NOAA Special Report

PROCEEDINGS AND RESULTS OF THE 2011 NTHMP MODEL BENCHMARKING WORKSHOP

National Tsunami Hazard Mitigation Program

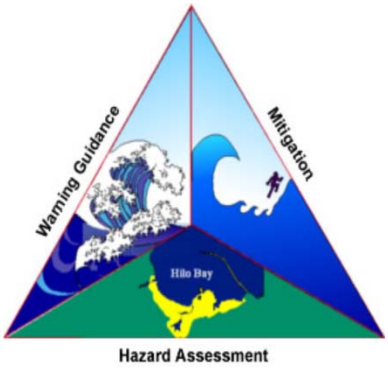

July 2012

U.S. DEPARTMENT OF COMMERCE

National Oceanic and Atmospheric Administration

Texas A&M University at Galveston

NOAA Special Report

PROCEEDINGS AND RESULTS OF THE 2011 NTHMP MODEL BENCHMARKING WORKSHOP

NTHMP Model Benchmarking Workshop Contributors:

Stéphane Abadie (University of Rhode Island)

Frank González (University of Washington)

Stephan Grilli (University of Rhode Island)

Juan Horrillo (Texas A&M at Galveston)

Bill Knight (West Coast & Alaska Tsunami Warning Center)

Dmitry Nicolsky (University of Alaska at Fairbanks)

Volker Roeber (University of Hawaii)

Fengyan Shi (University of Delaware)

Elena Tolkova (Joint Institute for the Study of the Atmosphere and Ocean, University of Washington/Pacific Marine Environmental Laboratory)

Yoshiki Yamazaki (University of Hawaii)

Joseph Zhang (Oregon Health & Science University)

Editor: **Loren Pahlke** (Cooperative Institute for Research in Environmental Sciences)

NTHMP Mapping and Modeling Co-Chairs:

Marie Eble (Pacific Marine Environmental Institute)

Bill Knight (West Coast & Alaska Tsunami Warning Center)

Rick Wilson (California Geological Survey)

July 2012

U.S. DEPARTMENT OF COMMERCE

National Oceanic and Atmospheric Administration

Texas A&M University at Galveston

NOTICE

Mention of a commercial company or product does not constitute an endorsement by NOAA/NTHMP. Use of information from this publication concerning proprietary products or the tests of such products for publicity or advertising purposes is not authorized.

This publication may be cited as:

[NTHMP] National Tsunami Hazard Mitigation Program. 2012. Proceedings and Results of the 2011 NTHMP Model Benchmarking Workshop. Boulder: U.S. Department of Commerce/ NOAA/NTHMP; (NOAA Special Report). 436 p.

A current PDF version of this document is maintained and available from the publications list at: http://nthmp.tsunami.gov

Contents

List of Tables

List of Figures

1 NTHMP Model Benchmarking Workshop

NTHMP Mapping and Modeling Subcommittee

1.1 Acknowledgements

The authors and participants in the National Tsunami Hazard Mitigation Program (NTHMP) Model Benchmarking Workshop wish to thank the NTHMP and the National Oceanic and Atmospheric Administration (NOAA) for providing the funding for the modeling activities associated with this work, and Texas A&M University at Galveston for hosting the workshop itself. In addition, we thank the collaborators and reviewers, especially those at the NOAA National Geophysical Data Center, who supported this work and provided invaluable discussion and review.

1.2 Executive summary

Model validation is essential to the production of accurate hazard mitigation and public safety products. Held March 31st to April 2nd, 2011 at Texas A&M University at Galveston under the auspices of the NTHMP Mapping and Modeling Subcommittee (MMS), the Model Benchmarking workshop participants were tasked with developing and implementing a strategy for the validation of tsunami inundation models. As stated in the NTHMP Strategic Plan, "All NTHMP-funded models will meet established standards by 2012." Accordingly, during this workshop, participants presented the results of applying their tsunami propagation models to a series of pre-established benchmark tests. The participants also began the process of clearly defining the validation procedure that all such models will be required to follow in order to obtain NTHMP funding for activities involving the development of public safety products such as inundation and evacuation maps. Specifically, participants, most representing nationally renowned tsunami modeling organizations, decided that a model will be deemed validated when it successfully simulates a series of tsunami benchmark tests covering all relevant tsunami processes targeted by a specific study. According to the analyses and model comparisons undertaken by the workshop participants, all the presented models tested as being capable of predicting propagation and runup of tsunami waves in most geophysical conditions.

The initial list of NTHMP benchmark tests, accessible at http://nctr.pmel.noaa.gov/benchmark, was established based on the OAR-PMEL-135 report (Synolakis et al., 2007). Because an additional important goal of the workshop was to revise the list of benchmark tests, participants proposed and discussed new benchmark tests, particularly in relation to landslide tsunamis and recent large co-seismic tsunami events.

The workshop results presented and described in these proceedings represent an important step in attaining consistency in tsunami inundation modeling and mapping among federal agencies, states, and communities.

1.3 Introduction

The coastal states and territories of the United States are vulnerable to devastating tsunamis similar to the 2004 Indian Ocean and 2011 Tohoku-oki events (Dunbar and Weaver, 2008). Over the past several decades, these states and territories have been developing tsunami inundation maps to form the basis of community evacuation plans. This map-making process drastically accelerated in 2005, following the catastrophic 2004 Indian Ocean tsunami, when the NTHMP received an increase of funding from the Tsunami Warning and Education Act for community-level tsunami preparedness activities, including inundation modeling and mapping. At the same time, the NTHMP was mandated by the National Science and Technology Council to implement a set of tsunami hazard mitigation recommendations. Because, at the time these recommendations were made, there were no commonly accepted tools for simulating potential tsunami inundation, the council recommended that NTHMP "develop standardized and coordinated tsunami hazard and risk assessment methodologies for all coastal regions of the U.S. and its territories." The standards were to be developed to ensure sufficient quality of the tsunami inundation maps and to ensure a basic level of consistency between efforts in terms of products. To this end, Synolakis et al. (2007) proposed a set of benchmark tests of tsunami computer models, aimed at ensuring that all models were vetted through a benchmarking process.

During the 2011 NTHMP Model Benchmarking Workshop, participants, as identified in Table 1-1, presented the hydrodynamic models currently in use by states and territories to produce inundation and evacuation products. The models ranged from a full application of the 3-D Navier-Stokes equations and Boussinesq approach to the depth-averaged non-linear shallow water equations (SWEs). Each model was put through a benchmarking process in which numerical model results were analyzed and compared with:

- The analytical solution for a specific benchmark test,
- The results of laboratory experiments,
- The observed field data for the July 1993 Okushiri Island event.

It should be noted that not all models were applied to all benchmark tests. Models were applied to only those tests corresponding to tsunami processes taken into account for developing inundation maps in the modelers' own geographic areas.

Results of systematic model testing exposed the limitations and clearly identified the attributes of each model. This led to collegial discussions, constructive criticisms, and proposed collaboration among participants to address outstanding issues. According to these analyses and comparisons, all the presented models were deemed capable of predicting the propagation and runup of tsunami waves in most of the geophysical conditions covered by the applicable benchmark tests. Brief descriptions of each model presented at the workshop and validated through the benchmarking process are given in the following section.

Table 1-1: NTHMP model benchmarking workshop participants. Participant affiliation and model of expertise are provided.

Name	Affiliation		Model
Stephane Abadie	University of Rhode Island (URI), East Coast		THETIS
Aggeliki Barberopoulou	University of Southern California (USC), CA		
Barry Eakins	National Geophysical Data Center (NGDC), NOAA		
Frank Gonzalez	University of Washington (UW), WA		GeoClaw
Stephan Grilli	URI, East Coast		FUNWAVE / THETIS
Roger Hansen	University of Alaska Fairbanks (UAF), AK		
Jeff Harris	URI, East Coast		
Juan Horrillo	Texas A&M at Galveston (TAMUG), Gulf of Mexico Coast	Conference sponsor & host	TSUNAMI3D
Victor Huerfano	Puerto Rico Seismic Network (PRSN), PR		
Bill Knight	West Coast & Alaska Tsunami Warning Center (WC/ATWC), NOAA	MMS co-chair	ATFM
Dmitry Nicolsky	UAF, AK		ALASKA GI-T / GI-L
Fengyan Shi	University of Delaware (UD), East Coast		FUNWAVE
Elena Tolkova	UW, Joint Institute for the Study of the Atmosphere and Oceans/Pacific Marine Environmental Laboratory, NOAA		MOST
Volker Roeber	University of Hawaii (UH), HI		BOSZ
Rick Wilson	California Geological Survey, CA	MMS co-chair	
Yoshiki Yamazaki	UH, HI		NEOWAVE
Joseph Zhang	Oregon Health & Science University (OHSU), OR		SELFE

1.4 NTHMP models

Over the past few decades, a variety of tsunami propagation models have been developed, based on a variety of governing equations, numerical methods, spatial and temporal discretization techniques, and wetting-drying algorithms used to predict tsunami runup.

Finite difference methods (FDM) were initially developed for solving linear shallow water wave equations (LSWEs), based on the work of Hansen (1956) and Fisher (1959). A detailed review of these methods can be found in Kowalik and Murty (1993a) and Imamura (1996). Based on these initial FDM approaches, the tsunami propagation model referred to as TUNAMI (Tohoku University's Numerical Analysis Model for Investigation; Imamura, 1995) was developed. In this work, the water level dynamics near the shoreline are computed by parameterizing a water flux quantity, the so-called ''discharge'' (Imamura, 1996), and nonlinear shallow water equations (NSWEs) are formulated in a flux-conservative form, which helps preserve water mass throughout the computations. A similar numerical model, also extensively used for tsunami modeling, is COMCOT (COrnell Multigrid COupled Tsunami; Liu et al., 1998), where a moving boundary algorithm is used to find the shoreline location. During the same period, Titov and Synolakis (1995) presented the VTCS model, now known as MOST (Method Of Splitting Tsunami), which can compute runup without adding an artificial viscosity or friction factor. An innovative idea of the MOST model is its ability to track the shoreline by adding new temporal grid points.

While the earlier models were hydrostatic and hence non-dispersive, more recently, long wave models have been developed on the basis of Boussinesq equations and applied to simulating tsunami propagation. While these equations were initially both weakly nonlinear and dispersive (Peregrine, 1967), fully nonlinear approximations with extended dispersion properties were developed (e.g., Wei et al., 1995; Kirby et al., 1998; Lynett et al., 2002). In shallow water, these fully nonlinear Boussinesq models (FNBMs) extend NSWEs to include non-hydrostatic dispersive effects. FNBMs have led to operational tsunami models (e.g., FUNWAVE), which were applied to simulating some of the recent significant tsunami events (e.g., Watts et al., 2003; Ioualalen et al., 2007; Tappin et al., 2008). An alternative governing equation describing a dispersive wave through non-hydrostatic pressure has been proposed by Stelling and Zijlema (2003). The models based on their formulations provide a slightly better dispersive property than Peregrine's (1967) depth-integrated model, and are comparative to FNBMs using a multiple-layer model. In total, more than ten tsunami simulation models were proposed over the past two decades or so, including, in addition to the earlier references, Mader and Lukas (1984), Kowalik and Murty (1993b), George and LeVeque (2006), and Zhang and Baptista (2008).

The next section briefly describes each of the numerical models presented and discussed during the 2011 NTHMP Model Benchmarking Workshop. Summaries of the main characteristics and capabilities of each model are given in Table 1-2 and Table 1-3, followed by a short write-up of each of the ten models run through the testing process.

Table 1-2: Summary of model characteristics (ALASKA, ATFM, BOSZ, FUNWAVE, GeoClaw)

Model Features	ALASKA	ATFM	BOSZ	FUNWAVE	GeoClaw
Approximation	Shallow Water	Shallow Water	Boussinesq	Boussinesq	Shallow Water
Wave dispersion	No	Yes (Optional)	Yes	Yes	No
Grid nesting	Two-way	Two-way (submeshes)	No	One-Way	Two-way AMR
Coordinate system	Cartesian/ Spherical	Cartesian/ Spherical	Cartesian	Cartesian/ Spherical	Cartesian/ Spherical
Numerical scheme	Finite difference	Finite difference	Finite volume	Hybrid finite vol./finite difference	Finite volume
Tsunami source	Co-seismic + Landslide	Co-seismic	Co-seismic	Co-seismic+ Landslide (Initiate THETIS)	Co-seismic+ Landslide
Runup approach	Moving boundary	Volume of Fluid	Shock-capturing/ Riemann solution	Slot technique	Shock-capturing/ Riemann solution
Parallelization	MPI	Co-array FORTRAN	OpenMP	MPI	OpenMP
Documentation	Limited	Limited	Limited	Yes	Yes
Execution	Graphics interface	Command line	Command line/ Graphics interface	Command line	Command line

Table 1-3: Summary of model characteristics (MOST, NEOWAVE, SELFE, THETIS, TSUNAMI3D)

Model Features	MOST	NEOWAVE	SELFE	THETIS	TSUNAMI3D
Approximation	Shallow Water	Hydro./ Nonhydro.	Hydro./ Nonhydro.	3-D Navier-Stokes	3-D Navier-Stokes
Wave dispersion	Yes (Numerical)	Yes	Yes (Optional)	Yes	Yes (Optional)
Grid nesting	One-way	Two-way	Two-way Unstructured mesh	Structured. Variable mesh	Structured. Variable mesh
Coordinate system	Cartesian/ Spherical	Cartesian/ Spherical	Cartesian/ Spherical	Cartesian/ Cylindrical	Cartesian
Numerical scheme	Finite difference	Finite difference	Finite element/ Finite volume	Finite volume	Finite volume
Tsunami source	Co-seismic	Co-seismic+ Landslide (Initiate TSUNAMI3D)	Co-seismic	Landslide (Coupled to FUNWAVE)	Landslide (Coupled to NEOWAVE)
Runup approach	Horizontal projection	Horizontal projection	Iterative projection	Volume of Fluid	Volume of Fluid
Parallelization	OpenMP	No	MPI	MPI	OpenMP/MPI
Documentation	Limited	Yes	Yes	Yes	Limited
Execution	Graphics interface	Command line	Command line	Command line	Command line

1.4.1 Alaska Geophysical Institute Parallel Robust Inundation Modeling Environment-Tectonic (GI'-T)

The ALASKA GI'-T is a numerical code that simulates the propagation and runup of co-seismic tsunami waves in the framework of NSWE theory. The numerical code adopts a staggered leapfrog FDM scheme to solve the shallow water equations formulated for depth-averaged water fluxes in spherical coordinates on Arakawa C-grid (Arakawa and Lamb, 1977). The spatial derivatives are discretized by central difference and upwind difference schemes (Fletcher, 1991). The friction term is discretized by a semi-implicit scheme according to Goto et al. (1997). A temporal position of the shoreline is calculated using a free-surface moving boundary algorithm, validated by Nicolsky et al. (2010). The FDM scheme is coded in FORTRAN using the Portable, Extensible Toolkit for Scientific computations (Balay et al., 2004) and the MPI standard. For large scale problems, the developed algorithm employs two-way nested grids.

The model can be accessed through a wizard-style internet-based interface that guides users through setup, execution, and retrieval of tsunami modeling results. The interface is based on Google Maps API, which simplifies interactions with the geospatial database of hypothetical, historical sources and elevation datasets needed to simulate propagation and runup of the tsunami.

For submarine landslide modeling the University of Alaska Fairbanks has developed the ALASKA GI'-L (Geophysical Institute Parallel Robust Inundation Modeling Environment – Landslide) code. The ALASKA GI'-L is a numerical code that simulates propagation and runup of landslide-generated tsunami waves in the framework of the long-wave approximation to water dynamics. The slide is an incompressible, isotropic 3-D viscous flow, propagating over realistic bathymetry. It is assumed that the horizontal velocities of the slide have a parabolic vertical profile. Equations for slide and water waves are two-way coupled. This coupling was initially proposed by Jiang and LeBlond (1992), and later improved by Fine et al. (1998). The numerical code adopts a staggered leapfrog finite difference scheme to solve the governing equations formulated for slide velocities and depth-averaged water fluxes in Cartesian coordinates. A temporal position of the shoreline is calculated using the same algorithm as in the GI'-T model. The finite difference scheme is coded in FORTRAN and can be implicitly parallelized.

This model was successfully applied to simulate a tsunami event in fjords near Seward, Whittier, and Skagway harbors, where tsunami waves were generated by submarine landslides in 1964 and 1994 (Fine et al., 1998; Thomson et al., 2001; Suleimani et al., 2009; Nicolsky et al., 2010).

1.4.2 The Alaska Tsunami Forecast Model (ATFM)

The Alaska Tsunami Forecast Model (ATFM) began as a collaborative effort between two researchers (Zygmunt Kowalik and Paul Whitmore) and became operational at the West Coast Alaska Tsunami Warning Center (WCATWC) in 1997 (Kowalik and Whitmore, 1991; Whitmore and Sokolowski, 1996). This is known as the "classic" model currently used in WCATWC operations. From 2004 until the present time, the model has been substantially reworked into a second forecasting model which is called ATFMv2. The benchmark challenge problems were computed with this newer model.

The ATFM solves the NSWEs. Two equations of motion and one continuity equation are formulated in spherical coordinates and solved on structured, nested meshes. The two horizontal components of velocity (u and v) are depth-averaged. The vertical component of velocity is not considered in this hydrostatic formulation. The solution technique for u and v is based on a differencing method described in Kowalik and Murty (1993a), and the sea level is computed with a second-order accurate, upwind scheme that conserves mass to machine accuracy (van Leer, 1977). The run-up / run-down method is based on the VOF approach pioneered by Nichols and Hirt (1980), and Hirt and Nichols (1981). There is no explicit dispersion in the model, although a non-hydrostatic addition is in the testing phase and was used for benchmarks BP4 and BP6 (Walters, 2005; Yamazaki et al., 2009). Submeshes are nested within parent meshes to increase spatial resolution where needed. Information is passed both from low to high-resolution meshes and back, based on a mass conserving interconnecting scheme (Berger and Leveque, 1998). Discretization for the three field variables uses the staggered "C grid" layout.

The model is coded in FORTRAN 90 and in Co-array FORTRAN. It has been run on PCs, a Cray X1, and a Penguin Computing cluster comprised of Opteron processors.

1.4.3 Boussinesq Model for Ocean and Surf Zones (BOSZ)

BOSZ is a numerical model for propagation, transformation, breaking, and runup of water waves. BOSZ was specifically designed for nearshore wave processes in the presence of fringing reefs in tropical and sub-tropical regions around the world. BOSZ was developed with the goal to obtain reliable and robust results in addressing the complementary but somewhat opposing

physical processes of flux and dispersion throughout a single numerical model. BOSZ was intentionally kept as simple as possible and yet containing the main features to accurately describe nearshore wave processes. BOSZ combines the weakly dispersive properties of a Boussinesq-type model with the shock capturing capabilities of the conservative form of the NSWEs. BOSZ allows the simulation of dispersive waves up to medium order as well as supercritical flows with discontinuities. The depth-integrated governing equations are derived from Nwogu (1993), an extended (with respect to linear dispersion) Boussinesq approach with conserved variables that satisfy conservation of mass and momentum for $Fr > 1$. The continuity and momentum equations contain the conservative form of the nonlinear shallow-water equations to capture shock-related hydraulic processes.

The governing equations are solved with a conservative finite volume Godunov-type scheme. The finite volume method benefits from a fifth-order Total Variation Diminishing (TVD) reconstruction procedure that evaluates the inter-cell variables. The exact Riemann solver of Wu and Cheung (2009) supplies the inter-cell flux and bathymetry source terms. The well-balanced scheme of Liang and Marche (2009) eliminates depth interpolation errors in the domain and preserves continuity at moving boundaries over irregular topography. The moving waterline is part of the Riemann solution and does not require additional treatments. A fourth-order explicit Adam-Bashforth-Moulton scheme integrates the governing equations in time and evaluates the conserved variables.

BOSZ is primarily used for modeling surf-zone and swash processes of swell and wind waves. The model can be applied to near-field tsunami scenarios. However, to date BOSZ is not based on spherical coordinates nor does it support nested grids. The code is written in MATLAB with most of its processing in embedded pre-compiled C++ MEX subroutines. This combines fast computations with a user-friendly code development interface for debugging, modifying, and demonstration. The current version of BOSZ runs on a serial processor.

1.4.4 FUNWAVE-TVD model

The FUNWAVE tsunami propagation and runup model is based on fully nonlinear and dispersive Boussinesq equations, retaining information to leading order in frequency dispersion $O[(kh)^2]$ and to all orders in nonlinearity (Wei and Kirby, 1995; Wei et al., 1995). Instead of tracking the moving boundary during wave run-up/run-down on the beach or coastlines, FUNWAVE treats the entire computational domain as an active fluid domain by employing an improved version of the slot or permeable-seabed technique, i.e., the moving shoreline algorithm proposed by Chen et al. (2000) and Kennedy et al. (2000) for the runup simulation. The basic idea behind this technique is to replace the solid bottom where there is little or no water covering the land with a porous seabed or to assume that the solid bottom contains narrow slots. This is incorporated in terms of mass flux and free surface elevation in order to conserve mass in the presence of slots. The model includes bottom friction, energy dissipation to account for the wave breaking and a subgrid turbulence scheme too. The bottom friction is modeled by the use of the quadratic law with bottom friction coefficient. The subgrid turbulence is modeled in terms of Smagorinsky-subgrid turbulent mixing type to account for the effect of the underlying current field. The energy dissipation due to wave breaking in shallow water is treated by the use of momentum mixing terms. The associated eddy viscosity is essentially proportional to the gradient of the horizontal velocity, which is strongly localized on the front face of the breaking wave.

FUNWAVE-TVD is an extension of FUNWAVE, formulated in both Cartesian coordinates (Shi et al., 2012) and in spherical coordinates with Coriolis effects (Kirby et al., 2009; 2012) for application to ocean basin scale problems. This new model uses a hybrid finite-volume and FDM-MUSCL-TVD scheme. As in FUNWAVE, improved linear dispersive properties are achieved, up to the deep water limit, by expressing the BM equations in terms of the horizontal velocity vector at 0.531 times the local depth, as in Nwogu (1993). Additionally, wave breaking is more accurately modeled by switching from the Boussinesq equations to the NSWE, when the local height to depth ratio exceeds 0.8. FUNWAVE-TVD's latest implementation is fully parallelized using MPI-FORTRAN, for efficient use on distributed memory clusters. One-way grid nesting was implemented to allow for grid refinement near tsunami sources and near the coast. This latest version was used for running the tsunami benchmarks.

FUNWAVE-TVD has been used to model landslide or co-seismic tsunamis. A pre-processor allows the user to specify the initial tsunami source condition in terms of a hot start, either from the underwater landslide (slides or slumps) solution of Grilli et al. (2002), Grilli and Watts (2005) and Watts et al. (2005), or for co-seismic tsunamis based on the standard Okada (1985) solution. More recently, both landslide and co-seismic tsunamis have also been dynamically generated (as a space and time-varying bottom boundary condition), using the non-hydrostatic, sigma coordinate model NHWAVE (Ma et al., 2012), whose solution is then interpolated into FUNWAVE's Cartesian or spherical grid.

1.4.5 GeoClaw model

The GeoClaw model is based on the NSWEs and uses a finite volume method on adaptively refined rectangular grids (Cartesian or lat-long). The method exactly conserves mass (except near the shoreline when refining or de-refining grids) and conserves momentum over a flat bottom. This method is based on Godunov's method: at each cell interface a one-dimensional Riemann problem is solved normal to the edge, which reduces to a one-dimensional shallow water model with piecewise constant initial data, with left and right values given by the cell averages on each side. The jump in bathymetry between the cells is incorporated into the Riemann solution in a manner that makes the method "well balanced": the steady state of the ocean at rest is exactly maintained. The shoreline is handled by allowing dry cells to have depth 0 and to dynamically change between wet and dry. The method is second order accurate in smooth regions but nonlinear limiters are used to create "shock-capturing" methods (LeVeque, 2002) that maintain sharp non-oscillatory solutions and non-negative depth even in the nonlinear regime. The method is stable to Courant number 1 and very robust. The Manning friction term is incorporated using a fractional step method.

Adaptive mesh refinement to several nested levels is allowed, with arbitrary refinement ratios at each level. Refinement is done by flagging cells for refinement (based on wave height and specification of the areas of interest). The flagged cells at each level are clustered into rectangular patches for refinement to the next level, as described in detail in Berger and LeVeque (1998). The high-resolution methods and adaptive refinement algorithms have been extensively tested in the Clawpack software that has been in development since 1994. GeoClaw includes special techniques to deal with bathymetry data, well-balancing, and wetting/drying, and is an outgrowth of the TsunamiClaw software developed in George (2006). The algorithms and software are described in more detail in Berger et al. (2011) and LeVeque et al. (2011).

For modeling earthquake-generated tsunamis, the co-seismic seafloor motion is modeled by adjusting the bathymetry dynamically each time step. An Okada (1985) model can be used to translate fault models to seafloor motion. For modeling landslide-generated tsunamis, the seafloor motion is modeled by adjusting the bathymetry dynamically each time step. The landslide motion is generally computed first, and GeoClaw has been used with a Savage-Hutter model to simulate the motion of the landslide itself, in current work by Ph.D. student Jihwan Kim. This has been compared with two-layer fully coupled models and found adequate for landslides in sufficiently deep water.

The main code is written in Fortran, with a Python user interface and plotting modules. All of the code is open source, hosted at https://github.com/organizations/clawpack. Additional documentation is available at http://www.clawpack.org/geoclaw.

1.4.6 Method Of Splitting Tsunamis (MOST)

The MOST model simulates propagation and runup of gravity waves according to depth-integrated NSWEs. The algorithm is based on the method of fractional steps which reduces the 2-D problem to a 1-D problem in each direction. To progress the solution through a time step, two 1-D problems are solved sequentially. Each 1-D problem is formulated in terms of Riemann invariants. MOST's computational algorithm uses a forward difference scheme in time and centered differences for spatial derivatives (Titov and Synolakis, 1998; Burwell et al., 2007). Friction is represented by a Manning term. The model operates on structured grids given in Cartesian or spherical coordinates. The algorithm is coded in Fortran 95 and parallelized using OpenMP.

MOST's inundation algorithm is a 1-D algorithm that uses horizontal projection of the water level in the last wet node onto the beach to move the instantaneous shoreline position (Titov and Synolakis, 1995). The simulation can be initiated given initial seafloor deformation or by providing lateral boundary conditions. The latter facilitates grid nesting with one-way coupling.

The operational version of the MOST model determines source parameters for the tsunami wave itself by incorporating observations into forecast methodology. Just as hurricane forecasts rely on observations (radar, aircraft, satellite, ocean systems) to forecast the path of a hurricane following generation, the operational forecast relies on deep-ocean bottom pressure observations of the tsunami waves after generation. The specific operational procedure is hard-coded for a three-nested-grid configuration forced through the boundary of the outer grid. The boundary input is supplied by the database of an ocean-wide 24-hour-long simulation of tsunami wave propagation, for numerous tsunamis generated by hypothetical M_w 7.5 earthquakes covering worldwide subduction zones (Gica et al., 2008). These data sets are linearly combined to imitate an arbitrary tsunami scenario in the deep ocean. Access to the operational version is offered via internet-enabled interface (ComMIT), which allows for the selection of model input data, use of shared databases, display of model output through a graphical user interface (GUI), and sharing simulation results.

1.4.7 Non-hydrostatic Evolution of Ocean WAVEs (NEOWAVE)

The Non-hydrostatic Evolution of Ocean WAVEs (NEOWAVE) model is a shock-capturing, dispersive model in a spherical coordinate system for basin-wide evolution and coastal runup of tsunamis using two-way nested computational grids (Yamazaki et al., 2011). This depth-integrated model describes dispersive waves through the non-hydrostatic pressure and vertical velocity (Stelling and Zijlema, 2003, and Yamazaki et al., 2009). The vertical velocity

term also facilitates modeling of tsunami generation from seafloor deformation to account for the time-sequence of the earthquake rupture process (Yamazaki et al., 2011). The semi-implicit, staggered finite difference model captures flow discontinuities associated with bores or hydraulic jumps through the momentum conserved advection (MCA) scheme, which embeds the upwind flux approximation of Mader (1988) in the shock-capturing scheme of Stelling and Duinmeijer (2003).

NEOWAVE builds on the nonlinear shallow-water model of Kowalik et al. (2005) with the non-hydrostatic terms and the momentum-conserved advection scheme (Yamazaki et al., 2009). The grid refinement scheme is implemented in the model to capture tsunami physics in adequate grid resolution. To ensure propagation of dispersive waves and discontinuities across computational grids of different resolution, a two-way grid-nesting scheme utilizes the Dirichlet condition of the non-hydrostatic pressure and both the horizontal velocity and surface elevation at the inter-grid boundary (Yamazaki et al., 2011). The present model tracks the wet/dry interface using the approach based on Kowalik and Murty (1993a) to compute the runup and inundation. The wet/dry interface is predicted by horizontal projection of sea level at the adjacent wet cell, and obtained through integration of the momentum and continuity equations (Yamazaki et al., 2009).

1.4.8 Semi-implicit Eulerian-Lagrangian Finite Elements (SELFE)

The tsunami propagation and inundation model SELFE (Zhang and Baptista, 2008a) was envisioned at its inception to be an open source, community supported, 3-D hydrodynamic/ hydraulic model. Originally developed to address the challenging 3-D baroclinic circulation in the Columba River estuary, the SELFE model has since been adopted by 100+ groups (most recent web count) around the world. It has evolved into a comprehensive modeling system encompassing such physical/biology processes as general circulation, tsunami and hurricane storm surge inundation, ecology and water quality, sediment transport, wave–current interaction and oil spill. A central web site dedicated to this model, http://www.stccmop.org/CORIE/modeling/selfe/, is maintained, along with a user mailing list and mail archive system, and an annual user group meeting has been organized since 2004, along with online training courses which are occasionally conducted for users.

SELFE combines numerical accuracy with efficiency and robustness. It is based on the 3-D NSWEs. The time stepping in SELFE is done semi-implicitly for the momentum and continuity equations, and together with the Eulerian-Lagrangian method for the treatment of the advection, the stringent CFL stability condition is bypassed. The use of unstructured grids in the horizontal dimension further enhances the model efficiency and flexibility due to their superior capability in fitting complex coastal boundary and resolving bathymetric and topographic features as well coastal structures. The model can be configured in multiple ways (e.g., hydrostatic or non-hydrostatic options, etc.), but in tsunami applications the 2-D depth-averaged hydrostatic configuration is typically applied for maximum efficiency. Since 2007, all components of the SELFE modeling system have been fully parallelized using domain decomposition and Message passing Protocol (MPI). The inundation algorithm in SELFE uses a simple iterative procedure to capture the moving shoreline (Zhang and Baptista, 2008b).

The model has been successfully applied in the recent simulation of the impact of the 1964 Alaska event on the US west coast (Zhang et al., 2011), and in the study of paleo-tsunamis near an Oregon town (Priest et al., 2010; Witter et al., 2011).

1.4.9 THETIS

THETIS is a multi-fluid Navier-Stokes (NS) solver developed by the TREFLE CNRS laboratory at the University of Bordeaux I. It is a multipurpose CFD code, freely available to researchers (http://thetis.enscbp.fr) and fully parallelized. For tsunami modeling, THETIS has been applied to tsunami generated by subaerial landslides (Abadie et al., 2010). In this case, the model solves the incompressible NS equations for water, air and the slide. Basically, at any time, the computational domain is considered as being filled by one "equivalent" fluid, whose physical properties (namely density and viscosity) vary with space. Subgrid turbulent dissipation is modeled based on a Large Eddy Simulation approach, using a mixed scale subgrid model (Lubin et al., 2006). The governing equations (i.e., conservation of mass and momentum) are discretized on a fixed mesh, which may be Cartesian, cylindrical or curvilinear, using the finite volume method. These governing equations are exact, except for interfacial meshes, where momentum fluxes are only approximated, due to the presence of several fluids. NS equations are solved using a two-step projection method. Fluid-fluid interfaces are tracked using the VOF method. For most flows, the PLIC algorithm (e.g., Abadie et al., 1998) allows ensuring an accurate tracking while keeping the interface discontinuous. However, for very violent flows with fast droplet ejection, the PLIC method may cause divergence of the projection algorithm. In such cases, the interface is smoothed either by allowing a slight diffusion process, after each PLIC iteration, or by using a TVD scheme solving Eulerian advection equations for the interfaces.

THETIS has been extensively validated for many theoretical and experimental flow cases. Hence, each new version of THETIS has to successfully solve more than 50 validation cases within a certain expected accuracy, before being released.

1.4.10 Tsunami Solution Using Navier-Stokes Algorithm with Multiple Interfaces (TSUNAMI3D)

The TSUNAMI3D model was developed by the University of Alaska Fairbanks (Horrillo, 2006) and Texas A&M University at Galveston (TAMUG). The TSUNAMI3D code solves transient fluid flows with free surface boundaries, based on the concept of the fractional VOF. The code uses an Eulerian mesh of rectangular cells having variable sizes. The fluid equations solved are the FDM approximation of the Navier-Stokes and the continuity equations. The basic mode of operation is for single fluid calculation having multiple free surfaces. However, TSUNAMI3D can also be used for calculations involving two fluids separated by a sharp or non-sharp (diffusive) interface, for instance, water and mud. In either case, the fluids may be treated as incompressible. Internal obstacles or topography are defined by blocking out fully or partially any desired combination of cells in the mesh.

The code is based on the developments originated in Los Alamos National Laboratory (LANL) during the 1970s, Hirt and Nichols (1981). In particular, the VOF algorithm for tracking the movement of a free surface interface between two fluids or fluid-void has been simplified specifically for the 3-D mode of operation, to account for the horizontal distortion of the computational cells with respect to the vertical scale that is proper in the construction of efficient 3-D grids for tsunami calculations. In addition, the pressure term has been split into two components, hydrostatic and non-hydrostatic. The splitting of the pressure term facilitates the hydrostatic solution by merely switching off the non-hydrostatic pressure term. Therefore, TSUNAMI3D can be used to separate non-hydrostatic effects from the full solution while keeping the 3-D structure. The TSUNAMI3D model is suitable for complex tsunami generation

because it has the capability to consider moving or deformable objects, subaerial/subsea landslide sources, soil rheology, and complex vertical or lateral bottom deformation.

1.5 Benchmark tests

As per NTHMP rules, it is mandatory that all numerical models used in inundation mapping be validated and verified by 2012. Although not required, the same should apply to models used in tsunami warning or emergency planning. This is best done by subjecting each model to a series of benchmark tests commonly accepted by the community. The three usual categories of reference data used for defining benchmark tests for tsunami numerical model validation and verification are: (i) analytical solutions; (ii) laboratory experiments; and (iii) field measurements. Various benchmark tests defined in these categories test some features, but not all, of the tsunami models. For instance, some benchmark tests are focused on validating and verifying model simulations of co-seismic tsunamis sources, while others are developed for landslide sources. Similarly, some analytic solutions solve NSWEs, which do not feature dispersion and hence do not include the more complete physics included in Boussinesq, non-hydrostatic, or NS models.

The validation of numerical models is a continuous process. Even proven numerical models must be subjected to additional testing as new knowledge/methods or better data are obtained. New benchmark tests must also be defined to address new tsunami source characteristics or complex coastal impact. Therefore all existing NTHMP numerical models, according to their capability, have to be tested regularly against a selected set of benchmark tests, for validation and verification. The official suite of benchmark tests was originally assembled based on the recommendations of Synolakis et al. (2007). This official set of benchmark tests has its origin in past tsunami model validation workshops that were organized to verify the performance of tsunami models according to the state of knowledge and new data obtained from recent tsunamis at the time, see Table 1-4. These were the 1995 Long-Wave Run-up Models Workshop held in Friday Harbor, Washington and the 2004 Workshop held in Catalina Island, California. A short description of each of the benchmark tests with their main intent can be found in Synolakis et al. (2007), and the complete suite of benchmark tests and related data are available at http://nctr.pmel.noaa.gov/benchmark/ and at the University of Washington (UW) Wiki, http://depts.washington.edu/clawpack/links/noaa-tsunami-benchmarks/.

Table 1-4: Current benchmark tests for model verification and validation

Benchmark Test	Category	Description
BP1*	Analytical Solution	Single Wave on a Simple Beach
BP2		Solitary Wave on a Composite Beach
BP3		Sub-aerial Landslide on Simple Beach (2-D Landslide)
BP4*	Laboratory Experiment	Solitary Wave on a Simple Beach
BP5		Solitary Wave on a Composite Beach
BP6*		Solitary Wave on a Conical Island
BP7		Tsunami Runup onto a Complex Three-Dimensional Beach. Monai Valley
BP8		Tsunami Generation and Runup Due to Three-Dimensional Landslide
BP9*	Field Measurements	Okushiri Island Tsunami
BP10		Rat Island Tsunami

* Benchmark test used for NTHMP's model comparison

During the detailed analysis of modeling results during the 2011 NTHMP workshop, it became apparent that some of the analytical benchmarks were formulated under certain conditions (i.e., to solve certain classes of equations such as NSWE) that prohibit the direct use of the derived analytical solution for accurate benchmarking of some tsunami models. For example:

- BP3 proposes to test the generation and propagation of the sub-aerial landslide-generated tsunami against an analytical solution that is obtained using overly simplified governing equations [i.e., linear shallow water (LSW) that do not feature dispersion]. In addition, the sliding mass in this problem is not conservative (the mass changes with time). During the workshop closing session, it was suggested that this benchmark be replaced in the future by a benchmark test that is similar in nature but presenting more realistic physics.
- BP5 (Solitary Wave in a Composite Beach) earned a similar recommendation from the workshop participants. This benchmark tests numerical models in extreme conditions that are not typical for geophysical tsunamis and can produce incongruent numerical results, e.g., the so-called "splash-type" runup at the vertical wall.
- BP8 (Tsunami Generation and Runup Due to Three-Dimensional Landslide) can only be realistically solved using a full 3-D Navier-Stokes model, which is not one of the preferred approximations used in most tsunami numerical models (e.g., NSWEs or Boussinesq). Models using NSWE approximation show numerical instabilities in this case that are due to a shock formation at the edge of the triangular wedge of sliding material. It is still unknown whether a Boussinesq approximation would help eliminate the shock formation and produce a good agreement with laboratory measurements. Therefore, it was suggested that this benchmark be replaced by one that can be applied to

a broader spectrum of numerical models or approximations, by changing the geometry of the sliding material.

Although each presented model was tested against nearly every benchmark test listed in Synolakis et al. (2007), for the sake of brevity, only a few benchmark tests have been selected for doing both the NTHMP model verification and a cross-model comparison. These are the benchmark tests which are the most applicable to testing geophysical tsunamis in realistic conditions: BP1, BP4, BP6 and BP9 (see Table 1-4). Following is a brief description of each of these tests.

1.5.1 BP1 analytical: Solitary wave on a simple beach

In this test, the bathymetry consists of a channel of constant depth $\bar{d}$, connected to a plane sloping beach of angle $\beta = \cot^{-1}(19.85) = 2.88^{o}$. A sketch (with distorted scale) of the canonical beach is displayed in Figure 1-1. The x coordinate increases monotonically seaward, $x = 0$ is the initial shore location, and the toe of the beach is located at $x = X_0 = \bar{d}\cot(\beta)$. The wave of height $\bar{H}$ is initially centered at $x = X_s$ at $t = 0$. This benchmark test is focused on modeling the runup of an incident non-breaking solitary wave such that $H = \bar{H} / \bar{d} = 0.0185$. H is the dimensionless wave height. The initial wave profile is given by,

$$\eta(x,0) = H\mathrm{sech}^2\left(\gamma\left(x - X_s\right)\right)$$

Where $\gamma = \sqrt{3H/4}$. The initial wave-particle velocity in the numerical experiments is set, following Titov and Synolakis (1995) as:

$$u(x,0) = -\sqrt{\bar{g}/\bar{d}}\ \eta(x,0)$$

The recommended procedure is to set a non-reflective boundary condition at the left side of the computational domain and then check that the computed non-dimensional variables such as $n/\bar{d}$, $u/\sqrt{\bar{g}\bar{d}}$ do not depend on the value of $\bar{d}$.

To perform this benchmark, it is necessary to compare numerically and analytically computed water level profiles at certain times, and then to compare the numerically and analytically computed water level dynamics at two locations along the beach during propagation and reflection of the wave. The analytical solution is derived based on NSWEs. All other requirements to satisfy BP1 can be found at https://github.com/rjleveque/nthmp-benchmark-problems.

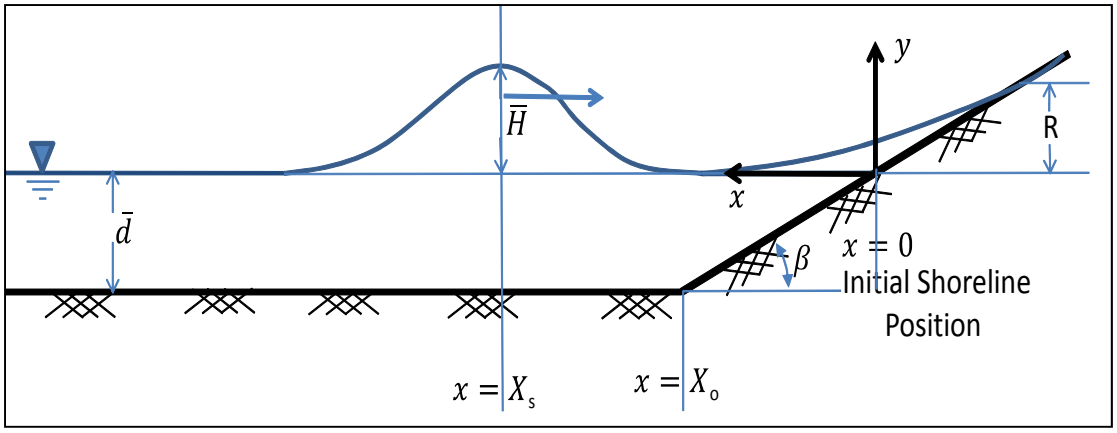

Figure 1-1: Definition Sketch for Canonical Bathymetry, i.e., Sloping Beach Connected to a Constant-depth Region.

1.5.2 BP4 laboratory experiment: Solitary wave on a simple beach

This benchmark is the laboratory experiment counterpart of BP1 and requires comparison of the model solution to laboratory measurements collected during experiments in a 32-meter long wave tank at the California Institute of Technology. The geometry of the tank and laboratory equipment used to generate long-waves is described by Hammack (1972), Goring (1978) and Synolakis (1986).

More than 40 experiments with solitary waves of varying heights were performed (Synolakis, 1986). The height-to-depth ratio $H = \overline{H} / \overline{d}$ in these experiments ranged from 0.021 to 0.626. The water level profiles at several times were measured for waves with $H = 0.0185$, $H = 0.045$, and $H = 0.3$. According to observations, the solitary wave breaking occurs when $H > 0.045$. The wave with $H = 0.0185$ did not break in the laboratory experiments, simulating a realistic tsunami, and hence this case is used to compare numerical results to laboratory data in this study. The initial and boundary conditions for this benchmark test are exactly the same as in the case of BP1. The choice for $\overline{d}$ is somewhat arbitrary, but the depth used in the laboratory experiments was approximately 0.3 m.

To perform this BP, it is first necessary to compare numerically computed water surface profiles to the laboratory data in the case of $H = 0.0185$ at certain given times. In addition, it is required to compare numerical model results and laboratory data in the case of $H = 0.3$ which corresponds to a breaking wave. All others requirements to satisfy BP4 can be found at https://github.com/rjleveque/nthmp-benchmark-problems.

1.5.3 BP6 laboratory experiment: Solitary wave on a conical island

To validate tsunami propagation models for a 3-D case, Synolakis et al. (2007) proposed the use of a laboratory experiment developed to study the inundation of Babi Island by the December 12, 1992 tsunami (Yeh et al., 1994). The tsunami attacked this conically shaped island from the north, but an extremely high inundation was observed in the south. A model of the conical island was constructed in a wave tank at the US Army Engineer Waterways Experimental Station (Briggs et al., 1995).

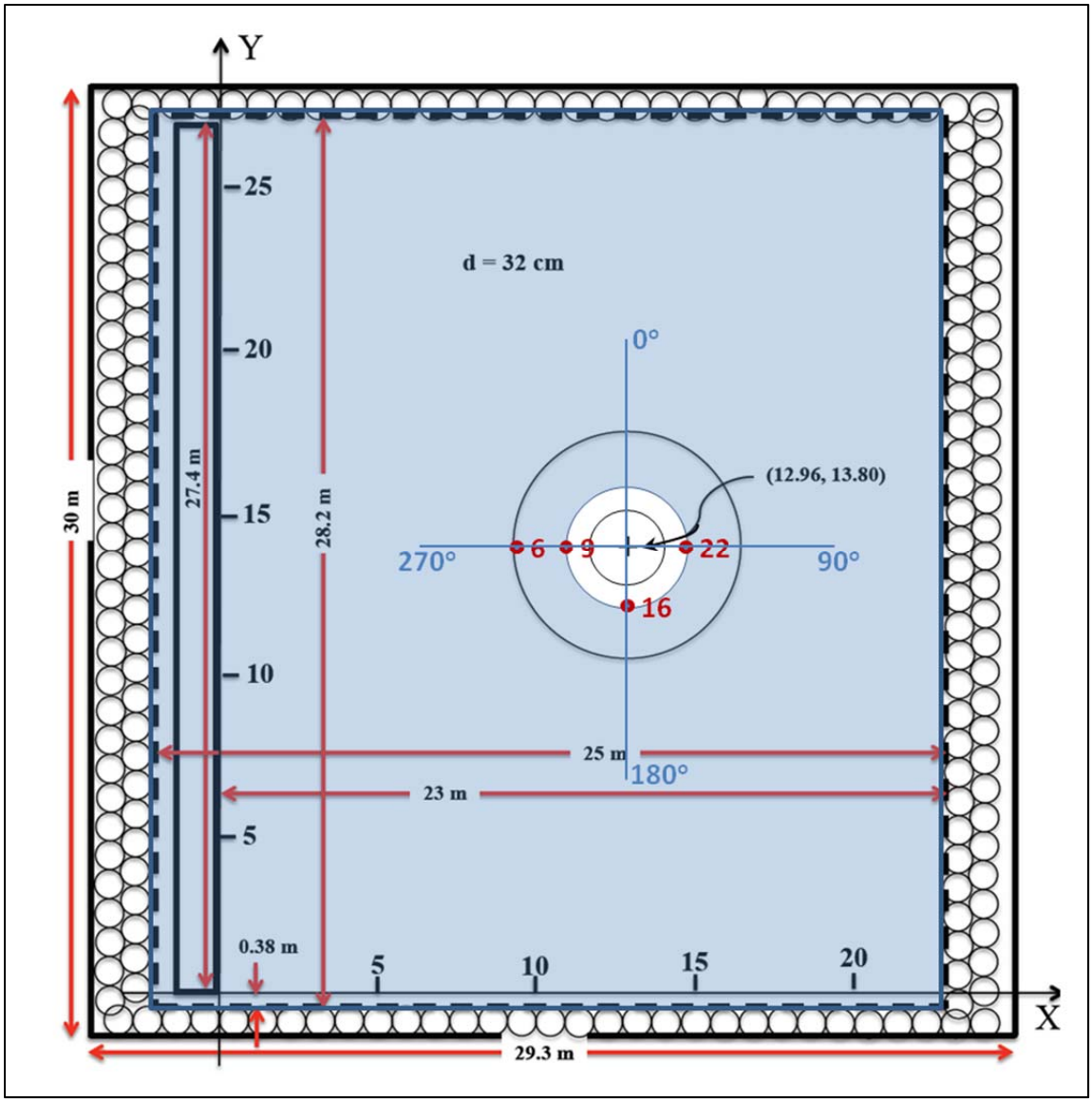

Figure 1-2: Basin Geometry, coordinate system and location of gauges. Solid lines represent approximate basin and wavemaker surfaces. Circles along walls and dashed lines represent wave absorbing material. Note the gaps of approximately 0.38 m between each end of the wavemaker and the adjacent wall. (Figure courtesy of Frank Gonzalez.)

Figure 1-2 was developed based on personal communications with Mike Briggs. The basin wall dimensions were 29.3 x 30 m. An absorbing material was installed to define a smaller, 25 x 28.2 m wave basin. The absorbing material used was synthetic horsehair about 2 inches thick, rolled into cylinders approximately 0.9 m in diameter, and characterized by a reflection coefficient that varied somewhat with wave frequency, but was of the order of 12%. The length of the wavemaker was 27.4 m. A few differences between Figure 1-2 and previously published figures of the wave basin stem primarily from the fact that (a) the wavemaker face extended about 2 m into the wave basin and (b) a gap of approximately 0.38 m was present between each end of the wavemaker and the bottom and top walls.

The island had the shape of a truncated, right circular cone with diameters of 7.2 m at the toe and 2.2 m at the crest. The vertical height of the island was approximately 0.625 m, with 1V on 4H beach face (i.e., $\beta = 14°$). The water depth was set at 0.32 m in the basin. The interested reader is referred to

http://chl.erdc.usace.army.mil/chl.aspx?p=s&a=Projects;35 or
http://nctr.pmel.noaa.gov/benchmark/Laboratory/Laboratory_ConicalIsland/index.html

for detailed descriptions of laboratory experiments and data files. All requirements to satisfy this benchmark test can be found at https://github.com/rjleveque/nthmp-benchmark-problems.

To perform this benchmark, it is necessary to demonstrate that two modeled wave fronts split in front of the island and collide behind it (as edge waves), while comparing computed water level and runup with the laboratory data at gauges.

1.5.4 BP9 field measurements: Okushiri Island Tsunami

On July 12, 1993, the M_w 7.8 Hokkaido-Nansei-Oki earthquake generated a tsunami that severely inundated coastal areas in northern Japan. Most of the damage was concentrated around Okushiri Island located west of Hokkaido. The tsunami runup around Okushiri Island was measured by the Hokkaido Tsunami Survey Group (1993), which reported up to 31.7 m runup near Monai village. The detailed runup measurements, together with high-resolution bathymetric surveys, done before and after the earthquake, allow for testing of numerical methods and validation of the shallow water approximation to simulate real tsunamis.

One of the difficulties in modeling a geophysical tsunami lies in specifying the initial conditions of the water surface displacement and velocities. In the absence of detailed earthquake models, the deformation in the Earth's crust is commonly computed by analytical formulae (Okada, 1985), which assumes a simple dislocation along an inclined plane in a homogeneous infinite half space. Owing to the near incompressibility of water and small rise times, the initial water surface displacement is typically set equal to the crustal surface displacement, while the initial water velocity is assumed to be zero. In the case of the Hokkaido-Nansei-Oki earthquake, several earth crustal deformation models were proposed. The interested reader is referred to a list of the deformation models for this earthquake in Yeh et al. (1996).

The original Kansai University bathymetry/topography Digital Elevation Models (DEMs) and the tectonic source were developed for the 1995 Friday Harbor Long Wave Runup Model workshop (Takahashi, 1996), and are available at the NOAA/PMEL Okushiri Benchmark test website http://nctr.pmel.noaa.gov/benchmark/Field/Field_Okushiri/index.html. Unfortunately, the developed Digital Elevation Models suffer from the apparent addition of rows and columns of so-called "ghost cells" to accommodate requirements of certain numerical models, and from significant horizontal and vertical misalignments of neighboring or embedded grids. The nesting between the Digital Elevation Models was attempted to be restored by finding an optimal alignment of the bathymetry/topography contours across boundaries of the fine-coarse grid. Despite all efforts, the final set of Digital Elevation Models still suffers from a lateral shift, due to conversion errors between the old Tokyo Datum and WGS84 datum.

To perform BP9, it is necessary to compute water level dynamics at Iwanai and Esashi tide gauges on Hokkaido Island, Figure 1-3-a; and the runup distribution around Okushiri Island at the regions enumerated in Figure 1-3-b. Other requirements to satisfy this benchmark test as well

as recommendations for potential improvements can be found at https://github.com/rjleveque/nthmp-benchmark-problems.

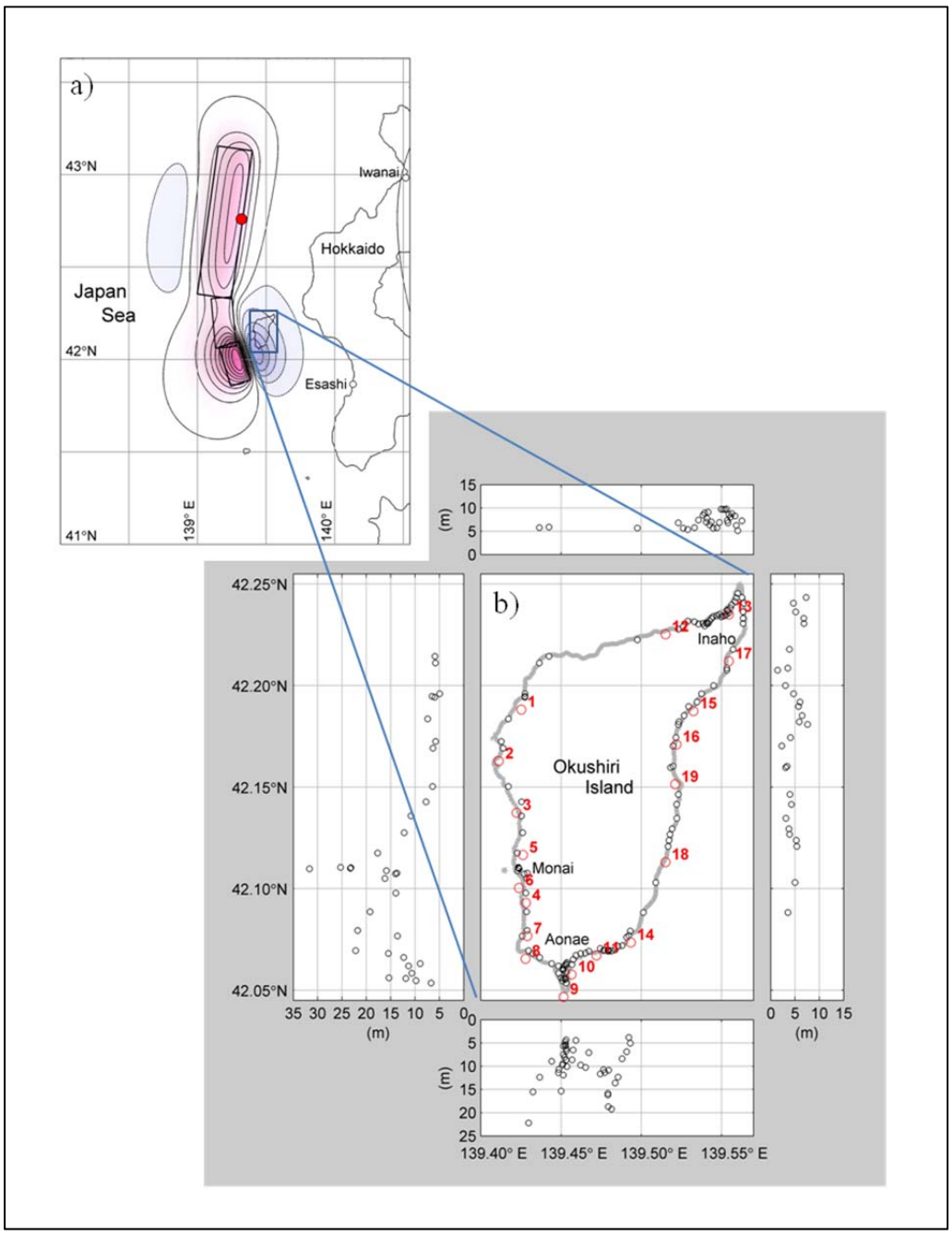

Figure 1-3: a) Tide gauge locations at Iwanai and Esashi. b) Maximum runup measurements around Okushiri Island. Numbers in red indicate regions to determine maximum runup. (Figure courtesy of Yoshiki Yamazaki).

1.6 Workshop section summary

The workshop comprised two parts. The first part was devoted to presentations by individual modelers of their benchmarking results, with each presentation followed by a general discussion with the NTHMP Mapping and Modeling Subcommittee members in attendance. The second part was focused entirely on crafting recommendations to the NTHMP Coordinating Committee, to critiquing model results, and setting goals to consolidate the validation process.

Most of the workshop attendees presented their model results for the existing benchmark tests, as defined in the report OAR-PMEL-135 (Synolakis et al., 2007). In view of the presented results, it became clear that some of these benchmark tests were not well enough defined and that others were missing supporting data, or at least some of the data were difficult to locate. The relevance of current benchmarks, how to conduct the required peer review of models and benchmarking results, how to develop "pass/fail" criteria for the benchmarks, and how to submit model results, were additional discussion topics. Several long-term recommendations for proposal to the NTHMP were identified as the result of these discussions. The long-term recommendations, along with short-term recommendations of note are summarized in the next section.

An additional topic focused on what mechanism should be employed for future validation of models. In general, future models may be verified by comparison with models having already passed benchmarking. A presentation of results showing new comparisons should be made to the Mapping and Modeling Subcommittee in order for newly tested models to be considered verified or validated.

1.7 Recommendations

Discussions that occurred during the NTHMP Model Benchmarking workshop led to a series of both short- and long-term recommendations. These are presented here for further consideration.

1.7.1 Short-term recommendations

1. Benchmarks shall include analytical, laboratory experiment, and field measurements benchmark tests.
2. Existing benchmark tests in OAR-PMEL-135 will be retained with the exception of BP3, to be replaced by laboratory experiments performed for an underwater rigid slide with Gaussian shape (Enet and Grilli, 2007) and BP8 (3-D slide), which will be replaced with a more carefully documented challenge problem. Case A in BP6, case B in BP4, as well as cases B and C in BP5, will be optional.
3. The UW github site (https://github.com/rjleveque/nthmp-benchmark-problems) will be the temporary repository for benchmark tests and model results.
4. A pass / fail criterion will be developed by consensus of NTHMP-MMS members, in consultation with state modelers, prior to reviewing model results deposited on the "results" directory of the UW github site.

1.7.2 Long-term recommendations

1. Establish and maintain a benchmark test repository, perhaps under NTHMP, NGDC or PMEL. This will require a partially funded position. Material accumulated on the UW site will eventually be transferred to the repository.

2. Conduct periodic reviews of current benchmarks with consideration of new proposed benchmarks.
3. Adopt additional BPs proposed for future use including: new field BPs for Samoa 2009, Chile 2010, Japan 2011; a sub-aerial slide laboratory BP; two submarine slide lab benchmark tests; a submarine slide field benchmark test (such as the PNG event proposed by Stephan Grilli); a seiche laboratory benchmark test (proposed by Aggeliki Barberopoulou); an analytical seiche benchmark test (proposed by Bill Knight); a grid alignment sensitivity benchmark test such as that briefly described in the GeoClaw Results Report and documented in Berger et al., 2011 (proposed by UW GeoClaw Tsunami Modeling Group). A proposal was made to create a folder on the UW repository to collect this information on new benchmark tests.
4. Provide financial support to develop and incorporate new, standardized Digital Elevation Models for the field benchmark tests; this is critical to the quality and credibility of benchmark test simulation results.
5. Provide modest financial support to individuals that agree to develop the necessary information and database for each benchmark test; this is sorely needed to improve the quality of these important resources and to minimize the time-consuming difficulties that beset modelers that attempt these benchmark tests.
6. Continue use of existing benchmarks for the immediate future, although cases well outside the shallow-water approximation should be omitted.
7. Immediately replace BP3 and BP8 (sub-aerial landslide on a simple beach, and 3-D slide) with similar, but more carefully documented and comprehensive, benchmark tests.
8. As agreed to in earlier MMS meeting discussions, models may be validated for either co-seismic or slide sources (or both). Slide source validation specifically requires passing the slide benchmarks. (NOTE: In the separate landslide workshop that followed the NTHMP benchmarking workshop in Galveston, there were some discussions about using justifiable initial conditions for a landslide source with validated, generic wave propagation models as an alternative for the completion of the slide benchmarks.)

1.8 Proposed benchmark tests and lessons learned

1.8.1 Proposed benchmark tests

1.8.1.1 Analytical: Convergence studies

By: Frank González et al.

The one-dimensional test problems currently involve exact solutions that are themselves difficult to calculate numerically, e.g. requiring numerical quadrature of Bessel functions. It is very useful that tabulated values of these solutions have been provided. However, rather than using limited tests for which such “exact” solutions are known, it might be preferable to carefully test a 1-D numerical model and show that it converges, and then use this with very fine grids to generate reference solutions. Fully converged solutions could be provided in tabulated form as well and could be as accurate as needed for a given class of equations. It would then be possible to generate a much wider variety of test problems. In particular, more realistic bathymetry could

be used, for example on the scale of the ocean, a continental shelf and beach, rather than modeling only a beach.

1.8.1.2 Analytical: Sloshing in a parabolic basin

By: Dmitry Nicolsky et al., Bill Knight, and Frank González et al.

We propose to test the model against the analytical solution in the cases of frictionless water flow in 2-D parabolic basins that can model fjord-type settings typical for the Alaska coast. The analytical solution to this problem is described as nonlinear normal mode oscillations of water (Thacker, 1981). This is a good test of wetting and drying as well as conservation. See Gallardo et al. (2007) and the test problem in GeoClaw: http://www.clawpack.org/clawpack-4.x/apps/tsunami/bowl-slosh/README.html.

1.8.1.3 Analytical: Symmetry preservation and grid alignment sensitivity studies

By: Frank González et al.

High-accuracy one-dimensional reference solutions can also be used to test a full two dimensional code, by creating bathymetry that varies in only one direction at some angle to the two-dimensional grid. A plane wave approaching such a planar beach would ideally remain one-dimensional, but at an angle to the grid this would test the two-dimensional inundation algorithms.

This idea can be extended to consider radially symmetric problems, such as a radially symmetric ocean with a Gaussian initial perturbation at the center. The waves generated should reach the shore at the same time in all directions, but the shore will be at different angles to the grid in different locations and it is valuable to compare the accuracy in different locations. The two-dimensional equations can be reformulated as a one-dimensional equation in the radial direction (with geometric source terms) and a very fine grid solution to this problem can be used as a reference solution. Features could also be added at one point along the shore and this location rotated to test the ability of the code to give orientation-independent results. Some GeoClaw results of this nature are presented in Berger et al. (2011) and LeVeque et al. (2011).

1.8.1.4 Analytical: Test for tolerance to depth discontinuities

By: Elena Tolkova

The appropriateness of representing differential equations with various difference schemes is based on the assumption that the physical variables do not change significantly within the sampling intervals in space and time. However, in tsunami propagation applications, the ocean depth supplied by Digital Elevation Models can undergo large changes between neighboring nodes. The suggested exercise aims to verify the correct operation of the tsunami model in the basin with abrupt depth changes.

1.8.1.5 Laboratory Experiment: Solitary wave over 2-D reef system

By: Volker Roeber and Kwok Fai Cheung

We conducted two series of laboratory experiments at Oregon State University in 2007 and 2009 that included 198 tests with 10 two-dimensional reef configurations at a range of water depths. Each test included a series of incident solitary wave heights. These test cases are a logical extension of the current benchmark for validation of inundation models. Though the laboratory experiments focus on shock-related hydraulic processes such as wave breaking and bore formation, the collected data allow examination of shoaling, reflection, wave breaking, and

swashing dynamics. We propose the results from one of the test configurations with $H/d = 0.3$ as a future NTHMP benchmark test and provide a detailed description of hydraulic processes with additional data from BOSZ.

1.8.1.6 Laboratory Experiment: Solitary wave over 3-D reef system

By: Volker Roeber and Kwok Fai Cheung

The National Science Foundation funded a workshop and a benchmarking exercise for inundation models at Oregon State University in 2009. The organizer provided two benchmark test cases with data from laboratory experiments at the Tsunami Wave Basin. Swigler and Lynett (2011) provided a detailed description of the experiments, instrumentation, and data post-processing. These test cases, which involve wave transformation over three-dimensional reef configurations, are logical extensions of the two-dimensional reef experiments from Roeber (2010). The laboratory data allow validation of models in handling dispersion and flux-dominated processes simultaneously.

1.8.1.7 Laboratory Experiment: Shoaling waves and runup along a wide continental shelf

By: Dmitry Nicolsky

It is noted in BP6 that the distance between the wave-maker and island is short and the wave dispersion effect does not have enough time to modify the wave and thus the runup of non-hydrostatic and hydrostatic models are more or less the same. A new benchmark test should be similar in nature to BP3, where the vertical wall is replaced by a sloping beach. The focus of this benchmark test will be on modeling propagation and shoaling of the wave across the continental shape and its runup at the beach.

1.8.1.8 Laboratory Experiment: The saucer slide

By: F. Enet and S. Grilli

Experiments were performed in the 3.7 m wide, 1.8 m deep, and 30 m long wave tank of the Ocean Engineering Department at the University of Rhode Island, Grilli and Watts (2001) and Grilli et al. (2002). The experimental setup was designed to be as simple as possible to build, while allowing one to illustrate and quantify the key physical phenomena occurring during landslide tsunami generation. In each experiment, a smooth and streamlined rigid body slides down a plane slope, starting from different initial submergence depths, and generates surface waves. Different conditions of wave nonlinearity and dispersion are generated by varying the model slide initial submergence depth. Surface elevations are measured with capacitance gauges. Runup is measured at the tank axis using a video camera. Landslide acceleration is measured with a micro accelerometer embedded within the model slide, and its time of passage is further recorded at three locations down the slope. The repeatability of experiments is very good. Landslide kinematics is inferred from these measurements and an analytic law of motion is derived, based on which the slide added mass and drag coefficients are computed. Characteristic distance and time of slide motion, as well as a characteristic tsunami wavelength, are parameters derived from these analyses. Measured wave elevations yield characteristic tsunami amplitudes, which are found to be well predicted by empirical equations derived in earlier work, based on two-dimensional numerical computations. The strongly dispersive nature and directionality of tsunamis generated by underwater landslides is confirmed by wave measurements at gauges. Measured coastal runup is analyzed and found to correlate well with initial slide submergence depth or characteristic tsunami amplitude.

1.8.1.9 Field Measurements: The 1964 Alaska tsunami

By: Joseph Zhang

The March 28, 1964 Prince William Sound (Alaska) earthquake produced a mega transoceanic tsunami that represented the largest tsunami that impacted the US and Canadian west coast on record. There is a wealth of field records for this event from tide gauges and eyewitness reports. Therefore we have been using this event as a representative of remote sources in our mitigation studies in Oregon.

1.8.1.10 Field Measurements: The Papua New Guinea (PNG) landslide-generated tsunami

By: Stephan Grilli

The tsunami that struck New Guinea on July 17, 1998 was the most devastating tsunami (in terms of casualties) generated by a landslide. The high reported runups, source definition and good runup data collected by tsunami survey teams makes this benchmark test a good candidate for benchmarking.

1.8.1.11 Field Measurements: Tsunami propagation for the 2004 Indian Ocean Tsunami

By: Stephan Grilli et al.

The Mw 9.3 earthquake on 26 December, 2004, ruptured over 1200 km along the Andaman-Sunda trench from Sumatra to the Nicobar and Andaman Islands, generating destructive tsunami affecting the coastal communities throughout the Indian Ocean. The 2004 Indian Ocean tsunami was recorded by satellite radar altimeters and many tide gauges. Three satellite radar altimeters, TOPEX/Poseidon, Jason-1, and Envisat, recorded the 2004 Indian Ocean tsunami propagating in deep water across the Indian Ocean and many nearshore tide gauges also measured the tsunami signal, both in far- and near-field. These are valuable data to validate tsunami models for open ocean propagation as well as for coastal impact.

1.8.1.12 Field Measurements: Propagation and runup for the 2009 South Pacific Tsunami

By: Yoshiki Yamazaki et al.

The South Pacific Tsunami on 29 September 2009 generated by Mw 8.1 earthquake south of the Samoan Islands struck Tutuila Island, American Samoa. Tsunami was recorded at DART buoys and Pago Pago Harbor at Tutuila. Tsunami arrived at mid tide and produced maximum runup of 17.6 m with detrimental impact on Tutuila. Several field survey teams measured runup and inundation around Tutuila. The high quality surface elevation data and runup/inundation measurements with available high resolution DEM data from NOAA NGDC provide the field benchmark to validate tsunami model to simulate propagation and runup.

1.8.1.13 Field Measurements: Tsunami induced currents for the 2006 Kuril, and 2010 Chile tsunamis

By: Yoshiki Yamazaki et al.

The Mw 8.3 earthquake on 15 November 2006 at the Kuril Islands and the Mw 8.8 earthquake on February 27, 2010 in Chile generated tsunamis that reached the Hawaiian Islands. Although Tsunami impacts due to these events were not severe along the Hawaii coastline, both tsunamis caused rapid changes in water level and unusual currents around the Hawaiian Islands. The Kilo Nalu Nearshore Reef Observatory located south of Oahu, Hawaii recorded clear signals of the flow velocity and surface elevation associated with the 2006 Kuril and 2010 Chile

tsunamis. Velocity measurements made during each of these tsunamis provide the opportunity to validate a tsunami model's capability to estimate tsunami induced currents for tsunamis arriving at the Islands from different directions.

1.8.1.14 Field Measurements: Distant and near-field tsunami impacts for the 2011 Tohoku Tsunamis

By: Many authors

The 2011 Tohoku earthquake of M_w 9.0 generated a massive tsunami that devastated the entire northeastern Japan coasts and damaged coastal infrastructure across the Pacific. The extensive the dense geodetic instruments, the numerous water level stations, post-event surveys across the Pacific provide the best quality datasets and coverage of any tsunami to date for model validation.

1.8.2 Lessons learned

An analytical solution in BP3 is derived under certain circumstances that prohibit any direct employment of the analytical solution in accurate benchmarking of the tsunami models. Therefore, it is suggested that this benchmark should be replaced by a problem that is similar in nature.

In BP8, the numerical results derived within the NSWE approximation show numerical instabilities that are due to a shock formation at the edge of the triangular wedge modeling sliding material. It is still unknown whether a Boussinesq approximation would help to eliminate the shock formation and produce better agreement with the laboratory measurements. However, 3-D full Navier-Stokes solutions do fairly well at reproducing BP8's free surface time series and runup. Anyway, we emphasize the rigid sliding block used in this benchmark test has an overly simplified geometry to represent an actual landslide. Therefore, it is suggested that this benchmark should be replaced by a problem with a more realistic geometry of the sliding material.

In BP9, the computed runup around Okushiri Island is within the variability of field observations. The computer simulation of the 1993 Okushiri tsunami captures the overland flow at the cape Aonae, where the maximum destruction was reported. However, the local extreme runup, e.g. in the narrow gully near the village of Monai, is sensitive to the near shore interpolation of bathymetry and topography.

During the benchmarking exercise, one of the most taxing problems we encountered was related to the incomplete information regarding field tests. We had to spend a considerable amount of time gleaning files from various sources. For the field test (Okushiri, etc.) some critical pieces of information (such as the horizontal datums of the Digital Elevation Models) are still missing. Perhaps the most serious problem with field tests is uncertainty about the geometry of the earthquake source. This issue causes serious errors in simulations for areas proximal to the source (e.g., poor match of simulated runup on the east coast of Okushiri Island).

The set of benchmark tests proposed in OAR-PMEL-135 was found to be mostly appropriate except for a few extreme cases (e.g., the larger wave breaking case C in the composite beach case). The combination of analytical, lab and field tests adequately tests the performance of models.

Going forward, we suggest that each model be validated by comparing it with recent well-documented tsunami events, such as 2004 Indian Ocean, 2010 Chile, and 2011 Tohoku. These

events have the advantage of being well documented in terms of witness accounts and a wealth of observations (e.g., satellite imagery, amateur and professional videos, and DART® deep-ocean bottom pressure) not previously captured on a wide scale. The synoptic look at these events makes them suitable for tsunami propagation model validation.

1.9 Models comparison

1.9.1 Summary

As stated in the NTHMP Strategic Plan, all numerical models used by NTHMP program partners for preparation of tsunami inundation and evacuation maps and associated products are required to meet standard criteria by the end of 2012. Accordingly, the primary objective of the NTHMP model benchmarking workshop held in Galveston, Texas in March 2012 was to ensure that each candidate model successfully simulate a series of pre-defined and accepted tsunami benchmark tests. Model results were compared against the relative reference solution for each benchmark test (e.g. analytic solutions, lab experiment, and tsunami field data for the case of the July 1993 Okushiri Island, Japan tsunami.) A subset of the benchmark tests listed in OAR-PMEL-135 was selected as benchmark priorities (BP) to adequately test the performance of each candidate NTHMP numerical model under the conditions of intended use. Results of each model were compared under the same data format and error formulation. Note that although each modeling group used benchmark tests in addition to those specified, the model comparisons presented here are limited in scope to the tests specified as part of the subset. The benchmark test priorities are as follows:

- Single wave on simple beach – analytical solution (BP1)
- Single wave on simple beach – laboratory experiment (BP4)
- Solitary wave on conical island – laboratory experiment (BP6)
- Okushiri Island – field measurements (BP9)

1.9.2 Error definition to measure model accuracy

To determine NTHMP models performance, three error formulae were selected and tailored to each of the four benchmark tests. These are:

- The normalized Root Mean Square deviations
- The Relative Error for maximum wave height or runup
- The Relative Error for multiple runup values recorded in a specific region

These three errors are described below.

RMS: The normalized Root Mean Square deviations error is applied within a space segment or time period to all observed data points. The error is defined as

$$RMS = \frac{1}{\zeta_{e_{max}} - \zeta_{e_{min}}} \sqrt{\frac{\sum_{i=1}^{n} (\zeta_{e.i} - \zeta_{m,i})^2}{n}} \tag{1}$$

The *RMS* is a frequently used measure of the differences between values predicted by a model (ζ_m) and values obtained/observed either from an analytical solution, laboratory experiments, or field measurements. The obtained/observed values are assumed as the benchmark test reference

data and hence assumed as true, although errors in their estimation are probable, especially for laboratory experiment and field measurements where systematic errors might exit. The *RMS* is normalized with respect to the magnitude between the maximum and minimum observed values, i.e., wave height $(\zeta_{e_{max}} - \zeta_{e_{min}})$, or the maximum wave amplitude or runup $\zeta_{e_{max}}$. The maximum wave height usually corresponds to the first or second wave in a tsunami wave train, measured from crest to trough and n is the number of observed points obtained within an arbitrary space segment or time period. This *RMS* error is thus a time or space-dependent error, based on model prediction, which are interpolated at the location/time of each observed point. Hence *RMS* error is sensitive to phase lags in the predicted values and its main use is only to assess the accuracy of the model in predicting the entire set of observed data (overall model performance).

MAX: To quantify each model's predictive accuracy for the maximum wave amplitude or runup regardless of the location where, or time this maximum occurs, the following formulation is used to measure differences between maximum predicted (ζ_m) and observed (ζ_e) values.

$$MAX = \frac{\left|\zeta_{e_{max}} - \zeta_{m_{max}}\right|}{\zeta_{e_{max}}} \tag{2}$$

Note that the expression used for MAX is a relative error based on the maximum magnitude of the observed values.

ERR: Another error used to measure the model performance is the relative error for multiple values that are collected in one specific location or region. This error is practically the same as *MAX* but it has been defined to determine model accuracy in predicting runup against multiple values that have been recorded by a tsunami survey team in a region with similar inundation characteristics or geomorphology. The regional data set is reduced to three values, minimum, maximum, and average, that represents the inundation at a specific location. The error is then defined as:

$$ERR = \begin{cases} 0 & If\ \left(\zeta_{e_{\min}} \le \zeta_{m_{avg}} \le \zeta_{e_{max}}\right) \\ \dfrac{\min[\,abs(\zeta_{e_{\min}} - \zeta_{m_{\min}}),\ abs(\zeta_{e_{avg}} - \zeta_{m_{avg}}),\ abs(\zeta_{e_{\max}} - \zeta_{m_{\max}})]}{D} & Otherwise \end{cases} \tag{3}$$

Where the denominator D is one of the following values $[\zeta_{e_{\min}}, \zeta_{e_{avg}}, \zeta_{e_{\max}}]$. D is selected according to the numerator minimum value. For example, if $abs(\zeta_{e_{avg}} - \zeta_{m_{avg}})$ is the minimum value in the numerator, then the denominator $D = \zeta_{e_{avg}}$.

The *MAX* and *ERR* errors are the only formulation used for verification and validation with observed data in the model comparison and discussion. However, *RMS* errors further help to assess the accuracy of the model in predicting the entire set of observed data (with the correct magnitude and phase); in other words, it is a good metric tool for assessing overall model performance.

1.9.3 Models comparison and discussion

To verify suitability of the NTHMP numerical models for the tsunami problem, the Mapping and Modeling Subcommittee decided, as a first attempt, to use as a threshold the allowable errors stated in the standard OAR-PMEL-135 for each benchmark test (Synolakis et al., 2007). For the

inter-model comparison, a subset of four benchmark tests that almost all models could simulate and which was deemed to adequately test the performance of each model was selected from the available list,. The selected benchmark tests represent all the categories of reference data used to assess each model, namely: a) analytical solution, b) laboratory measurements and c) field measurements. The allowable errors vary according to these categories, the tested parameter (e.g., maximum amplitude/runup), and wave condition (e.g., breaking, non-breaking). Model accuracy is quantified by way of the error formulae previously defined, i.e., *RMS*, *MAX,* and *ERR*. According to OAR-PMEL-135, the models' maximum predicted values should not differ by more than the pre-established error threshold indicated in Table 1-5.

Table 1-5: Current allowable errors for model validation and verification, after Synolakis et al. (2007)

Benchmark Test	Category	Tested Quantity and Wave Condition	OAR-PMEL-135 Allowable Error
BP1	Analytical Solution	Runup/amplitude (non-breaking wave)	<5%
BP4	Laboratory Measurements	Runup/amplitude (non-breaking wave) Runup/amplitude (breaking wave)	<5% <10%
BP6	Laboratory Measurements	Runup	<20%
BP9	Field Measurements	Runup	<20%

1.9.4 Summary of comparisons for the four selected benchmark tests

The following sections summarize NTHMP model comparisons for the four selected benchmark tests.

1.9.4.1 BP1 Analytical Solution: Single wave on simple beach

Let us define the following non-dimensional variables: $H = \overline{H}/\overline{d}$, $x = \overline{x}/\overline{d}$, and $t = \overline{t}\sqrt{\overline{g}/\overline{d}}$. A focus in developing a tsunami modeling algorithm is to simulate extreme positions of the shoreline - the maximum runup and rundown. Figure 1-4 and Figure 1-5 show comparisons of analytical (i.e., NSW) and computed water surface profiles during runup and rundown of a solitary wave of initial height H = 0.0185 over a beach of slope 1:19.85 ($\cot\beta = 19.85$) (see Figure 1-1), at t = 35 to 65 by Δt = 5 increments. The maximum runup and rundown occur in the numerical simulation at t = 55 and 70, respectively. Note, the t = 70 plot is not shown in the figures. Results indicate that all the numerical solutions match very well the analytical solution during runup, while the maximum rundown shows some variability between the computed water surface profiles. This is likely due to the use of different shoreline tracking (i.e., wetting-drying) algorithms, different model schemes, and different spatial and temporal discretizations. In future benchmark validations, it is recommended that the numerical solutions be computed to show convergence to the analytical prediction for maximum rundown, i.e., here at t = 70. It is noteworthy to mention that for BP1, dispersive models such as SELFE, NEOWAVE, and FUNWAVE were restricted to run in a non-dispersive mode, because the validation data are based on an analytical solution of the non-dispersive NSW equations

Table 1-7-a (case $H = 0.0185$, non-breaking wave) shows, for all NTHMP models, the mean *RMS* errors (for computed surface profiles) range between 1- 4% and mean *MAX* errors (for maximum wave amplitude or runup, regardless of location) range between 1 - 5%. Based on these results, the overall performance of all the models is deemed very good ($RMS \leq 4\%$ and for *MAX*, the model errors are kept below 5%). According to Synolakis et al. (2007), "any well-benchmarked code should produce results within 5% of the calculated value from the analytical solution."

Figure 1-6 compares numerical and analytical solutions of water level dynamics at locations $x = 0.25$ (near the initial shoreline) and 9.95 (between the beach toe and initial wave crest) during propagation and reflection for the case $H = 0.0185$. During rundown, both numerical and analytical solutions predict a water backwash between $t = 67$ and 82, with the location $x = 0.25$ becoming temporarily dry, while $x = 9.95$ remains wet throughout the entire duration of the experiment. Comparison of the analytical and numerical solutions at these two locations reveals that the computational error (*RMS*) is typically less that 3% (see Table 1-7-b), and the agreement is quite good for all NTHMP models. For *MAX* (maximum wave amplitude), the models' mean errors range between 0 - 2%. Therefore, one can conclude that all NTHMP models predicted extremely well the analytical solution of BP1. The models' *MAX* errors are kept below the allowable threshold of 5%, although some small differences between models occur, presumably due to the variety of numerical schemes used and the different space and time discretization methods adopted for the solution.

1.9.4.2 BP4 Laboratory Experiment: Single wave on simple beach

The time evolution of the free surface profile for an initial wave of height $H = 0.0185$ (Case A) shoaling over a sloping beach with 1:19.85 slope, is shown in Figure 1-7, between $t = 30$ and 70 by $\Delta t = 10$ increments. Laboratory measurements of the surface elevation at these times are compared to the NTHMP models solutions. Overall, we see a good agreement between the numerical solutions and the laboratory measurements for all times corresponding to the propagation and runup of the wave. One noticeable observation is that differences among numerical solutions are smaller than differences between any of the model solutions and the laboratory data.

At time $t = 50$, which is near the maximum runup ($t = 55$), two models based on the NSWE (ALASKA and GEOCLAW) predict a slightly higher runup than the other models and the experimental data. These differences could be attributed in part to the zero friction assumption and fine spatial discretization used in the numerical solution. However, other NSWE models (MOST and ATFM) captured the runup somewhat better. In the case of ATFM, the improvement is likely due to the addition of the non-hydrostatic component. It is noticeable from Figure 1-7 that the models that include dispersive effects produce better results at $t = 50$ and 60 than non-dispersive models. The numerical solutions vary the most at $t = 70$, which corresponds to the maximum rundown. There, we see that the non-dispersive models (MOST, ALASKA and GEOCLAW) compute larger rundowns than the dispersive models.

The estimation of model errors are shown in Figure 1-6-a. The mean *RMS* errors range between 7 - 11% and, for the maximum wave amplitude or runup (*MAX*), regardless of its location, mean errors range between 2 - 10%. Hence, model errors are kept below 10%, the threshold agreed upon for laboratory measurement benchmarks during the Catalina Island model validation workshop, in 2004.

Figure 1-8 similarly presents the time evolution of free surface profiles for an initial wave of height $H = 0.30$ (Case B) between $t = 15$ and 30 by $\Delta t = 5$ increments, computed by NTHMP models, as compared to laboratory experiments. This is a very challenging case, in which the wave breaks during runup in laboratory experiments. For non-dispersive or NSWE models, this case becomes even more challenging. For instance, NSWE models predict that the leading front of the solitary wave will steepen and become singular shortly after the initiation of the computations. The numerical singularity propagates towards the beach until it meets the shoreline where the singularity dissipates. The existence of strong wave breaking does prevent a good agreement of the NSWE solutions with the laboratory measurements (for details on a non-dispersive solution see each individual reports that use NSWE). However, since numerical dispersion can compensate for the absence of physical dispersion in NSWE models (e.g., by adjusting the spatial discretization as the MOST model does), the effective simulation of breaking waves in NSWE models is still an active area of research. Results show that the inclusion of wave dispersion in the models allows the wave to initially steepen-up without breaking, between $t = 15$ and 20, which results in a good match with laboratory measurements. Table 1-6-b indicates for Case B, mean *RMS* errors ranging from 5 - 8% and mean *MAX* errors for the maximum wave amplitude ranging from 5% to 12%. Although, for some models, the latter errors are slightly larger than the accepted threshold for laboratory measurements (≤10%), these errors are still deemed more than acceptable, considering the difficulty in reproducing this benchmark test that features breaking waves.

1.9.4.3 BP6 Laboratory Experiment: Solitary wave on conical island

In BP6, experiments with different wave heights were conducted in the large-scale wave tank at Coastal Engineering Research Center, Vicksburg, Mississippi. The time series of surface elevation comparison and associated errors at gauges 6, 9, 16, and 22 for a variety of incident solitary waves impinging into a conical island are shown in Figure 1-9 through Figure 1-12, and in Table 1-9 and Table 1-10. Three different wave heights or cases were selected from the laboratory experiment to validate the numerical models, i.e., Case A, $H = 0.045$; Case B, $H = 0.096$ and Case C, $H = 0.181$.

Figure 1-9, Figure 1-10, and Figure 1-11 show the computed and observed sea levels at the four gauges around the island, for the various cases of incident waves. The model comparison times have been selected to avoid the first reflection of the wave. One of the challenges in modeling the observed waves was the application of appropriate boundary conditions and generating the wave in the numerical models. Although various techniques were employed to address these challenges, all computed solutions matched well the observed water level dynamics at the given locations or gauges. For all SWE models, such as ALASKA, GEOCLAW and MOST, the simulated waves are seen to steepen faster than in laboratory experiments (e.g., in Case C; $H = 0.181$). This is a well-known effect of the shallow water approximation, where the lack of dispersive terms yields so-called “shallow water steepening” of waves. Visual examination of the models' results reveals that the dispersive models, such as BOSZ, FUNWAVE, NEOWAVE, and SELFE, capture the water level dynamics slightly better than the non-dispersive models. However, while models based on the Boussinesq-type or non-hydrostatic approximations feature wave dispersion effects, they did not show an appreciable improvement over the SWE models in matching this particular set of laboratory observations. This can also be deduced from Table 1-9, where the models' mean *RMS* errors for cases A, B and C have a narrow range of variation, i.e., between 7% and 10%. For maximum wave amplitude at gauges,

regardless of the location the maxima occurred, the mean models' errors (*MAX*) range between 4% and 19%. These models' errors have a wider variation, and there is a clear trend that dispersive models perform slightly better. One non-dispersive model, ALASKA, was the exception, with its performance for this specific BP case being quite good (perhaps due to numerical dispersion). All models' errors for BP6 are below the 20% threshold recommended in OAR-PMEL-135 (see Table 1-5).

Figure 1-12 shows the modeled maximum runup distribution versus laboratory experiments, around the conical island, for all three wave height cases. We again observe that, in general, dispersive models reproduce the maximum runup slightly better. The models' *RMS* errors for maximum runup around the conical island range from 12% to 22%, and the mean relative errors *MAX*, range between 3% and 10%. As they do not differ by more than 20% from the laboratory measurements, maximum runup values predicted by all the models are considered to be fairly good.

1.9.4.4 BP9 Field Measurement: Okushiri Island

BP9 provides model validation and as such is an important check of the ability of the presented models to simulate realistic tsunami events. The sea level dynamic results modeled with various NTHMP models are compared to the tidal gauge records taken during the first hour following the earthquake. Figure 1-13 shows the computed and observed water level dynamics at Iwanai and Esashi, respectively. For the Esashi tide gauge, the arrival time of each computed wave matches well the arrival of the recorded leading tsunami wave. The correlation of positive and negative phases between the computed and observed waves is also rather good, although the computed waves at both locations have a larger range and frequency of variability than the observed waves. For the Iwanai case, the time shift discrepancies between the measured and observed waves could be explained by the lack of detailed bathymetry or coastal geomorphology near tide stations, inaccuracies in the specified initial conditions, and a potential delayed response of the tide gauge hardware (Yeh et al., 1996). The models' relative errors on maximum amplitude (*MAX*) at Iwanai and Esashi are shown in Table 1-11-a. In the Esashi case, the ATFM, FUNWAVE and NEOWAVE models predicted the free surface time series and the maximum wave amplitude with maximum amplitude relative errors in the range of 10%-19%, below the 20% error threshold recommended in OAR-PMEL-135. Other models did not perform as well, but during the benchmarking exercise, many modelers struggled with incomplete information regarding this benchmark. They reported having to spend considerable time collecting files from various sources, which instead of helping, actually increased the uncertainties. Some critical pieces of information, such as the horizontal datum of the DEMs, are still missing and the geometry of the earthquake source is doubtful too. These information gaps caused serious errors in the simulations for areas both near to and far from the source. Therefore, the workshop participants recommend that BP9 be revised to address these issues, if possible, and that additional historic events be simulated for model validation.

In the Iwanai case, the errors on maximum amplitude modeled are very large. In view of the close similarity among model results and the large discrepancy with respect to measurements, it is quite clear that the Iwanai tide record is too uncertain and likely not adequate to be used as a validation case. After a closer examination of the Iwanai gauge location, it seems that the gauge is surrounded by a complex port layout, which is not resolved well in the current grid resolution used in the models. Therefore, it is suggested that Iwanai's tide records be replaced with another

(nearby) tide gauge for which adequate surrounding bathymetry and coastal geomorphology data exist.

Figure 1-3-b shows the locations (black circles) on Okushiri island where the runup was measured shortly after the 1993 tsunami. These measurements were obtained from Imamura-Shuto's group (data researched by Yoshiki Yamazaki) (regional data are enumerated in red). From Table 1-11-b, based on the models' runup relative errors *ERR*, it can be seen that all NTHMP's models obtained mean runup relative error below the permissible 20%. A closer examination of the modelers' individual reports, however, shows that there are several exceptions where the modeled runup underestimates the observations by a larger amount. For example, the modeled runup in the narrow gully near the village of Monai is underestimated in most of the models. The discrepancy between the measured and computed runup values there might be explained by the lack of accurate bathymetry and topography data near Monai, uncertainties in the initial water surface displacement, or by limitations of the current models when high vertical acceleration occurs. Almost all presented models capture a sequence of events related to the inundation of the city of Aonae (model runup relative *ERR* = 0% at regional location 9 on Table 1-11-b). In computer experiments, it is easy to observe an approximately 5 m high wave approaching the Aonae peninsula from the west. The wave drastically steepens over the shallow areas, runs up on the western side on the Aonae peninsula, and then sweeps across the tip of the peninsula. Then due to the shallow depth around the peninsula, the wave front bows, bends around the Aonae peninsula, and subsequently hits the town of Hamatsumae. Although some computed results show discrepancies with measured runup regional data, all the presented models reproduced this overall pattern quite well. Probably, the largest source of discrepancy is associated with the interpretation of incomplete information regarding the field data, horizontal datums of the DEM, and uncertainties in the sea floor deformation.

1.9.5 Benchmarking results for landslide generated tsunami models

To benchmark numerical models to simulate landslide-generated tsunamis, Synolakis et al. (2007) propose two benchmark problems, namely BP3 and BP8. The first BP is based on an analytical solution, while the other is a laboratory experiment. The analytical solution in BP3 is derived under certain conditions that prohibit any direct use of the solution to accurately benchmark some tsunami models (i.e., dispersive/non-hydrostatic models). All models that attempted to predict the landslide-generated wave according to BP3 have a good qualitative agreement with the analytical solution provided in Liu et al. (2003), although quantitative agreement may be lacking for the reason discussed before. Therefore, it is suggested that this benchmark be replaced by a problem that is similar in nature.

Only two SWE models (GEOCLAW and ALASKA) and two Navier-Stokes models (THETIS and TSUNAMI3D) were used to compare the simulated water dynamics to laboratory observations in BP8. Before comparing the numerical results to the laboratory observations, it was observed, that for this particular BP, the SWEs are not applicable to simulate 3-D flows, especially around the sliding wedge. Away from the shore, the water depth is comparable with or greater to the observed wavelength and thus the shallow water assumption is no longer valid.

The SWE models produce computational results that exhibit severe numerical oscillations due to the formation of a shock wave (see individual reports). The Navier-Stokes models achieve a much better comparison of numerical results with laboratory observations. The THETIS model shows that it is possible both to predict a slide location and wave dynamics at the same time. The

TSUNAMI3D model also shows a good match of the computed water level to the laboratory observations. Unfortunately, the computational resources required for meaningfully running Navier-Stokes models are still prohibitive. However, the coupling of Navier-Stokes model (landslide tsunami generation region) and SWEs model (tsunami propagation and inundation) for practical tsunami application is possible. The coupling of the two approaches has been applied successfully for construction of inundation map in the Gulf of Mexico, Horrillo et al. (2009) and recently for the US east coast inundation assessment, Kirby and Grilli (2011). Moreover, a closer examination of BP8 reveals that this BP does not constitute a good test for the tsunami models, due to an unrealistic landslide profile - a rigid wedge (with vertical front and side walls) sliding into the water. Therefore, it is suggested that BP8 be replaced by a problem with a more realistic geometry of the sliding material. In Section 1.8, we briefly mention some proposed benchmark problems for the future validation and verification of landslide tsunami models.

1.9.6 Conclusions

Workshop participants recommend continuing to use the existing benchmark tests listed in OAR-PMEL-125 in the immediate future, although the cases well outside the shallow-water approximation can be omitted. In particular, BP3 should be replaced with a newly proposed laboratory benchmark for an underwater landslide with a Gaussian shape, and BP8 should be replaced by a more carefully documented challenge problem; in BP4, Case B should be optional; in BP5, Cases B and C should be optional, and in BP6, Case A should be optional. Historic events in addition to the 1993 Hokkaido-Nansei-Oki (Okushiri Island, Japan) should be added to the suite of benchmark tests to further validate all models.

The 1993 Hokkaido-Nansei-Oki Tsunami event remains one of the most important and thoroughly documented cases of extensive tsunami runup available to the tsunami community. But the bathymetric and topographic computational grids are flawed by severe horizontal and vertical misalignment errors. It is necessary to build improved, nested coastal digital elevation models (DEMs) of the Okushiri, Japan area to replace the 8 existing DEMs that have large, known inaccuracies that negatively impact tsunami modeling results. The best publicly available bathymetry and topographic data should be obtained through collaboration with Japanese institutions and both structured and unstructured nested DEMs should be developed to support multiple tsunami modeling codes. It was evident after examination of numerical models results that the Iwanai tide record is faulty too. The workshop participants suggest that this tide record be replaced by another (nearby) tide gauge record where surrounding bathymetry and coastal geomorphology data are better suited for unambiguous model validation.

In BP1, all NTHMP's models predicted very well the analytical solution of the wave evolution ($H = 0.0185$) at different times, with errors less than the allowable 5%. In BP4, for Case A (H = 0.0185), all mean model errors were kept below 10% (which the 2004 Catalina Island model validation workshop suggested is an allowable error for laboratory measurements benchmark tests). For Case B ($H = 0.30$, breaking wave), the maximum wave amplitude model errors range from 5% to 12%. Although, the mean amplitude model errors are slightly larger than the accepted standard error for laboratory measurements benchmark tests (≤10%), the workshop participants concluded that these errors are more than acceptable, considering the difficulty in reproducing this benchmark test, which features breaking waves. In BP6, Case A ($H = 0.045$), Case B ($H = 0.096$), and Case C ($H = 0.181$), a clear trend was observed showing that dispersive models perform slightly better than non-dispersive models. However, one non-

dispersive model, ALASKA, was the exception, with its performance for this specific test case being quite good. For BP6, model errors are kept below the 20% recommended in OAR-PMEL-135 (see Table 1-5). For BP9, runup around Okushiri Island, participants concluded that, although some computed results show discrepancies with measured runup regional data, all the presented models reproduced the overall observed pattern of wave arrival quite well. All NTHMP models obtained mean runup relative errors below the acceptable 20%.

The workshop participants represent nationally renowned tsunami modeling organizations and, therefore, are well qualified for validating each numerical model. A pass / fail criteria for the verification and validation based on comparison with observations of each numerical model was developed by consensus of NTHMP MMS members during the benchmarking workshop, in consultation with state modelers and based on the review of modeling results. Future model validation testing and acceptance will follow the existing criteria, and will also be reviewed by the MMS members and their modeling experts.

The following table summarizes the allowable errors for the main three categories used for benchmarking. These errors are quite similar to those recommended in OAR-PMEL-135, Synolakis et al. (2007). The only difference is in the allowable error for the laboratory measurement category. For the sake of simplicity, the error criterion of 10% is applied to both breaking and non-breaking waves.

Table 1-6: Allowable errors for the main three categories used for benchmarking

Category	Allowable Errors MAX /ERR/ RMS
Analytical Solution	<5%
Laboratory Measurements	<10%
Field Measurements	<20%

1.9.7 Model comparisons: Summary figures and tables

1.9.7.1 Single Wave on a Simple Beach – Analytical Solutions (BP1)

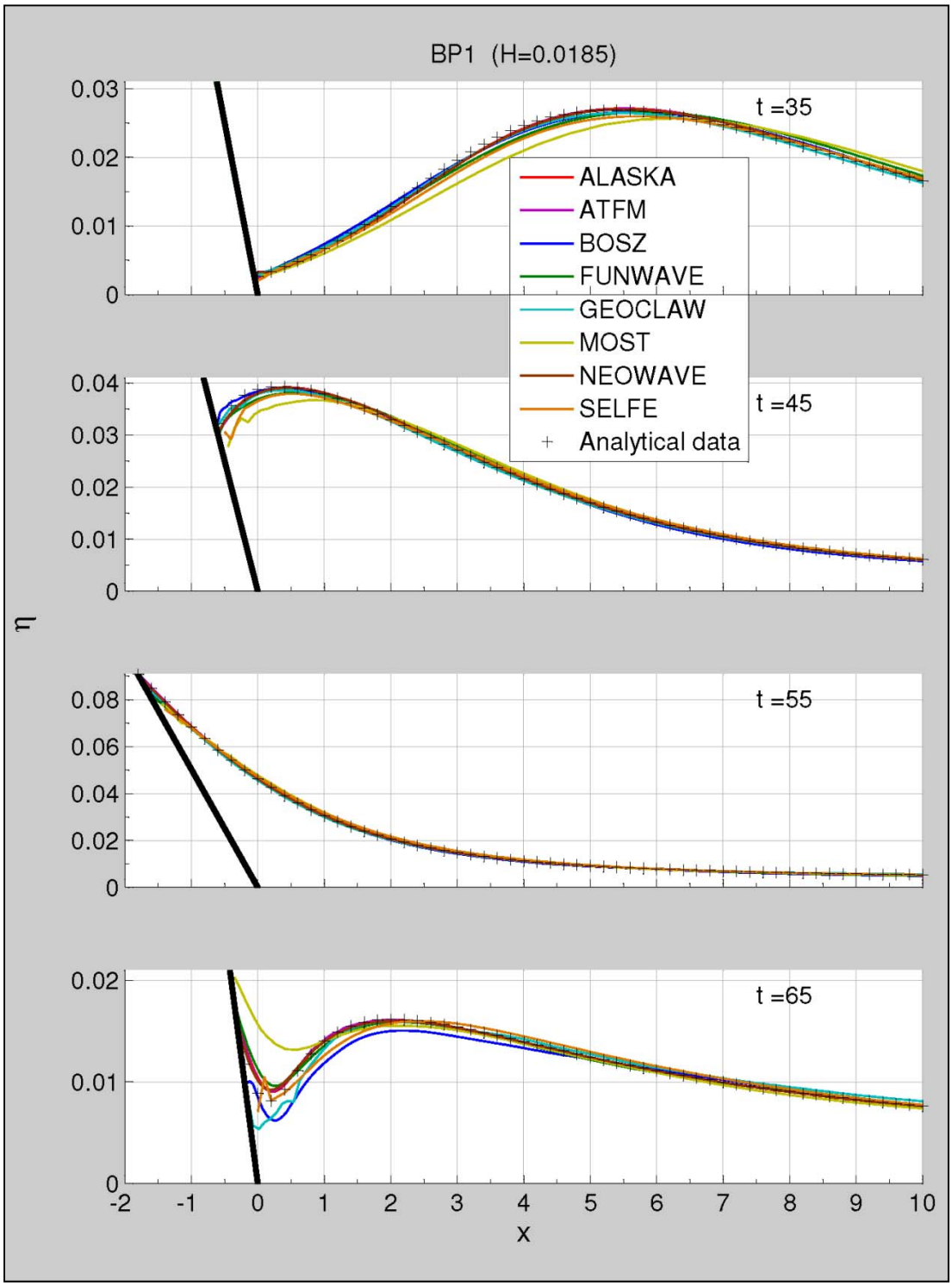

Figure 1-4: Comparison of analytical solution (crosses) versus NTHMP's models surface profiles (solid lines) during runup of a non-breaking wave of H = 0.0185 at t = [35, 45, 55, 56]. The analytical solution can be found in Synolakis (1986).

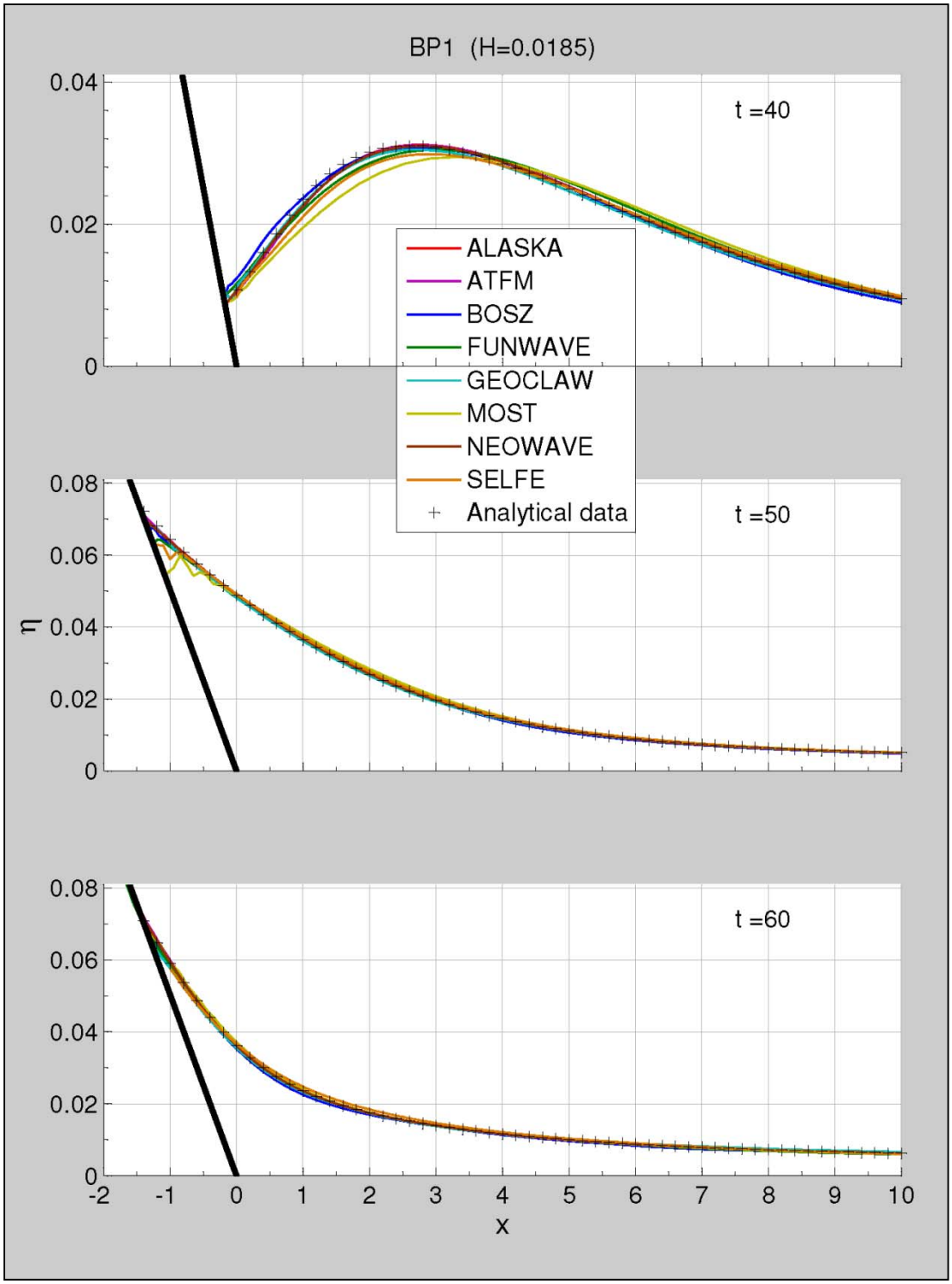

Figure 1-5: Comparison of analytical solution (crosses) versus NTHMP's models surface profiles (solid lines) during runup of a non-breaking solitary wave of H = 0.0185 at t = [40, 50, 60]. The analytical solution can be found in Synolakis, (1986).

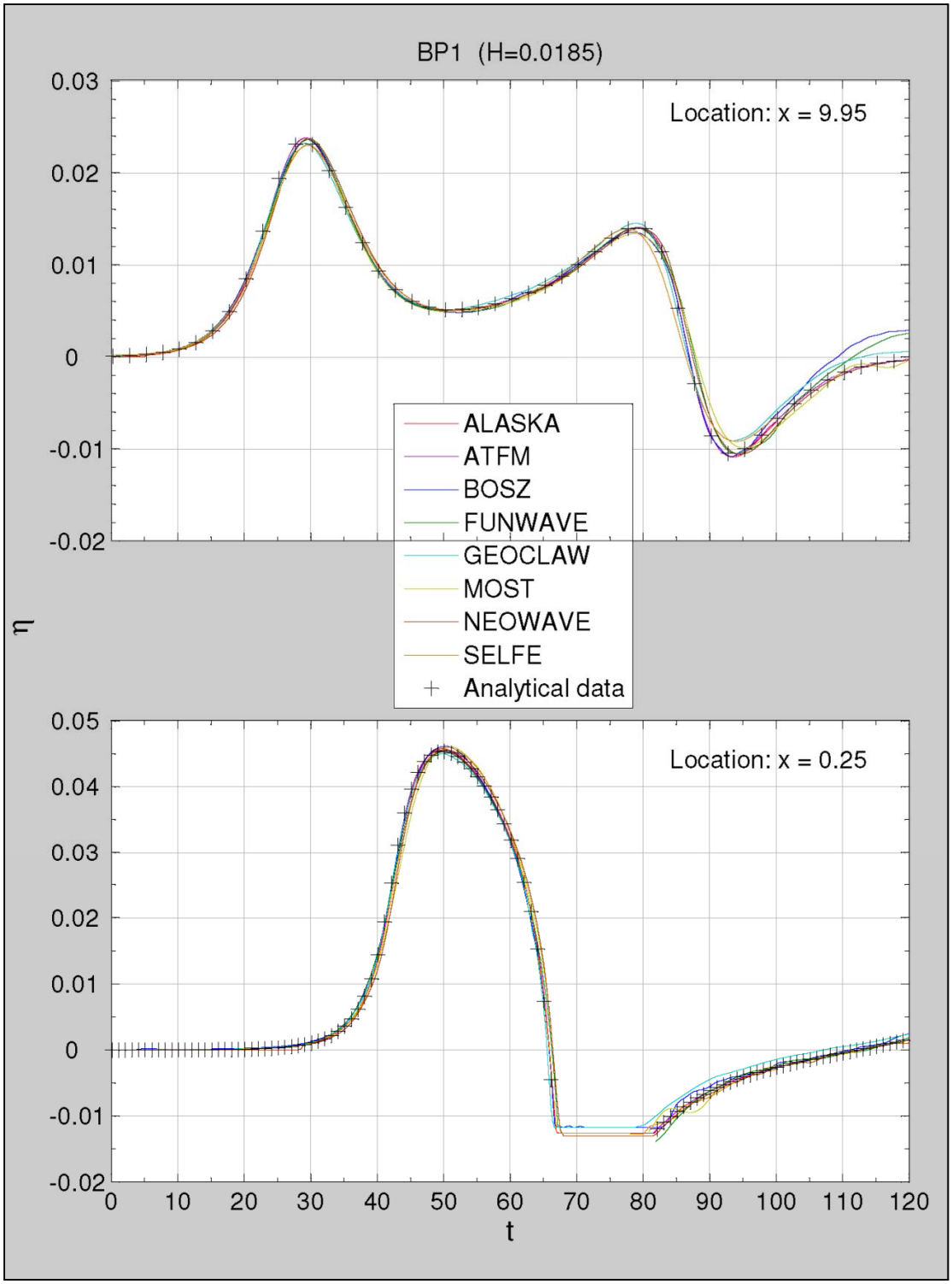

Figure 1-6: Comparison between the analytical solution (crosses) versus NTHMP's models (solid lines) during the runup of a non-breaking solitary wave of H = 0.0185 on 1:19.85 beach. The top and bottom plots represent comparisons at x = 9.95 and x = 0.25, respectively. The analytical solution is taken from Synolakis (1986).

Table 1-7: BP1: NTHMP models' errors with respect to the analytical solution for H = 0.0185. a) surface profile errors at t = [35, 40, 45, 50, 55, 60, 65]. b) sea level time series errors at x = 9.95 and x = 0.25. RMS: Normalized root mean square deviation. MAX: Maximum amplitude or runup error.

a)

	MODEL ERROR for CASE H=0.0185															
	t = 35		t = 40		t = 45		t = 50		t = 55		t = 60		t = 65		Mean	
MODEL	RMS	MAX	RMS	MAX	RMS	MAX	RMS	MAX	RMS	MAX	RMS	MAX	RMS	MAX	RMS	Max
ALASKA	1%	1%	1%	0%	1%	0%	0%	2%	0%	0%	0%	2%	2%	0%	1%	1%
ATFM	1%	1%	1%	0%	1%	1%	0%	1%	0%	1%	0%	2%	2%	0%	1%	1%
BOSZ	2%	1%	2%	1%	1%	1%	1%	2%	0%	0%	1%	0%	6%	7%	2%	2%
FUNWAVE	3%	1%	2%	2%	2%	3%	1%	4%	1%	2%	0%	2%	4%	2%	2%	2%
GEOCLAW	1%	2%	1%	2%	1%	2%	0%	2%	0%	0%	1%	1%	5%	1%	1%	1%
MOST	6%	5%	5%	5%	4%	7%	2%	2%	1%	0%	0%	0%	10%	13%	4%	5%
NEOWAVE	1%	0%	1%	0%	1%	1%	0%	2%	0%	0%	0%	1%	2%	1%	1%	1%
SELFE	3%	4%	3%	4%	2%	3%	1%	2%	1%	0%	1%	0%	5%	1%	2%	2%
Mean	2%	2%	2%	2%	2%	2%	1%	2%	0%	0%	0%	1%	5%	3%		

b)

	MODEL ERROR					
	x = 9.95		x = 0.25		Mean	
MODEL	RMS	MAX	RMS	MAX	RMS	Max
ALASKA	1%	1%	1%	1%	1%	1%
ATFM	2%	2%	2%	1%	2%	2%
BOSZ	3%	0%	1%	2%	2%	1%
FUNWAVE	3%	0%	2%	0%	3%	0%
GEOCLAW	2%	1%	2%	1%	2%	1%
MOST	3%	2%	3%	1%	3%	2%
NEOWAVE	2%	1%	2%	0%	2%	1%
SELFE	2%	2%	1%	1%	2%	2%
Mean	2%	1%	2%	1%		

1.9.7.2 Single Wave on a Simple Beach – Laboratory Experiment (BP4)

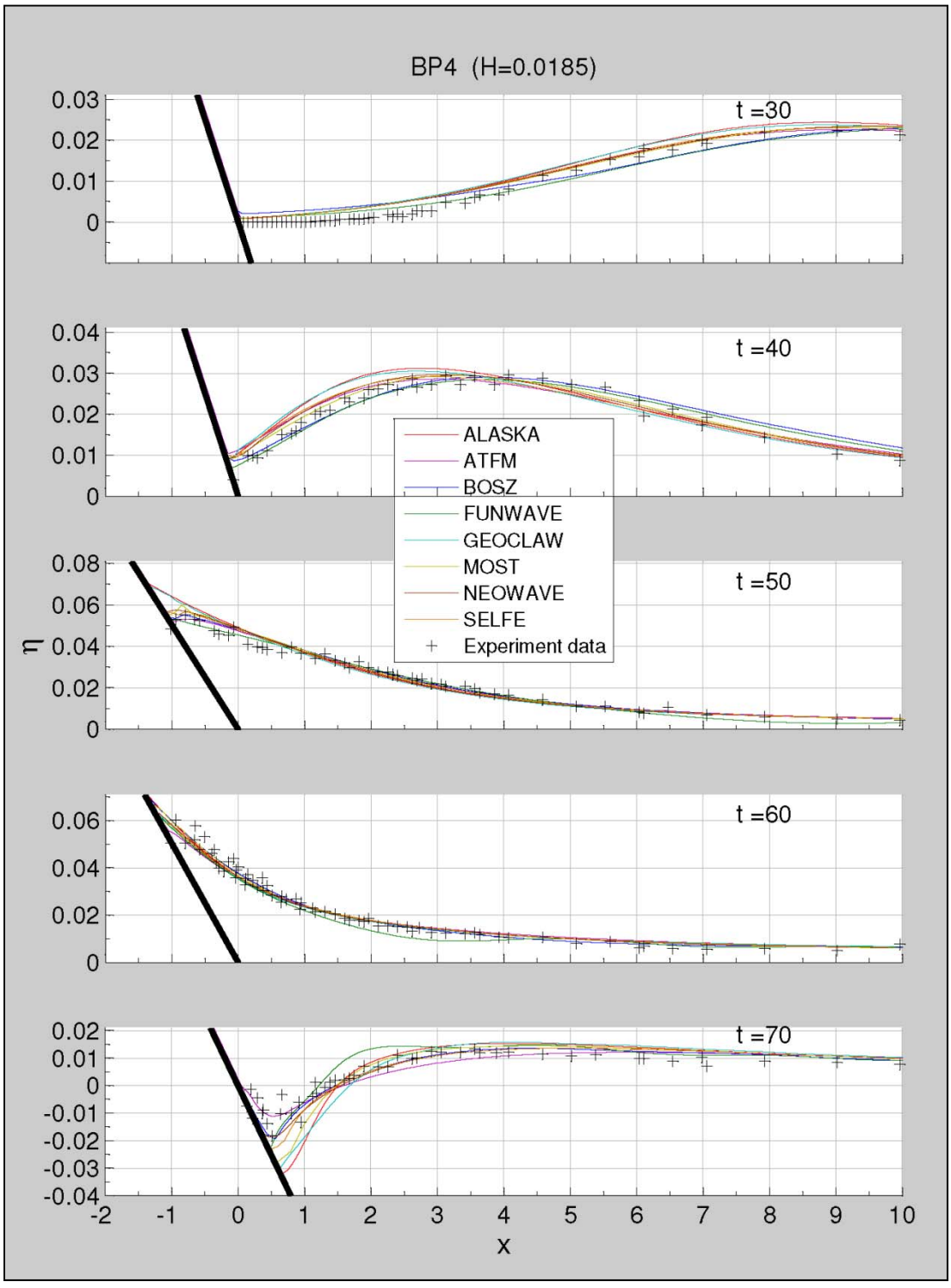

Figure 1-7: Comparison of experimental data (crosses) versus NTHMP's models surface profiles (solid lines) during runup of a non-breaking wave (Case A, H = 0.0185) at t = [30, 40, 50, 60, 70].

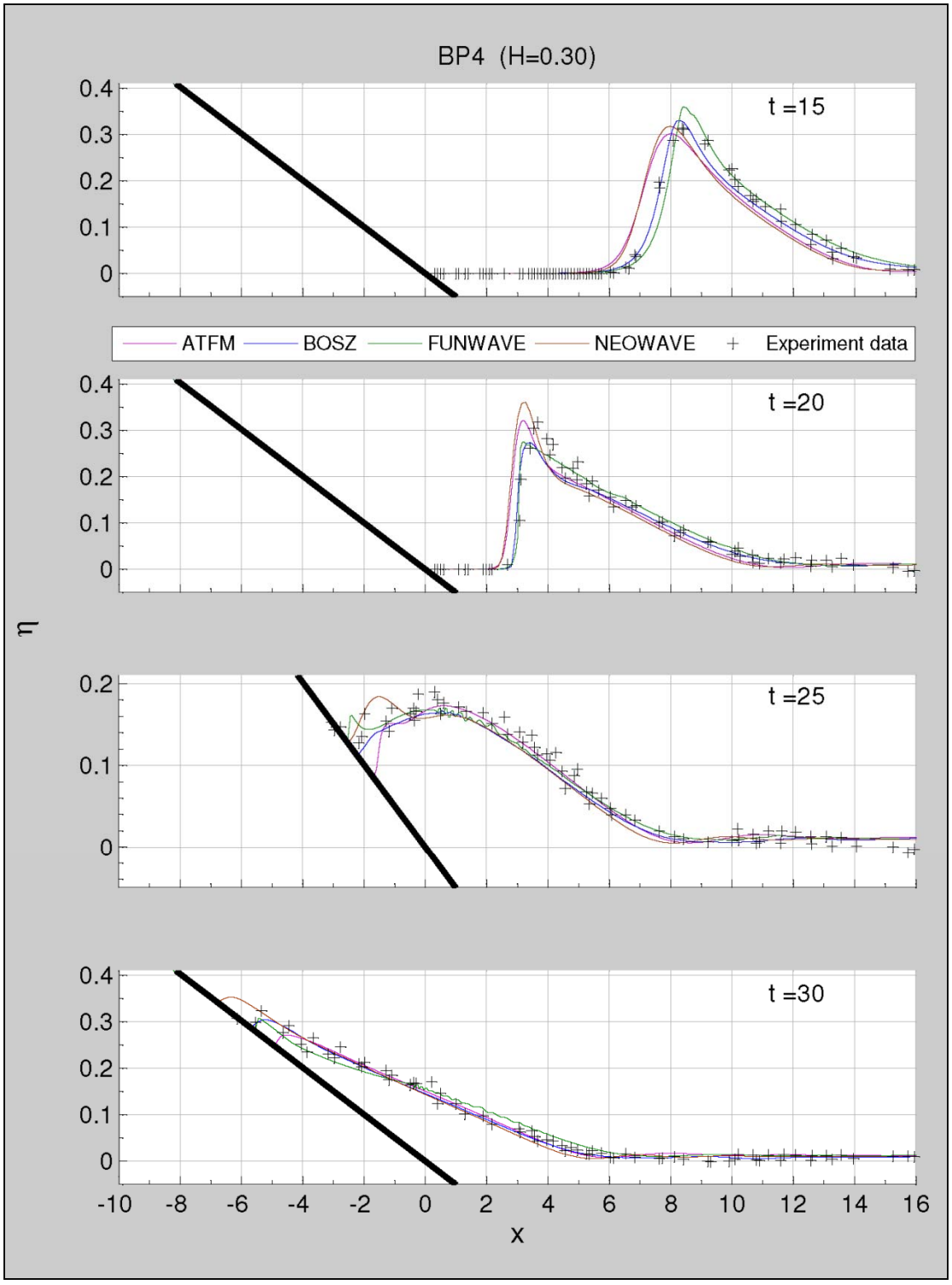

Figure 1-8: Comparison of experimental data (crosses) versus NTHMP's models surface profiles (solid lines) during runup of a breaking wave (Case B, H = 0.30) at t = [15, 20, 25, 30].

Table 1-8: BP4: NTHMP's models errors with respect to the lab experiment data. a) surface profile errors for Case A, H = 0.0185. b) surface profile errors for Case B, H = 0.30. RMS: Normalized root mean square deviations. MAX: Maximum amplitude or relative runup error.

a)

	MODEL ERROR for CASE H=0.0185											
	$t = 30$		$t = 40$		$t = 50$		$t = 60$		$t = 70$		Mean	
MODEL	RMS	MAX	RMS	MAX	RMS	MAX	RMS	MAX	RMS	MAX	RMS	Max
ALASKA	10%	9%	11%	6%	7%	17%	4%	0%	24%	16%	11%	10%
ATFM	10%	1%	8%	3%	4%	2%	5%	8%	10%	9%	7%	5%
BOSZ	13%	3%	7%	2%	4%	0%	4%	0%	10%	3%	8%	2%
FUNWAVE	11%	2%	6%	4%	3%	4%	6%	5%	14%	12%	8%	5%
GEOCLAW	11%	6%	11%	3%	7%	16%	5%	4%	22%	19%	11%	10%
MOST	10%	4%	6%	0%	5%	6%	4%	0%	19%	9%	9%	4%
NEOWAVE	10%	5%	8%	1%	5%	4%	4%	3%	12%	3%	8%	3%
SELFE	10%	3%	9%	1%	5%	3%	4%	3%	14%	2%	8%	2%
Mean	11%	4%	8%	3%	5%	7%	5%	3%	16%	9%		

b)

	MODEL ERROR for CASE H=0.30									
	$t = 15$		$t = 20$		$t = 25$		$t = 30$		Mean	
MODEL	RMS	MAX	RMS	MAX	RMS	MAX	RMS	MAX	RMS	Max
ALASKA	NA	NA	NA	NA	NA	NA	NA	NA	NA	NA
ATFM	9%	4%	11%	1%	6%	9%	3%	4%	7%	5%
BOSZ	4%	5%	7%	14%	7%	13%	3%	4%	5%	9%
FUNWAVE	5%	15%	6%	16%	5%	11%	4%	6%	5%	12%
GEOCLAW	NA	NA	NA	NA	NA	NA	NA	NA	NA	NA
MOST	NA	NA	NA	NA	NA	NA	NA	NA	NA	NA
NEOWAVE	9%	1%	13%	11%	7%	5%	4%	8%	8%	6%
SELFE	NA	NA	NA	NA	NA	NA	NA	NA	NA	NA
Mean	7%	6%	9%	11%	6%	10%	4%	6%		

1.9.7.3 Solitary Wave on Conical Island – Laboratory Experiment (BP6)

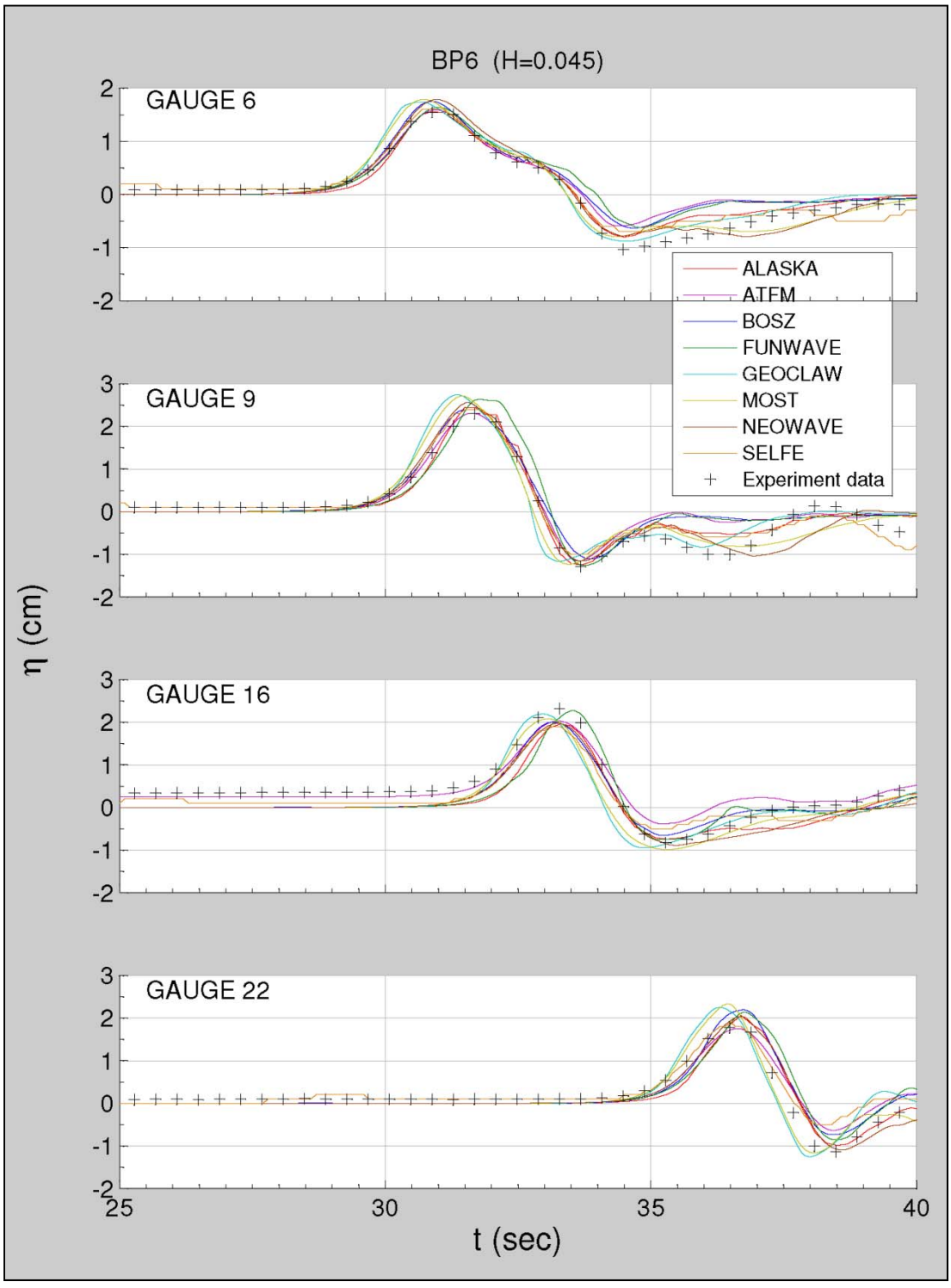

Figure 1-9: Sea level time series comparison between experimental data (crosses) versus NTHMP's models results (solid lines) of a solitary wave of H = 0.045 (Case A) at gauges shown in Figure 1-2.

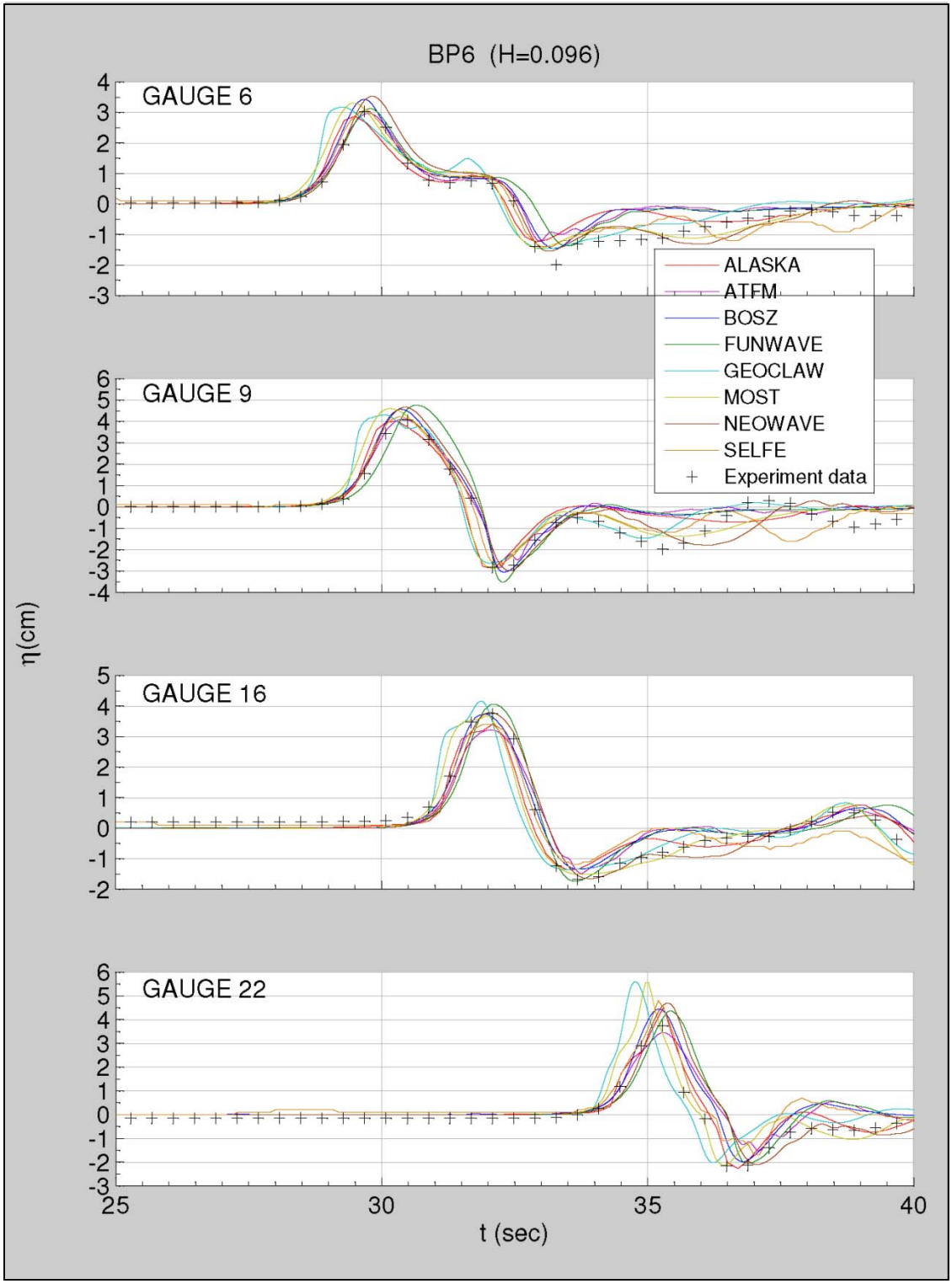

Figure 1-10: Sea level time series comparison between experimental data (crosses) versus NTHMP's models results (solid lines) of a solitary wave of H = 0.096 (Case B) at gauges shown in Figure 1-2.

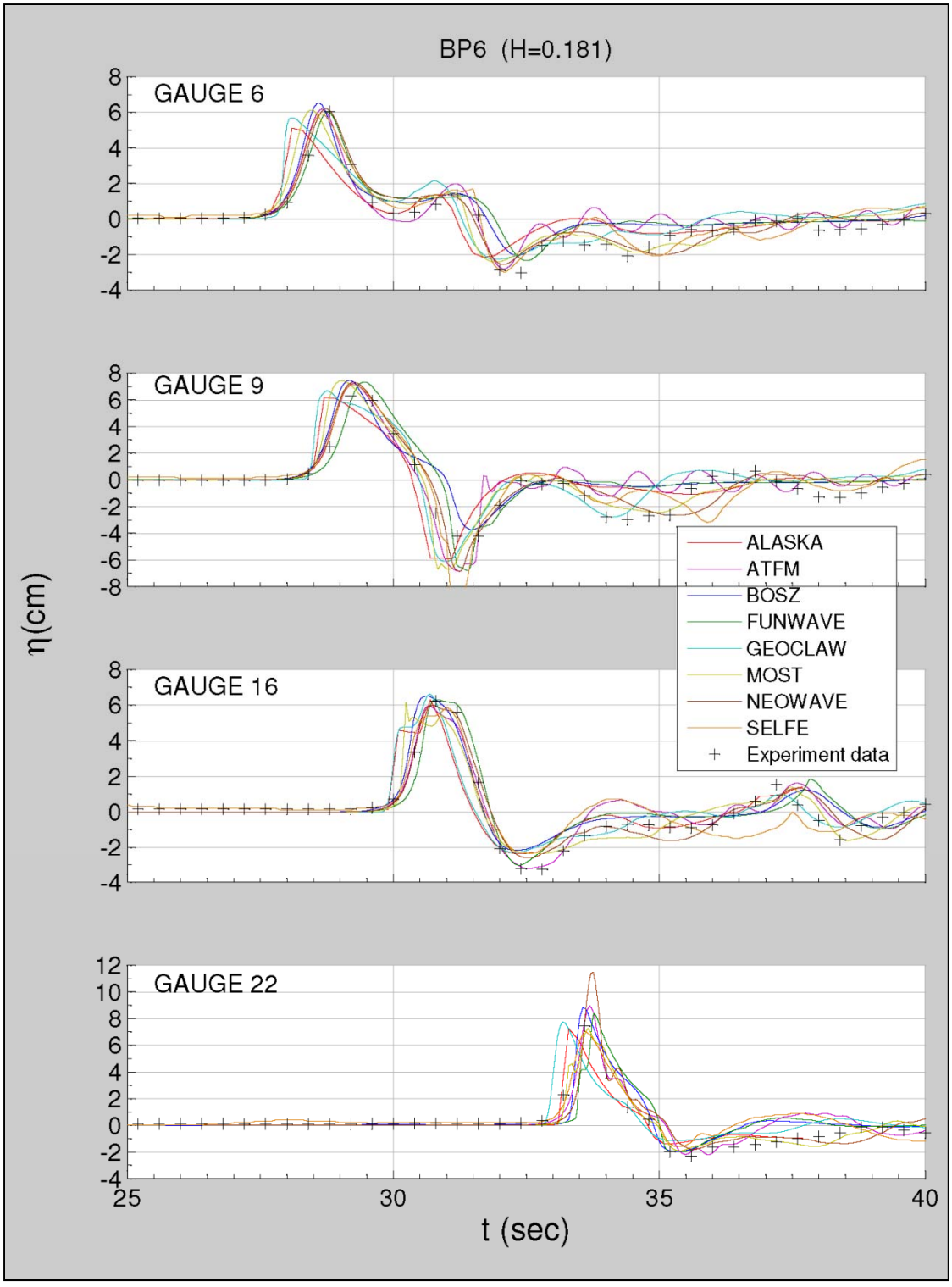

Figure 1-11: Sea level time series comparison between experimental data (crosses) versus NTHMP's models results (solid lines) of a solitary wave of H = 0.181 (Case C) at gauges shown in Figure 1-2.

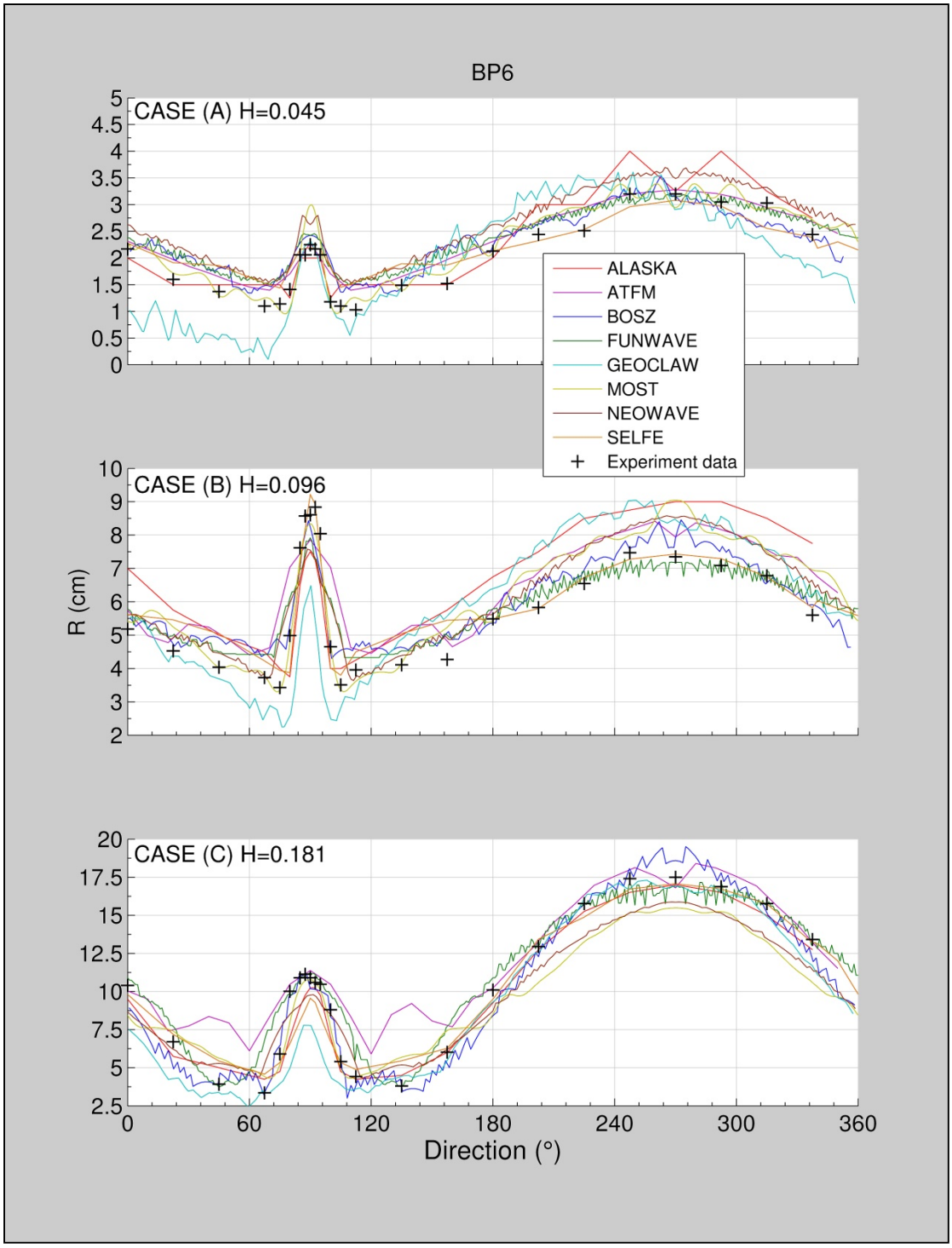

Figure 1-12: Runup comparison around a conical island between experimental (crosses) versus NTHMP models' results (solid lines) for H = [0.045, 0.096, 0.181] (Cases A, B, and C). Briggs et al. (1995)

Table 1-9: BP6: Sea level time series NTHMP models' errors with respect to laboratory experiment data. a) Case A, H = 0.045; b) Case B, H = 0.096; and c) Case C, H = 0.181. RMS: Normalized root mean square deviation error. MAX: Maximum amplitude or runup relative error.

a)

SEA LEVEL MODEL ERROR for CASE (A) H=0.045										
	Gauge #6		*Gauge #9*		*Gauge #16*		*Gauge #22*		Mean	
MODEL	RMS	MAX	RMS	MAX	RMS	MAX	RMS	MAX	RMS	Max
ALASKA	6%	0%	6%	6%	10%	15%	7%	16%	7%	9%
ATFM	9%	2%	8%	0%	8%	13%	8%	2%	8%	4%
BOSZ	9%	12%	9%	4%	8%	14%	8%	23%	9%	13%
FUNWAVE	10%	5%	10%	14%	10%	2%	10%	20%	10%	10%
GEOCLAW	6%	12%	8%	19%	10%	5%	9%	27%	8%	16%
MOST	6%	14%	8%	18%	9%	11%	7%	31%	8%	19%
NEOWAVE	6%	14%	7%	11%	9%	15%	6%	15%	7%	14%
SELFE	6%	2%	5%	4%	8%	18%	8%	7%	7%	8%
Mean	7%	8%	8%	10%	9%	12%	8%	18%		

b)

SEA LEVEL MODEL ERROR for CASE (B) H=0.096										
	Gauge #6		*Gauge #9*		*Gauge #16*		*Gauge #22*		Mean	
MODEL	RMS	MAX	RMS	MAX	RMS	MAX	RMS	MAX	RMS	Max
ALASKA	8%	6%	9%	1%	6%	9%	5%	21%	7%	9%
ATFM	8%	3%	8%	1%	6%	15%	9%	8%	8%	7%
BOSZ	8%	12%	7%	13%	6%	1%	8%	19%	7%	11%
FUNWAVE	9%	2%	9%	17%	7%	8%	12%	17%	9%	11%
GEOCLAW	9%	4%	9%	6%	9%	10%	13%	50%	10%	18%
MOST	7%	8%	8%	13%	6%	2%	8%	49%	7%	18%
NEOWAVE	6%	15%	7%	15%	5%	0%	10%	26%	7%	14%
SELFE	6%	1%	7%	3%	7%	10%	9%	28%	7%	11%
Mean	8%	6%	8%	9%	7%	7%	9%	27%		

c)

SEA LEVEL MODEL ERROR for CASE (C) H=0.181										
	Gauge #6		*Gauge #9*		*Gauge #16*		*Gauge #22*		Mean	
MODEL	RMS	MAX	RMS	MAX	RMS	MAX	RMS	MAX	RMS	Max
ALASKA	13%	16%	13%	2%	10%	1%	5%	20%	10%	10%
ATFM	8%	2%	11%	15%	6%	4%	8%	2%	8%	6%
BOSZ	7%	7%	11%	18%	7%	5%	8%	3%	8%	8%
FUNWAVE	8%	1%	11%	16%	8%	1%	11%	8%	10%	7%
GEOCLAW	10%	6%	11%	6%	9%	6%	8%	15%	10%	8%
MOST	8%	1%	9%	18%	7%	1%	6%	20%	8%	10%
NEOWAVE	5%	2%	8%	16%	6%	4%	10%	26%	7%	12%
SELFE	6%	3%	12%	13%	8%	5%	8%	22%	9%	11%
Mean	8%	5%	11%	13%	8%	3%	8%	15%		

Table 1-10: Runup NTHMP models' errors with respect to laboratory experiment data for Case A (H = 0.045), Case B (H = 0.096), and Case C (H = 0.181). RMS: Normalized root mean square deviation error. MAX: Maximum runup relative error.

	RUNUP MODEL ERROR							
	CASE (A) H=0.045		*CASE (B) H=0.096*		*CASE (C) H=0.181*		*Mean*	
MODEL	RMS	MAX	RMS	MAX	RMS	MAX	RMS	MAX
ALASKA	17%	25%	25%	2%	8%	3%	17%	10%
ATFM	13%	2%	22%	8%	15%	3%	17%	4%
BOSZ	17%	0%	13%	7%	5%	6%	12%	4%
FUNWAVE	17%	2%	16%	10%	10%	3%	14%	5%
GEOCLAW	24%	9%	24%	2%	17%	3%	22%	5%
MOST	14%	1%	13%	2%	11%	11%	13%	5%
NEOWAVE	24%	11%	18%	4%	11%	9%	18%	8%
SELFE	14%	4%	11%	4%	10%	2%	12%	3%
Mean	18%	7%	18%	5%	11%	5%		

1.9.7.4 Models Comparison: Okushiri Island – Field Measurement (BP9)

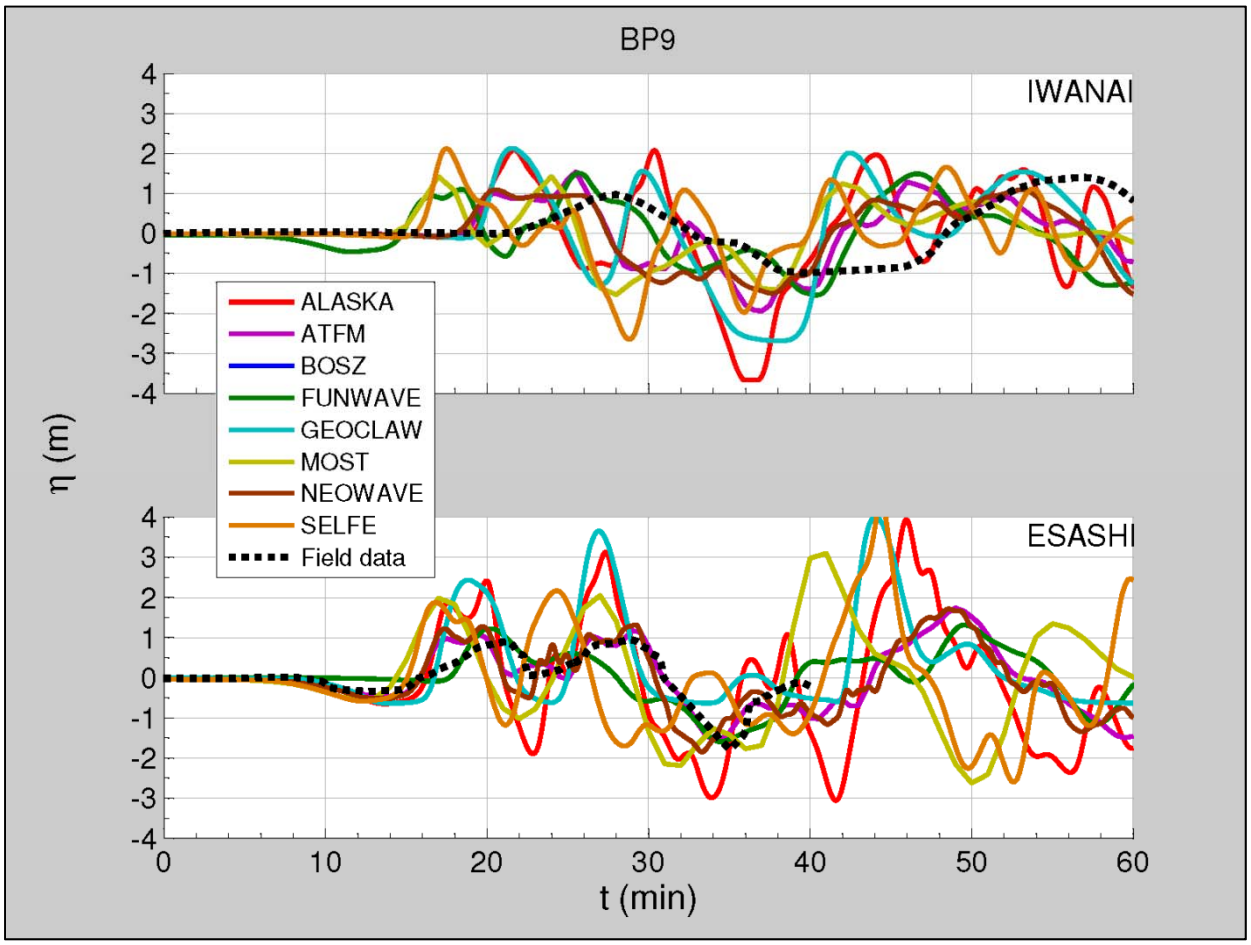

Figure 1-13: Sea level time series at two tide stations (Iwanai and Esashi) along the west coast of Hokkaido island during 1993 Okushiri tsunami. NTHMP models' results (solid lines), observed water level (dashed line). Observations courtesy of Yeh et al. (1996).

Table 1-11: BP9: NTHMP Models' relative error with respect to field measurement data, Okushiri Tsunami, 1993. a) Models' maximum amplitude error for Iwanai and Esashi gauges. b) Models' runup errors around Okushiri Island (see Figure 1-3). MAX: Maximum amplitude relative error. ERR: Runup relative error.

a)

	SEALEVEL MODEL ERROR		
	IWANAI	*ESASHI*	
MODEL	MAX	MAX	Mean
ALASKA	57%	80%	69%
ATFM	19%	8%	14%
FUNWAVE	27%	10%	19%
GEOCLAW	59%	99%	79%
MOST	23%	42%	33%
NEOWAVE	6%	14%	10%
SELFE	59%	45%	52%
Mean	36%	43%	

b)

			RUNUP MODEL ERROR							
			ALASKA	ATFM	FUNWAVE	GEOCLAW	MOST	NEOWAVE	SELFE	
Region	Longitude	Latitude	ERR	ERR	ERR	ERR	ERR	ERR	ERR	Mean
1	139.4292117	42.18818149	8%	0%	16%	0%	0%	12%	0%	5%
2	139.4111857	42.16276287	5%	5%	8%	0%	9%	21%	11%	8%
3	139.4182612	42.13740439	14%	23%	25%	41%	4%	25%	58%	27%
4	139.4280358	42.09301238		1%	4%	1%	16%	6%	12%	7%
5	139.4262450	42.11655479	0%	2%	4%	7%	11%	6%	14%	6%
6	139.4237147	42.10041415	0%	0%	0%	0%	13%	30%	0%	6%
7	139.4289018	42.07663658	22%	22%	8%	4%	29%	18%	5%	15%
8	139.4278534	42.06546152	28%	0%	0%	0%	44%	0%	0%	10%
9	139.4515399	42.04469655	0%	0%	0%	0%	0%	0%	0%	0%
10	139.4565284	42.05169226	0%	16%	37%	0%	0%	0%	0%	8%
11	139.4720138	42.05808988	11%	0%	0%	0%	0%	0%	0%	2%
12	139.5150461	42.21524909	0%	13%	0%	12%	17%	11%	14%	10%
13	139.5545494	42.22698164	15%	43%	17%	0%	21%	0%	0%	14%
14	139.4934307	42.06450128	24%	71%	16%	161%	82%	95%	71%	74%
15	139.5474599	42.18744879	10%	7%	36%	0%	5%	27%	10%	14%
16	139.5258982	42.17101221	0%	17%	8%	8%	34%	0%	13%	11%
17	139.5625242	42.21198369	4%	23%	11%	23%	1%	3%	41%	15%
18	139.5190997	42.11305805	10%	27%	16%	54%	53%	59%	20%	34%
19	139.5210766	42.15137635	3%	9%	14%	21%	24%	6%	58%	19%
		Mean	9%	15%	12%	17%	19%	17%	17%	

1.10 References

Abadie S, Caltagirone JP, Watremez P. 1998. Mecanisme de generation du jet secondaire ascendant dans un deferlement plongeant. *C. R. Mecanique*, 326:553-559.

Abadie S, Morichon D, Grilli S, Glockner S. 2010. A three fluid model to simulate waves generated by subaerial landslides. *Coastal Engineering,* 57, 9, 779-794.

Arakawa A, Lamb V. 1977. Computational design of the basic dynamical processes of the UCLA general circulation model. In: *Methods in Computational Physics*. Vol. 17. Academic Press, 174–267.

Balay S, Buschelman K, Eijkhout V, Gropp WD, Kaushik D, Knepley MG, Curfman McInnes L, Smith B, Zhang H. 2004. PETSc Users Manual. Tech. Rep. ANL-95/11 - Revision 2.1.5, Argonne National Laboratory.

Berger MJ, LeVeque RJ. 1998. Adaptive mesh refinement using wave-propagation algorithms for hyperbolic systems. 1998. SIAM *J. Numer. Anal*. 35, 2298-2316.

Berger MJ, George DL, LeVeque RJ, Mandli KT. 2011. The GeoClaw software for depth-averaged flows with adaptive refinement. *Adv. Water Res*. 34, 1195-1206.

Briggs MJ, Synolakis CE, Harkins GS, Green D. 1995 Laboratory experiments of tsunami runup on a circular island. *Pure Appl. Geophys.*, 144, 569–593.

Burwell D, Tolkova E, Chawla A. 2007. Diffusion and Dispersion Characterization of a Numerical Tsunami Model. *Ocean Modelling*, Vol.19/1-2, pp. 10-30. doi:10.1016/j.ocemod.2007.05.003

Chen Q, Kirby JT, Dalrymple RA, Kennedy AB, Chawla A. 2000. Boussinesq modeling of wave transformation, breaking, and runup. II: 2D. *J Wtrwy Port Coast and Oc Engrg* ASCE 126(1):48–56.

Dunbar PK, Weaver CS. 2008. U.S. States and Territories National Tsunami Hazard Assessment: Historical Record and Sources for Waves. Prepared for the National Tsunami Hazard Mitigation Program by NOAA and USGS. 59 pp.

Enet F, Grilli ST. 2007. Experimental Study of Tsunami Generation by Three-dimensional Rigid Underwater Landslides. *Journal of Waterway Port Coastal and Ocean Engineering*, 133(6), 442-454.

Fine IV, Rabinovich AB, Kulikov EA, Thomson RE, Bornhold BD. 1998. Numerical Modelling of Landslide-Generated Tsunamis with Application to the Skagway Harbor Tsunami of November 3, 1994. In Proceedings, International Conference on Tsunamis (Paris, 1998) pp. 211–223.

Fischer G. 1959. Ein numerisches verfahren zur errechnung von windstau und gezeiten in randmeeren. *Tellus* 11, 60–76.

Fletcher C. 1991. Computational Techniques for Fluid Dynamics 1. Springer-Verlag, 401 pp.

Gallardo JM, Parés C, Castro M. 2007. On a well-balanced high-order finite volume scheme for shallow water equations with topography and dry areas. *J. Comput. Phys.* 227, 574–601.

George DL. 2006 Finite Volume Methods and Adaptive Refinement for Tsunami Propagation and Inundation, PhD Dissertation, University of Washington.

George DL, Leveque RJ. 2006. Finite volume methods and adaptive refinement for global tsunami propagation and inundation. *Science of Tsunami Hazards* 24(5), 319–328.

Gica E, Spillane MC, Titov VV, Chamberlin CD, Newman JC. 2008. Development of the forecast propagation database for NOAA's Short-Term Inundation Forecast for Tsunamis (SIFT). NOAA Tech. Memo. OAR PMEL-139, 89 pp.

Goring DG. 1978. Tsunamis—the propagation of long waves onto a shelf. WM. Keck Laboratory of Hydraulics and Water Resources, California Institute of Technology, Report No. KH-R-38.

Goto C, Ogawa Y, Shuto N, Imamura F. 1997. Numerical method of tsunami simulation with the leap-frog scheme. Manuals and Guides 35, UNESCO: IUGG/IOC TIME Project.

Grilli ST, Watts P. 2001. Modeling of tsunami generation by an underwater landslide in a 3-D numerical wave tank. Proc. of the 11th Offshore and Polar Engrg. Conf., ISOPE01, Stavanger, Norway, 3, 132–139.

Grilli ST, Vogelmann S, Watts P. 2002. Development of a 3-D Numerical Wave Tank for modeling tsunami generation by underwater landslides. *Engineering Analysis with Boundary Elements,* 26(4), 301-313

Grilli ST, Watts P. 2005. Tsunami generation by submarine mass failure Part I : Modeling, experimental validation, and sensitivity analysis. *J. Waterway Port Coastal and Ocean Engng.*, 131(6), 283-297.

Hammack JL. 1972. Tsunamis—A model for their generation and propagation. WM. Keck Laboratory of Hydraulics and Water Resources, California Institute of Technology, Report No. KH-R-28.

Hansen W, 1956. Theorie zur errechnung des wasserstands und derstromungen in randemeeren. *Tellus* 8, 287–300.

Hirt CW, Nichols BD. , 1981. Volume of Fluid (VOF) Method for the dynamics of free boundaries. *J. of Computational Physics*, 39, pp. 201-225.

Hokkaido Tsunami Survey Group, 1993. Tsunami devastates Japanese coastal regions. EOS, Transactions AGU 74 (37), 417–432.

Horrillo J. 2006. Numerical Method for Tsunami Calculation Using Full Navier-Stokes Equations and Volume of Fluid Method. Thesis dissertation presented to the University of Alaska Fairbanks.

Horrillo J, Wood AL, Williams C, Parambath A, Kim G-B. 2009. Construction of Tsunami Inundation Maps in the Gulf of Mexico. A report to the National Tsunami Hazard Mitigation Program, NOAA.

Imamura F. 1995. Tsunami numerical simulation with the staggered leap-frog scheme. Tech. rep., School Disaster Control Research Center, Tohoku University, Manuscript for TUNAMI code, 33 pp.

Imamura F. 1996. Review of tsunami simulation with a finite difference method. In: Yeh H, Liu P, Synolakis C. (Eds.), Long-Wave Runup Models. World Scientific, pp. 25–42.

Ioualalen M, Asavanant J, Kaewbanjak N, Grilli ST, Kirby JT, Watts P. 2007. Modeling the 26 December 2004 Indian Ocean tsunami: Case study of impact in Thailand. *J. of Geophys. Res.*, 112, C-07024.

Jiang L, LeBlond PH. (1992). The coupling of a submarine slide and the surface waves which it generates. *J. Geoph. Res.*, 97(C8), 12731-12744.

Kennedy AB, Chen Q, Kirby JT, Dalrymple RA. 2000 Boussinesq modeling of wave transformation, breaking, and run-up. I: 1D. *J Wtrwy Port Coast and Oc Engrg* ASCE 126(1):39–47.

Kirby J, Grilli S. 2011. Modeling Tsunami Inundation and Assessing Tsunami Hazards for the U. S. East Coast. NTHMP Semi-Annual Report March 29, 2011. Award Number: NA10NWS4670010.

Kirby JT, Pophet N, Shi F, Grilli ST. 2009. Basin scale tsunami propagation modeling using boussinesq models: Parallel implementation in spherical coordinates. *In Proc. WCCE-ECCE-TCCE Joint Conf. on Earthquake and Tsunami (Istanbul, Turkey, June 22-24)*, paper 100:(published on CD).

Kirby JT, Shi F, Harris JC, Grilli ST. 2012. Sensitivity analysis of trans-oceanic tsunami propagation to dispersive and Coriolis effects. *Ocean Modeling*, (in preparation):42 pp.

Kirby J, Wei G, Chen Q, Kennedy A, Dalrymple R. 1998. FUNWAVE 1.0, fully nonlinear boussinesq wave model documentation and users manual. Tech. Rep. Research Report No. CACR-98-06, Center for Applied Coastal Research, University of Delaware.

Kowalik Z, Murty TS. 1993a. Numerical modeling of ocean dynamics. *World Scientific Publ*., 481 pp

Kowalik Z, Murty TS. 1993b. Numerical simulation of two-dimensional tsunami runup. *Marine Geodesy* 16, 87–100.

Kowalik Z, Whitmore PM. 1991. An investigation of two tsunamis recorded at Adak, Alaska. *Science of Tsunami Hazards*, 9, 67-83.

Kowalik Z, Knight W, Logan T, Whitmore P. 2005. Numerical modeling of the global tsunami: Indonesian Tsunami of 26 December 2004. *Science of Tsunami Hazards*, 23(1), 40-56.

LeVeque RJ. 2002. Finite Volume Methods for Hyperbolic Problems, Cambridge University Press.

LeVeque RJ, George DL, Berger MJ. 2011. Tsunami modeling with adaptively refined finite volume methods. *Acta Numerica* 2011 211-289.

Liang Q, Marche F. 2009. Numerical resolution of well-balanced shallow water equations with complex source terms. *Advances in Water Resources* 32(6):873-884.

Liu PL-F, Woo S, Cho Y. 1998. Computer programs for tsunami propagation and inundation. Tech. rep., Cornell University, 104 pp.

Liu PL-F, Lynett P, Synolakis CE. (2003): Analytical solutions for forced long waves on a sloping beach. *J. Fluid Mech., 478*, 101–109.

Lubin P, Vincent S, Abadie S, Caltagirone JP. 2006. Three-dimensional Large Eddy Simulation of air entrainment under plunging breaking waves. *Coastal Engineering*, Volume 53, issue 8, .631-655.

Lynett P, Wu T-R., Liu PL-F. 2002. Modeling wave runup with depth-integrated equations. *Coastal Engineering* 46(2), 89–107.

Ma G, Shi F, Kirby JT. 2012. Shock-capturing non-hydrostatic model for fully dispersive surface wave processes. *Ocean Modeling*, 43-44:22–35.

Mader CL. 1988. Numerical Modeling of water waves. University of California Press, Berkeley, California.

Mader C, Lukas S. 1984. SWAN-A Shallow Water, Long Wave Code. Tech. Rep. HIG-84-4, Hawaii Institute of Geophysics, University of Hawaii.

Nichols BD, Hirt CW, Hotchkiss RS. 1980. SOLA-VOF: a solution algorithm for transient fluid flow with multiple boundaries. Los Alamos Scientific Laboratory Report, LA-8355.

Nicolsky DJ, Suleimani EN, Hansen RA. 2010. Validation and Verification of a Numerical Model for Tsunami Propagation and Runup. *Pure Appl. Geophys*. 168 (2011), 1199–1222.

Nwogu O. 1993. Alternative form of Boussinesq equations for near shore wave propagation. *J. Wtrwy., Port, Coast., and Oc. Engrg.*, ASCE, 119(6), 618–638.

Okada Y. 1985. Surface deformation due to shear and tensile faults in a half-space. *Bulletin of the Seismological Society of America* 75, 1135–1154.

Peregrine D. 1967. Long waves on a beach. *Journal of Fluid Mechanics* 27(4), 815–827.

Priest GR, Goldfinger C, Wang K, Witter RC, Zhang Y, Baptista AM. 2010 Confidence levels for tsunami-inundation limits in northern Oregon inferred from a 10,000-year history of great earthquakes at the Cascadia subduction zone. *Natural Hazards*, 54(1), 27-73.

Roeber V. 2010. Boussinesq-type model for nearshore wave processes in fringing reef environment. PhD Dissertation, University of Hawaii, Honolulu.

Shi F, Kirby JT, Harris JC, Geiman JD, Grilli ST. 2012. A highorder adaptive time-stepping TVD solver for Boussinesq modeling of breaking waves and coastal inundation. *Ocean Modeling*, 43-44:36–51.

Stelling GS, Duinmeijer SPA, 2003. A staggered conservative scheme for every Froude number in rapidly varied shallow water flows. *Int. J. Numer. Meth. Fluids*; 43:1329–1354 (DOI: 10.1002/fld.537)

Stelling GS, Zijlema M. 2003. An accurate and efficient finite-difference algorithm for non-hydrostatic free-surface flow with application to wave propagation. *International Journal for Numerical Methods in Fluids*, 43(1), 1-23.

Suleimani E, Hansen R, Haeussler P. 2009. Numerical study of tsunami generated by multiple submarine slope failures in Resurrection Bay, Alaska, during the M9.2 1964 earthquake. *Pure appl. geophys., v. 166, 131-152, doi: 10.1007/s00024-004-0430-3*.

Swigler DT, Lynett P. (2011) Laboratory study of the three-dimensional turbulence and kinematic properties associated with a solitary wave traveling over an alongshore-variable, shallow shelf. In review.

Synolakis CE. 1986 The Runup of Long Waves. Ph.D. Thesis, California Institute of Technology, Pasadena, California, 91125, 228 pp.

Synolakis CE, Bernard EN, Titov VV, Kanoglu U, González FI. 2007. OAR PMEL-135 Standards, criteria, and procedures for NOAA evaluation of tsunami numerical models. Technical report, NOAA Tech. Memo. OAR PMEL-135, NOAA/Pacific Marine Environmental Laboratory, Seattle, WA.

Takahashi T. 1996. Benchmark problem 4; the 1993 Okushiri tsunami—Data, conditions and phenomena. In *Long-Wave Runup Models*, World Scientific, 384–403.

Tappin DR, Watts P, Grilli ST. 2008. The Papua New Guinea tsunami of 17 July 1998: anatomy of a catastrophic event. *Nat. Hazards Earth Syst. Sci.* 8, 243–266.

Thacker C-T. 1981. Some exact solutions to the nonlinear shallow-water wave equations. *J.Fluide Mech*., vol.107, pp.499-508, 1981.

Thomson RE, Rabinovich AB, Kulikov EA, Fine IV, Bornhold BD. 2001. On numerical simulation of the landslide-generated tsunami of November 3, 1994 in Skagway Harbor, Alaska. In: Hebenstreit G. (Ed.), Tsunami Research at the End of a Critical Decade. Kluwer, Dorderecht, pp. 243–282.

Titov V, Synolakis C. 1995. Evolution and runup of breaking and nonbreaking waves using VTSC2. *Journal of Waterway, Port, Coastal and Ocean Engineering* 121 (6), 308–316.

Titov VV, Synolakis CE, 1998. Numerical modeling of tidal wave runup. *J. Waterw. Port Coast. Ocean Eng.*, 124(4), 157-171.

van Leer B. 1977, Towards the ultimate conservative difference scheme III. Upstream-centered finite-difference schemes for ideal compressible flow. *J. Comp. Phys*. 23 (3): 263–275

Walters RA. 2005. A semi-implicit finite element model for non-hydrostatic (dispersive) surface waves. *International Journal for Numerical Methods in Fluids* 49(7):721–737.

Watts P, Grilli ST, Tappin D, Fryer GJ. 2005. Tsunami generation by submarine mass failure Part II: Predictive Equations and case studies. *J. Waterway Port Coastal and Ocean Engng.*, 131(6), 298-310

Wei G, Kirby JT. 1995 Time-dependent numerical code for extended Boussinesq equations. *J Wtrwy Port Coast and Oc Engrg* ASCE 121(5):251–261

Wei G, Kirby JT, Grilli ST, Subramanya R. 1995 A fully nonlinear Boussinesq model for free surface waves. Part 1: highly nonlinear unsteady waves. *J Fluid Mech* 294:71–92

Whitmore PM, Sokolowski TJ. (1996). Predicting tsunami amplitudes along the North American coast from tsunamis generated in the northwest Pacific Ocean during tsunami warnings. *Science of Tsunami Hazards*, 14, 147-166.

Witter R, Zhang Y, Wang K, Priest G, Goldfinger C, Stimely L, English J, Ferro P. 2011. Simulating tsunami inundation at Bandon, Coos County, Oregon, using hypothetical Cascadia and Alaska earthquake scenarios. Special paper 43, Oregon Department of Geology and Mineral Industries.

Wu Y, Cheung KF. 2008. Explicit solution to the exact Riemann problem and application in nonlinear shallow-water equations. *International Journal for Numerical Methods in Fluids*, v. 57, pp 1649-1668.

Yamazaki Y, Kowalik Z, Cheung KF. 2009. Depth-integrated, nonhydrostatic model for wave breaking and run-up. *Int. J. Numer. Methods Fluids*, 61(5), 473–497.

Yamazaki Y, Cheung KF, Kowalik Z. 2011. Depth-integrated, non-hydrostatic model with grid nesting for tsunami generation, propagation, and run-up. *Int. J. Numerical Methods Fluids*, 67(12), 2081-2107.

Yeh H, Liu PL-F, Briggs M, Synolakis CE. 1994. Tsunami catastrophe in Babi Island. *Nature,* 372, 6503–6508.

Yeh H, Liu PL-F, Synolakis CE. 1996. *Long-Wave Runup Models*. World Scientific, 403 pp.

Zhang Y, Baptista AM. 2008a SELFE: A semi-implicit Eulerian-Lagrangian finite-element model for cross-scale ocean circulation. *Ocean Modelling*, 21(3-4), 71-96.

Zhang Y, Baptista AM. 2008b An Efficient and Robust Tsunami Model on Unstructured Grids. Part I: Inundation Benchmarks. *Pure and Applied Geophysics*, 165, 2229–2248.

Zhang Y, Witter RW, Priest GP. 2011 Nonlinear Tsunami-Tide Interaction in 1964 Prince William Sound Tsunami. *Ocean Modelling* (submitted).

2 Alaska Tsunami Model

Dmitry Nicolsky

Geophysical Institute of the University of Alaska Fairbanks and the State of Alaska Division of Geological & Geophysical Surveys

2.1 Introduction

NTHMP-funded efforts in Alaska are focused on improvement of the emergency response to the tsunami hazards in coastal communities. Typical tsunami-related hazards originate from vertical and horizontal coseismic tectonic displacements and the failure of unconsolidated materials from above and below the sea surface.

To help mitigate the tsunami hazards, we subject our tsunami model, developed at the Geophysical Institute, University of Alaska Fairbanks, to a series of benchmark problems proposed by Synolakis et al., (2007). The benchmark problems deal with validating and verifying the ability of the model to accurately simulate a tsunami caused by vertical coseismic tectonic displacement or by the failure of unconsolidated material. There is, however, no benchmark problem focused on validating the model's ability to simulate seiche waves caused by lateral coseismic displacements. In certain Alaska fjords, lateral tectonic displacements might produce a seiche wave comparable in size with a landslide-generated tsunami (Plafker et al., 1969).

In this report, we provide a brief description of three tsunami models used to predict a potential inundation. Each model addresses one of the above-mentioned tsunami hazards.

2.2 Model description

The suit of numerical models employed by the State of Alaska for the tsunami inundation mapping project comprises:

- Tectonic tsunami model
- Landslide-generated tsunami model
- Seiche tsunami model

2.2.1 Tectonic tsunami model

This is a numerical model that has been described and tested through a set of analytical, laboratory, and field benchmark problems (Nicolsky et al., 2011). This model solves nonlinear shallow water equations, commonly used to predict the propagation of long waves in the ocean and the inundation of coastal areas (Synolakis and Bernard, 2006).

The water depth, η, and the horizontal water velocity, **u,** in the ocean are described in the spherical coordinates by the mass and linear momentum conservation principles:

$$\frac{\partial}{\partial t}\eta + \nabla \cdot (\eta \mathbf{u}) = 0, \tag{1}$$

$$\frac{\partial}{\partial t}(\eta \mathbf{u}) + \nabla \cdot (\eta \mathbf{uu}) + g\eta \nabla \xi + f\eta(\mathbf{e}_r \times \mathbf{u}) + \eta \boldsymbol{\tau} = 0, \quad (2)$$

Here,

$$\xi = h + \eta \quad (3)$$

is the water level, h is the bathymetry, g is the acceleration of gravity, f is the Coriolis parameter, $\mathbf{e_r}$ and $\mathbf{e}_r$ is the outward unit normal vector on the sphere. The system of equations (1) and (2) is approximated in spherical coordinates by finite differences on Arakawa C-grid (Arakawa and Lamb, 1977). The spatial derivatives are discretized by central difference and upwind difference schemes (Fletcher, 1991). The friction term $\boldsymbol{\tau}$ is discretized by a semi-implicit scheme according to Goto et al. (1997). Equations (1) and (2) are solved semi-implicitly in time using a first order scheme (Kowalik and Murty, 1993). The finite difference scheme is coded in FORTRAN using the Portable, Extensible Toolkit for Scientific computations (Balay et al., 2004) and the MPI standard (Gropp et al., 1999).

The initial water deformation is assumed to be equal to a coseismic uplift and subsidence of the sea floor. The vertical displacement can be set arbitrarily or computed by Okada (1985) formulae, requiring the epicenter location, area, dip, rake, strike, and amount of slip on the fault.

2.2.2 Landslide-generated tsunami model

To simulate tsunamis produced by underwater slope failures, we use a numerical model of a viscous underwater slide with full interactions between the deforming slide and the water waves that it generates. The shallow viscous slide equations are coupled with shallow water equations (1) and (2) by substituting equation (3) with

$$\xi = h + \eta + s$$

where s is the landslide thickness. The thickness is computed according to the model initially proposed by Jiang and LeBlond (1992), improved by Fine et al. (1998). The full system of equations is provided by Suleimani et al. (2011), who successfully used it to model landslide-generated tsunami in Resurrection Bay, Alaska. The Fine model's assumptions and applicability to simulating underwater mudflows are discussed by Jiang and LeBlond (1992, 1994) in their formulation of the viscous slide model. The model uses long-wave approximation for water waves and the deforming slide, which means that the wavelength is much greater than the local water depth, and the slide thickness is much smaller than the characteristic length of the slide along the slope (Jiang and LeBlond, 1994).

2.2.3 Seiche tsunami model

Nicolsky and others, (2010) considered a fixed coordinate system to model runup of the seiche tsunami by considering motion of the reservoir by solving equations (1) and (2), while taking into account that h = h(x,y,t). If there is no vertical displacement and the lateral ground velocity, $\mathbf{u}_g$, is known then

$$\frac{\partial h}{\partial t} + \nabla h \cdot \mathbf{u}_g = 0. \quad (4)$$

To facilitate computations, it is convenient to simulate water dynamics in the reference frame moving with the land. The change of reference coordinate systems, i.e., from a fixed system to a moving one, introduces new terms into the original mass and momentum conservation principles,

i.e., equations (1) and (2), respectively. At the same time, equation (4) reduces to h = const and thus the final system of equations is

$$\frac{\partial}{\partial t}\eta - \nabla\eta\cdot\mathbf{u}_g + \nabla\cdot(\eta\mathbf{u}) = 0 \tag{1a}$$

$$\frac{\partial}{\partial t}(\eta\mathbf{u}) - \nabla\eta\mathbf{u}\cdot\mathbf{V}_L + \nabla\cdot(\eta\mathbf{u}\mathbf{u}) + g\eta\nabla\xi = 0. \tag{2a}$$

Equations (1a) and (2a) are discretized in Cartesian coordinates by finite differences on Arakawa C-grid (Arakawa and Lamb, 1977). The spatial derivatives are discretized by central difference and upwind difference schemes (Fletcher, 1991). The runup is modeled by the method employed to simulate the runup of tectonic waves (Nicolsky, 2011).

2.3 Benchmark results

2.3.1 BP1: Solitary wave on simple beach – analytical

We verify our numerical method by comparing numerical and analytical solutions that describe 1-D solitary wave runup. The analytical solution to a specific solitary wave runup on the sloping beach was derived by Synolakis (1986). In this problem, the wave of height *H* is initially centered at distance *L* from the beach toe and is schematically shown in Figure 2-1.

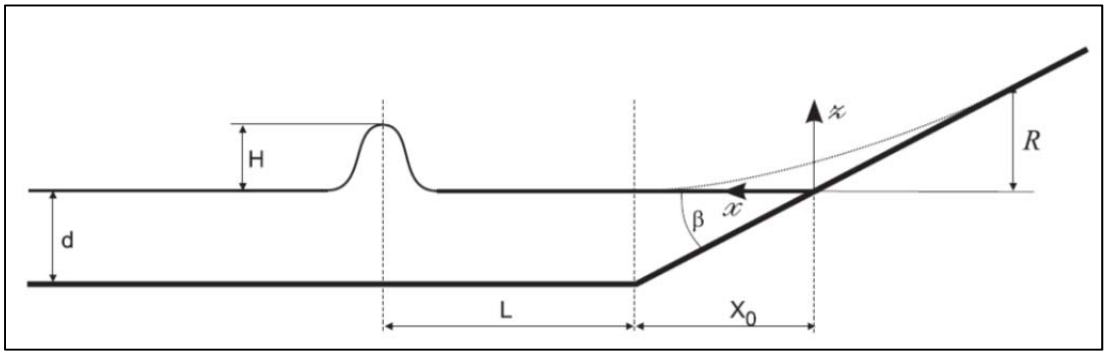

Figure 2-1: Non-scaled sketch of a canonical beach with a wave climbing up.

The value of L = arccosh (√20)/γ is the half-length of the solitary wave, and the initial depth profile is given by

$$\eta(x,0) = H\sec h^2(\lambda(x - X_1)/d),$$

where $X_1 = X_0 + L$, and $\gamma = \sqrt{3H/4d}$. The initial wave-particle velocity in the computer experiments is set, following Titov and Synolakis (1995), as:

$$u(x,0) = \sqrt{g/d}\ \eta(x,0).$$

First, we check the ability of the method to model runup on a beach by simulating the runup of a solitary wave when *d* = 1, 100, and 500 m, and then comparing the numerical and analytical solutions. In these numerical experiments, the 1-D domain, with total length 400d, is discretized with spacing Δx = d/20. The computational time step $\Delta t = 10^{-3}\sqrt{d/g}$ satisfies the Courant-Friedrichs-Levy stability criterion (Courant et al., 1928). The results suggest that the computed nondimensional variables such as η/d, **v**/√gd do not depend on the value of d, and further that the numerical predictions are in good agreement with analytical solutions for *H/d* = 0.019. We

discuss comparison of numerical and analytical solutions for H/d = 12 0.019 in greater detail later in this section. For error analysis, the water mass before and after wave reflection from the beach is calculated, finding a total mass decrease of less than 0.01% in each case. This negligibly small error in the mass conservation is well within established criteria (Synolakis et al., 2007).

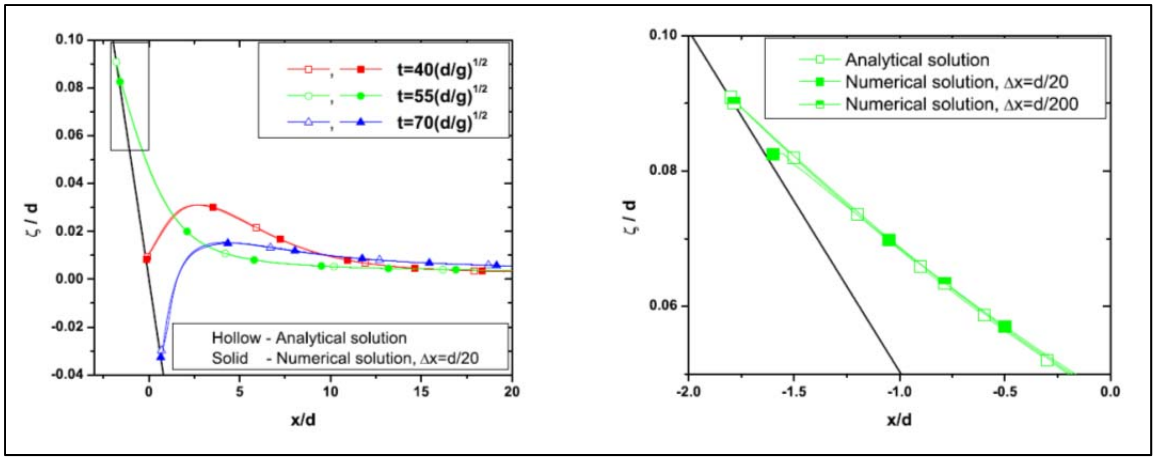

Figure 2-2: Left plot: comparison between the analytically and numerically computed solutions simulating runup of the non-breaking wave in the case of H/d = 0.019 on the 1:19.85 beach. Right plot: an enlarged version of the left plot within the rectangle region. Two numerical solutions computed on grids with Δx = d/20 and Δx = d/200 are shown at t = 55√d/g. The numerical solution is shown to be converging to the analytical one as the spatial discretization is refined. The analytical solution is according to Synolakis (1986).

A focus in developing a tsunami modeling algorithm is to simulate extreme positions of the shoreline–the maximum runup and rundown. Figure 2-2 shows computed water surface profiles at the maximum runup and rundown of a solitary wave in the case of H/d = 0.019. The maximum runup in the numerical simulation occurs at $t \approx 55\sqrt{d/g}$ and this solution has a 15% error with respect to the derived analytical solution. After refining the computational grid from $\Delta x = d/20$ to $\Delta x = d/200$, the analytically and numerically computed maximum runup values differ by less than 2%, which is within the recommended criteria (Synolakis et al., 2008). We additionally checked convergence of numerically computed maximum rundown to its analytical prediction. For the computational grid with $\Delta x = d/20$, the difference between the numerical and analytical rundown values is at most 16%. After the grid refinement to $\Delta x = d/200$, the difference is less than 3%. The results show that the numerical solution converges to the analytical prediction at the extreme locations of the shoreline, and that the recommended 5% error in numerical solution is achieved.

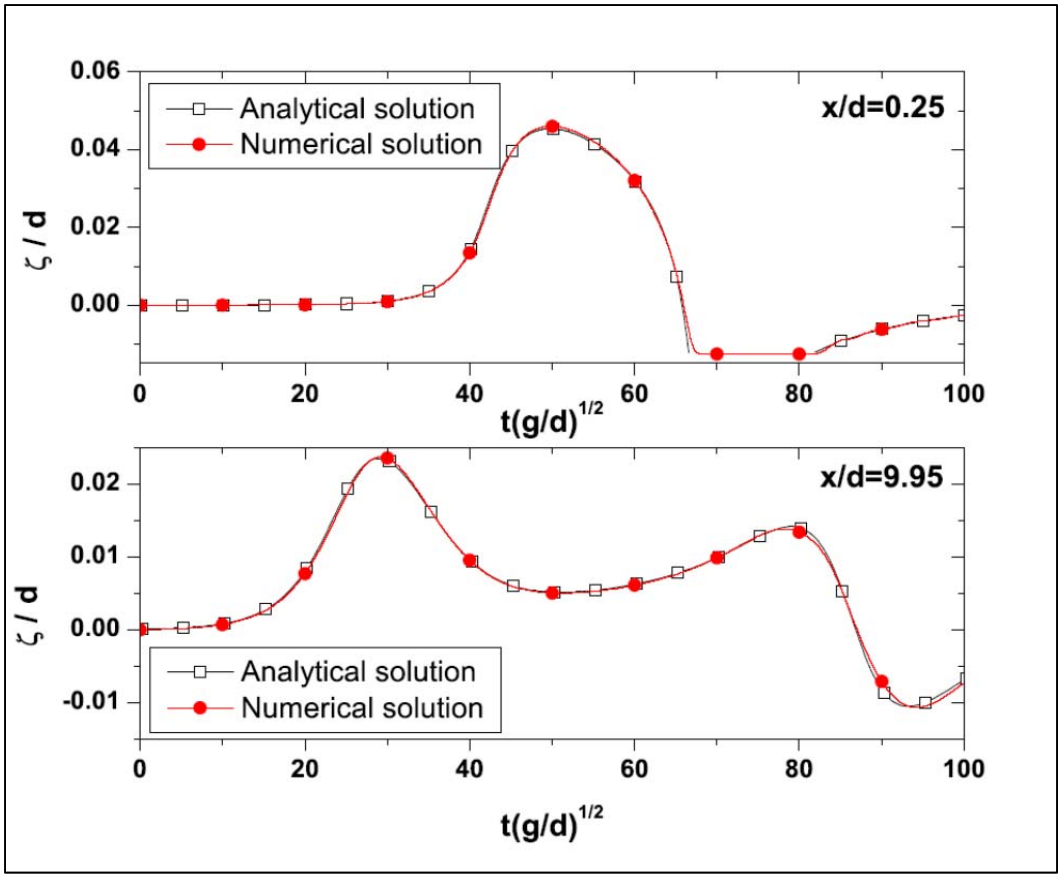

Figure 2-3: Comparison between the analytical solution (hollow symbols) and the finite difference solution (filled symbols) during the runup of the non-breaking solitary wave with H/d = 0.019 on 1:19.85 beach. The top and bottom plots represent comparisons at x = 0.25d and x = 9.95d, respectively. The analytical solution is according to Synolakis (1986).

Figure 2-3 shows numerically and analytically computed water level dynamics at locations x/d = 0.25 (near the initial shoreline) and x/d = 9.95 (between the beach toe and initial wave crest) during propagation and reflection in the case H/d = 0.019. During rundown, both numerical and analytical solutions show that water retreats from $t = 67\sqrt{d/g}$ to $t = 82\sqrt{d/g}$, and the point x/d = 0.25 temporally becomes dry, while the point x/d = 9.95 remains wet throughout the entire length of the computer experiment. Comparison of the analytical and numerical solutions at these two points reveals that the computational error is typically less that 2% for $\Delta x = d/20$, and that the agreement between the two solutions is quite good even on the coarse grid.

2.3.2 BP2: Solitary wave on composite beach – analytical

Typically, a real-life beach has an irregular bathymetry, which is much more complicated than the one described in the previous benchmark problem. One of the simplest approximations to the irregular bathymetry is obtained by utilizing piece-wise linear functions. Kânoğlu and Synolakis (1998) developed an exact analytical solution to the linearized shallow water equations (1-2) in order to predict propagation and runup of wave over the piece-wise linear beach. In this benchmark, we compare our finite difference solution to the analytical solution (Kânoğlu and Synolakis, 1998) in the case of waves propagating over a composite beach.

A composite beach simulating the geometrical dimensions of Revere Beach, Massachusetts, was built in a U.S. Army Corps of Engineers, Coastal Engineering Research Center in Vicksburg, Mississippi. The beach consists of three piece-wise linear segments and a vertical wall, shown in Figure 2-4.

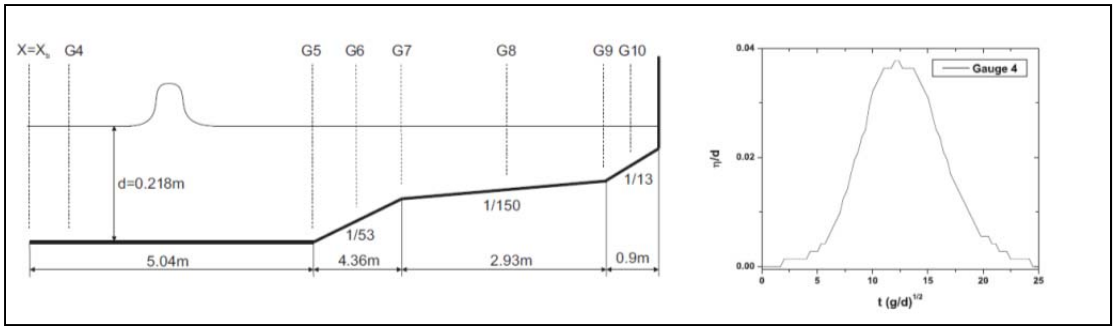

Figure 2-4: Left, non-scaled sketch of the composite beach modeling Revere Beach, Massachusetts. Vertical lines mark the locations of gauges measuring the water level in laboratory experiments. Right, an incident wave recorded by Gauge 4. This record was used to set the water height $h(X_b; t)$ at the inflow boundary condition.

The laboratory equipment and the beach profile are described in Yeh, et al. (1996) and Kânoğlu and Synolakis (1998). The slopes of the segments, starting from the wall, are 1 = 13, 1 = 150, and 1 = 53, respectively. At the beginning and in the middle of each sloping segment a water gauge measuring time dynamics of the water surface height was installed

We compare our numerical solution to the analytical solution modeling propagation of waves over the composite beach. We note that in the numerical experiments, we neglect all non-linearities in (1-2) and solve the linear shallow water equations. In Figure 2-5, we show the comparison between the analytical solution (5) and the obtained numerical solution at the locations where the gauges were installed. The numerical solution was computed using the grid size $\Delta x \approx d/20$, where the quantity d stands for the still water equal to 0:218 m at Gauge 4. Analyzing the results, we observe that the numerical solution closely matches the analytical one, and the difference between them is typically less than 5%.

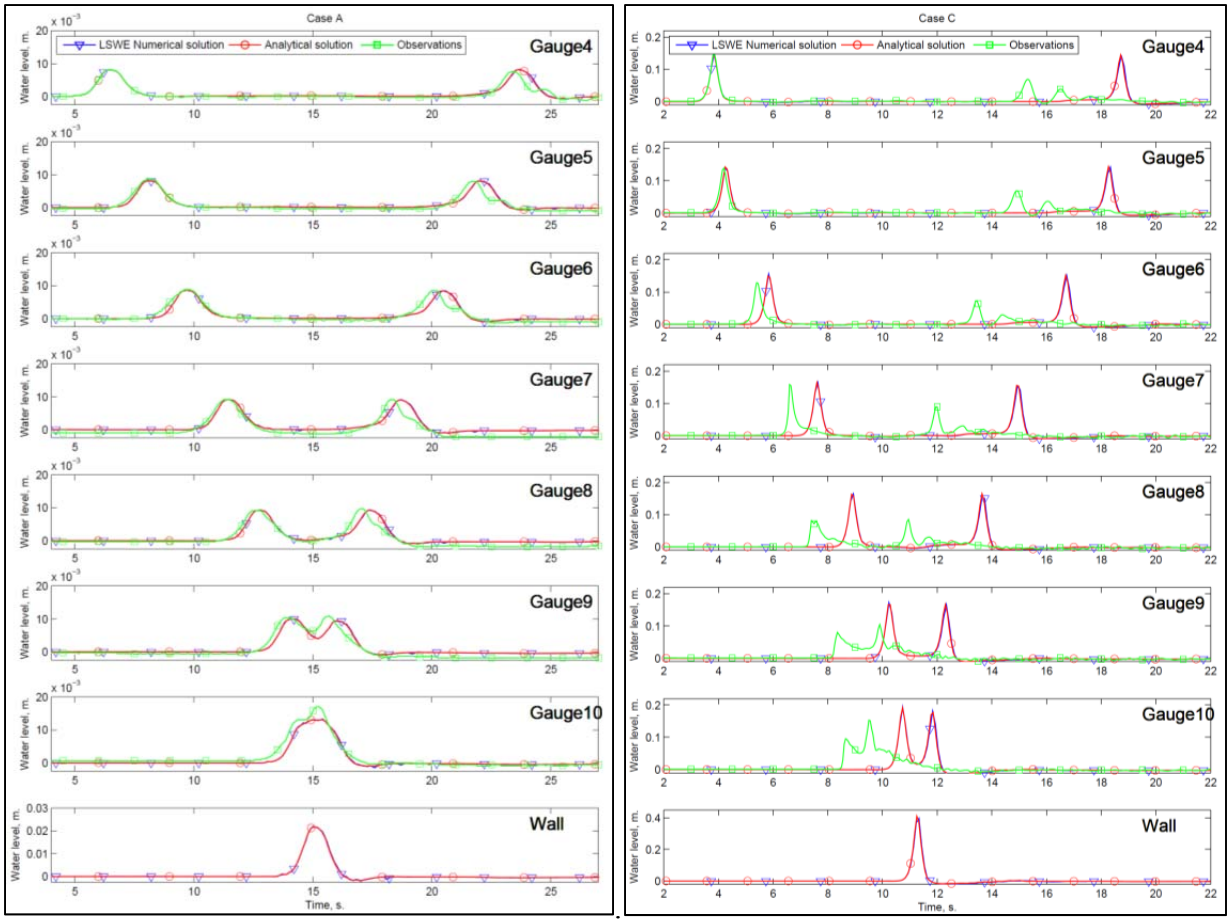

Figure 2-5: Comparison between the analytically and numerically computed solutions at the gauge locations shown in Figure 2-4. Left plot: Case A, Right plot Case C.

2.3.3 BP3: Subaerial landslide on simple beach – analytical

Liu et al. (2003) considered tsunami generation by a moving slide on a uniformly sloping beach, using the forced linear shallow water-wave equation as in Tuck and Hwang (1972);

$$\frac{\partial^2 \xi}{\partial t^2} - \frac{\tan\beta}{\mu}\frac{\partial}{\partial x}\left(x\frac{\partial \xi}{\partial x}\right) = \frac{\partial^2 s}{\partial t^2}, \qquad x \geq 0,$$

where the quantities β and μ specify the beach slope. Following Liu et al. (2003), Synolakis et al. (2007) consider a translating Gaussian shaped mass, described by $s(x,t) = \exp(-(\xi - t)^2)$ with $\xi^2 = 4\mu x/\tan\beta$. The analytical solution for this translating Gaussian shape is given by Liu et al. (2003)

The goal of this benchmark problem is to compare the numerical predictions with the analytical solution. Figure 2-6 presents a comparison between the analytical and numerical solutions to equations (1) and (2). Note that the analytical solutions and the numerical solutions to the linear shallow water equations are derived using two different boundary conditions. Therefore, the discrepancy between these solutions is rather large.

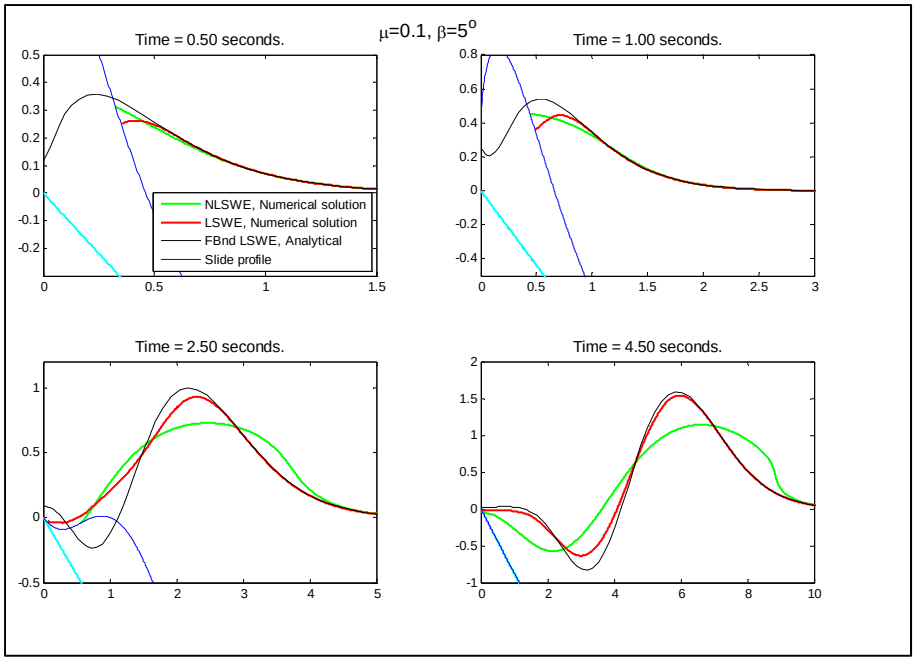

Figure 2-6: Comparison between the analytically and numerically computed solutions at several moments of time. LSWE and NLSWE stand for the numerical solutions computed with linear and non-linear assumptions, respectively. The analytical solution is according to Liu et al. (2003).

2.3.4 BP4: Solitary wave on simple beach – laboratory

More than 40 laboratory experiments were conducted in the wave tank by Synolakis (1986). In this benchmark problem, we perform numerical modeling of the water dynamics observed during these experiments. In the computer experiment, we assume that the wave tank is 400d in length and discretized by a uniformly spaced grid with $\Delta x = d/200$. To model common geophysical conditions, we assume that d = 500 m, although scalability shows that appropriately scaled results do not depend on d. Additionally, we assume that there is no bottom friction, i.e., $v = 0$. We analyze the effects of bottom friction on water dynamics later in this sub-section.

In the first series of laboratory experiments, the runup of a non-breaking solitary wave with $H/d = 0.019$ is studied. We plot laboratory measured water level by black rectangles in Figure 2-7. In the same Figure, the numerical and analytical solutions are plotted by lines with solid and hollow triangles, respectively. Agreement between analytical and numerical computed solutions is more than sufficient for all snapshots; the discrepancy between the solutions is much smaller than the discrepancy between any one of the solutions and the laboratory data.

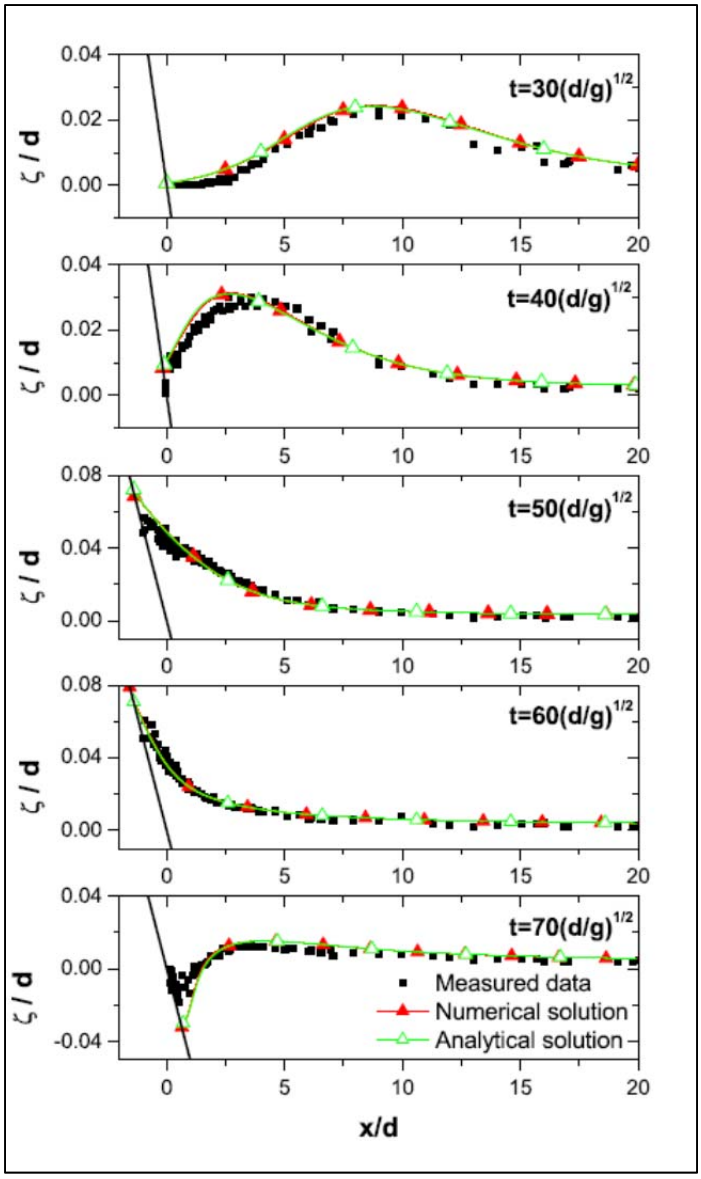

Figure 2-7: Comparison of observed and simulated water profiles during runup of a non-breaking wave in the case of H/d = 0.019. Observations are shown by dots. The analytical predictions and numerical calculations are marked by hollow and filled symbols, respectively. The measurements are provided courtesy of Synolakis (1986).

The computed solutions have slightly higher runup than observations, and the computed maximum runup also exceeds the physical measurements, visible in Figure 2-8 where we show the numerically modeled and observed waterfront path $X_w(t)$. Here, the measured data are plotted by rectangles while the computed path is plotted by a line with hollow triangles. For a detailed analysis of the discrepancy between the analytical solution and laboratory results, which we prescribe to the zero friction assumption in the computer modeling, we refer interested readers to Synolakis (1986).

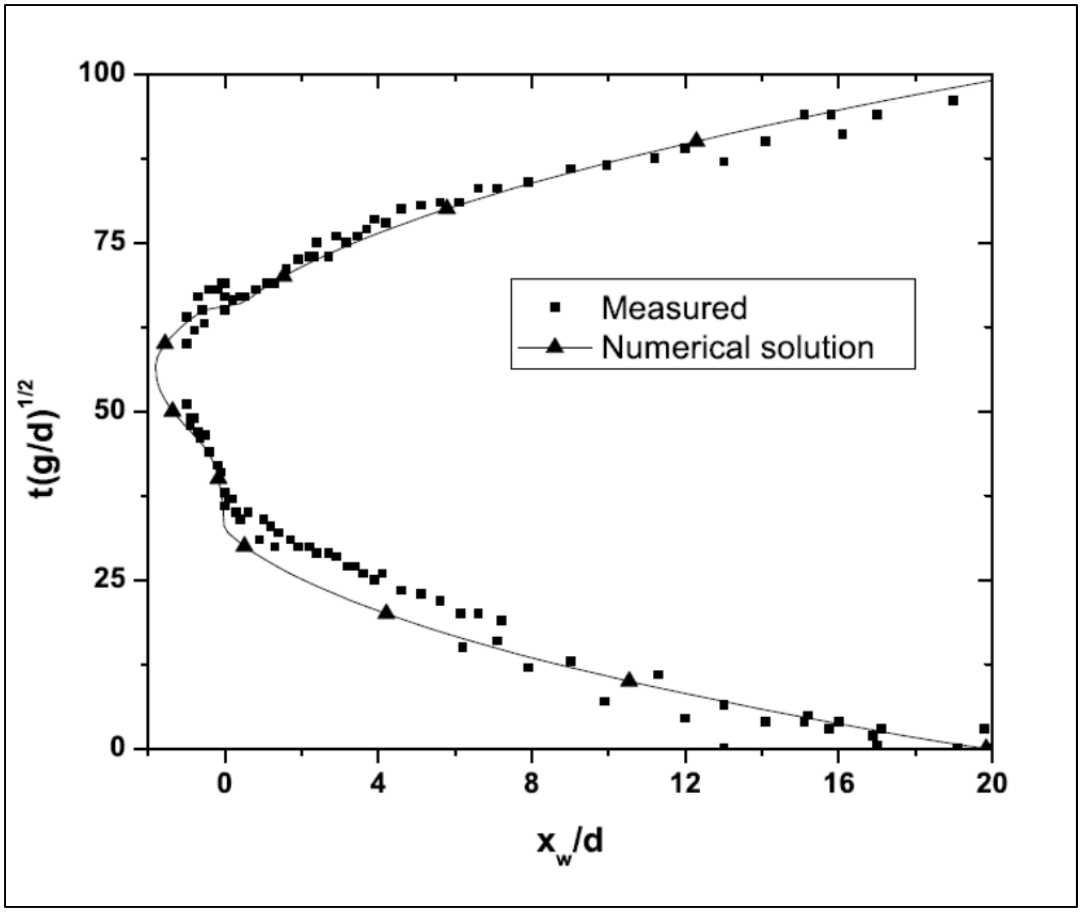

Figure 2-8: Laboratory measured and simulated waterfront path X_w of a solitary wave running up on a canonical beach. Measurements are represented by squares and numerical simulations by a line. The measurements are provided courtesy of Synolakis (1986).

In the second series of laboratory experiments, a solitary wave with the initial amplitude H/d = 0.04 propagates and inundates the sloping beach. We display laboratory data by black rectangles and the results of numerical modeling by lines with solid triangles in Figure 2-9. According to analytical predictions derived using the zero bottom friction assumption, the solitary wave breaks only if its initial height satisfies $H/d \geq 0.029$ (Synolakis, 1987). The ratio of $H/d = 0.04$ for which the laboratory data are collected satisfies this condition, so a breaking wave is expected. Laboratory experiments, however, show that this wave does not break. This lack of breaking in the laboratory experiment is explained by bottom friction and dispersion effects on wave dynamics. Further, the numerically simulated wave also fails to break, but is on the verge of breaking at $t = 38\sqrt{d/g}$ during runup and at $t = 62\sqrt{d/g}$ during rundown. This behavior in the numerical solution is explained by numerical dispersion and dissipation, introduced by the finite difference discretization of the partial derivatives. The slight numerical dissipation brings stability into the calculations and produces computational results that are in good agreement with laboratory measurements.

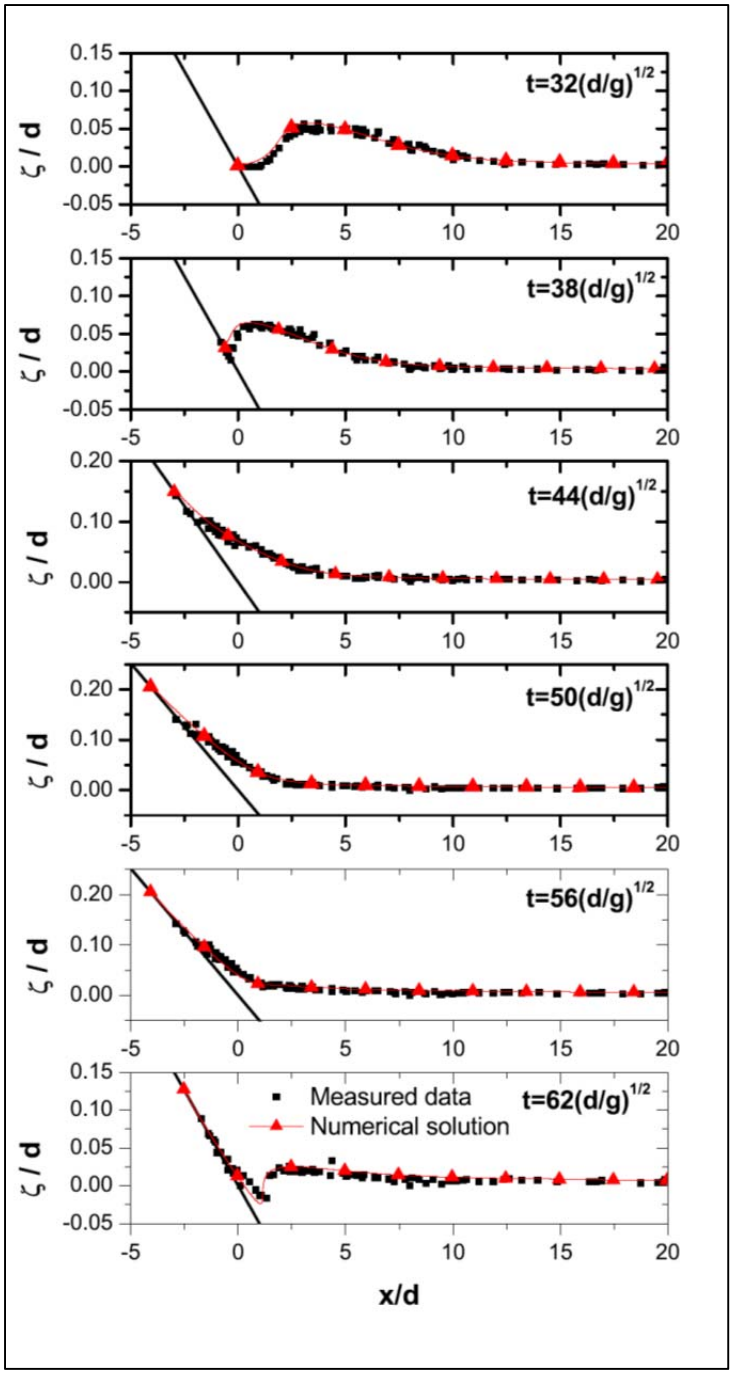

Figure 2-9: Comparison of measured and simulated water profiles during runup of a non-breaking wave in the case of H/d = 0.04. Observations are shown by squares. The analytical predictions and numerical calculations are marked by hollow and filled symbols, respectively. The measurements are provided courtesy of Synolakis (1986).

Finally, in the third series of laboratory experiments, the runup in the H/d = 0.3 case is studied. Both in computer and in laboratory experiments, the wave severely breaks. The leading front of the solitary wave steepens and becomes singular shortly after the beginning of computations. The numerical singularity propagates towards the beach until it meets the

shoreline where the singularity dissipates. Figure 2-10 shows our numerical solution, plotted by a line with solid triangles. The existence of strong wave breaking prevents a good agreement of our solution with the laboratory measurements. We observe that between moments $t = 15\sqrt{d/g}$ and $t = 20\sqrt{d/g}$, the computed wave propagates faster than the measured wave, because the numerical solution is computed using the primitive shallow water approximation (2-3) where dispersive terms are neglected. Inclusion of the wave dispersion leads to Boussinesq-type equations.

In all previous computations, for both breaking and non-breaking waves, the computed maximum runup, denoted by R, is found to be higher than its laboratory measured value. One possible explanation for this discrepancy is the assumption of zero bottom friction in the model. In the following sensitivity study, we examine whether the bottom friction can effectively parameterize wave breaking and eddy viscosity to accurately predict the maximum runup height R both for breaking and non-breaking waves. We begin with a discussion of non-breaking waves.

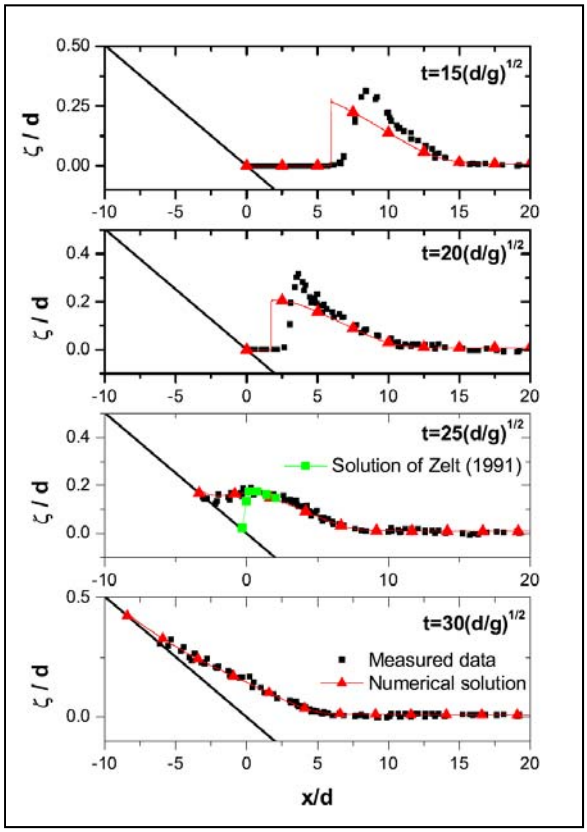

Figure 2-10: Comparison of measured and simulated water profiles during runup of a non-breaking wave in the case of H/d = 0.3. Observations are shown by squares. The analytical predictions and numerical calculations are marked by hollow and filled symbols, respectively. The measurements are provided courtesy of Synolakis (1986).

In several series of computer experiments, we model inundation of the sloping beach by waves with different H/d ratios. In each series, the bottom water friction is parameterized by the Manning friction coefficient ν, a certain fixed number. In Figure 2-11, we plot the computed maximum runup R/d versus H/d for $\nu = 0$, $\nu = 0.02$, and $\nu = 0.04$. In the same plot, we also

display laboratory measurements (Synolakis, 1987). We observe that for small non-breaking waves with $H/d \leq 0.01$, numerically simulated maximum runup heights do not depend on v and are in good agreement with laboratory data. For intermediate non-breaking waves $0.01 \leq H/d \leq 0.03$, the computed runup heights show little dependence on the bottom friction coefficient ν; similar results were reported by Lynett et al. (2002). In the case of breaking waves, those with $H/d > 0.03$, the maximum runup height strongly depends on v because a wave becomes a thin layer of liquid traveling up the slope after breaking, and friction is inversely proportionally to the water depth. Analyzing our computer experiments, we conclude that the measured runup height can be well approximated for the case in which the Manning friction coefficient $v = 0.03$.

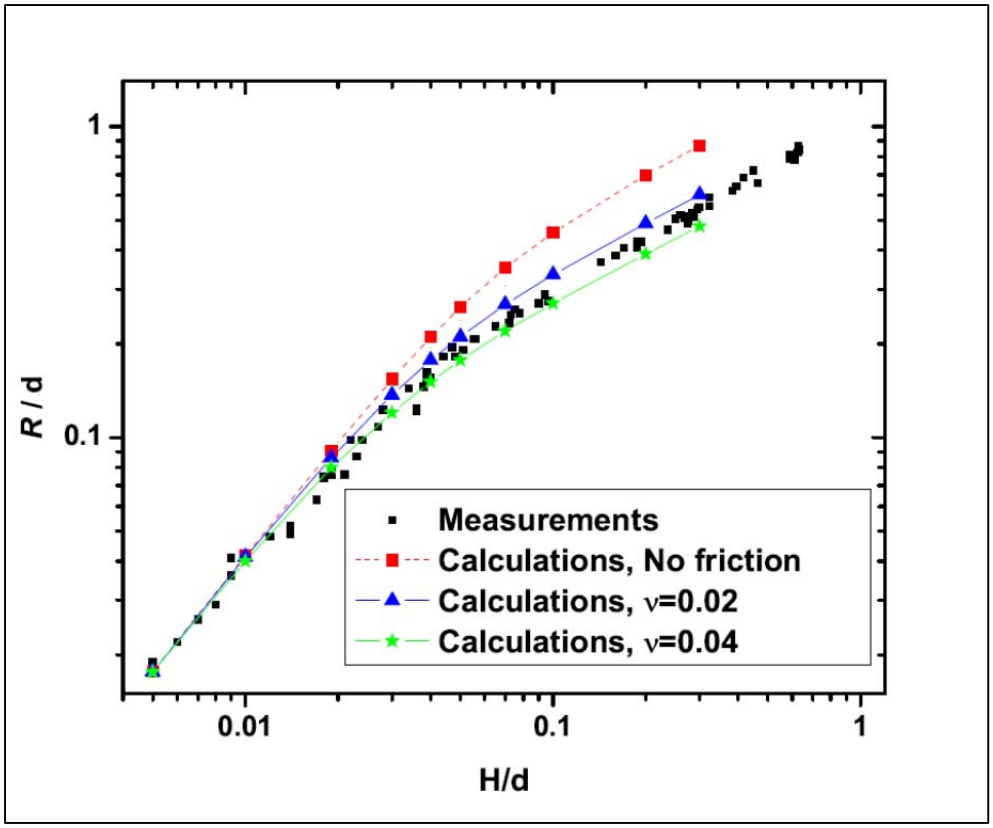

Figure 2-11: Non-dimensional maximum runup of solitary waves on the 1:19.85 sloping beach versus the height of the initial wave. The measured runup values (Synolakis, 1986) are marked by dots. The dashed line represents maximum runup values computed without an effect of bottom friction, i.e., v = 0. The solid lines represent maximum runup values computed with the effect of bottom friction, i.e., v = 0.02 and v = 0.04. The measurements are provided courtesy of Synolakis (1986).

2.3.5 BP5: Solitary wave on composite beach – laboratory

In a series of laboratory experiments, solitary waves of various heights H were generated in the tank by paddle motion. Their water surface height dynamics were recorded by ten capacitance gauges. Additionally, the maximum runup on the vertical wall was visually measured. Records of propagation of solitary waves with various ratios of H/d, where d is the still water depth, and values of the maximum runup can be found in Briggs et al. (1995). In Yeh et al. (1996) computational results from several numerical models are compared to certain

laboratory records, namely cases A, B, and C related to $H/d = 0.038$, $H/d = 0.259$, and $H/d = 0.681$, respectively.

To simulate the laboratory recorded wave dynamics, we discretize the computational domain shown in Figure 2-4 into grid cell of the length $\Delta x \approx d/20$ and use the time step $\Delta t = 0.05\sqrt{d/g}$. To model the incident solitary wave, we specify the water surface height at the inflow boundary located at Gauge 4. Once the wave was generated, the boundary condition is modified to simulate the non-reflective behavior.

In Figure 2-12, we display the laboratory measured water level in Cases A and C by a line with hollow circles. In Case A, the generated wave has the ratio $H/d = 0.038$ and it does not break in either the laboratory or computer experiments. The computational results in the case of non-linear shallow water equations are shown by lines with triangles in Figure 2-12. The comparison of the numerical results in the case of linear shallow water equations is provided in Figure 2-5.

We note that the wave simulated by the linearized equations does not break while shoring, whereas the solution to non-linear equations indicates that the wave front sharpens and finally the wave breaks after reflection from the vertical wall. We conclude that the linear solution reproduces the observations satisfactorily, while the non-linear solution clearly indicates shortcomings of the primitive shallow water approximation, due to negligence of the dispersion.

In Case C, the wave front of the numerical non-linear solution sharpens and approaches the limiting case of a vertical leading edge as the wave approaches the vertical wall. There is also a timing error with the predicted wave traveling ≈5% faster than the observed wave. The sharpening of the wave front and the timing error are probably due to the dispersive terms being neglected in the primitive shallow water approximation.

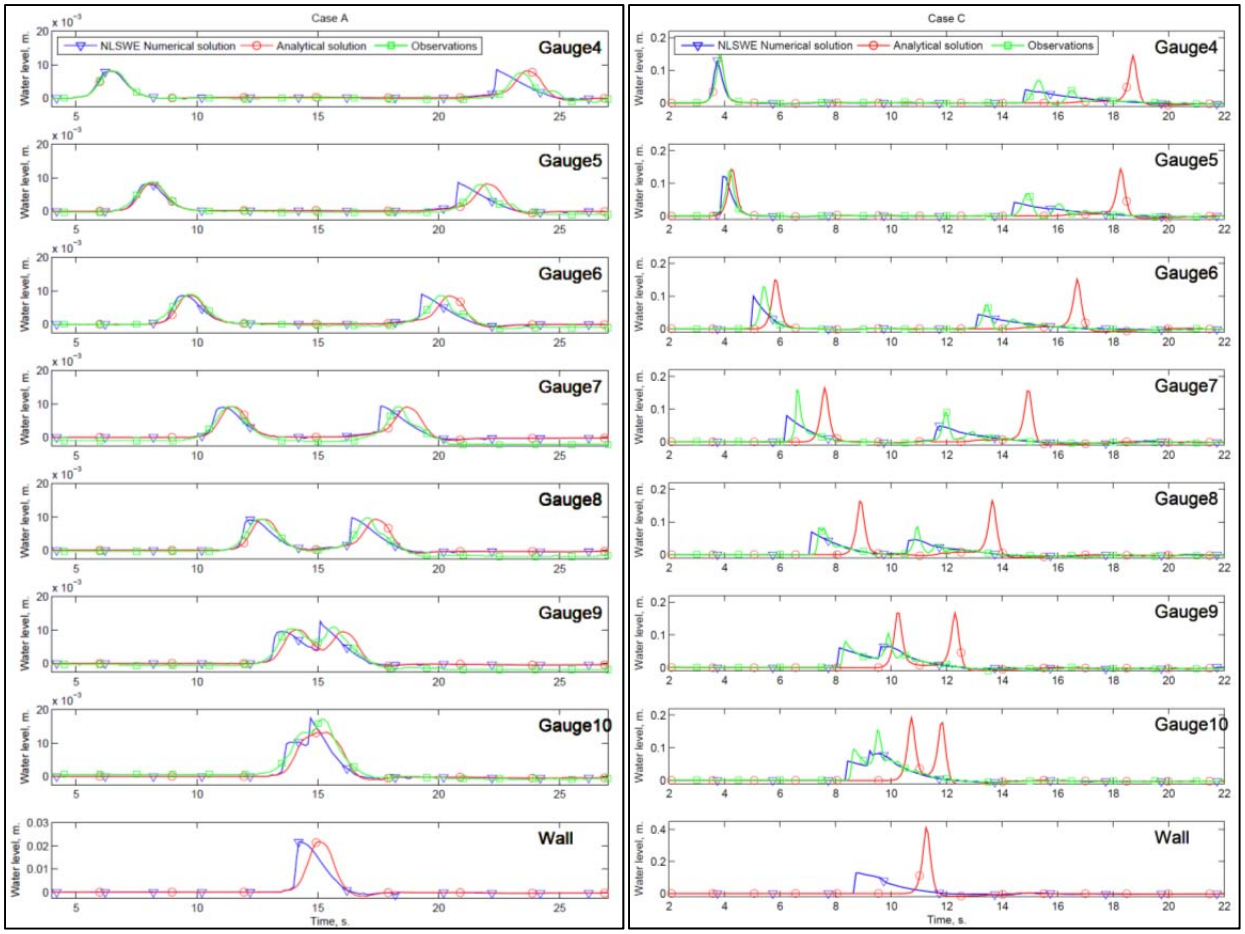

Figure 2-12: Comparison between the numerically computed solutions and laboratory measurements at the gauge locations shown in Figure 2-4. Left plot: Case A, Right plot Case C.

In Table 2-1, we list values of the maximal computed runup at the vertical wall versus the observed values. For case A, the predicted runup is under-predicted by 10%. For cases B and C, the error is significantly larger because when the breaking wave collapses into the vertical wall, the shallow water theory is no longer applicable and more complicated models are necessary to model the observed runup more precisely.

Table 2-1: Comparison between the numerically computed and measured runup at the vertical wall.

	Measured		Computed	
	R, cm	R/d	R	R/d
Case A	2.74	0.13	2.18	0.1
Case B	45.72	2.10	8.81	0.4
Case C	27.43	1.26	12.91	0.6

2.3.6 BP6: Solitary wave on a conical island – laboratory

We simulate propagation and runup of a solitary wave on a conically shaped island. To validate our numerical method, we use a laboratory experiment focused on studying inundation

of the Babi island by the 12 December 1992 tsunami. The tsunami attacked the conically shaped Babi island from the north, but extremely high inundation was observed in the south. A model of the conical island was constructed in a wave tank at the US Army Engineer Waterways Experimental Station (Briggs et al., 1995). Figure 2-13 shows a sketch of the conical island and the location of several sensors that recorded the water level dynamics. Along one side of the tank, a wave generator directed plane solitary waves toward the island. Interested readers are referred to Liu et al. (1995) where the laboratory experiments and measured data are described in detail.

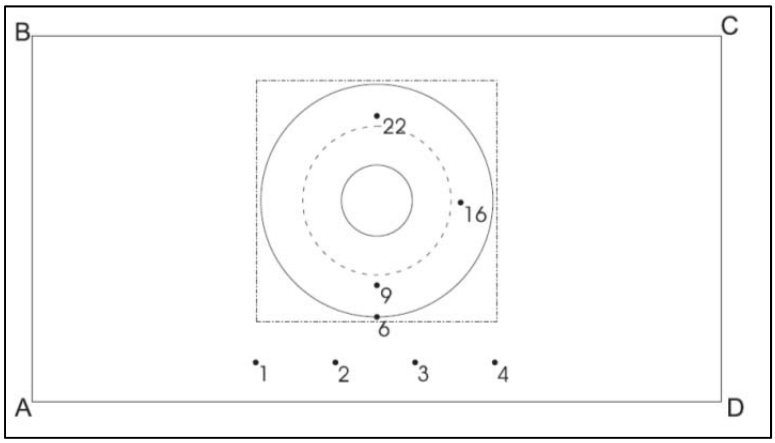

Figure 2-13: Top-down non-scaled sketch of a conically-shaped island. The solid circles represent exterior and interior bases of the island. The dotted line shows an initial location of the shoreline. The dash-dotted line shows the extent of the high resolution computational grid. The dots mark gauge locations where laboratory measured water level is compared to numerical calculations. The in-flow boundary condition is simulated on the segment AD, while the open boundary condition is modeled on the segments AB, BC, and CD. Location of gauges 1, 2, 3, and 4 is schematic, while locations of the rest of gauges are precise.

Experiments with different wave heights, H, were conducted in the wave tank. A goal of the experiments was to demonstrate that after the tsunami hits the island, it splits into two waves traveling with their crests perpendicular to the shoreline. Once these waves meet behind the island, they collide and produce a local extremum in runup. In this work, we model the highest generated wave. This is a formidable test of the numerical algorithm because the modeled wave is steeper than most realistic tsunamis (Titov and Synolakis, 1998).

In our computer experiment, we discretize the entire basin with a coarse resolution grid with spacing $\Delta x/d = \Delta y/d = 5/32$, where the undisturbed water depth $d = 0.32$ m. However, in the vicinity of the conical island, we also construct a fine resolution grid with a cell size $\Delta x/d = \Delta y/d = 1/32$ to include the entire island and its exterior base. To couple these two grids, we use an algorithm described by Kowalik and Murty (1993) and Goto et al. (1997) in which the water flux from the coarse resolution grid is passed to the fine resolution grid, and the water level η from the fine resolution grid is returned back to the coarse grid at each time step. To simulate the incident wave, the water level at the boundary AD is set according to measurements at gauges 1-4, instead of modeling the action of generator paddles. On all other sides of the computational domain, we define open boundary conditions. The choice of boundary conditions in the model differs from conditions imposed by horsehair-type absorbers along the tank wall, so the

computed water dynamics cannot model laboratory data after the time τ when wave crest reaches BC. Therefore, the computer simulation is terminated at τ.

On the left plots in Figure 2-14 and Figure 2-15, we compare computed and measured water level dynamics in the case of H/d = 0.05 and H/d = 0.2, respectively. The computations are terminated after the first reflection of the wave from the island. The simulated wave breaks and steepens faster than in laboratory measurements, a well-known effect of the shallow water approximation in which dispersive terms are neglected. Despite the extensive wave breaking, the computed runup is in good agreement with laboratory data, as shown on the right plots in Figure 2-14 and Figure 2-15. The error between the measured and simulated runup everywhere around the island, except the lee side, is within 10%, below suggested errors (Synolakis et al., 2008). The simulated runup does not match the measured runup at the lee side, due to low order wave theory used to simulate the vertical velocity in the computer experiment. Still, the error between the measured and simulated runup at the lee side of the island is less than 20% and is within acceptable criteria (Synolakis et al., 2007).

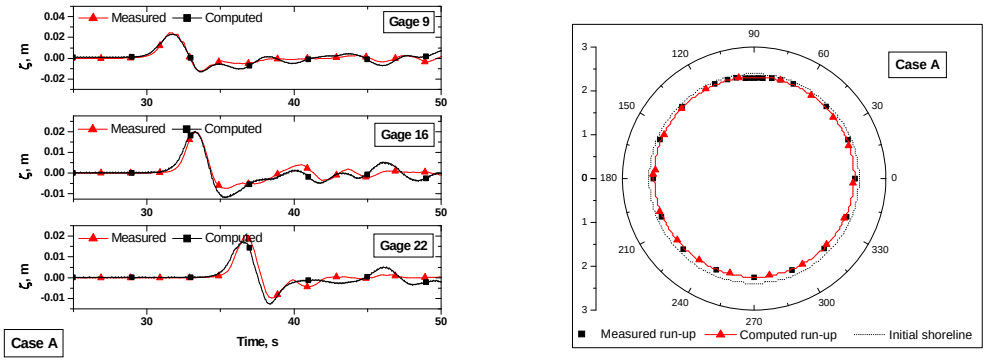

Figure 2-14: Left plot: comparison between the computed and measured water level at gauges shown in Figure 2-13 for an incident solitary wave in the case of H/d = 0.05. Right plot: comparison between computed and measured inundation zones. Top view of the island, with the lee side at 90^{O}. The dotted line represents the initial shoreline. The measurements are provided courtesy of Briggs et al. (1995).

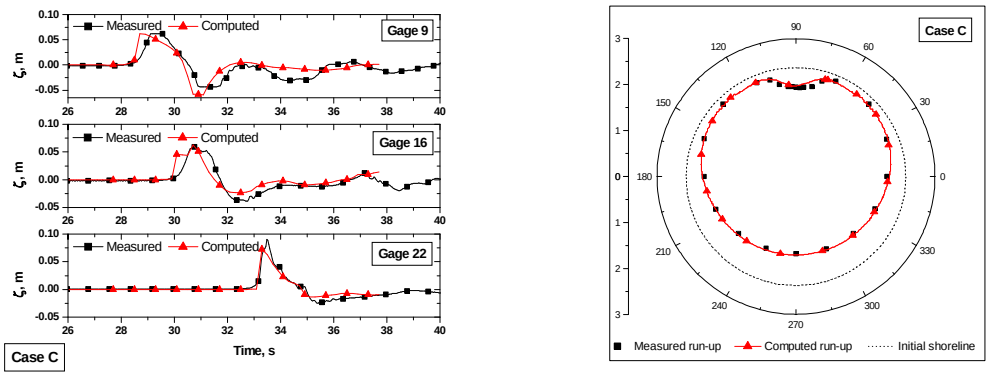

Figure 2-15: Left plot: comparison between the computed and measured water level at gauges shown in Figure 2-13 for an incident solitary wave in the case of H/d = 0.2. Right plot: comparison between computed and measured inundation zones. Top view of the island, with the lee side at 90^{O}. The dotted line represents the initial shoreline. The measurements are provided courtesy of Briggs et al. (1995).

2.3.7 BP7: Tsunami runup onto a complex three-dimensional model of the Monai Valley beach – laboratory

A laboratory experiment, using a large-scale tank at the Central Research Institute for Electric Power Industry, was focused on modeling runup of a long wave on a complex beach near the village of Monai (Liu et al., 2007). The beach in the laboratory wave tank was a 1:400 scale model of the bathymetry and topography around a very narrow gully, where extreme runup was measured. The incoming wave in the experiment was created by wave paddles located away from the shoreline, and the induced water level dynamics were recorded at several locations by gauges. Figure 2-16 shows a snapshot of the simulated water level and the relative location of the gauges with respect to the shoreline.

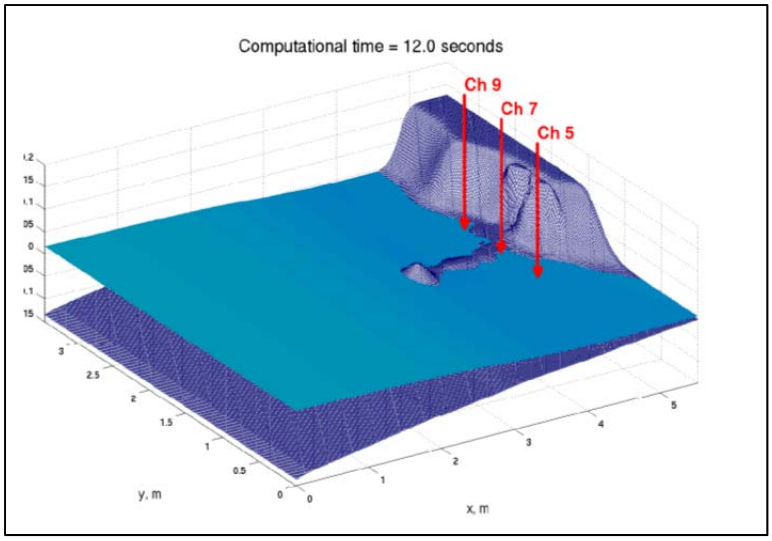

Figure 2-16: The 3-D view of the computational domain and numerical solution at 12 seconds. Locations of gauges, at which the modeled and measured water level dynamics are compared, are shown by arrows. Abbreviations Ch5, Ch7, and Ch9 stand for Channel 5, 7, and 9, respectively. The inlet boundary is modeled at x = 0. At y = 0 and y = 3.4, the reflective boundary conditions are set.

The computational domain represents a 5.5 by 3.4 m portion of the wave tank near the shore and is divided into 0.014 × 0.014 m grid cells. The incident wave is prescribed at $x = 0$ for the first 22.5 seconds, after which a non-reflective boundary condition is set at $x = 0$. The boundary conditions along segments $y = 0$, $y = 3.4$, and $x = 5.5$ are set to be totally reflective. To model the bottom friction, we select $v = 0.01$, which is the closest value of the Manning's coefficient for the smooth bottom material of the wave tank. The time step is set to $5 \cdot 10^{-4}$ seconds to satisfy the stability condition.

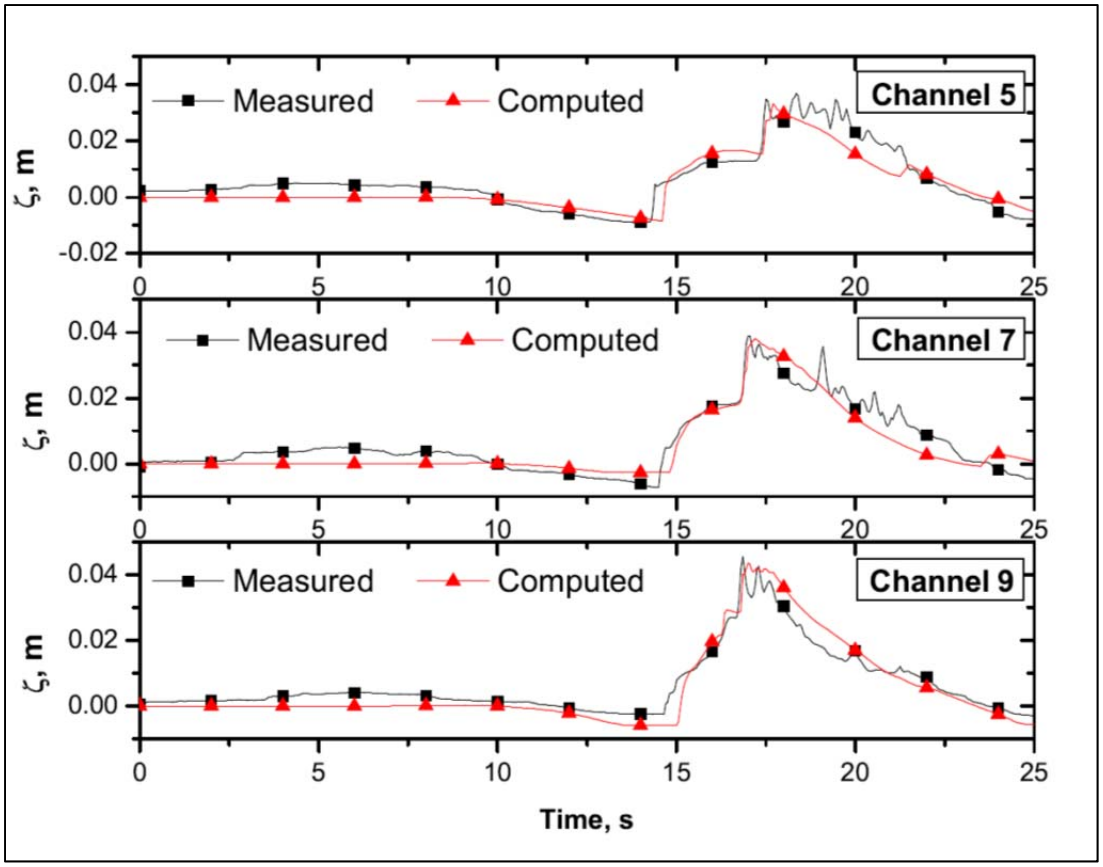

Figure 2-17: Comparison of the computed water height with the laboratory measurements at water gauges Ch5, Ch7, and Ch9. The measurements are provided courtesy of the Third International Workshop on Long-Wave Runup Models (Liu et al., 2007).

Figure 2-17 shows plots of the computed and measured water surface dynamics by lines marked with triangles and rectangles, respectively. The water level dynamics are shown at channels 5, 7, and 9 for the first 25 seconds, during which the maximum runup occurs. As noted by (Zhang and Baptista, 2008), the observed water elevation for the first 10 seconds cannot be accurately modeled due to the existence of initial water disturbances in the wave tank. In the computer experiment, the positive wave arrives at the gauges less than 0.3 seconds after the measured wave. Also, the maximum computed water level at each gauge is less than the measurements by less than 5%. Therefore, we conclude that despite minor inconsistencies, the numerical solution matches well with observations at each gauge.

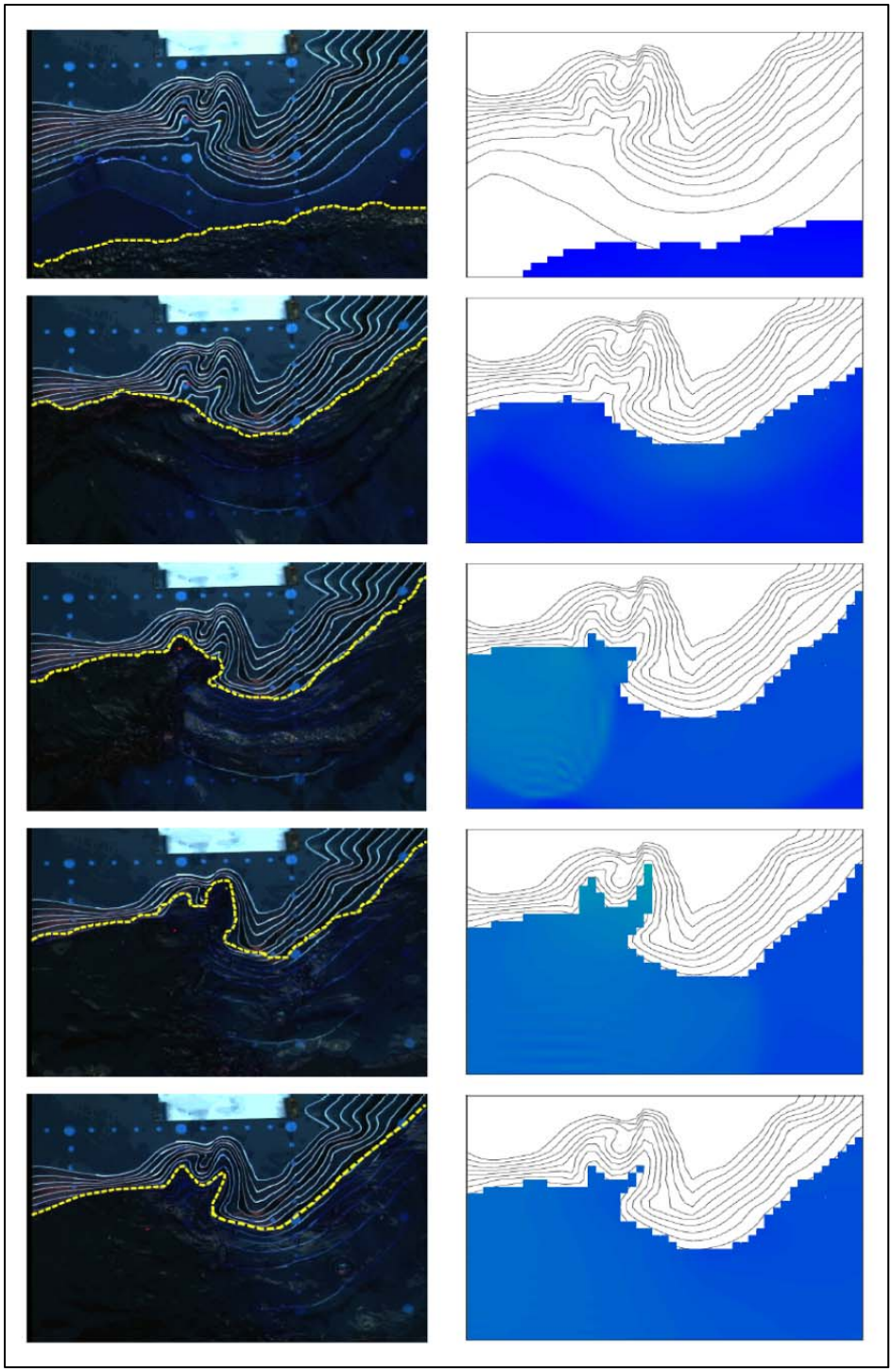

Figure 2-18: Left side: frames 10, 25, 40, 55, and 70 from the overhead movie of the laboratory experiment. The time interval between frames is 0.5 seconds. The dashed yellow line shows the instantaneous location of the shoreline. Right side: snapshots of the numerical solution at the time intervals corresponding to the movie frames. The blue shaded area corresponds to the water domain and is considered to be wet. The frames are provided courtesy of the Third International Workshop on Long-Wave Runup Models (Liu et al., 2007).

In addition to point-wise comparison at the gauges, we plot snapshots of the computed and observed water height of the whole domain. On the left side in Figure 2-18, we display five frames extracted from a video taken during the laboratory experiment. These frames are 0.5 seconds apart and are focused on the narrow gully where the highest runup is observed. On the right side in Figure 2-18, we show snapshots of the numerically computed water level at times synchronous with those of the video frames. Side-by-side comparison of these series of frames reveals a good agreement of the numerical solution to the observations throughout the domain, where the maximum runup occurred. Furthermore, Figure 2-18 shows that the numerical method is able to capture a rapid sequence of runup and rundown.

2.3.8 BP8: Three-dimensional landslide – laboratory

Large-scale experiments have been conducted in a wave tank with a plane slope (1:2) located at one end of the tank. Detailed description of the tank geometry and experimental equipment can be found in Liu et al. (2005). A solid wedge was used to model the landslide. The horizontal surface of the wedge was initially positioned either a small distance, Δ, above or below the still water level to reproduce a subaerial or submarine landslide.

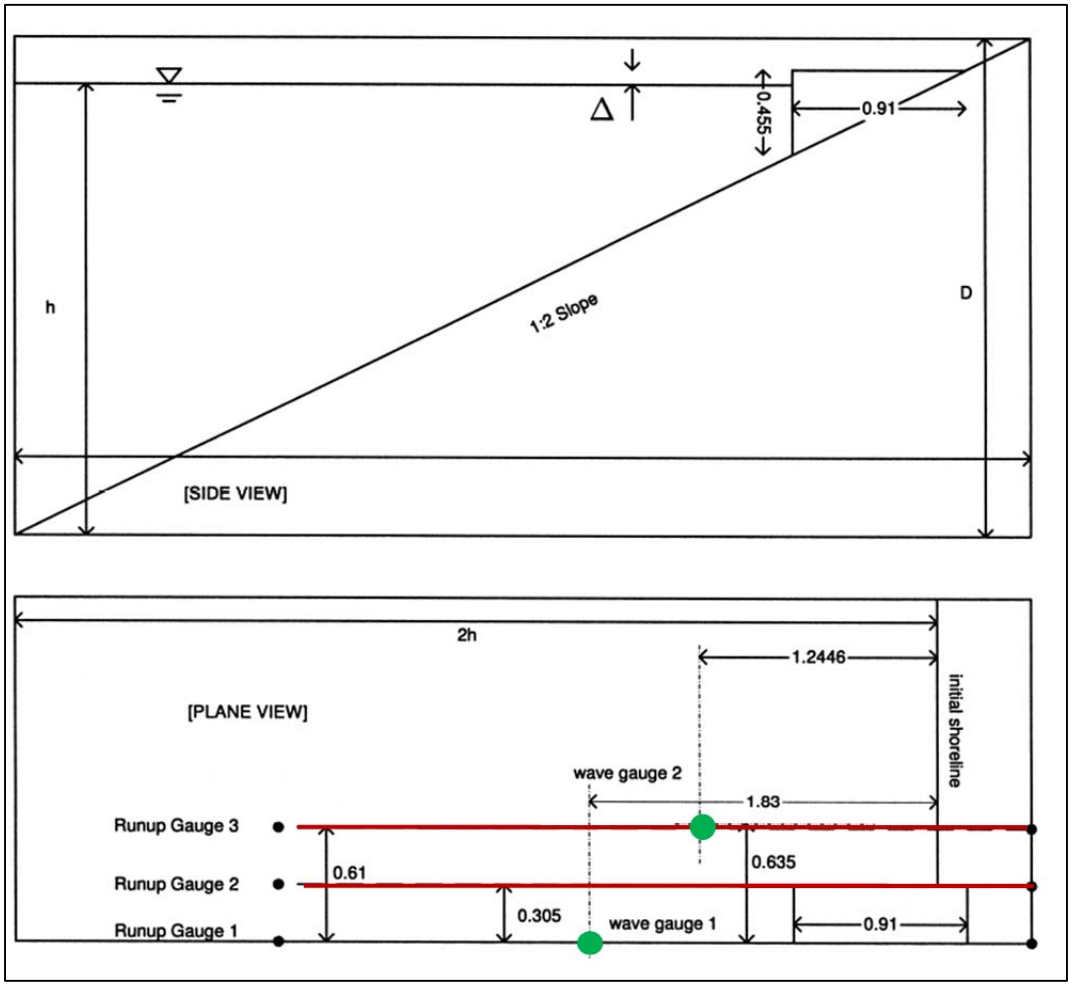

Figure 2-19: Schematic of the experimental setup. Locations of the water gauges are marked by green dots. The profiles along which the runup is measured are shown by red lines.

The wedge was released from rest, abruptly moving downslope under gravity. The wedge was instrumented with a position indicator to determine the velocity and position time histories.

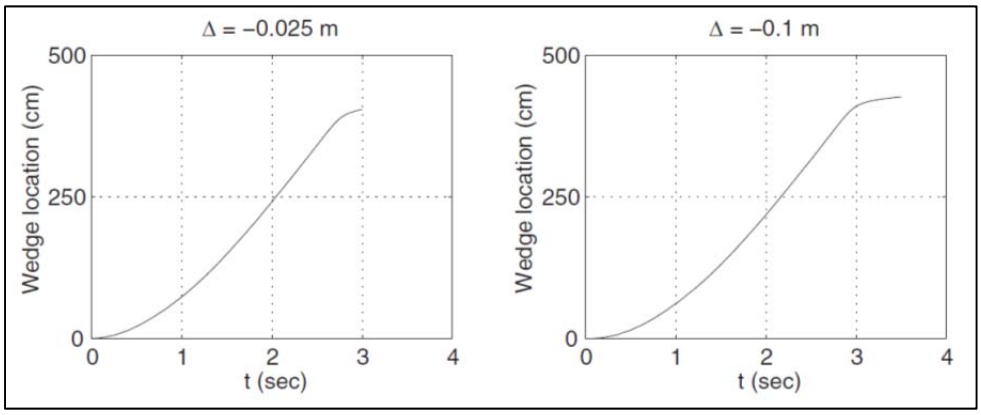

Figure 2-20: Time histories of the block motion for the submerged case with Δ = −0.025 m and Δ = −0.1 m.

The goal of this benchmark problem is to compare the numerical predictions with the laboratory measurements. The domain, shown in Figure 2-19, was discretized with $\Delta x = \Delta y = 5 \cdot 10^{-3}$ meter spatial resolution and a time step of 10^{-5} seconds. Location of the wedge was prescribed according to the time histories of the block motion, shown in Figure 2-20. Figure 2-21 displays the comparison between the measurements and the numerical solution.

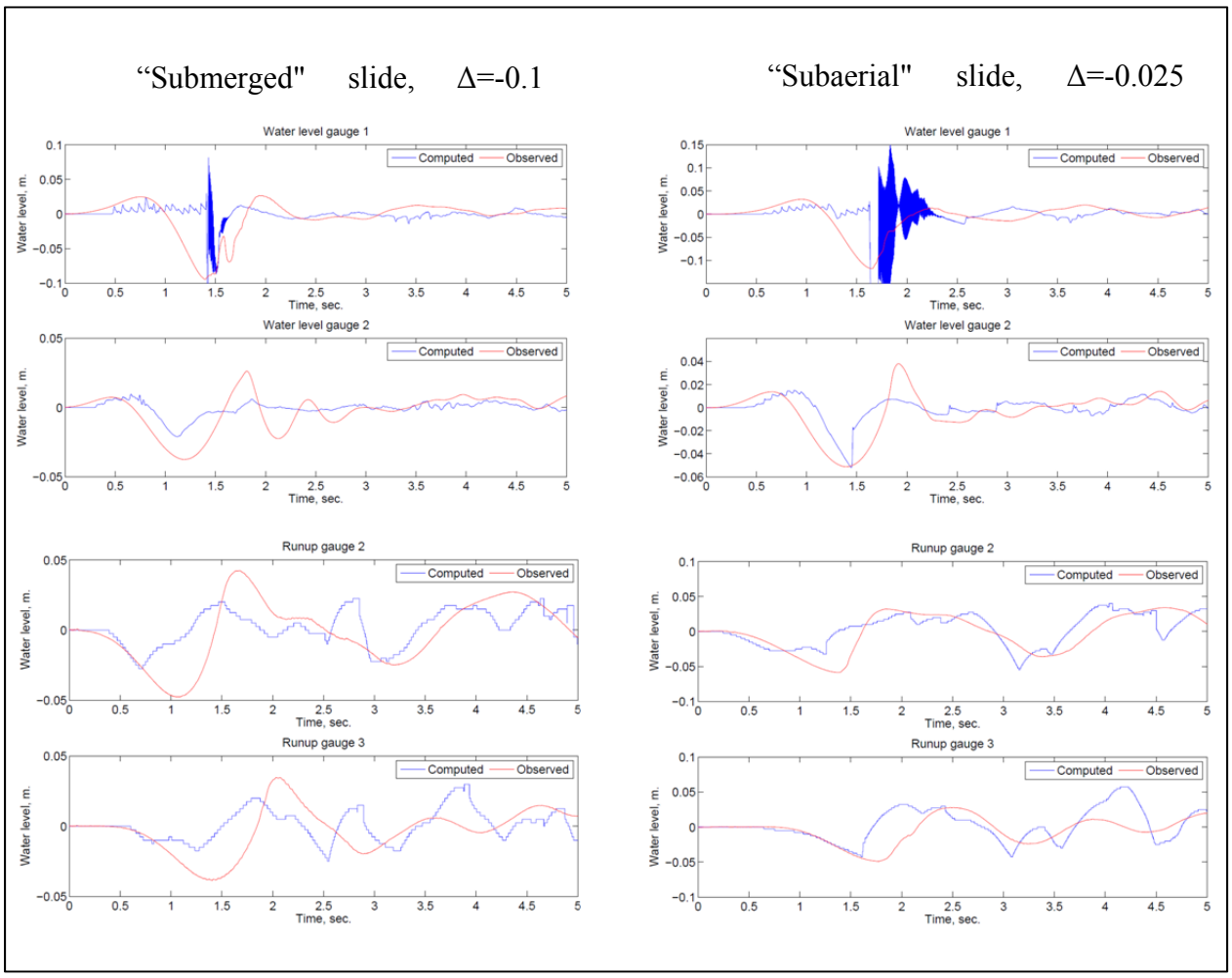

Figure 2-21: The top plots show the comparison between the computed and measured water level dynamics at two gauges, shown in Figure 2-19. The bottom plots show the comparison between the computed and measured runup along two profiles, shown in Figure 2-19.

We note that the numerical solution to the non-linear shallow water equations has some numerical instability due to the formation of the shock wave.

2.3.9 BP9: Okushiri Island tsunami – field

The bathymetry/topography digital elevation model (DEM) for Okushiri island was provided by the Disaster Control Research Center (DCRC) at Tohoku University, Japan. The data consist of several nested grids of increasing spatial resolution ranging from 450 m to 5 m. The grids are focused on the Monai and Aonae regions where the maximum runup and devastation was reported in 1993.

We began to analyze computational results by comparing the numerically computed water level dynamics to tidal gauge records of the first hour after the earthquake. Figure 2-23 shows the computed and observed water level dynamics at the stations, marked in Figure 2-22 by triangles. The arrival time of the computed wave matches well with the arrival of the leading tsunami wave. The correlation of positive and negative phases between the computed and observed waves is rather good, although the computed wave at both locations has a larger range

and frequency of variability than the observed wave. The discrepancies between the measured and observed waves can be explained by the lack of detailed bathymetry near tide stations, limitations of the shallow water approximation model, and inaccuracy of the specified initial conditions.

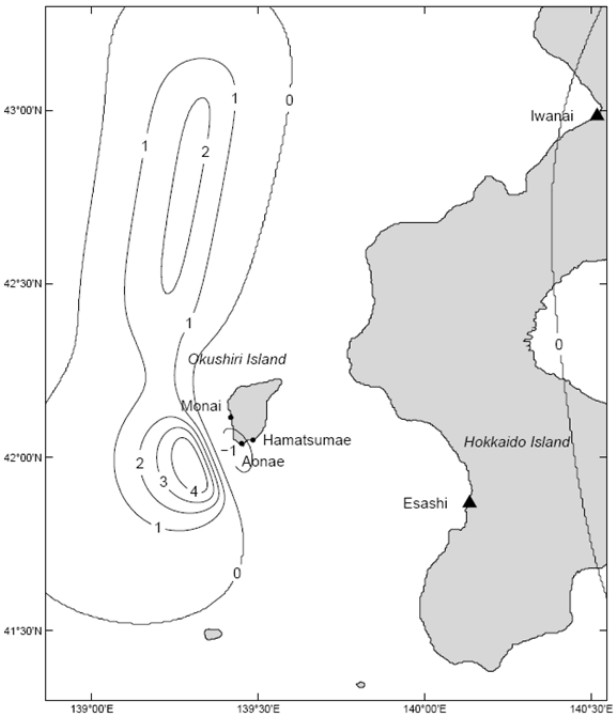

Figure 2-22: The computational domain used to simulate 1993 Okushiri tsunami. The triangles mark the locations of the tide gauge stations that observed water levels to which we compare model dynamics. The contours mark the seafloor displacement caused by the Hokkaido-Nansei-Oki earthquake (Takahashi et al., 1995).

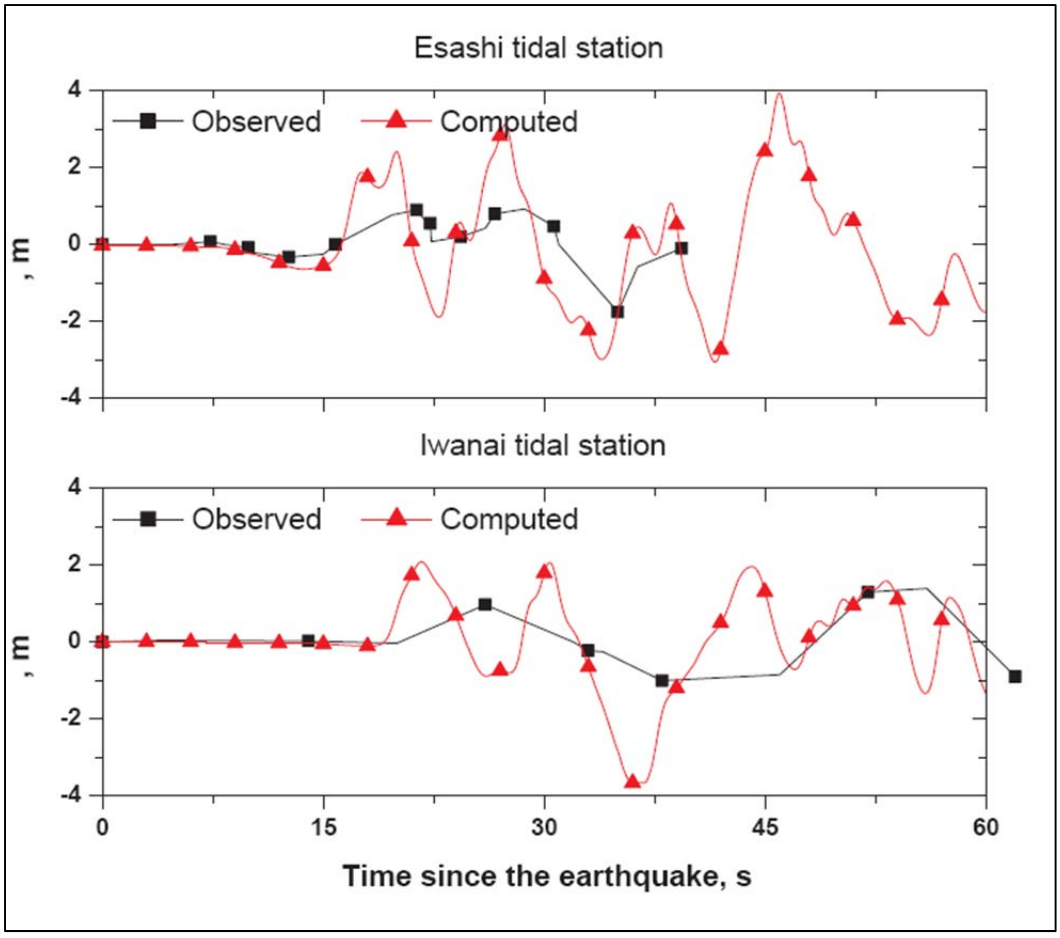

Figure 2-23: Computed and observed water levels at two tide stations located along the west coast of Hokkaido island during 1993 Okushiri tsunami. The observations are provided courtesy of Yeh et al. (1996).

Figure 2-24 shows the locations on Okushiri island where the runup was measured shortly after the 1993 tsunami. To compare the computed and observed runup, we discretize the shoreline into several regions, with each region enclosing the part of the shoreline lying closer to a certain observation point than to any other. Within each region, we compute the maximum and minimum values of the simulated runup and compare this variability to the observations at each point. We note that almost everywhere around the island, the observed values lie within the modeled range of variability. There are, however, several exceptions where the modeled runup underestimates the observations. For example, the modeled runup in the narrow gully near the village of Monai is underestimated partially because of the reasons discussed below.

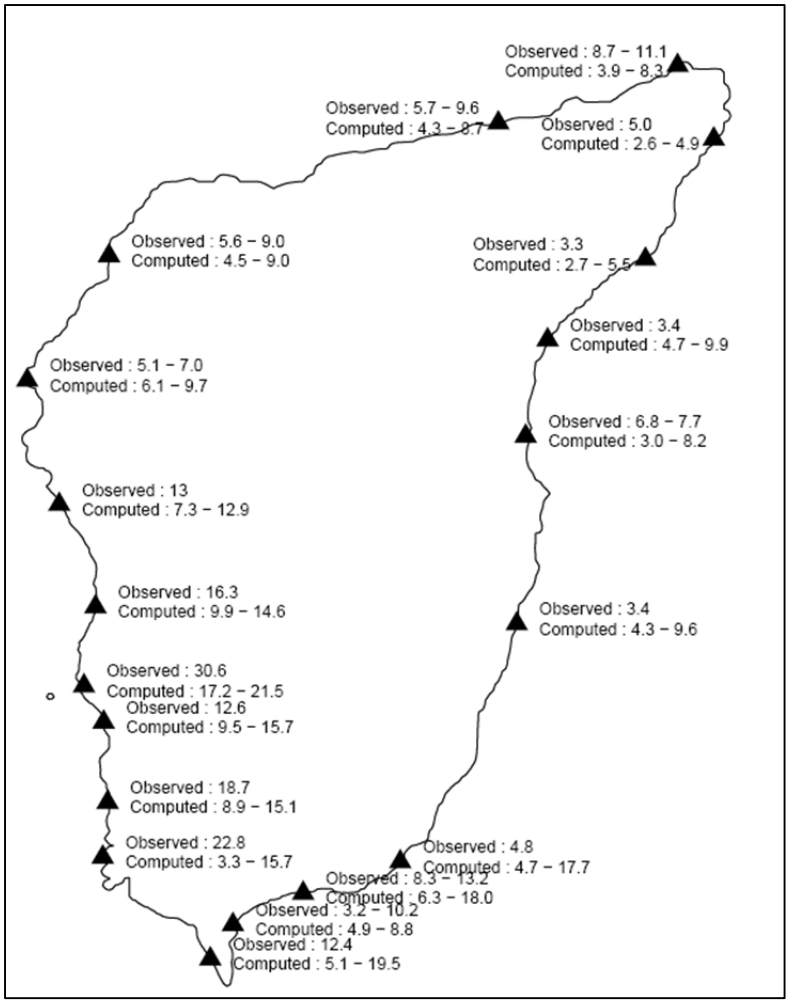

Figure 2-24: The computed and observed runup in meters at 19 locations along the coast of Okushiri island after the 1993 Okushiri tsunami. The observations are provided courtesy of Kato and Tsuji (1994).

We recall that near Monai village the runup is modeled using 5 meter resolution computational grids. The bathymetry/topography data within the 5 meter grid are based either on the DEM provided by the DCRC, or on the DEM used to construct a wave tank in the laboratory experiment discussed in the previous sub-section. In both DEMs, the narrow gully is identical, but there is a small difference in elevation near the shoreline. The numerical computations using the DCRC DEM show that the computed maximum runup in the narrow gully is 17.2 m. By comparison, utilizing the wave tank DEM, the resulting runup in the gully is 21.5 m. We emphasize that model parameters as well as bathymetry/topography in computational grids coarser than 5 m are the same in both simulations. The difference between the maximum runup values in these two simulations reveals the high sensitivity of the runup to nearshore bathymetry/topography, and underlines the importance of the near-shore bathymetry data for accurate runup predictions. Therefore, the discrepancy between the measured and computed runup values may be explained by the lack of accurate bathymetry/topography data near Monai,

uncertainties in the initial water surface displacement, or finally by limitations of the shallow water approximation to model 3-D flows.

In Figure 2-25, we show a sequence of snapshots depicting the simulated waves inundating the city of Aonae. The 0, 5, and 10 meter ground elevations contours are shown by thick lines. The first snapshot corresponds to 280 seconds after the earthquake, and each snapshot is 60 second after the previous one. In the first snapshot, it is easy to observe the approaching 5 meter high wave via water level contours shown by the dashed lines. While the wave approaches the Aonae peninsula, it drastically steepens over the shallow areas as shown in the second snapshot, shown upper right. The wave runs-up on the western side on the Aonae peninsula and reaches the 10 meter high mark. In the third snapshot, shown lower left, the wave sweeps across the peninsula. The speed of the water traveling across the tip of the peninsula, where the greatest destruction occurred, is numerically estimated at up to 12 m/s, which is in good agreement with observations. In the last snapshot, shown lower right, we show the Aonae peninsula after the retreat of the computed wave.

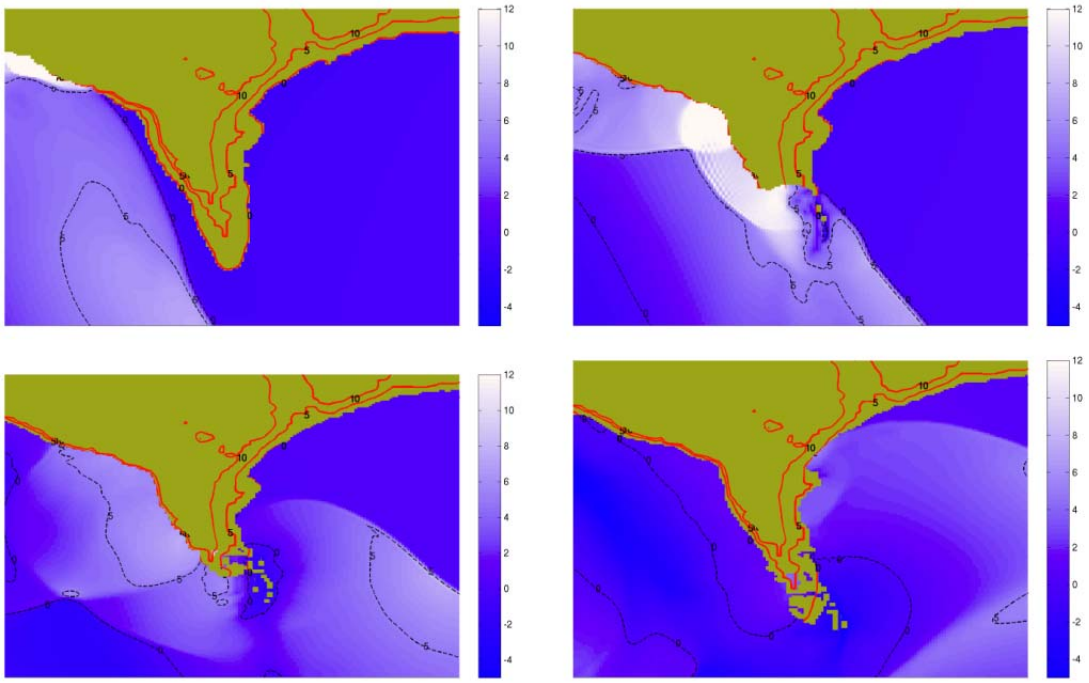

Figure 2-25: Numerical modeling of a tsunami wave overflowing the Aonae peninsula, viewed from above. The dashed black and solid red contours represent the water level and land elevation, respectively. The upper left plot shows an approaching 5 meter high wave. As the wave approaches, it steepens and overtops the peninsula as illustrated by the upper right plot. In the lower left plot, the wavefront bends around the peninsula and propagates in the direction of Hamatsumae. In the lower right plot, the water retreats and the seabed becomes partially dry.

We note that due to the shallow depth around the peninsula, the simulation reveals that the wavefront bows, then bends around the Aonae peninsula, and subsequently hits the town of Hamatsumae. The computed runup at Hamatsumae reaches 15 m and matches well with field observations. Numerical modeling shows that during the reflection of the first wave that hit Hamatsumae, a wave traveling toward the Aonae peninsula has formed. Both in the computer

experiment and in eyewitness reports, this second wave hits the Aonae peninsula from the south-east direction approximately 10 minutes after the first wave. The damage due to the second wave is localized on the eastern side as reported by eyewitnesses. In Figure 2-26, we provide the contours of the maximum computed runup around the Aonae peninsula. This computer experiment shows that the numerical algorithm is stable, successfully models the overland flow, and captures the runup of reflected waves.

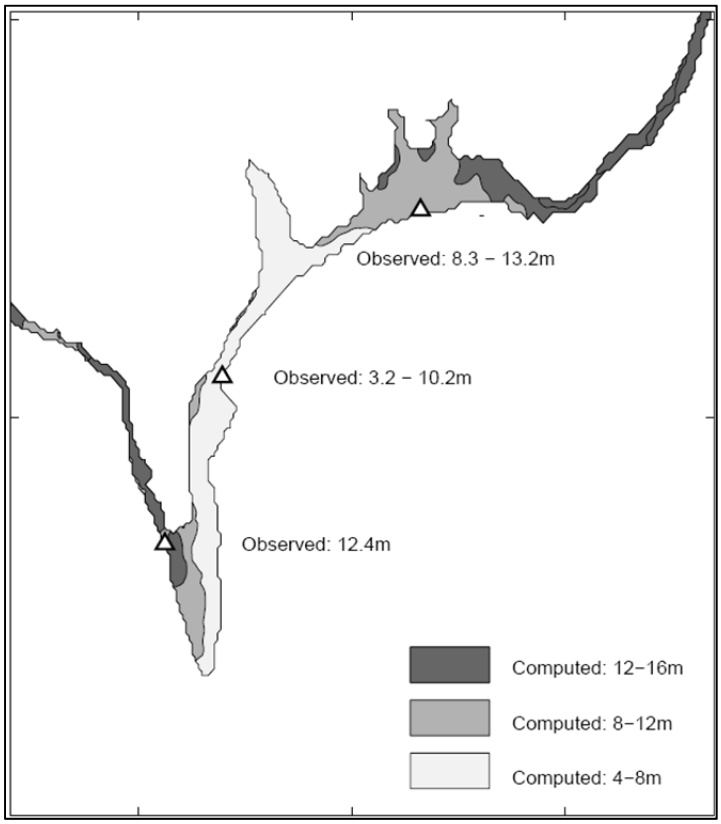

Figure 2-26: The computed and observed runup in the vicinity of the Aonae peninsula after 1993 Okushiri tsunami. The triangles mark the locations where the observations were conducted. The computed runup distribution has a local maximum near Hamatsumae, as observed by eyewitnesses. The observations are provided courtesy of Kato and Tsuji (1994).

2.4 Lessons learned

A numerical model for the simulation of tsunami propagation and runup is verified and validated using NOAA standards and criteria. In computer experiments modeling the propagation and runup of tsunami waves, specified by BP1, BP2, BP4, BP6 and BP7, numerical calculations are within the established errors proposed by Synolakis et al., (2008).

The analytical solution in BP3 is derived under circumstances that prohibit any direct employment of the analytical solution in accurate benchmarking of the tsunami models. Therefore, we suggest that this benchmark should be replaced by a problem that is similar in nature.

The numerical results agree with the runup measurements in Case A of BP5, but do not predict the runup in Case B and Case C, if the water dynamics is modeled by using the non-

linear shallow water equations. It seems that in these lab experiments, a wave hitting the vertical wall creates air bubbles that produce a splash that is actually measured in Case B and Case C.

In BP8, the numerical results derived within the non-linear shallow water approximation show numerical instabilities that are due to a shock formation at the edge of the triangular wedge modeling sliding material. It is still unknown whether a Boussinesq approximation would help to eliminate the shock formation and produce better agreement with the laboratory measurements. Anyway, we emphasize that the geometry of the rigid sliding block used in this BP is too simple to represent an actual landslide. Therefore, we suggest that this benchmark should be replaced by a problem with a more realistic geometry of the sliding material.

In BP9, the computed runup around Okushiri island is within the variability of field observations. However, the local extreme runup, e.g., in the narrow gully near the village of Monai, is sensitive to the near shore interpolation of bathymetry/topography. The computer simulation of the 1993 Okushiri tsunami also captures the overland flow at the Aonae peninsula, where the maximum destruction was reported.

2.5 Proposed benchmarks

Benchmarking of the seiche tsunami model (1a)-(2a) that shares the same runup algorithm as the tectonic tsunami model is partially addressed by the list of considered BPs. Unfortunately, it is hard to derive an analytical solution for the full system (1a)-(2a). However, it is possible to model a physical effect of these terms as follows. The ground velocity $\mathbf{u_g}$ has non-zero values only for a few seconds, i.e., over the period when the horizontal tectonic displacement occurs. Within this time period the water velocity, $\mathbf{u}$, can be considered small and then the water surface displacement can be approximated by $\nabla h \cdot \mathbf{u}_g$. In the case of the parabolic water basin, this initial disturbance is a plane profile. Therefore, we propose to test the model against the analytical solution in the cases of frictionless water flow in 2-D parabolic basins that can model fjord-type settings typical of the Alaska coast. The analytical solution to this problem is described as nonlinear normal mode oscillations of water (Thacker, 1981). We assume that the bathymetry is given by

$$h = h_0\left(x^2 + y^2 - l^2\right)$$

Then, an analytical solution to (1)-(2) is described by oscillations such that the water surface remains planar:

$$\xi = ah_0\left(2x\cos\omega' t - 2y\sin\omega' t - a\right),$$

where a is the amplitude of the motion, $2\omega' = f + \sqrt{\omega}$, and $\omega^2 = f^2 + 8gh_0$.

To conduct numerical experiments, we set $L = 500$, $g = 9.8$, $h_0 = 10$, $a = 1$, and $f = 0.01$. To estimate accuracy of the numerical scheme we compute the numerical solution on the series of grids ($\Delta x = 5$, $\Delta x = 2.5$, and $\Delta x = 1.25$) and compare it to the analytical ones. In all computations, the time step Δt is fixed and is equal to $10^{-3}T$, where the constant T is a period of oscillations, i.e., $T = 2\pi/\omega'$. The numerical water surfaces after the third revolution are shown in Figure 2-27.

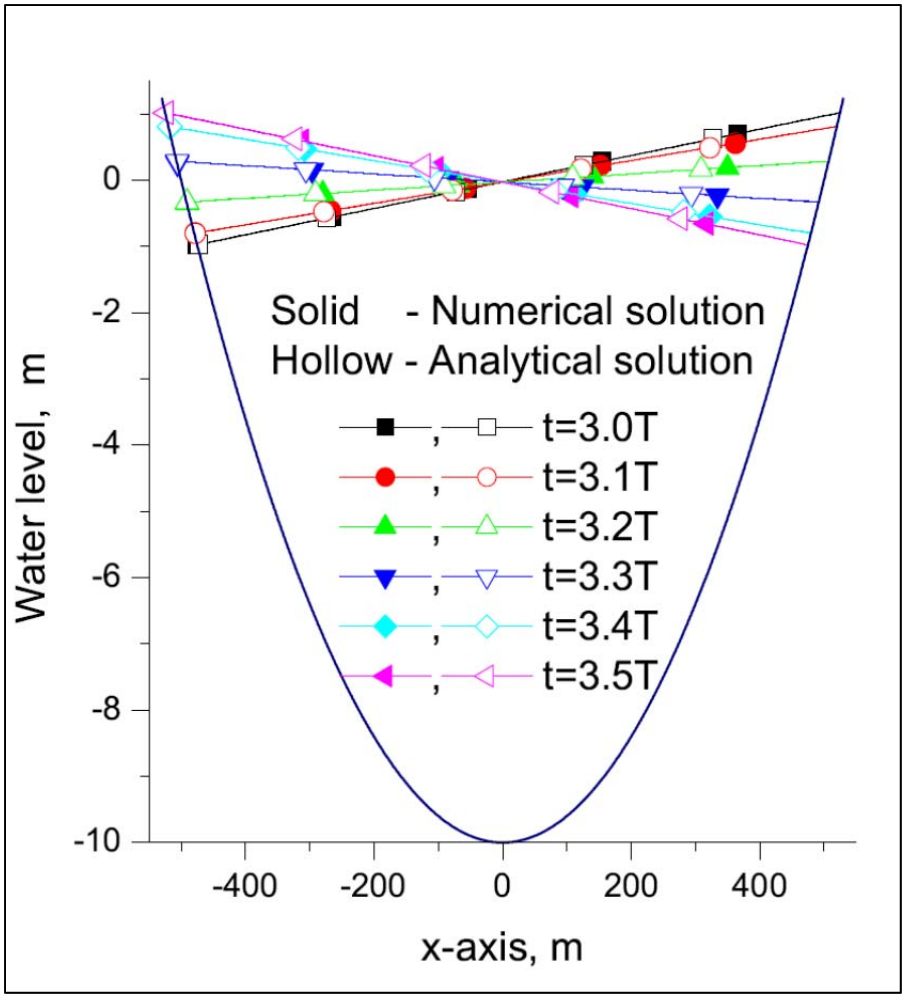

Figure 2-27: Water height profiles ξ(x, 0, t) for numerical (solid) and analytical (hollow) solutions at t = 3T, 3.1T, 3.2T, 3.3T, 3.4T, and 3.5T, where T is the period of the corresponding oscillatory mode.

2.6 References

Arakawa A, Lamb V. 1977. Computational design of the basic dynamical processes of the UCLA general circulation model. In: *Methods in Computational Physics*. Vol. 17. Academic Press, pp. 174–267.

Balay S, Buschelman K, Eijkhout V, Gropp WD, Kaushik D, Knepley MG, McInnes LC, Smith BF, Zhang H. 2004. PETSc Users Manual. *Tech. Rep. ANL-95/11 - Revision 2.1.5*, Argonne National Laboratory.

Briggs M, Synolakis C, Harkins G, Green D. 1995. Laboratory experiments of tsunami runup on a circular island. *Pure and Applied Geophysics* 144, pp. 569–593.

Courant R, Friedrichs K, Lewy H. 1928. Uber die partiellen differenzengleichungen der mathematischen physic. *Mathematische Annalen* 100, pp. 32–74.

Fine I, Rabinovich A, Kulikov E, Thomson R, Bornhold B. 1998. Numerical modeling of landslide-generated tsunamis with application to the Skagway Harbor tsunami of

November 3, 1994. In *Proceedings of international conference on tsunamis: Paris*, pp. 211–223.

Fletcher C. 1991. Computational Techniques for Fluid Dynamics 1. Springer-Verlag, 401 pp.

Goto C, Ogawa Y, Shuto N, Imamura F. 1997. Numerical method of tsunami simulation with the leap-frog scheme. Manuals and Guides 35, UNESCO: IUGG/IOC TIME Project.

Gropp W, Lusk E, Skjellum A. 1999. Using MPI: Portable Parallel Programming with the Message-Passing Interface. The MIT press, 406 pp.

Jiang L, LeBlond P. 1992. The coupling of a submarine slide and the surface waves which it generates: *Journal of Geophysical Research*, 97(C8), 12731–12744.

Jiang L, LeBlond P. 1994. Three-dimensional modeling of tsunami generation due to a submarine mudslide. *Journal of Physical Oceanography*, 24(3):559–572.

Kânoğlu U, Synolakis C. 1998. Long wave runup on piecewise linear topographies. *Journal of Fluid Mechanics* 374, 1-28.

Kato K, Tsuji Y. 1994. Estimation of fault parameters of the 1993 Hokkaido-Nansei-Oki earthquake and tsunami characteristics. *Bulletin of the Earthquake Research Institute* 69, 39–66, University of Tokyo.

Kowalik Z, Murty T. 1993. Numerical modeling of ocean dynamics.World Scientific, 481 pp.

Liu PL-F, Cho YS, Briggs MJ, Kânoğlu U, Synolakis CE. 1995. Runup of solitary waves on a circular island. *J. Fluid Mech*, 302, 259-285.

Liu PL-F, Lynett P, Synolakis CE. 2003. Analytical solutions for forced long waves on a sloping beach. *J. Fluid Mech*, 478, 101–109.

Liu PL-F, Wu T-R, Raichlen F, Synolakis CE, Borrero J. 2005. Runup and rundown generated by three-dimensional sliding masses. *J. Fluid Mech*, 536, 107–144.

Liu PL-F, Yeh H, Synolakis C. 2007. Advanced Numerical Models for Simulating Tsunami Waves and Runup. Vol. 10 of Advances in Coastal and Ocean Engineering. World Scientific, Proceedings of the Third International Workshop on Long-Wave Runup Models, Catalina, (2004) Benchmark problems, pp. 223–230.

Lynett P, Wu T-R, Liu PL-F. 2002. Modeling wave runup with depth-integrated equations. *Coastal Engineering* 46 (2): 89–107.

Nicolsky DJ, Suleimani EN, Hansen RA. 2010. Numerical modeling of the 1964 Alaska tsunami in western Passage Canal and Whittier, Alaska. *Natural Hazards and Earth System Sciences*, 10, 2489-2505, doi:10.5194/nhess-10-1-2010.

Nicolsky DJ, Suleimani E, Hansen R. 2011. Validation and verification of a numerical model for tsunami propagation and runup. *Pure and Applied Geophysics*, 168:1199–1222, doi 10.1007/s00024-010-0231-9.

Okada Y. 1985. Surface deformation due to shear and tensile faults in a half-space. *Bulletin of the Seismological Society of America* 75, 1135–1154.

Plafker G, Kachadoorian R, Eckel E, Mayo L. 1969. Effects of the Earthquake of March 27, 1964 on various communities: U.S. Geological Survey Professional Paper 542-G, 50 p.

Suleimani E, Nicolsky D, Haeussler P, Hansen R. 2011. Combined effects of tectonic and landslide-generated tsunami runup at Seward, Alaska during the Mw9.2 1964 earthquake, *Pure Appl. Geophys* 168, pp. 1053--1074, doi:10.1007/s00024-010-0228-4.

Synolakis C. 1986. The Runup of Long Waves. Ph.D. thesis, California Institute of Technology, Pasadena, California, 228 pp..

Synolakis C, Bernard E. 2006. Tsunami science before and beyond Boxing Day 2004: *Philosophical Transactions of the Royal Society A*, v. 364, n. 1845, p. 2231–2265.

Synolakis C, Bernard E, Titov V, Kânoğlu U, González F. 2007. Standards, criteria, and procedures for NOAA evaluation of tsunami numerical models. OAR PMEL-135 Special Report, NOAA/OAR/PMEL, Seattle, Washington, 55 pp.

Synolakis C, Bernard E, Titov V, Kânoğlu U, González F. 2008. Validation and verification of tsunami numerical models. *Pure and Applied Geophysics* 165, 2197–2228.

Takahashi T, Takahashi T, Shuto N, Imamura F, Ortiz M. 1995. Source models for the 1993 Hokkaido-Nansei-Oki earthquake tsunami. *Pure and Applied Geophysics* 144, 747–768.

Thacker W. 1981. Some exact solutions to the nonlinear shallow-water wave equations. *Journal of Fluid Mechanics* 107, 499–508.

Titov V, Synolakis C. 1995. Evolution and runup of breaking and nonbreaking waves using VTSC2. *Journal of Waterway, Port, Coastal and Ocean Engineering* 121 (6): 308–316.

Titov V, Synolakis C. 1998. Numerical modeling of tidal wave runup. *Journal of Waterway, Port, Coastal and Ocean Engineering* 124, 157–171.

Tuck EO, Hwang LS. 1972. Long wave generation on a sloping beach. *J. Fluid Mech.* 51, 449–461.

Yeh H, Liu PL-F, Synolakis C. 1996. Long-Wave Runup Models. World Scientific, 403 pp.

Zhang Y, Baptista A. 2008. An efficient and robust tsunami model on unstructured grids. Part I: Inundation benchmarks. *Pure and Applied Geophysics* 165, 2229–2248.

3 ATFM (Alaska Tsunami Forecast Model)

Bill Knight

Zygmunt Kowalik: University of Alaska, Fairbanks- Institute of Marine Sciences (UAF-IMS)

Paul Whitmore: NOAA/NWS/West Coast and Alaska Tsunami Warning Center (WCATWC), Palmer, AK

Bill Knight: WCATWC, Palmer AK, UAF-IMS, Fairbanks, AK

3.1 Introduction

The Alaska Tsunami Forecast Model (ATFM) began as a collaborative effort between two of the members (Kowalik and Whitmore) and became operational at the WCATWC in 1997 (Kowalik and Whitmore, 1991; Whitmore and Sokolowski, 1996). This is known as the "classic" model currently used in WCATWC operations. This model has been tested against the analytical solutions of Carrier and Greenspan (1958) and Thacker (1981). From 2004 on, the model has been substantially reworked into a second forecast model, which is called ATFMv2. The benchmark challenge problems were computed with this newer model.

The design philosophy behind both models is to focus on tectonic sources and to use the models to pre-compute hundreds of tsunami "scenarios". Because of the tectonic-only usage, a subset of the benchmarks proposed in Synolakis et al. (2007) has been validated here.

3.2 Model description

The ATFM solves the non-linear shallow water equations. Two equations of motion and one continuity equation are formulated in spherical coordinates and solved on structured, nested meshes. The two horizontal components of velocity (U and V) are depth averaged. The vertical component of velocity (W) is not considered in the hydrostatic formulation.

The solution technique for U and V is based on a differencing method described in Kowalik and Murty (1993), and the sea level (η) is computed with a second-order accurate, upwind scheme that conserves mass to machine accuracy (Van Leer, 1977). The runup / run-down method is based on the VOF approach pioneered by Nichols and Hirt (1980), and Hirt and Nichols (1981). There is no explicit dispersion in the model, although a non-hydrostatic addition is under development and is in the testing phase (Walters, 2005, Yamazaki et al. 2009). Sub-meshes are nested within parent meshes to increase spatial resolution where needed. Information is passed both from low to high resolution meshes and back, based on a mass conserving interconnect scheme (Berger and Leveque, 1998). Discretization for the 3 field variables (U, V, and η) uses the staggered "C grid" layout.

The model is coded in FORTRAN 90 and in Co-array FORTRAN. It has been run on PCs, a Cray X1, and a Penguin Computing cluster comprised of Opteron processors.

Some notation:

R_e = radius of earth (assumed uniform)
Ω = earth's rotation rate
λ = longitude, φ = latitude
U and V are the east, and north pointing velocity components
η = sea surface elevation
h = still water depth
ξ = ocean bottom uplift
α = dimensionless bottom friction parameter
G = gravity acceleration

The equations solved are:

$$\frac{\partial U}{\partial t}+\frac{U}{R_e\cos\phi}\frac{\partial U}{\partial \lambda}+\frac{V}{R_e}\frac{\partial U}{\partial \emptyset}-\frac{UV}{R_e}\tan\phi=2\Omega \mathrm{V}\sin\phi-\frac{G}{R_e\cos\phi}\frac{\partial \eta}{\partial \lambda}-\alpha\sqrt{U^2+V^2}\frac{U}{(\eta+h-\xi)} \quad (1)$$

$$\frac{\partial V}{\partial t}+\frac{U}{R_e\cos\phi}\frac{\partial V}{\partial \lambda}+\frac{V}{R_e}\frac{\partial V}{\partial \emptyset}+\frac{U^2}{R_e}\tan\phi=-2\Omega U\sin\phi-\frac{G}{R_e}\frac{\partial \eta}{\partial \phi}-\alpha\sqrt{U^2+V^2}\frac{V}{(\eta+h-\xi)} \quad (2)$$

$$\frac{\partial \eta}{\partial t}-\frac{\partial \xi}{\partial t}+\frac{1}{R_e\cos\phi}\frac{\partial}{\partial \lambda}\big((\eta+h-\xi)U\big)+\frac{1}{R_e\cos\phi}\frac{\partial}{\partial \phi}\big((\eta+h-\xi)V\cos\phi\big)=0 \quad (3)$$

The UV and U^2 terms in the equations of motion (1 and 2) are small and are neglected in the ATFM. Note that for benchmark problems 1, 4, and 6, the equations were also re-formulated in simpler 2-D Cartesian coordinates.

3.2.1 BP1: Solitary wave on a simple beach – analytical

The model solution is compared to an analytical solution of the one dimensional, hydrostatic shallow water equations. With that comparison in mind, the bottom friction parameter has been set to zero. Numerical dispersion is also near zero through the choice of high spatial resolution. The problem set up is shown in Figure 3-1.

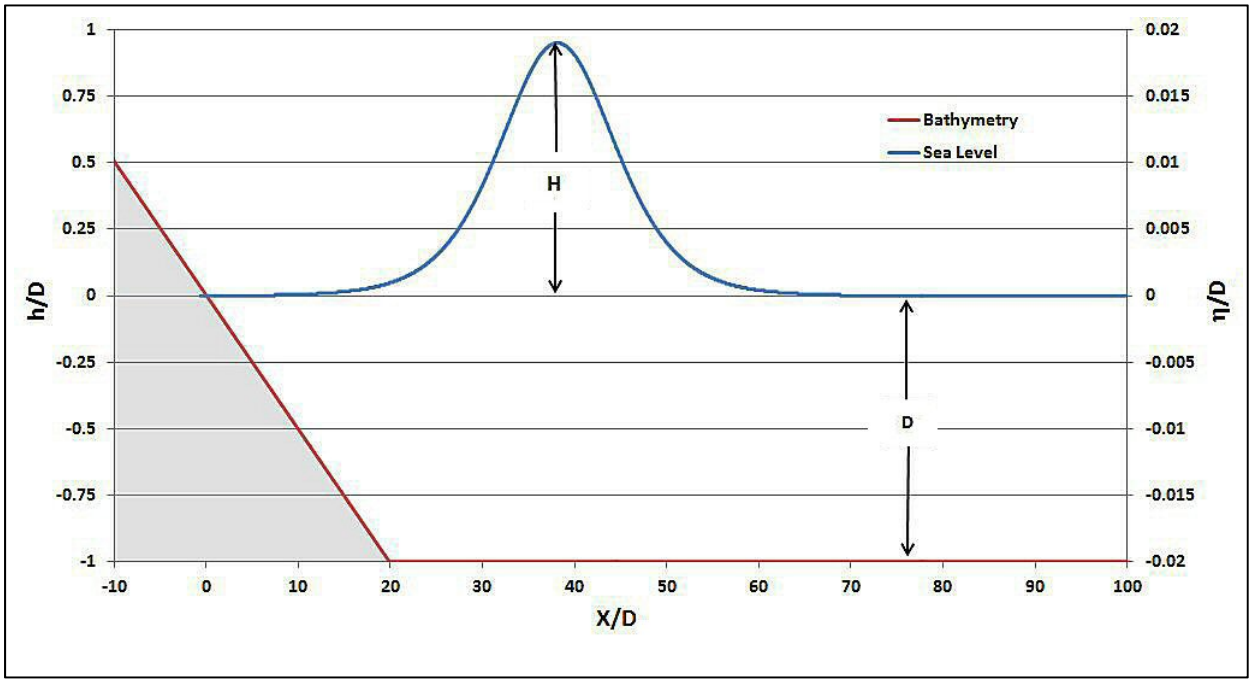

Figure 3-1: Initial condition for BP1. Note figure is not drawn to scale. The right vertical scale shows the range of sea level used in the benchmark, and the left vertical scale shows the ratio of maximum heights (H) to depth (D).

The runup (R) in this and in later benchmarks is defined as maximum height reached by the water on dry land. In this benchmark, runup (R), sea level (η), and time (t) are replaced with their dimensionless counterparts $\frac{R}{D}, \frac{\eta}{D}, and\ t * \sqrt{\frac{G}{D}}$. The beach slope is fixed at 2.88 degrees and the initial non-dimensional amplitude (H/D) is set to 0.019. At t_0, the solitary wave is positioned such that the sea level equals e^{-3} of the maximum height H at the toe of the slope (X/D = 20). The "beach" is the origin of the coordinate x, with x increasing towards deep water. A uniform mesh with resolution D/20 was used to compute sea level profiles at six dimensionless times. The time step was set at $\frac{1}{200}\sqrt{\frac{D}{g}}$ to insure the Courant-Friedrichs-Lewy (CFL) condition was met. Results are displayed in Figure 3-2 and Figure 3-3.

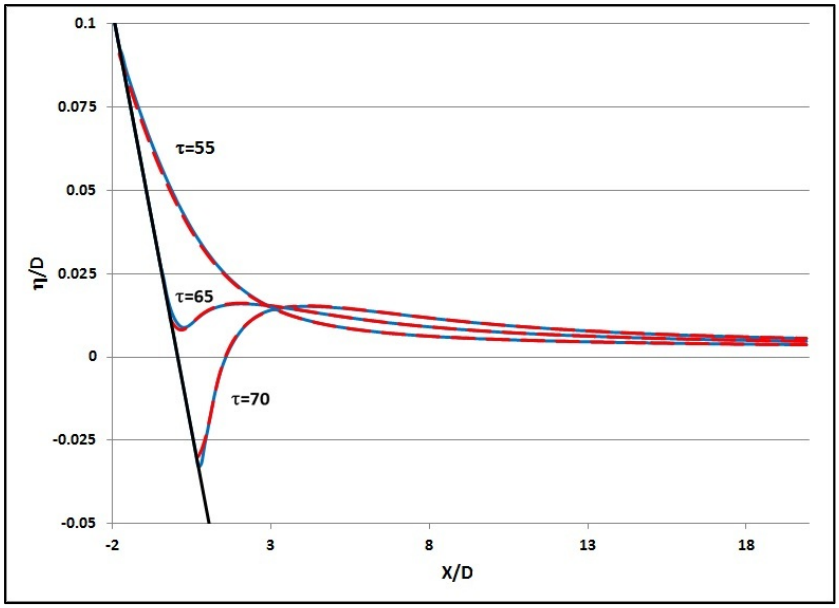

Figure 3-2: Non-dimensional sea level profiles as a function of non-dimensional distance for BP1. Dashed red lines are the analytic result while the solid blue are modeled results for dimensionless times τ = 35 to 45.

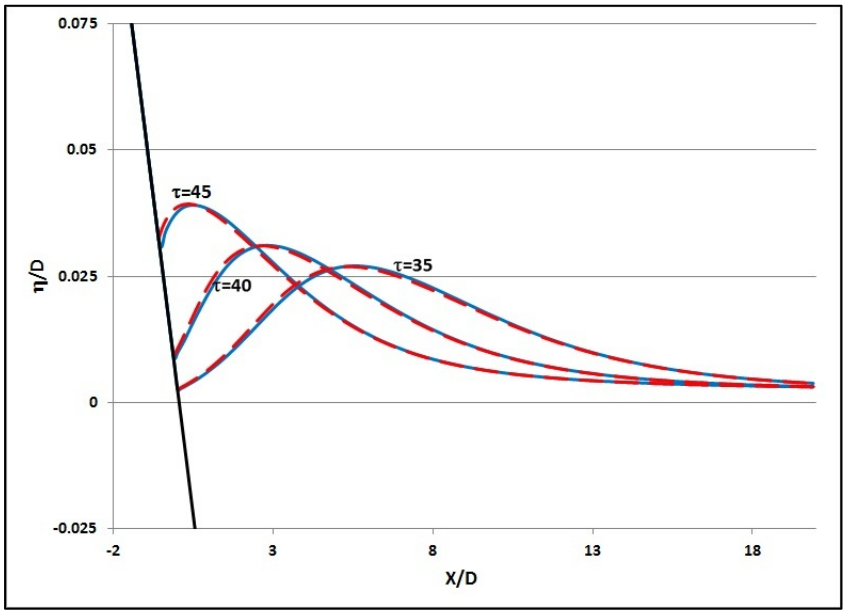

Figure 3-3: Non-dimensional sea level profiles as a function of non-dimensional distance for BP1. Dashed red lines are the analytic result while the solid blue are the modeled results for dimensionless times τ = 55 to 70.

The maximum predicted runup (R/D) is 0.0901 at $\tau = 55.4$. This is within 2% of the theoretical runup value. The total system mass, normalized to the initial solitary wave mass, varies by only 1.0×10^{-6} during the model run. Additional plots of sea surface elevation vs. time at two positions x/D = 0.25 (near the initial shoreline) and x/D = 9.95 (between beach and initial

solitary wave crest are displayed in Figure 3-4. The data gap at x/D = 0.25 for dimensionless times 67 <τ< 82 occurs when the beach is temporarily dry. Normalized *RMS* errors (Horrillo and Kim, 2011), are under 3% in all cases.

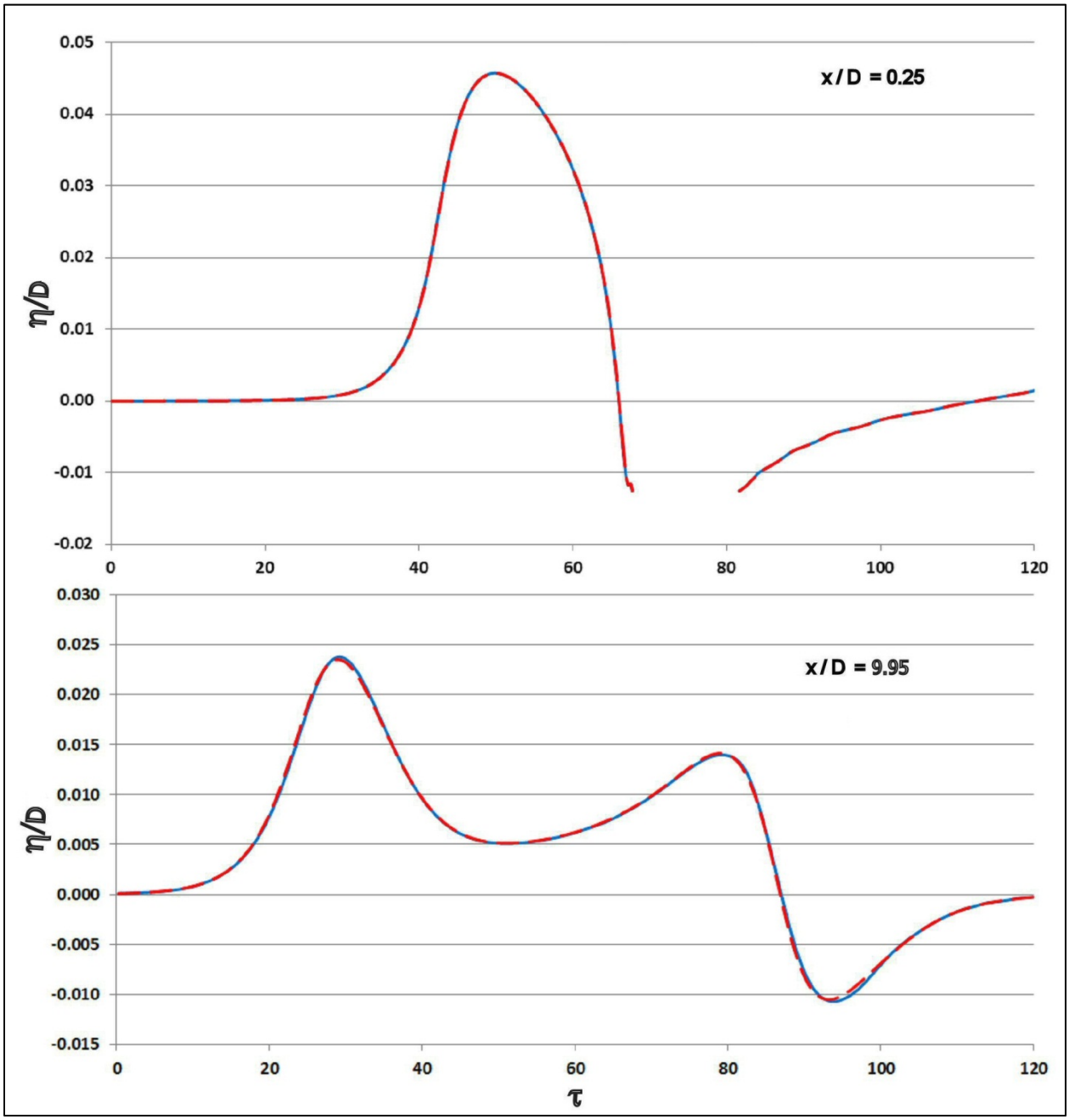

Figure 3-4: Non-dimensional sea level as a function of non-dimensional time at two positions for BP1. Dashed red lines are the analytic result while the solid blue lines are model results.

The results previously shown were obtained with a mesh resolution of D/20. To investigate the approach to mesh independence, the maximum runup was recomputed with resolutions

increasing from D/2 to D/256. Figure 3-5 shows the approach to a final value of R/D which is within 3.1% of the theoretical value of 0.0889.

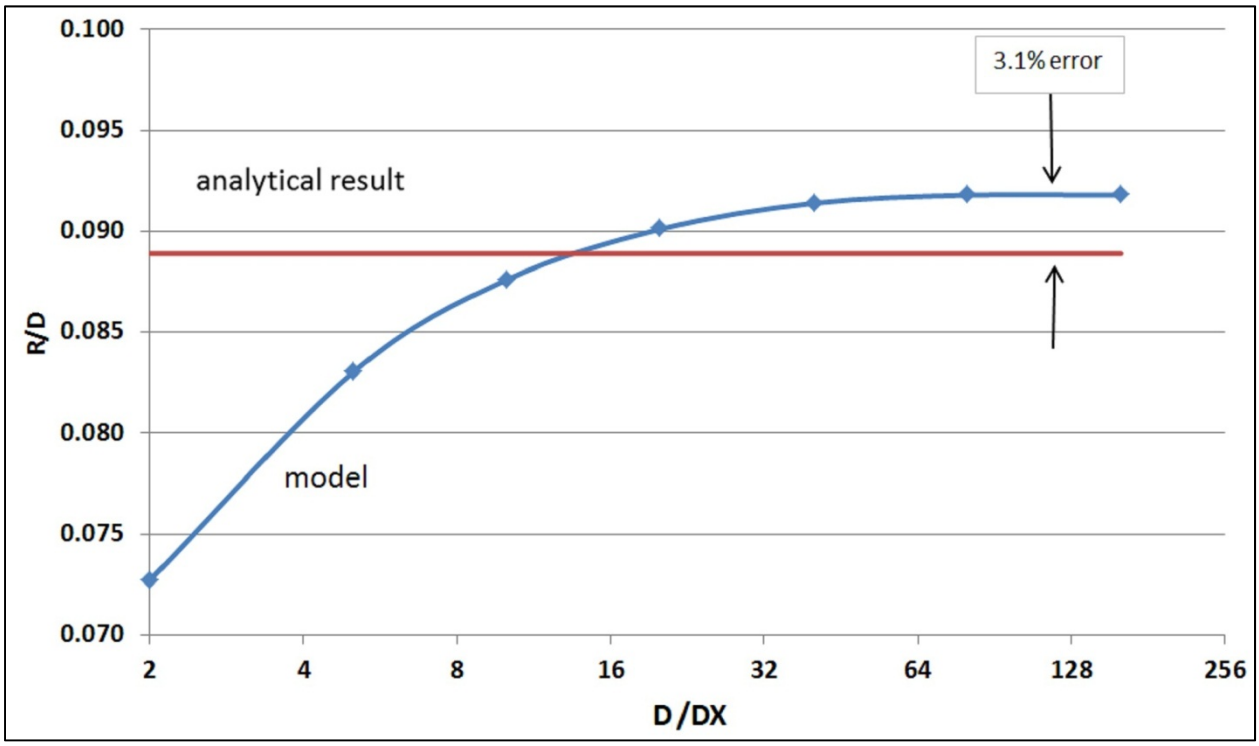

Figure 3-5: Comparison of non-dimensional model runup (blue line) to the analytical result (red line) with increasing mesh resolution. All other computations for this benchmark were computed with D/DX = 20.

3.2.2 BP4: Solitary wave on a simple beach – experimental

This benchmark is the experimental counterpart of BP1. The model results are compared to data obtained in a rectangular flume tank (Synolakis, 1986). In this benchmark test, the ATFM used more realistic non-zero values of bottom friction and horizontal friction. Some dependence on these parameters is noted. Two cases are modeled: one is a non-breaking solitary wave (H/D = 0.0185) and the second is a breaking wave (H/D = 0.3), using initial conditions as illustrated in Figure 3-1 In the latter case, a reasonable fit to observation could only be obtained with the non-hydrostatic pressure field included in the ATFM. The model depth D was set at 30 cm and resolution at D/20 for both runs. Results are displayed in **Error! Reference source not ound.** and Figure 3-7. Model results are in black and experimental data in red. The plots show the best model result obtained, which occurred with bottom friction $\alpha = 0.01$ (dimensionless) and horizontal friction $\nu = 0.01$ m^2/s. The hydrostatic ATFM result for H/D = 0.3 is shown in Figure 3-8 for comparison.

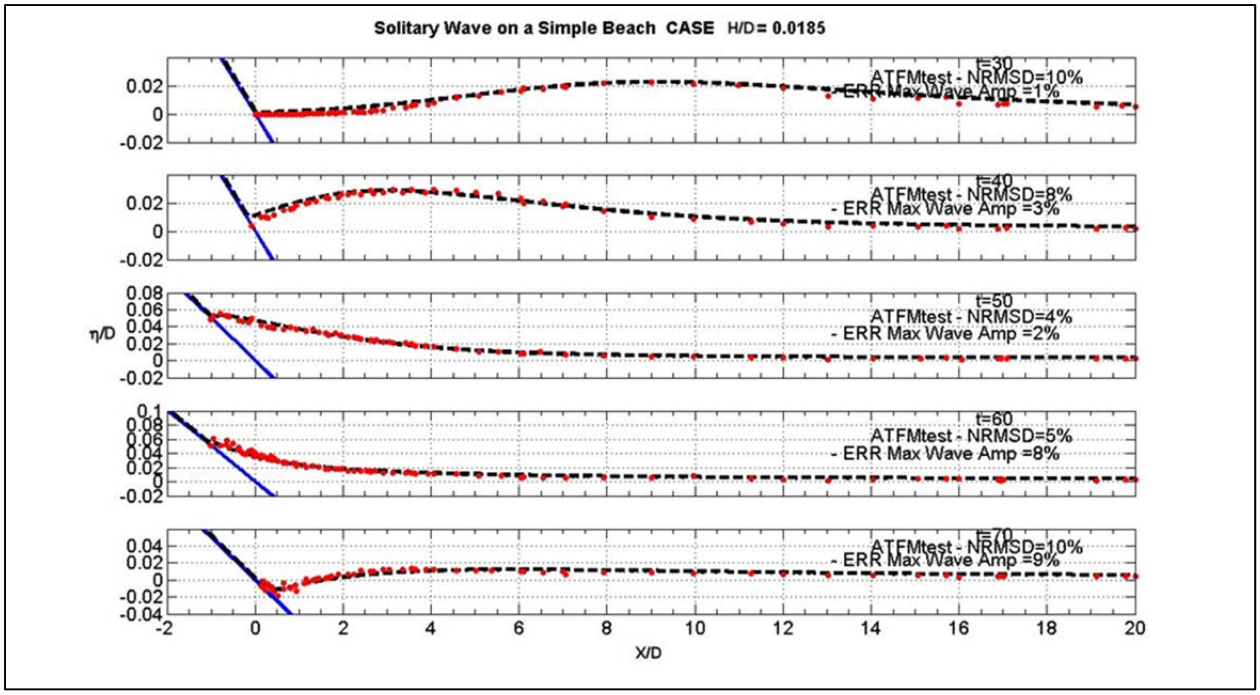

Figure 3-6: Non-dimensional sea level vs. non-dimensional distance for several non-dimensional times. Model results and experimental data for H/D = 0.0185. Model results in black, experimental data in red.

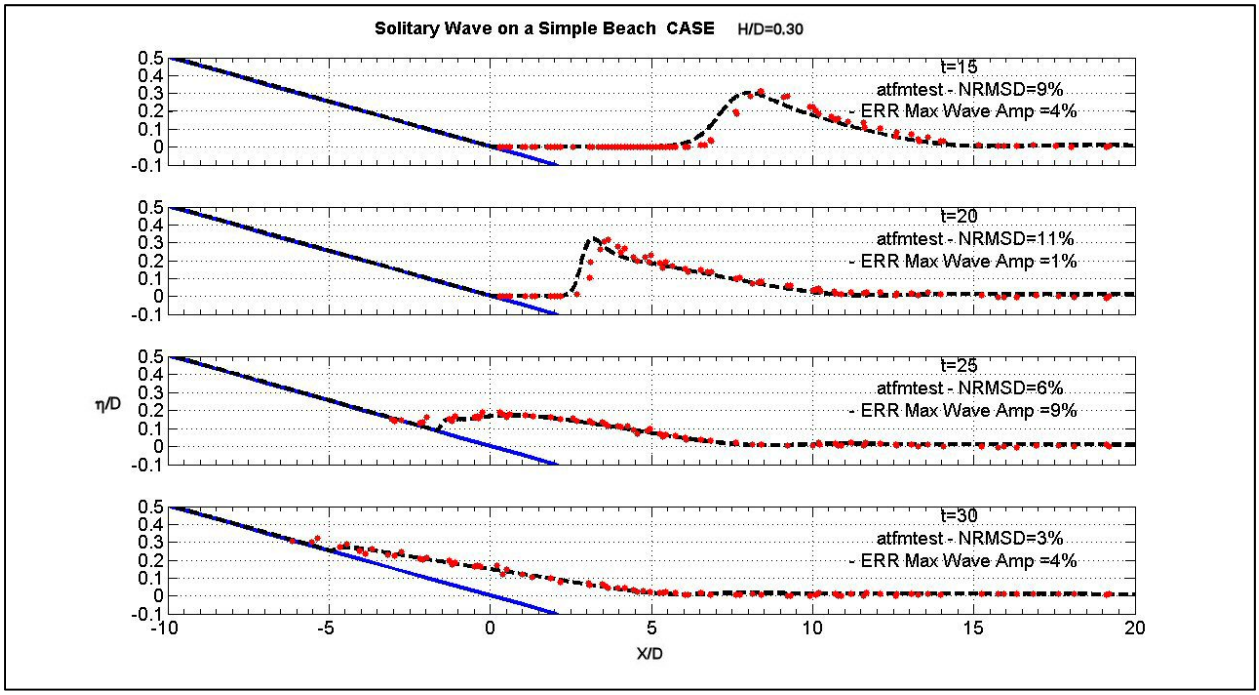

Figure 3-7: Non-dimensional sea level vs. non-dimensional distance for several non-dimensional times. Model results and experimental data for H/D = 0.3. Model results in black, experimental data in red.

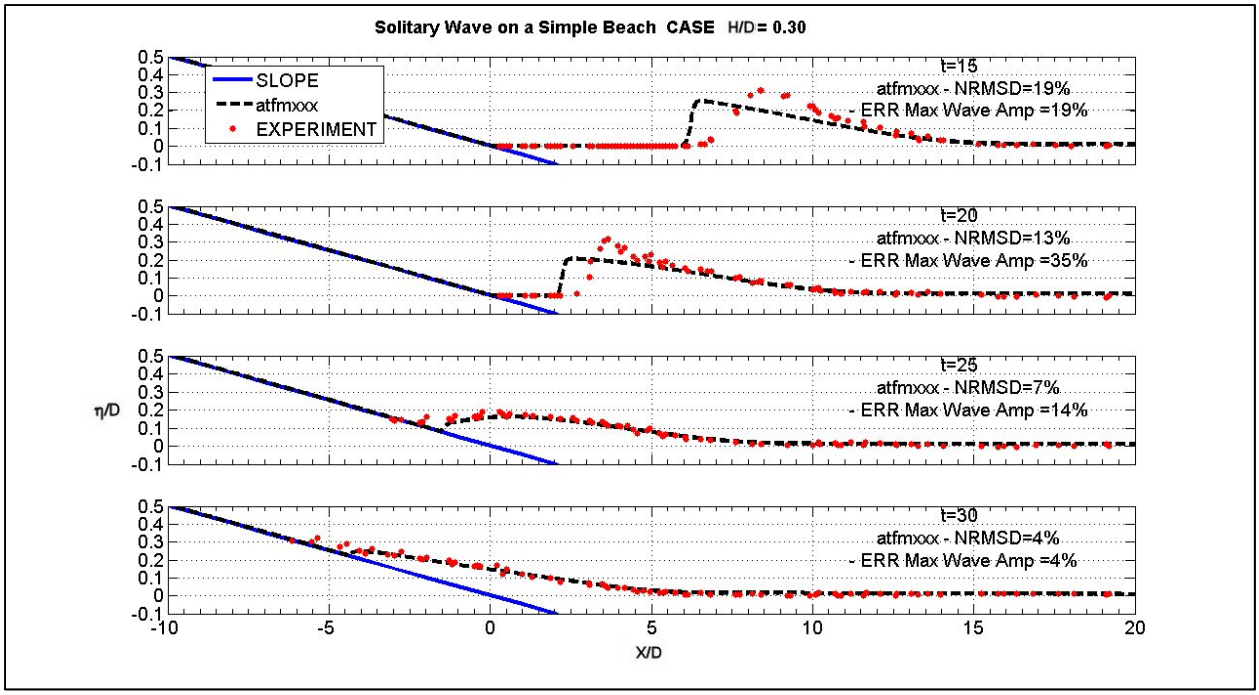

Figure 3-8: Hydrostatic model results and experimental data for H/D = 0.3. Model results in black, experimental data in red.

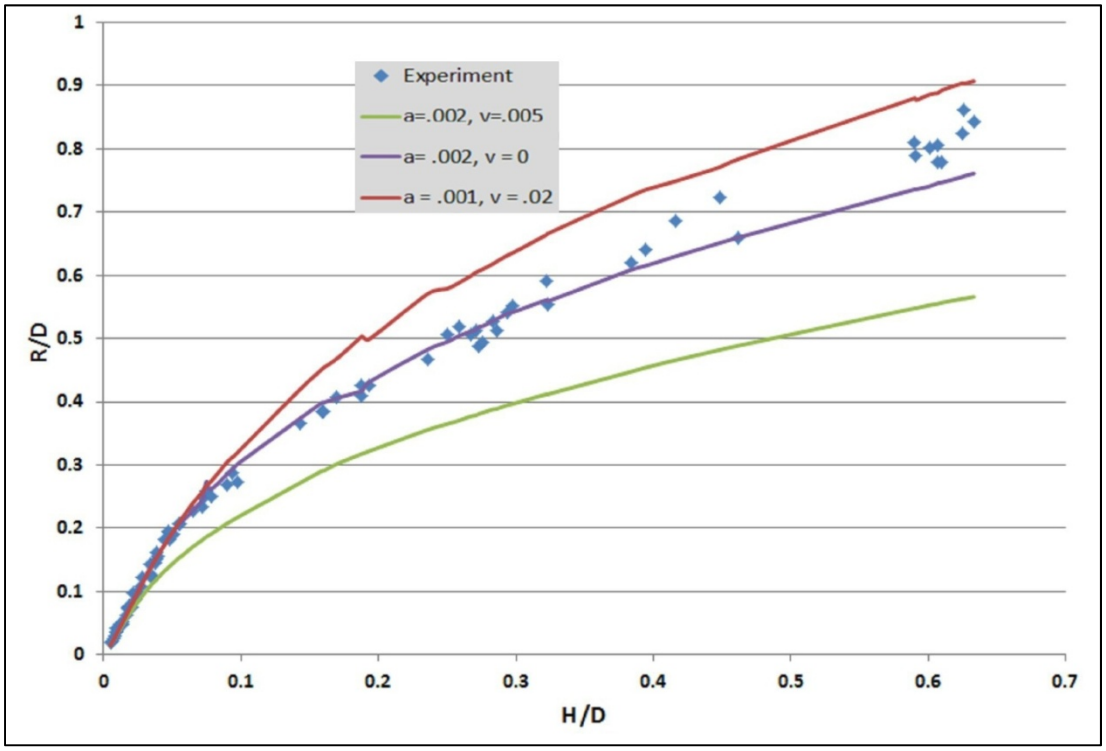

Figure 3-9: Model results for R/D_0 for increasing H/D_0 with various values of α and υ.

A sequence of solitary waves with increasing *H*/*D* was modeled and compared to experimental results (shown in Figure 3-9). The model results are quite sensitive to variations in the friction parameters, although with suitable choices, the experimental results are reproduced fairly well.

3.2.3 BP6: Runup around a conical island – experimental

This benchmark is based on a series of experiments conducted at the U.S. Army Engineer Waterways Experiment Station in Vicksburg, MS (Briggs et al., 1995). Details can be found at http://chl.erdc.usace.army.mil/chl.aspx?p=s&a=Projects;35. An island, idealized as a conical frustum, is placed near the center of a flat-bottomed rectangular tank. The tank dimensions are 30 m wide by 25 m long and the island is 7.2 m in diameter at the base, 2.2 m at the top, with a uniform slope of 1 in 4. The water depth (D) is 0.32 m. In three separate experiments, a plane solitary wave is produced with wave paddles. The waves are generated at one side of the tank and overtake the island as they travel toward the opposite side. Gauges placed at several locations record the "sea surface" time series. The angular distribution of runups is also recorded. The three cases, labeled "A", "B", and "C", have starting *H*/*D* ratios of 0.045, 0.096 and 0.181 respectively. The benchmark task is to replicate the time series from 4 of these gauges along with the island runups for the three cases. A "zeroth order" model challenge is to reproduce the wave splitting at the forward side of the island, refractive wrapping around both sides, and then recombining at the lee side of the island to produce a runup spike. Figure 3-10 shows the model result for Run C.

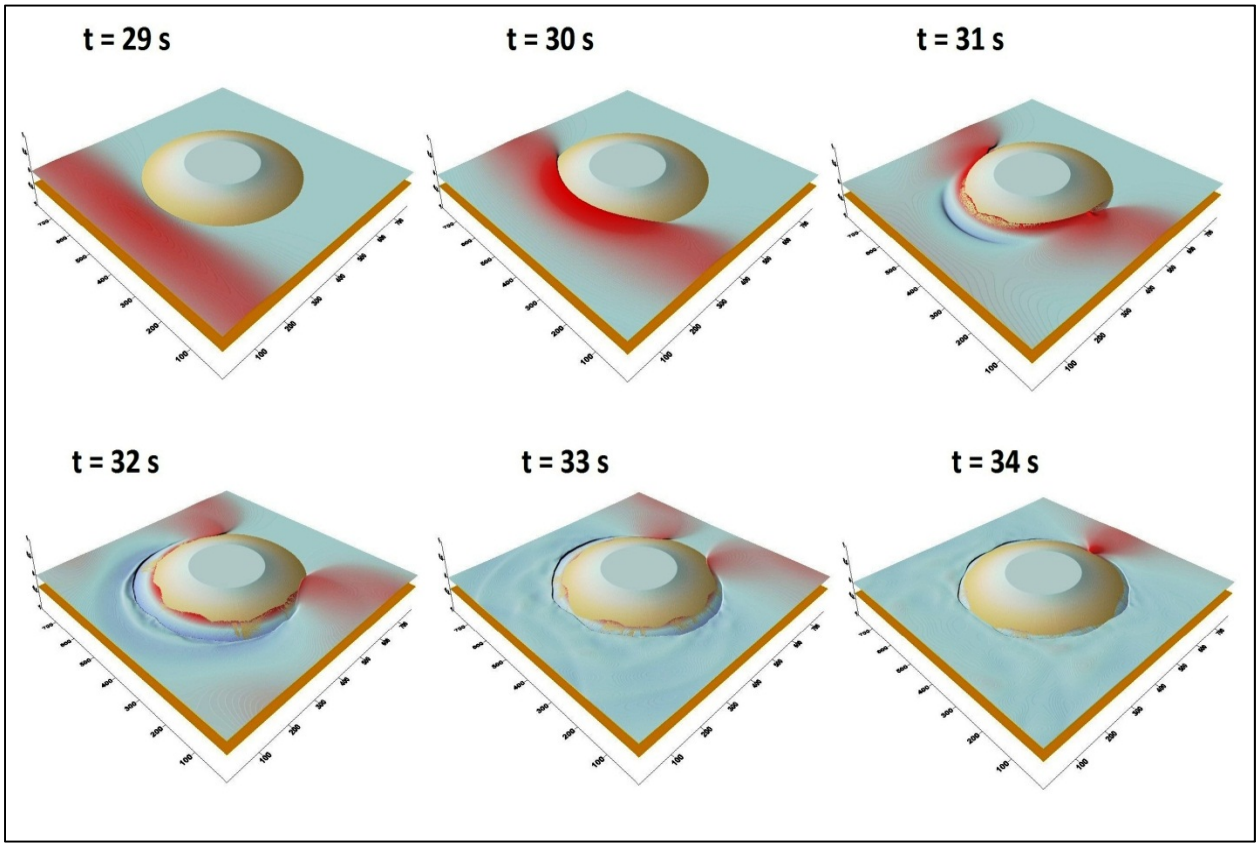

Figure 3-10: Run C model results for BP6 in one second steps from time t = 29 to 34 seconds.

Case C required the non-hydrostatic version of the ATFM to both adequately resolve the initial wavelength and to prevent the wave front from steepening prior to island impact. All runs were then treated as non-hydrostatic problems. In the three cases, a "parent" mesh resolution of D/2 was chosen, and a single nested sub-mesh with spatial resolution of D/32, centered on the island, was added. The sub-mesh length and width equaled the base diameter of the island. The arrangement is illustrated in Figure 3-11. Gauges 9 through 22 are placed in 8 cm of still water depth, and gauge 6 at the base of the island at 32 cm depth. The experimental wavemaker trajectory data were splined to produce a smooth driving function for the left side of the domain. The absorbing sides of the experimental wave tank were modeled with a telescoping mesh along three walls to replicate radiation boundary conditions. The amplitude of the initial modeled waves were higher than predicted from the nearest gauge data, so all amplitudes in the wavemaker paddle trajectory files were scaled by 0.9 to get a better match. No further alterations to the experimental data were made. Results with the non-hydrostatic model using a single grid at a resolution of D/8 were comparable, although the run time was significantly longer.

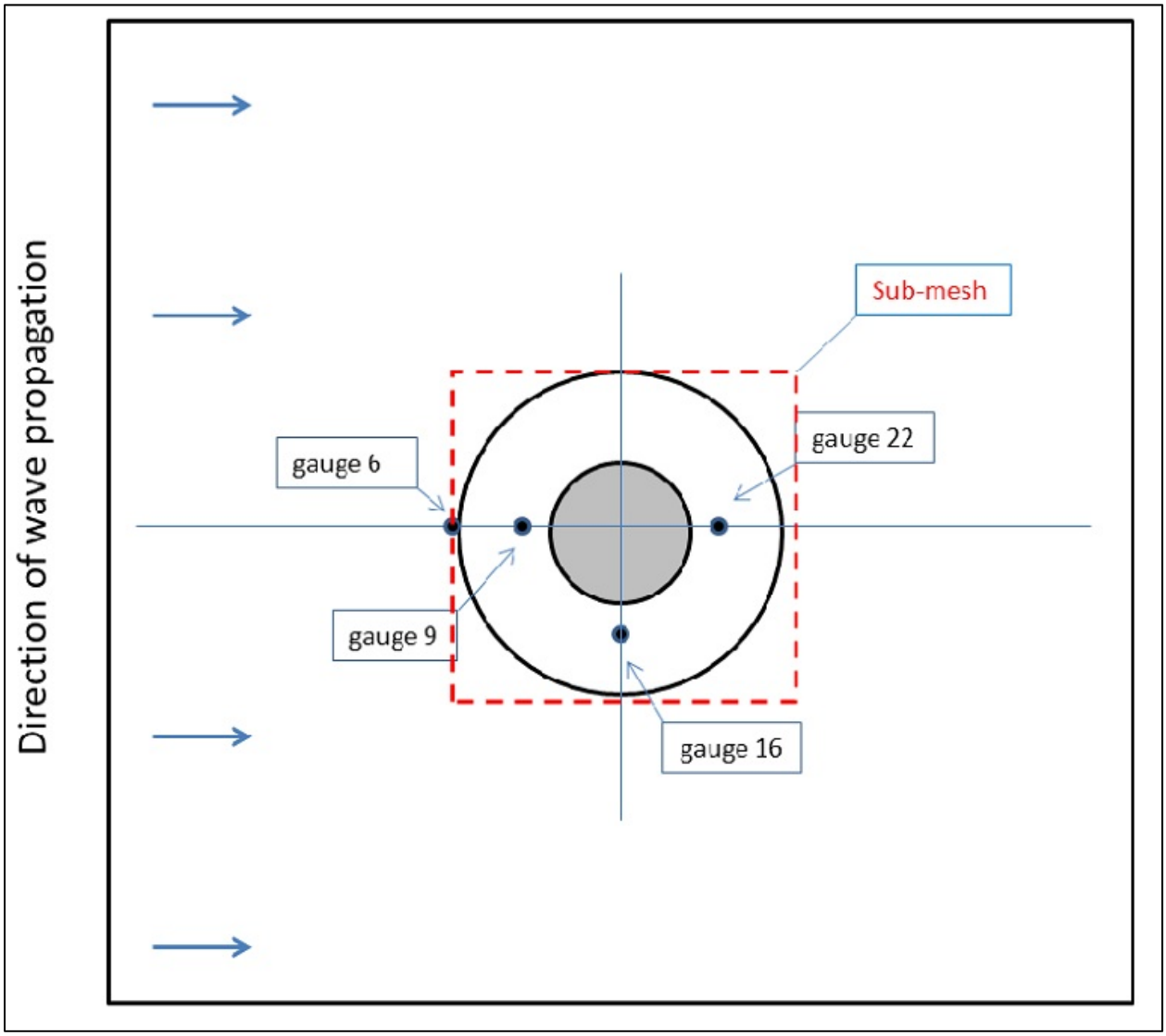

Figure 3-11: Plan view sketch of BP6 domain, sub-mesh, and gauge locations.

The gauge time series for runs A, B, and C are displayed in Figure 3-12 and the runup results in Figure 3-13.

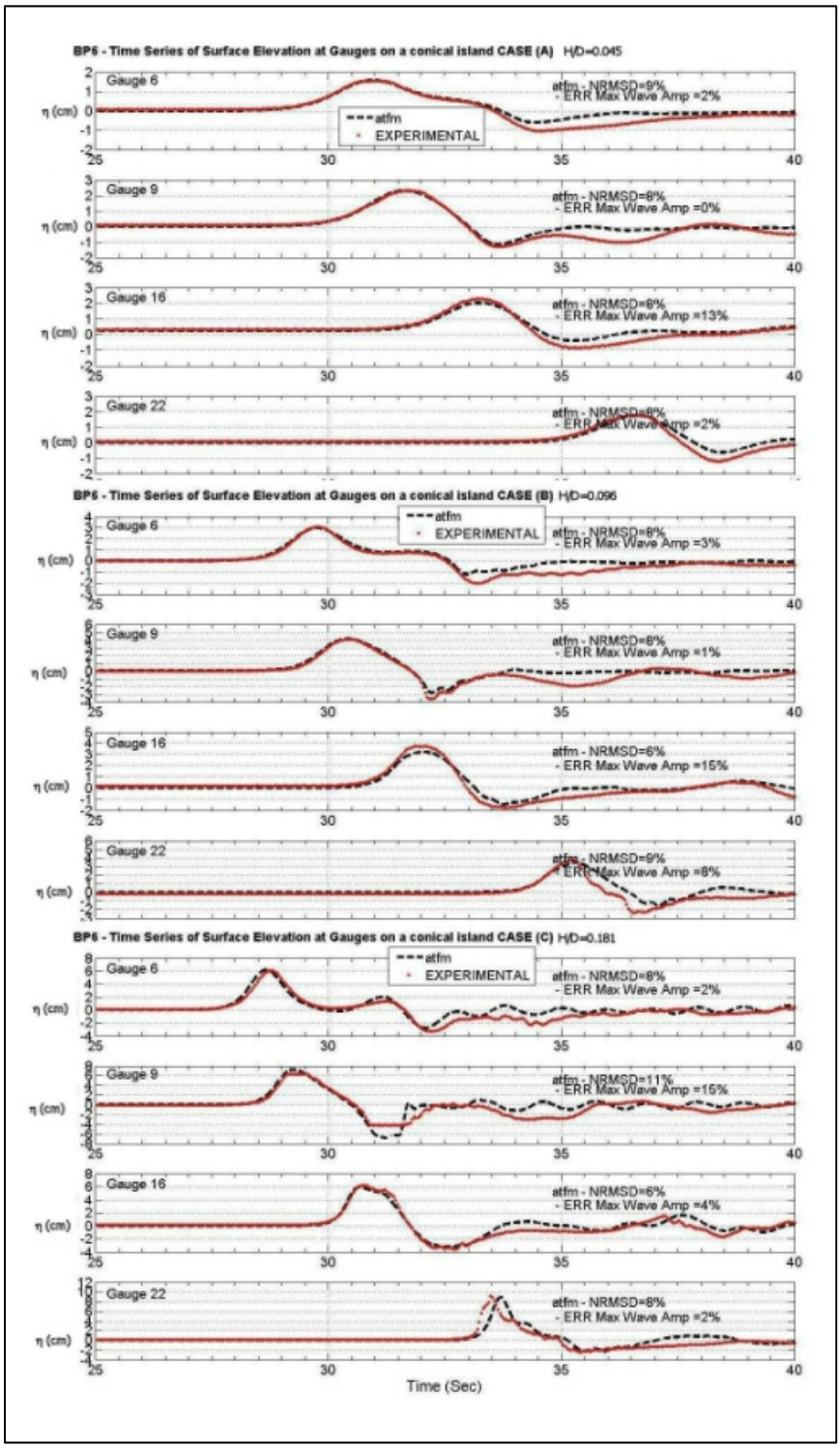

Figure 3-12: Surface elevation vs. time at four gauge locations for BP6, Cases A, B, and C. Model results are in black, and the experimental data are in red.

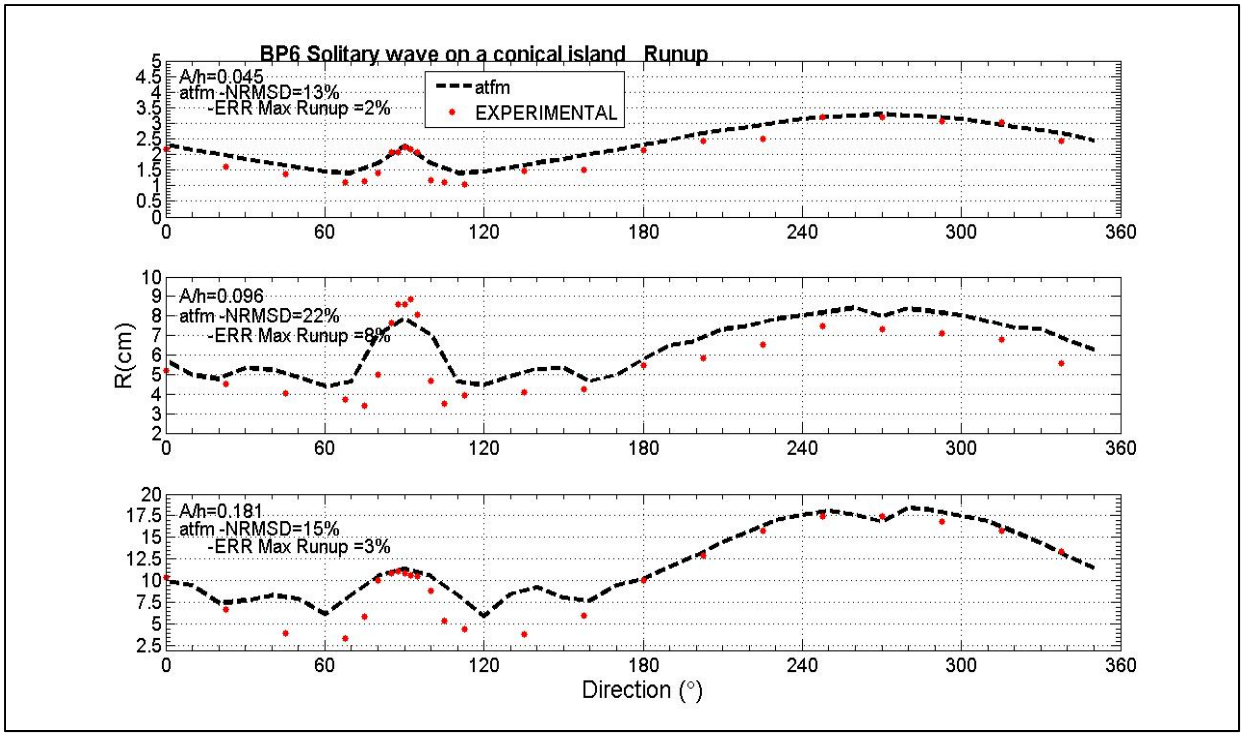

Figure 3-13: Comparison of model runup results with experimental runups for BP6: cases A, B, and C.

3.2.4 BP9: Okushiri Island tsunami – field

Bathymetry and sea surface deformation data files for this study were copied directly from the PMEL download site (http://nctr.pmel.noaa.gov/benchmark/Field/Field_Okushiri/index.html) and used without modification. This benchmark is based on the Sea of Japan earthquake and tsunami of 1993.

The first challenge is to reproduce tide gauge data for Iwanai and Esashi, located on the western side of Hokkaido. A 3x3 array of model grid points centered on each of the two corresponding coastal coordinates produced 9 time series for each location. The best fit from each set of nine model results for these two cases was kept and these are displayed in Figure 3-14. The results for Esashi replicate the observed data rather well while the case for Iwanai is not as good.

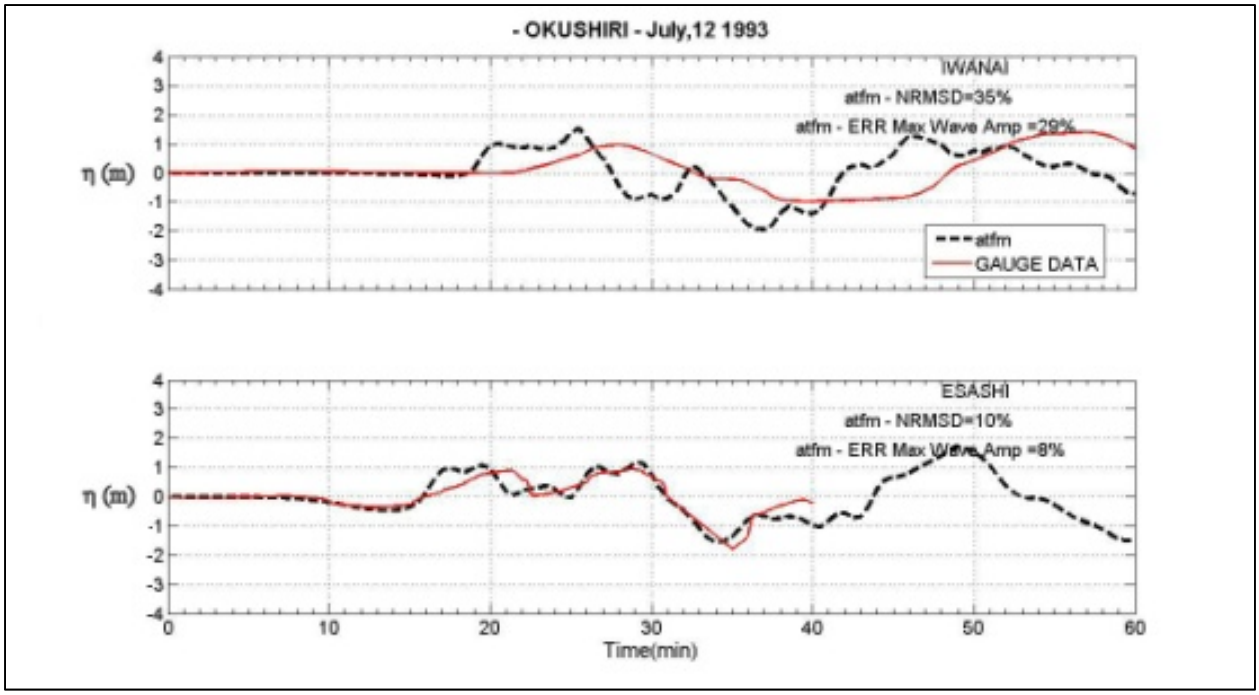

Figure 3-14: Comparison of model results with tide gauge data from the Iwanai and Esashi gauges. Model results are in black, and the measured data are in red.

There appears to be an extensive harbor structure at Iwanai – note map link at: www.tiptopglobe.com/city?n=Iwanai&p=15584#lat=42.98519&lon=140.51308&zoom=14. If this structure was present at the time of the tsunami and if the tide gauge was positioned within the harbor, results obtained with more realistic bathymetry would be required.

The next benchmark test is to reproduce the inundation sequence and its timing for the region around the Aonae peninsula and at Hamatsumae on the southern coast of Okushiri Island. One minute model snapshots are shown in Figure 3-15. The first inundating wave arrives 310 seconds following the earthquake event time. After arriving on the western edge of Aonae, the wavefront is refracted around the tip of the peninsula and arrives at Hamatsumae approximately four minutes later. A reflected wave front, moving westward at this time produces a second inundation on the east side of Aonae fourteen minutes following the initial arrival. Maximum runup and amplitude contours in the vicinity of Aonae are plotted atop local bathymetry and elevations in Figure 3-16. The predicted runup exceeds 12 m near Hamatsumae. Runup predictions for points along the coast of Okushiri Island are compared to field data in Figure 3-17.

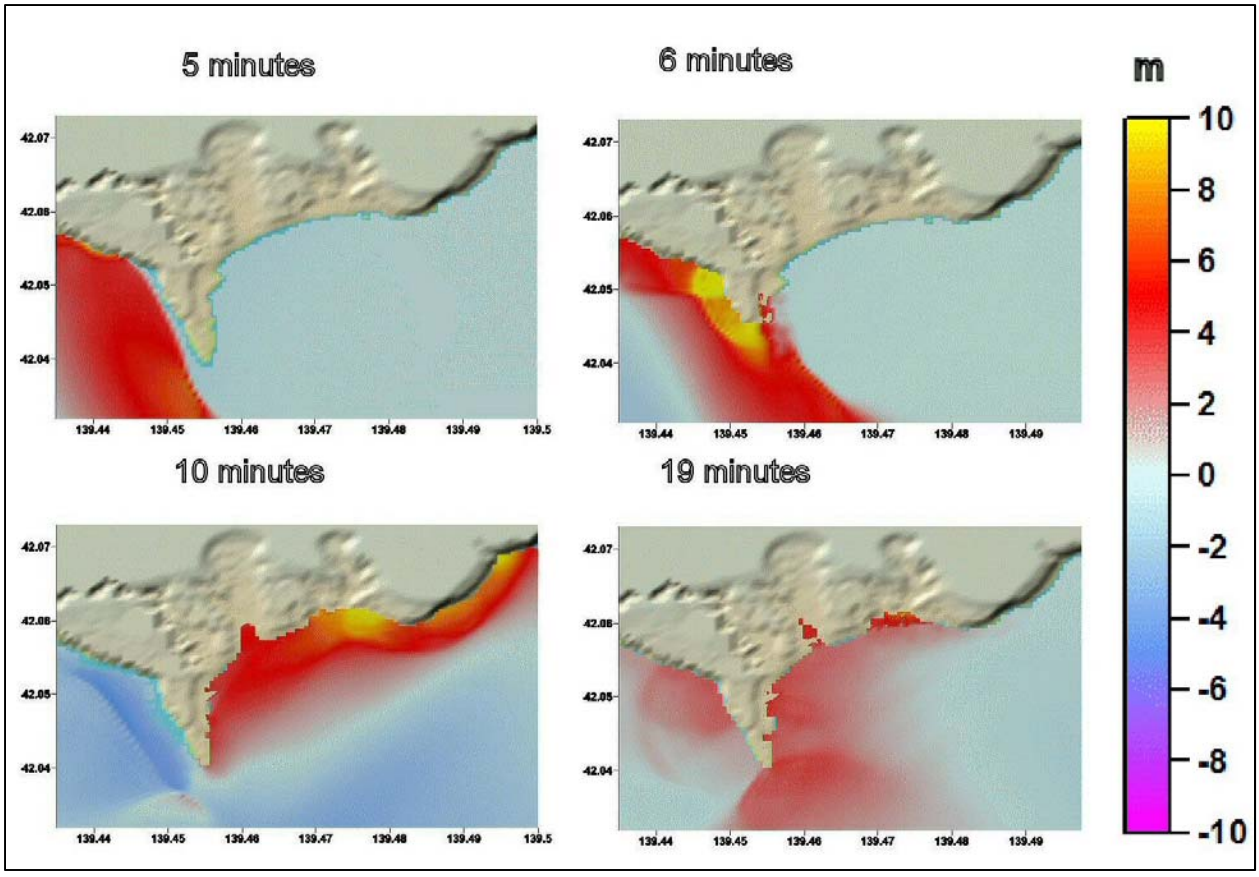

Figure 3-15: Model inundation sequence along the Aonae Peninsula from the 1993 Okushiri Island Tsunami.

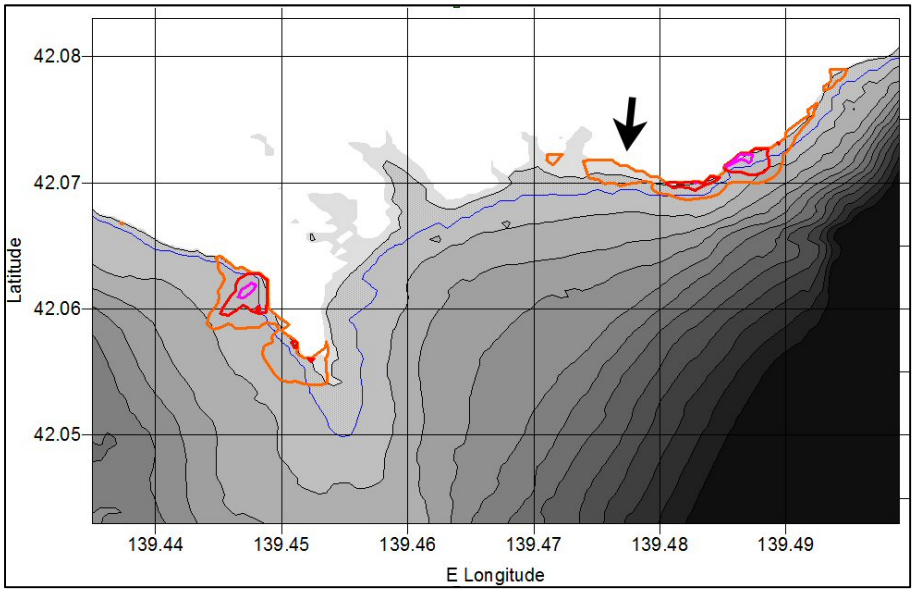

Figure 3-16: Maximum model runups and tsunami amplitudes. Magenta is 14 m, red is 12 m, and orange is 10 m. The original coastline is drawn in blue. The arrow locates the region near Hamatsumae.

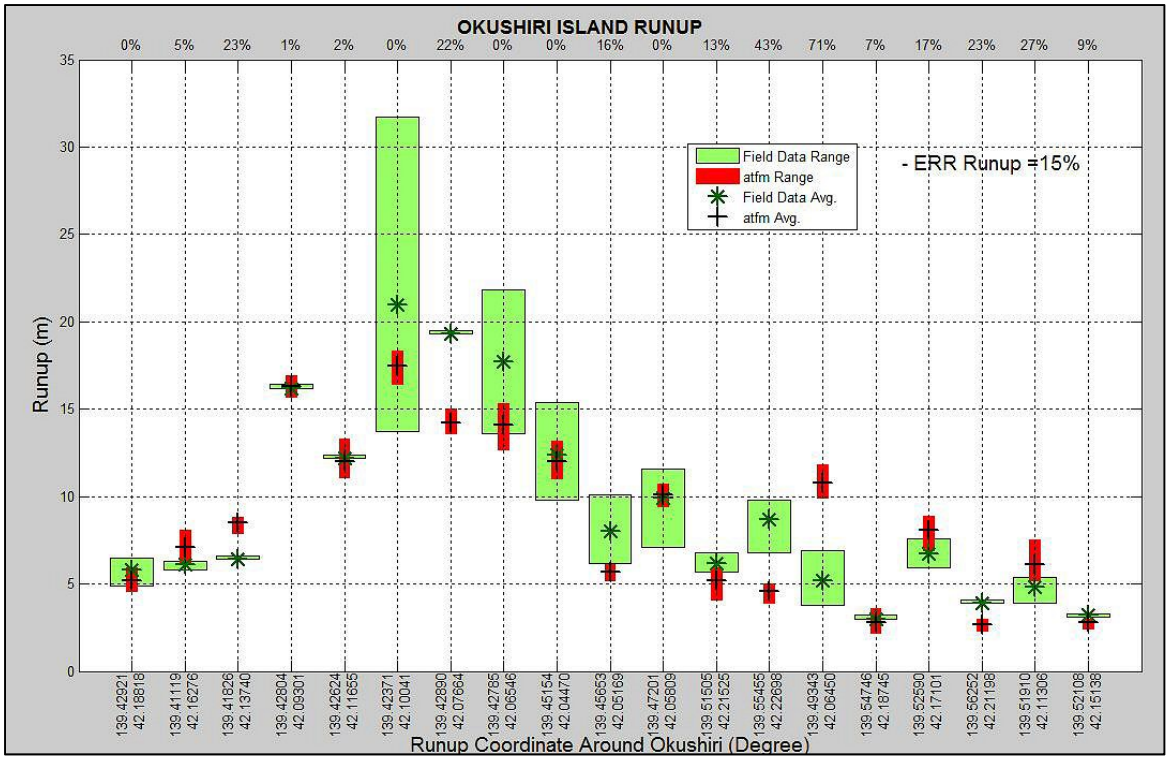

Figure 3-17: Comparison of model inundation forecasts with observations for the 1993 Okushiri Island Tsunami. The spread in model results is from a series of runups at grid points near the test point.

3.3 Observations and next steps

The tests in this report show that the ATFM does a good job of meeting the NOAA tsunami model validation tests set forth in the standards document (Synolakis et al., 2007). In order to get reasonable correspondence with experimental data for some parts of benchmarks 4 and 6, a non-hydrostatic treatment was required. This brings up some questions: does a non-dispersive model leave out important tsunami physics? For large wavelength tectonic sources, is some essential predictive skill left out with the hydrostatic simplification?

Other questions pertain to the use of nested meshes. There are many ways to connect meshes and some of the schemes in use might be unacceptable in certain situations. Are two nested sub-meshes with refinements of 3 and 3 better than a single sub-mesh with a refinement of 9? Under what conditions is two-way data flow between child and parent meshes important? What guidelines can be developed to determine the minimum level of spatial resolution required for various coastline geometries? How should the shorter wavelengths generated within the high resolution meshes be coupled to the coarse parent mesh at mesh / sub-mesh boundaries?

The questions indicate that further research is needed for better matching the tsunami physical process with numerical approximations, and that the additional research would be best addressed by an inter-agency study group with the findings from their investigation reported back to the larger modeler community.

Somewhat unrelated to the above discussion is the observation that there is at least one additional analytical solution to the shallow water equations that includes runup. This solution is

derived for motion in 1-D or 2-D parabolic basins (Thacker, 1981). The solution would be a particularly useful benchmark challenge for future developments in seiche forecasting.

3.4 References

Berger M, Leveque R. 1998. Adaptive mesh refinements using wave propagation algorithms for hyperbolic systems. *SIAM J. Num. Anal.*, 35, 2298-2316.

Briggs M, Synolakis C, Harkins G, Green D. 1995. Laboratory experiments of tsunami runup on a circular island. *Pure and Applied Geophysics*, 144, 569–593.

Carrier GF, Greenspan HP. 1958. Water waves of finite amplitudes on a sloping beach. *J. Fluid Mech.*, 4, 97-109.

Hirt, C, Nichols B. 1981. Volume of fluid (VOF) method for the dynamics of free boundaries. *J. Comp. Phys*, 39, 201-225.

Horrillo J, Kim B. 2011. MATLAB script "ANALY_BM1_SW", Tsunami Model Validation Workshop, Texas A&M campus, Galveston, TX.

Kowalik Z, Whitmore P. 1991. An Investigation of two tsunamis recorded at Adak, Alaska. *Science of Tsunami Hazards*, 9, 67-84.

Kowalik Z, Murty T. 1993. Numerical Modeling of Ocean Dynamics. World Scientific Press, 481 pp.

Nichols B, Hirt C. 1980. Los Alamos National Labs report LA-8355.

Synolakis C. 1986. The runup of long waves. Ph.D. thesis, California Institute of Technology, Pasadena, California, 228 pp.

Synolakis C, Bernard E, Titov V, Kânoğlu U, González F. 2007. Standards, criteria, and procedures for NOAA evaluation of tsunami numerical models. OAR PMEL-135 Special Report, NOAA/OAR/PMEL, Seattle, Washington, 55 pp.

Thacker WC. 1981. Some exact solutions to the nonlinear shallow water wave equations. *J. Fluid. Mech.*, 107, 499-508.

Van Leer B. 1977. Towards the ultimate conservative difference scheme-IV. *J. Comp. Phys.*, 23, 276-299.

Walters RA. 2005. A simple-implicit finite element model for non-hydrostatic (dispersive) surface waves. *Int. J. for Numer. Meth.in Fluids*, 49, 721-737.

Whitmore P, Sokolowski T. 1996. Predicting tsunami amplitudes along the North American coast from tsunamis generated in the northwest Pacific Ocean during tsunami warnings. *Science of Tsunami Hazards*, 14, 147-166.

Yamazaki Y, Kowalik Z, Cheung KF. 2009. Depth integrated, non-hydrostatic model for wave breaking and run-up. *Intl. J. for Num. Meth. in Fluids*, 61, 473-497.

4 Fully Nonlinear Boussinesq Wave Model FUNWAVE-TVD, v. 1.0

Babak Tehranirad, Fengyan Shi, James T. Kirby, Jeffrey C. Harris, Stephan Grilli

Babak Tehranirad. Fengyan Shi, James T. Kirby: Center for Applied Coastal Research, University of Delaware, Neward, DE 19716

Jeffrey C. Harris, Stephan Grilli: Department of Ocean Engineering, University of Rhode Island, Narragansett, RI 02882

4.1 Introduction

This report describes the benchmark testing of the Boussinesq model FUNWAVE-TVD which has been carried out as part of the Benchmark Workshop exercise for the National Tsunami Hazard Mitigation Program. The benchmark tests described here are taken from Synolakis et al. (2007). The report is organized as follows. Section 4.2 provides a description of the model equations and numerical scheme. Section 4.3 provides basic information on hydrodynamic considerations used to judge basic model validity. Sections 4.4 and 4.5 describe benchmark tests for analytical and laboratory cases, respectively. Data for each benchmark are obtained from http://nctr.pmel.noaa.gov/benchmark/. FUNWAVE-TVD is distributed as open source code. General users may obtain the most recent tested version from the web site http://chinacat.coastal.udel.edu/kirby/programs/index.html//, which provides this code along with other programs developed at the Center for Applied Coastal Research. The code is provided along with a UNIX/Linux makefile, a users manual (Shi et al., 2011), and input files for executing the tests described in the manual. The present report will also be updated with each major change in program version. Input files and scripts for executing the benchmark tests described here are provided at

http://chinacat.coastal.udel.edu/programs/funwave/funwave.html.

Version control for FUNWAVE-TVD is done using SVN (Collins-Sussman et al. 2004). Users who would like to become part of the development team should contact Fengyan Shi (fyshi@udel.edu) or Jim Kirby (kirby@udel.edu).

4.2 Model description

In this section, we describe the set of Boussinesq equations that are used as the basis for FUNWAVE-TVD. FUNWAVE-TVD is formuiated in both Cartesian coordinates and in spherical (lat-long) coordinates for application to ocean basin scale problems. The benchmarks considered here are all treated in Cartesian coordinates, and we therefore omit description of the spherical coordinate model. This may be found in Shi et al. (2011). We retain dimensional forms below but will refer to the apparent $O(\mu^2)$ ordering of terms resulting from deviations from hydrostatic behavior in order to identify these effects as needed. Here. μ is a parameter characterizing the ratio of water depth to wave length, and is assumed to be small in classical

Boussinesq theory. The model equations used here follow from the work of Chen (2006). In this and earlier works starting with Nwogu (1993), the horizontal velocity is written as

$$u = u_\alpha + u_2(z) \tag{1}$$

Here, u_α denotes the velocity at a reference elevation $z = z_\alpha$, and

$$u_2(z) = (z_\alpha - z)\nabla A + \frac{1}{2}\left(z_\alpha^2 - z^2\right)\nabla B \tag{2}$$

represents the depth-dependent correction at $O(\mu^2)$, with A and B given by

$$A = \nabla \cdot (h u_\alpha)$$

$$B = \nabla \cdot u_\alpha \tag{3}$$

The derivation follows Chen (2006) except for the additional effect of letting the reference elevation z_α vary in time according to

$$z_\alpha = \zeta h + \beta \eta \tag{4}$$

where h is local still water depth, η is local surface displacement, and ζ and β are constants, as in Kennedy et al. (2001). This addition does not alter the details of the derivation, which are omitted below.

4.2.1 Governing equations

The equations of Chen (2006) extended to incorporate a possible moving reference elevation follow. The depth-integrated volume conservation equation is given by

$$\eta_t + \nabla \cdot M = 0 \tag{5}$$

where

$$M = H\left\{u_\alpha + \bar{u}_2\right\} \tag{6}$$

is the horizontal volume flux. $H = h + \eta$ is the total local water depth and $\bar{u}_2$ is the depth averaged $O(\mu^2)$ contribution to the horizontal velocity field, given by

$$\bar{u}_2 = \frac{1}{H}\int_{-h}^{\eta} u_2(z)dz = \left(\frac{z_\alpha^2}{2} - \frac{1}{6}(h^2 - h\eta + \eta^2)\right)\nabla B + \left(z_\alpha + \frac{1}{2}(h - \eta)\right)\nabla A \tag{7}$$

The depth-averaged horizontal momentum equation can be written as

$$u_{\alpha,t} + (u_\alpha \cdot \nabla)u_\alpha + g\nabla\eta + V_1 + V_2 + V_3 + R = 0 \tag{8}$$

where g is the gravitational acceleration and R represents diffusive and dissipative terms including bottom friction and subgrid lateral turbulent mixing. V_1 and V_2 are terms representing the dispersive Boussinesq terms given by

$$V_1 = \left\{\frac{z_\alpha^2}{2}\nabla B + z_\alpha \nabla A\right\}_t - \nabla\left[\frac{\eta^2}{2}B_t + \eta A_t)\right] \tag{9}$$

$$V_2 = \nabla\left\{(z_\alpha - \eta)(u_\alpha \cdot \nabla)A + \frac{1}{2}(z_\alpha^2 - \eta^2)(u_\alpha \cdot \nabla)B + \frac{1}{2}[A + \eta B]^2\right\} \tag{10}$$

The form of (9) allows for the reference level z_α to be treated as a time-varying elevation, as suggested in Kennedy et al. (2001). If this extension is neglected, the term reduces to the form given originally by Wei et al. (1995). The expression (10) for V_2 was also given by Wei et al. (1995), and is not altered by the choice of a fixed or moving reference elevation.

The term V_3 in (8) represents the $O(\mu^2)$ contribution to the expression for $\omega \times u = \omega i^z \times u$ (with i^z the unit vector in the z direction) and may be written as

$$V_3 = \omega_0 i^z \times \bar{u}_2 + \omega_2 i^z \times u_\alpha \tag{11}$$

where

$$\omega_0 = (\nabla \times u_\alpha) \cdot i^z = v_{\alpha,x} - u_{\alpha,y} \tag{12}$$

$$\omega_2 = (\nabla \times \bar{u}_2) \cdot i^z = z_{\alpha,x}(A_y + z_\alpha B_y) - z_{\alpha,y}(A_x + z_\alpha B_x) \tag{13}$$

Following Nwogu (1993), z_α is usually chosen to optimize, in some sense, the apparent dispersion relation of the linearized model relative to the full linear dispersion. In particular, the choice $\alpha = (z_\alpha/h)^2/2 + z_\alpha/h = -2/5$ recovers a Padé approximant form of the dispersion relation, while the choice $\alpha = -0.39$, corresponding to the choice $z_\alpha = -0.53\,h$, minimizes the maximum error in wave phase speed occuring over the range $0 \le kh \le \pi$. Kennedy et al. (2001) showed that allowing z_α to move up and down with the passage of the wave field allowed a greater degree of flexibility in optimizing nonlinear behavior of the resulting model equations. In the examples chosen here, where a great deal of our focus is on the behavior of the model from the break point landward, we adopt the Kennedy et al. "datum invariant" form

$$z_\alpha = -h + \beta H = (\beta - 1)h + \beta\eta = \zeta h + (1 + \zeta)\eta \tag{14}$$

with $\zeta = -0.53$ as in Nwogu (1993) and $\beta = 1 + \zeta = 0.47$. This corresponds in essence to a σ coordinate approach which places the reference elevation at a level 53% of the total local depth below the local water surface. This also serves to keep the model reference elevation within the actual water column over the entire wetted extent of the model domain.

4.2.2 Treatment of the surface gradient term

The hybrid numerical scheme requires a conservative form of continuity equation and momentum equations, thus requiring a modification of the leading order pressure term in the momentum equation. A numerical imbalance problem occurs when the surface gradient term is conventionally split into an artificial flux gradient and a source term that includes the effect of the bed slope for a non-uniform bed. To eliminate errors introduced by the traditional depth gradient method (DGM), a so-called surface gradient method (SGM) proposed by Zhou et al. (2001) was adopted in the TVD based-Boussinesq models in the recent literature. Zhou et al. discussed an example of SGM in 1-D and verified that the slope-source term may be canceled out by part of the numerical flux term associated with water depth, if the bottom elevation at the cell center is constructed using the average of bottom elevations at two cell interfaces. Zhou et al. also showed a 2-D application but without explicitly describing 2-D numerical schemes. Although this scheme can be extended into 2-D following the same procedure as in 1-D, it was found that the 2-D extension may not be trivial in terms of the bottom construction for a 2-D arbitrary bathymetry. Kim et al. (2008) pointed out that the water depth in the slope-source term

should be written in a discretized form rather than the value obtained using the bottom construction, implying that their revised SGM is valid for general 2-D applications.

For the higher-order schemes such as the fourth-order TVD-MUSCL scheme (Yamamoto and Daiguji, 1993, Yamamoto et al., 1998) used in the recent Boussinesq applications, the original SGM and the revised SGM may not be effective in removing the artificial source. This problem was noticed by some recent authors such as Roeber et al. (2010) who kept a first-order scheme (second-order for normal conditions) for the numerical flux term and the slope-source term in order to ensure a well-balanced solution without adding noise for a rapidly varying bathymetry.

In fact, the imbalance problem can be solved by a reformulation of this term in terms of deviations away from an unforced but separately specified equilibrium state (see general derivations in Rogers et al., 2003 and recent application in Liang and Marche, 2009). Using this technique, the surface gradient term may be split into

$$gH\nabla\eta = \nabla\left[\frac{1}{2}g(\eta^2 + 2h\eta)\right] - g\eta\nabla h \tag{15}$$

which is well-balanced for any numerical order under an unforced stationary condition (still water condition).

4.2.3 Conservative form of fully nonlinear Boussinesq equations

For Chen's (2006) equations or the minor extension considered here, Hu_α can be used as a conserved variable in the construction of a conservative form of Boussinesq equations, but resulting in a source term in the mass conservation equation such as in Shiach and Mingham (2009) and Roeber et al. (2010). An alternative approach is to use M as a conserved variable in terms of the physical meaning of mass conservation. In this study, we used M, instead of Hu_α, in the following derivations of the conservative form of the fully nonlinear Boussinesq equations.

Using M from (6) together with the vector identity

$$\nabla\cdot(uv) = \nabla u\cdot v + (\nabla\cdot v)u \tag{16}$$

allows (8) to be rearranged as

$$M_t + \nabla\cdot\left(\frac{MM}{H}\right) + gH\nabla\eta = H\left\{\bar{u}_{2,t} + u_\alpha\cdot\nabla\bar{u}_2 + \bar{u}_2\cdot\nabla u_\alpha - V_1 - V_2 - V_3 - R\right\} \tag{17}$$

Following Wei et al. (1995), we separate the time derivative dispersion terms in V_1 according to

$$V_1 = V_{1,t}^{'} + V_1^{''} \tag{18}$$

where

$$V_1^{'} = \frac{z_\alpha^2}{2}\nabla B + z_\alpha\nabla A - \nabla\left[\frac{\eta^2}{2}B + \eta A\right] \tag{19}$$

and

$$V_1^{''} = \nabla\left[\eta_t(A + \eta B)\right] \tag{20}$$

Using (15), (19) and (20), the momentum equation can be rewritten as

$$M_t+\nabla\cdot\left[\frac{MM}{H}\right]+\nabla\left[\frac{1}{2}g(\eta^2+2h\eta)\right]=H\left\{\bar{u}_{2,t}+u_\alpha\cdot\nabla\bar{u}_2+\bar{u}_2\cdot\nabla u_\alpha-V_{1,t}'-V_1''-V_2-V_3-R\right\}+g\eta\nabla h \quad (21)$$

A difficulty usually arises in applying the adaptive time-stepping scheme to the time derivative dispersive terms $\bar{u}_{2,t}$ and $V_{1,t}'$ which are usually calculated using values stored in several time levels in the previous Boussinesq codes such as in Wei et al. (1995) and Shi et al. (2001). The equation can be re-arranged by merging the time derivatives on the right hand side into the time derivative term on the left hand side, giving

$$V_t+\nabla\cdot\left[\frac{MM}{H}\right]+\nabla\left[\frac{1}{2}g(\eta^2+2h\eta)\right]=\eta_t(V_1'-\bar{u}_2)+H\left(u_\alpha\cdot\bar{u}_2+\bar{u}_2\cdot\nabla u_\alpha-V_1''-V_2-V_3-R\right)+g\eta\nabla h \quad (22)$$

where

$$V=H(u_\alpha+V_1') \quad (23)$$

In (23), η_t can be calculated explicitly using (5) as in Roeber et al. (2010). Equations (5) and (22) are the governing equations solved in this study. As V is obtained, the velocity u_α can be solved by a system of tridiagonal matrix equations formed by (23) in which all cross-derivatives are moved to the right-hand side of the equation.

4.2.4 Numerical schemes

The governing equations in FUNWAVE-TVD are discretized on a regular grid using a hybrid finite-volume / finite-difference approach. The numerical scheme is described in detail in Shi et al. (2011, 2012) and is omitted here for conciseness. Examples described below are based on discretizations on regular Cartesian grids with uniform grid spacings in x and y. Terms in conservative form in equations (5) and (22) are written in finite volume form using a MUSCL-TVD scheme, while additional terms are written in cell-centered finite differences. An adaptive third-order Strong Stability Preserving (SSP) Runge-Kutta scheme is used for time stepping (Gottlieb et al., 2001).

4.2.5 Wave breaking and wetting-drying schemes for shallow water

The wave breaking scheme follows the approach of Tonelli and Petti (2009) who successfully used the ability of NSWE with a TVD scheme to model moving hydraulic jumps. The fully nonlinear Boussinesq equations are switched to NSWE at cells where the Froude number exceeds a certain threshold. Following Tonelli and Petti, the ratio of wave height to total water depth is chosen as the criterion used to switch from Boussinesq to NSWE. The threshold value is set to be 0.8 as suggested by Tonelli and Petti.

The wetting-drying scheme for modeling of a moving boundary is straightforward. The normal flux $n\cdot M$ at the cell interface of a dry cell is set to zero. A mirror boundary condition is applied to the fourth-order MUSCL-TVD scheme and discretization of dispersive terms in ψ_x,ψ_y at dry cells.

4.2.6 Boundary conditions and wavemaker

We implemented various boundary conditions including the wall boundary condition, the absorbing boundary condition following Kirby et al. (1998), and the periodic boundary condition following Chen et al. (2003).

Wavemakers implemented in the study include Wei et al. (1999) internal wavemakers for regular waves and irregular waves. For the irregular wavemaker, an extension was made to incorporate the alongshore periodicity into wave generation in order to eliminate a boundary effect on wave simulation. The technique exactly follows the strategy in Chen et al. (2003) who adjusted the distribution of wave directions in each frequency bin to obtain alongshore periodicity. This approach is effective in modeling of breaking wave-induced nearshore circulation such as alongshore currents and rip currents.

4.2.7 Parallelization

In parallelizing the computational model, we use the domain decomposition technique to subdivide the problem into multiple regions and assign each subdomain to a separate processor core. Each subdomain region contains a three-rows-deep overlapping area of ghost cells, as dictated by the fourth order MUSCL-TVD scheme. The Message Passing Interface (MPI) with non-blocking communication is used to exchange the data in the overlapping region between neighboring processors. Velocity components are obtained from Equation (23) by solving tridiagonal matrices using the parallel pipelining tridiagonal solver described in Naik et al. (1993).

4.3 Basic hydrodynamic considerations

There are two basic states that are required in ensuring that any numerical model works for predicting evolution and inundations. The first step is ensuring that the model conserves mass; the second basic step is checking convergence of this numerical code to an asymptotic limit.

4.3.1 Mass conservation

Conservation of mass can be checked by calculating water volume at the beginning and at the end of the computation. This should be done by integrating disturbed water depth $\eta(x,y,t)$ over the entire flow domain, i.e., if the flow domain extends from the maximum penetration during inundation $x = X_{max}$ to the outer location of the source region X_S, and $y = Y_{max}$ to Y_s, then the total displaced volume $V(t)$ is,

$$V(t) = \int_{X_{max}}^{X_S} \int_{Y_{max}}^{Y_S} \eta(x,y,t)\,dxdy \tag{24}$$

The integral of $\eta(x,y,t)$ should be used instead of the integral of the entire flow depth $h(x,y,t) = \eta(x,y,t) + d(x,y,t)$ where $d(x,y,t)$ is the undisturbed water depth, because the latter is likely to conceal errors in the calculation. Typically, $\eta << d$ offshore, so integrating h will simply produce the entire volume of the flow domain and will mask errors. Note that testing of the conservation of mass as above involves placing a closed domain within reflective boundaries (Synolakis et al., 2007).

Calculations of conservation of mass have been done for all of the benchmark problems reviewed in this report such that the total initial displaced volume $V(t = 0)$ was within less than 1% of the total displaced volume at the end of the computation $V(t = T)$ where T represents the computation end time. It is assumed that the end of the computation is when the initial wave is entirely reflected and reached offshore. However, with a few changes in Δx and Δy the conservation of mass can be improved.

4.3.2 Convergence

Convergence is another basic hydrodynamic consideration that is checked for all of the benchmarks in this research. Actually, this means checking the convergence of the numerical code to a certain asymptotic limit, presumably the actual solution of the equations solved. The grid steps Δx and Δy have been halved, and the time step Δt has been automatically reduced to conform to the Courant-Friedrics-Levy (CFL) criterion. As recommended in the literature, convergence of the code has been checked through the extreme runup and rundown. Table 4-1 displays convergence of the code tested during the conical island test problem, which is discussed in Section 5.3 below.

Table 4-1: Maximum runup for gauge 9 for different grid size.

	Maximum Runup		
Grid Size	H/d = 0.045	H/d = 0.091	H/d = 0.181
0.1	0.02302	0.04061	0.06311
0.05	0.02303	0.04063	0.06315
0.01	0.02303	0.04064	0.06316
0.005	0.02303	0.04064	0.06316

4.4 Analytical benchmarks

In this section, we compare the numerical results for test cases to the analytical solutions for the same test cases obtained by using shallow water (SW) wave equations. We also present several analytic solutions to the 1+1 version of the shallow water wave equations. Although 1+1 models are not completely reliable for tasks such as tsunami inundation mapping, they are the first step toward testing and validating models (Synolakis et al., 2007).

The following benchmark problems are studied in this section:

1. Solitary wave on a simple beach
2. N-wave on a simple beach
3. Solitary wave on a composite beach

4.4.1 BP1: Solitary wave on a simple beach – analytical

This section covers the canonical problem of the shallow water wave equations, the calculation of a long wave climbing up a sloping beach of angle β attached to a constant-depth region (Figure 4-1). The origin of the coordinate system is at the initial position of the shoreline and x increases seaward.

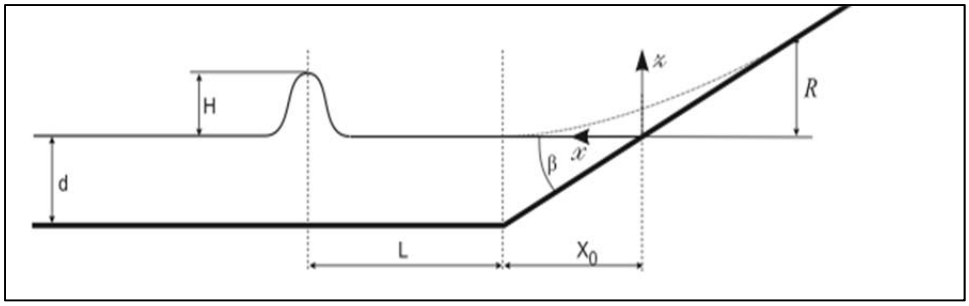

Figure 4-1: Definition sketch for simple beach bathymetry (from Synolakis et al. (2007, Figure A1)).

It is possible to use linear theory to derive exact results for the evolution and runup of solitary waves (Synolakis, 1986, 1987). Solitary waves have long been used as a model for the leading wave of tsunamis. Russell (1845) defined solitary waves as great waves of translation, each consisting of a single elevation wave. While capturing some of the basic physics of tsunamis, solitary waves do not model the physical manifestation of tsunamis in nature, which are invariably N-wave like with a leading-depression wave followed by an elevation wave (Synolakis et al., 2007). The following runup law for the maximum nondimensional runup R is provided based on the slope of the beach and the nondimensional wave height of the solitary wave

$$R = 2.831\sqrt{\cot\beta}\,H^{\frac{5}{4}} \tag{25}$$

Table 4-2: Runup data from numerical calculations compared with runup law values.

				R/d		
d(m)	$\Delta x(m)$	H/d	$\cot(\beta)$	Runup Law	Numerical Calculations	Error(%)
0.5	0.1	0.03	10.0	0.112	0.110	1.6
0.5	0.1	0.05	10.0	0.212	0.204	3.6
0.5	0.1	0.1	3.333	0.291	0.282	3.0
0.5	0.1	0.48	1.0	1.131	1.109	2.0
0.5	0.1	0.01	20.0	0.040	0.042	4.9
5.0	1.0	0.03	10.0	0.112	0.112	0.4
5.0	1.0	0.05	10.0	0.212	0.212	0.2
5.0	1.0	0.10	3.372	0.308	0.315	2.4
5.0	1.0	0.10	3.372	0.731	0.734	0.3
5.0	1.0	0.294	2.747	1.016	1.058	4.2
5.0	1.0	0.005	20.0	0.017	0.017	1.1
5.0	1.0	0.01	20.0	0.040	0.039	3.0
100	5.0	0.05	10.0	0.212	0.202	4.5
100	5.0	0.03	2.747	0.257	0.266	3.4
100	5.0	0.03	2.747	0.600	0.598	0.4
100	5.0	0.03	20.0	0.040	0.040	0.2

The benchmark problems studied here have depths that range from 50 cm to 1000 m. Also, for each depth, different slopes and wave heights has been studied. Table 4-2 provides a list of selected examples that have been modeled, including their maximum runup and the grid size for each case. Figure 4-2 compares the results of numerical simulations with the runup law predictions.

In addition, the analytical solution for different times is available for a specific case in which $H/d = 0.0019$ and $\beta = \text{arccot}(19.85)$. To have the same time with the data it was recommended that $L = \text{arccosh}(\sqrt{20})/\gamma$ in which $\gamma = \sqrt{3H/4d}$; therefore, the distance of the wave from the initial shoreline (X_1) can be written as $X_1 = X_0 + L$ (with respect to Figure 4-1). Figure 4-3 shows the profiles and time series of the water at eight different times. Extreme positions of the shoreline are shown in Figure 4-3 (the maximum runup and rundown occur $t;\ 55(d/g)^{1/2}$ and $t;\ 70(d/g)^{1/2}$). Figure 4-4 shows the water level fluctuations at two gauge locations, $X/d = 0.25$ and $X/d = 9.95$. As the figure shows, the point $X/d = 0.25$, which is closer to the initial shoreline, becomes temporarily dry during the process but the point $X/d = 9.95$ remains wet throughout the entire length of the numerical simulation.

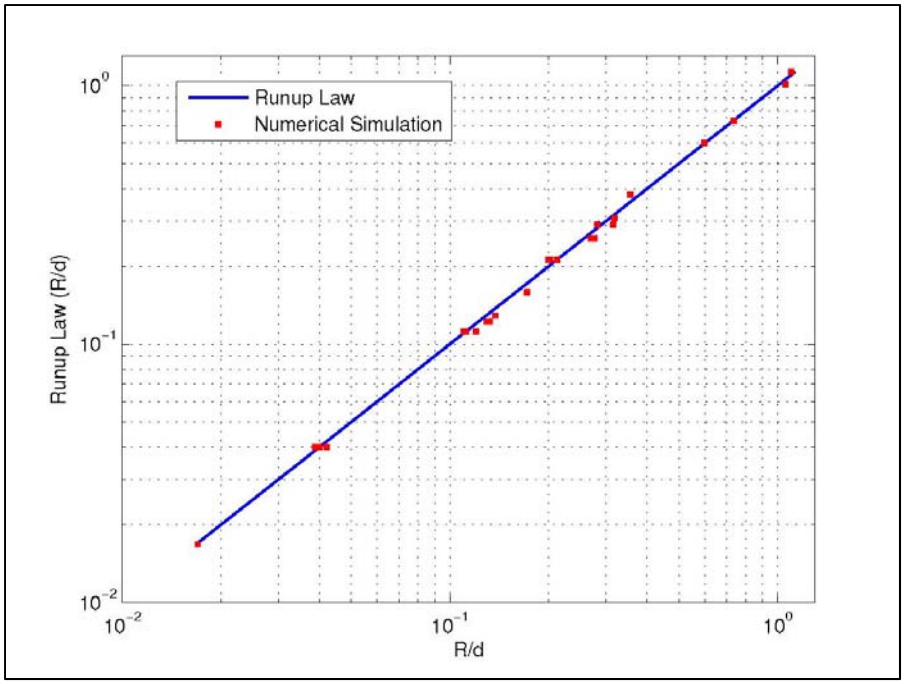

Figure 4-2: Numerical simulation data for maximum runup of nonbreaking waves climbing up different beach slopes. Solid line represents the runup law (25).

4.4.2 N-wave runup on a simple beach – analytical

Most tsunami eyewitness accounts suggest that tsunamis are N-wave like, i.e., they are dipolar, which means they appear as a combination of a depression and an elevation wave, and frequently as a series of N-waves, sometimes known as double N-waves (Synolakis et al., 2007).

Tadepalli and Synolakis (1994) described an N-wave with leading elevation and depression waves of the same height and at a constant separation distance. They refer to this wave as an isosceles N-wave with a surface profile given by

$$\eta(x,0) = \frac{3\sqrt{3}H}{2}\operatorname{sech}^2[\gamma(x - X_N)]\tanh[\gamma(x - X_N)] \tag{26}$$

where

$$\gamma = \frac{3}{2}\sqrt{\sqrt{\frac{3}{4}}H} \tag{27}$$

which is a nondimensional equation.

The benchmark problems that are studied here have depths that range from 50 cm to 1000 m. Also, for each depth, various slope and wave heights have been studied. Table 4-3 provides a list of selected different cases that have been modeled, including their maximum runup and the grid size for each case. Figure 4-5 compares the numerical simulation results and the predictions of the runup law for the N-wave problem.

As for the solitary wave problem discussed in the previous part, the following expression for the maximum nondimensional runup of N-waves has been provided based on the slope of the beach and the nondimensional wave height of the N-wave,

$$R = 3.86\sqrt{\cot\beta}\,H^{\frac{5}{4}} \tag{28}$$

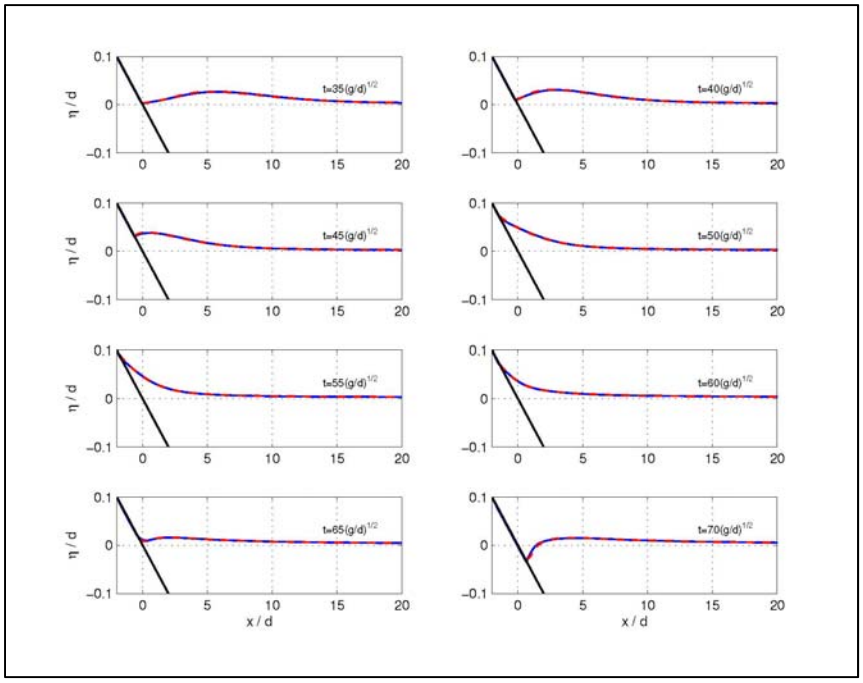

Figure 4-3: The water level profiles during runup of the non-breaking wave in the case of H/d = 0.019 on a 1:19.85 beach. The solid blue line represents the analytical solution according to Synolakis (1986), and the dashed red line represents the results of numerical simulation.

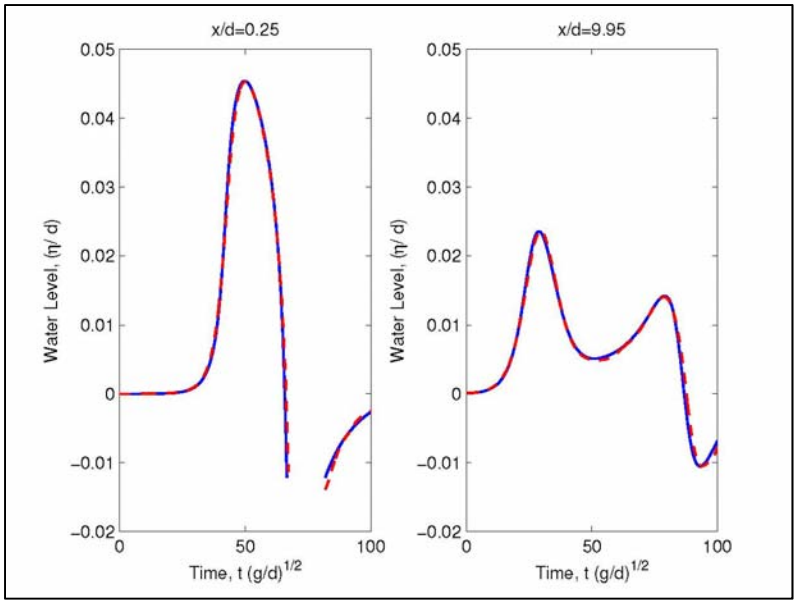

Figure 4-4: The water level dynamics at two locations *X/d* = 0.25 and *X/d* = 9.95. Solid blue line represents the analytical solution in according to Synolakis (1986), and dashed red line represents the numerical simulation.

Table 4-3: Runup data from numerical calculations compared with runup law for *N*-wave.

					R/d		
d (m)	γ	Δx (m)	H/d	$\cot(\beta)$	Runup Law	Numerical Calculations	Error (%)
0.5	0.22	0.1	0.05	3.333	0.167	0.165	1.0
0.5	0.44	0.1	0.2	1.0	0.516	0.505	2.2
5.0	0.54	1.0	0.03	10.0	0.152	0.157	3.0
5.0	0.70	1.0	0.05	10.0	0.289	0.286	0.9
5.0	0.99	1.0	0.1	3.732	0.419	0.433	3.3
5.0	1.69	1.0	0.294	2.747	1.385	1.388	0.2
5.0	0.22	1.0	0.005	20.0	0.023	0.023	0.2
5.0	0.31	1.0	0.01	20.0	0.055	0.056	2.6
100.0	3.12	5.0	0.05	10.0	0.289	0.277	4.0
100.0	6.13	5.0	0.193	2.747	0.818	0.826	0.9
100.0	1.40	5.0	0.01	20.0	0.055	0.056	2.6
1000.0	9.87	20.0	0.05	10.0	0.289	0.275	4.7
1000.0	9.87	20.0	0.05	3.333	0.167	0.173	3.8

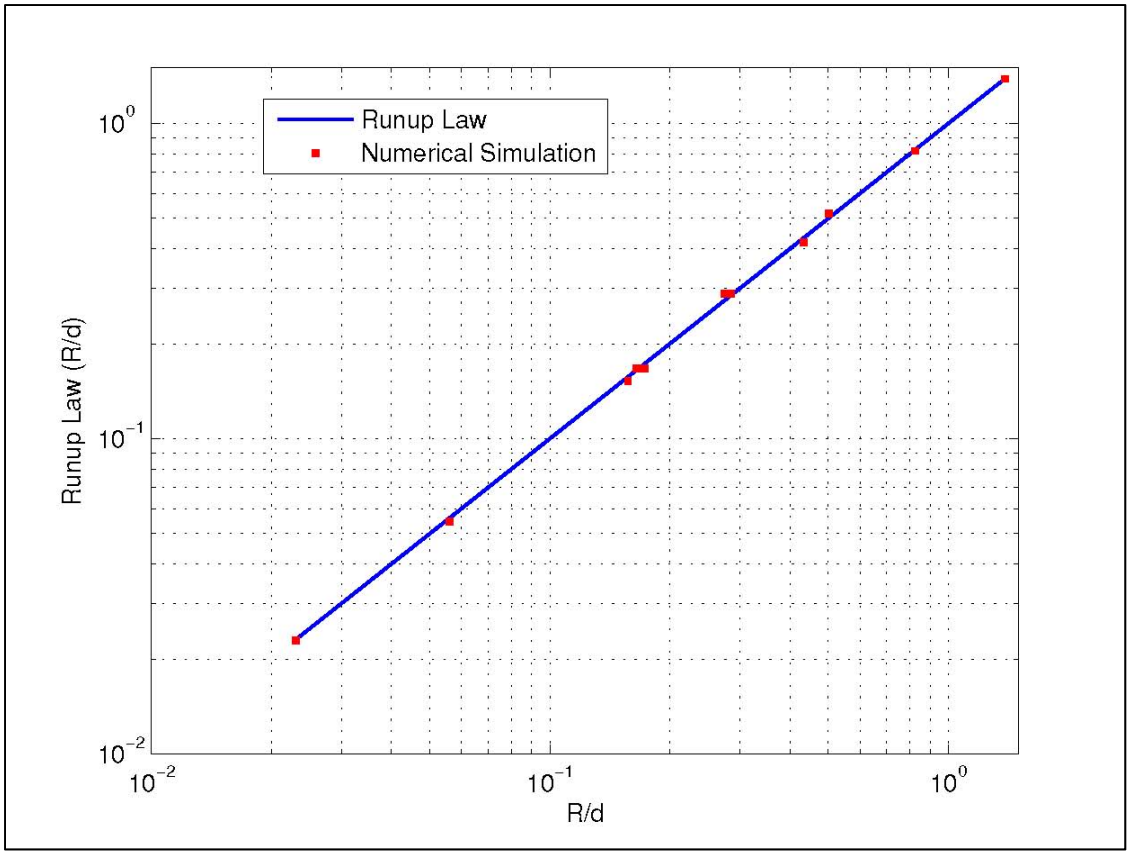

Figure 4-5: Numerical simulation data for the maximum runup of N-waves climbing up different beach slopes. The solid line represents the runup law (28).

4.4.3 BP2: Solitary wave on composite beach – analytical

In this benchmark problem, a complex topography consisting of three segments and a vertical wall is considered (Figure 4-6). The benchmark test is described in Appendix A, Section 2.2 of Synolakis et al. (2007). Runup of non-breaking solitary waves on the vertical wall is simulated in this case. Results have been compared with the analytical solution. Laboratory data exist for this topography from a U.S. Army Corps of Engineers, Coastal Engineering Research Center, Vicksburg, Mississippi experiment of wave runup on a model of Revere Beach, Massachusetts. However, the maximum runup for solitary waves propagating up Revere Beach (Composite Beach) is given by the runup law

$$R = 2h_w^{-\frac{1}{4}}H \tag{29}$$

where h_w is the initial depth at the right vertical wall and H is the solitary wave height.

Two initial depths have been studied here; $d = 18.8$ cm, and $d = 21.8$ cm. For all cases, a grid size of $\Delta x = 0.10$ m has been used. Table 4-4 demonstrates a comparison of runup law with the numerical data for both depths studied here.

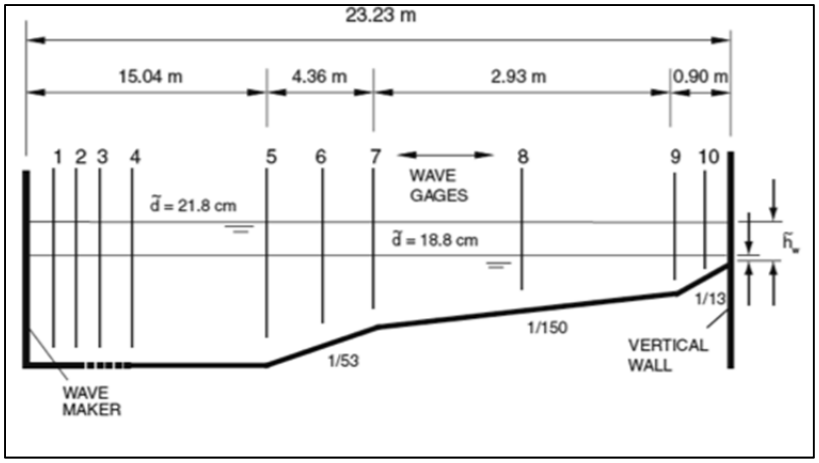

Figure 4-6: Definition sketch for Revere Beach (from Synolakis et al. (2007, Figure A7)).

Table 4-4: Maximum runup of solitary wave on composite beach compared to runup law (29).

(m)	(Runup Law)	(Numerical)	Error (%)	(m)	(Runup Law)	(Numerical)	Error (%)
0.005	0.0146	0.0141	3.7	0.005	0.0152	0.0148	2.5
0.01	0.0293	0.0288	1.6	0.01	0.0304	0.0310	2.1
0.03	0.0878	0.0850	3.2	0.03	0.0911	0.0871	4.4
0.05	0.1463	0.1390	5.0	0.05	0.1519	0.1440	5.2

In addition, for this benchmark problem three different waves have been modeled (H/d = 0.0378, 0.2578, 0.6404 for cases A, B and C). Recorded data are compared with the analytical data for gauge 4 to gauge 10 and also on the wall in Figure 4-7, Figure 4-8, and Figure 4-9. Grid size for this case is $\Delta x = 0.010$ m. It should be mentioned that for analytical results, the model has been used in linear, non-dispersive, and no friction mode.

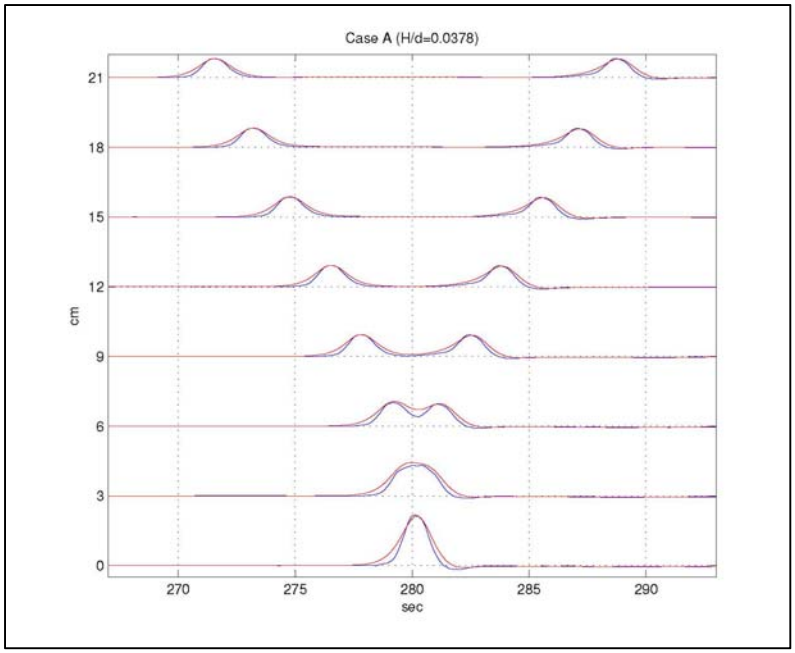

Figure 4-7: Time evolution of nonbreaking *H/d* = 0.0378 wave on composite beach. The red line shows the numerical solution and the blue line represents the analytic solution.

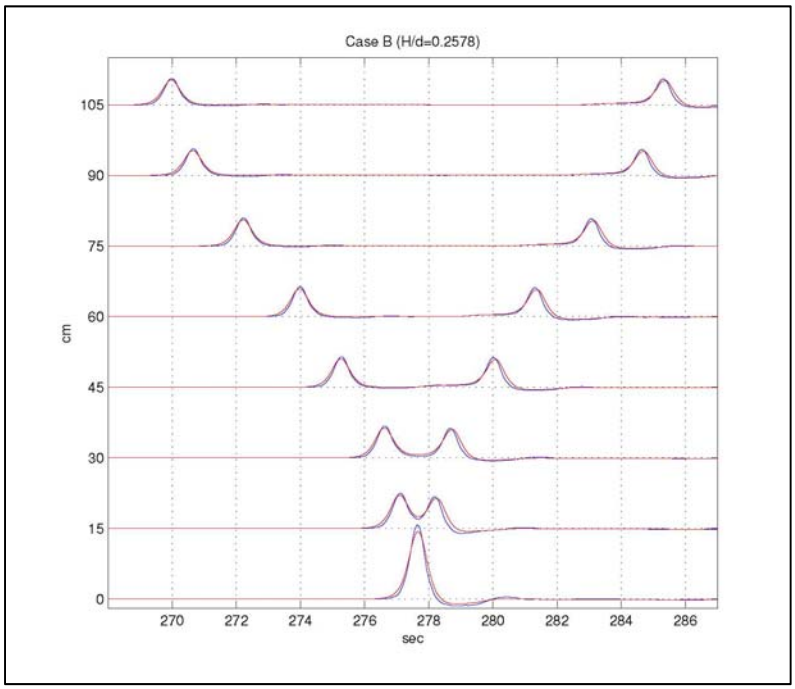

Figure 4-8: Time evolution of breaking *H/d* = 0.2578 initial wave on composite beach. The red line shows the numerical solution and the blue line represents the analytic solution.

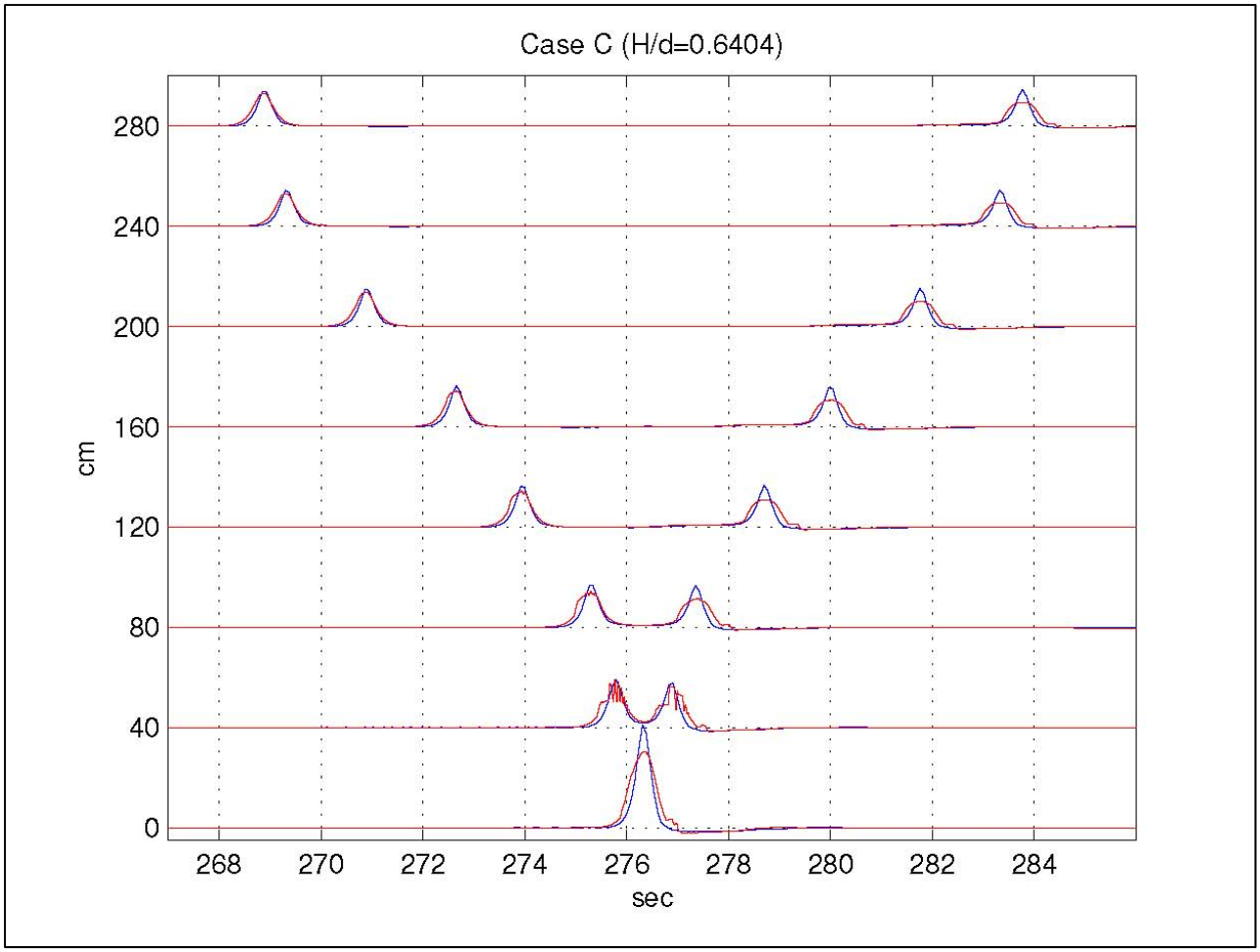

Figure 4-9: Time evolution of breaking *H/d* = 0.6404 initial wave on composite beach. The red line shows the numerical solution and the blue line represents the analytic solution.

4.5 Laboratory benchmarks

In this section, data from different laboratory benchmarks are studied and compared to the results of numerical calculations. The following benchmark problems are studied in this section:

1. Solitary wave on a simple beach
2. Solitary wave on a composite beach
3. Solitary wave on a conical island
4. Tsunami runup onto a complex three-dimensional beach; Monai Valley

4.5.1 BP4: Solitary wave on a simple beach – laboratory

In this laboratory test, the 31.73 m-long, 60.96 cm-deep and 39.97 cm wide California Institute of Technology, Pasadena, California wave tank was used with water at varying depths. The tank is described by Synolakis (1986, 1987). The bottom of the tank consisted of painted stainless steel plates. A ramp was installed at one end of the tank to model the bathymetry of the canonical problem of a constant-depth region adjoining a sloping beach. The ramp had a slope of

1:19.85. The ramp was sealed to the tank side walls. The toe of the ramp was distant 14.95 m from the rest position of the piston generator used to generate waves.

This set of laboratory data has been widely used for many code validations. In this modeling test, the data sets for the $\tilde{H}/\tilde{d} = 0.0185$ nonbreaking and $\tilde{H}/\tilde{d} = 0.30$ breaking solitary waves are the most frequently used and most appropriate for code validation.

For these cases, a grid size of $\Delta x = 0.10$ m has been used. Figure 4-10 and Figure 4-11 display the accuracy of the model for both nonbreaking and breaking waves. The runup error for the nonbreaking wave was 3.3% and for the breaking wave was 5.8%.

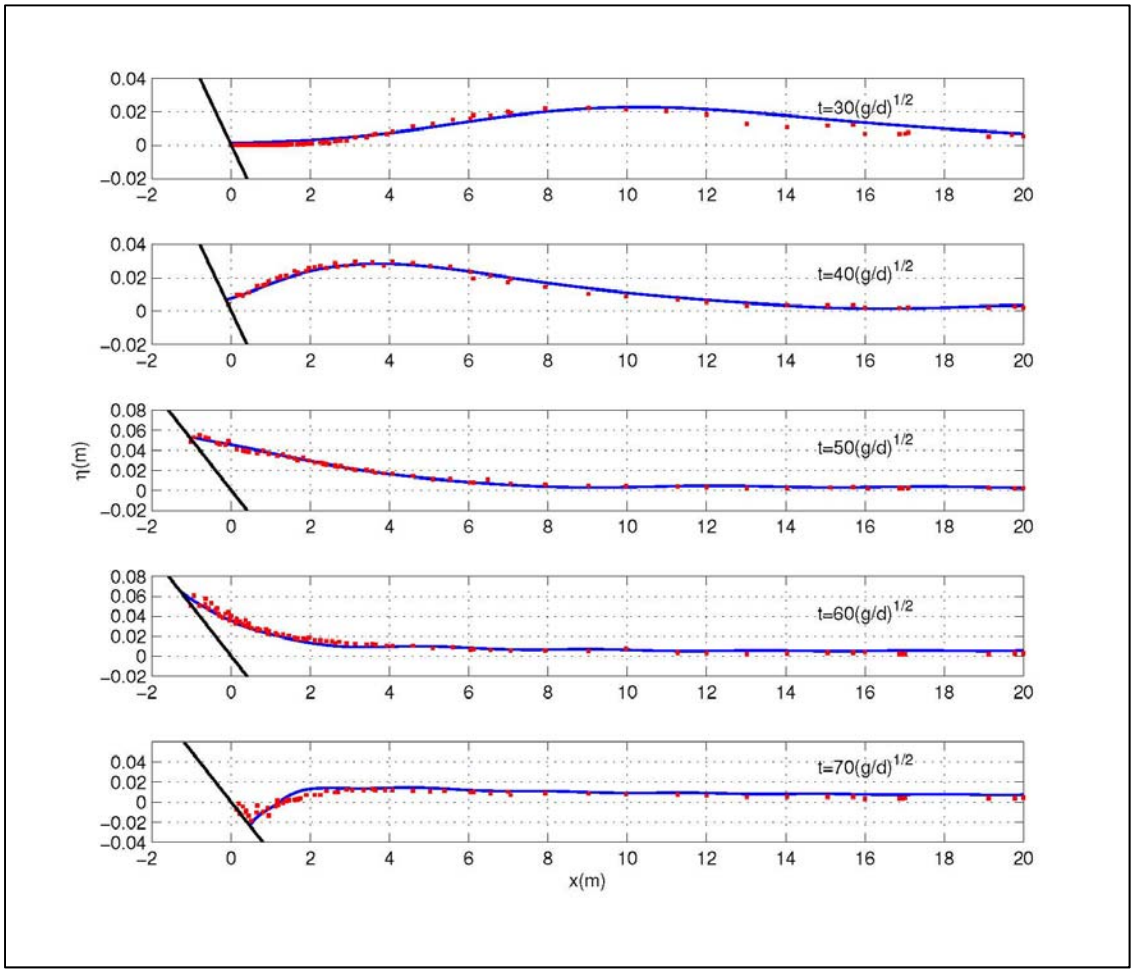

Figure 4-10: Time evolution of nonbreaking *H/d* = 0.0185 initial wave. The solid line shows the numerical solution and the dots represent the laboratory data.

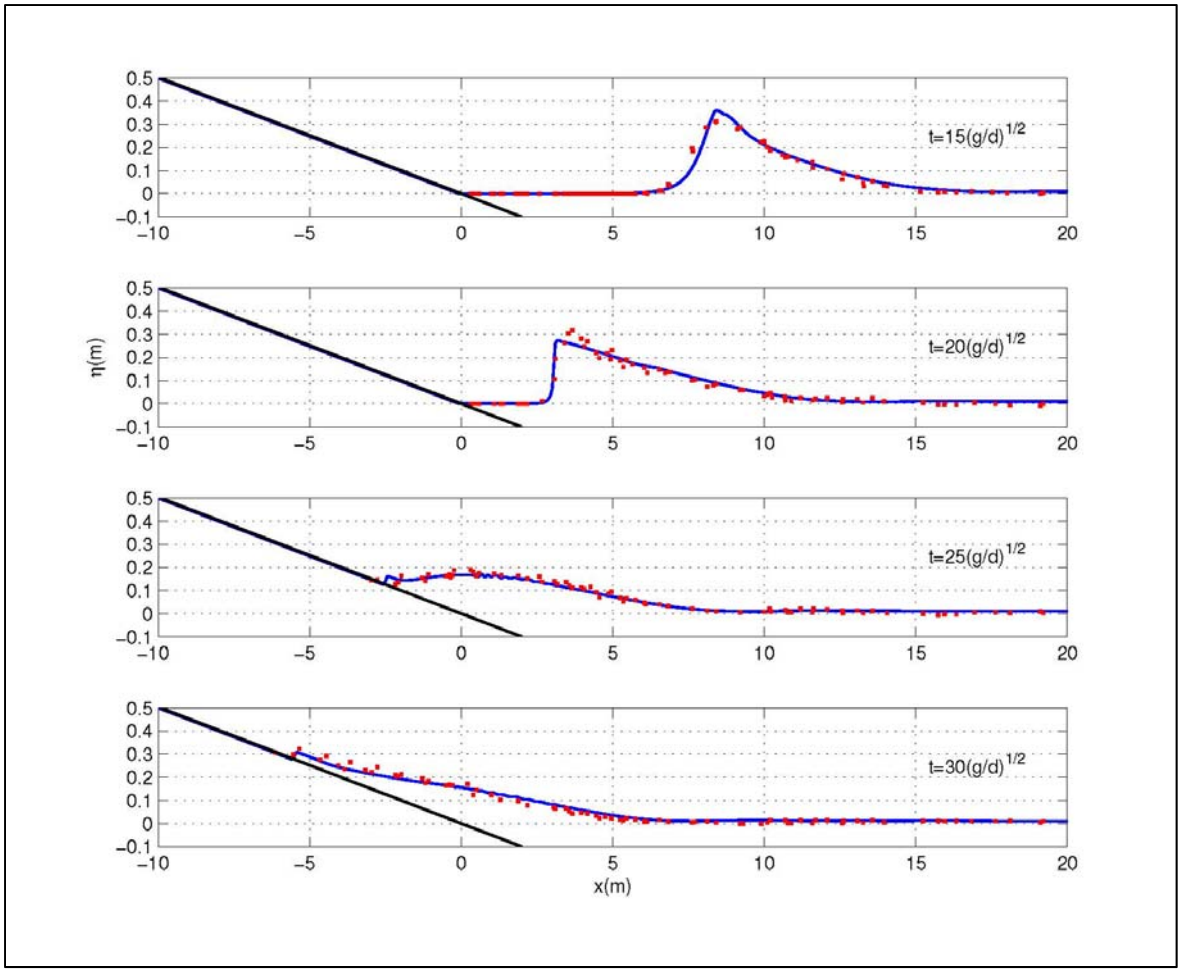

Figure 4-11: Time evolution of breaking *H/d* = 0.3 initial wave. The solid line shows the numerical solution and the dots represent the laboratory data.

4.5.2 BP5: Solitary wave on a composite beach – laboratory

Revere Beach is located approximately 6 miles northeast of Boston, in the City of Revere, Massachusetts. To address beach erosion and severe flooding problems, a physical model of the beach was constructed at the Coastal Engineering Laboratory of the U.S. Army Corps of Engineers, Vicksburg, Mississippi facility, earlier known as Coastal Engineering Research Center. This benchmark is described in Section 3.2 of Appendix A of Synolakis et al. (2007).

The beach characteristics are exactly the same as the composite beach described in Section 4.3. In this benchmark problem, three different waves are modeled ($H/d = 0.0378, 0.2578, 0.6404$ for cases A, B, and C) and the numerical data are compared with the laboratory data for gauges 4 to 10 in Figure 4-12, Figure 4-13, and Figure 4-14). The grid size for this case is $\Delta x = 0.010$ m.

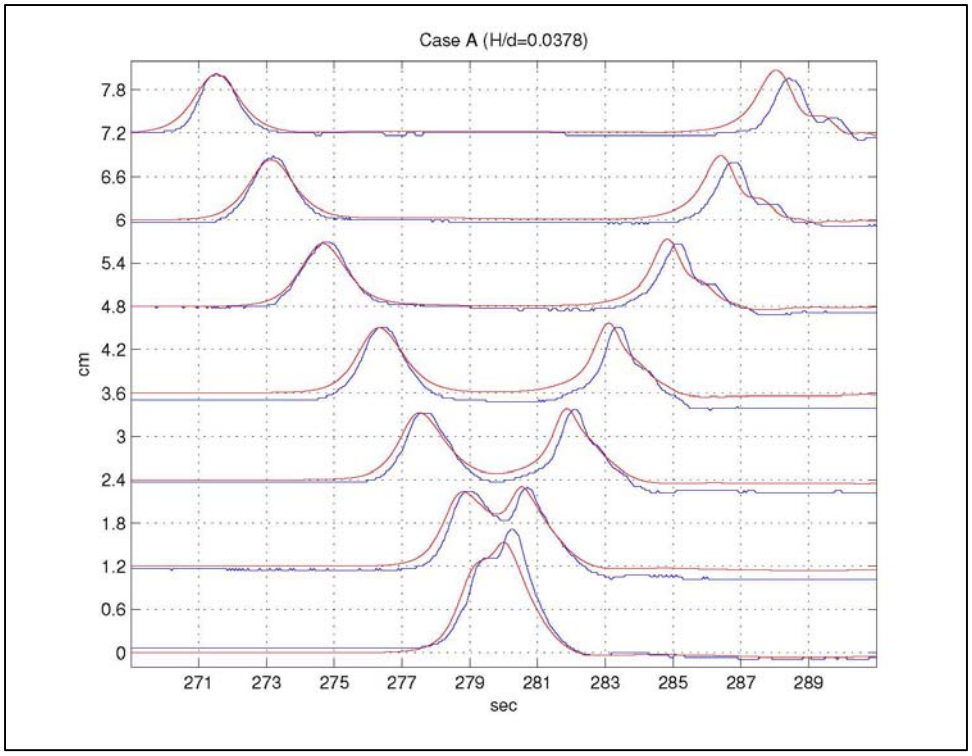

Figure 4-12: Time evolution of nonbreaking *H/d* = 0.0378 initial wave on composite beach. The red line shows the numerical solution and the blue line represents the laboratory data.

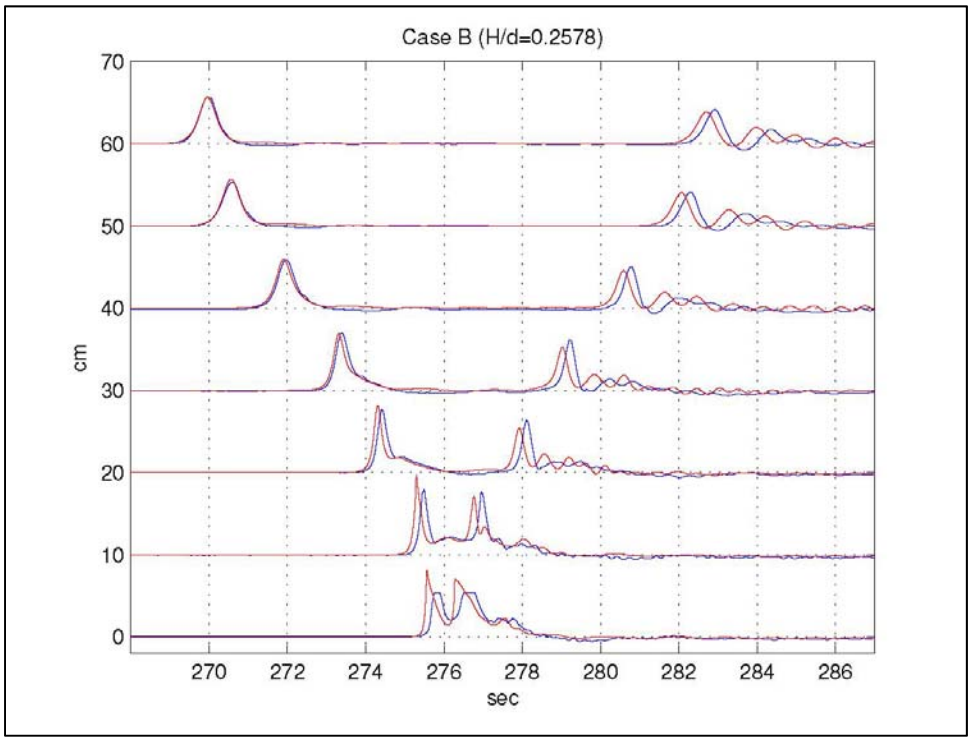

Figure 4-13: Time evolution of breaking *H/d* = 0.2578 initial wave on composite beach. The red line shows the numerical solution and the blue line represents the laboratory data.

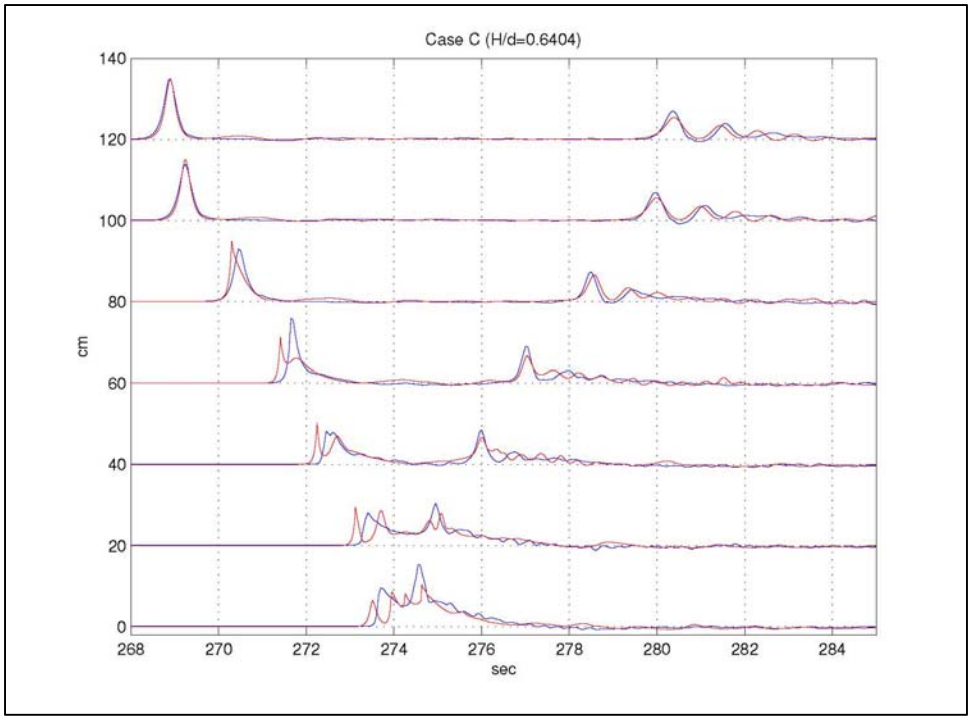

Figure 4-14: Time evolution of breaking *H/d* = 0.6404 initial wave on composite beach. The red line shows the numerical solution and the blue line represents the laboratory data.

4.5.3 BP6: Solitary wave on a conical island – laboratory

Laboratory experiments on the interaction between solitary waves and a conical island were conducted by Briggs et al. (1995). The three cases from this test illustrate the important fact that runup and inundation heights on the sheltered back sides of an island can exceed the incident wave height on the exposed front side, due to trapping of wave fronts propagating around the island circumference. These tests have been used in a number of validation studies for a variety of models, including nonlinear shallow water equations (Liu et al. 1995) and Boussinesq equations (Chen et al., 2000). The benchmark test is specified in Section 3.3 of Appendix A of Synolakis et al. (2007).

Large-scale laboratory experiments were performed at the Coastal Engineering Research Center, Vicksburg, Mississippi, in a 30 m wide, 25 m long, and 60 cm deep wave basin (Figure 4-15). In the physical model, a 62.5 cm -high, 7.2 m toe-diameter, and 2.2 m crest-diameter circular island with a 1:4 slope was located in the basin (Figure 4-16). Experiments were conducted at depth of 32cm, with three different solitary waves (H/d = 0.045, 0.091, 0.181). Water-surface time histories were measured with 27 wave gauges located around the perimeter of the island (Figure 4-17).

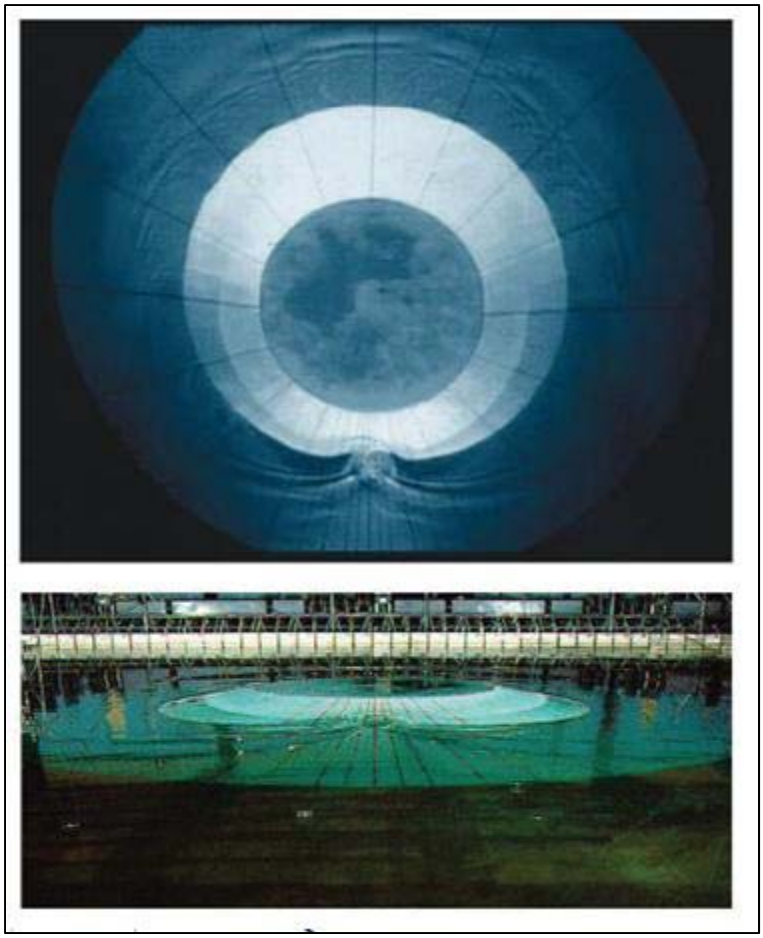

Figure 4-15: View of conical island (top) and basin (bottom) (from Synolakis et al. (2007, Figure A16)).

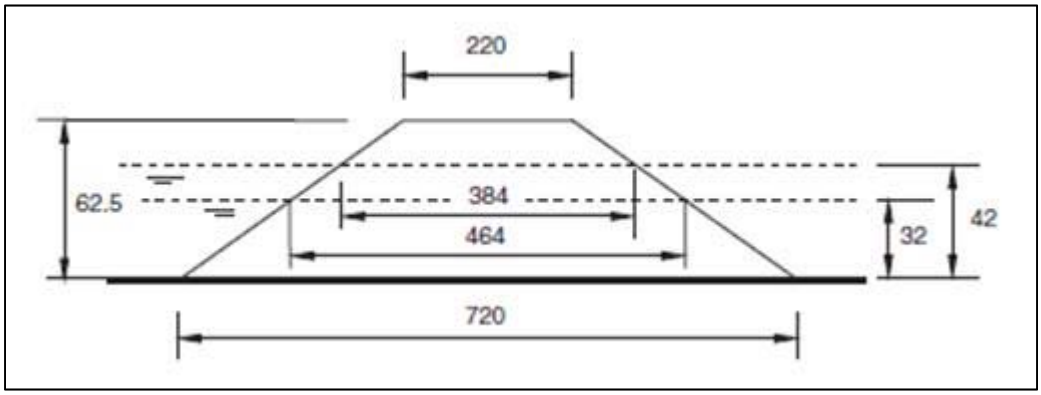

Figure 4-16: Definition sketch for conical island. All dimensions are in cm (from Synolakis et al. (2007, Figure A17)).

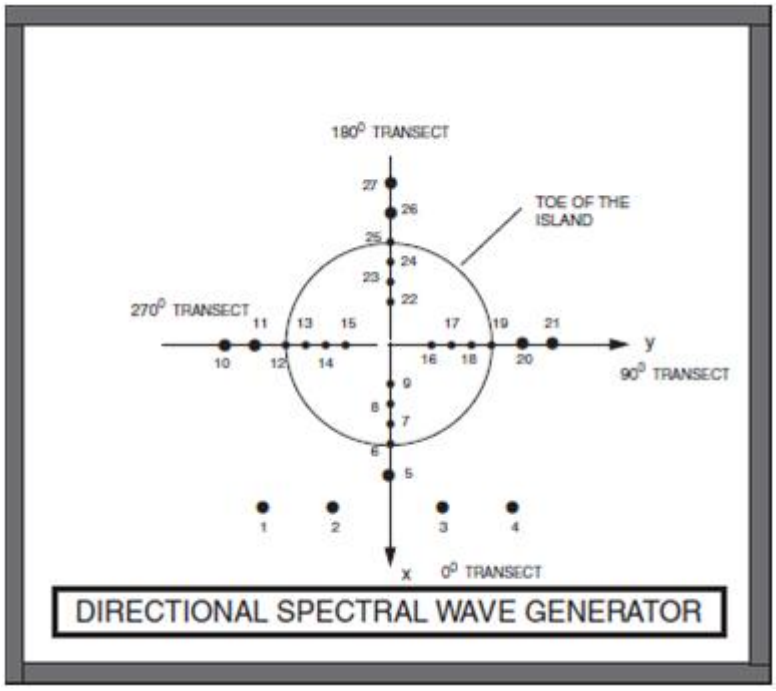

Figure 4-17: Schematic gauge locations around the conical island. From Synolakis et al. (2007, Figure A18).

For this benchmark test, time histories of the surface elevation around the circular island are given at four locations, i.e., in the front of the island at the toe (Gauge 6) and gauges closest to the shoreline with the numbers 9, 16, and 22 located at the 0°, 90°, and 180° radial lines (Figure 4-17). A grid size of $\Delta x = 0.10m$ is considered for proper numerical simulation of this benchmark. Figure 4-18, Figure 4-19, and Figure 4-20 show the comparison of the laboratory data with the numerical calculations. Table 4-5 represents the error of the maximum runup for each gauge for different wave heights.

Table 4-5: Percent error of predicted maximum runup calculated for each gauge in conical island test.

	Gauge Number			
H/*d*	6	9	16	22
0.045	6.0	13.2	0.1	18.9
0.091	3.2	16.6	11.6	0.26
0.181	1.6	13.33	13.8	13.3

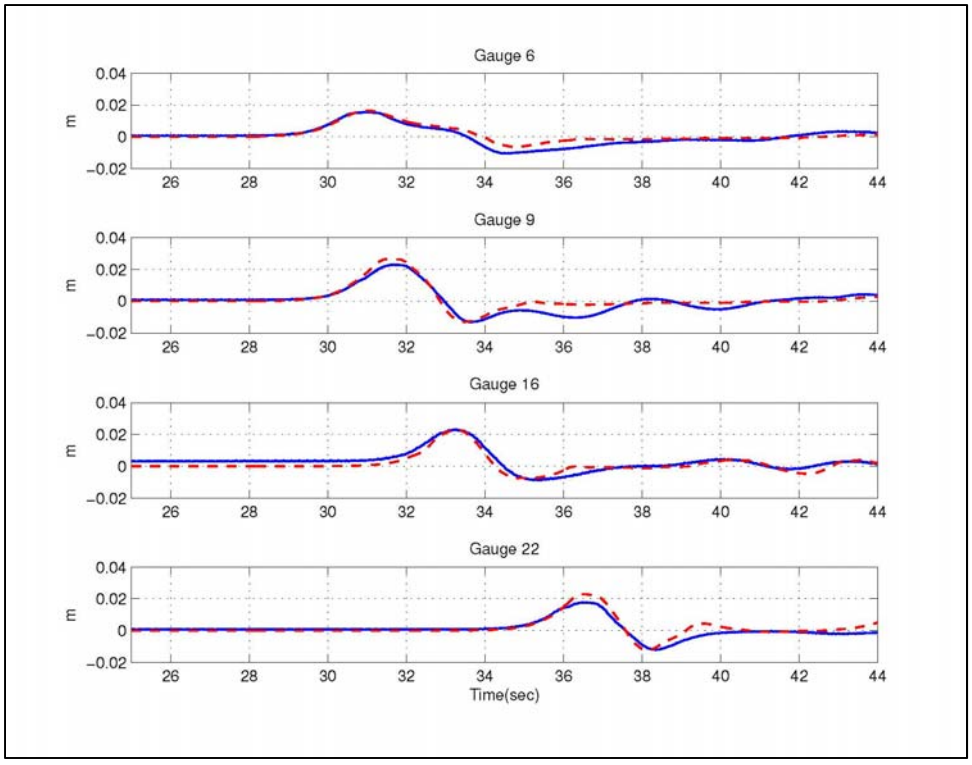

Figure 4-18: Comparison of computed and measured time series of free surface for *H/d* = 0.045. Solid lines: measured, Dashed lines: Computed.

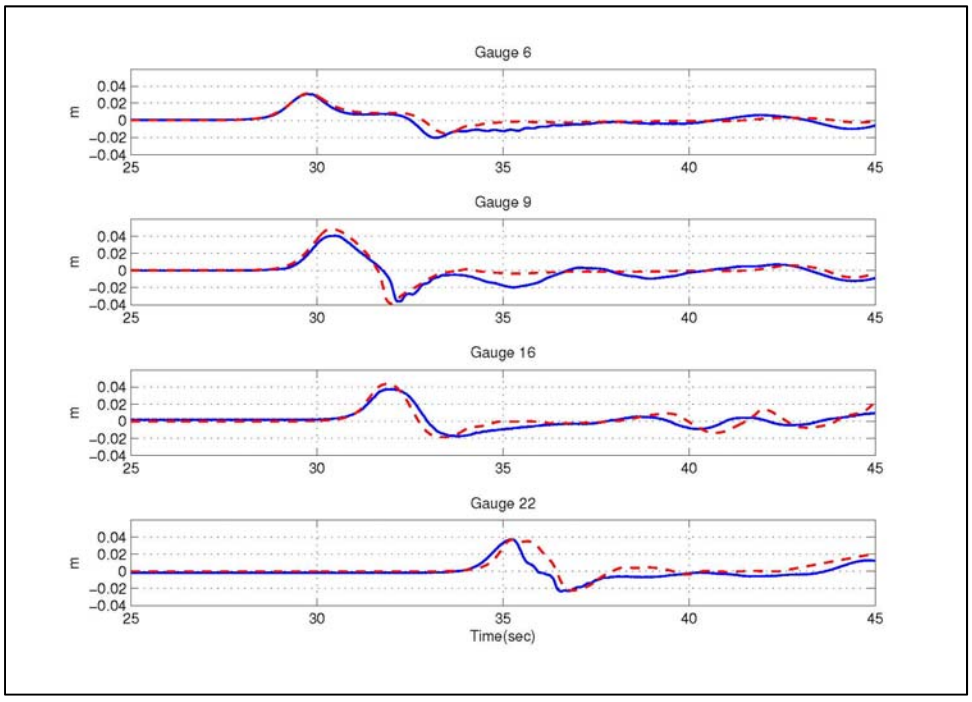

Figure 4-19: Comparison of computed and measured time series of free surface for *H/d* = 0.091. Solid lines: measured, Dashed lines: Computed.

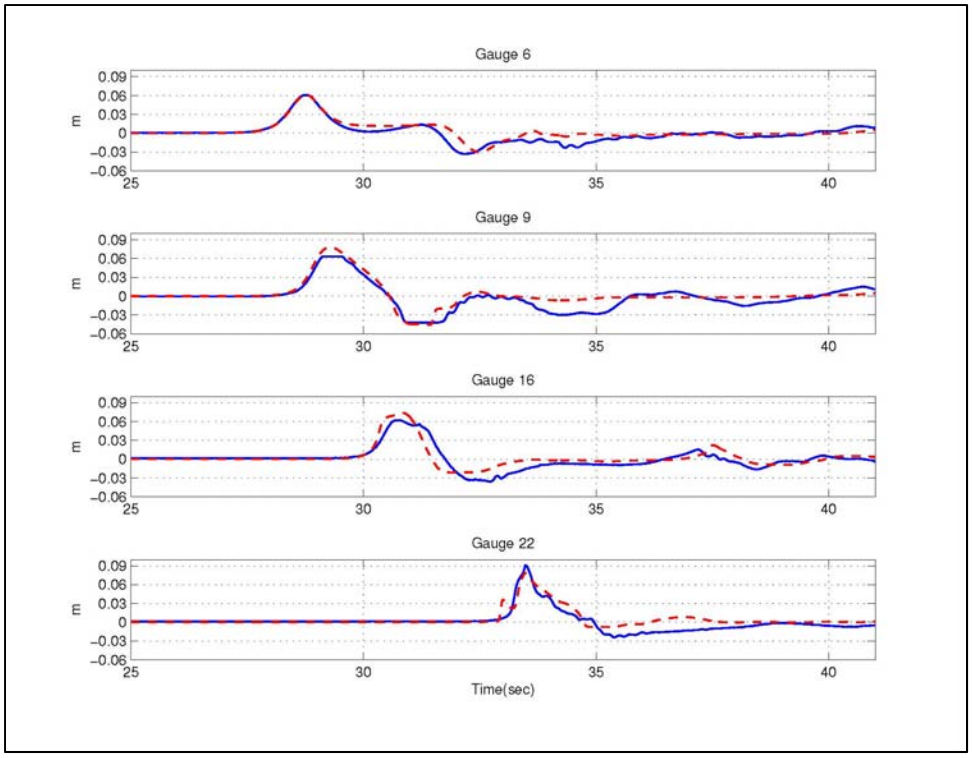

Figure 4-20: Comparison of computed and measured time series of free surface for *H/d* = 0.181. Solid lines: measured, Dashed lines: Computed.

4.5.4 BP7: Tsunami runup onto a complex three-dimensional beach; Monai Valley – laboratory

The Hokkaido-Nansei-Oki tsunami of 1993 that struck Okushiri Island, Japan, provided high-quality data for tsunami researchers. Because the maximum tsunami runup mark was discovered at the tip of a very narrow gully within a small cove at Monai, a laboratory benchmark was designed based on Monai valley bathymetry and the tsunami wave that struck the area. Based on the high resolution seafloor bathymetry that existed before the event, a 1/400 laboratory model of Monai was constructed in a 205 m long, 6m deep, and 3.5 m-wide tank at Central Research Institute for Electric Power Industry (CRIEPI) in Abiko, Japan. The model is partly shown in Figure 4-21. The incident wave from offshore, at the water depth of d = 13.5 cm is known and it is shown in Figure 4-22. There are reflective vertical sidewalls at y = 0 and 3.5 m (Figure 4-23). The entire computational area for the laboratory test is $5.448\ \text{m} \times 3.402\ \text{m}$, and the grid sizes recommended for numerical simulations are $\Delta x = \Delta y = 1.4\ \text{cm}$. However, due to numerical limitations, the computational domain that is used in numerical simulation is longer in order to generate waves without any reflection disturbance from the back wall ($12.488\ \text{m} \times 3.402$ m) (Figure 4-24). The input wave is an LDN with a leading-depression height of 2.5 mm with a crest of 1.6 cm behind it, which is produced in the model using FFT analysis and the WK TIME SERIES wavemaker option (Figure 4-22). Data for water surface elevations during the laboratory experiment are given and compared with numerical simulations at three locations (Gauge 5, 7 and 9), i.e., (x, y) = (4.521, 1.196), (4.521, 1.696), and (4.521, 2.196) in meters (Figure 4-25). Figure 4-26 compares extracted movie frames from the overhead movie of the

laboratory experiment with the result of numerical simulations. Finally, maximum runup in the narrow gully in the numerical solution was 7.43 cm, which is comparable with the laboratory data (maximum runup of 7.5 cm in the lab data or 30 m in field tsunami data).

Figure 4-21: Bathymetric profile for experimental setup for Monai Valley experiment (2007, Figure A24)).

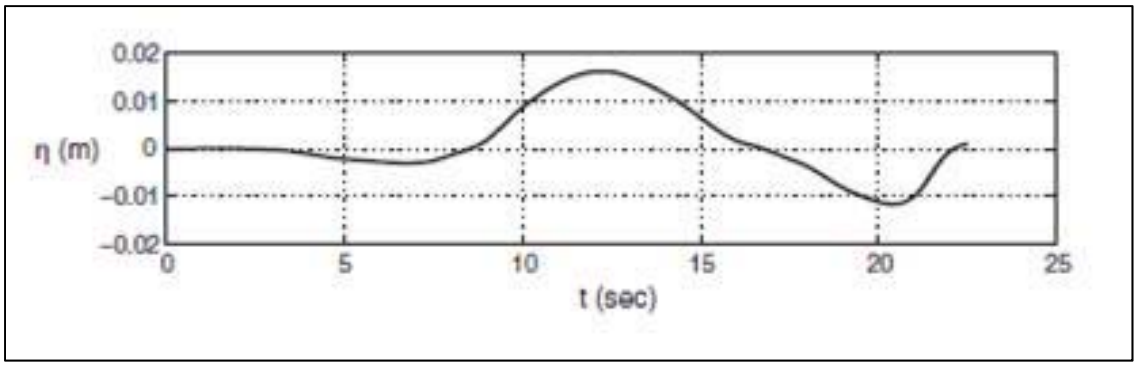

Figure 4-22: Initial wave profile for Monai Valley experiment (2007, Figure A25)).

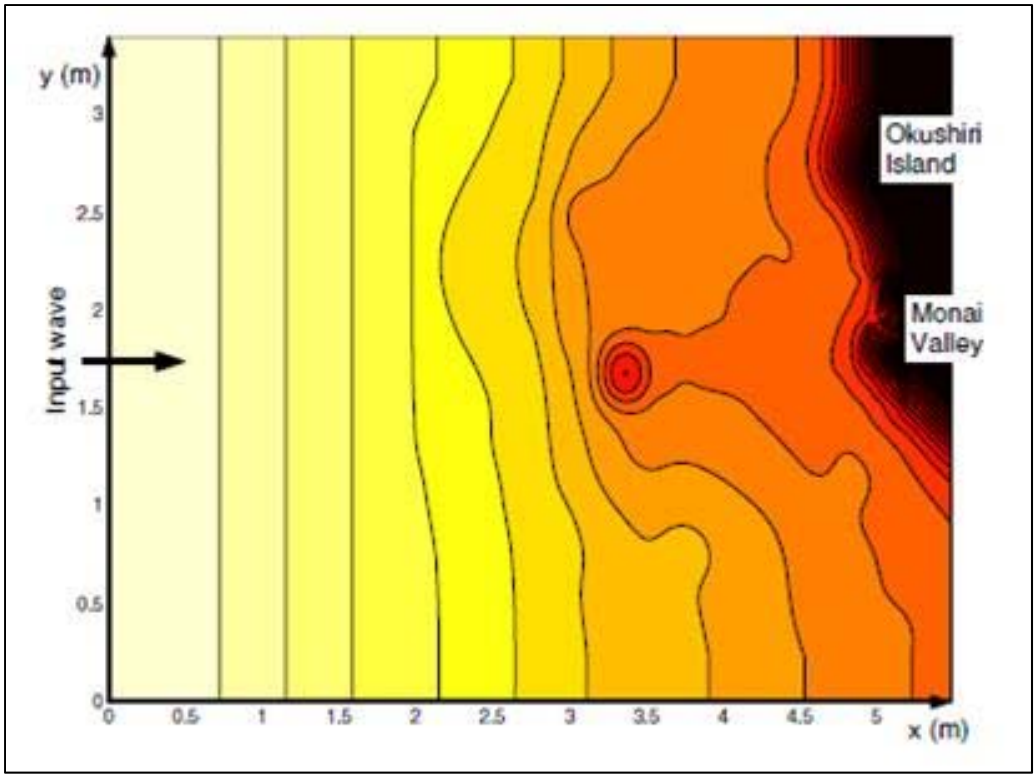

Figure 4-23: Computational area for Monai Valley experiment (2007, Figure A26)).

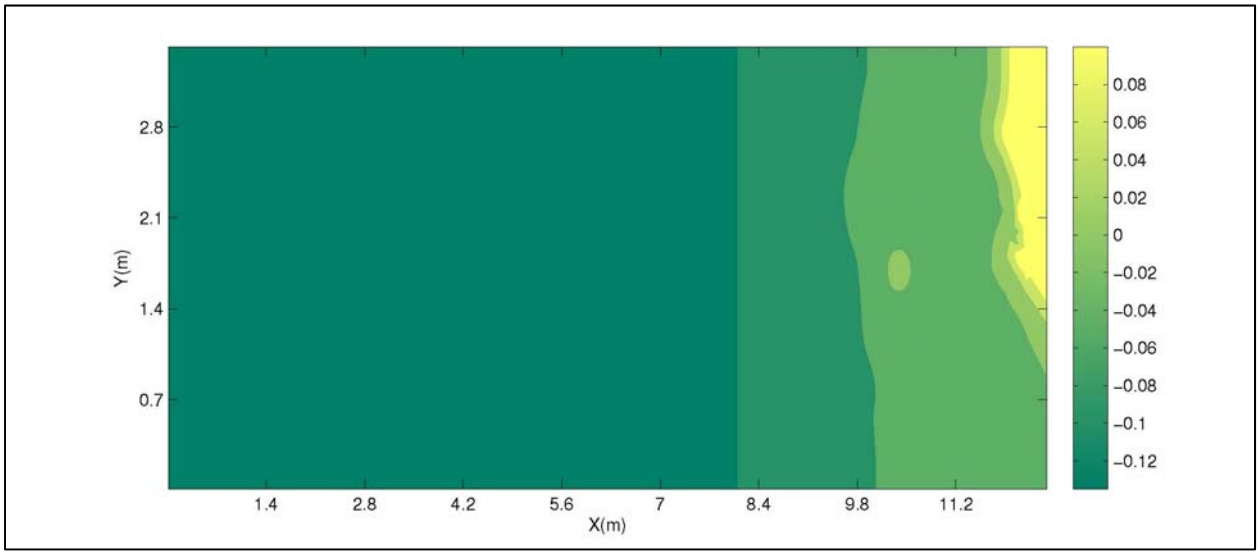

Figure 4-24: Computational area for Monai Valley numerical simulation.

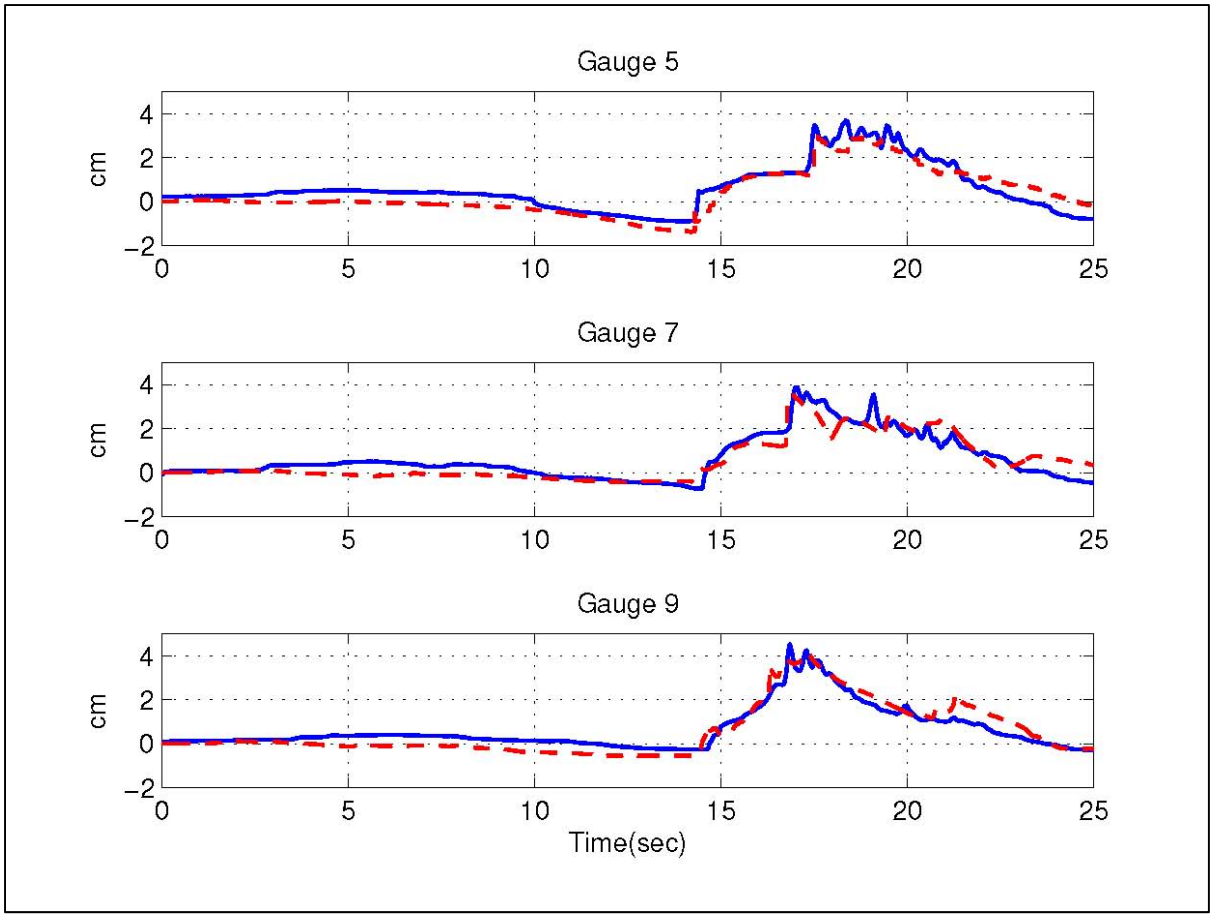

Figure 4-25: Comparison of computed and measured time series of free surface. Dashed lines: Computed, Solid lines: Measured.

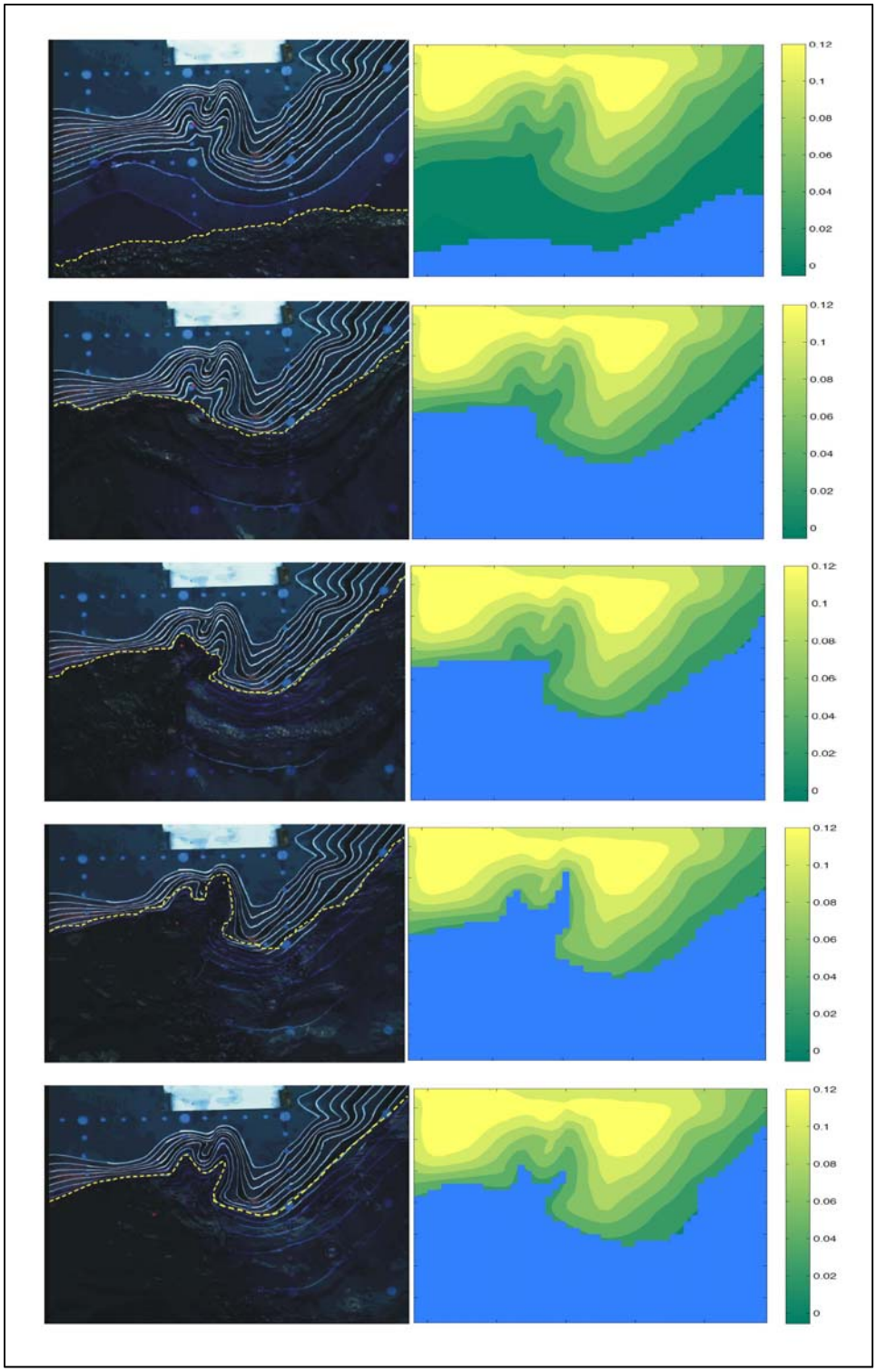

Figure 4-26: Comparison between extracted movie frames from the overhead movie of the laboratory experiment (left) (from http://burn.giseis.alaska.edu/file_doed/Dmitry/BM7_description.zip) and numerical simulation (right).

4.6 References

Briggs MJ, Synolakis CE, Harkins GS, Green D. 1995. Laboratory experiments of tsunami runup on a circular island, *Pure Appl. Geophys.*, 144, 569-593.

Chen Q, Kirby JT, Dalrymple RA, Kennedy AB, Chawla A. 2000. Boussinesq modelling of wave transformation, breaking and runup. II: Two horizontal dimensions, *J. Waterway, Port, Coast. Ocean Engnrng*, 126, 48-56.

Chen Q, Kirby JT, Dalrymple RA, Shi F, Thornton EB. 2003. Boussinesq modelling of longshore currents, *J. Geophys. Res.*, 108(C11), 3362, doi:10.1029/2002JC001308.

Chen Q. 2006. Fully nonlinear Boussinesq-type equations for waves and currents over porous beds, *J. Eng. Mech.*, 132, 220-230.

Collins-Sussman B, Fitzpatrick BW, Pilato CM. 2004. Version Control with Subversion. O'Reilly Media Inc.

Gottlieb S, Shu C-W, Tadmore E. 2001. Strong stability-preserving high-order time discretization methods, *SIAM Review*, 43 (1), 89 - 112.

Kennedy AB, Kirby JT, Chen Q, Dalrymple RA. 2001. Boussinesq-type equations with improved nonlinear performance, *Wave Motion*, 33, 225-243.

Kim DH, Cho YS, Kim HJ. 2008. Well balanced scheme between flux and source terms for computation of shallow-water equations over irregular bathymetry, *J. Eng. Mech.*, 134, 277-290.

Kirby JT, Wei G, Chen Q, Kennedy AB, Dalrymple RA. 1998. FUNWAVE 1.0, Fully nonlinear Boussinesq wave model. Documentation and user's manual, Research Report No. CACR-98-06, Center for Applied Coastal Research, University of Delaware.

Liang Q, Marche F. 2009. Numerical resolution of well-balanced shallow water equations with complex source terms, *Adv. Water Res.*, 32, 873 - 884.

Liu PL-F, Cho YS, Briggs MS, Kânoğlu U, Synolakis CE. 1995. Runup of solitary waves on a circular island, *J. Fluid Mech.*, 320, 259-285.

Naik NH, Naik VK, Nicoules M. 1993. Parallelization of a class of implicit finite difference schemes in computational fluid dynamics, *Int. J. High Speed Computing*, 5, 1-50.

Nwogu O. 1993. An alternative form of the Boussinesq equations for nearshore wave propagation, *J. Waterway, Port, Coastal, and Ocean Engineering*, 119, 618-638.

Roeber V, Cheung KF, Kobayashi MH. 2010. Shock-capturing Boussinesq-type model for nearshore wave processes, *Coastal Engineering*, 57, 407-423.

Rogers BD, Borthwick AG. L, Taylor PH. 2003. Mathematical balancing of flux gradient and source terms prior to using Roe's approximate Riemann solver, *J. Comp. Phys.*, 192, 422-451.

Russel JS. 1845. Report on waves, Rp. Meet. Brit. Assoc. Adv. Sci. 14th, 311- 390, John Murray, London.

Shi F, Dalrymple RA, Kirby JT, Chen Q, Kennedy A. 2001. A fully nonlinear Boussinesq model in generalized curvilinear coordinates, *Coastal Engineering*, 42, 337-358.

Shi F, Kirby JT, Tehranirad B, Harris JC, Grilli ST. 2011. FUNWAVE-TVD Version 1.0. Fully nonlinear Boussinesq wave model with TVD solver. Documentation and user's manual, Research Report No. CACR-11-04, Center for Applied Coastal Research, University of Delaware.

Shi F, Kirby JT, Harris JC, Geiman JD, Grilli ST. 2012. A high-order adaptive time-stepping TVD solver for Boussinesq modelling of breaking waves and coastal inundation, *Ocean Modelling*, 43-44, 36-51.

Shiach JB, Mingham CG. 2009. A temporally second-order accurate Godunov-type scheme for solving the extended Boussinesq equations, *Coast. Eng.*, 56, 32-45.

Synolakis CE. 1986. The runup of long waves, Ph.D. Thesis, California Institute of Technology, Pasadena, California, 91125, 228 pp.

Synolakis CE. 1987. The runup of solitary waves, *J. Fluid Mech.*, 185, 523-545.

Synolakis CE, Bernard EN, Titov VV, Kâno ğ lu U, González FI. 2007. Standards, criteria, and procedures for NOAA evaluation of tsunami numerical models, NOAA Tech. Memo. OAR PMEL-135, Pacific Marine Env. Lab., Seattle.

Tadepalli S, Synolakis CE. 1994. The runup of N -waves on sloping beaches, *Proc. R. Soc. A*, 445, 99-112.

Tonelli M, Petti M. 2009. Hybrid finite volume - finite difference scheme for 2DH improved Boussinesq equations, *Coast. Engrng.*, 56, 609-620.

Wei G, Kirby JT, Grilli ST, Subramanya R. 1995. A fully nonlinear Boussinesq model for surface waves: Part I. Highly nonlinear unsteady waves, *J. Fluid Mech.*, 294, 71-92.

Wei G, Kirby JT, Sinha A. 1999. Generation of waves in Boussinesq models using a source function method. *Coastal Eng.*, 36, 271-299.

Yamamoto S, Daiguji H. 1993. Higher-order-accurate upwind schemes for solving the compressible Euler and Navier-Stokes equations, *Computers and Fluids*, 22, 259-270.

Yamamoto S, Kano S, Daiguji H. 1998. An efficient CFD approach for simulating unsteady hypersonic shock-shock interference flows, *Computers and Fluids*, 27, 571-580.

Zhou JG, Causon DM, Mingham CG, Ingram DM. 2001. The surface gradient method for the treatment of source terms in the shallow-water equations, *J. Comp. Phys.*, 168, 1-25.

5 GeoClaw Model

GeoClaw Tsunami Modeling Group, University of Washington

Frank I. González, Randall J. LeVeque, Paul Chamberlain, Bryant Hirai, Jonathan Varkovitzky and David L. George (USGS)

5.1 Introduction

5.1.1 Geographic area

The west coast, with a focus on Washington State, including Puget Sound, the San Juan Island group, and other islands in the Strait of Juan de Fuca.

5.1.2 NTHMP support

This group has no current or past support from NTHMP.

NTHMP approval of this model will allow us to seek funding in the future to perform tsunami hazard and risk assessment modeling, such as from NTHMP partner FEMA Risk Mapping, Assessment, and Planning (Risk MAP) Program. Funding will also be sought to provide Washington State with tsunami modeling and mapping in support of tsunami hazard assessment and emergency management planning and education. Tsunami sources in these geographic areas include earthquakes and landslides, and we will therefore address benchmark problems that deal with these sources.

5.2 Model description

5.2.1 Model equations

For all benchmark problems we used the two-dimensional nonlinear shallow water equations

$$h_t + (hu)_x + (hv)_y = 0,$$

$$(hu)_t + (hu^2 + \frac{1}{2}gh^2)_x + (huv)_y = -ghB_x - Du,$$

$$(hv)_t + (huv)_x + (hv^2 + \frac{1}{2}gh^2)_y = -ghB_y - Dv,$$

where $u(x, y, t)$ and $v(x, y, t)$ are the depth-averaged velocities in the two horizontal directions, $B(x, y, t)$ is the topography or bathymetry, and $D = D(h, u, v)$ is the drag coefficient.

Most of the benchmark problems use no bottom friction, so $D = 0$. When used, it has the form

$$D = \frac{gM^2\sqrt{u^2 + v^2}}{h^{5/3}}$$

where M is the Manning coefficient, generally taken to be 0.025. Comparisons with and without friction have been performed in Section 5.3.9 for BP9 and Section 5.3.6 for BP6.

Coriolis terms can be turned on in GeoClaw, but have not been used for any of the benchmark problems.

5.2.2 Methods implemented in GeoClaw

GeoClaw is a variant of the Clawpack open source software (LeVeque et al., n.d.) that LeVeque and collaborators have been developing since 1994. The "wave-propagation algorithms" used in this software are described in great detail in the textbook (LeVeque, 2002) and in several journal publications (LeVeque, 1996; LeVeque, 1997; Langseth and LeVeque, 2000).

Adaptive mesh refinement (AMR) has been incorporated since the inception of this software, in joint work with Marsha Berger at the Courant Institute of Mathematical Sciences, one of the foremost authorities on block structured AMR technology, often referred to as Berger-Colella-Oliger style AMR (Berger and Colella, 1989; Berger and Oliger, 1984). The AMR algorithms in Clawpack are described in detail in Berger and LeVeque (1998). Berger has also played a significant role in adapting the AMR routines to work well in GeoClaw (Berger et al., 2011; LeVeque et al., 2011) in connection with well-balancing and inundation modeling.

The GeoClaw software is described in some detail in (Berger et al., 2011), an invited contribution to a special issue of *Advances in Water Resources* on "New Computational Methods and Software Tools," and in (LeVeque et al., 2011), an invited paper in *Acta Numerica*, which serves as an "annual review of numerical analysis." There is also on-line documentation (GeoClaw documentation, 2011) that is part of the extensive documentation of Clawpack. The Riemann solvers and inundation model are described in more detail in (George, 2006; George, 2008).

The open source Clawpack software (including GeoClaw) can be freely downloaded from the website http://www.clawpack.org. Recent developments have taken place using a Subversion repository that is openly accessible (linked from the Clawpack webpage), using issue tracking and a wiki, as well as the claw-dev Google group to discuss development issues. Claw-pack is currently transitioning to use of the Git, a more modern distributed version control system, and the future home of Clawpack is on Github (https://github.com/organizations/ clawpack).

GeoClaw was initiated in the PhD work of David George (George, 2006; LeVeque and George, 2004; George and LeVeque, 2006; George, 2008) and was originally called TsunamiClaw. It has more recently been extended to handle other geophysical flows such as storm surge (Mandli, 2011), dam break problems (George, 2010), and debris flows (George and Iverson, 2010).

The GeoClaw model solves the two-dimensional nonlinear shallow water equations using high-resolution finite volume methods. Values of h, hu, and hv in each grid cell represent cell averages of the depth and momentum components. With flat bathymetry, the methods are exactly conservative for both mass and momentum, and conserve mass for arbitrary bathymetry when used on a fixed grid. They do not exactly conserve mass during regridding when AMR is used because, for example, a grid cell that is dry on a coarse grid may contain part of the shoreline on a finer grid. This is not an issue as long as the region of interest is refined before the main wave arrives.

These methods are based on Godunov's method, which means that at each cell interface a one-dimensional Riemann problem is solved normal to the edge, which reduces to a one-

dimensional shallow water model with piecewise constant initial data, with left and right values given by the cell averages on each side. The jump in bathymetry between the cells is incorporated into the Riemann solution in a manner that makes the method "well balanced": the steady state of the ocean at rest is exactly maintained. This is done using the "f-wave formulation" of the wave propagation method, as discussed in Bale et al. (2002), George (2008), LeVeque (2002), and LeVeque (2010).

Godunov's method consists of solving the Riemann problem and using the resulting wave structure to update cell averages in the adjacent finite volume cells. In practice, an approximate Riemann solution is used, which reduces to the standard Roe solver (LeVeque, 2002; Roe, 1981) in f-wave form in general, but is modified to also handle dry states in order to model inundation (George, 2008).

Accuracy is improved by adding in high-resolution correction terms. These terms are based on Taylor series approximation of the exact solution at time t_{n+1} about time t_n, using the same approach as used to derive the classical second-order accurate Lax-Wendroff method (LeVeque, 2007). However, the terms are only added where the solution is smooth. Near steep gradients, these terms lead to severe numerical dispersion and potential undershoots or overshoots that can lead to instability or unphysical states (e.g., negative fluid depth). A limiter is applied to the correction term using the standard approach described in detail in LeVeque (2002) and references found there, based on the theory of total variation diminishing (TVD) methods that has been well developed since the early 1980s. The resulting "high-resolution" shock-capturing methods exhibit minimal numerical dispersion or dissipation and have been shown to be very robust for both linear and nonlinear hyperbolic problems, even when the solution contains strong shock waves.

5.2.3 Boundary conditions

Boundary conditions at edges of the computational domain are handled as described in Chapter 7 of LeVeque (2002). At the start of each time step, solution values are assigned in two rows of ghost cells surrounding the computational domain. This allows the high-resolution finite volume methods to be applied on all cells that lie inside the computational domain. One row of ghost cells is required in order to solve Riemann problems at edges of the physical cells adjacent to the boundary. The second row is required in order to apply limiters. Here we summarize the boundary conditions used in the benchmark problems.

5.2.3.1 Non-reflecting boundaries

Zero-order extrapolation from the grid cells along the boundary to ghost cells in every time step is used to implement non-reflecting boundary conditions, for example when truncating the ocean or wave tank. The Godunov-type methods implemented in GeoClaw solve Riemann problems at each grid interface and having equal values in the grid cell at the boundary and the adjacent ghost cell results in no incoming wave. These boundary conditions are described in more detail in Section 7.3.1 of LeVeque (2002). Although not perfectly absorbing for waves hitting the boundary at a non-normal angle, they perform very well in practice and have been extensively used for similar problems.

5.2.3.2 Solid wall boundaries

Several benchmark problems are posed in wave tanks with solid (reflecting) walls. Solid wall boundary conditions are implemented as described in Section 7.3.3 of LeVeque (2002). The

values in each grid cell adjacent to the boundary are extrapolated into ghost cells and then the normal velocity is negated. When solving the Riemann problem, this anti-symmetric setup results in a Riemann solution with zero normal velocity at the interface, modeling the correct boundary condition at this boundary.

5.2.3.3 Inflow boundaries

Some benchmark problems specify an incoming wave, typically by tabulated values of the depth at a gauge near the inflow boundary. This can be implemented by filling ghost cells at each time step with the desired values of the fluid depth and momentum values that are determined using the Riemann invariants for the shallow water equations, by assuming the depth and momentum are related in such a way that the solution is a simple wave in the incoming wave family.

For example, at the left edge of the computational domain, an incoming wave would be a right-going wave with constant values of the Riemann invariant $u - 2\sqrt{gh}$ throughout the wave.

This value must be $-2\sqrt{gh_0}$ where $h0$ is the depth of the undisturbed water before the wave arrives. From this the velocity $u = 2\left(\sqrt{gh} - \sqrt{gh_0}\right)$ can be determined for any depth h. Hence the given depth as a function of time at a wave gauge can be used to determine the depth and momentum at this point as a function of time, which in turn is used to fill ghost cells.

5.2.3.4 Initial conditions

In other problems, an initial wave form $h(x, t = 0)$ is specified as a function of x at time $t = 0$, representing a propagating wave form. Again the Riemann invariants can be used to determine the momentum at each point in order to specify initial conditions.

For BP9 (Section 5.3.9) the seafloor displacement is specified. This is what is generally done in real applications. GeoClaw allows specifying a time-varying seafloor displacement as well, to model the dynamic rupture of faults. This capability has also been used in the landslide problems (Section 5.3.3 and Section 5.3.8) to model the changing bathymetry.

5.2.4 Other validation studies

Several of the benchmark problems were solved using TsunamiClaw, an early version of Geo-Claw, in preparation for the Catalina benchmarking workshop in 2004. These results are available in the proceedings paper (LeVeque and George, 2004).

Validation studies of the more recent GeoClaw software have been presented in several peer-reviewed papers:

In Berger et al. (2011), a test problem is used that consists of a radially symmetric ocean with a continental shelf, and a radially symmetric initial hump of water at the center. At one position along the coast an island is placed on the shelf. Several gauges are located near the island. If the island is rotated to a different position on the coast the results at the gauges should be identical. Numerically they will not be identical due to differences in how the coast intersects the Cartesian grid. Very similar results are obtained for locations near an axis and near the diagonal, both in gauge results and in plots of the surface and inundation. This is true even when AMR is used to concentrate fine grids only in the direction towards the island. In Berger et al. (2011), the Chile 2010 tsunami is also used as a test problem and good agreement with measured

results at DART Buoy 32412 are obtained, on two different grid resolutions to test convergence. See also http://www.clawpack.org/links/awr11/ for codes and animations.

Further tests of this same problem are presented in LeVeque et al. (2011). See also http://www.clawpack. org/links/an11/ for codes and animations.

Grid refinement studies and comparison with field data for the widely studied Malpasset dam failure are presented in George (2010).

In Berger et al. (2009), tests are performed for a tsunami-like wave propagating on the full sphere, using a novel mapped grid that covers the sphere with a logically rectangular finite volume grid. Tests are presented in which the bathymetry and the initial conditions are axisymmetric so that the solution should remain so and can be compared to fine grid one-dimensional simulations. See also http://www.amath.washington.edu/~rjl/pubs/amrsphere09/index.html for codes used in this paper.

Independent validation of GeoClaw has also been performed by Spatial Vision Group (http://www.spatialvisiongroup.com/), a private consulting company in Vancouver, BC. David Alexander and Bill Johnstone from this group used the TsunamiClaw software to perform hazard studies of the communities of Ucluelet and Tofino on Vancouver Island. As part of their validation, they compared TsunamiClaw results to those obtained using MOST for a standard model of a Magnitude 9.0 Cascadia Subduction Zone event. Comparisons were performed for several tide gauges on the coast of Washington and Oregon.

Our group is currently using GeoClaw to model the Great Tohoku Tsunami of 11 March 2011 and preliminary comparisons with DART buoy data look very good. Some results were posted online as computed in the days after the event and can be viewed at http://www.clawpack.org/links/honshu2011/. Some comparisons were also presented in a recent article in SIAM News on tsunami modeling (Behrens and LeVeque, 2011). Preliminary results have also been obtained by other groups, e.g., (Zhang et al., 2011).

5.3 Benchmark results

The sections below contain the GeoClaw results for each benchmark problem. Benchmark problem descriptions can be found in the Github repository https://github.com/rjleveque/ nthmp-benchmark-problems (LeVeque, 2011) along with data that were provided as part of the problem specification.

5.3.1 BP1: Single wave on a simple beach – analytical

- A description of this benchmark problem is provided by LeVeque (2011) and Synolakis et al. (2007).
- Problem description provided by Dmitry Nicolsky, at LeVeque (2011): BP01-DmitryN-Single_wave_on_simple_beach/description.pdf

5.3.1.1 Problem Description

The focus is on comparing computed and analytic solutions for a wave incident on a simple beach, in which:

- The bathymetry consists of a deep region of constant depth d connected to a sloping beach of angle $\beta = \text{arccot}(19.85)$. Note that the toe of the beach is located at $x = X0 = d\cot\beta$.

- The initial waveform of the wave is given by

  $\eta(x,0) = Hsech^2(\gamma(x - X1)/d)$

  where $L = arccosh(\ (20))/\gamma$, $X1 = X0 + L$, and $\gamma = (3H/4d)$. The speed of the wave is given by the following:

  $u(x,0) = -\sqrt{g/d}\eta(x,0)$

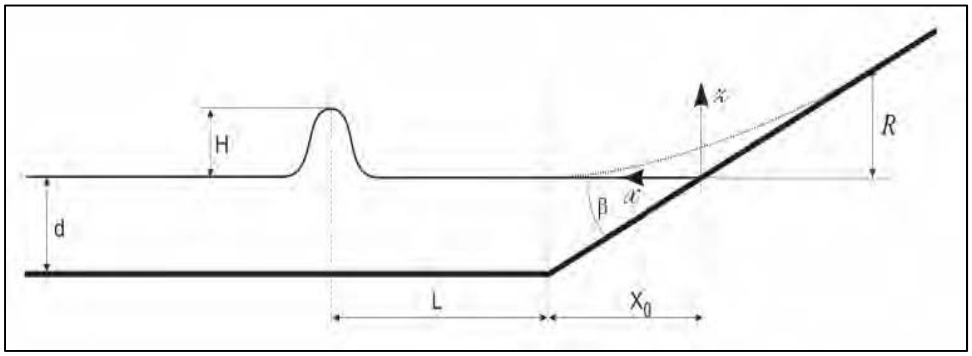

Figure 5-1: Sketch of canonical beach and approaching wave.

5.3.1.2 Problems encountered

- The analytic solution of the wave equation was hard to determine and compute. The analytic solution was obtained from the benchmark problem champion; it would be very helpful if it were provided in an Excel file as part of the benchmark problem description.
- No analytical solution was provided for time $t = 25s$.
- The Clawpack code does not currently include maximum runup calculations. An additional module had to be written.

5.3.1.3 What we did

- Used $g = 1$ and no friction.
- The problem was solved on an 800 × 2 grid, where the *x* domain spanned *x* = -10 to 60.
- Variable time stepping was allowed, based on a CFL number of 0.9.

5.3.1.4 Results

- Task 1. Good agreement between computed and analytic water level profiles at $t = 35(d/g)^{1/2}$, $t = 45(d/g)^{1/2}$, $t = 55(d/g)^{1/2}$, $t = 65(d/g)^{1/2}$ are presented in Figure 5-2. Data were missing from file canonical_profiles.txt for $t = 25(d/g)^{1/2}$, so this time was omitted.
- Task 2. Good agreement between computed and analytic water levels at locations $x/d = 0.25$ and $x/d = 9.95$ during the propagation and reflection of the wave is presented in Figure 5-3.
- Task 3. Maximum runup on the beach was 0.085, as presented in the time series of runup values in Figure 5-4.
- Task 4. The optional demonstration of convergence was not performed.

5.3.1.5 Lessons learned

- This benchmark problem is a good test of the shallow water wave computation against an analytic solution in one dimension.
- Because of its complexity, the analytical solution should be provided in a data file on the benchmark problem website to ensure all participants are solving the same problem.

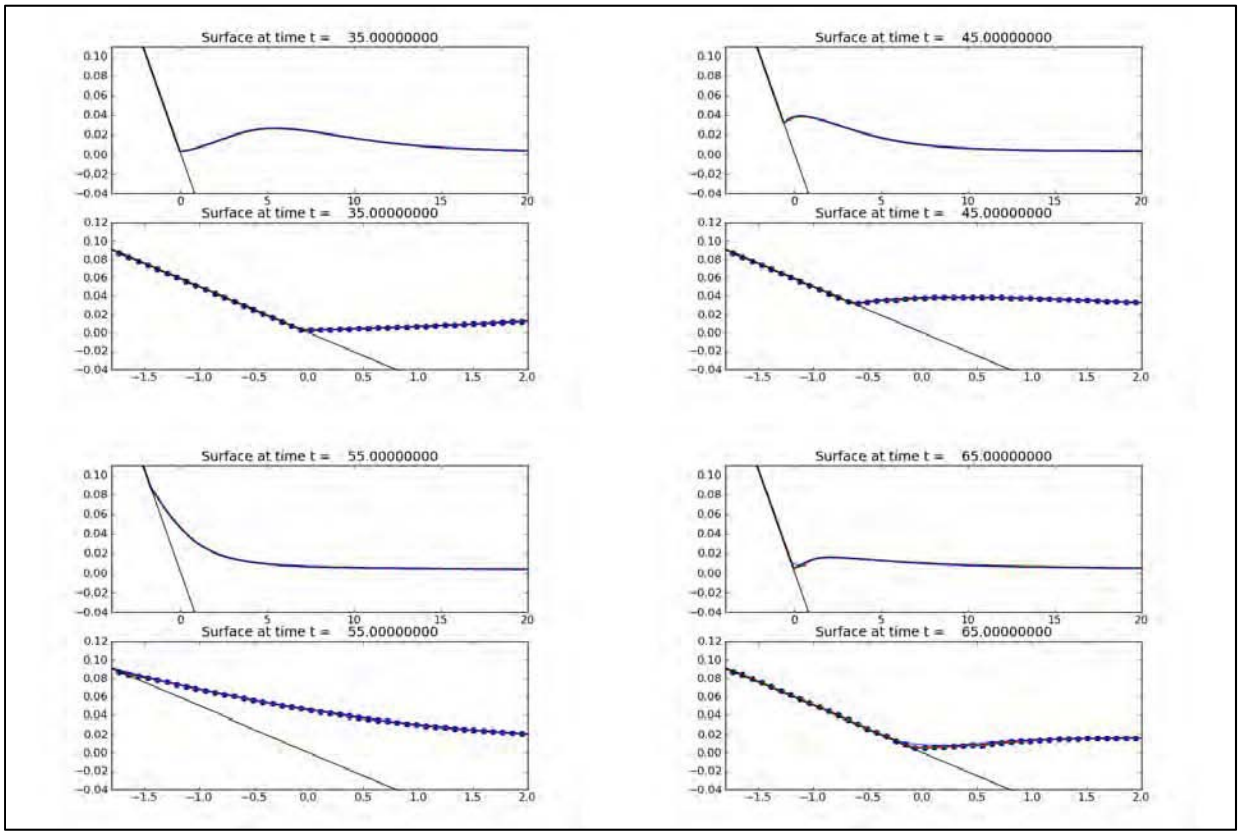

Figure 5-2: Profile plots for the times specified in Task 2. For each pair of plots at a particular time, the top frame provides a full view of the incoming wave and the bottom frame provides an expanded view of the inundation area. In some regions, the analytic and GeoClaw solutions lie atop one another.

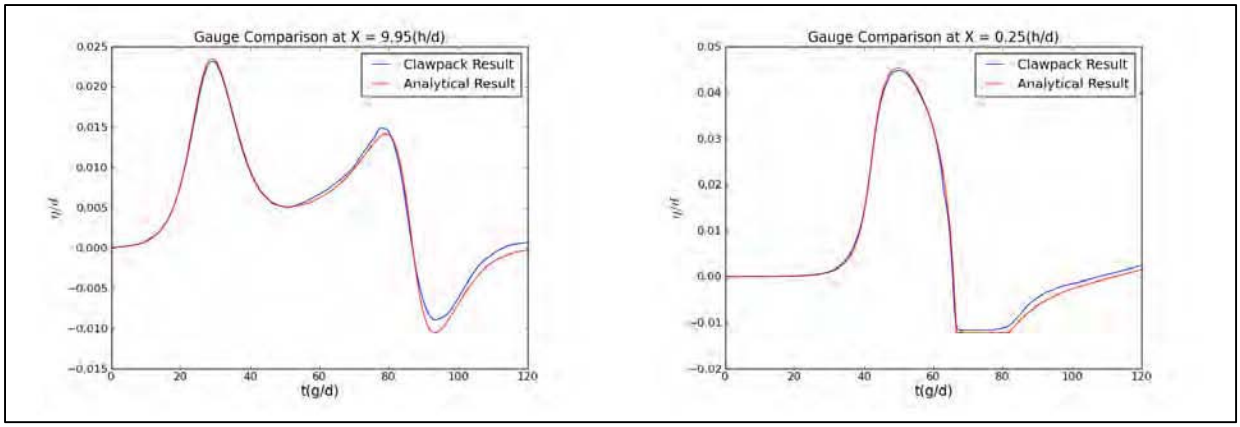

Figure 5-3: Left column: Water level time series at location $x/d = 9.95$. Right column: Water level time series at location $x/d = 0.25$.

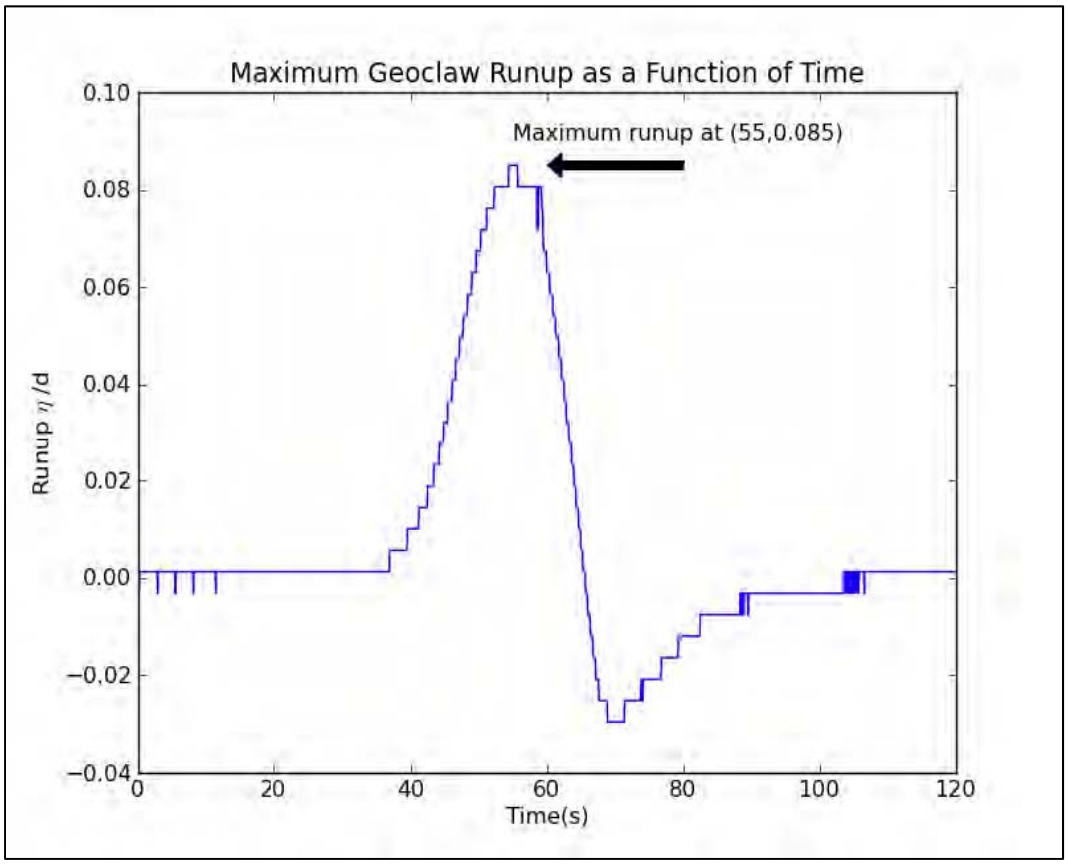

Figure 5-4: Runup on canonical beach as a function of time.

5.3.2 BP2: Solitary wave on composite beach – analytical

Documentation:

- PMEL-135, pp. 5 & 30-33 (Synolakis et al., 2007).

- Problem description provided by Dmitry Nicolsky, at LeVeque (2011): BP02-DmitryN-Solitary_wave_on_composite_beach_analytic/description.pdf
- Coastal Hydraulics Laboratory Problem Description (Briggs, n.d.).

5.3.2.1 What we did

- We solved the shallow water wave equation in Cartesian coordinates with $g = 9.81$ and no friction.
- To specify the incoming wave from the left boundary of our computational domain, we used the first ten seconds of measurements taken at Gauge 4. After ten seconds, the left boundary switched to be a non-reflecting boundary. This boundary is selected since the end of our computational domain is not the end of the physical wave tank. The implementation of these boundary conditions is described in Sections 5.2.3.1 and 5.2.3.3.
- Because the problem is one-dimensional, we solved on a 600 × 2 grid with no adaptive mesh refinement.
- To impose linearization, we scaled the incoming wave by 10^{-4} to remove any nonlinear behavior, then scaled up the gauge readings by 10^{4} to compare with the analytical solution.

5.3.2.2 Gauge comparisons

For these gauge comparisons, we ran our code linearly with friction set to zero.

The results for cases A, B, and C are shown in Figure 5-5, Figure 5-6, and Figure 5-7 respectively, where Gauge 11 is placed at the vertical wall.

5.3.2.3 Convergence Study

We performed a test to see how well Clawpack converged to the analytic solution as we increased the number of grid cells in our computational domain (using 200, 400, and 600 cells). We found that as the number of grid cells was increased, the computed solution approached the analytic solution. The convergence plot is shown in Figure 5-8.

5.3.2.4 Lessons learned

In this benchmark problem, we found that using the analytic solution at Gauge 4 as boundary conditions on a shorter domain, starting at gauge 4, provided more accurate results than using the wavemaker position and a longer domain to model the entire tank. It appears that a similar assumption is made in the provided analytic solutions, as they match up nearly perfectly with the lab data for the first ten seconds.

Overall this benchmark problem is a good test for one-dimensional codes. The benchmark problem specifications could be improved by specifying the computational domain and the specific data source that should be used to model the incoming wave.

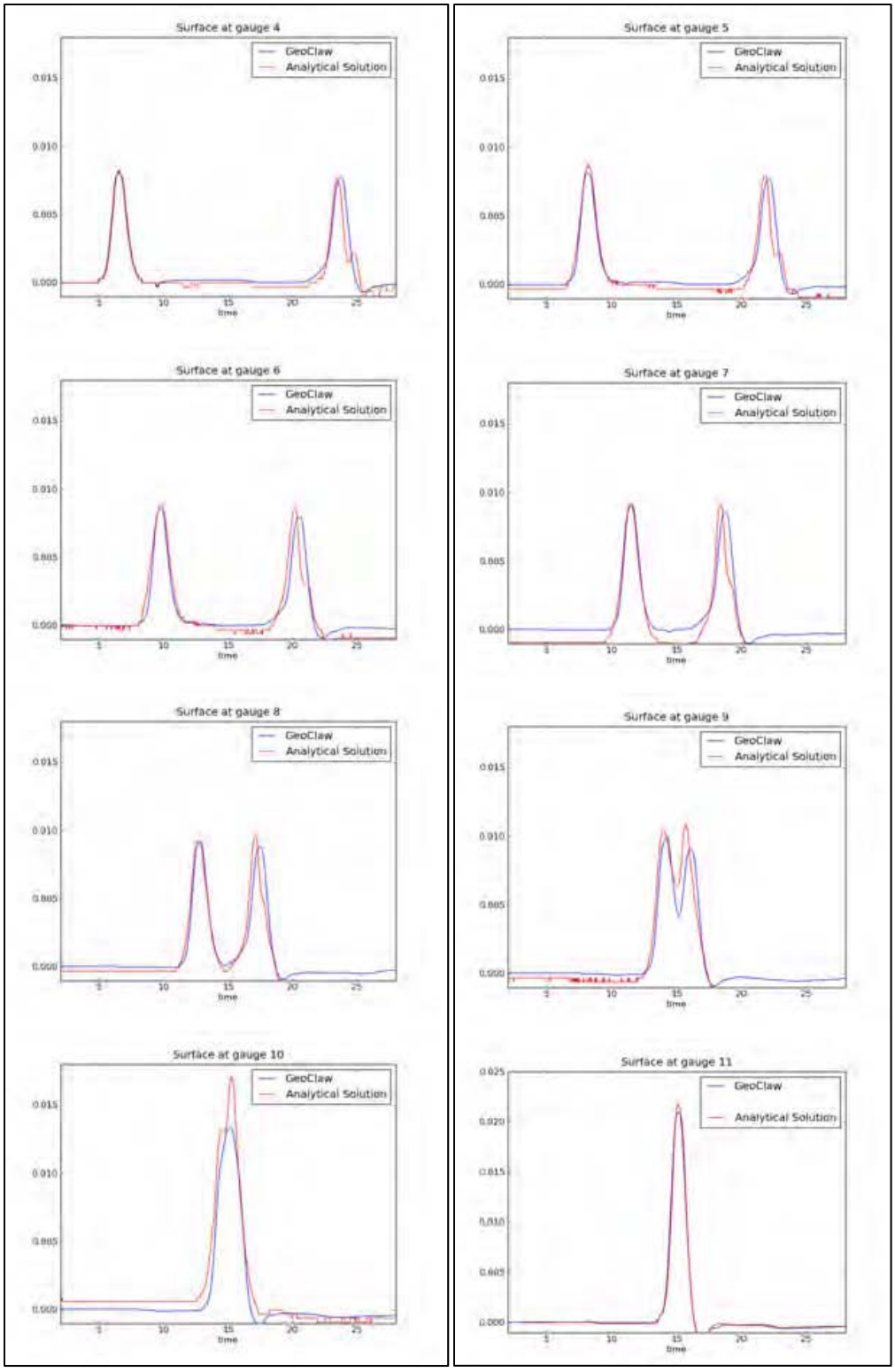

Figure 5-5: Case A

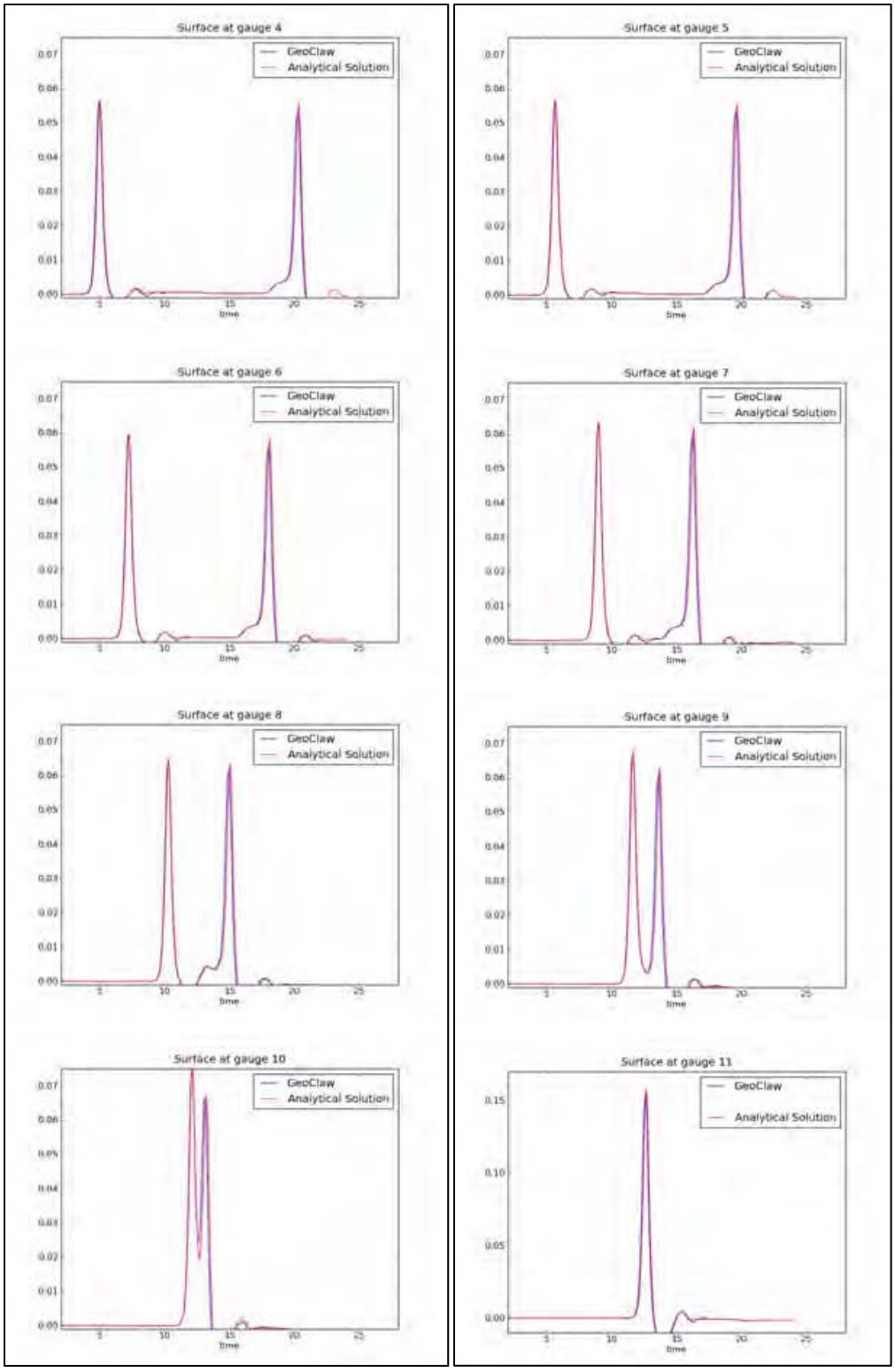

Figure 5-6: Case B

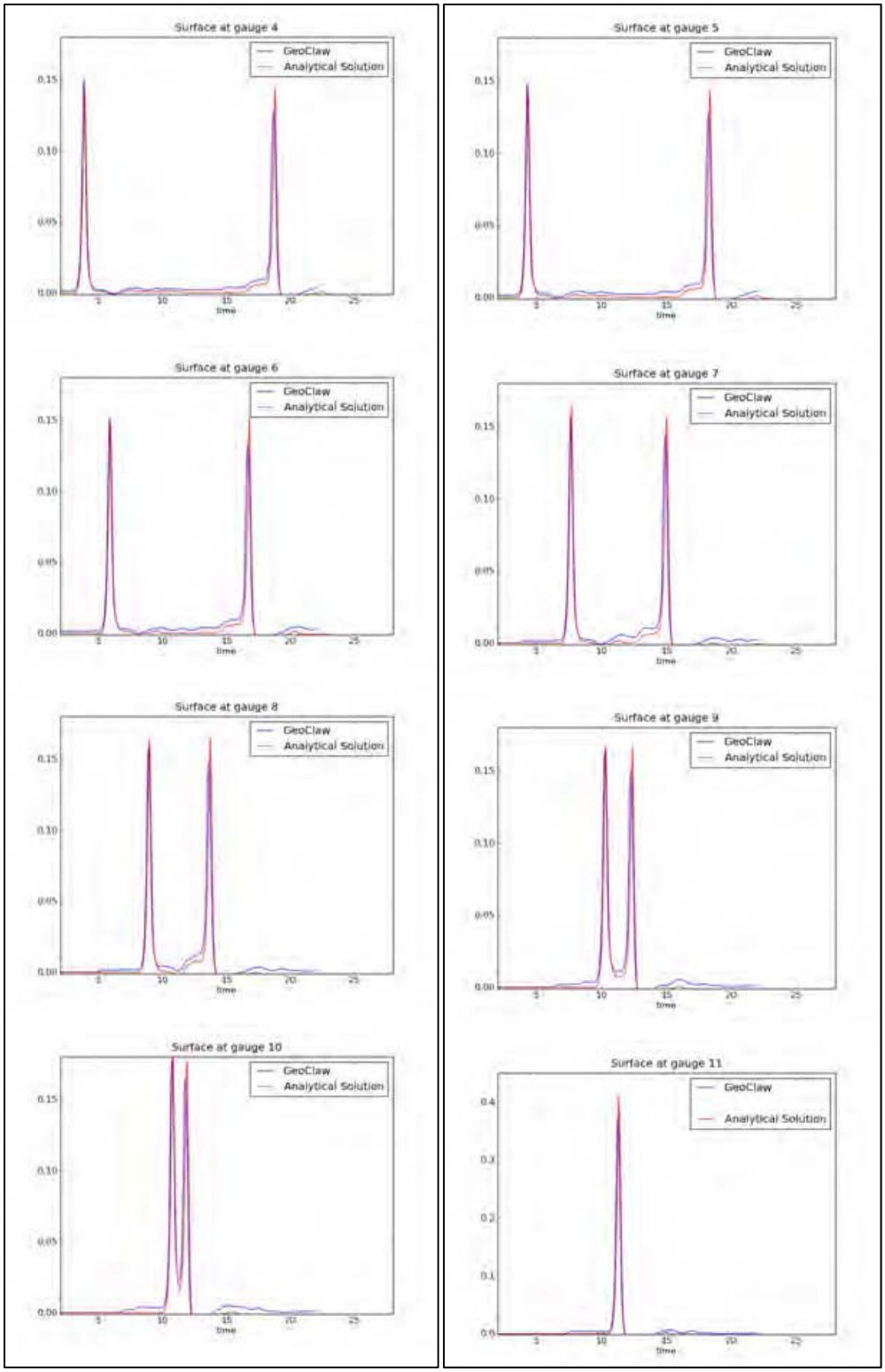

Figure 5-7: Case C

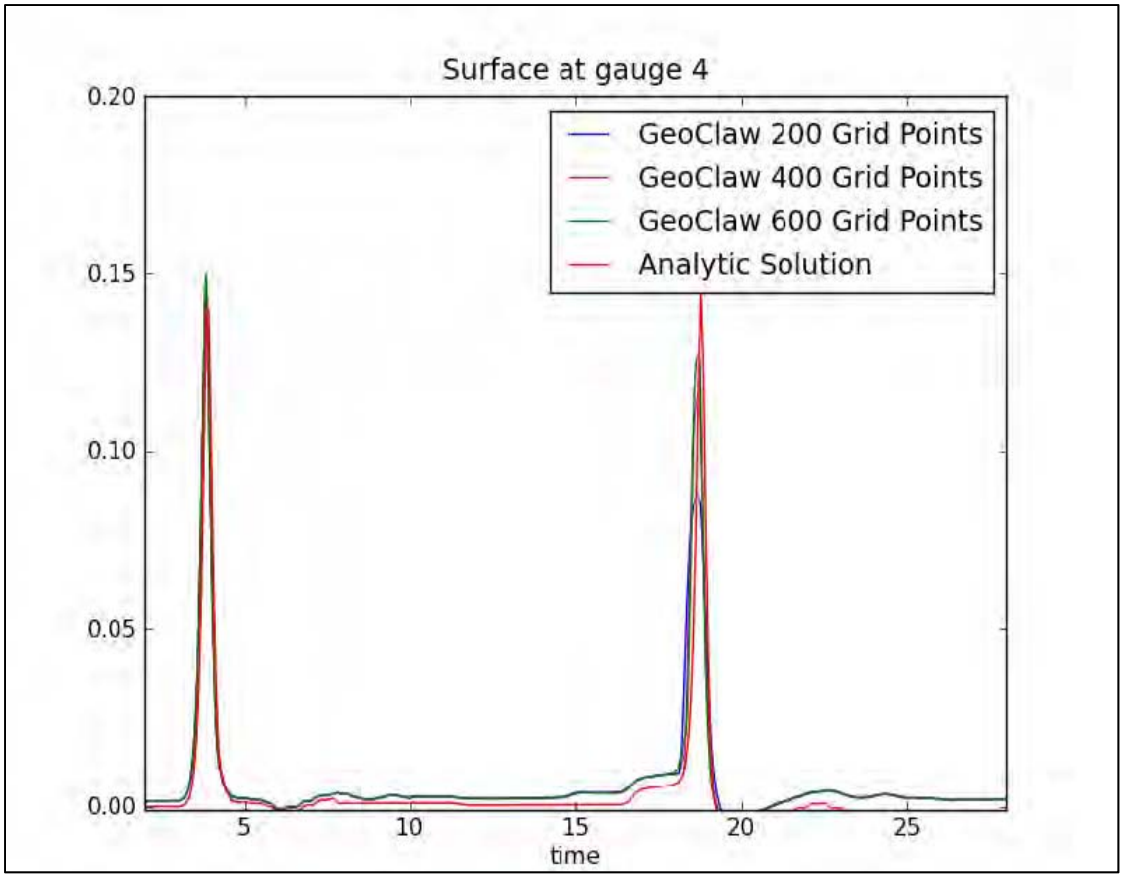

Figure 5-8: Convergence Plot for Gauge 4 in Case C

5.3.3 BP3: Saucer landslide – laboratory

5.3.3.1 Problem specification

- Problem description provided by Stephan Grilli: BP03-StephanG-Saucer_landslide/EG07_slide_benchmark.pdf at LeVeque (2011).
- Original paper of Enet and Grilli (2003) describing laboratory experiments.

5.3.3.2 Problems encountered

The moving bathymetry is specified in terms of $\zeta(\xi, \eta)$, the thickness of the sliding mass in the direction orthogonal to the sloping beach. In each time step, this must be converted into values $B(x, y, t)$ in the vertical z-direction, at horizontal distance x from the initial shore. Note that

$$x = \xi \cos(\theta), y = \eta$$

The bathymetry of the wave tank and beach without the sliding mass is given by

$$B_0(x, y) = \begin{cases} -\tan(\theta)\mathrm{x} & \text{if x} < 5.598 \\ -1.5 & \text{if x} \geq 5.598 \end{cases}$$

The value 5.598 ≈ 1.5/ tan(θ) is determined by the fact that the water has a depth of 1.5 m on the flat portion and the beach slope is 15° so θ = 15π/180 ≈ 0.2618.

At time $t = 0$ the sliding mass is located at $x = x_0$, determined by the initial depth d according to

$$x_0 = \frac{d}{\tan(\theta)} + \frac{T'}{\sin(\theta)}$$

At time t the sliding mass is centered at $x_c = x_0 + s(t)\cos(\theta)$ where $s(t)$ is the function discretized in the data file kinematics.txt. However, this is only true for small t. After some time the mass hits the horizontal bottom of the tank. According to paper by Enet and Grilli (2003) and communication with Stephan Grilli, the mass stops at this point. This is not made clear in the problem specification (LeVeque, 2011).

To determine $B(x, y, t)$ for each finite volume grid cell with center (x_i, y_j) the value ξ must be found so that

$$\xi\cos(\theta) + \zeta(\xi - \xi_c, y_j)\sin(\theta) = x_i$$

where $\xi_c = x_c/\cos(\theta) + s(t)$ is the ξ location of the center of mass at this time. Determining ξ requires solving the nonlinear equation

$$\cos(\theta)\xi + \zeta(\xi - \xi_c, y_j)\sin(\theta) - x_i = 0.$$

In our Fortran code this equation is solved using the library routine zeroin, available from Netlib (http://www.netlib.org/go/zeroin.f).

Once ξ has been found, the bathymetry is

$$B(x_i, y_j, t) = -\tan(\theta)\xi + \cos(\theta)\zeta(\xi - \xi_c, y_j).$$

5.3.3.3 What we did

- The moving bathymetry is handled by recomputing $B_{ij}^n = B(x_i, y_j, t_n)$ in each time step at the center of each finite volume grid cell, by solving a nonlinear equation as described above. This is the standard approach for handling moving bathymetry in GeoClaw: the value B_{ij}^n is adjusted but the fluid depth h_{ij}^n remains the same, so that the water column is simply displaced vertically in any cell where the bathymetry changes. For bathymetry that is smoothly varying in space and time, as in this problem, this is considered a reasonable approach. Note, however, that no momentum is directly imparted to the water by the moving bathymetry.
- The problem was solved using a fixed grid with $72n \times 18n$ grid cells on the domain $-1 \le x \le 6.2$ and $0 \le y \le 1.8$ m. Three resolutions corresponding to $n = 1, 2, 4$ were used to test convergence.

  A second level of refined grid was used in the region $-0.1 \le x \le 0.1$ and $0 \le y \le 0.1$ surrounding the point $x \approx 0, y = 0$ on the shoreline where the runup R_u must be calculated. In each case this grid was 10 times finer in each direction than the base grid.

  Adaptive mesh refinement (with moving grids) was not used.
- The problem was solved on $0 \le y \le 1.8$ with solid wall boundary conditions at $y = 0$. This gives the correct solution in this domain and the solution in the other half of the wave tank $-1.8 \le y \le 0$ is easily constructed by symmetry if desired.

  Solid wall boundary conditions were also used at $y = 1.8$. At $x = -1$ the boundary condition doesn't matter since this region is always dry, and at $x = 6.2$ outflow boundary conditions were used. Zero-order extrapolation, which generally gives a very

good approximation to non-reflecting boundary conditions as described in Section 5.2.3.1. Solid wall boundary conditions are implemented as described in Section 5.2.3.2. See Section 5.2.3 for more information about these boundary conditions.

5.3.3.4 Numerical simulations

Figure 5-9 shows two frames from a sample computation for the case $d = 0.061$. Colors indicate the surface elevation $\eta(x, y, t)$ and contours show the bathymetry with the upper half of the sliding mass.

5.3.3.5 Gauge comparisons

Simulated gauges were placed at the 4 locations that match the wave tank measurements, as indicated in Figure 5-9.

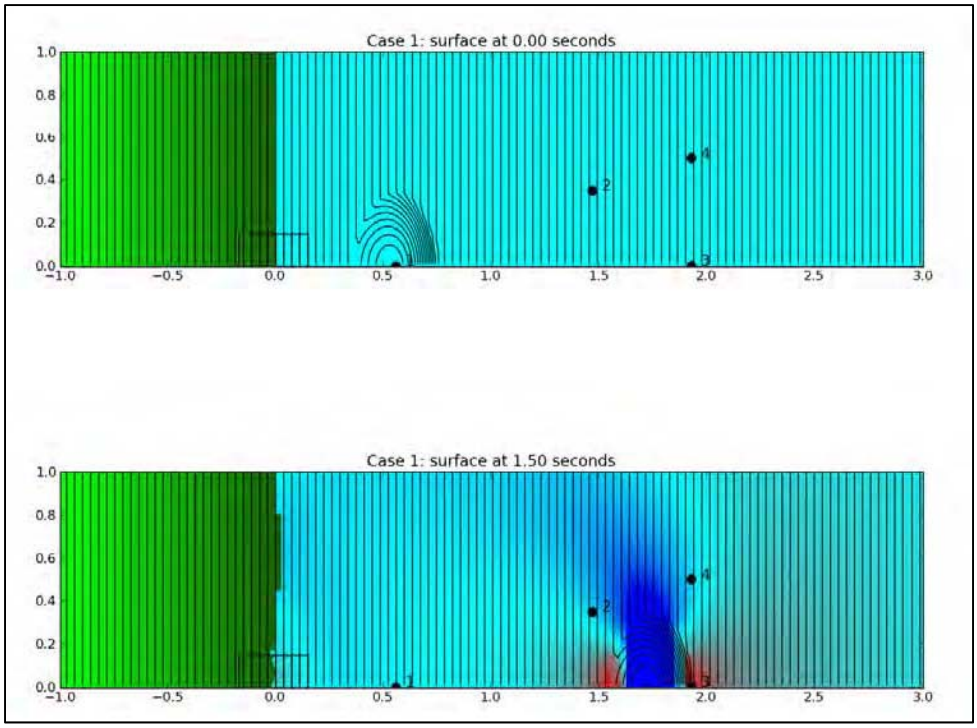

Figure 5-9: Sample results for d = 0.061. The water surface η(x, y, t) (colors with dark red +0.02 m and dark blue −0.02 m) and bathymetry (0.01 m contour levels). Only a portion of the computational domain is shown. Grid resolution: Δx = Δy = 0.025 m on the full domain, with refinement to Δx = Δy = 0.0025 m in the nearshore region in the rectangular box. The full domain goes to x = 6.2 and to y = 1.8.

The surface elevation $\eta(t)$ at each gauge was recorded every time step. These results are shown in Figure 5-10 through Figure 5-16 for the 7 test cases.

Reasonable agreement is generally seen for the initial peak and trough at Gauges 1, 2, and 4. On the other hand, Gauge 3, located along the centerline, shows quite different results than the measurements and generally exhibits a steeper dip in η as the mass passes this point. The measurements also show an oscillatory wave train behind the initial peak and trough that is not captured in the simulations obtained with the shallow water equations. This is consistent with claims in LeVeque (2011) and Enet and Grilli (2003) that dispersive effects are important for these short wavelength waves that cannot be captured by the non-dispersive shallow water

equations. By contrast, the Boussinesq model used in Fuhrman and Madsen (2009) does display these dispersive ripples.

5.3.3.6 Runup measurements

The runup is measured near $y = 0$ by keeping track of the approximate shoreline position in the first row of grid cells $j = 1$, whose centers lie at $y = \Delta y/2$. In each time step, we loop over all cells $i = 1,2,\ldots$ and look for the first cell for which $h_{ij} > f$, where $f = 0.001$ (1 mm) was chosen as a depth below which the cell is considered dry. The value $x_s = i\Delta x$, the right edge of this finite volume cell, was then used as the shoreline location at this time. The runup at each time is then computed as $x_s \tan(\theta)$, and this value was output for later plotting, and for computing the maximum runup R_u required for the benchmark.

Figure 5-10 through Figure 5-16 show the runup as functions of time for each test case. Some of these plots exhibit strange behavior for later times. This was due to the fact that we used a limited domain and also that we used a refined grid over only a fairly small region near the origin.

Approximate maximum runup values are tabulated in Table 5-1. These values are based on the minimum values seen in the figures for early times. It is not clear if these are correct in all cases. Also these grids are fairly coarse. But because the gauge data do not match particularly well and we do not believe shallow water is a suitable model for this problem, we did not pursue this further.

Table 5-1: Runup values in mm. Lab results taken from Table 1 of LeVeque (2011). Two different resolutions with 36 and 72 points in the y direction were compared, with mx = 4my points in the x direction.

D	Lab	My = 36	My = 72
0.061	6.2	8.0	8.7
0.080	5.7	5.4	6.0
0.100	4.4	2.7	4.3
0.120	3.4	2.7	3.4
0.140	2.3	2.7	2.7
0.149	2.7	2.7	2.7
0.189	2.0	1.4	2.0

5.3.3.7 Lessons learned and suggestions for improvement

- It might be useful to other groups doing this problem in the future if the bathymetry $z = B_0(x, y)$ were tabulated, corresponding to the mass centered at $x_0 = 0$ on the slope with $\theta = 15°$. From this, the bathymetry at later times could be interpolated by shifting by x_c. Computing $B_0(x, y)$ from the given $\zeta(\xi, \eta)$ requires solving a nonlinear equation at each (x, y) as outlined in Section 5.3.3.3.
- It is stated in LeVeque (2011) that $\zeta(\xi, \eta)$ represents a "Gaussian mass" but this is not a Gaussian function.
- The non-dispersive shallow water equations do not appear adequate to model the oscillatory wave train observed in the laboratory. The shallow water equations may still

be useful for modeling landslides of this nature because the initial peak amplitude and run up values are in the right ballpark, but comparison with laboratory measurements is not a suitable means of judging convergence or accuracy of the numerical method. For this reason, it would be valuable if the community could agree on what the "correct" converged solution to the shallow water equations is for this problem, and if this solution (or at least the values at the gauges) were tabulated for comparison in future benchmark studies.

- The runup results in the laboratory might be affected by the rail along which the mass slides, which is visible in Figure 1 of LeVeque (2011) and is along $y = 0$, the point where it is stated that the runup should be measured. In fact, the runup must have been measure slightly above this point, as indicated in Figure 9 of Enet and Grilli (2003). The rail appears to be several mm high and should affect the fluid dynamics. This rail could easily be added to the bathymetry if its dimensions were known.

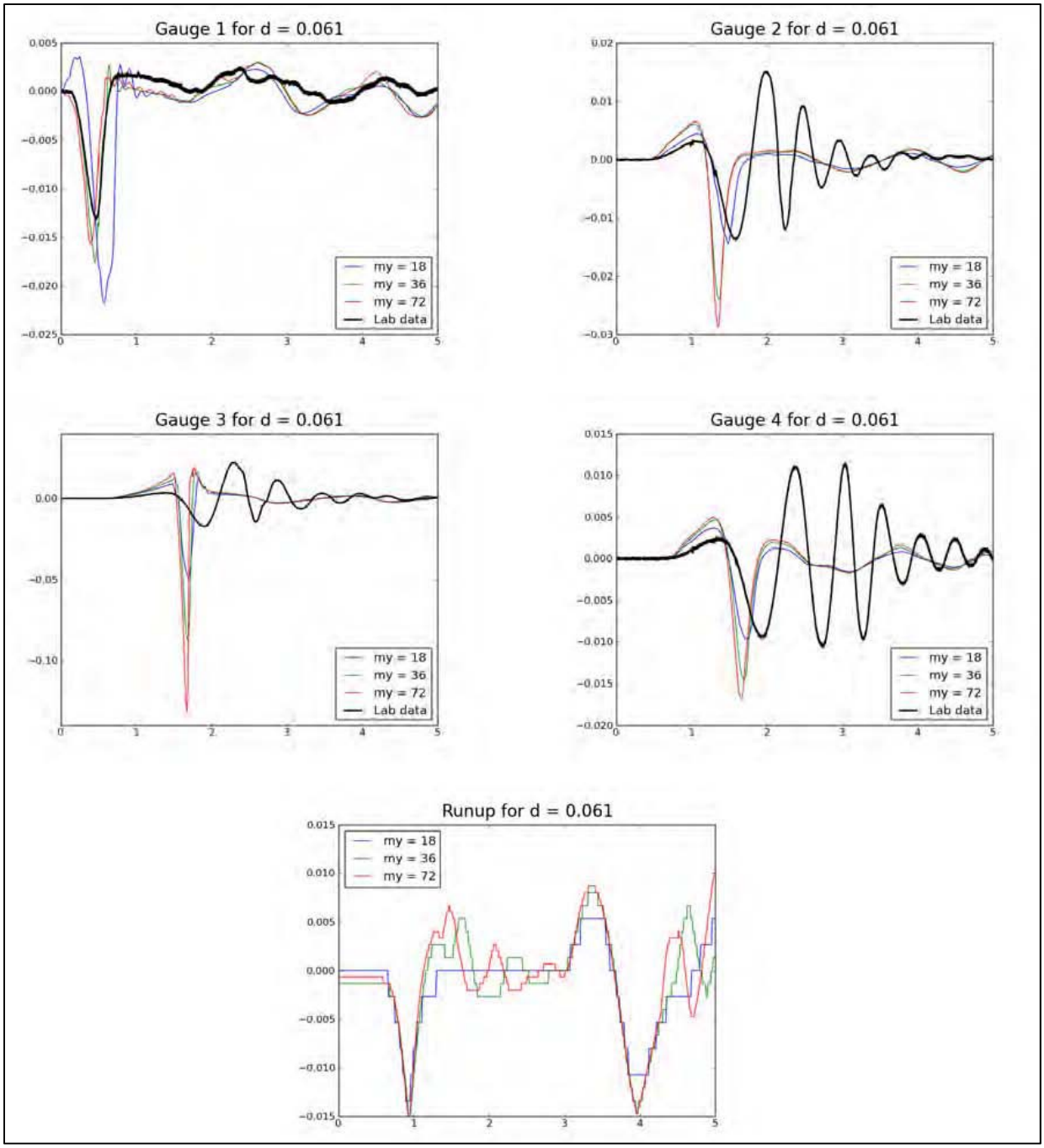

Figure 5-10: Gauge and runup results for d = 0.061. Three different resolutions with my = 18, 36, and 72 points in the y direction were compared, with mx = 4my points in the x direction.

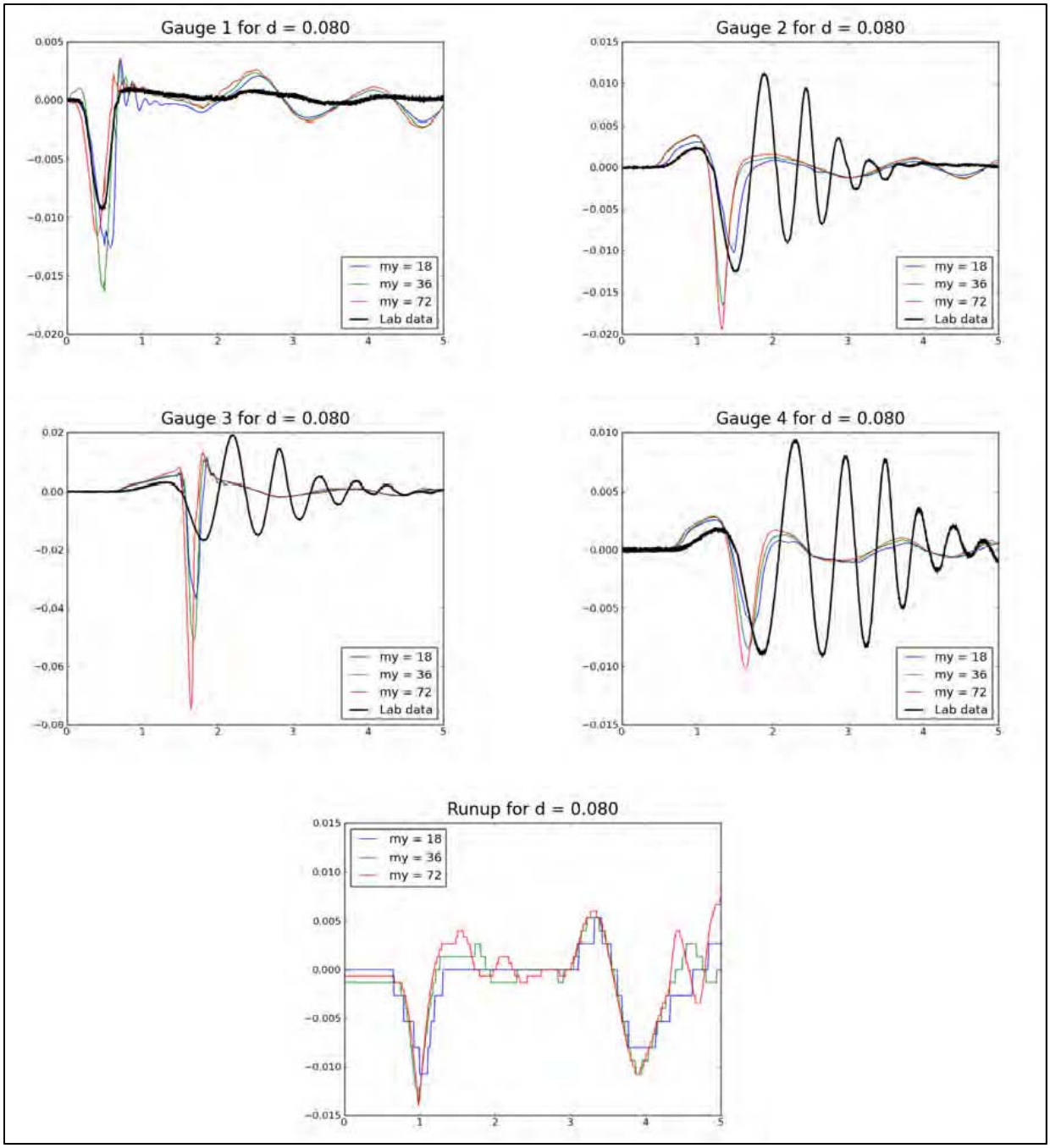

Figure 5-11: Gauge and runup results for d = 0.08.

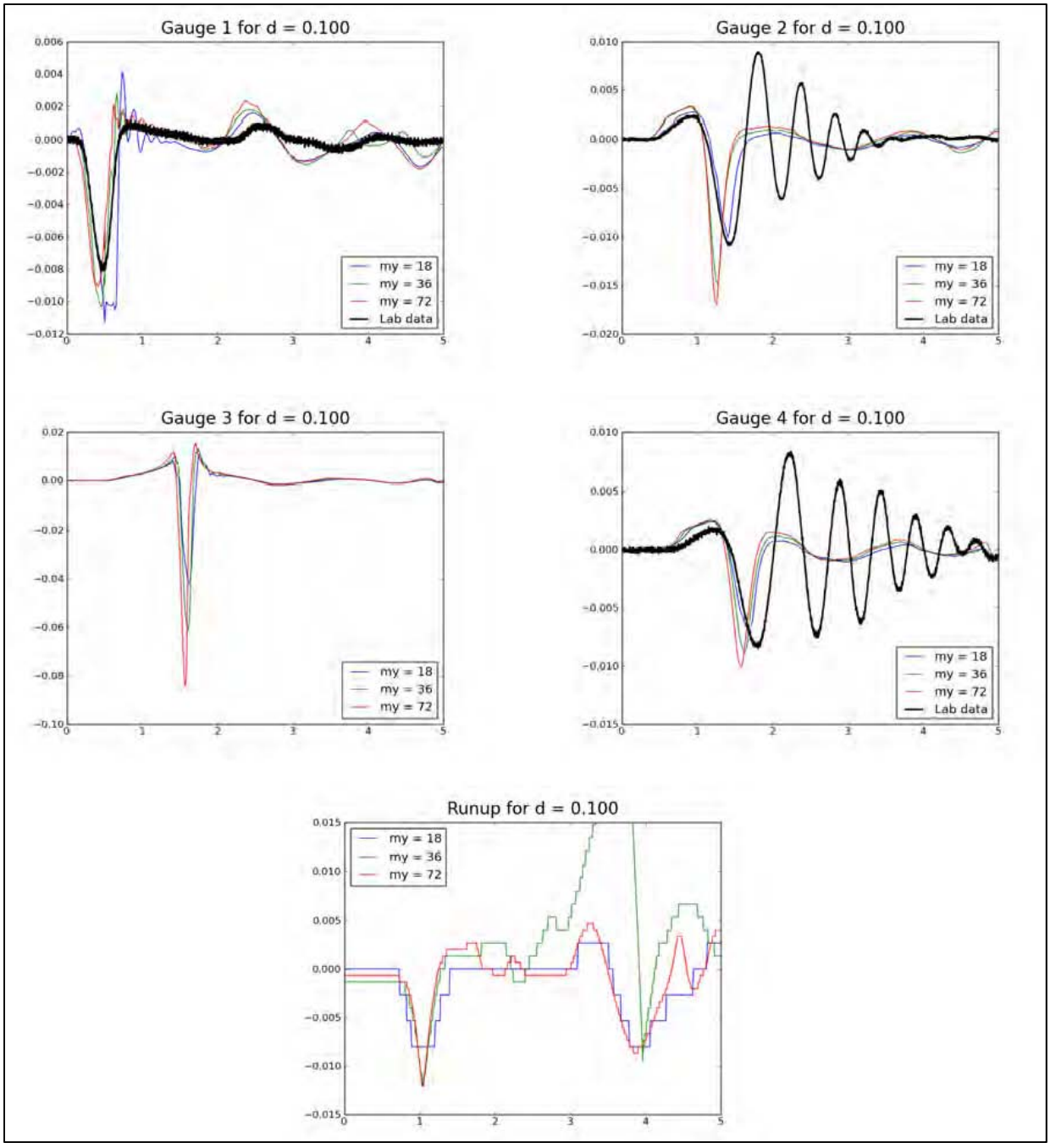

Figure 5-12: Gauge and runup results for d = 0.1.

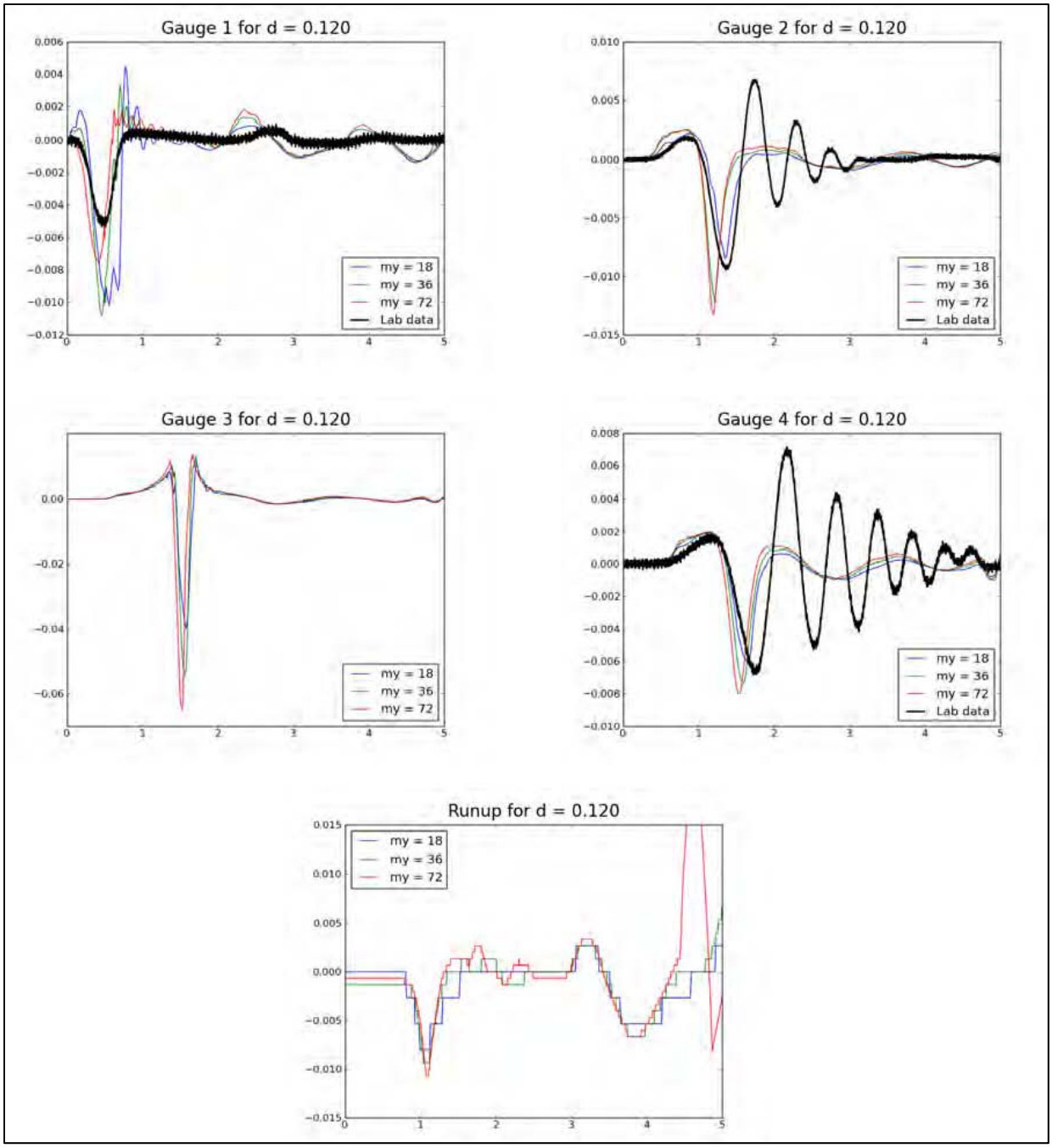

Figure 5-13: Gauge and runup results for d = 0.12.

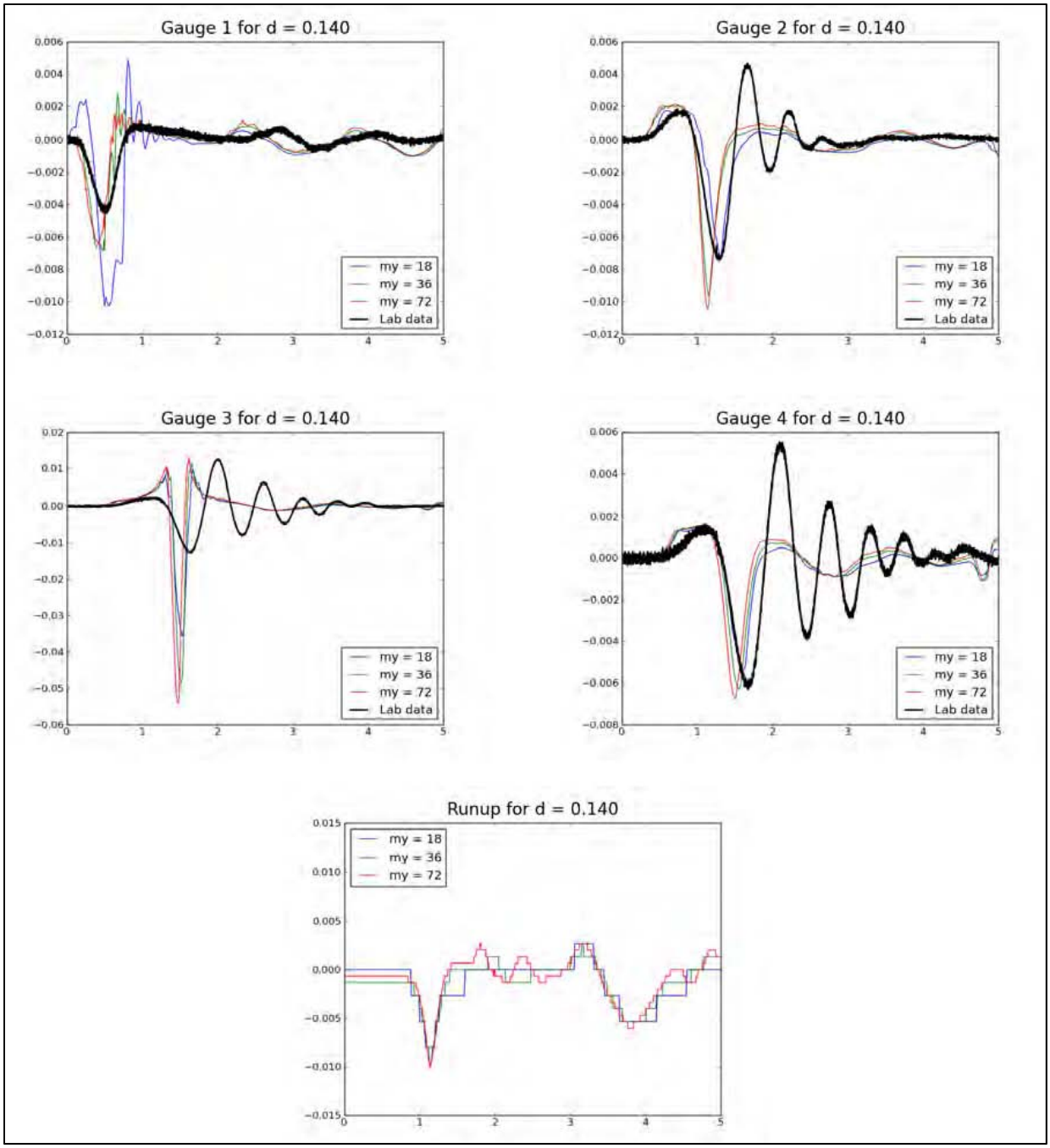

Figure 5-14: Gauge and runup results for d = 0.14.

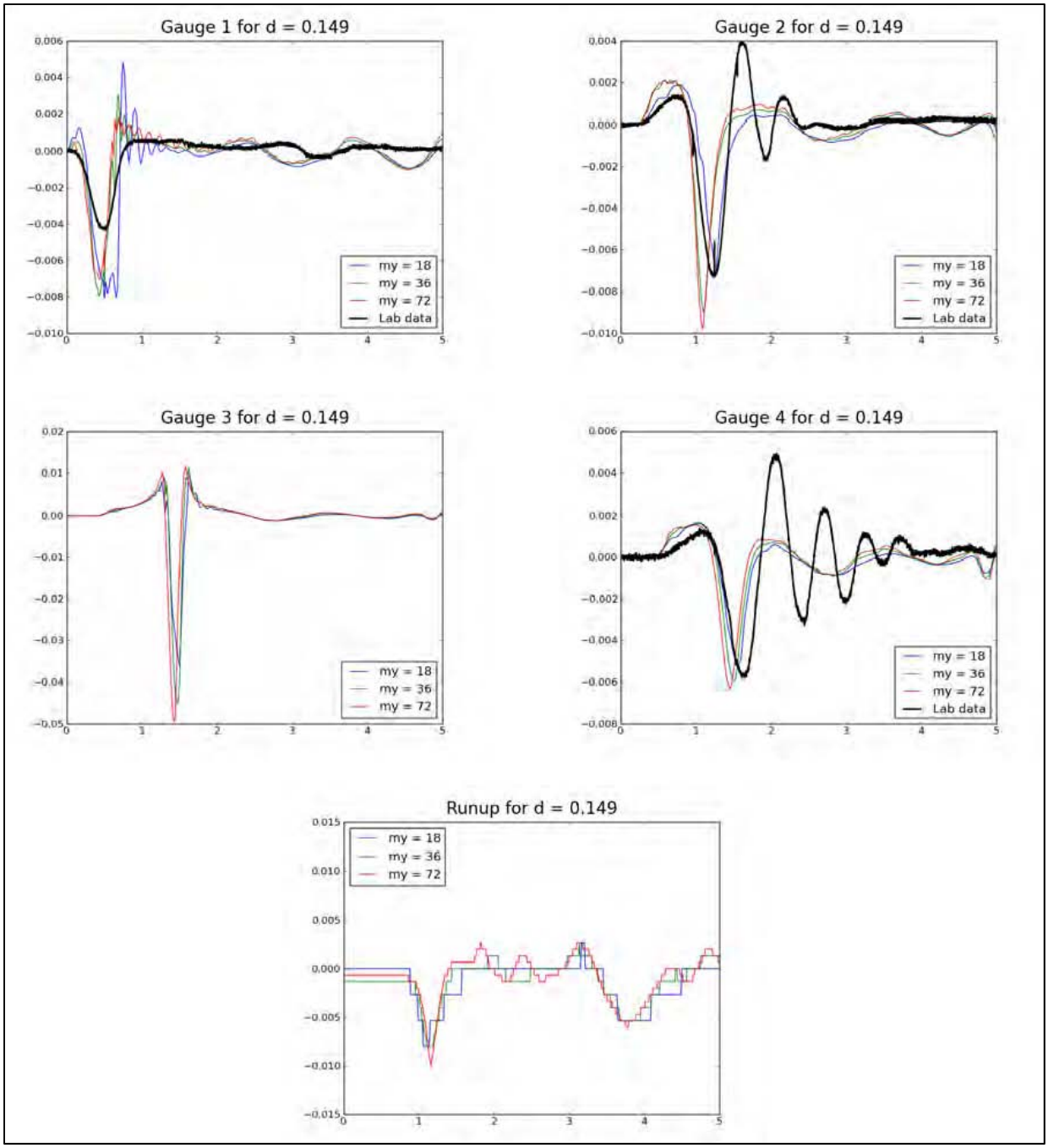

Figure 5-15: Gauge and runup results for d = 0.149.

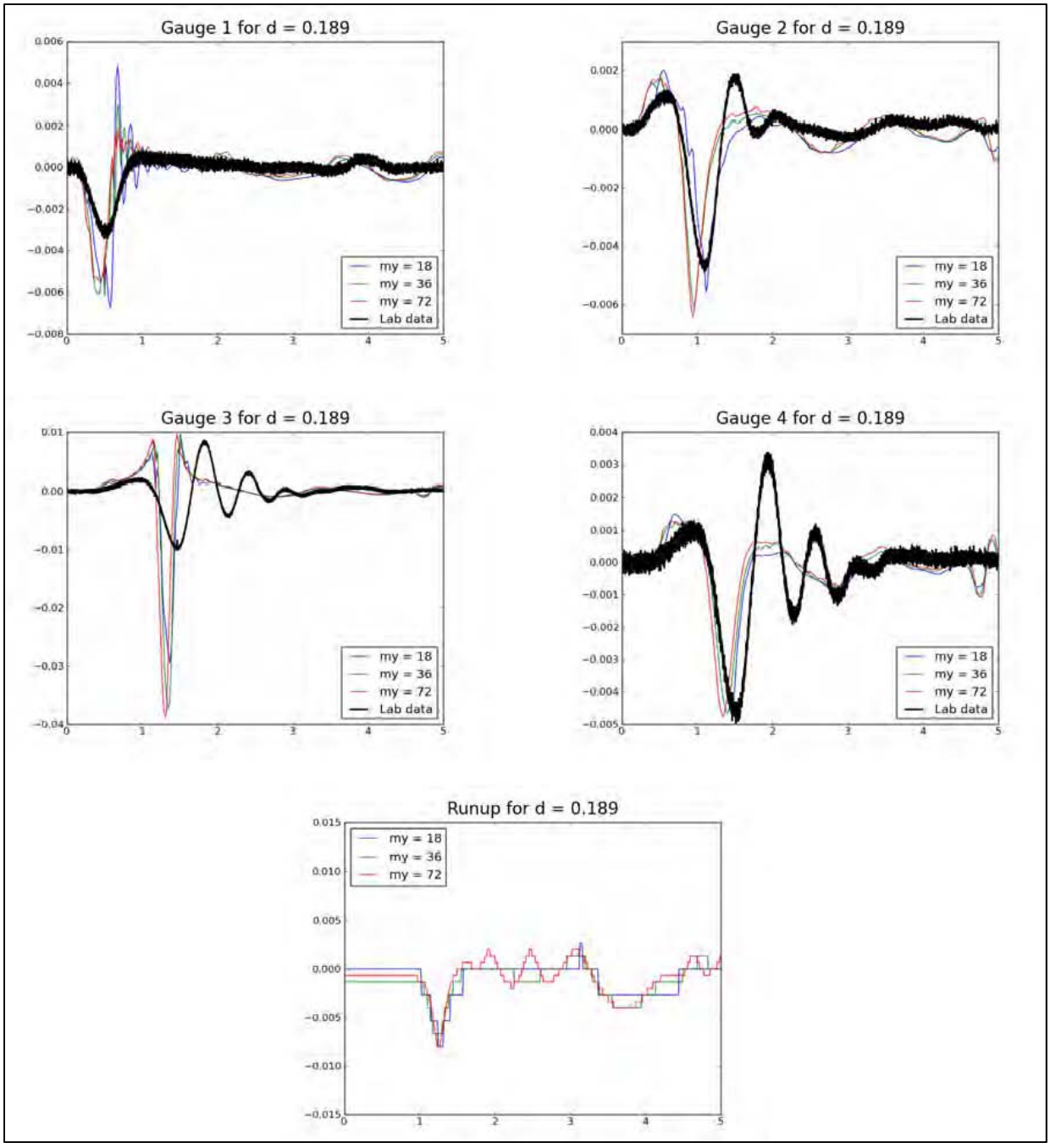

Figure 5-16: Gauge and runup results for d = 0.189.

5.3.4 *BP4: Single wave on simple beach – laboratory*

- PMEL-135, pp. 5 & 30-33
- Problem description provided by Y. Joseph Zhan, at LeVeque (2011).

5.3.4.1 Description

This benchmark is the laboratory counterpart to BP1 (Single wave on a simple beach: Analytic). A wave tank at the California Institute of Technology in Pasadena was used. The tank was 31.73 m long, 60.96 cm deep, and 39.97 cm wide; the bottom of the tank consisted of painted stainless steel plates. An instrument carriage was mounted on rails that ran along the entire length of the tank, permitting the arbitrary positioning of measurement sites. A ramp was installed at one end of the tank to model the bathymetry of the canonical beach configuration – i.e., a constant-depth region adjoining a sloping beach. The beach ramp was sealed to the tank side walls and the beach slope corresponded to angle $\beta = \text{arccot}(19.85)$. Figure 5-17 presents the computational domain used in this test.

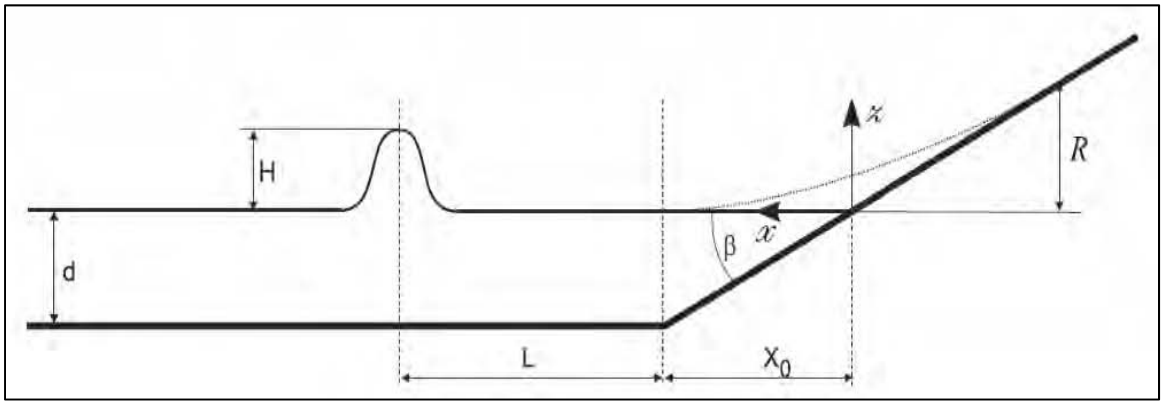

Figure 5-17: Schematic of computational domain.

5.3.4.2 Tasks

- a. Compare numerically calculated surface profiles at $t/T = 30:10:70$ for the non-breaking case $H/d = 0.0185$ with the lab data.
- b. Compare numerically calculated surface profiles at $t/T = 15:5:30$ for the breaking case $H/d = 0.3$ with the lab data
- c. (Optional) Demonstrate the scalability of the code by using different d
- d. Compute maximum runups for at least one non-breaking and one breaking wave case.

5.3.4.3 Problems encountered

Problems that prevented completion of the benchmark were not encountered.

5.3.4.4 What we did

- Used $g = 1$ and no friction.
- The bathymetry consisted of a deep plateau of constant depth d connected to a sloping beach of angle $\beta = \text{arccot}(19.85)$. Note that the toe of the beach was located at $x = X0 = d\cot\beta$
- The initial waveform of the wave was given by

  $\eta(x,0) = H\text{sech}^2(\gamma(x - X_1)/d)$

  where $L = \text{arccosh}(\sqrt{(20)})/\gamma$, $X1 = X0 + L$, and $\gamma = \sqrt{(3H/4d)}$. The speed of

the wave is given by:

$u(x,0) = -\sqrt{g/d}\eta(x,0)$

- For the low amplitude case, we set $d = 1$ cm, $H = 0.0185$ cm, and ran the computations on an 800 × 2 grid, where the x domain spanned from $x = -10\ to\ x = 60$.
- For the high amplitude case, we set $d = 1$ cm, $H = 0.3$ cm, and ran the computations on a 1200 × 2 grid, where the x domain spanned from $x = -10\ to\ x = 60$.
- We allowed variable time stepping based on a CFL number of 0.9

5.3.4.5 Results

- Tasks a and b in Figure 5-18 and Figure 5-19 present the computed and measured surface profiles for the low and high amplitude cases, respectively. Correspondence is excellent in the low amplitude case. In the high amplitude case the computed amplitude is smaller and the steepness greater than that of the measured wave – a consequence of the fact that the experimental parameters violate the shallow water wave assumptions.
- Task c: This optional task was not addressed.
- Task d: Figure 5-20 and Figure 5-21 present the results for maximum runup computations for the low amplitude and high amplitude wave cases. The results can be expressed as the non-dimensional data pairs (H/d, R/d) = (0.0185, 0.085) and (0.3, 0.42) for the high and low amplitude cases, respectively. The low amplitude result falls well within the scatter plot results of Zhan (LeVeque, 2011) presented in Figure 5-22, while the high amplitude result falls somewhat below, as might be expected in light of the comments made in the Task a and b discussion, above.

5.3.4.6 Lessons learned

For test cases in which amplitudes are so large that the shallow water wave assumptions are violated, it can be expected that computed and observed wave height and runup will not agree as well as in cases characterized by amplitudes for which the shallow water wave assumptions are valid.

For the amplitude $H/d = 0.3$ case, our observed runup of 0.42 agrees well with the experimental results shown in Figure 5-22.

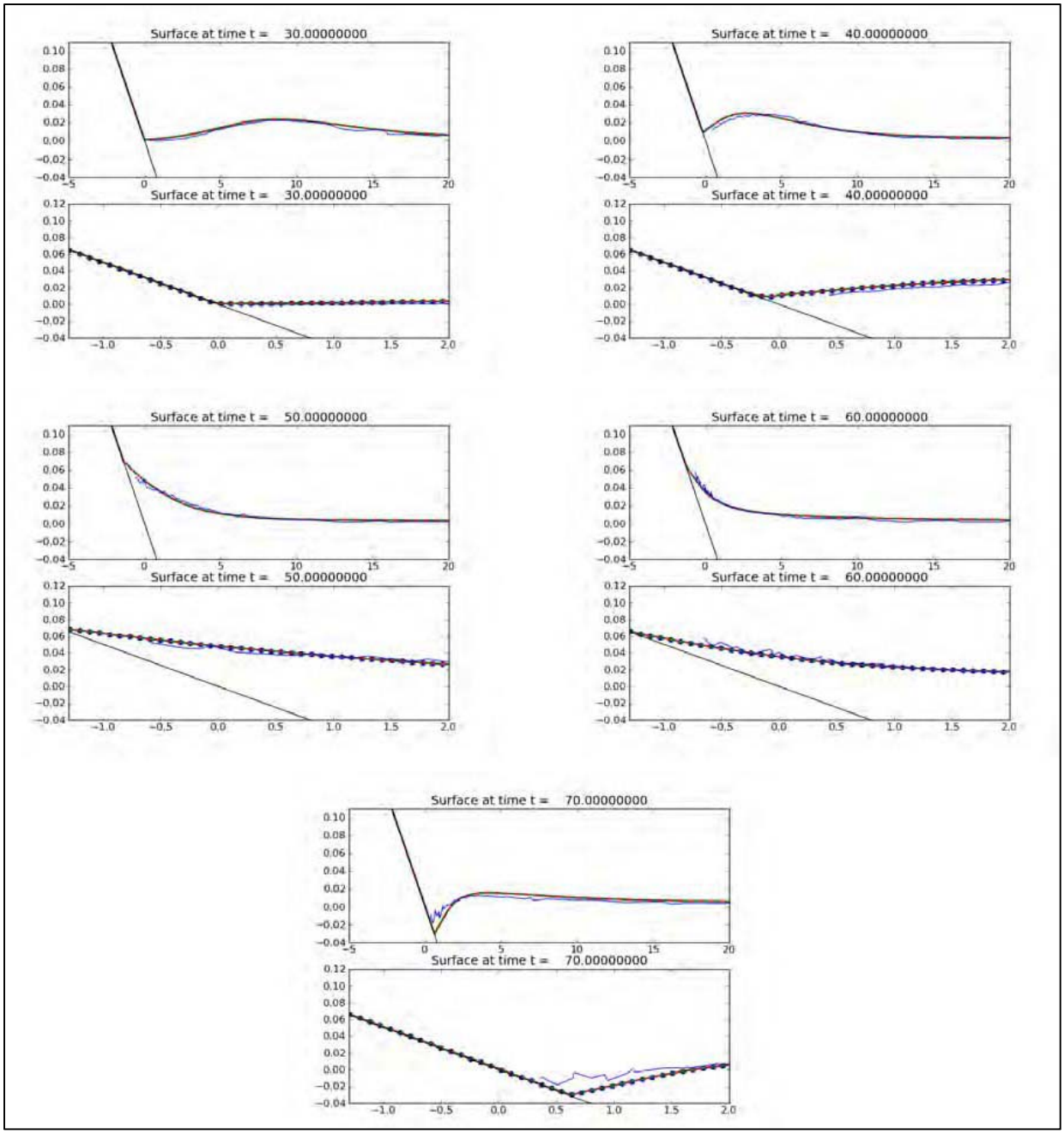

Figure 5-18: Runup computations and lab measurements for the low amplitude case. In the paired plots for each time value, the bottom frame provides a zoomed view of the inundation area for the incident wave presented in the top frame.

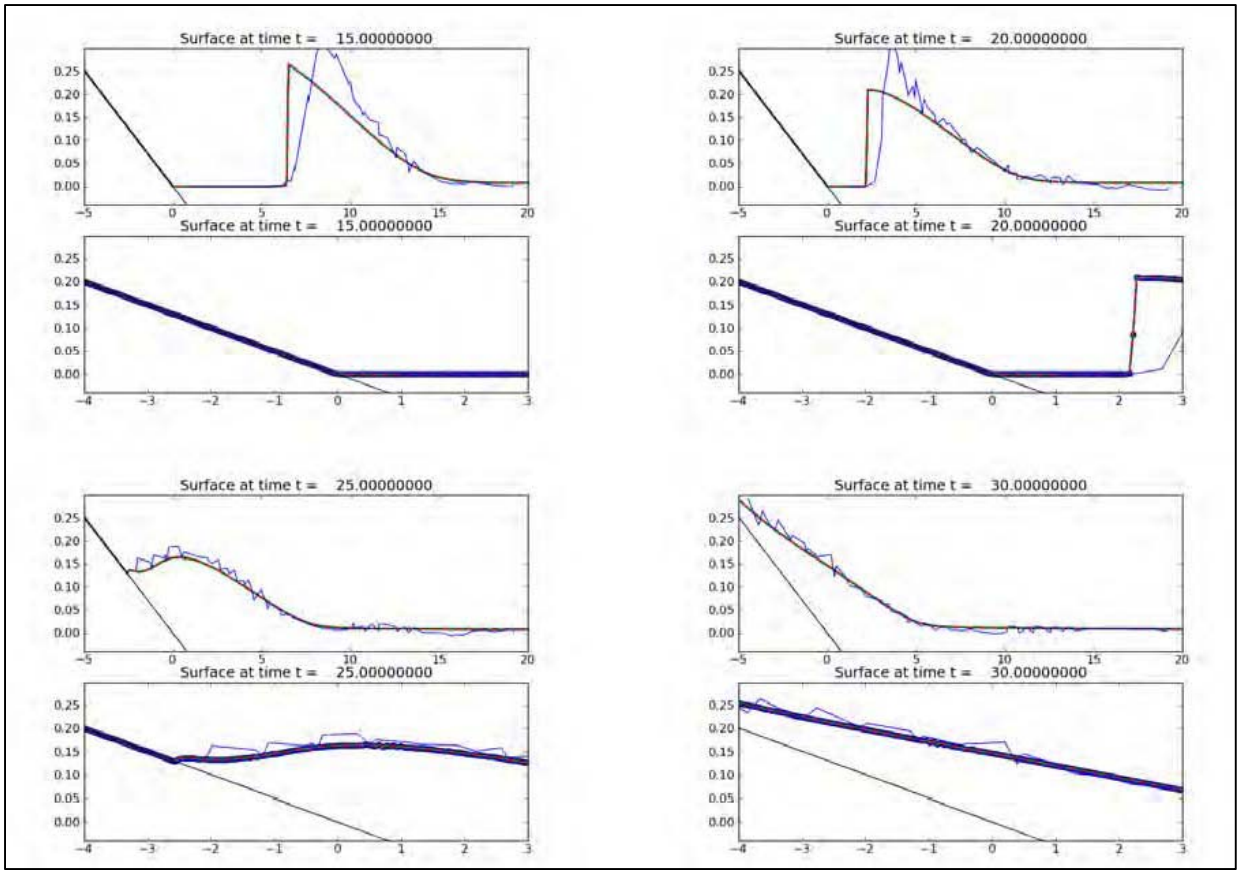

Figure 5-19: Runup computations and lab measurements for the high amplitude case. In the paired plots for each time value, the bottom frame provides a zoomed view of the inundation area for the incident wave presented in the top frame.

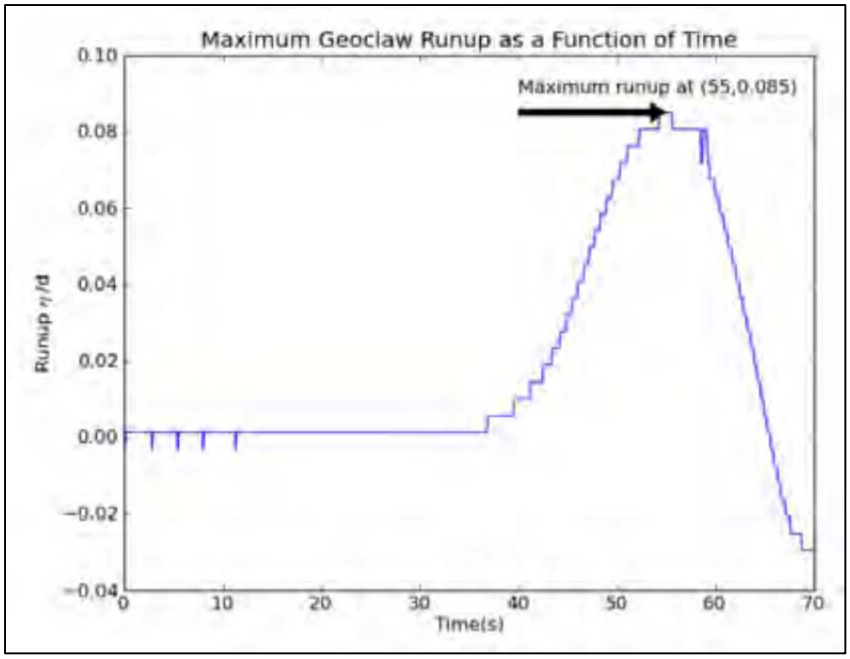

Figure 5-20: Maximum runup estimate of 0.085 cm for the low amplitude case, occurring at 55 seconds of the computation.

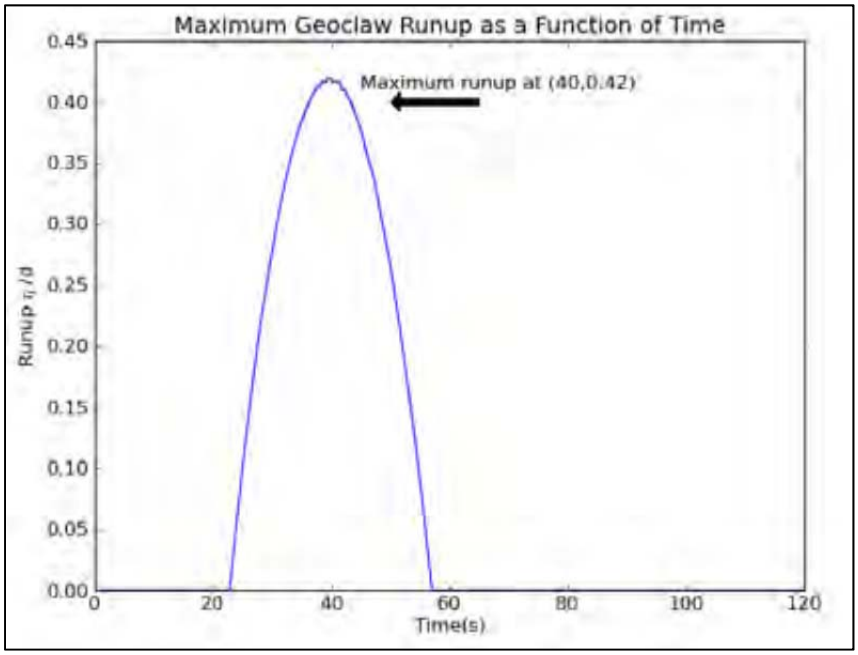

Figure 5-21: Maximum runup estimate of 0.42 cm for the high amplitude case, occurring at 40 seconds of the computation.

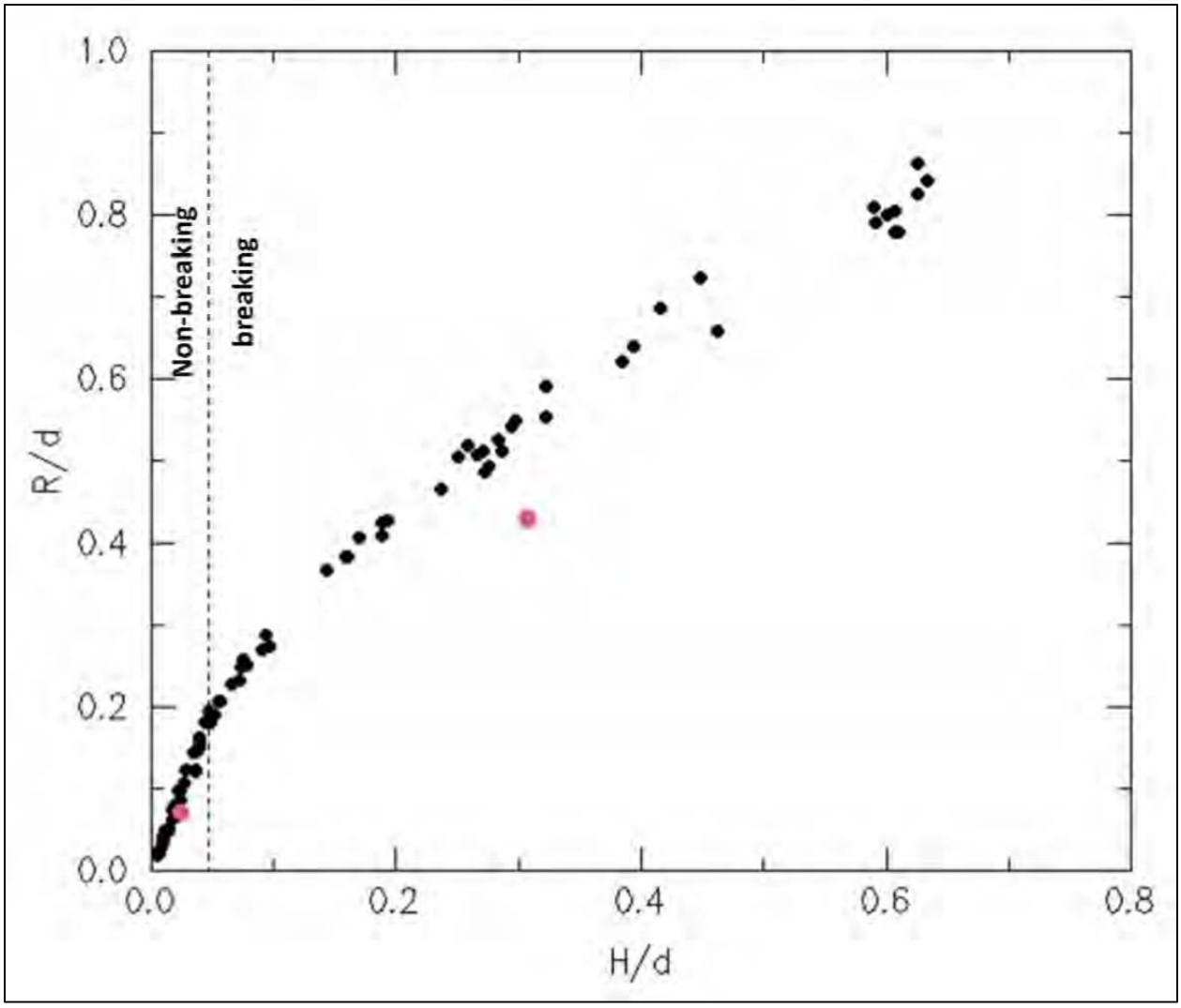

Figure 5-22: Scatter plot of nondimensional maximum runup, R/d, versus nondimensional incident wave height, H/d, resulting from a total of more than 40 experiments conducted by Y. Joseph Zhan and described at LeVeque (2011). Red dots indicate the numerical results.

5.3.5 BP5: Solitary wave on composite beach – laboratory

5.3.5.1 Problem specification

- PMEL-135, pp. 6 & 37-39.
- Problem description provided by Elena Tolkova at LeVeque (2011): BP05-ElenaT-Solitary_wave_on_composite_beach_laboratory/BP5_description.pdf
- Coastal Hydraulics Laboratory Problem Description (Briggs, n.d.).

This is the same problem as in BP2, but using the nonlinear shallow water equations and comparing to laboratory data rather than to the analytic solution of the linear equations.

5.3.5.2 What we did

- We solved the shallow water wave equation in Cartesian coordinates with $g = 9.81$ and no friction.
- To specify the incoming wave from the left boundary of our computational domain we used the first ten seconds of measurements taken at Gauge 4. After ten seconds the left boundary switched to be a non-reflecting boundary. This boundary is selected because the end of our computational domain is not the end of the physical wave tank. The implementation of these boundary conditions is described in Section 5.2.3.
- We solved on a 600 × 2 grid with no adaptive mesh refinement.

5.3.5.3 Gauge comparisons

The results for cases A, B, and C are shown in Figure 5-23, Figure 5-24, and Figure 5-25 respectively, where Gauge 11 is placed at the vertical wall.

5.3.5.4 Convergence Study

We performed a test to see how well Clawpack converged to the gauge measurements as we increased the number of grid cells in our computational domain. We found that as the number of grid cells was increased that the computed solution converged and had a shock in approximately the same location as in the gauge data. The results are shown in Figure 5-26.

5.3.5.5 Lessons learned

In this benchmark problem, we found that using the measured data from Gauge 4 as boundary conditions on a shorter domain, starting at this gauge, provided more accurate results than using the wavemaker position and a longer domain to model the entire tank. It appears that a similar assumption is made in the provided analytic solutions, as they match up nearly perfectly with the lab data for the first ten seconds.

Overall this benchmark problem is a good test for one-dimensional codes. Case C exhibits dispersion in the laboratory results not seen with the nonlinear shallow water equations.

The benchmark problem specifications could be improved by specifying the computational domain and the specific data source that should be used to model the incoming wave.

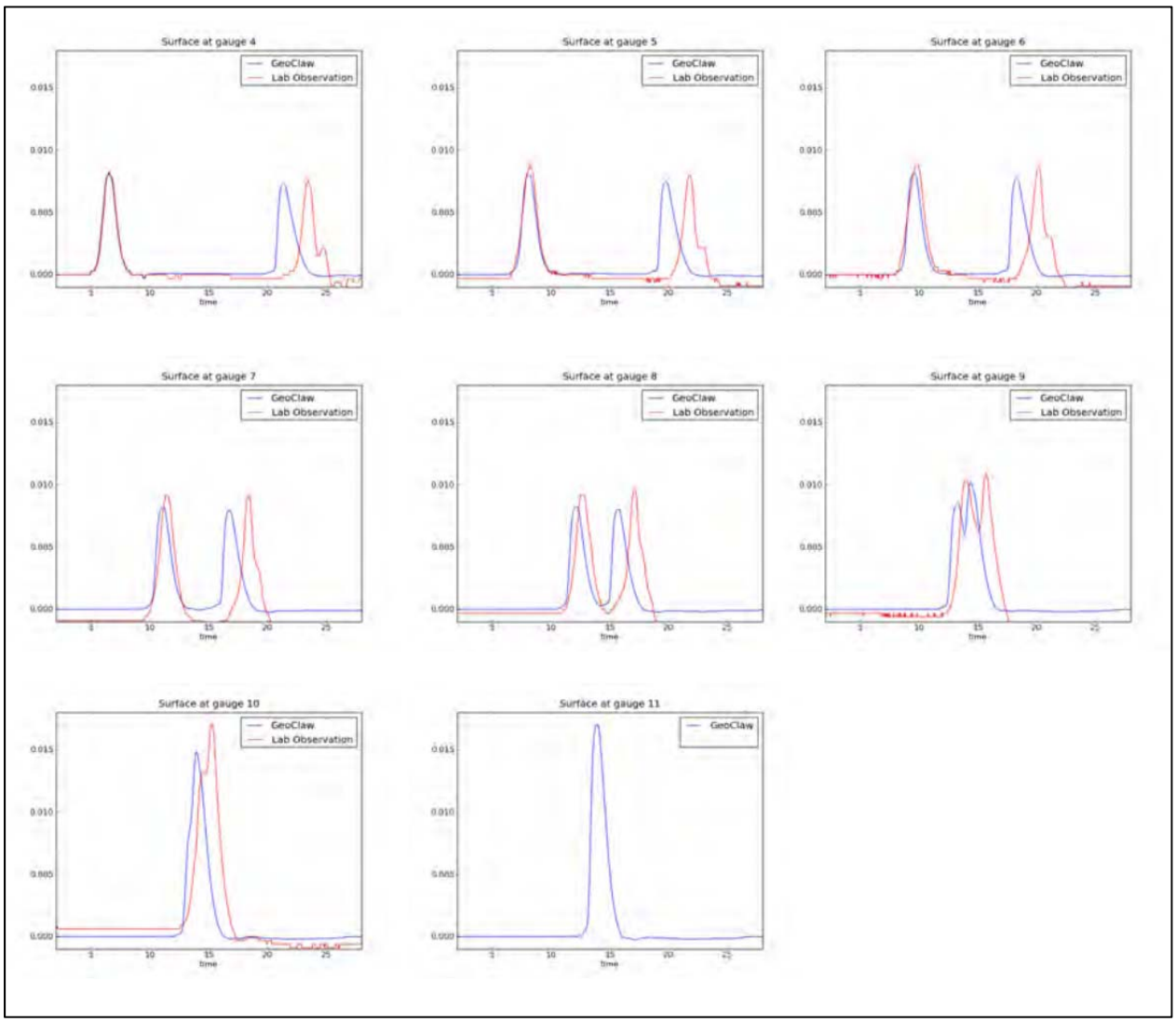

Figure 5-23: Case A

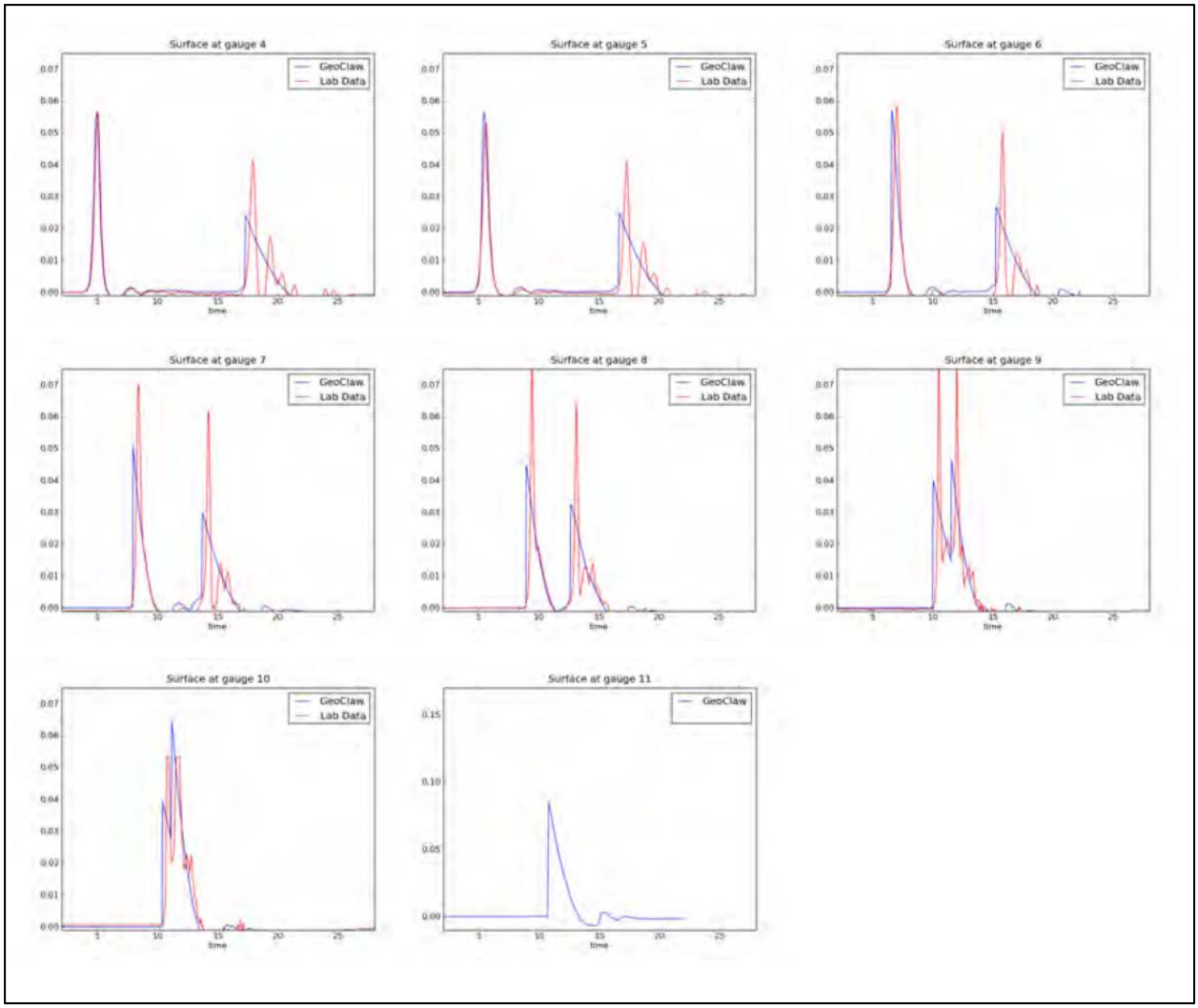

Figure 5-24: Case B

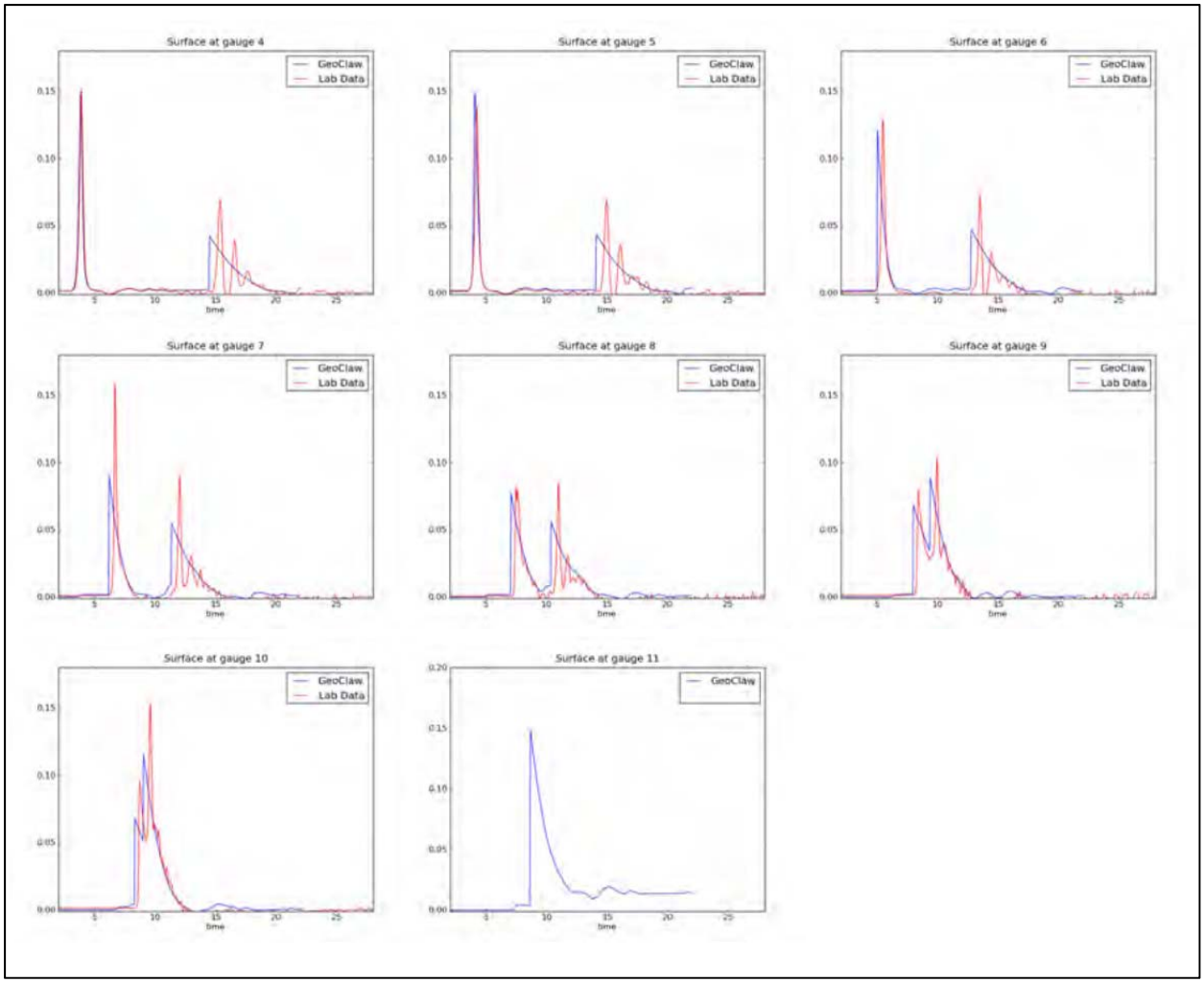

Figure 5-25: Case C

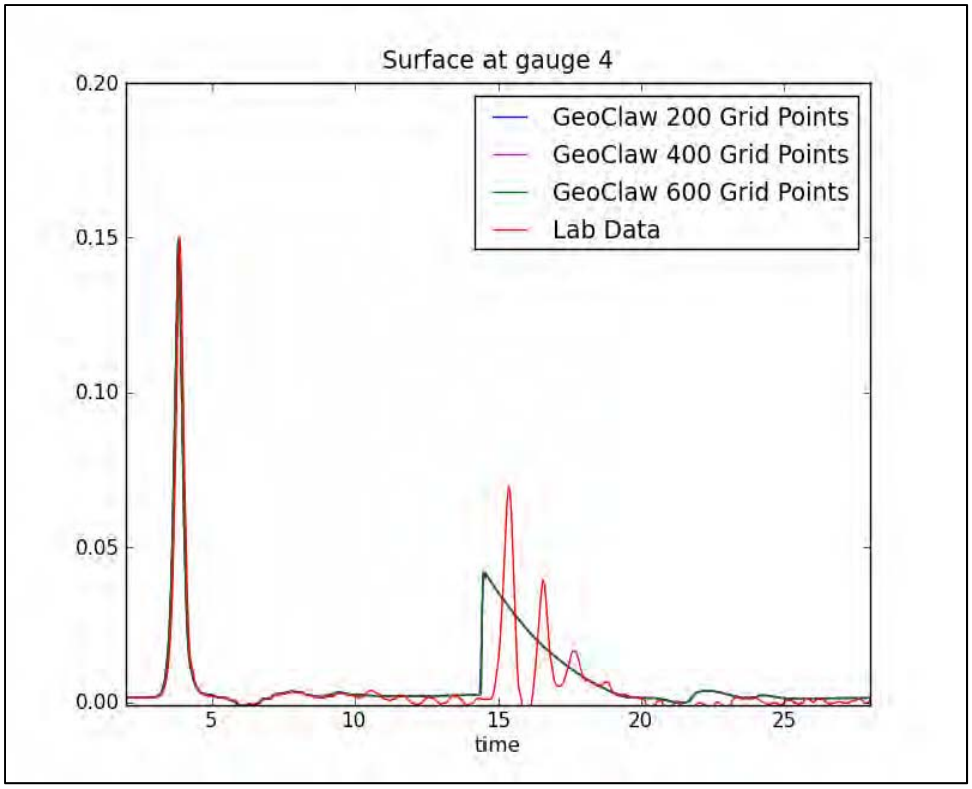

Figure 5-26: Convergence plot for Gauge 4 in Case C

5.3.6 BP6: Solitary wave on a conical island – laboratory

- The Corps of Engineers website is the primary documentation for this benchmark problem: http://chl.erdc.usace.army.mil/chl.aspx?p=s&a=Projects;35
- A problem description is also provided by Frank González at LeVeque (2011): BP06-FrankG-Solitary_wave_on_a_conical_island/Description.pdf
- Numerous other publications also describe this experiment, in varying detail: (Synolakis et al., 2007; Briggs et al., 1994; Liu et al., 1994; Briggs et al., 1995; Liu et al., 1995; Briggs et al., 1996; Fujima et al., 2000)

5.3.6.1 Description

The goal of this benchmark problem (BP) is to compare computed model results with laboratory measurements obtained during a physical modeling experiment conducted at the Coastal and Hydraulic Laboratory, Engineering Research and Development Center of the U.S. Army Corps of Engineers. The laboratory physical model was constructed as an idealized representation of Babi Island in the Flores Sea, Indonesia, to compare with Babi Island runup measured shortly after the 12 December 1992 Flores Island tsunami (Yeh et al., 1994).

5.3.6.2 Problems encountered

- Details of the laboratory setup and, therefore, of the computational domain could not be determined by the available documentation (above). The version of the domain used in this report is presented in Figure 5-27; this specification of the domain was developed after personal communication with Michael Briggs, U.S. Army Corps of Engineers, who

provided additional information on physical details of the laboratory experiment. Unfortunately, it is not certain that accurate specification of details of the laboratory setup have been resolved. In particular, the following items were not well documented and remain open to question: (a) the distance from the wavemaker face to the island center and (b) open gaps at each end of the wavemaker.

- Erroneous entries were found in data files ts2a.txt, ts2b.txt and ts2cnew1.txt. Several entries of the letter 'M' triggered read-in error messages; they were replaced by linear interpolation or extrapolation of neighboring values.
- Initial values for some laboratory data were non-zero, rather than the zero values expected for initial wave basin conditions corresponding to still water.

5.3.6.3 What we did

- Used $g = 9.81$ and no friction.
- Used the computational domain presented in Figure 5-27.
- Used open boundary conditions for the top, bottom and right walls, and for the gaps between the ends of the wavemaker and the top and bottom walls.
- Used inflow boundary conditions for the face of the wavemaker, as described in the Model Description section of this report.
- Simulated Cases A and C, each with three different grid sizes and resolution, to demonstrate convergence: 28 X 24 (100 cm), 56 X 47 (50 cm) and 223 X 185 (12.5 cm)
- Simulated optional Case B; the results are not presented here, but they were submitted for analysis and inclusion in the workshop summary report.
- An additional computational experiment was conducted to document the effect of varying two model parameters on the results – the Manning coefficient of friction (M) and the Dry Cell Depth (DCD) threshold. Several values of each parameter were used in this experiment.

5.3.6.4 Results

Requirements of this benchmark test were to:

- Demonstrate that two wave fronts split in front of the island and collide behind it.
- Demonstrate convergence of the solution as the computational grid is refined.
- Compare computed water level with laboratory data for Cases A and C at gauges 1, 2, 3, 4, 6, 9, 16, and 22 (files ts2a.txt, ts2cnew1.txt).
- Compare computed island runup with laboratory gauge data (files run2a.txt, run2c.txt)

The first benchmark requirement was satisfied, as seen in Figure 5-29 and Figure 5-30. Thus, for Cases A and C we see in frames t = 30 to t = 36 seconds that the initial wave splits into two wave fronts in front of the island, which then collide behind the island.

The second benchmark requirement was satisfied, as seen in Figure 5-31, Figure 5-32, and Figure 5-33. The agreement between Lab and GeoClaw time series is seen to improve as the computational grid resolution is decreased from 100 to 12.5 cm. The most obvious manifestation of this convergence is the improved value of the first wave amplitude.

The third benchmark requirement is satisfied by the comparisons presented in Figure 5-34 and Figure 5-33. Good agreement is seen overall and, in particular, between computed and measured time series for the first wave. The agreement for later wave details becomes progressively worse, as multiple reflections and refraction occur at the basin boundaries, the wavemaker face, and the island. Note that in some cases, the laboratory gauge data are characterized by non-zero initial values, which would be expected in the case of an initial condition corresponding to still water in the wave basin (see, e.g., gauge 2 for Cases A and C).

The final benchmark requirement is satisfied by the runup values presented in Figure 5-35 and Figure 5-36, in which good agreement is seen between the computed and measured runup on the conical island.

5.3.6.5 Sensitivity of runup to friction and 'Dry Cell Depth' parameters

Nine additional simulations of Case C were run on the 12.5 cm grid to test the sensitivity of computed runup values to variations in Manning's friction coefficient and the threshold depth for which a "Dry Cell" is identified by GeoClaw. The results are presented in Figure 5-37. We see that runup estimates can be significantly affected by changes in the value of each parameter. Because the friction term is a function of water depth, we also see that these effects vary spatially over the computational domain; for example, the frame (DCD, M) = (0.01, 0.0) provides the best fit for inundation values on the lower side of the conical island, but increasing the friction degrades this fit and improves the fit to runup measurements directly behind the conical island – see frames (DCD, M) = (0.01, 0.012) and (0.01, 0.025). Similar frictional effects are seen in the Okushiri Island field benchmark problem, in which runup computations with M = 0.0 and M = 0.25 are compared with field observations (see Figure 5-51).

5.3.6.6 Lessons learned

- Accurate specification of the computational domain is essential, and every effort should be made to acquire this information.
- Results demonstrate that the long wave equations are adequate to describe the major features of propagation, refraction, and runup observed in the laboratory experiment.
- Even with the unresolved details of the computational domain and lab data (i.e., non-zero initial values) the available data still provide a good benchmark test.
- Both the friction and the dry cell depth parameters have a significant, spatially variable, effect on runup computations.

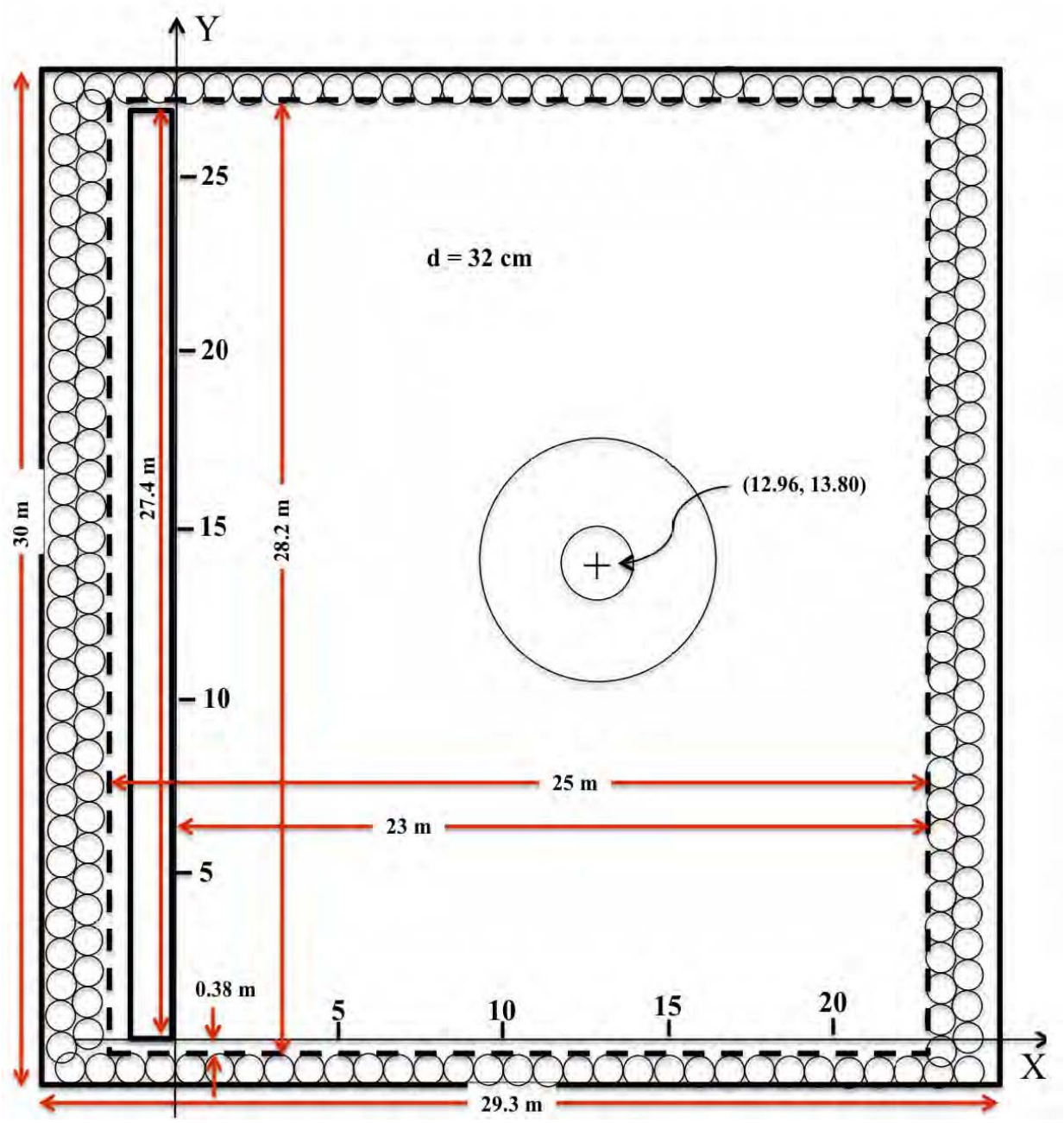

Figure 5-27: Basin geometry and coordinate system. Solid lines represent approximate basin and wavemaker vertical surfaces. Circles along walls and dashed lines represent rolls of wave absorbing material. Note the gaps of approximately 0.38 m between each end of the wavemaker and the adjacent wall. Gauge positions are given in Figure 5-28.

Gage ID	X, m	Y, m	Z, cm	Comment
1	A: 5.76 B: 6.82 C: 7.56	16.05	32.0	Incident gage
2		14.55	32.0	
3		13.05	32.0	
4		11.55	32.0	
6	9.36	13.80	31.7	270 deg transect
9	10.36	13.80	8.2	
16	12.96	11.22	7.9	0 deg transect
22	15.56	13.80	8.3	90 deg transect

Figure 5-28: Coordinates of laboratory gauges 1, 2, 3, 4, 6, 9, 16, and 22.

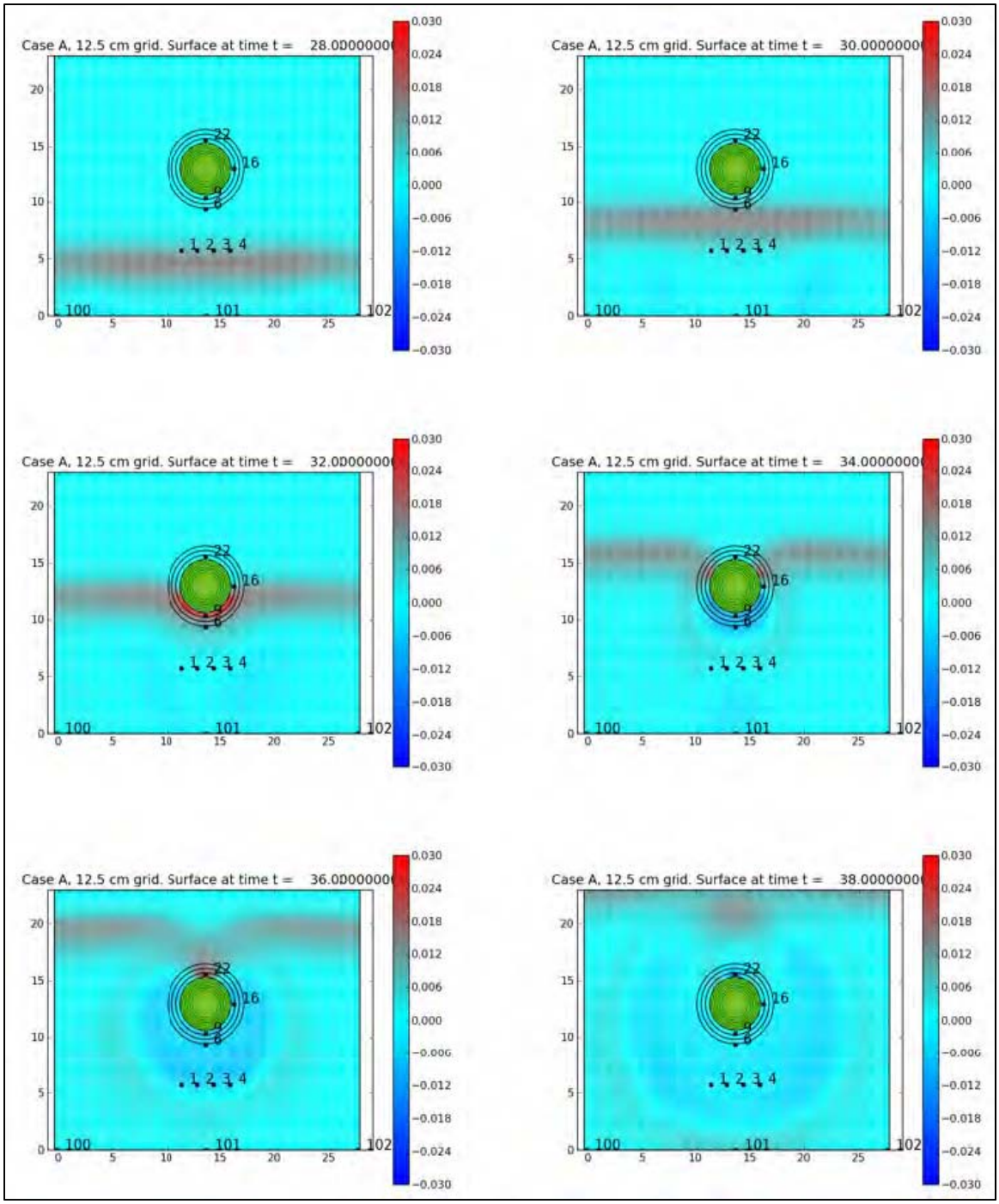

Figure 5-29: Animation snapshots of Case A for the 12.5 cm resolution computational grid.

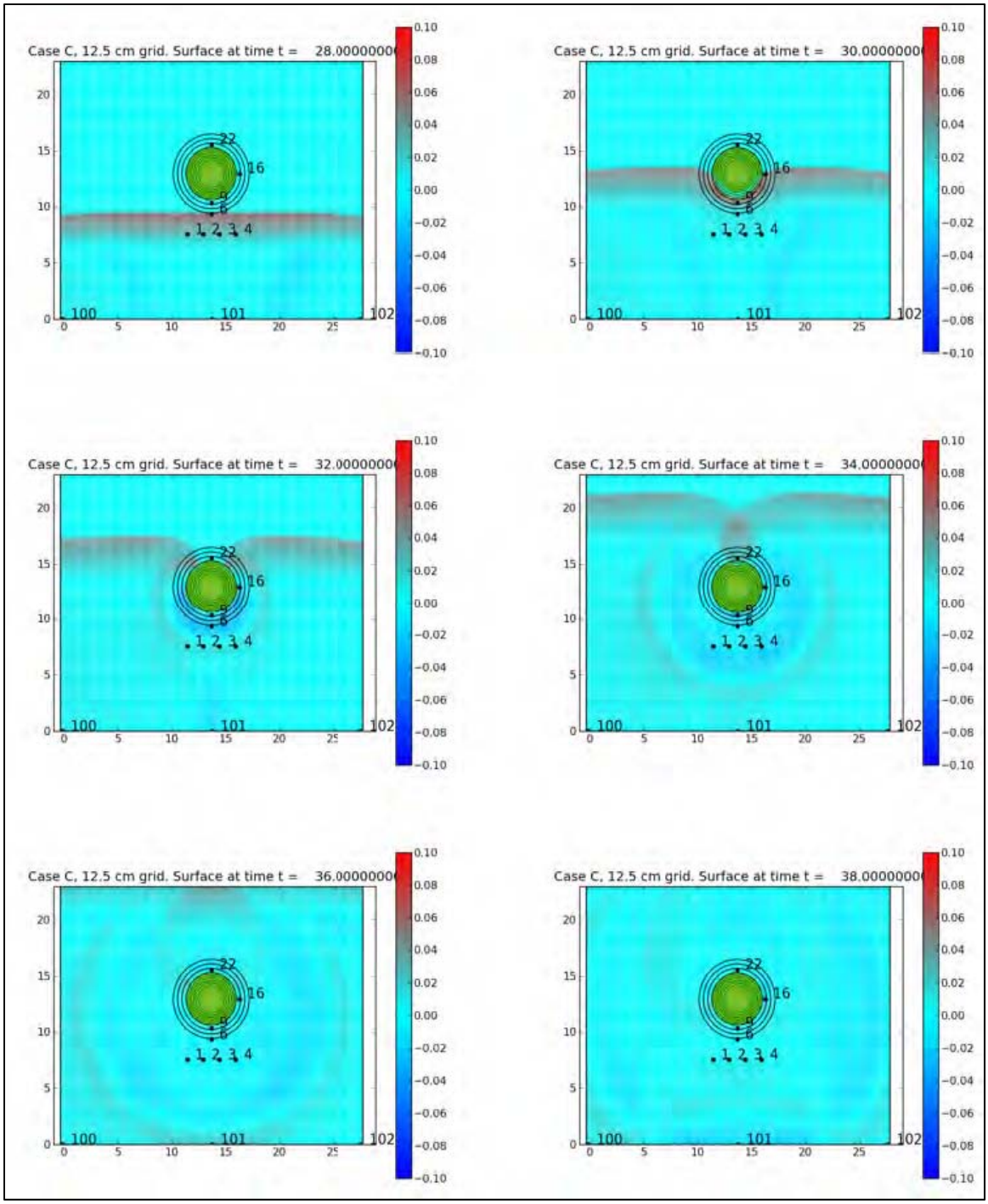

Figure 5-30: Animation snapshots of Case C for the 12.5 cm resolution computational grid.

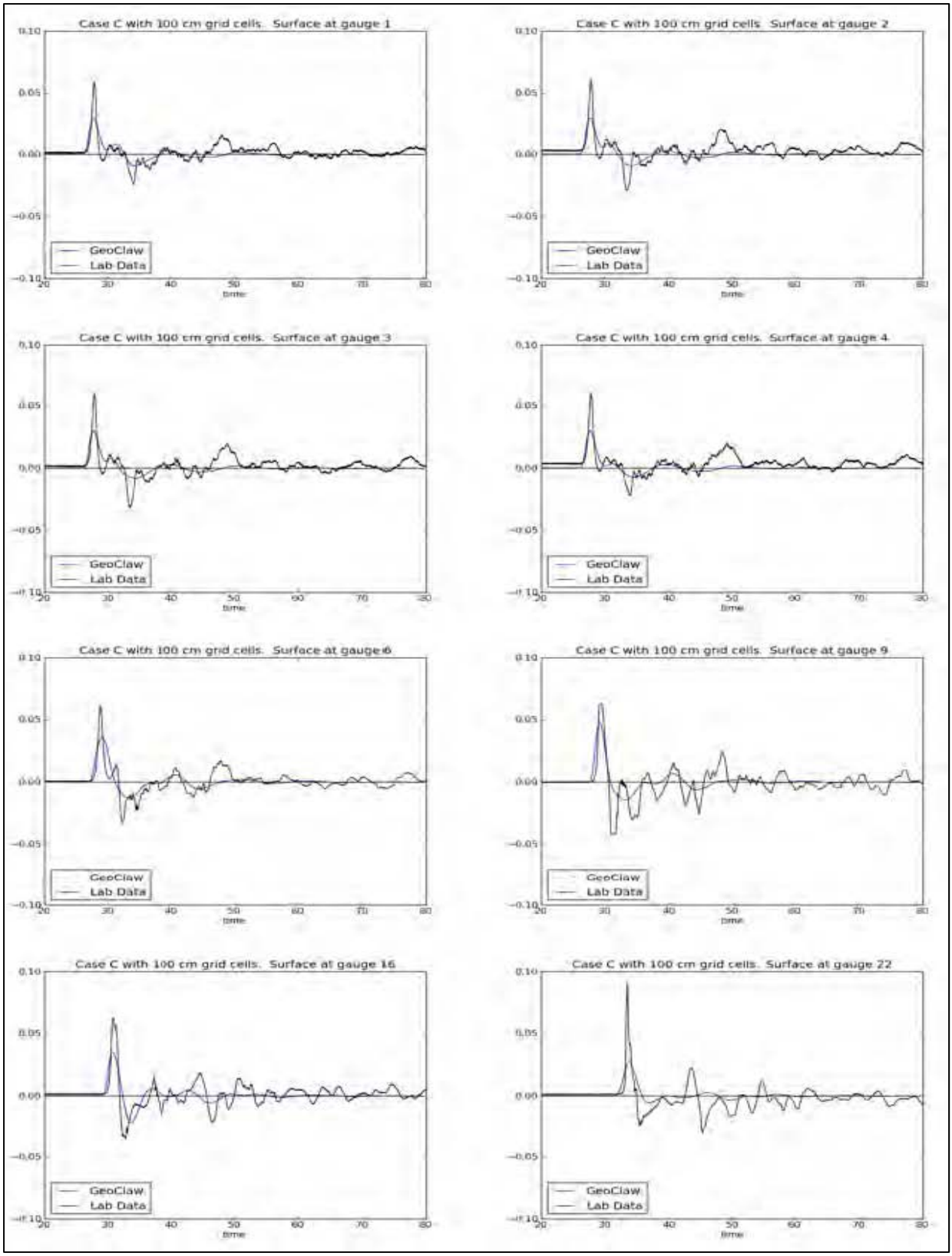

Figure 5-31: Comparison of laboratory gauge and GeoClaw time series for the Case C, 100 cm resolution grid.

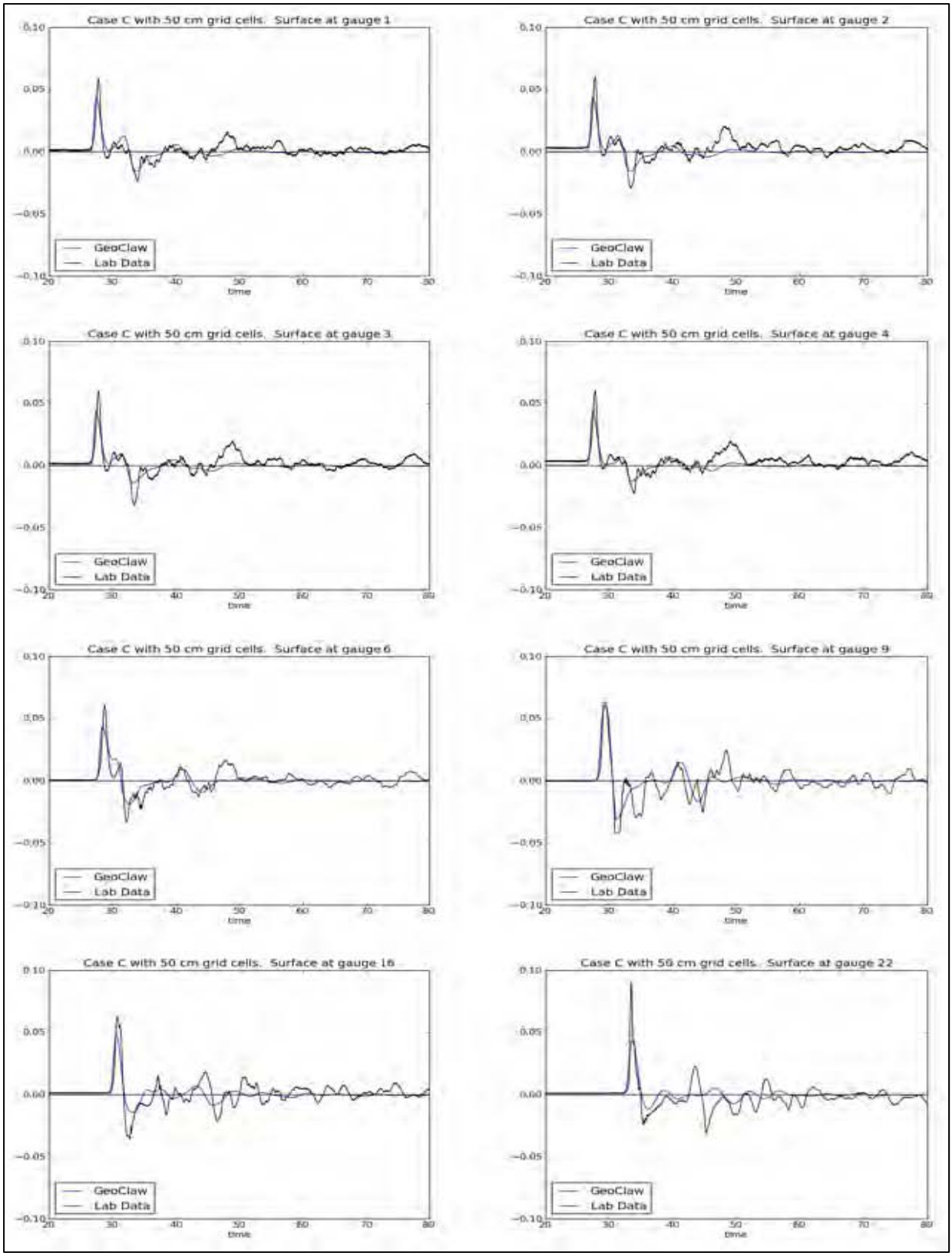

Figure 5-32: Comparison of laboratory gauge and GeoClaw time series for the Case C, 50 cm resolution computational grid.

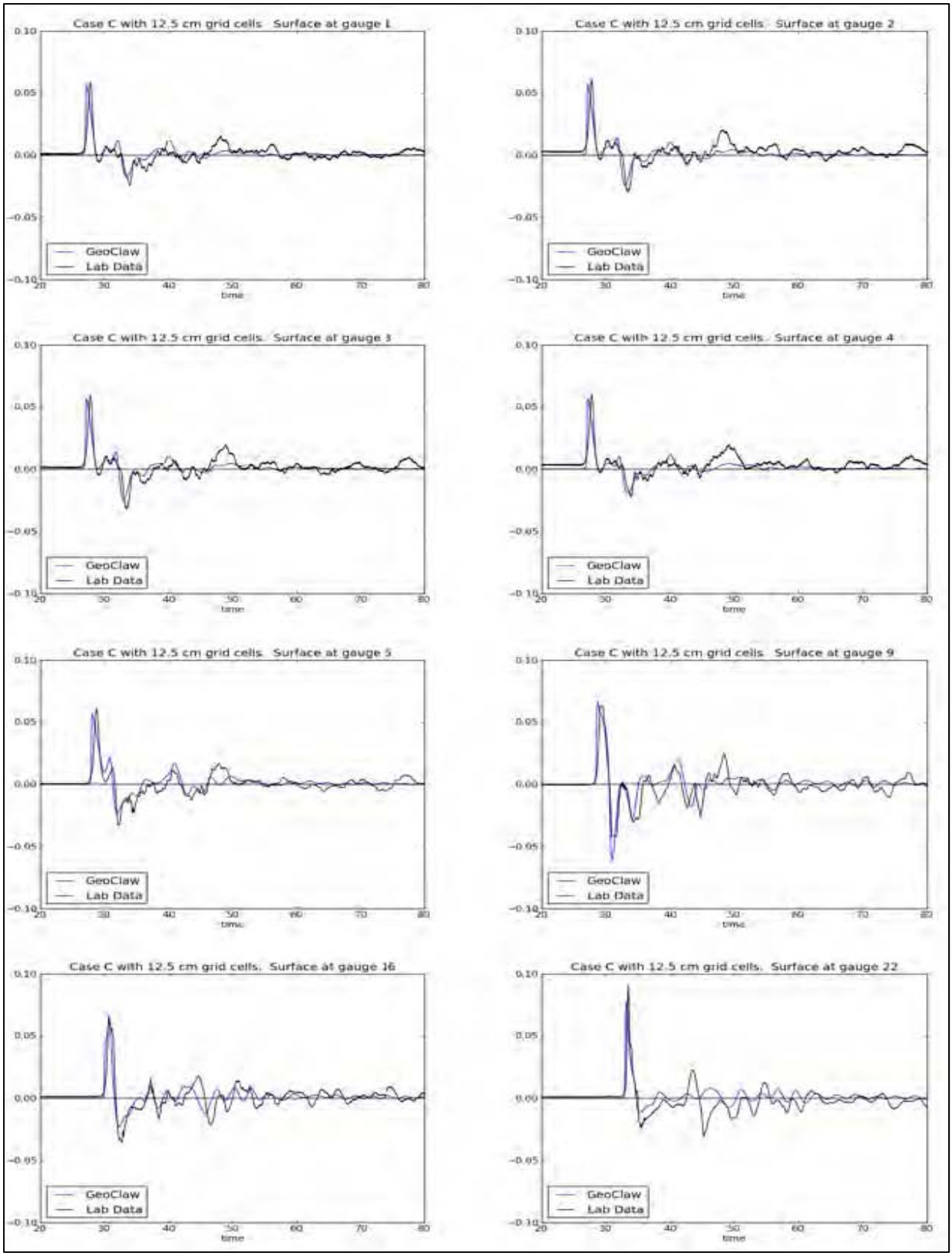

Figure 5-33: Comparison of laboratory gauge and GeoClaw time series for the Case C, 12.5 cm resolution computational grid.

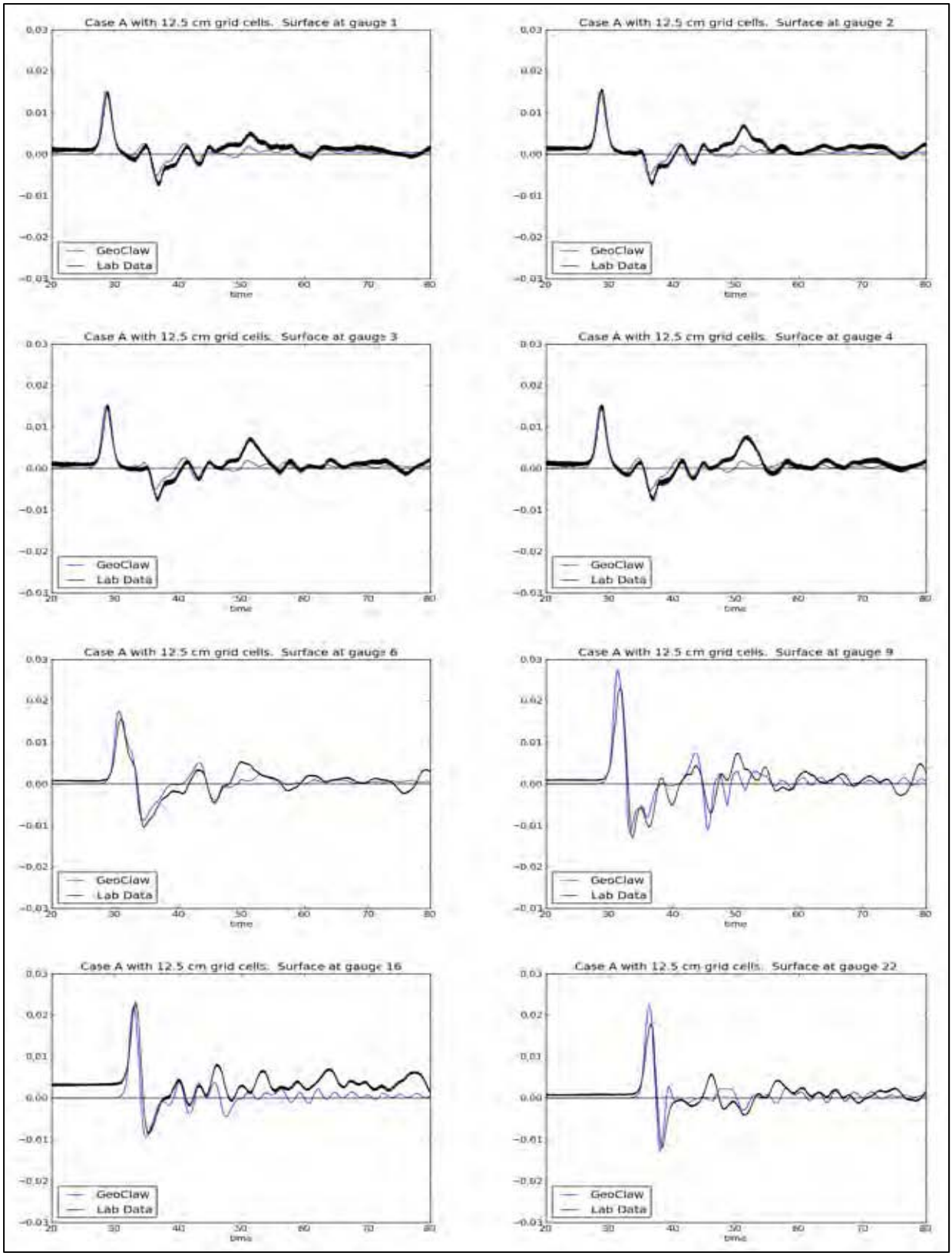

Figure 5-34: Comparison of laboratory gauge and GeoClaw time series for the Case A, 12.5 cm resolution computational grid.

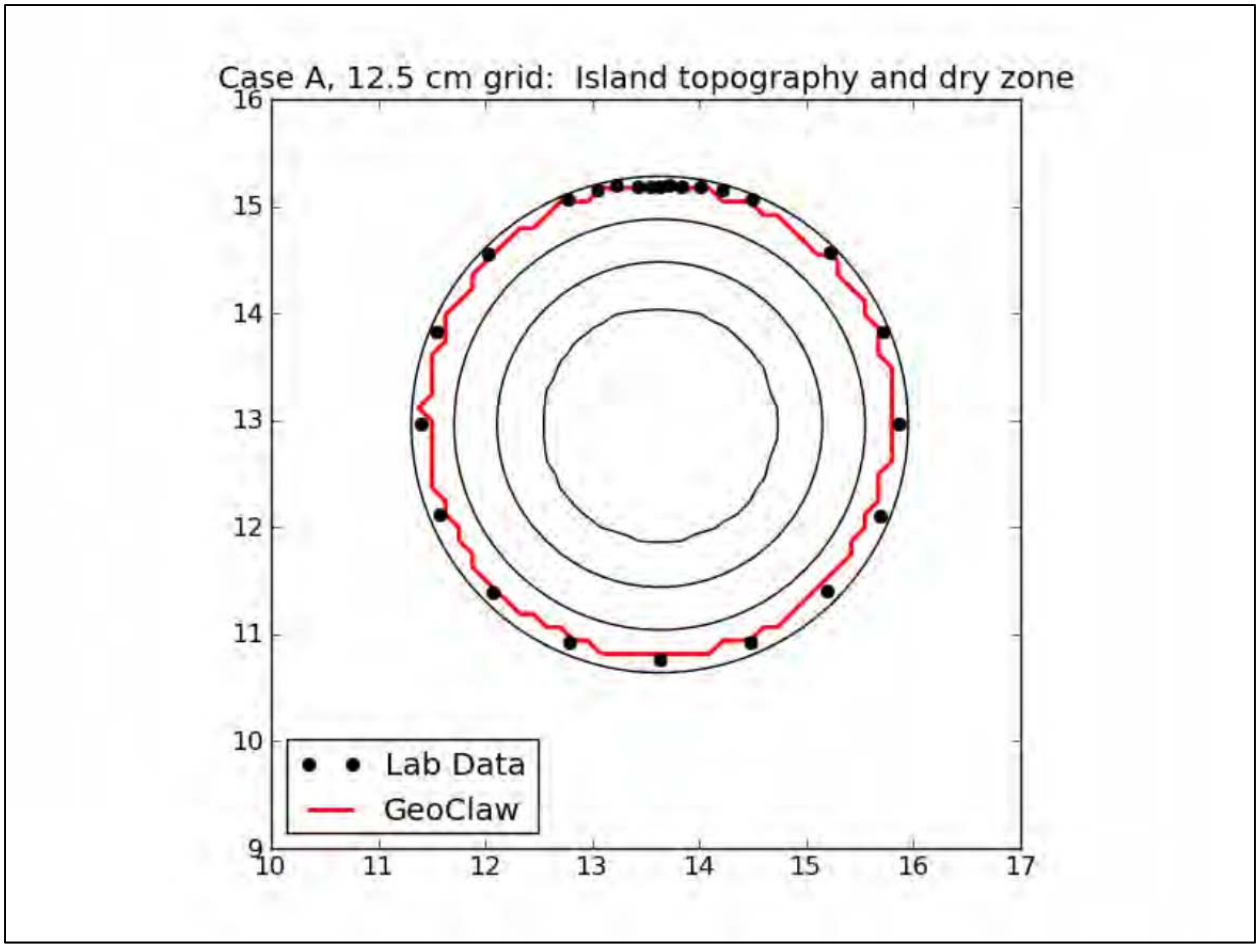

Figure 5-35: Island runup for Case A, using a 12.5 cm resolution computational grid.

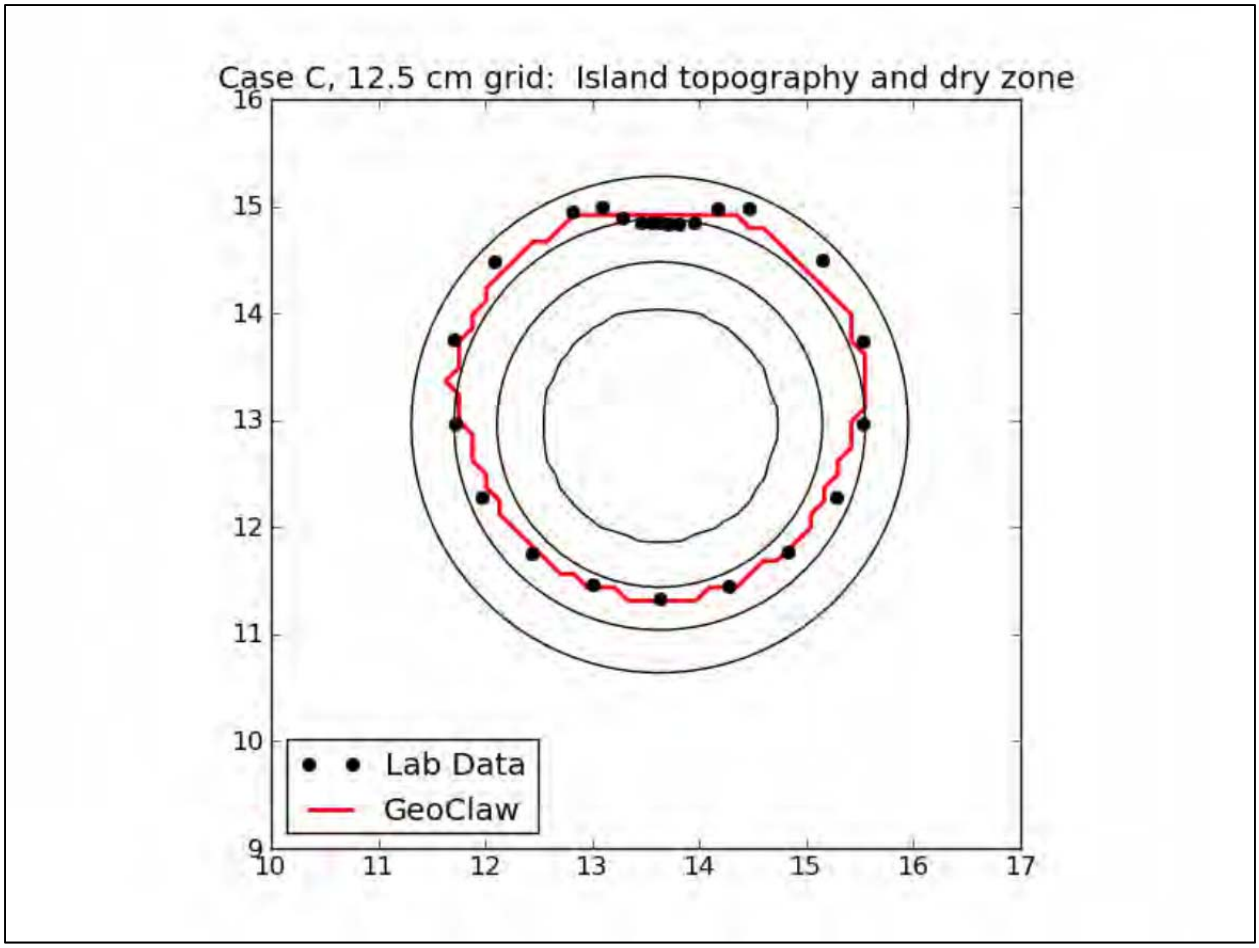

Figure 5-36: Island runup for Case C, using a 12.5 cm resolution computational grid.

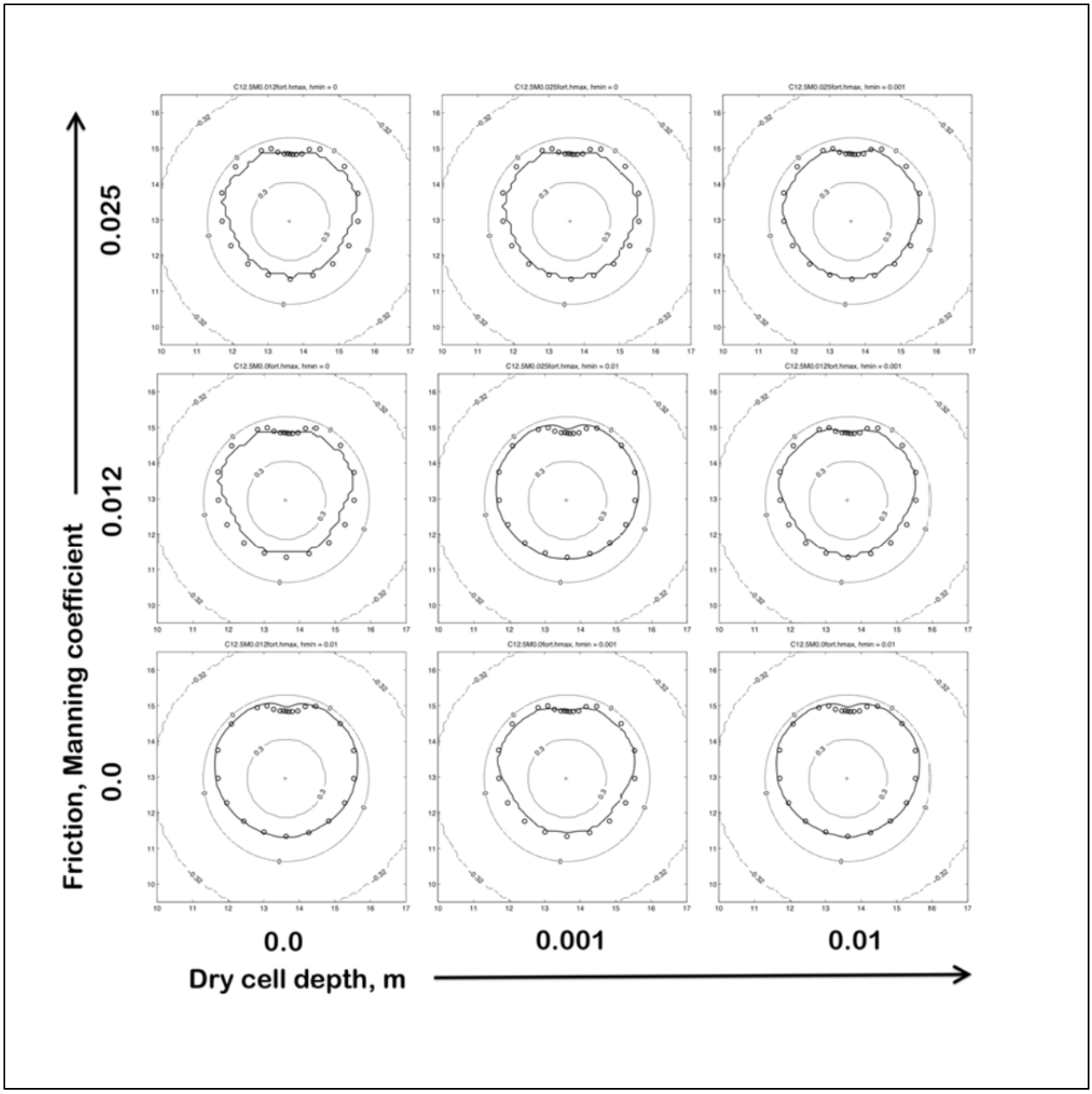

Figure 5-37: Island runup for Case C on a 12.5 cm grid, for differing values of Manning's friction coefficient, M, and the 'Dry Cell Depth', DCD, threshold.

5.3.7 BP7: Monai valley beach – laboratory

5.3.7.1 Problem specification

- PMEL-135, pp. 6 & 45-46.
- Problem description provided by Dmitry Nicolsky, at LeVeque (2011): BP07-DmitryN-Monai_valley_beach/description.pdf
- The original experiment is fully described by Matsuyama and Tanaka (2001).

5.3.7.2 What we did

- We solved the nonlinear shallow water equations in Cartesian coordinates with $g = 9.81$ and no friction.
- We used the given initial wave to specify a boundary condition at the left boundary up to time 20. This was done by filling ghost cells each time step at the left edge of the computational domain with depth values interpolated from the given time trace at $x = 0$. Momentum values were determined as described in Section 5.2.3.3.
- After time 20, the boundary condition procedure switched to non-reflecting boundary conditions (see Section 5.2.3.1) at the left boundary, so reflected waves exit. (Note that the wave tank was much longer than the specified computational domain.)
- We solved on 423 × 243 grid (same as bathymetry), with no adaptive mesh refinement. Solid wall boundary conditions were used at the top and bottom.
- We also solved on 211 × 121 grid, coarser by roughly a factor of 2, for comparison as a test of convergence.

5.3.7.3 Gauge comparisons

Figure 5-38 shows a comparison of the GeoClaw results with the laboratory values at the three gauges requested, with both grid resolutions. The two resolutions give very comparable results, indicating that the solution presented is close to a converged solution of the shallow water equations. The results are, in general, a good match to the laboratory measurements.

5.3.7.4 Frame comparisons

See Figure 5-39 and Figure 5-40 for comparisons of the Frames 10, 25, 40, 55, and 70 from the overhead movie with GeoClaw results at roughly corresponding times. These results are from the 423 × 243 grid (same as given bathymetry).

The movie had a rate of 30 fps, so the frames are 0.5 seconds apart. However, it is not clear what the starting time was for Frame 1 relative to the simulation time. In the Benchmark Description (LeVeque, 2011), it is stated that "frame 10 approximately occurs at 15.3 seconds," but then later "it is recommend that each modeler find times of the snapshots that best fit the data." We found reasonably good agreement starting at 15.0 seconds for Frame 1 and then taking 0.5 second increments, as shown in Figure 5-39 and Figure 5-40.

The yellow dashed lines on the frames from the movie show the approximate shoreline, and were provided as part of the benchmark specification (LeVeque, 2011). The actual shoreline location is, of course, somewhat ambiguous in the movie, and also in the computation. The figures of the Geo-Claw computation show the shoreline two different ways:

- The cells colored blue are finite volume cells where the fluid depth is greater than 0.0001 m. Those colored green have less fluid or are dry.
- The black dashed line is a contour line where depth = 0.002 m, which agrees better with the movie frames and might be a depth that can actually be detected in the movie frames.

5.3.7.5 Runup in the valley

The file OBS_RUNUP.txt from the benchmark specification contains the runup at 3 locations as observed in 6 runs of the same wavetank experiment. The relevant location for runup

in the valley is the first point at $x = 5.1575$, $y = 1.88$ m. The six values given are 0.0875, 0.09, 0.08, 0.09, 0.1, 0.09, with an average value of approximately 0.09.

In the computation, the maximum runup was observed at time $t \approx 16.5$. This frame is shown in Figure 5-41 with a white dot at the location $x = 5.1575, y = 1.88$ and several contour levels marked. The contour lines are at levels 0.01 m apart. The maximum runup appears to be around 0.08 to 0.10 m depending on what water depth is used to judge.

5.3.7.6 Lessons learned

- This problem has data that are fairly well specified, and has wave tank geometry that scales up to a reasonable physical tsunami problem (because it was designed by scaling down a physical problem).
- Solutions to the shallow water equations fit the data quite well, as found both in our experiments and by other modelers. This gives a reassuring test of the validity of shallow water equations for real tsunamis.
- This benchmark problem appears to be a good test for tsunami models. It has been widely used and many models have been shown to give results that agree quite well with the laboratory measurements.
- The laboratory test also appears to agree very well with the actual tsunami it was designed to model. Compare Figure 5-41 to Figure 5-53.
- The benchmark problem specification could be improved by specifying the computational grids that are to be used. We show results for a grid that matches the resolution of the bathymetry provided and a second computation at half the resolution, but this should be specified as part of the problem.
- The input data only go out to 20 seconds. The first waves are modeled well, but later waves in the laboratory data (not shown here) are not seen in the computation. If a longer time history were provided for the input data, it might be possible to match later waves better. Note that the computational domain is only part of the wave tank, which was 205 m long (Matsuyama and Tanaka, 2001). Presumably it is impossible to obtain more data at this point.

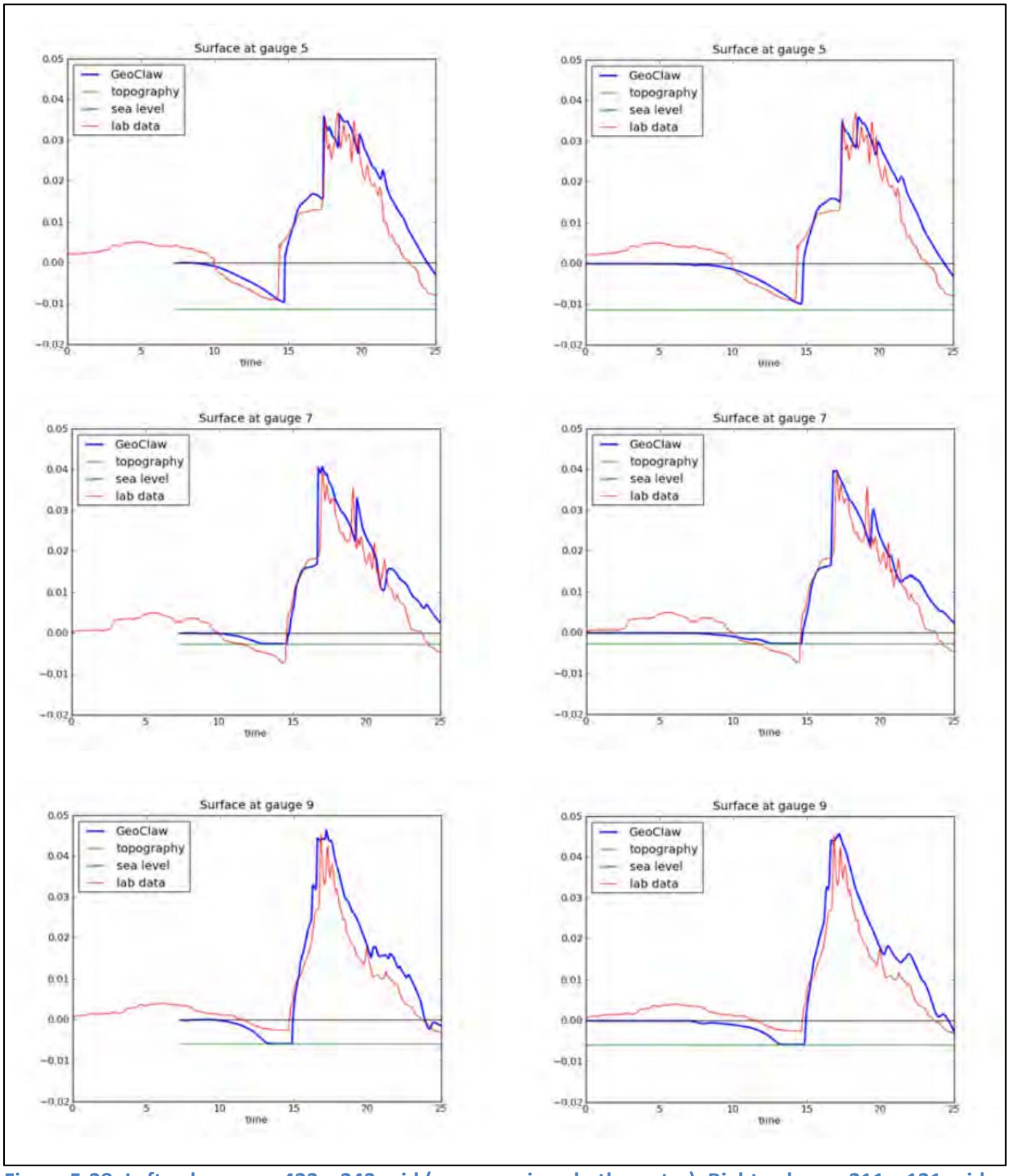

Figure 5-38: Left column: on 423 x 243 grid (same as given bathymetry). Right column: 211 x 121 grid.

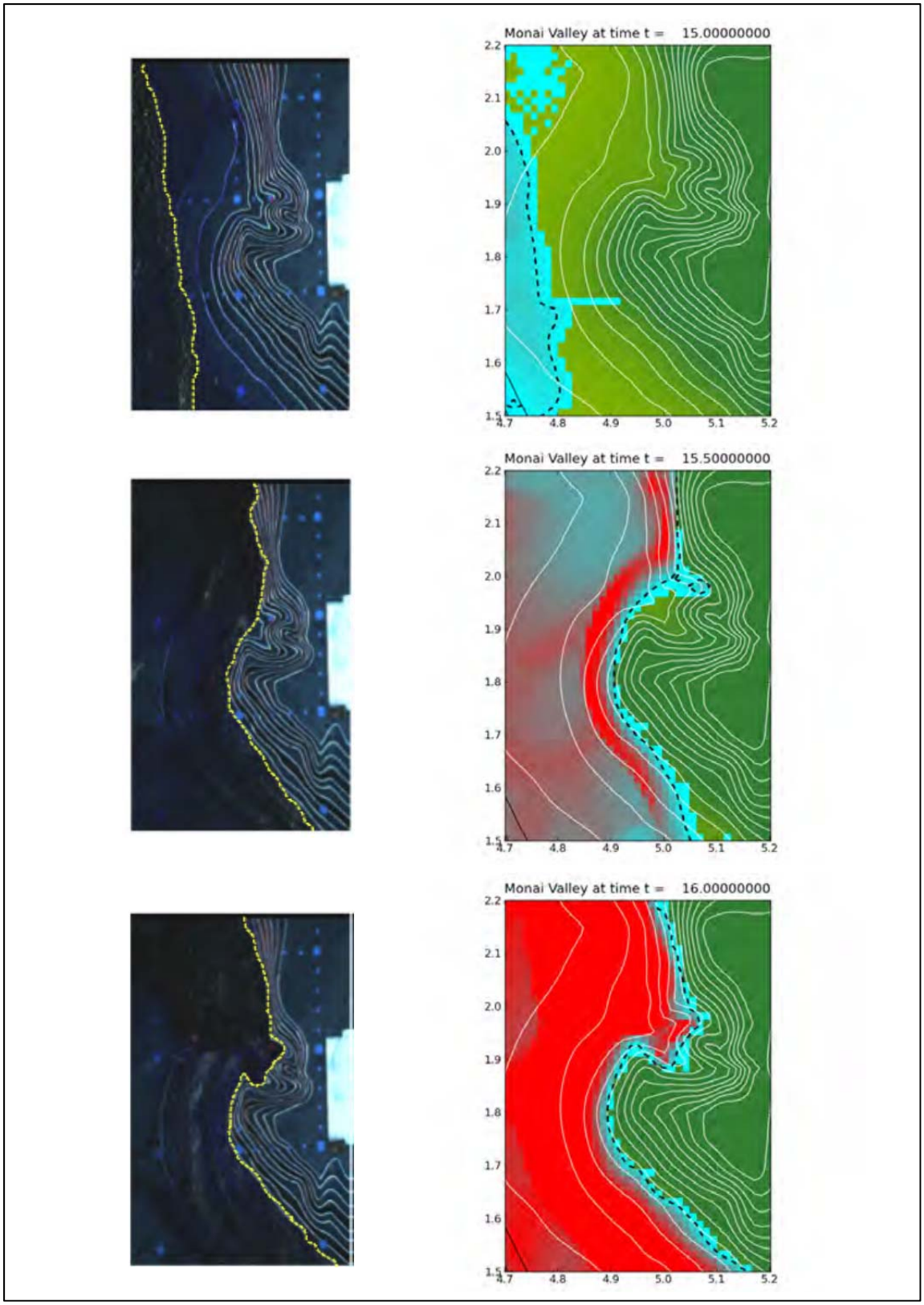

Figure 5-39: Left column: Frames 10, 25, and 40 from the movie. Right column: Zoomed view of computation.

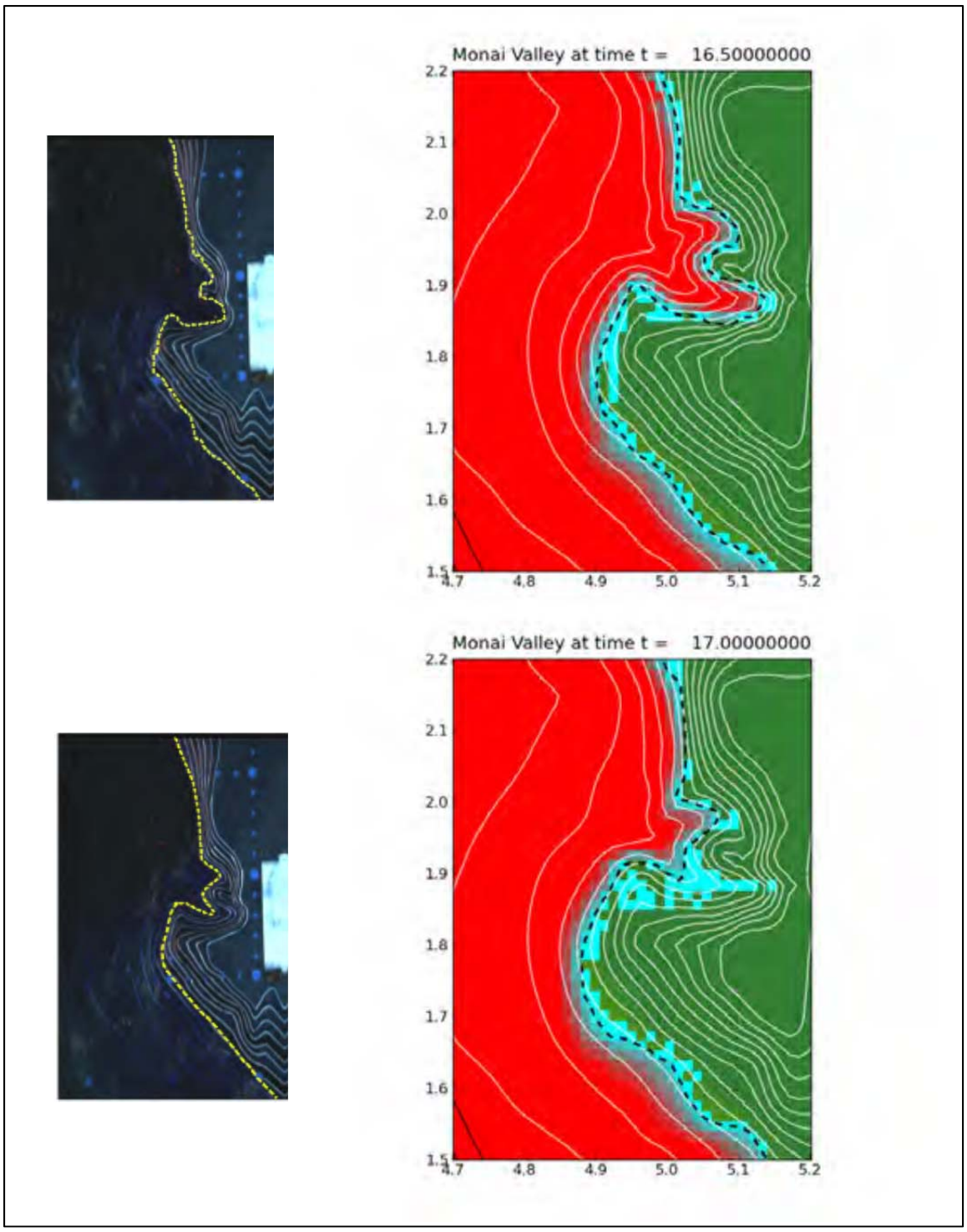

Figure 5-40: Left column: Frames 55 and 70 from the movie. Right column: Zoomed view of computation.

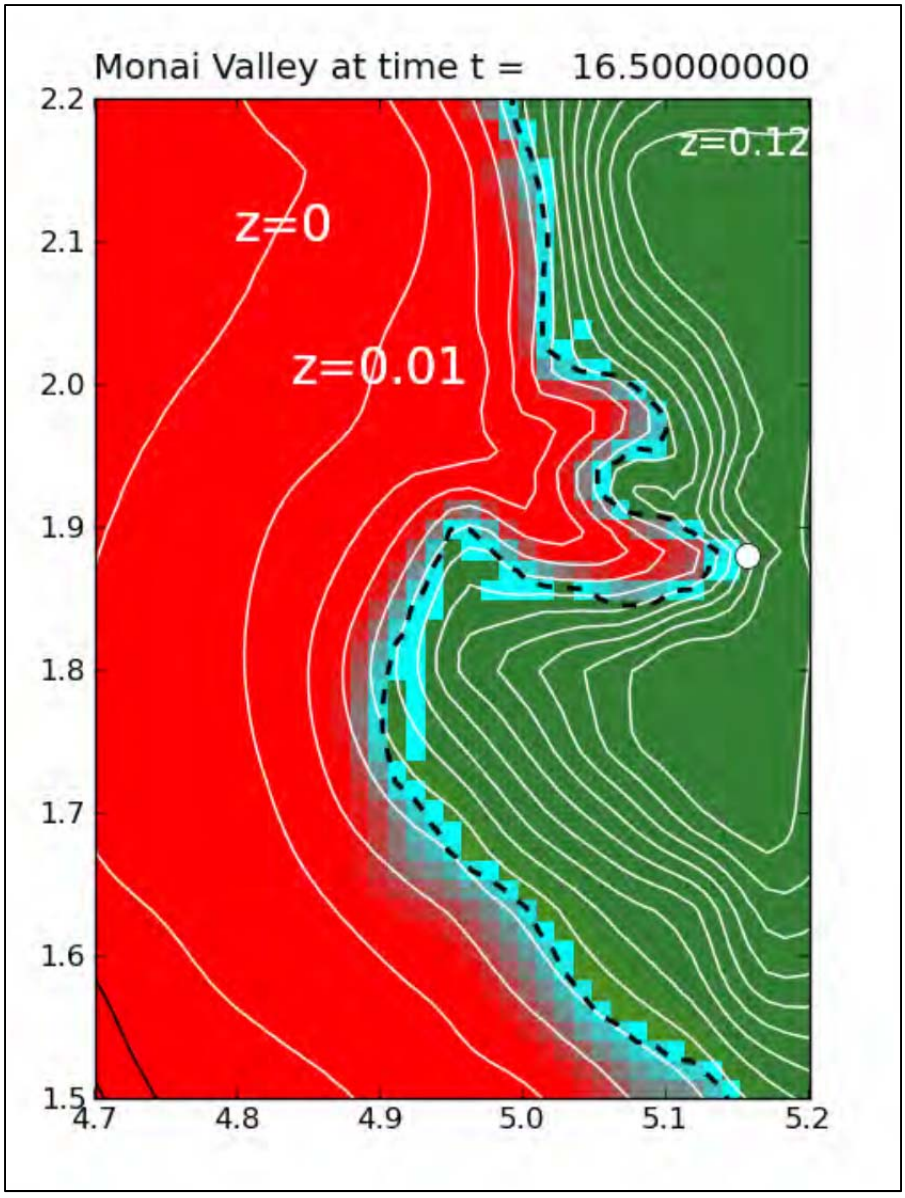

Figure 5-41: Maximum runup relative to observed location (white dot).

5.3.8 BP8a: Old 3-D landslide – laboratory

There are plans to replace this benchmark problem with a new one. This has not yet happened. This old benchmark problem consists of a wedge sliding on a plane beach. See Figure 5-42.

5.3.8.1 Problem specification

- PMEL-135, pp. 7 & 47-48 (Synolakis et al., 2007).
- The original experiment is fully described on NOAA's benchmarking website which can be found at http://nctr.pmel.noaa.gov/benchmark/Laboratory/

5.3.8.2 What we did

- We solved the nonlinear shallow water equations in Cartesian coordinates with $g = 9.81$ and no friction.
- We used the given laboratory data and problem setup to create our initial topography and bathymetry. While there were data provided up to time 20 s, we only conducted simulations up to time 10 s, as was done on NOAA's benchmarking website. We specified the movement of the wedge by using the time histories of the block motion provided for the problem. In order to implement this, we adjusted the bathymetry every time step to capture the wedge sliding down the linear beach. The slope of this linear beach was 12. Due to the symmetry of the problem, we simplified the problem to half of the domain of the tank, specifying an outflow or non-reflecting boundary condition at the right boundary so reflected waves exit. We also specified a solid wall boundary condition at all other boundaries. (Note that the wave tank was much longer than the specified computational domain.) We used zero-order extrapolation, which generally gives a very good approximation to non-reflecting boundary conditions as described in Section 5.2.3.1. Solid wall boundary conditions are implemented as described in Section 5.2.3.2. See Section 5.2.3 for more information on how these boundary conditions were specified.
- The moving bathymetry is handled by recomputing $B_{ij}^n = B(x_i, y_j, t_n)$ in each time step, at the center of each finite volume grid cell, based on the specified bathymetry. This is the standard approach for handling moving bathymetry in GeoClaw: the value B_{ij}^n is adjusted but the fluid depth h_{ij}^n remains the same, so that the water column is simply displaced vertically in any cell where the bathymetry changes. For bathymetry that is smoothly varying in space and time this is considered a reasonable approach (see Section 5.3.3, for example). Note, however, that no momentum is directly imparted to the water by the moving bathymetry.

  For this problem, the vertical face of the wedge makes this approach inadequate. The discontinuity in the moving bathymetry means that in each time step the bathymetry near the face will gain an increment of 0.455 m, lifting the water in this cell by this amount. This is not at all physical. Instead, the moving face should impart horizontal momentum to the water.

  Given this inaccuracy and the full three-dimensional nature of the physical flow, we do not expect to obtain very good comparisons computationally.
- We solved on a 35 × 10 grid with 3 levels of adaptive mesh refinement. We refined in the x-and y-directions by a factor of 6 from levels 1 to 2 and levels 2 to 3. We refined in time by a factor of 3. We specified level 3 refinement on a rectangle with x values of $[-0.4, 2]$ and y values of $[0, 1]$.
- We compared the simulated gauge data with the laboratory gauge data to determine GeoClaw's accuracy on this problem.

5.3.8.3 Gauge comparisons

Figure 5-43 shows a comparison of the GeoClaw results with the laboratory values at the two wave gauges and two runup gauges requested for case 1. The gauge data for gauge 1 is initially very "noisy" but the overall behavior seems to be captured well. We suspect that because gauge 1 was in the wedge's path of travel and because the wedge was specified as part

of our bathymetry, this created strong oscillations in our wave formations and an overshoot relative to the lab results.

Figure 5-44 shows a comparison of the GeoClaw results with the laboratory values at the two wave gauges and two runup gauges requested for case 2. As for case 1, the gauge data for gauge 1 is initially very “noisy" but the overall behavior seems to be roughly consistent with the lab results.

5.3.8.4 Lessons learned

- It is not clear that the shallow water equations are a good model for this problem. The flow should be fully three-dimensional around this sliding wedge and it is not clear that any depth-averaged model will do well.
- At some distance away from the shore, the depth will be greater than wave length and the shallow water equations will no longer be valid.
- The vertical face causes numerical difficulties.
- Overall, GeoClaw seems to model the surface elevations with respect to still water level well for both cases. However, gauge 1 seems to have issues from shortly after the start of the simulation to about 2 seconds. As mentioned earlier, it seems that this phenomenon is more of a result of how the bathymetry is specified than GeoClaw’s ability to model this landslide. To smooth the data, one could try interpolating the data so that the moving bathymetry is smooth instead of piecewise. This should greatly reduce the heavy oscillations. Another approach would be to add a slope to the leading face of the wedge. This would ensure a more gradual drop in bathymetry as the wedge propagates across the linear beach.
- This benchmark problem does not appear to be a good test for tsunami models. The dimensions do not seem to be reasonable relative to true submarine landslide problems. The vertical face does not seem realistic and causes numerical difficulties.

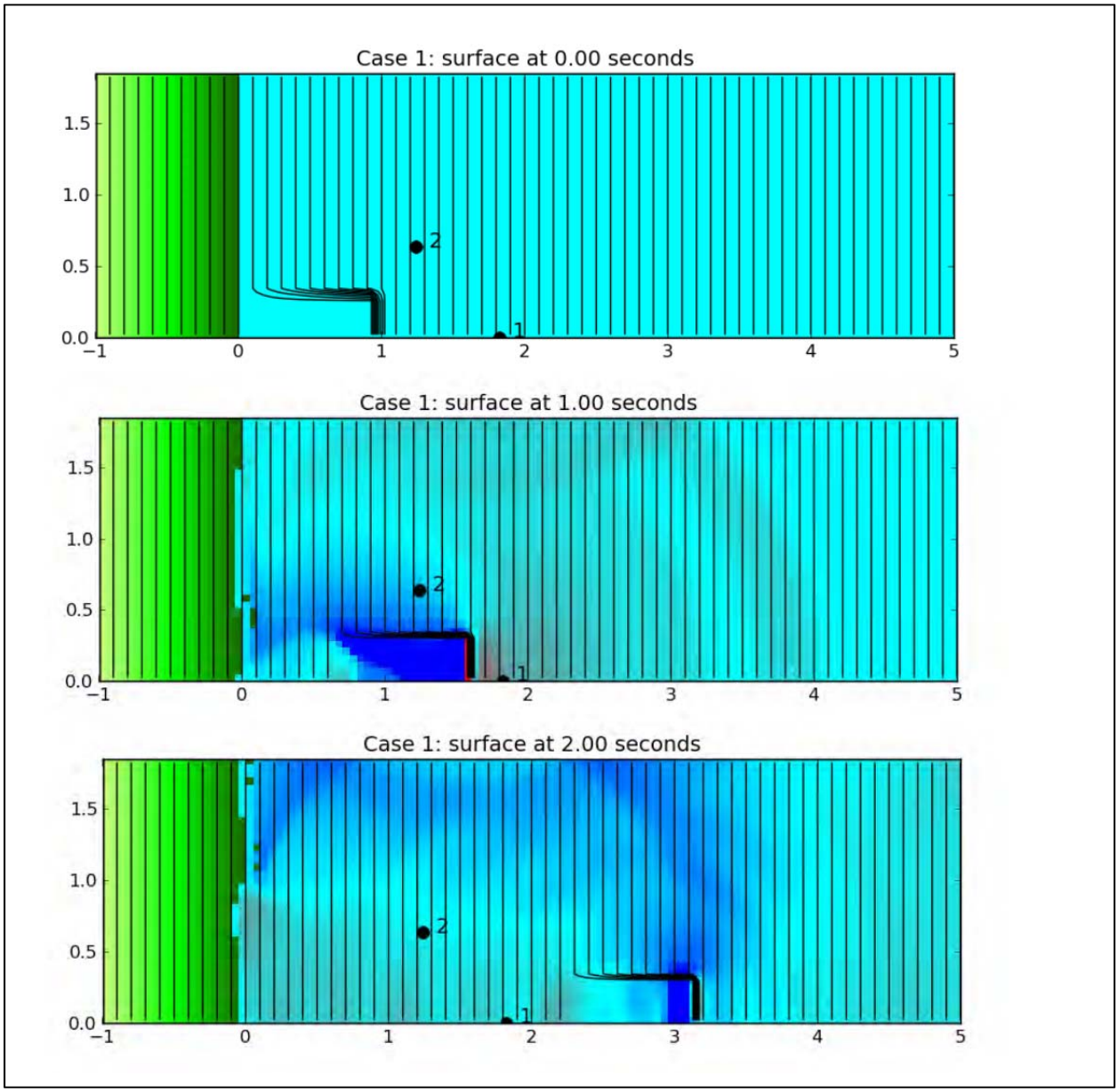

Figure 5-42: Single grid 140 x 40 GeoClaw simulation of Case 1 to illustrate moving bathymetry and gauge locations.

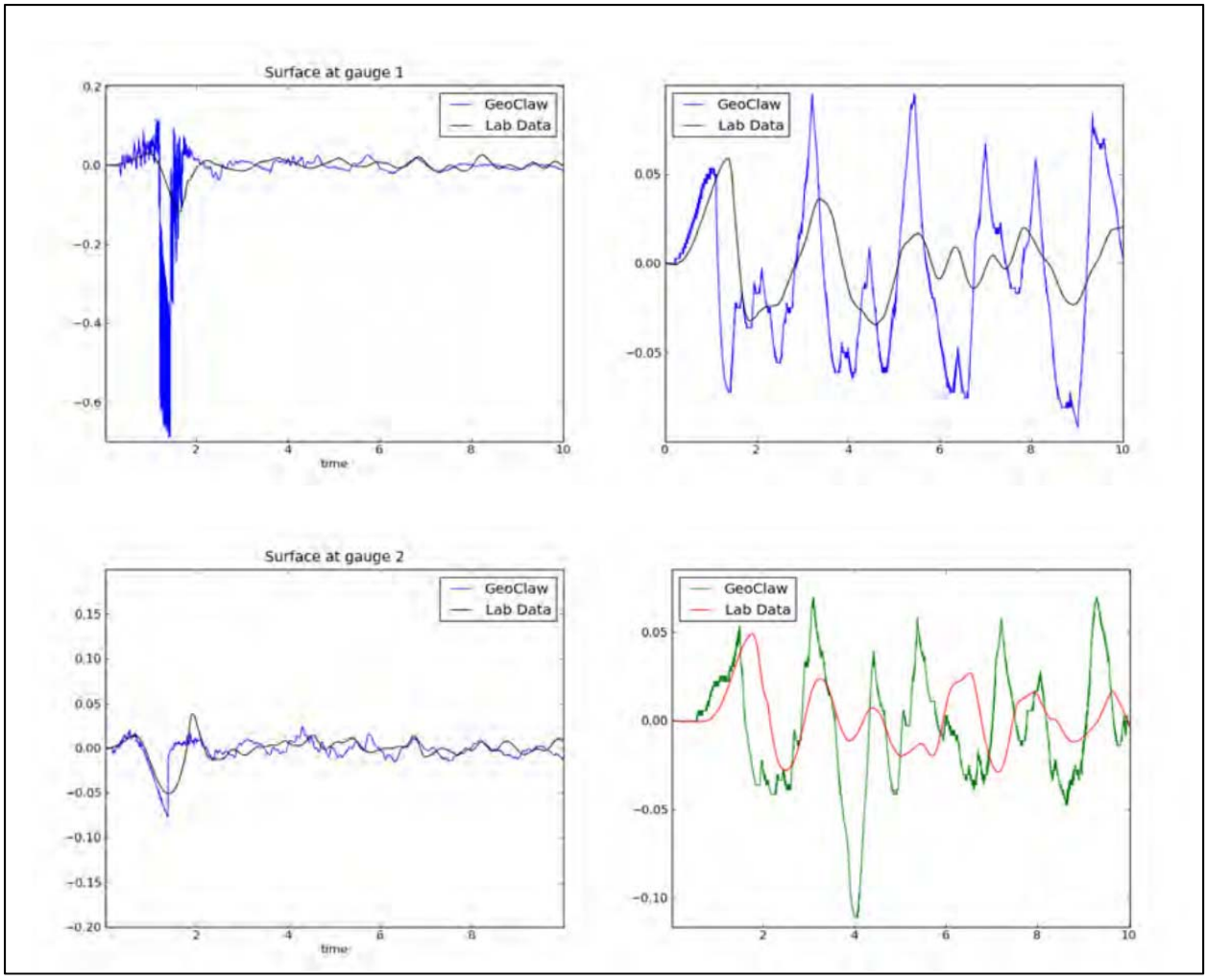

Figure 5-43: Left column: Time histories of the surface elevation with respect to still water level for case 1. Right column: Time histories of the runup measurements with respect to still water level for case 1, at Runup gauges 2 and 3. Note: runup values are negated in this figure for both GeoClaw and lab data due to a programming glitch.

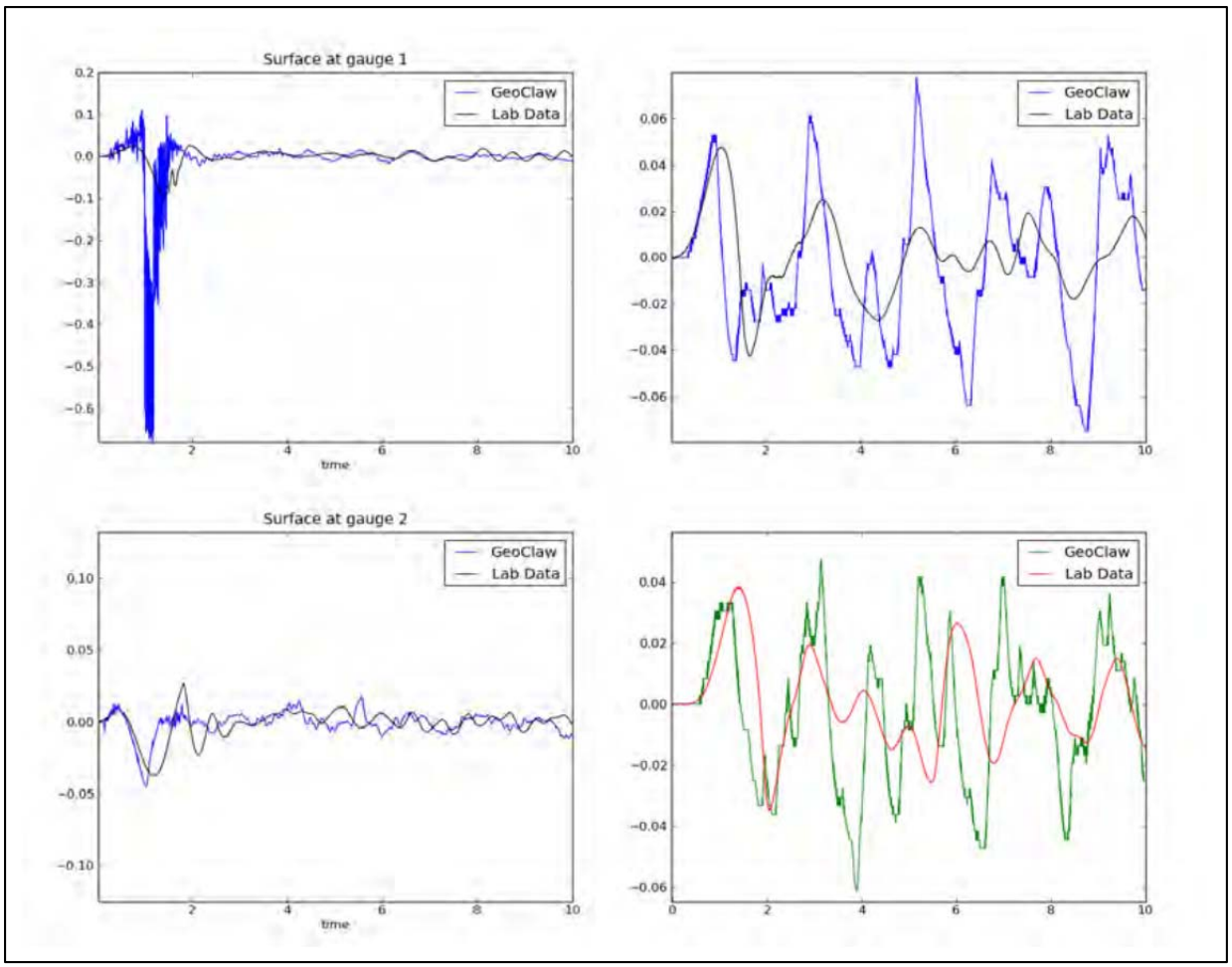

Figure 5-44: Left column: Time histories of the surface elevation with respect to still water level for case 2. Right column: Time histories of the runup measurements with respect to still water level for case 2, at Runup gauges 2 and 3. Note: runup values are negated in this figure for both GeoClaw and lab data due to a programming glitch.

5.3.9 BP9: Okushiri Island – field

- PMEL-135, pp. 8 & 48-53 (Synolakis et al., 2007).
- A problem description is provided by Frank González at LeVeque (2011) BP09-FrankG-Okushiri_island/Description.pdf
- Numerous other publications also describe this event, in varying detail: (DCRC, 1994; HTSG, 1993; Kato and Tsuji, 1994; Takahashi et al., 1995; Yeh et al., 1994).

5.3.9.1 Description

The goal of this benchmark problem (BP) is to compare computed model results with field observations of the 1993 Okushiri Island tsunami.

5.3.9.2 Problems encountered

Two basic problems were encountered:

- Poor quality of the computational bathymetric/topographic grids.

- Inaccurate spatial registration of field observational data with the model grids.

5.3.9.3 What we did

- Used $g = 9.81$ and Manning coefficient 0.025 for the friction term. We also ran many of the tests with no friction for comparison.
- Used bathy/topo grids and source grid for the Disaster Control Research Center solution DCRC17a. Dmitry Nicolsky provided improved versions of the originals developed by Kansai University, in which severe misalignments in the original data were reduced (but not eliminated).

5.3.9.4 Problem Requirements

Requirements of this benchmark test were to compute:

1. Runup around Aonae.
2. Arrival of the first wave to Aonae.
3. Two waves at Aonae approximately 10 min apart; the first wave from the west, the second from the east.
4. Water level at Iwanai and Esashi tide gauges.
5. Maximum modeled runup distribution around Okushiri Island.
6. Modeled runup height at Hamatsumae.
7. Modeled runup height at a valley north of Monai.

5.3.9.5 Results

Figure 5-45 through Figure 5-48 show results of one computation where AMR is used to concentrate grid points near the southern Aonae peninsula and (Requirements 1, 2, 3). The rectangular boxes show regions of refinement. The coarsest grid is a 60 × 60 grid on a 1-degree square as shown in Figure 5-45. Five levels of refinement are used going down by factors 2, 4, 4, and 6 from each level to the next. In this computation, Level 4 is only allowed on the southern half of Okushiri Island and Level 5 only around the Aonae peninsula.

Figure 5-46 shows a zoom on the island and Figure 5-47 a further zoom on the peninsula. Arrival of the first wave at Aonae (Requirement 2) is seen from the west at about $t = 5$ minutes. The second major wave arrives from the east at about 10 minutes.

Figure 5-48 shows the inundation level on the peninsula. The color scale indicates the maximum depth of water recorded at each point on a fixed grid that is placed around this region. This can be compared to the photographs shown in Figure 5-49.

A slight modification of this run was done to focus on the Hamatsumae region just east of the peninsula. Figure 5-50 shows the maximum inundation in this region.

The bottom panel of Figure 5-51 shows the runup at various other points around the island as measured by the team of Y. Tsuji (top panel), along with values computed using GeoClaw. Figure 5-52 shows a scatter plot of the correlation between the observations and the computed values. The GeoClaw values were obtained by placing a small fixed grid around each observation point and recording the maximum water depth at each point on this grid at each timestep of the computation, using the built-in feature of GeoClaw. The maximum depth over time can also be accumulated at these points and updated each time step. Plots of the maxima

over these grids give a visualization of the maximum extent of inundation. Such plots are shown in Figure 5-48 and Figure 5-53, with 4-meter contours. For most other observation points contours of topography at 2-meter increments were plotted in order to better estimate the maximum runup in a small region centered about each observation point.

Figure 5-53 shows the inundation map for the Valley north of Monai, with 4-meter contour lines (Requirement 7). Inundation to roughly 32 m is observed, in accordance with observations. For this run a finer grid was used in the region around the value (refining by a factor 24 rather than 6 in the level 5 grid), and the finer scale bathymetry provided in this region was used.

Requirement 4 is the comparison of observed and computed water levels at the Iwanai and Esashi tide gauge stations; the analog records are shown in Figure 5-54, taken from Takahashi et al. (1995). The digitized tide gauge data are compared with the GeoClaw time series in Figure 5-55 and Figure 5-56. At Iwanai, the digitized tide gauge record is clearly undersampled (compare Figure 5-54 and Figure 5-55), but does capture the peaks and troughs of the analog record. We see that the first wave arrival time and the overall wave amplitudes are comparable, but that the GeoClaw tsunami waves are about half the period of the waves recorded by the Iwanai tide gauge. Considering the regularity of the long train of waves in the tide gauge record, it is probable that longer period resonance modes at Iwanai were excited by the incident tsunami; if so, then higher resolution bathy/topo grids would be required to capture these resonant oscillations in a numerical simulation. At Esashi, it appears that the digitized tide record reflects the main features of the analog record (compare Figure 5-54 and Figure 5-56). However, the strange shape of the analog wave form makes it likely that there are problems with the tide gauge record; the record suffers from either mechanical/electronic, or damage by debris, or simply a damped or mismatched response function in the tsunami frequency band. In spite of this, the first arrival and timing of the first two tsunami waves are in good correspondence, though the amplitude and individual wave forms are not.

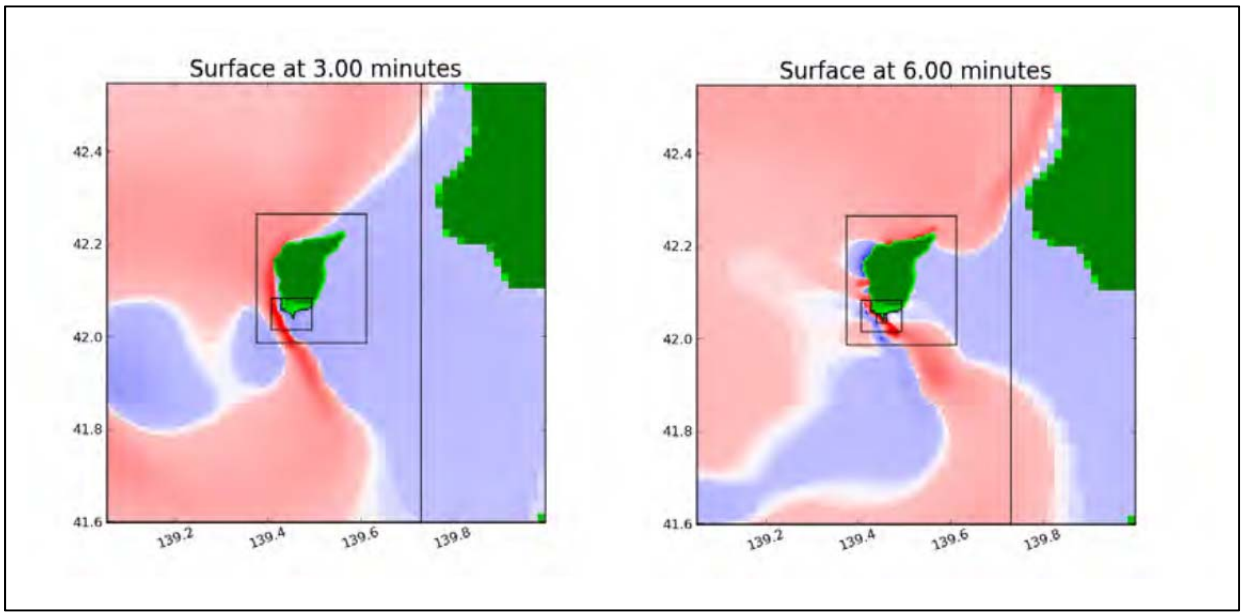

Figure 5-45: Full computational domain for one simulation, in which AMR grids are focused near the Aonae peninsula at the south of Okushiri Island.

5.3.9.6 Lessons learned

This benchmark problem requires much more work to qualify as a credible test of tsunami inundation models. We have little confidence in:

- The quality of the bathy/topo computational grids. A number of mismatches and discontinuities still exist in the system of grids.
- The accuracy of the geospatial registration of observational data with model latitude and longitude positions. Figure 5-51 presents the observation locations of each of three field survey teams – Professor Yoshinobu Tsuji, Tokyo University (Tsuji), the United States-Japan Cooperative Program on Natural Resources (UJNR) and the Tohoku University (Tohoku) teams. The bathy/topo computational grids were adjusted to match the positions of the Tsuji observations, but it is clear that this created a systematic error in the registration of the grids with the Tohoku field observations and, in all likelihood, the UJNR field observations. As another example, there appear to be discrepancies in the several field team reports of the latitude and longitude of the highest runup observed, i.e., the value of over 30 m in a " ... small valley north of Monai ...." Such positioning errors can be critical with respect to accurate comparisons of observed and computed runup.

5.3.9.7 Recommendations

The Okushiri event tsunami runup and eyewitness reports remains one of the most valuable datasets for model comparisons in existence, but the quality of this dataset must be improved to qualify as a credible benchmark problem. We recommend that an effort be supported to

- Develop a high quality bathy/topo grid system.
- Resolve ambiguities and discrepancies currently found in the various team data reports, and improve the geospatial registration of observed and modeled values.
- Provide adequate documentation of the resulting benchmark problem dataset.

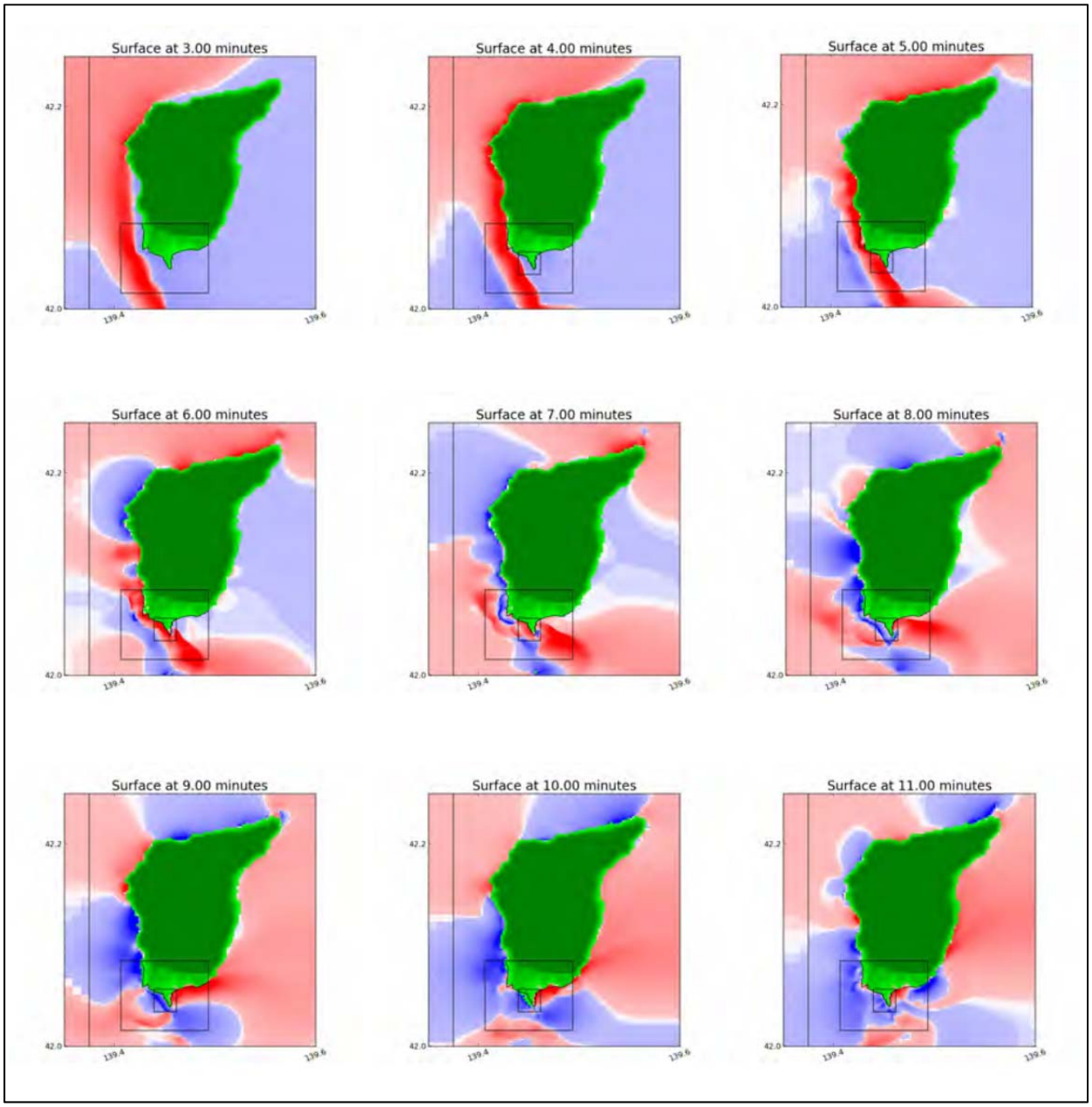

Figure 5-46: Zoom on Okushiri Island.

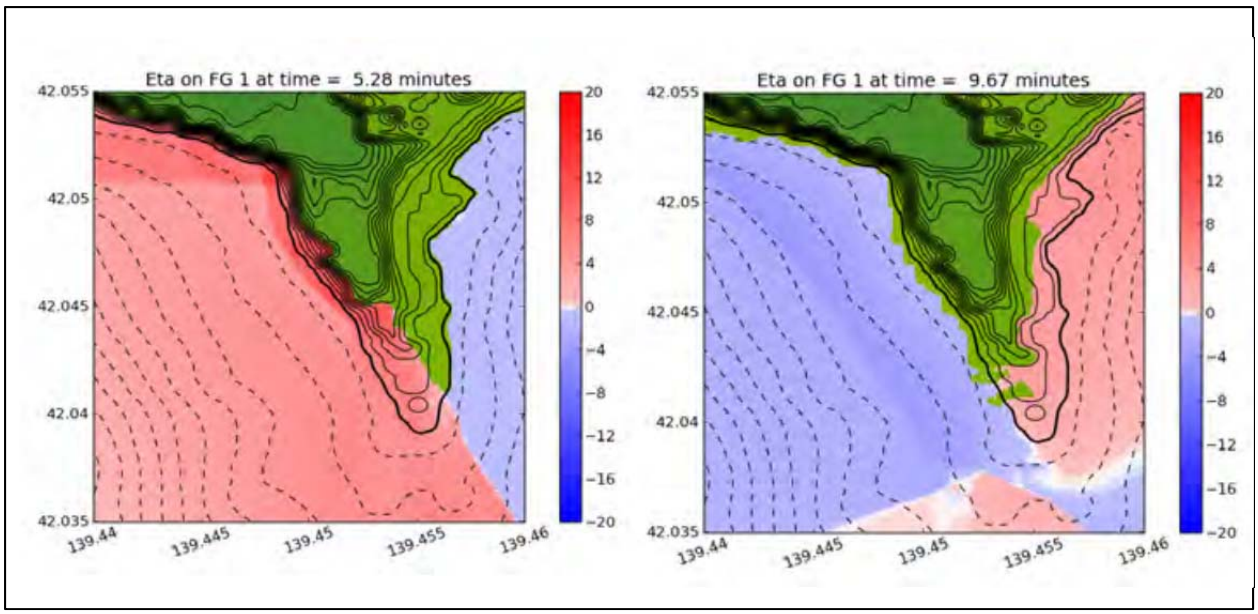

Figure 5-47: Zoom on the Aonae peninsula showing the first wave arriving from the west and the second from the east. Color map shows elevation of sea surface. 4-meter contours of bathymetry and topography are shown.

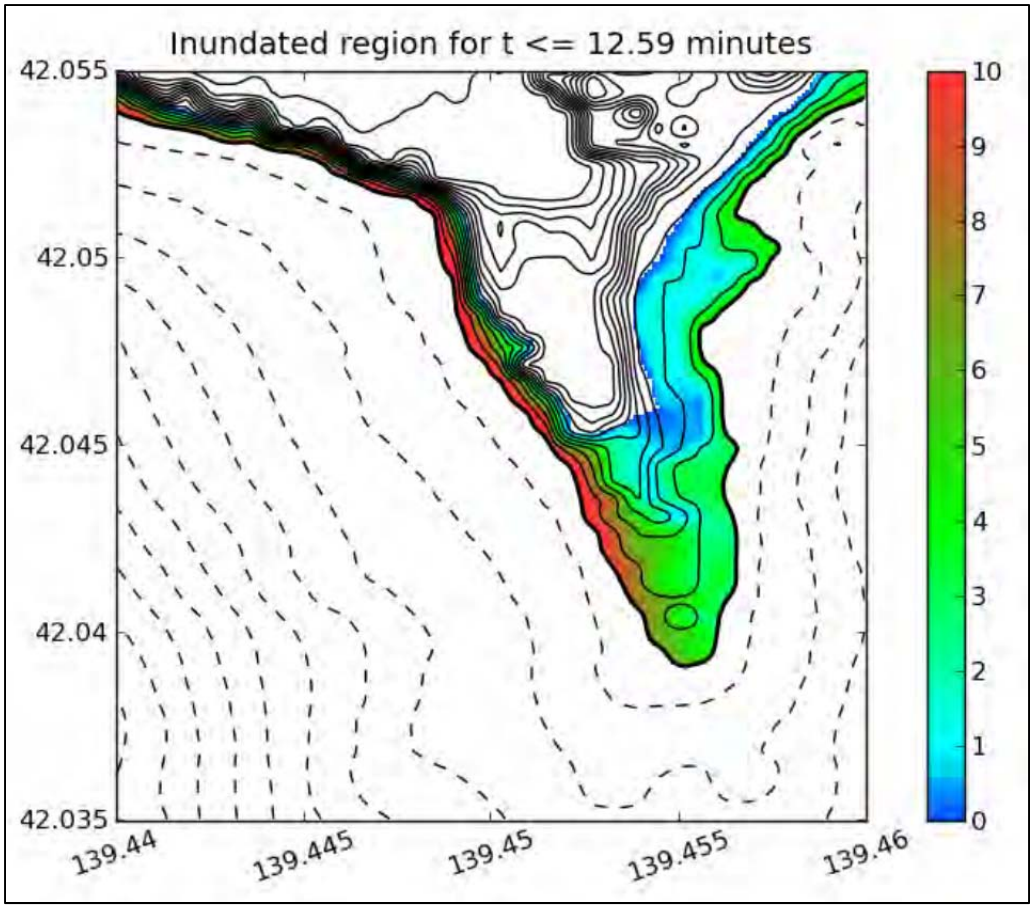

Figure 5-48: Inundation map of the Aonae peninsula. Color map shows maximum fluid depth over entire computation at each point. 4-meter contours of bathymetry and topography are shown.

Figure 5-49: Photographs of the Aonae peninsula taken shortly after the event.
Left: From http://www.usc.edu/dept/tsunamis/hokkaido/aonae.html.
Right: From http://nctr.pmel.noaa.gov/okushiri_devastation.html, credited to Y. Tsuji.

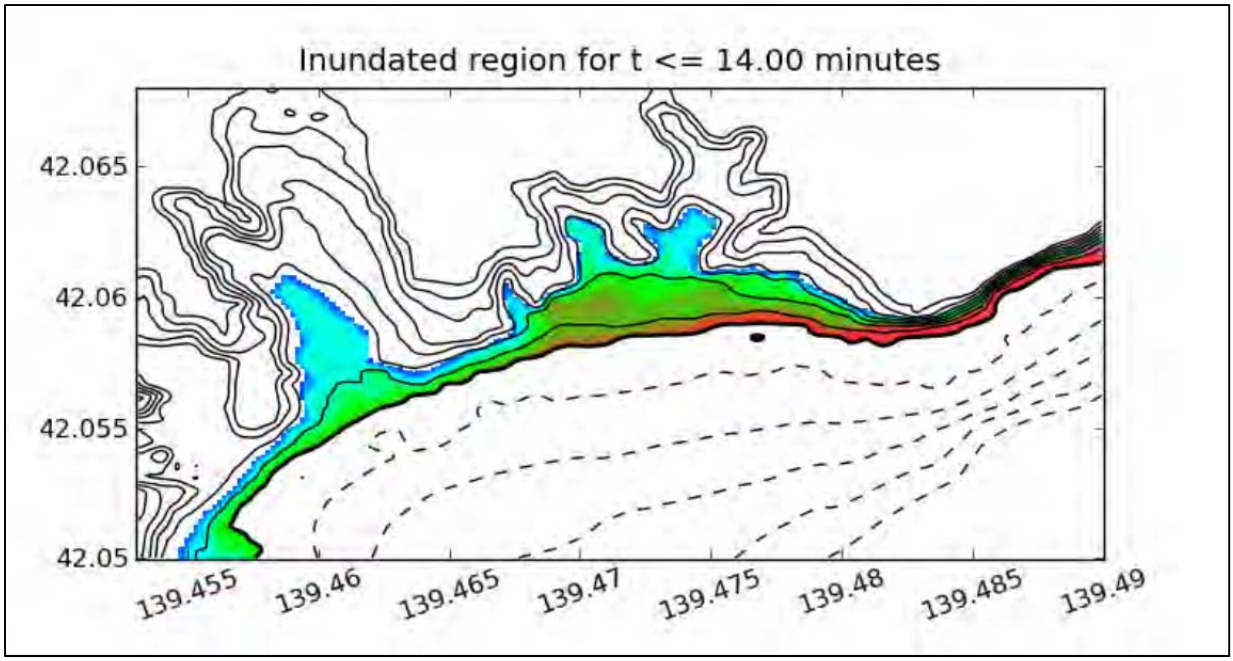

Figure 5-50: Inundation map of the Hamatsumae neighborhood just east of the Aonae peninsula. Color map shows maximum fluid depth over entire computation at each point, with the same color scale as Figure 5-48. 4-meter contours of bathymetry and topography are shown.

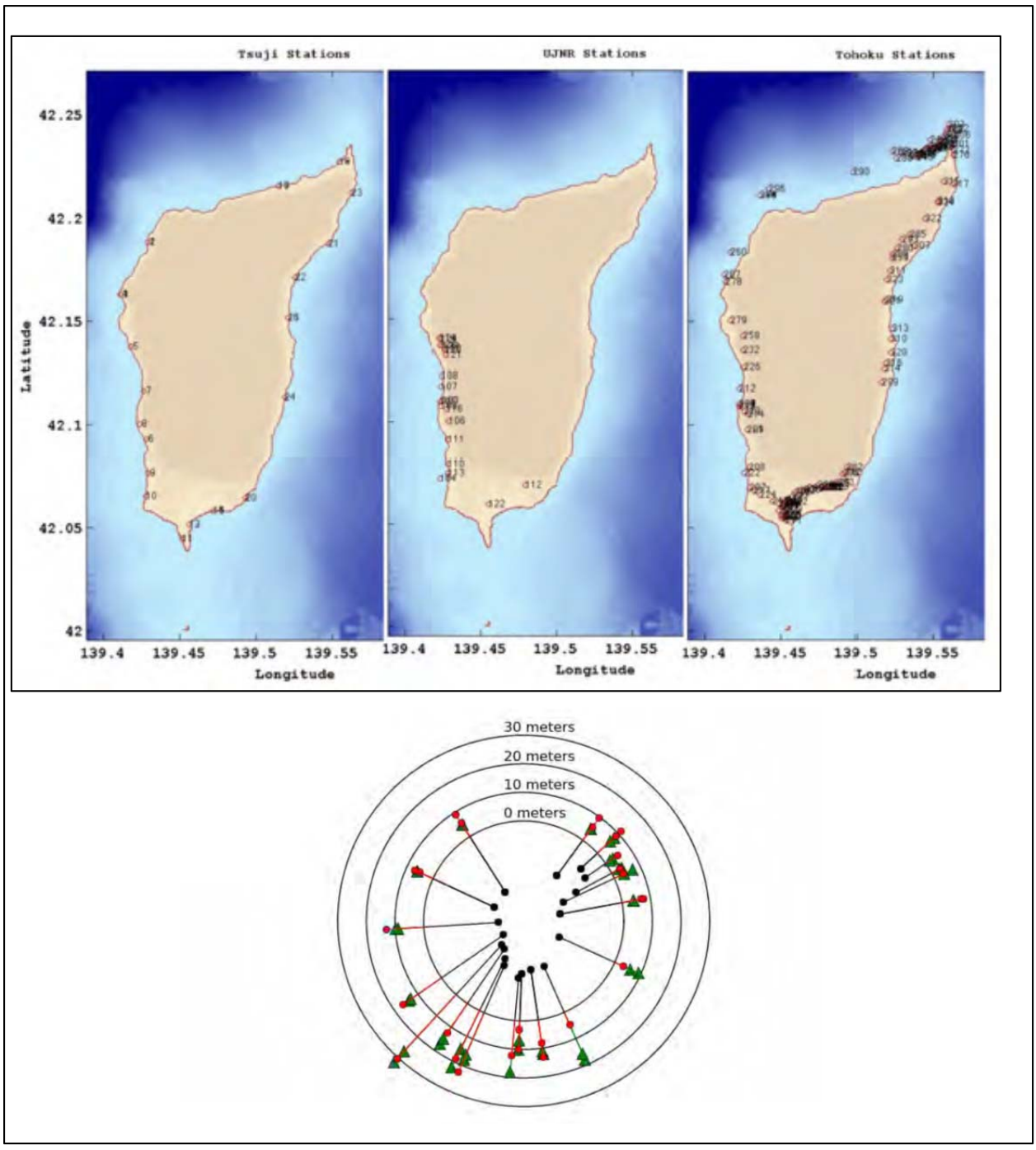

Figure 5-51: Top: Locations of field observations by three independent field survey teams, relative to the computational bathy/topo grid system. Only the observations of Tsuji (left figure) were used in this study due to misregistration of the other two data sets. Bottom: Measured and computed runup at 21 points around Okushiri Island where measured by the Tsuji team. Red circles are measurements; green diamonds are estimated from the computation. Two red circles at the same point represent estimates of minimum and maximum inundation observed near the point. Two green diamonds at the same point represent values estimated when the model was run with and without bottom friction (Manning coefficient 0.025). The runup computed with bottom friction is the smaller value.

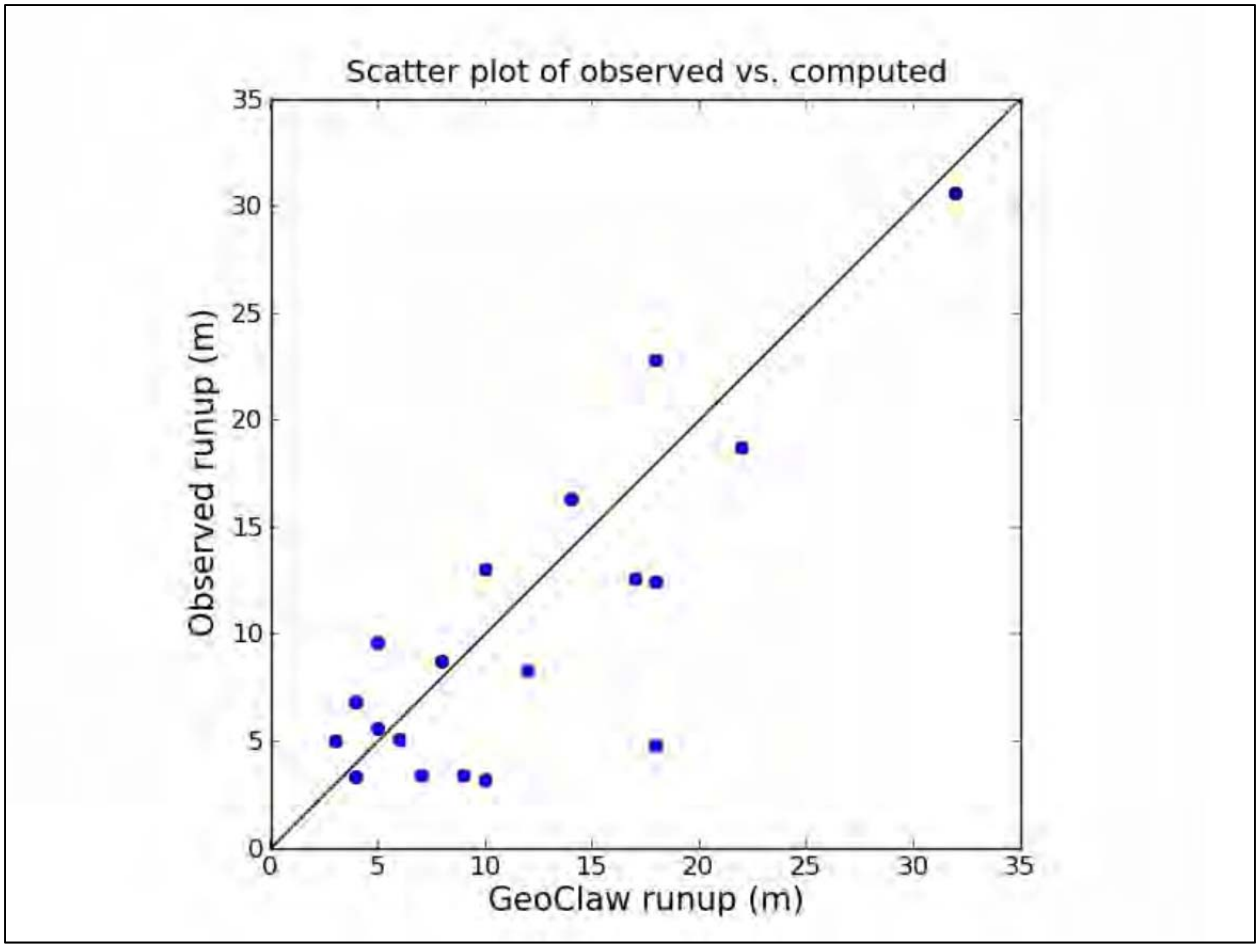

Figure 5-52: Scatter plot illustrating the correlation between measured and computed values for the values shown in Figure 5-51.

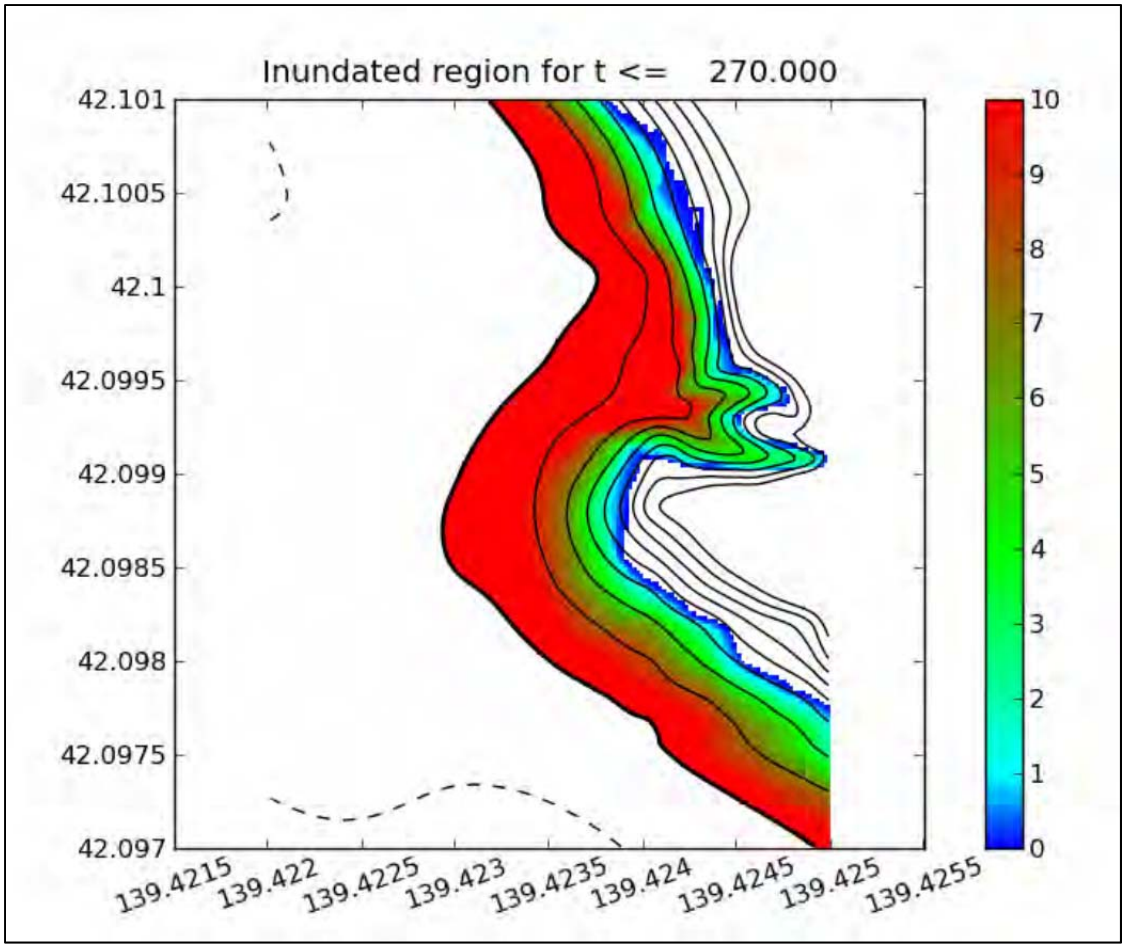

Figure 5-53: Inundation map of the valley north of Monai. Color map shows maximum fluid depth over entire computation at each point. 4-meter contours of bathymetry and topography are shown. Compare to Figure 5-41 showing the related wave tank simulation.

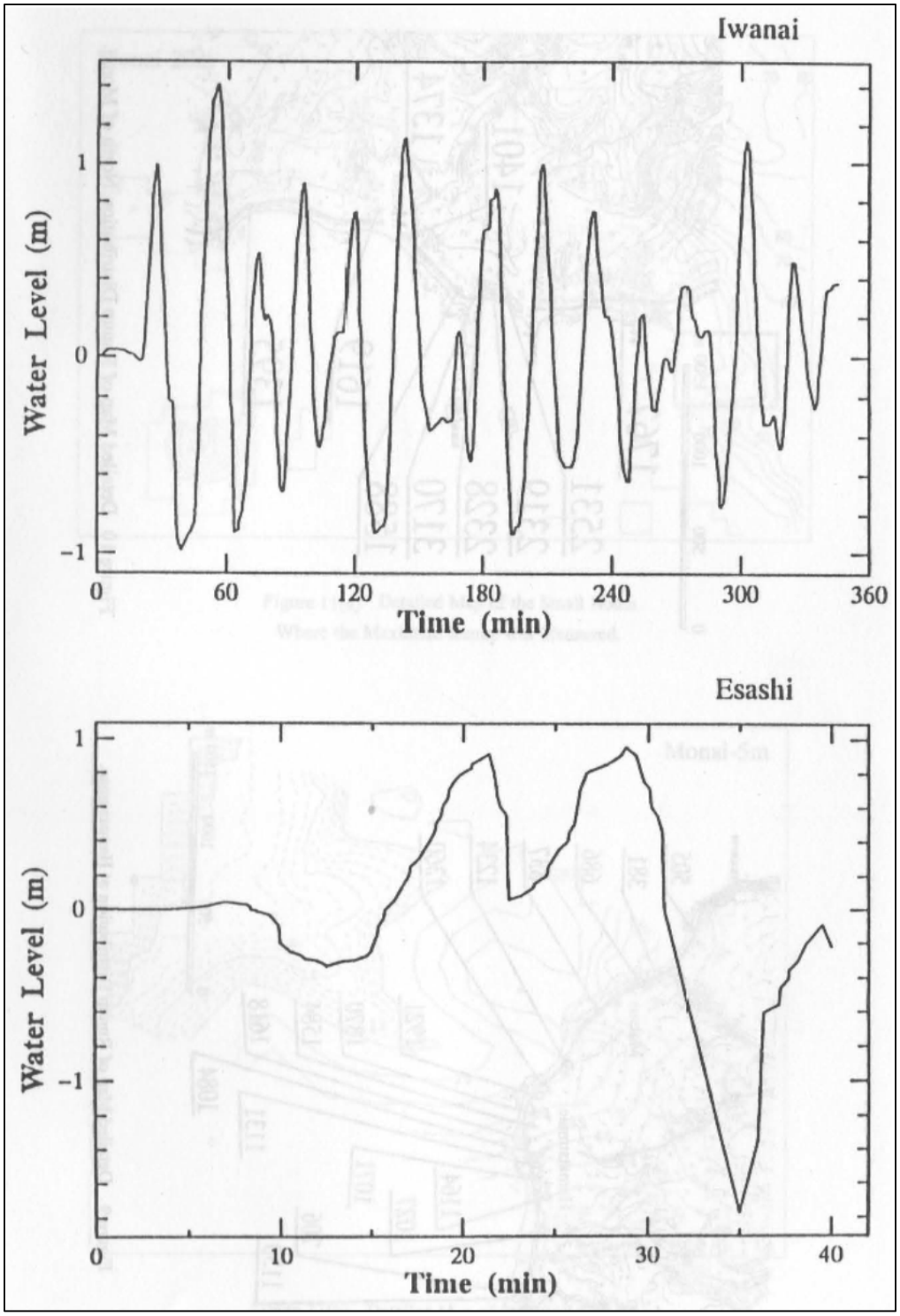

Figure 5-54: Analog tide gauge records at Iwanai and Esashi.

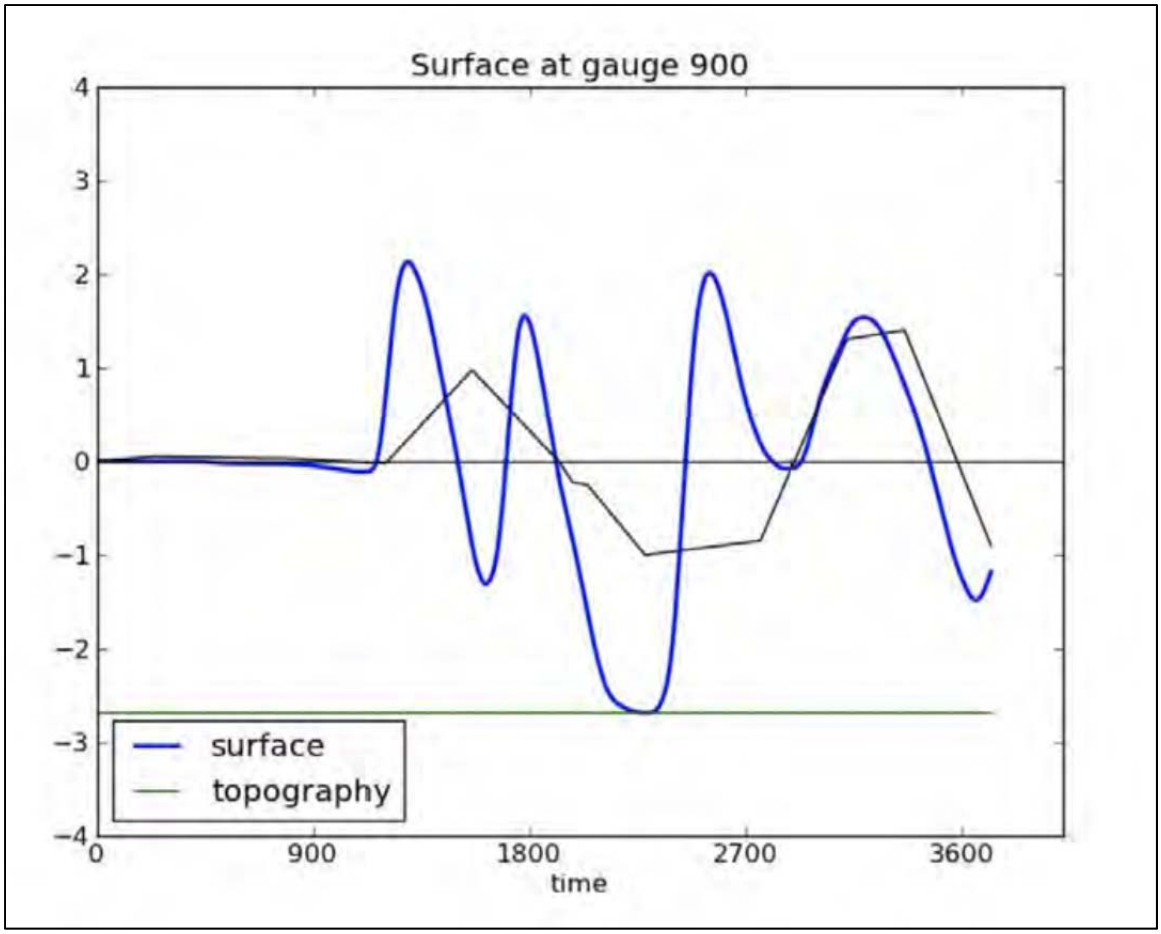

Figure 5-55: Iwanai digitized tide gauge record (black line) and GeoClaw (blue line) time series.

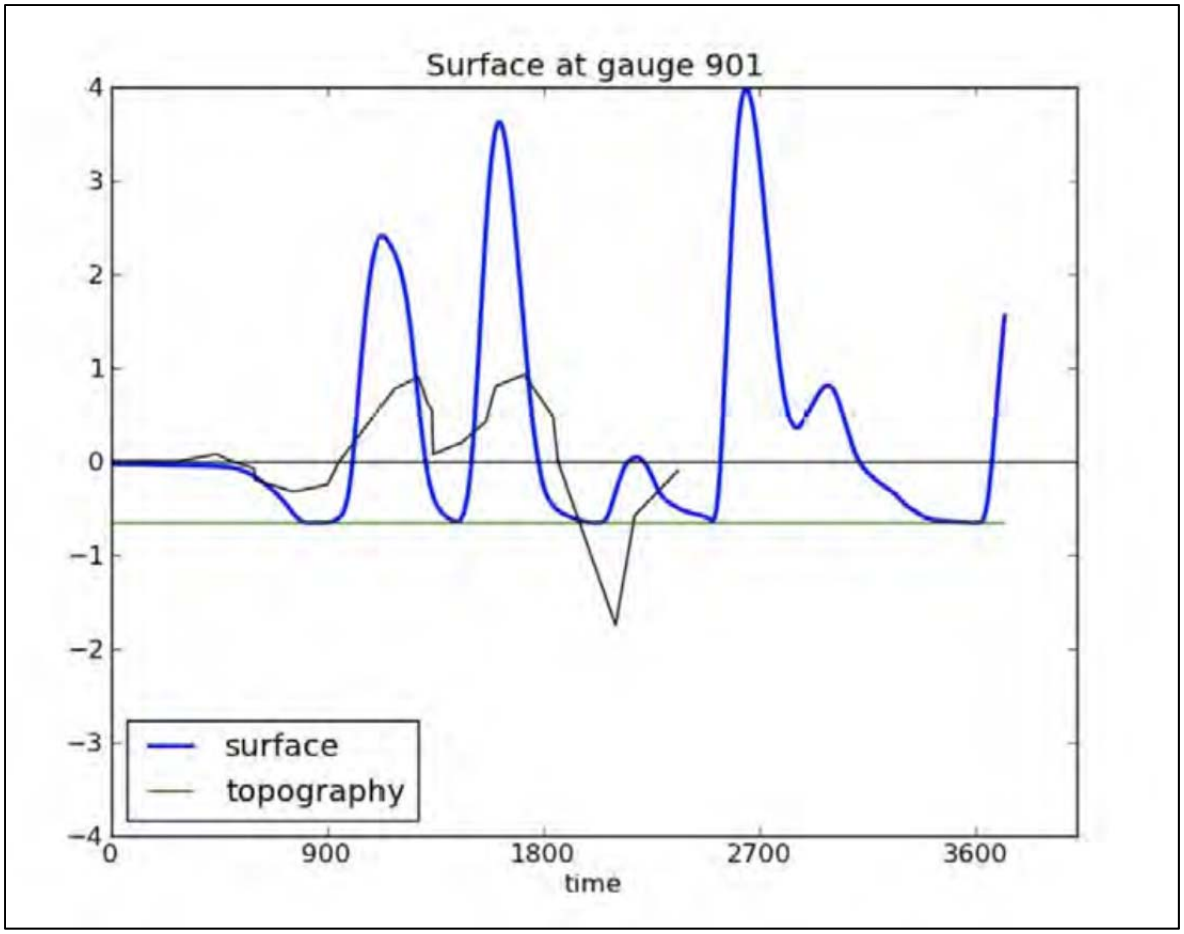

Figure 5-56: Esashi digitized tide gauge record (black line) and GeoClaw (blue line) time series.

5.4 Further remarks and suggestions

5.4.1 Comments on the current benchmark problems

The current set of benchmark problems do a good job of testing some aspects of a tsunami simulation code. However, there are some shortcomings that have become apparent to us in the course of working through these problems and that could be addressed in the future.

- Several of the problems are not well specified in terms of the data provided. These difficulties have been noted in our discussion of the individual problems.
- In some problems there is not a clear description of how the simulation is supposed to be set up, or how the accuracy of the solution should be quantified. Allowing flexibility is perhaps necessary to allow for differences in capabilities of existing simulation codes, but we feel this could be better constrained. In particular, there is no indication in the problem descriptions of what grid resolution should be used. There are requirements to "demonstrate convergence," but for practical applications it is important to know that adequately accurate results can be obtained on grids with a reasonable resolution in terms of computing time constraints.

- Friction parameter values significantly affect model runup computations at both laboratory and field experiment scales (see Figure 5-37 and Figure 5-51). Different models may use different formulations of the friction terms and some consideration should be given to testing and reporting on the effect of different values of the friction parameter when conducting benchmark problem simulations.
- Runup computational algorithms frequently employ a parameter that sets a threshold level below which a cell is declared dry, i.e., the Dry Cell Depth. As in the case of friction, the value of this parameter can also affect the resulting runup computation (see Figure 5-37), and some consideration should be given to testing and reporting on how variations in such model parameters can affect runup computation results for benchmark problems.
- Currently there is no requirement to report CPU time required to solve each problem. This would be interesting information to have when comparing different approaches, and would be a necessary component if the benchmark did require a particular grid resolution, because grid resolution alone is not necessarily a good indication of computational effort needed.
- Some of the benchmark problems compare numerical results to the exact solutions of the linear or nonlinear shallow water equations. For these problems, any code that solves the equations in question should converge to the correct solution, but it may also be of interest to know how rapidly the error goes to zero, and how good the solution is on under-resolved grids that may be more representative of what would be used in actual tsunami simulations.
- Other benchmark problems require comparison with wave tank experiments. In some cases (e.g., with breaking waves) it cannot be expected that the code converges to the experimental results because the equations used in tsunami modeling are only approximations. Different codes may use different approximations and so this comparison may be valuable, but because many codes use the same shallow water approximations, for these problems it would be valuable to have some agreement as to what a "converged solution" of the shallow water equations looks like.
- BP8a, studied in Section 5.3.8, does not seem to scale well as a model of a real landslide, and has difficulties associated with the vertical face that are not likely to be seen in real landslides, where momentum transfer is probably secondary to the vertical displacement of the water column in creating a tsunami. The short wavelength waves generated by the discontinuity in this problem also accentuate the need to use dispersive corrections in order to obtain reasonable approximations. While dispersive terms may be very important for some submarine landslide generated tsunamis, there may be other cases where they are less important and the ability to model such events with shallow water equations is important because these equations can be solved with explicit methods that are often orders of magnitude faster than implicit dispersive solvers. (This may be particularly important in doing probabilistic hazard assessment requiring a large number of scenarios.) We believe it would be valuable to develop landslide benchmarks that model events such as a large mass failure on the continental slope, which the current benchmarks do not address.

- The Okushiri Island BP9 requires comparison to field observations. Beyond the technical difficulties with datasets for this problem, there are also questions regarding (a) the accuracy of the earthquake source being used, (b) the accuracy of some of the field observations and tide gauges. This makes it difficult to assess the accuracy of a simulation code. This will always be a problem in comparing with actual events, but our feeling is that to form a meaningful benchmark there should be some agreement in the community regarding how large the deviation between the computed solutions and the observations are expected to be, rather than an expectation that results converge to observations as the grid is refined.

5.4.2 Suggestions for future benchmark problems

We believe there are other possible benchmark problems that should be considered by the community in order to better test tsunami simulation codes.

- The one-dimensional test problems currently involve exact solutions that are themselves difficult to calculate numerically, e.g., requiring numerical quadrature of Bessel functions. It is very useful that tabulated values of these solutions have been provided. However, rather than using limited tests for which such "exact" solutions are known, it might be preferable to carefully test a 1-D numerical model and show that it converges, and then use this with very fine grids to generate reference solutions. Fully converged solutions could be provided in tabulated form and could be as accurate as needed. It would then be possible to generate a much wider variety of test problems. In particular, more realistic bathymetry could be used, for example on the scale of the ocean, a continental shelf and beach, rather than modeling only a beach.
- High-accuracy one-dimensional reference solutions can also be used to test a full two dimensional code, by creating bathymetry that varies in only one direction at some angle to the two-dimensional grid. A plane wave approaching such a planar beach would ideally remain one-dimensional, but at an angle to the grid this would test the two-dimensional inundation algorithms.
- This idea can be extended to consider radially symmetric problems, such as a radially symmetric ocean with a Gaussian initial perturbation at the center. The waves generated should reach the shore at the same time in all directions, but the shore will be at different angles to the grid in different locations and it is valuable to compare the accuracy in different locations. The two-dimensional equations can be reformulated as a one-dimensional equation in the radial direction (with geometric source terms) and a very fine grid solution to this problem can be used as a reference solution.
- Features could also be added at one point along the shore and this location rotated to test the ability of the code to give orientation-independent results. Some GeoClaw results of this nature are presented in Berger et al. (2011) and LeVeque et al. (2011).
- A very simple exact solution is known for water in a parabolic bowl, in which the water surface is linear at all times but the water sloshes around in a circular motion. This is a good test of wetting and drying as well as conservation. See for example Gallardo et al. (2007), Thacker (1981), and the test problem in GeoClaw: http://www.clawpack.org/clawpack-4.x/apps/tsunami/bowl-slosh/ README.html

- Extensive observations are available for recent events such as Chile 2010 or Tohoku 2011, including DART buoys, tide gauges, and field observations of inundation and runup. It would be valuable to develop new benchmark problems based on specific data sets, including specified bathymetry and earthquake source (or seafloor displacement).

5.5 References

Bale DS, LeVeque RJ, Mitran S, Rossmanith JA. 2002. A wave propagation method for conservation laws and balance laws with spatially varying flux functions. *SIAM J. Sci. Comput.*, 24:955–978.

Behrens J, LeVeque RJ. 2011. Modeling and simulating tsunamis with an eye to hazard mitigation. *SIAM News*, 44(4), May.

Berger MJ, Calhoun DA, Helzel C, LeVeque RJ. 2009. Logically rectangular finite volume methods with adaptive refinement on the sphere. *Phil. Trans. R. Soc. A*, 367:4483– 4496.

Berger MJ, Colella P. 1989. Local adaptive mesh refinement for shock hydrodynamics. *J. Comput. Phys.*, 82:64–84.

Berger MJ, George DL, LeVeque RJ, Mandli KT. 2011. The GeoClaw software for depth-averaged flows with adaptive refinement. *Adv. Water Res*.

Berger MJ, LeVeque RJ. 1998. Adaptive mesh refinement using wave-propagation algorithms for hyperbolic systems. *SIAM J. Numer. Anal.*, 35:2298–2316.

Berger MJ, Oliger J. 1984. Adaptive mesh refinement for hyperbolic partial differential equations. *J. Comput. Phys.*, 53:484–512.

Briggs M. No date (n.d.) Runup of solitary waves on a vertical wall. Coastal Hydraulics Laboratory http://chl.erdc.usace.army.mil/chl.aspx?p=s&a=Projects;36. Accessed n.d.

Briggs MJ, Synolakis CE, Harkins GS. 1994. Tsunami runup on a conical island. In *Proc. of Waves T Physical and Numerical Modelling, 21-24 August 1994, Vancouver, Canada*, pages 446–455, August (1994).

Briggs MJ, Synolakis CE, Harkins GS, Green D. 1995. Laboratory experiments of tsunami runup on a circular island. *Pure Appl. Geophys.*, 144:569–593.

Briggs MJ, Synolakis CE, Harkins GS, Green DR. 1996. Runup of solitary waves on a circular island. In *Proceedings of the Second International Long-Wave Runup Models, Friday Harbor, Washington, 12-16 September (1995)*, pages 363–374.

DCRC (Disaster Control Research Center). 1994. *Tsunami Engineering Technical Report No. 11*. Tohoku University, Tohoku, Japan.

Enet F, Grilli ST. 2003. Experimental study of tsunami generation by three-dimensional rigid underwater landslides. *Journal of Waterway, Port, Coastal, and Ocean Engineering*, 133:442–454.

Fuhrman DR, Madsen PA. 2009. Tsunami generation, propagation, and run-up with a high-order boussinesq model. *Coastal Eng.*, 56:747–758.

Fujima K, Briggs MJ, Yuliadi D. 2000. Runup of tsunamis with transient wave profiles incident on a conical island. *Coastal Engineering Journal*, 42:175–195.

Gallardo JM, Parés C, Castro M. 2007. On a well-balanced high-order finite volume scheme for shallow water equations with topography and dry areas. *J. Comput. Phys.*, 227:574–601.

GeoClaw documentation. 2011. http://www.clawpack.org/geoclaw.

George DL. 2006. *Finite Volume Methods and Adaptive Refinement for Tsunami Propagation and Inundation*. PhD thesis, University of Washington.

George DL. 2008. Augmented Riemann solvers for the shallow water equations over variable topography with steady states and inundation. *J. Comput. Phys.*, 227(6):3089–3113, March.

George D. 2010. Adaptive finite volume methods with well-balanced Riemann solvers for modeling floods in rugged terrain: Application to the Malpasset dam-break flood (France, 1959). *Int. J. Numer. Meth. Fluids*.

George DL, Iverson RM. 2010. A two-phase debris-flow model that includes coupled evolution of volume fractions, granular dilatency, and pore-flud pressure. Submitted to *Italian Journal of Engineering, Geology and Environment*.

George DL, LeVeque RJ. 2006. Finite volume methods and adaptive refinement for global tsunami propagation and local inundation. *Science of Tsunami Hazards*, 24:319–328.

HTSG (Hokkaido Tsunami Survey Group). 1993. Tsunami devastates japanese coastal region. *Eos Trans. Am. Geophys. Union*, 74:417, 432.

Kato K, Tsuji Y. 1994. Estimation of fault parameters of the 1993 hokkaido-nansei-oki earthquake and tsunami characteristics. *Bull. Earthq. Res. Inst., Univ. Tokyo*, 69:39–66.

Langseth JO, LeVeque RJ. 2000. A wave-propagation method for three-dimensional hyperbolic conservation laws. *J. Comput. Phys.*, 165:126–166.

LeVeque RJ. 1996. High-resolution conservative algorithms for advection in incompressible flow. *SIAM J. Numer. Anal.*, 33:627–665.

LeVeque RJ. 1997. Wave propagation algorithms for multi-dimensional hyperbolic systems. *Journal of Computational Physics*, 131:327–335.

LeVeque RJ. 2002. *Finite Volume Methods for Hyperbolic Problems*. Cambridge University Press.

LeVeque RJ. 2007. *Finite Difference Methods for Ordinary and Partial Differential Equations, Steady State and Time Dependent Problems*. SIAM, Philadelphia.

LeVeque RJ. 2010. A well-balanced path-integral f-wave method for hyperbolic problems with source terms. *J. Sci. Comput.* To appear, www.clawpack.org/links/wbfwave10.

LeVeque RJ. 2011. rjleveque / nthmp-benchmark-problems. https://github.com/rjleveque/nthmp-benchmark-problems. Accessed n.d.

LeVeque RJ, Berger MJ, et al. No date (n.d.) Clawpack. http://www.clawpack.org. Accessed n.d.

LeVeque RJ, George DL. 2004.. High-resolution finite volume methods for the shallow water equations with bathymetry and dry states. In PL-F. Liu, H. Yeh, and C. Synolakis, editors, *Proceedings of Long-Wave Workshop, Catalina*, volume 10, pages 43–73. World Scientific. http://www.amath.washington.edu/~rjl/pubs/ catalina04/.

LeVeque RJ, George DL, Berger MJ. 2011. Tsunami modeling with adaptively refined finite volume methods. *Acta Numerica*, pages 211–289.

Liu PL-F, Cho Y-S, Briggs MJ, Kânoğlu U, Synolakis CE. 1995. Runup of solitary waves on a circular island. *J. Fluid Mech.*, 302:259–285.

Liu PL-F, Cho Y-S, Fujima K. 1994. Numerical solutions of three-dimensional run-up on a circular island. In *Proceedings of the International Symposium: Waves – Physical and Numerical Modeling, 21-24 August 1994, Vancouver, Canada*, volume 2, pages 1031–1040.

Mandli KT. 2011. *Finite Volume Methods for the Multilayer Shallow Water Equations with Applications to Storm Surges*. PhD thesis, University of Washington.

Matsuyama M, Tanaka H. 2001. An experimental study of the highest run-up height in the 1993 Hokkaido Nansei-oki earthquake tsunami. *ITS Proceedings*, pages 879–889.

Roe PL. 1981. Approximate Riemann solvers, parameter vectors, and difference schemes. *J. Comput. Phys.*, 43:357–372.

Synolakis CE, Bernard EN, Titov VV, Kanoglu U, Gonzáles F. 2007. Standards, criteria, and procedures for NOAA evaluation of tsunami numerical models. NOAA Tech. Memo. OAR PMEL-135, http://nctr.pmel.noaa.gov/benchmark/SP_3053.pdf.

Takahashi Tomo., Takahashi Take., Shuto N, Imamura F, Ortiz M. 1995. Source models for the 1993 hokkaido nansei-oki earthquake tsunami. *Pure and Applied Geophysics*, 144:74–767.

Thacker WC. 1981. Some exact solutions to the nonlinear shallow water wave equations. *J. Fluid Mech.*, 107:499–508.

Yeh H, Liu P, Briggs M, Synolakis C. 1994. Propagation and amplification of tsunamis at coastal boundaries: *Nature*, 372:353–355.

Yeh H, Liu P, Synolakis C, editors. 1996. *Benchmark Problem 4. The 1993 Okushiri Data, Conditions and Phenomena*. Singapore: World Scientific Publishing Co. Pte. Ltd..

Zhang S, Yuen DA, Zhu A, Song S. 2011. Use of many-core architectures for high-resolution simulation of Tohoku 2011 Tsunami waves. Submitted to Supercomputing 2011 conference.

6 MOST (Method Of Splitting Tsunamis) Numerical Model

Elena Tolkova

Joint Institute for the Study of the Atmosphere and Ocean, University of Washington / PMEL.
etolkova@u.washington.edu

6.1 Model description

The Method Of Splitting Tsunamis (MOST) numerical model (Titov and Synolakis, 1998) is a set of code developed to simulate three processes of tsunami evolution: generation by an earthquake, transoceanic propagation, and inundation of dry land. MOST has been used by the NOAA Center for Tsunami Research (NCTR) in the development of tsunami inundation forecast models. These forecast models are supported by an ocean-wide database of 24-hour-long tsunami wave propagation simulations of numerous tsunami scenarios, each generated by hypothetical earthquakes from unit sources covering worldwide subduction zones (Gica et al., 2008). As a tsunami wave propagates across the ocean and reaches tsunameter observation sites, the forecasting system uses a data inversion technique coupled with these pre-computed tsunami generation scenarios to deduce the tsunami source, in terms of the earthquake unit sources identified in the database (Percival et al., 2009). A linear combination of the pre-computed tsunami scenarios is then used to determine the offshore tsunami waves and to incorporate synthetic boundary conditions of water elevation and flow velocities into site-specific forecast models. The main objective of the forecast model is to provide an accurate estimate of wave arrival time, wave height, and inundation extent at a particular location within minutes of the earthquake, in advance of wave arrival. Previous and present development of forecast models in the Pacific (Titov and González, 1997; Wei et al., 2008; Titov, 2009; Tang et al., 2009) have validated the accuracy and efficiency of each forecast model currently implemented in the real-time tsunami forecast system.

6.1.1 Governing equations

The MOST model is intended to solve a system of depth-averaged continuity and momentum equations:

$$\frac{\partial h}{\partial t} + div(h\vec{V}) = 0 \tag{1a}$$

$$\left(\frac{\partial}{\partial x} + \vec{V}\cdot\nabla\right)\vec{V} + g\nabla h + \gamma\frac{g|V|\vec{V}}{h^{4/3}} = g\nabla d \tag{1b}$$

where $h(x_1, x_2, t) = \eta(x_1, x_2, t) + d(x_1, x_2)$, and η and d refer to the free surface displacement and undisturbed water depth, respectively, $\vec{V}(x_1, x_2, t)$ is the depth-averaged velocity vector in the horizontal plane, g is the acceleration due to gravity, and $\gamma = n^2$ is the Manning friction coefficient. The solution is based on the method of fractional steps (Yanenko, 1971; Durran, 1999) which reduces the 2-D problem to two 1-D problems by setting either spatial derivative to

zero. The majority of the benchmark problems below were simulated in the Cartesian coordinates (x_1, x_2) with friction set to zero. In those settings, the two 1-D problems yielded by splitting are:

$$\frac{\partial h}{\partial t} + \frac{\partial}{\partial x_1}\left(hV_1\right) = 0 \tag{2a}$$

$$\frac{\partial V_1}{\partial t} + V_1 \frac{\partial V_1}{\partial x_1} + g\frac{\partial h}{\partial x_1} = g\frac{\partial d}{\partial x_1} \tag{2b}$$

$$\frac{\partial V_2}{\partial t} + V_1 \frac{\partial V_2}{\partial x_1} = 0 \tag{2c}$$

and

$$\frac{\partial h}{\partial t} + \frac{\partial}{\partial x_2}\left(hV_2\right) = 0 \tag{3a}$$

$$\frac{\partial V_2}{\partial t} + V_2 \frac{\partial V_2}{\partial x_2} + g\frac{\partial h}{\partial x_2} = g\frac{\partial d}{\partial x_2} \tag{3b}$$

$$\frac{\partial V_1}{\partial t} + V_2 \frac{\partial V_1}{\partial x_2} = 0. \tag{3c}$$

The MOST method is a numerical technique of solving system (1) by computing solutions for the next time step of the simplified systems (2) and (3) sequentially.

The first two equations in (2) (and in (3) analogically) can be re-written in terms of Riemann invariants

$$p = V_1 + 2\sqrt{gh},\ \ q = V_1 - 2\sqrt{gh}$$

and eigenvalues $\lambda_{1,2} = V_1 \pm \sqrt{gh}$ as

$$\frac{\partial p}{\partial t} + \lambda_1 \frac{\partial p}{\partial x_1} = g\frac{\partial d}{\partial x_1} \tag{4a}$$

$$\frac{\partial q}{\partial t} + \lambda_2 \frac{\partial q}{\partial x_1} = g\frac{\partial d}{\partial x_1} \tag{4b}$$

Adding equations (4) together simplifies to (2b). Subtracting the two equations simplifies to (2a). Equations (4) and (2c) are the set of equations that are solved in MOST to propagate the solution in the x_1-direction. The corresponding primitive variables V_1 and h are then obtained from the characteristics *p* and *q* as

$$V_1 = (p+q)/2,\ \ h = (p-q)^2/16g, \tag{5}$$

and propagation in the x_2-direction is computed according to (3), with the first two equations being solved in terms of

$$\tilde{p} = V_2 + 2\sqrt{gh},\ \ \tilde{q} = V_2 - 2\sqrt{gh},\ \ \tilde{\lambda}_{1,2} = V_2 \pm \sqrt{gh}.$$

The numerical scheme for solving the characteristic equations (4) in one dimension, with (optionally) varying space step followed by runup on a beach, has been given in Titov and Synolakis (1995). Details of the MOST numerical scheme can also be found in Titov and Synolakis (1998) and Burwell et al. (2007). The MOST model solver is second-order accurate in Δx, except on boundaries.

Two-dimensional extension of the 1-D model in either Cartesian or spherical coordinates is described in Titov and Synolakis (1998) and Titov and González (1997). MOST adaptation to an arbitrary orthogonal curvilinear coordinate system is developed in Tolkova (2008).

6.1.2 Wetting/drying interface

The MOST model inundation algorithm uses a horizontal projection of the water level in the last wet node onto the beach to adjust the length of the last wet cell, as discussed in Titov and Synolakis (1998). As the moving shoreline position steps over a fixed grid node, the algorithm would add or exclude a wet node so the wet area would expand at runup and shrink at rundown. A node is considered dry when the water height at this node is less than a threshold.

6.1.3 Boundary conditions

Two types of boundary conditions are implemented in MOST: totally reflective and totally transparent, as discussed in detail in Titov and Synolakis (1998).

At either boundary, the outgoing Riemann invariant is advanced for the next time step t_n using a 1st order difference scheme applied to the solution at t_{n-1}, while the incoming invariant is specified according to the type of the boundary. It is assumed that the flow is subcritical, and therefore $\lambda_1 > 0$ and the p-invariant propagates to the right, while $\lambda_2 < 0$ and the q-invariant propagates to the left.

On the reflecting left boundary, the p-invariant at the 1st node is set to –q at each time step. This procedure implies $V_1 = 0$ at the 1st node, which sets the reflective wall immediately behind the 1st node.

On the transparent left boundary, the p-invariant is assigned to

$$p_1(t_n) = u_l(t_n) + 2\sqrt{g(d_1 + \eta_l(t_n))}, \tag{6}$$

where d_1 is depth at the 1st node, and u_l and η_l represent external forcing through given velocity and elevation.

In general, values u_l and η_l would not coincide with the solution in the 1st node, except when they are consistent with the value of the outgoing Riemann invariant, that is, satisfying

$$u_l(t_n) - 2\sqrt{g(d_1 + \eta_l(t_n))} = q_1(t_n). \tag{7}$$

The last equation reflects the fact that, for an initial-boundary-value problem in the quadrant $x > 0$, $t > 0$, only one boundary condition (either velocity or elevation) is needed on the t-axis (Mei, 1983).

In particular, if near the left boundary at t_n there is no wave inside the domain propagating toward the boundary, then $q_1(t_n) = -2\sqrt{gd_1}$ and condition (7) defines the velocity of the incoming wave, given its elevation (or vice versa) as:

$$u_l(t_n) = 2\sqrt{g(d_1 + \eta_l(t_n))} - 2\sqrt{gd_1}. \tag{8}$$

In the absence of any inflow through the left boundary, u_l and η_l are set to zero.

Likewise, in the N-th (last) node, the p-invariant at t_n is computed with the solution at t_{n-1} in the last two nodes, while the q-invariant at t_n is set to either $-p_N(t_n)$ (reflective right boundary), or

$$q_N(t_n) = u_r(t_n) - 2\sqrt{g(d_N + \eta_r(t_n))} \tag{9}$$

(transparent right boundary), where d_N is depth at the last node, and u_r and η_r represent forcing through the right boundary. As long as no wave escapes through the right boundary, velocity and elevation in a wave entering the domain from the right satisfy

$$u_r(t_n) = 2\sqrt{gd_N} - 2\sqrt{g(d_N + \eta_r(t_n))}. \tag{10}$$

6.1.4 Numerical dispersion and dissipation in MOST

Designed to solve non-dispersive shallow-water equations, the MOST model nevertheless possesses significant numerical dispersion and, in some cases, dissipation properties for the higher wave numbers. The numerical dispersion can be used to mimic physical dispersion. As shown in Burwell et al. (2007), MOST dispersive and dissipative properties are determined by a single parameter $\beta = V_0 / C$, also referred to as the Courant number, where $V_0 = \sqrt{gd}$ and $C = \Delta x / \Delta t$.

MOST yields the non-dispersive solution traveling at exactly long-wave velocity V_0 only when $\beta = 1$. This is also the edge case, because at $\beta > 1$ the numerical scheme becomes unstable.

When $1/\sqrt{2} < \beta < 1$, the harmonic component with the highest wave number of $\pi / \Delta x$ always travels at phase speed C. At the same time, in this range of β, the components with higher wave numbers are subject to numerical dissipation, which is greater the closer β is to $1/\sqrt{2}$.

When $\beta < 1/\sqrt{2}$, the shortest wave of $2\Delta x$-length always travels with zero phase speed. Numerical dissipation also drops down and remains lower, the smaller the value of β. For $\beta < 0.3$, MOST phase velocities (function of wave number k) are very close to the limit

$$V_k = V_0 \cdot \frac{\sin k\Delta x}{k\Delta x} \tag{11}$$

For well-resolved waves ($k\Delta x << 1$), MOST velocities coincide with Linear Wave Theory (LWT) phase velocities

$$V_k = V_0 \cdot \sqrt{\frac{\tanh kd}{kd}} \tag{12}$$

when $\Delta x = d$, whereas the time step should be just small enough to provide for low β.

Maintaining a specific Δx and Courant number in a basin with variable depth is straightforward in the 1-D case. The grid spacing should vary as $\sqrt{d}$ and the Courant number should be as close as possible to 1, to keep the solution stable, if the objective is to approach a nonlinear shallow water (NSW) solution over the wide range of wave numbers. If, however, the wave is well resolved (containing only low wave numbers), then keeping β close to 1 is not essential. The grid spacing is set equal to depth while the Courant number is kept low, whenever a benchmark test calls for matching laboratory measurements taken in dispersive settings. Emulating LWT dispersion is not possible with finer (spacing less than depth) grids.

6.2 Benchmark problems

The MOST model has been benchmarked against benchmark problems 1, 2, 4–7, and 9, which focus on verifying the simulations of wave propagation and subsequent inundation with laboratory, analytical, and field data. The results are presented below.

6.2.1 BP1: Solitary wave on a simple beach – analytical

The solitary wave on a simple beach problem for BP1 is focused on modeling runup of a non-breaking solitary wave of height *H*, normally incident to a plane sloping beach. The simulation was performed using a 384-node grid, which encompassed a 45*d*-long segment of constant depth *d* connected to a 50*d*-long slope of angle $\beta = \operatorname{arccot}(19.85)$. In simulations, the depth of the flat part of the basin was d = 1 m and the initial wave height was H = 0.0185d. The grid spacing was set to 1 m (depth) over the flat segment, then varied as $\sqrt{d}$, but not less than 0.1*d*. The time increment Δt = 0.03 s provided for β = 0.1. Results with dimension of length are expressed in units of depth; time is expressed in units of $\tau = \sqrt{d / g}$.

Computed time histories of surface elevation at x / d = 0.25 and x / d = 9.95 vs. the analytical solution are shown in Figure 6-1. Water level profiles at t / τ = 35, 45, 55, and 65 are shown in Figure 6-2. Maximum computed runup is 0.08*d*.

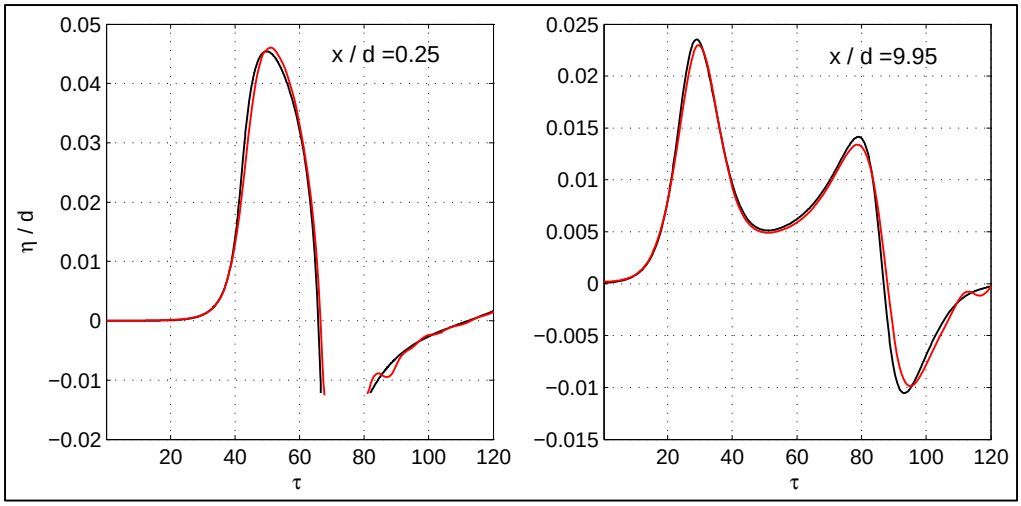

Figure 6-1: Time histories at locations *x/d* = 0.25 (left) and *x/d* = 9.95 (right), analytical NSW solution (black), and numerical solution (red), in dimensionless units.

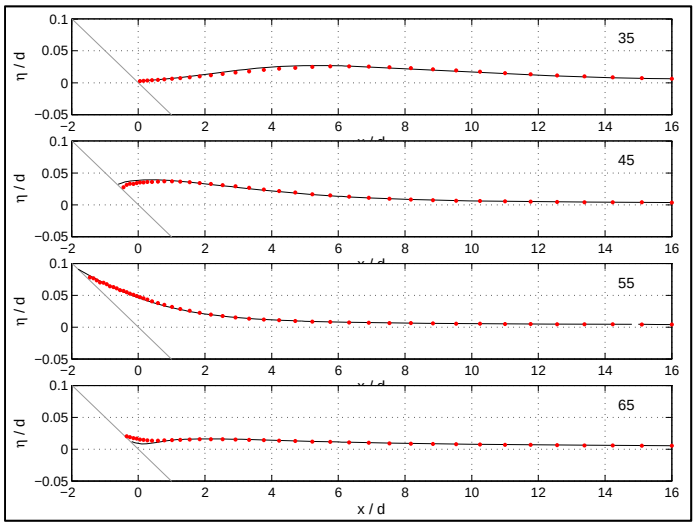

Figure 6-2: Water level profiles at t/τ = 35, 45, 55, and 65: analytical NSW solution (black), and numerical solution in grid nodes (red dots), in dimensionless units.

6.2.2 BP4: Solitary wave on a simple beach – laboratory

This problem is a laboratory counterpart to BP1. It was simulated under the same settings as BP1 for initial wave heights $H = 0.0185d$ and $H = 0.3d$.

Computed water level profiles are shown in Figure 6-3 and Figure 6-4. Maximum computed runup is $0.08d$ for $H/d = 0.0185$, and $0.265d$ for $H/d = 0.3$.

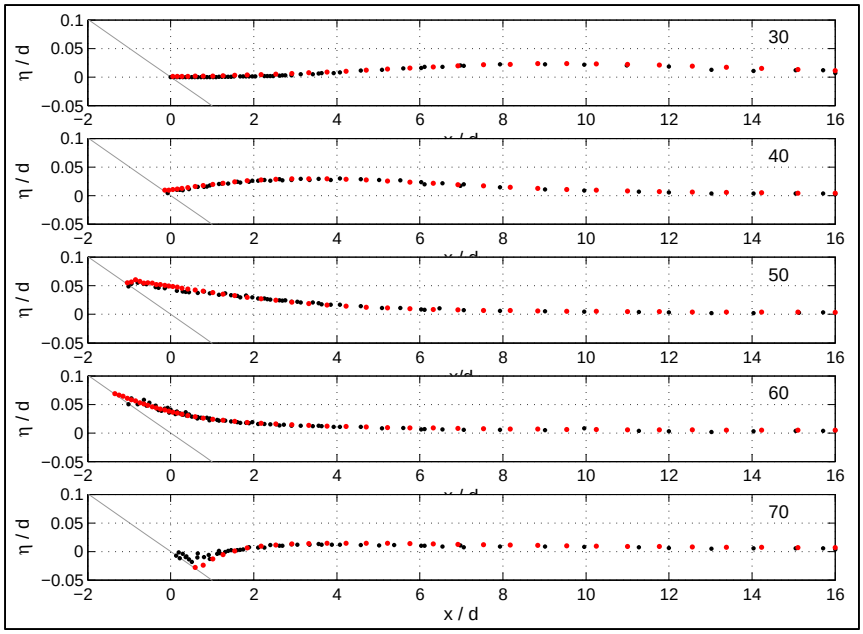

Figure 6-3: Water level profiles for H/d = 0.0185 at t/τ = 30, 40, 50, 60, and 70: measurements (black dots) and numerical solution in grid nodes (red dots), in dimensionless units.

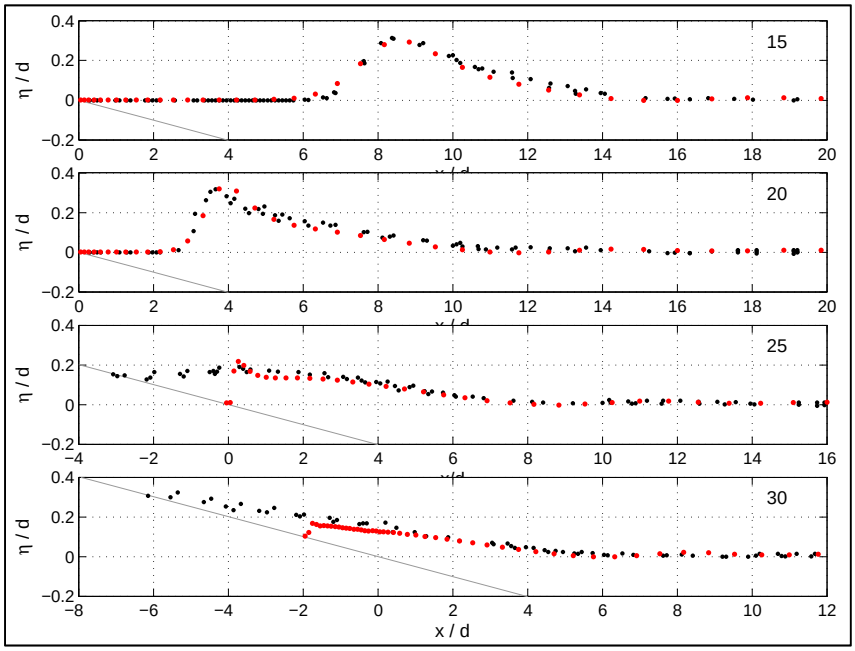

Figure 6-4: Water level profiles for H/d = 0.3 at t/τ = 15, 20, 25, and 30: measurements (black dots) and numerical solution in grid nodes (red dots), in dimensionless units.

6.2.3 BP2/5: Solitary wave on a composite beach – analytical, laboratory

The objective of this benchmark is modeling propagation of incident and reflected solitary waves of different heights (cases A, B, and C) in a basin of complex geometry.

The experiment was modeled as a 1-D problem. The computational domain starts at gauge 4 (whose position x_4 is different among the three cases A, B, and C). The simulation is initiated with the boundary input of $\eta_0(t)$ and $v_0(t)$ at $x = x_4$, where η is taken from an actual record of a direct pulse (prior to 275 s) at the incident gauge. Given η, velocity v is computed according to equation (8).

The grid parameters were selected with the intent to use numerics to mimic physical dispersion; that is, the grid spacing dx equals depth (but is no smaller than 0.05 m), starting with $d = 0.218$ m on the deep end. The resulting grid size was 72 nodes (case A), 66 nodes (case B), and 64 nodes (case C). The time increment was 0.02 s (A), 0.003 s (B), and 0.01 s (C), which kept the Courant number under 0.3 everywhere.

No attempt was made to match the analytical LSW solution because, as can be seen from the figures, nonlinearity affects propagation speed even for the lowest pulse (case A). For this problem, the MOST model does not have a "linear" mode for meaningful comparisons with the LSW solution.

Computed time histories of surface elevation at gauges 4–10 vs. the lab measurements and analytical solutions for the three heights of the incident pulse are shown in Figure 6-5 through Figure 6-7; time histories by the wall are shown in Figure 6-8. The maximum simulated runup at the wall was 2.24 cm / 0.1d (case A), 18.2 cm / 0.84d (case B), and 22.4 cm / 1.03d (case C).

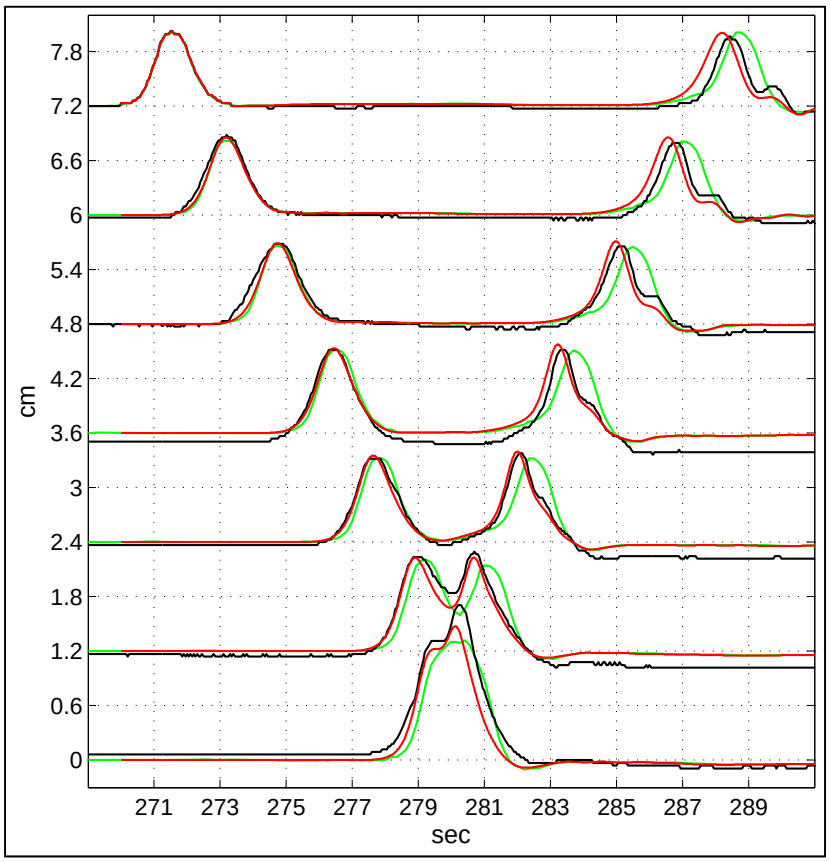

Figure 6-5: Time histories at gauges 4–10 (top to bottom), provided by measurements (black), analytical LSW solution (green), and numerical solution (red). Case A.

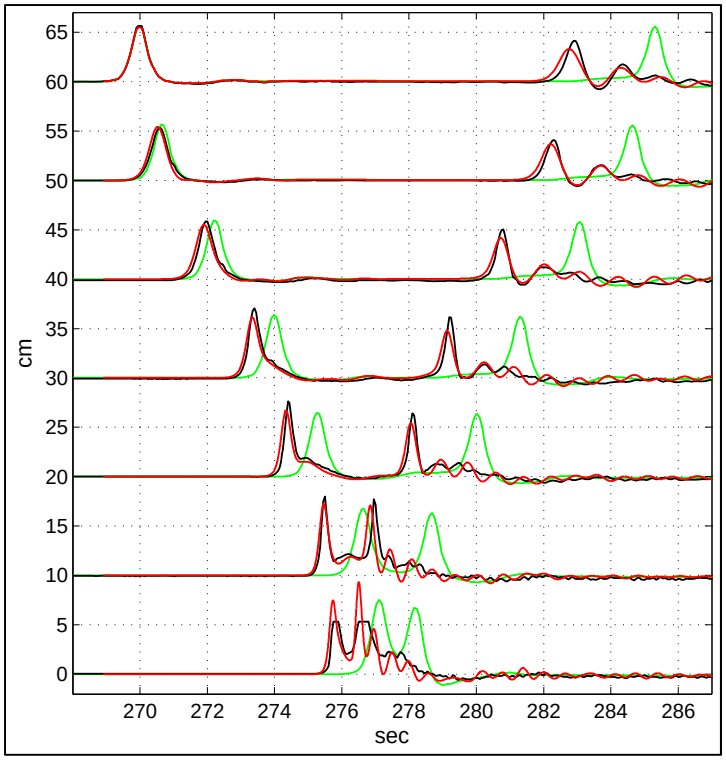

Figure 6-6: Time histories at gauges 4–10 (top to bottom), provided by measurements (black), analytical LSW solution (green), and numerical solution (red). Case B.

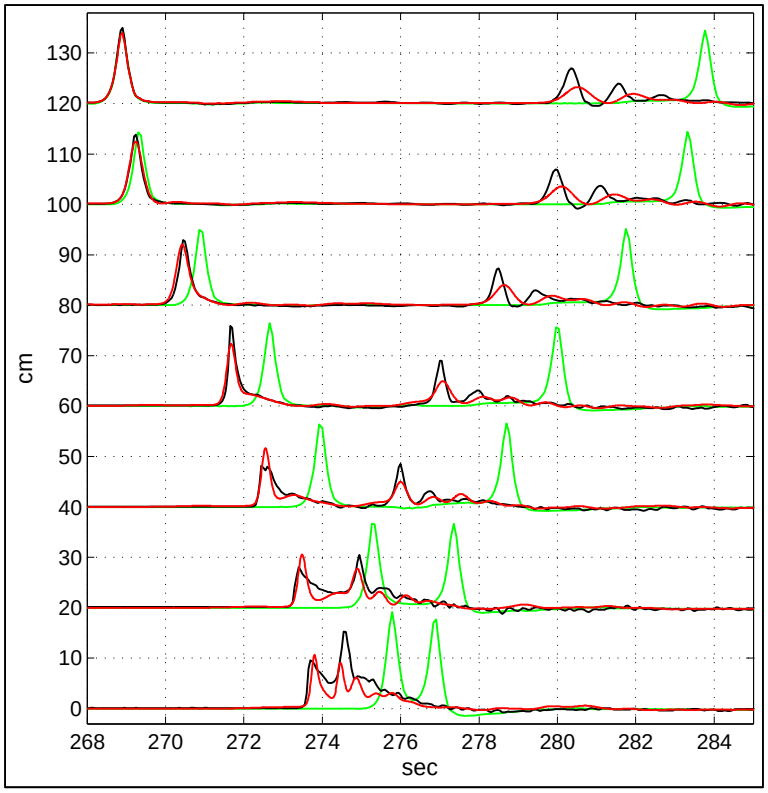

Figure 6-7: Time histories at gauges 4–10 (top to bottom), provided by measurements (black), analytical LSW solution (green), and numerical solution (red). Case C.

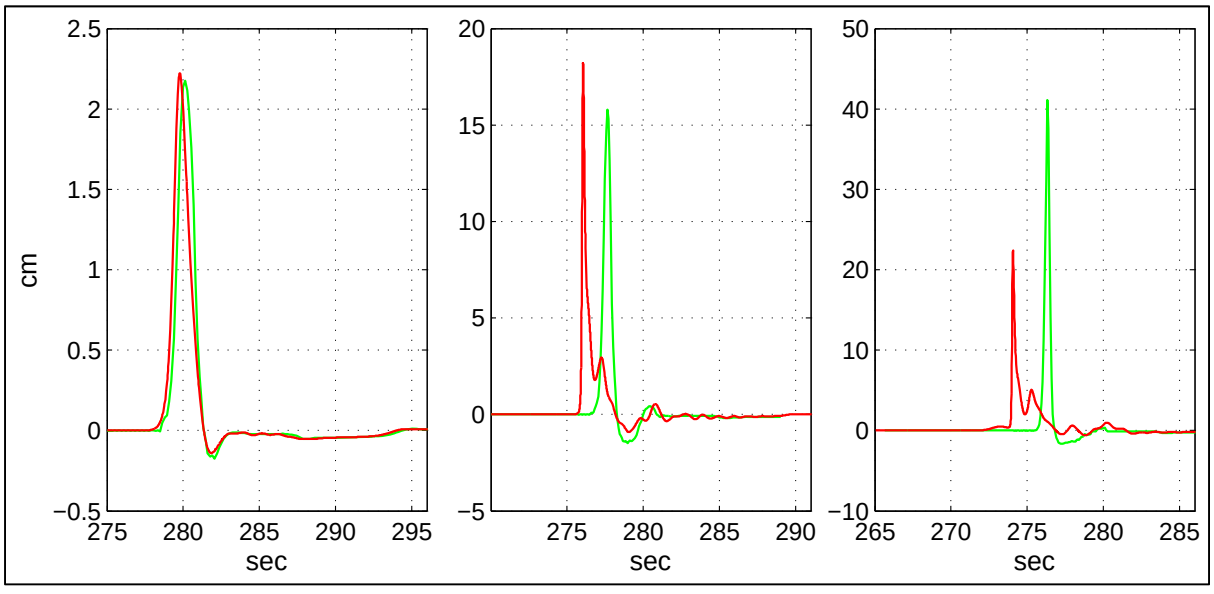

Figure 6-8: Time histories at the wall, provided by analytical LSW solution (green) and numerical solution (red). Left to right: cases A, B, and C.

6.2.4 BP6: Conical island

This benchmark problem was simulated using two nested grids. The outer grid enclosed the entire basin area starting with the wavemaker at $x = 0$. Radiative boundary conditions were applied on the other three sides (basin walls). The size of the grid was 25 m × 30 m, or 84 × 101 nodes at $dx = 30$ cm spacing. The time increment of $dt = 0.01$ s with the depth-equal spacing provided for imitating physical dispersion as the pulse propagates from the wavemaker toward the island.

Boundary input to the domain was provided according to the paddle velocities (computed by differentiating the given paddle trajectory $x(t)$, with some smoothing applied) complemented with elevation computed according to equation (8). The boundary conditions were applied at $x = 0$. Because the paddle stroke was under 30 cm, that is, under the grid cell size in all the cases, no actual reduction in the size of the basin was accounted for. After the stroke was completed (in 158 s in case A, 123 s in case B, and 65 s in case C), reflective boundary conditions were applied at $x = 0$.

Runup onto the island was simulated within a finer 10 m × 10 m grid enclosing the island. Boundary input on the four sides was provided from the outer grid. Two resolutions for the inner grid were considered: 201 × 201 nodes at $dx = 5$ cm spacing and $dt = 0.02$ s time increment, and 401 × 401 nodes at $dx = 2.5$ cm spacing and $dt = 0.01$ s time increment.

Simulated time histories at eight gauges vs. the laboratory measurements for the three cases are shown in Figure 6-9 through Figure 6-11. Time histories at the incident gauges 1–4 were obtained in the outer grid, while those at the gauges around the island (6, 9, 16, and 22) were computed in the inner grid with $dx = 5$ cm resolution. The boundary of the inundated area around the island, computed at 5 and 2.5 cm grid spacing for each of the three cases, is shown in Figure 6-12 through Figure 6-14.

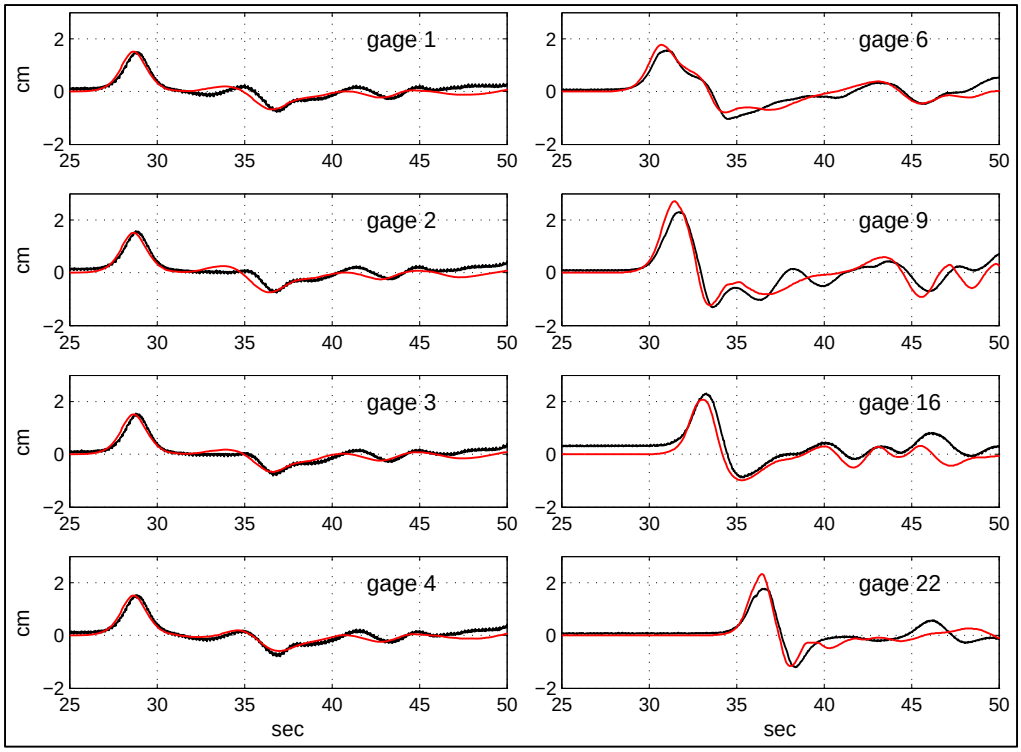

Figure 6-9: Time histories at gauges 1-4, 6, 9, 16, and 22: simulated with MOST (red) and laboratory measurements (black). Case A.

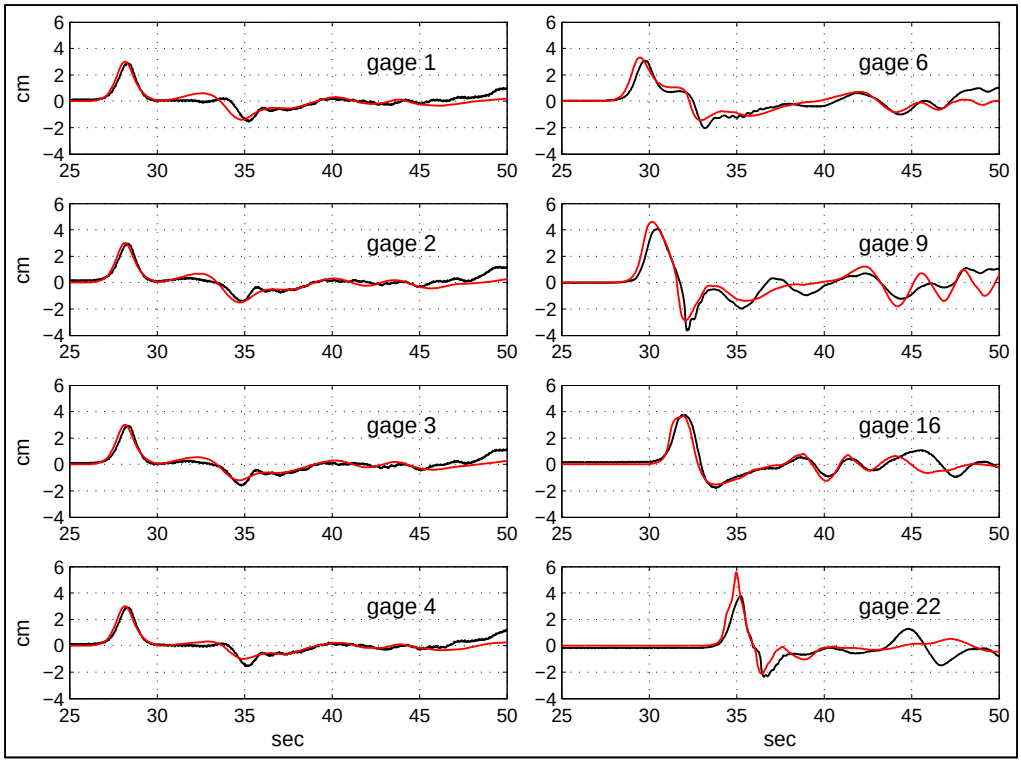

Figure 6-10: Time histories at gauges 1-4, 6, 9, 16, and 22: simulated with MOST (red) and laboratory measurements (black). Case B.

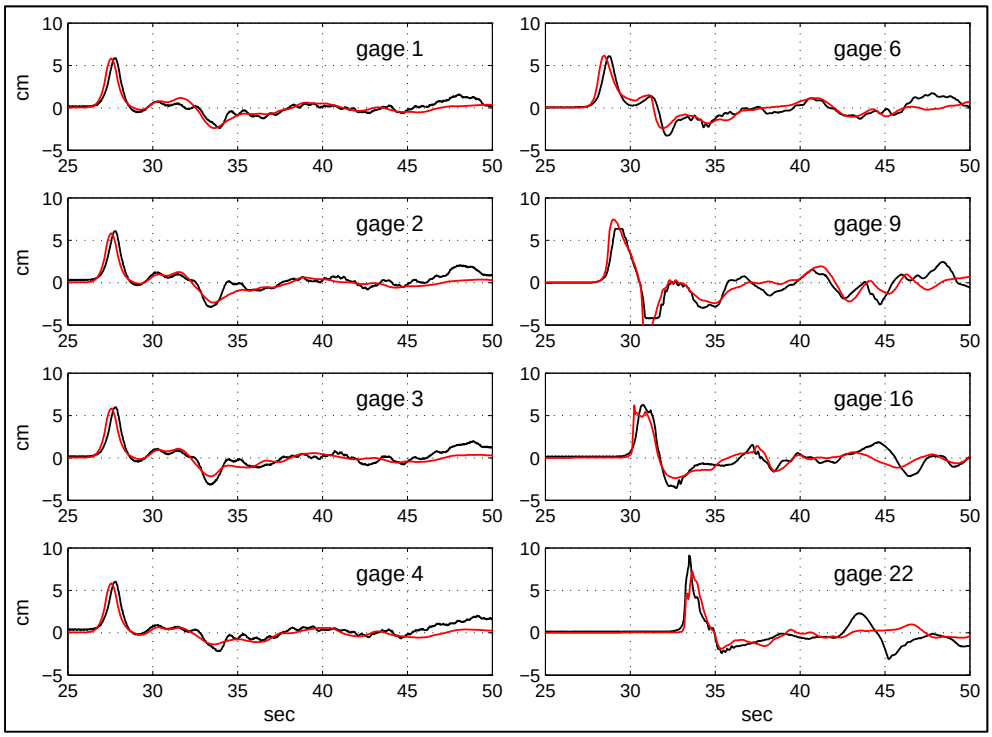

Figure 6-11: Time histories at gauges 1-4, 6, 9, 16, and 22: simulated with MOST (red) and laboratory measurements (black). Case C.

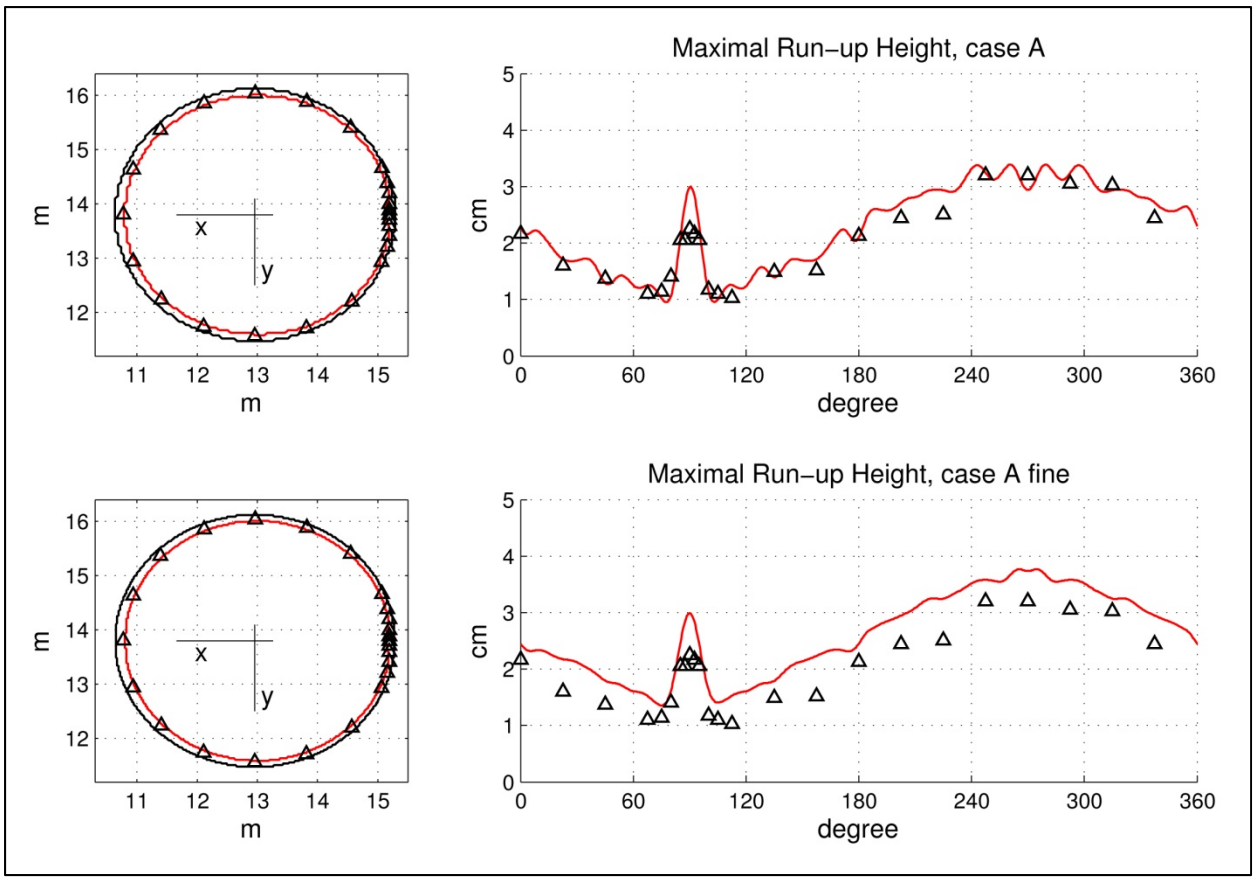

Figure 6-12: Maximum runup height around the island: computed with MOST (red) at dx = 5 cm (top) and dx = 2.5 cm (bottom), and laboratory measurements (black triangles). Case A.

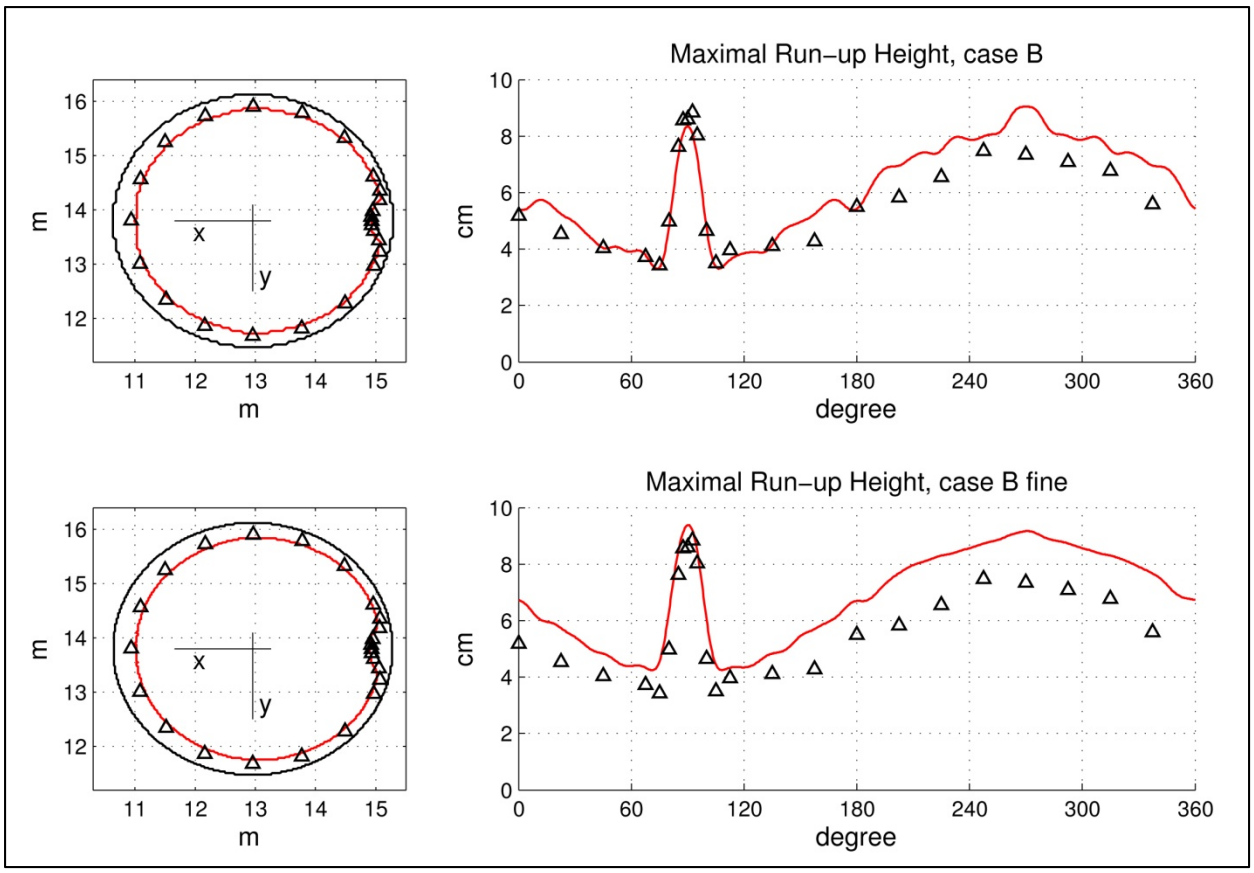

Figure 6-13: Maximum runup height around the island: computed with MOST (red) at dx = 5 cm (top) and dx = 2.5 cm (bottom), and laboratory measurements (black triangles). Case B.

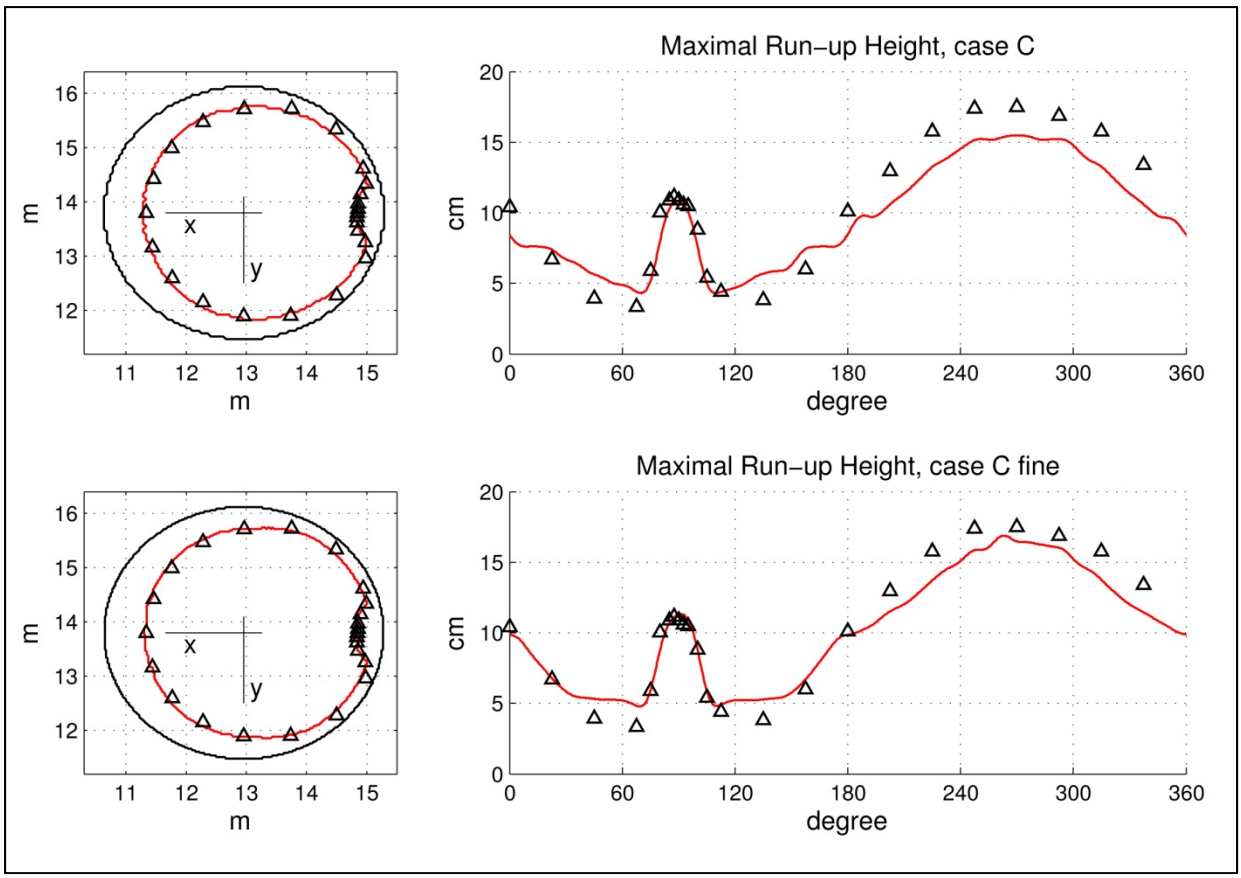

Figure 6-14: Maximum runup height around the island: computed with MOST (red) at dx = 5 cm (top) and dx = 2.5 cm (bottom), and laboratory measurements (black triangles). Case C.

6.2.5 BP7: Runup onto a laboratory model of Monai Beach

Computations were performed with 0.01 s time step using the original grid of 393 × 244 nodes at 1.4 cm spacing, covering the region of 5.488 m × 3.402 m. Reflective walls were imposed at two sides, $y = 0$ and $y = 3.402$. Boundary input into the domain was provided according to the given elevation time history at $x = 0$, complemented with x-direction velocity computed according to (8).

Shown in Figure 6-15 and Figure 6-16 are time histories at the gauges and snapshots of the simulation to be compared with the laboratory data and recordings.

The area shown in the snapshots is 4.6 m $\leq x \leq$ 5.3 m, 1.43 m $\leq y \leq$ 2.3 m, with x-axes pointing up and y-axes pointing left. Twelve isolines are drawn with a 1 cm interval from the original shoreline to 11 cm land elevation. The first snapshot, supposedly corresponding to frame 10 of the video recording, occurs at 16 sec.

The maximum runup computed in the "valley" is 10.4 cm.

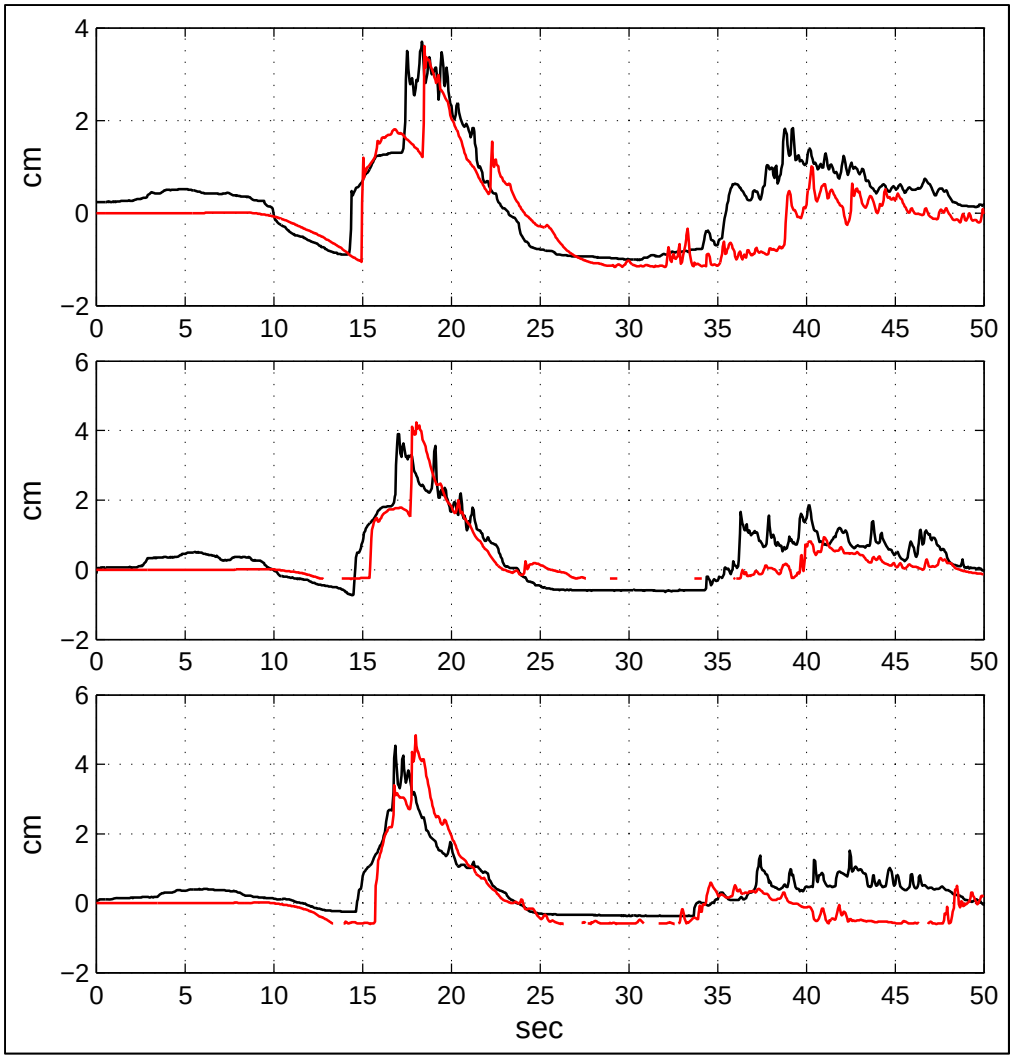

Figure 6-15: Time histories at gauges 5, 7, and 9: simulated with MOST (red) and laboratory measurements.

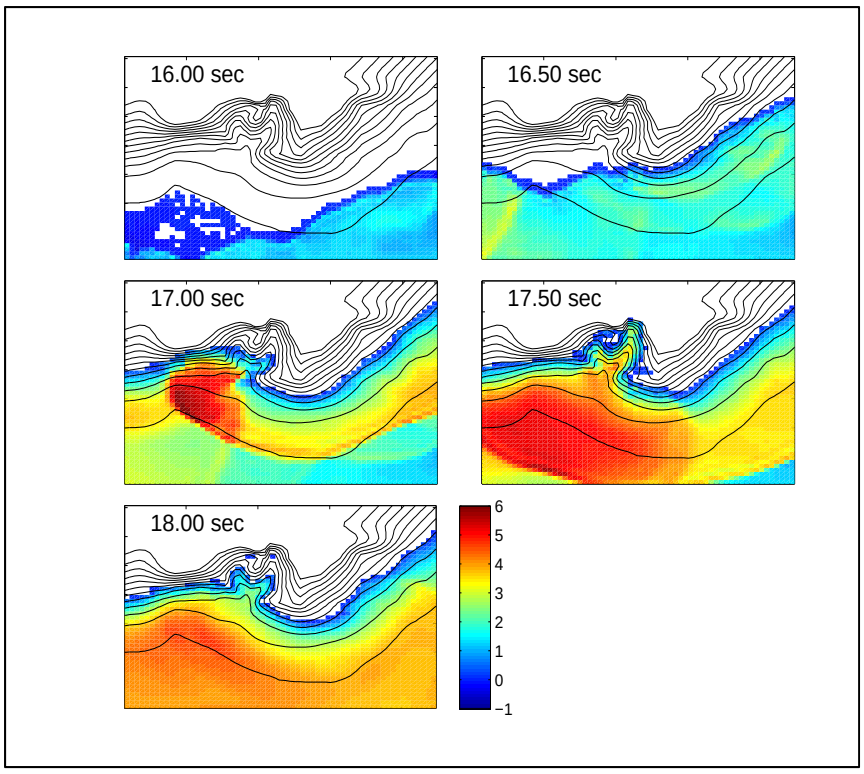

Figure 6-16: Snapshots of computed water surface, to be compared with video frames 10, 25, 40, 55, and 70. The time when each snapshot is taken is shown in the plot. Water elevation is shown with respect to still surface (sea) or with respect to inundated land level. Color scale - cm.

6.2.6 BP9: 1993 Hokkaido-Nansei-Oki (Okushiri tsunami) – field

The set of nested grids to model the Okushiri tsunami is shown in Figure 6-17. The set comprises:

- Grid A: 566 (lat) × 356 (lon) node grid with a space increment of 30 arc sec of the Great Circle, or 30 arc sec in latitude and 40.3 arc sec in longitude, interpolated from OK24.xyz. Simulated with a time increment of 4 s.
- Grid B: 224 (lat) × 307 (lon) node grid with a space increment of 10 arc sec of the Great Circle, in rotated spherical coordinates, interpolated from OK08.xyz. Simulated with a time increment of 1.5 s. Enclosed in grid A.
- Grid C: 660 (lat) × 387 (lon) node grid enclosing Okushiri Island with a space increment of 1.5 arc sec of the Great Circle, interpolated from OK03.xyz. Simulated with a time increment of 0.3 s. Enclosed in grid B.
- Grid Da: 280 (lat) × 220 (lon) node grid around the southern tip of Okushiri with a space increment of 15 m, cut from AO15.xyz. Simulated with a time increment of 0.5 s. Enclosed in grid C.
- Grid Dm: 252 (lat) × 255 (lon) node grid around the southern tip of Okushiri with a space increment of 6 m, cut from MB05.xyz. Simulated with a time increment of 0.2 s. Enclosed in grid C.

In all cases, the Manning friction coefficient $n = 0.03$ was used.

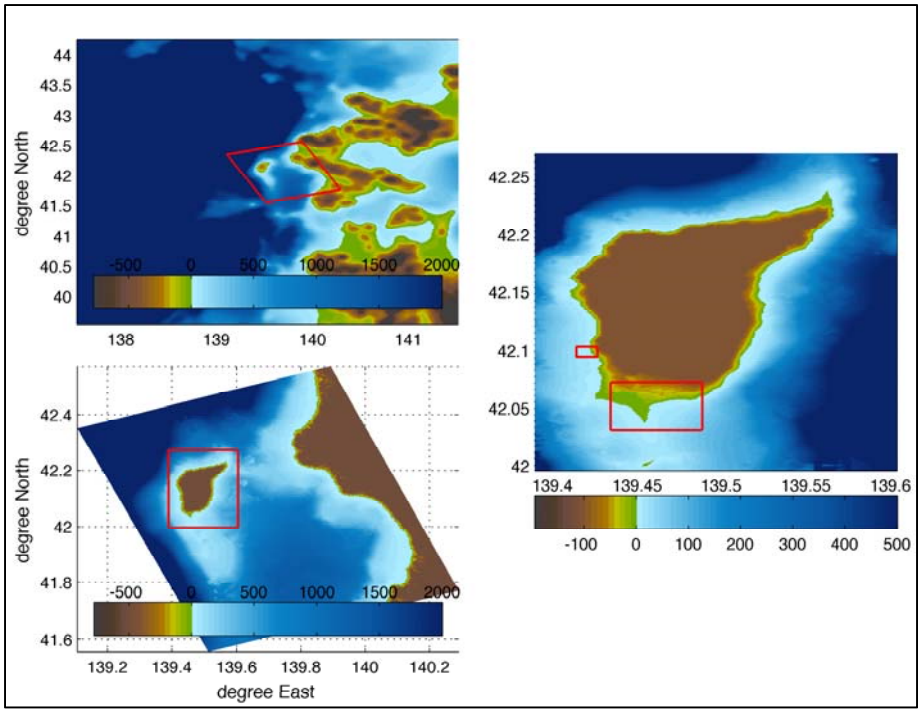

Figure 6-17: Top left: grid A with grid B contour shown in red. Bottom left: grid B with grid C contour shown in red. Right: grid C with contours of grids Da and Dm shown in red. Color scale - m.

6.2.6.1 Tsunami arrival at Aonae

According to the simulation using three nested grids (A, B, and C), the first wave arrives at Aonae from the west 5 min after the earthquake. The second wave comes from the east 9 min after the first wave. Figure 6-18 shows sea surface snapshots and corresponding flow fields at the maxima of the first and second waves at the southern tip of Okushiri.

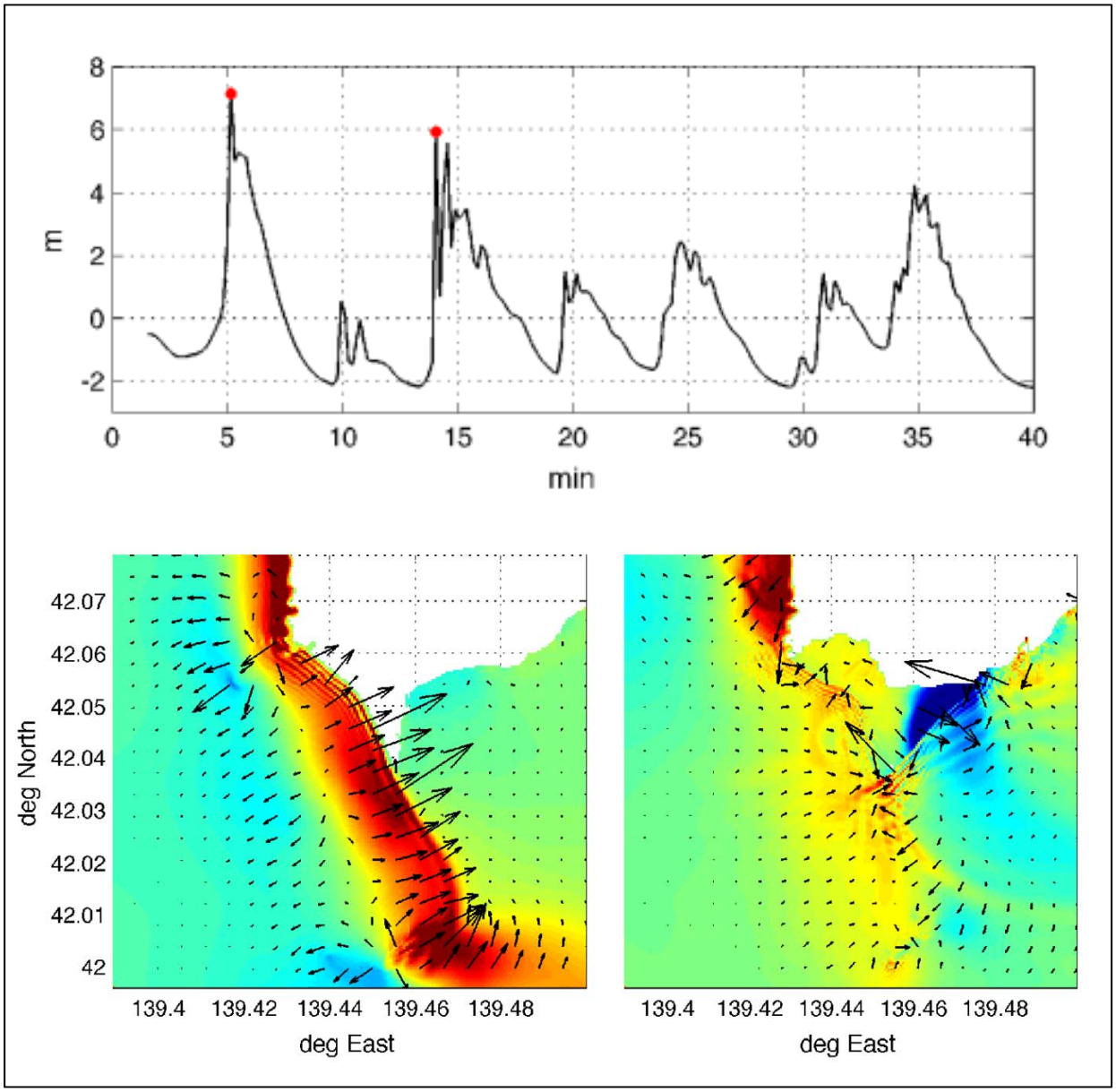

Figure 6-18: Top: simulated time history at the southern tip of Okushiri Island; red dots mark wave phases at which snapshots below were taken. Bottom: snapshot of the sea surface displacement / water height over inundated land (color) and the velocity field (arrows), 5 min (left) and 14 min (right) after the earthquake. Color scale - m.

6.2.6.2 Comparison at Iwanai and Esashi tide gauges

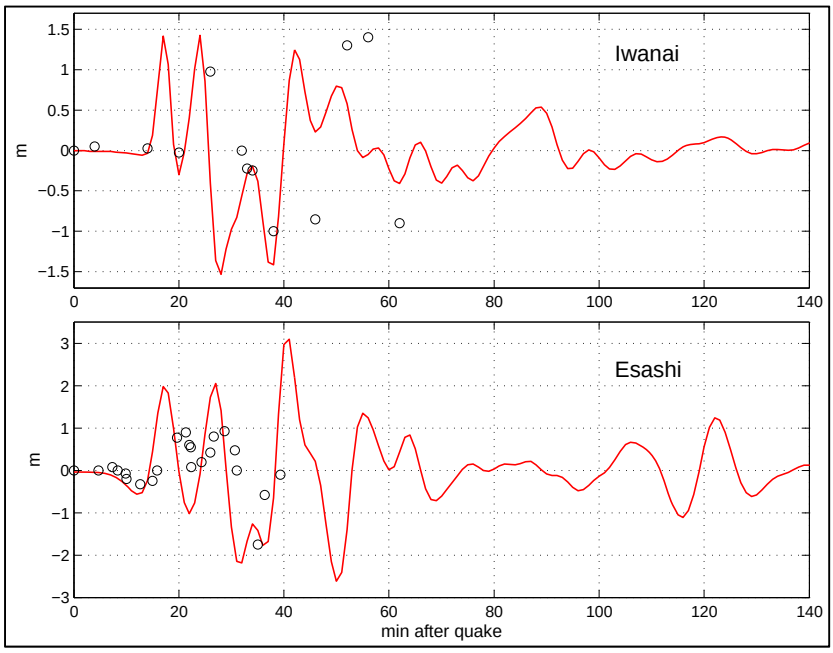

Figure 6-19: Computed water level at Iwanai and Esashi tide gauges (red) vs. measurements (black circles).

6.2.6.3 Runup distribution

Runup was computed as the maximal modeled water height over land added to the land elevation, with respect to sea level. Runup around Okushiri Island was modeled with nested A, B, and C grids. The solution in the Aonae and Monai areas was refined with the use of a fourth nested grid, Da or Dm, respectively.

Maximum modeled runup height obtained at Hamatsumae (139.4728°E, 42.0622°N) was 10.5 m, in Monai valley, 17.1 m, and in Aonae, 15.5 m.

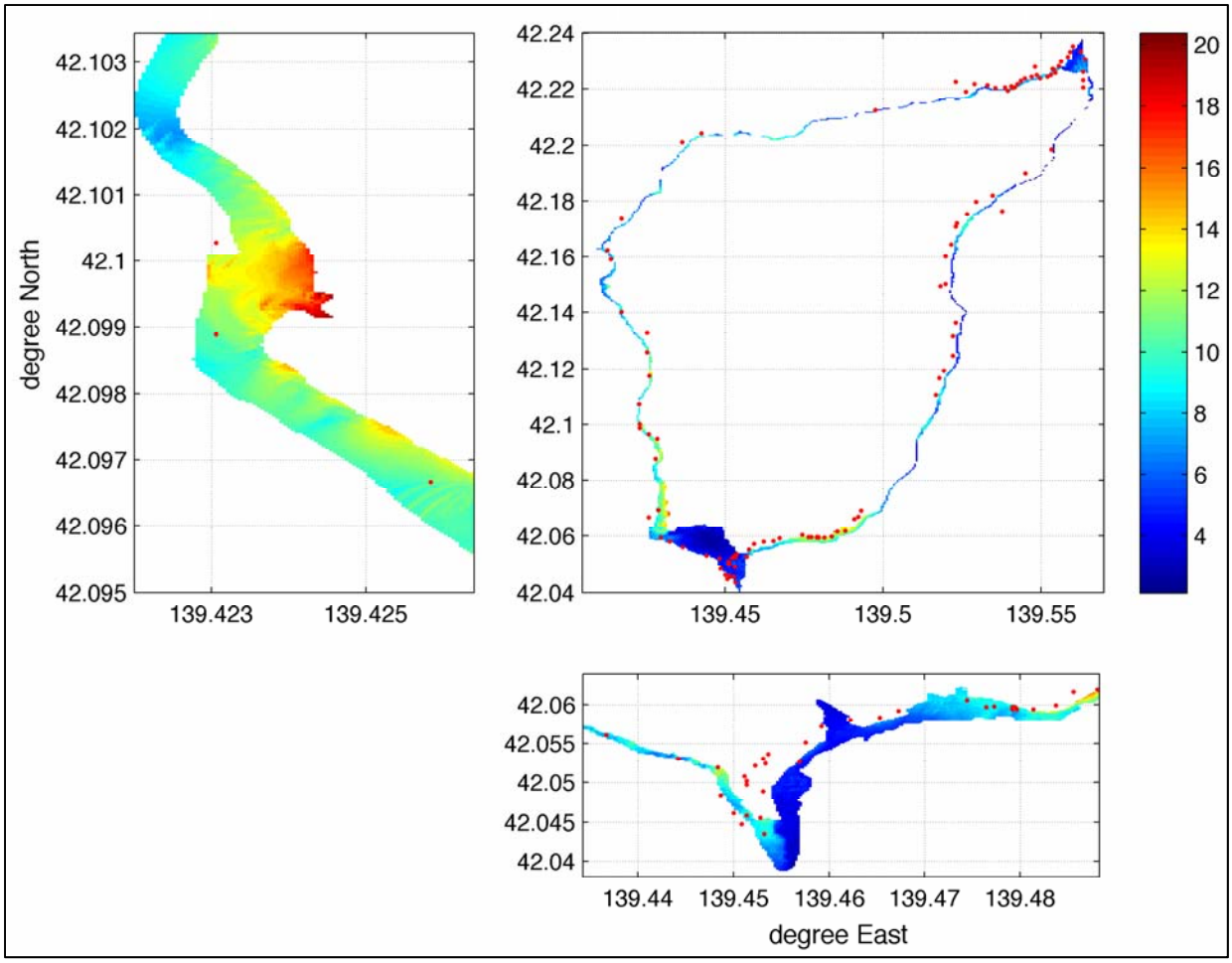

Figure 6-20: Maximum modeled runup distribution around Okushiri Island (center pane), Aonae area (bottom), Monai area (left). Red dots show locations of field measurements (0.01° was subtracted from the latitude vector). Color scale – m.

6.3 Proposed benchmark problem: test for tolerance to depth discontinuities

6.3.1 Objectives

The appropriateness of representing differential equations with various difference schemes is based on the assumption that the physical variables do not change significantly within the sampling intervals in space and time. However, in tsunami propagation applications, the ocean depth supplied by digital elevation models can undergo large changes between neighboring nodes. This suggested exercise aims to verify the correct operation of the tsunami model in the basin with abrupt depth changes.

6.3.2 Preliminaries

Let us consider the evolution of a pulse in a one-dimensional basin with depth $D(x)$ composed of three flat segments:

$$D(x) = \{\mathrm{d\_1}, \mathrm{x} < -L/2; \mathrm{d}, -L/2 < \mathrm{x} < L/2; d\_2, \mathrm{x} > L/2\} \quad (13)$$

Initially, the pulse $\eta_0(x)$ is localized in the central segment. Its evolution in the central segment can be described as a sequence of partial reflections at $x = \pm L/2$ (see Figure 6-21). Thus the solution in the central segment is identical to the solution for a series $\eta_0(x)$ of pulses centered at $x = 0, \pm L, \pm 2L, \pm 3L, \ldots$ propagating over the constant depth *d*:

$$\tilde{\eta}_0(x) = \eta_0(x) + \sum_{k\geq 1} R_1^k R_2^k \left(\eta_0(x-2kL) + \eta_0(x+2kL)\right) + \sum_{k\geq 1} R_1^{k-1} R_2^{k-1} \left(R_2\eta_0(x-(2k-1)L) + R_1\eta_0(x+(2k+1)L)\right) \quad (14)$$

where R_1 and R_2 are the amplitude reflection coefficients on the left and right discontinuity. The corresponding time history at $x = 0$, for a symmetric pulse, is:

$$\tilde{s}(\tau) = \eta_0\left(L\tau\right) + \sum_{k\geq 1} R_1^k R_2^k \eta_0\left(L\left(\tau - 2k\right)\right) + \sum_{k\geq 1} R_1^{k-1} R_2^{k-1} (R_1 + R_2)\eta_0\left(L\left(\tau - (2k-1)\right)\right) \quad (15)$$

where $\tau = t/T$, $T = L/\sqrt{gd}$, g being the gravity acceleration.

In the shallow-water approximation, the reflection coefficients are:

$$R_1 = \frac{\sqrt{d} - \sqrt{d_1}}{\sqrt{d} + \sqrt{d_1}}, \quad R_2 = \frac{\sqrt{d} - \sqrt{d_2}}{\sqrt{d} + \sqrt{d_2}} \quad (16)$$

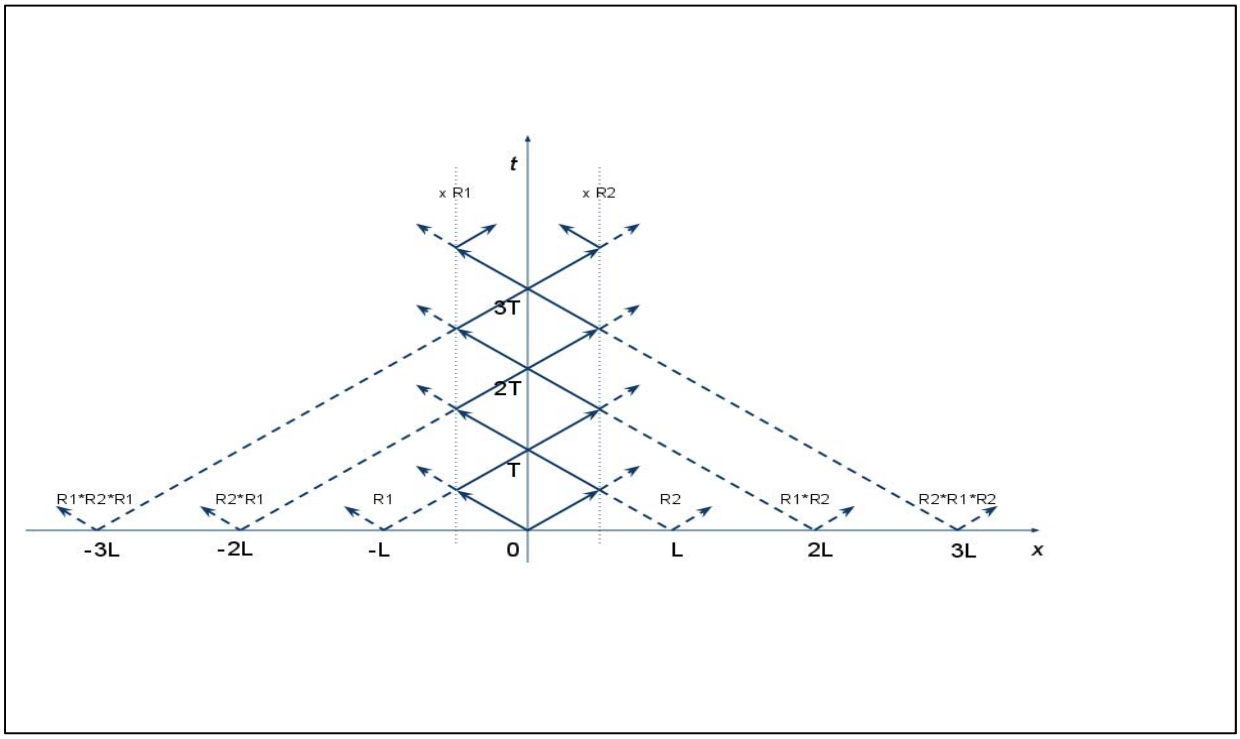

Figure 6-21: Pulse trajectory in x-t plane.

6.3.3 Procedure

- For a given pulse $\eta_0(x)$ localized within the central segment, model its evolution over the depth (13).

- Under the same computational settings, model the evolution of (14) over the constant depth *d*.
- Compare the solutions in the central segment, in particular the time histories at $x = 0$.

Comment: comparing the model outputs as above, rather than comparing a model output to the analytical solution (15), ensures that the discrepancies between the solutions are only due to reflections in the first solution. Other numerical artifacts, if any, contribute equally to both model outputs.

6.3.4 MOST example

The next example illustrates the suggested test performed with the MOST model, with d_1 set equal to d_2, and, consequently, $R_1 = R_2 = R$. Four cases were considered, representing different ratios of the outer depths (d_1) to the depth of the central segment (d) in the segmented basin: $d_1/d =$ 0.8, 0.6, 0.4, 0.2. Figure 6-22 shows the corresponding pulse series (14) whose propagation over the constant depth d in the flat basin is to be modeled. Ideally, within the central segment, the solution for a single pulse in the segmented basin (13) should coincide with the solution for the corresponding pulse series in the flat basin.

As seen in Figure 6-23, in the first three cases, the MOST model reproduced the theoretical reflection very closely. In the last case, representing the largest change in depth, the MOST model over-estimated the amplitude of the reflected wave.

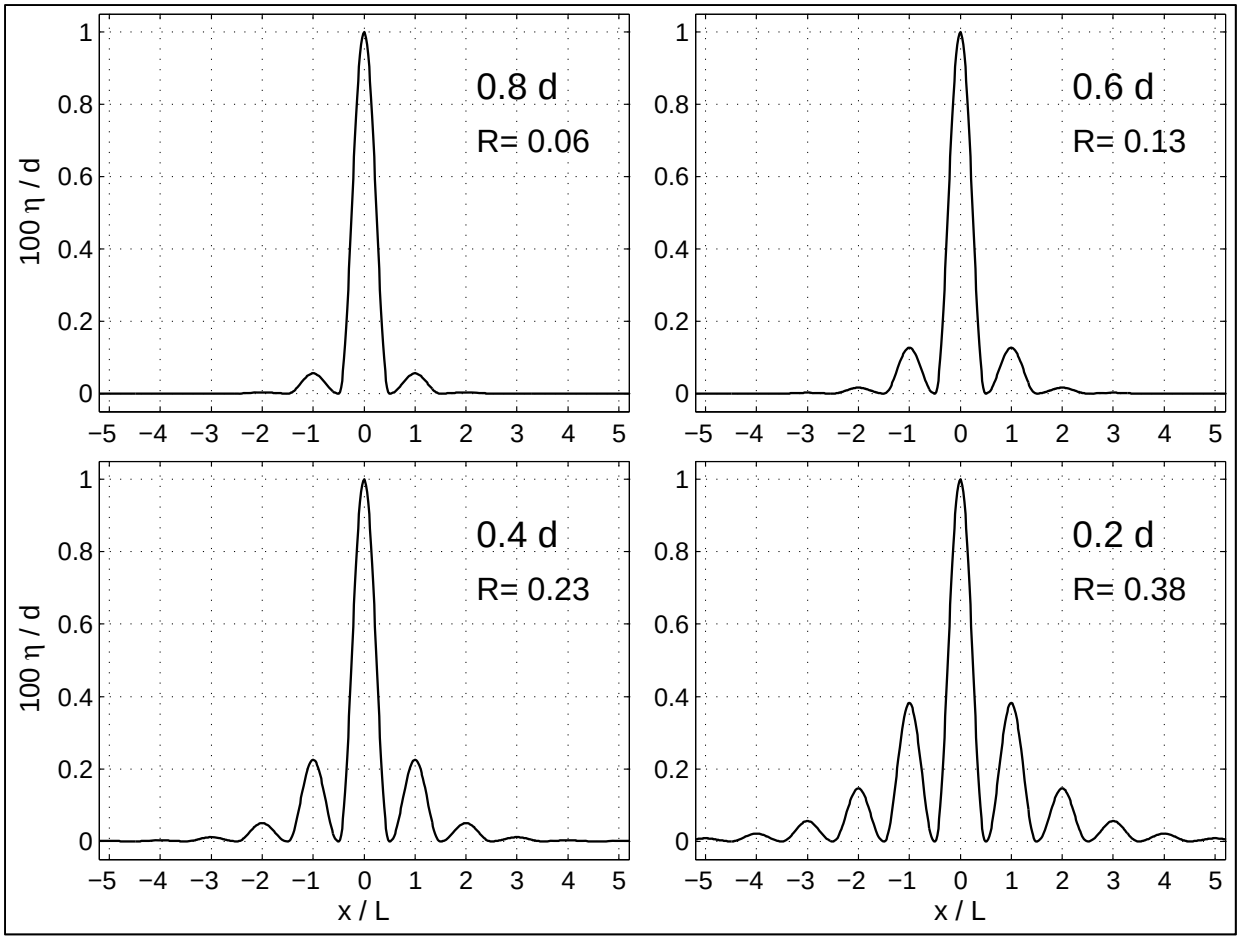

Figure 6-22: Corresponding pulse series (14) whose propagation over the constant depth d in the flat basin was modeled by MOST.

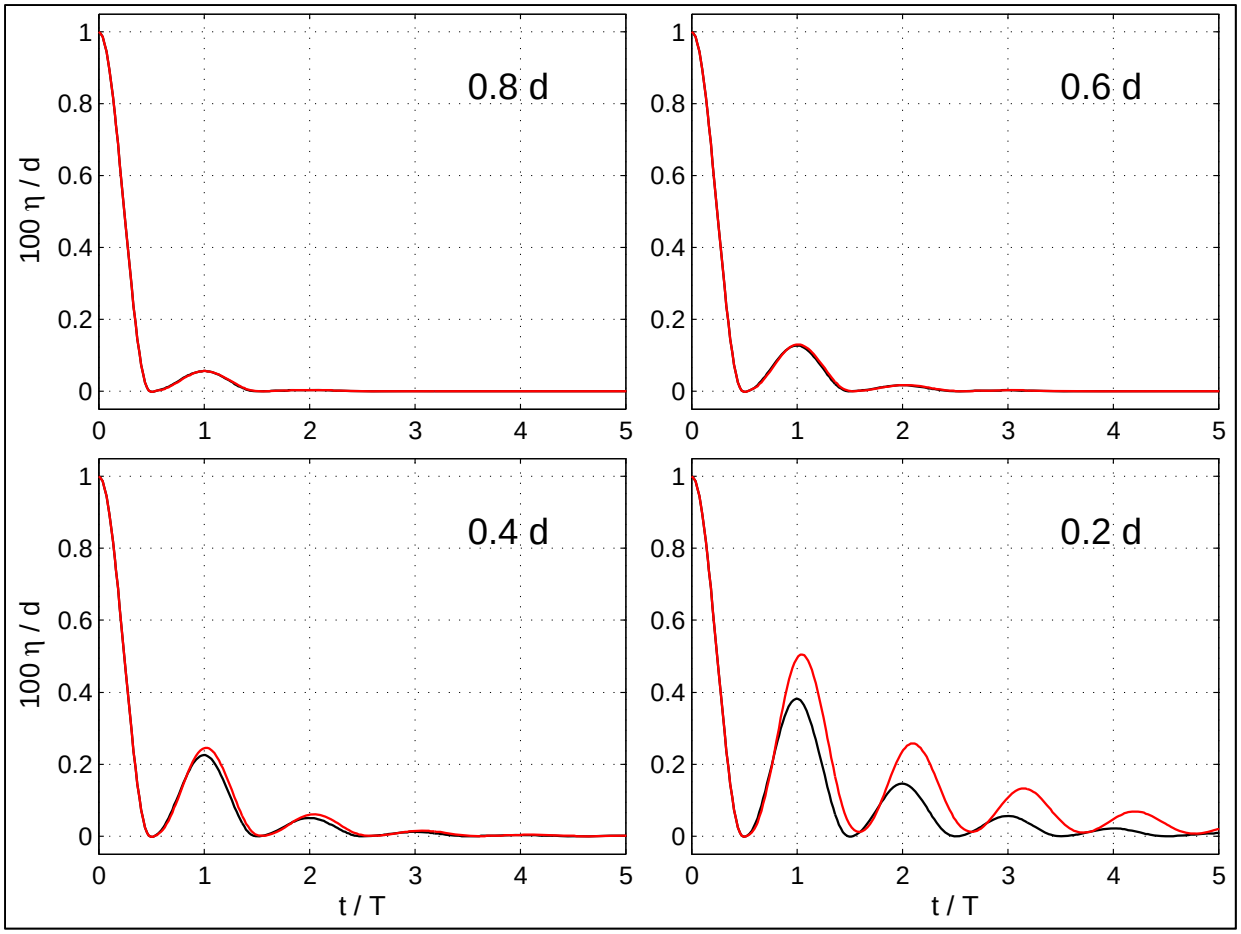

Figure 6-23: Time histories at $x = 0$ of the evolution of a single pulse in a basin (13) for $d_1 = d_2 = 0.8d$, 0.6d, 0.4d, 0.2d (red) and that of the corresponding pulse series over the flat bottom (black).

6.4 References

Burwell D, Tolkova E, Chawla A. 2007. Diffusion and dispersion characterization of a numerical tsunami model. *Ocean Modelling*, 19(1–2), 10–30, doi:10.1016/j.ocemod.2007.05.003.

Durran DR. 1999. Numerical Methods for Wave Equations in Geophysical Fluid Dynamics. Springer-Verlag, New York, Berlin, Heidelberg. 465 pp.

Gica E, Spillane MC, Titov VV, Chamberlin CD, Newman JC. 2008. Development of the forecast propagation database for NOAA's Short-Term Inundation Forecast for Tsunamis (SIFT), NOAA Tech. Memo. OAR PMEL-139, 89 pp.

Percival DB, Arcas D, Denbo DW, Eble MC, Gica E, Mofjeld HO, Spillane MC, Tang L, Titov VV. 2009. Extracting tsunami source parameters via inversion of DART® buoy data. NOAA Tech. Memo. OAR PMEL-144, 22 pp.

Mei CC. 1983. The Applied Dynamics of Ocean Surface Waves. John Wiley & Sons, New York, Chichester, Brisbane, Toronto, Singapore. 740 pp.

Tang L, Titov VV, Chamberlin CD. 2009. Development, testing, and applications of site-specific tsunami inundation models for real-time forecasting. *J. Geophys. Res.*, 114, C12025, doi:10.1029/2009JC005476.

Titov VV. 2009. Tsunami forecasting. Chapter 12 in The Sea, Volume 15: Tsunamis. Harvard University Press, Cambridge, MA and London, England, 371-400.

Titov VV, Synolakis CE. 1995. Modeling of breaking and nonbreaking long-wave evolution and runup using VTCS-2. *J. Waterw. Port Coast. Ocean Eng.*, 121(6), 308–316.

Titov VV, González FI. 1997. Implementation and testing of the Method of Splitting Tsunami (MOST) model. NOAA Tech. Memo. ERL PMEL-112, NTIS: PB98-122773, NOAA/Pacific Marine Environmental Laboratory, Seattle, WA, 11 pp.

Titov VV, Synolakis CE. 1998. Numerical modeling of tidal wave runup. *J. Waterw. Port Coast. Ocean Eng.*, 124(4), 157–171.

Tolkova E. 2008. Curvilinear MOST and its first application: Regional Forecast version 2. In: Burwell D and Tolkova E, Curvilinear version of the MOST model with application to the coast-wide tsunami forecast. NOAA Tech. Memo. OAR PMEL-142, Part 2, 28 pp.

Wei Y, Bernard E, Tang L, Weiss R, Titov V, Moore C, Spillane M, Hopkins M, Kanoglu U. 2008. Real-time experimental forecast of the Peruvian tsunami of August 2007 for U.S. coastlines. *Geophys. Res. Lett.*, 35, L04609, doi: 10.1029/2007GL032250.

Yanenko NN. 1971. The Method of Fractional Steps. Translated from Russian by M. Holt. Springer, New York, Berlin, Heidelberg.

7 NEOWAVE

Yoshiki Yamazaki, Kwok Fai Cheung, Zygmunt Kowalik, Thorne Lay, and Geno Pawlak

Yoshiki Yamazaki, Kwok Fai Cheung, Geno Pawlak: Department of Ocean and Resources Engineering, University of Hawaii at Manoa, Honolulu, Hawaii

Zygmunt Kowalik: Institute of Marine Science, University of Alaska, Fairbanks, Alaska

Thorne Lay: Department of Earth and Planetary Sciences, University of California Santa Cruz, Santa Cruz, California

7.1 Model description

NEOWAVE (Non-hydrostatic Evolution of Ocean WAVEs) is a shock-capturing, dispersive model in the spherical coordinate system for tsunami generation, basin-wide evolution and coastal inundation and runup using two-way nested computational grids (Yamazaki et al., 2011). The depth-integrated model describes dispersive waves through the non-hydrostatic pressure and vertical velocity, which also account for tsunami generation from kinematic seafloor deformation. The semi-implicit, staggered finite difference model captures flow discontinuities associated with bores or hydraulic jumps through the momentum-conserved advection scheme with an upwind flux approximation (Yamazaki et al., 2009). A two-way grid-nesting scheme utilizes the Dirichlet condition of the non-hydrostatic pressure and both the horizontal velocity and surface elevation at the inter-grid boundary to ensure propagation of dispersive waves and discontinuities across computational grids of different resolution.

7.1.1 Theoretical formulation

NEOWAVE utilizes a spherical coordinates system (λ, ϕ, z), in which λ is longitude, ϕ is latitude, and z denotes normal distance from the ocean surface, to model basin-wide propagation and coastal inundation of tsunamis. Figure 7-1 provides a schematic of the free-surface flow generated by seafloor deformation. The boundary conditions at the free surface and seafloor facilitate the depth-integration of the Euler equations. The flow depth D is the distance between the two boundaries defined as

$$D = \zeta + (h - \eta) \tag{1}$$

where ζ is the surface elevation from the still-water level, h is the water depth, and η is the seafloor displacement.

The depth-integrated, non-hydrostatic governing equations, which include the λ, ϕ, and z momentum equations as well as the continuity equation, are

$$\frac{\partial U}{\partial t} + \frac{U}{R\cos\phi}\frac{\partial U}{\partial \lambda} + \frac{V}{R}\frac{\partial U}{\partial \phi} - \left(2\Omega + \frac{U}{R\cos\phi}\right)V\sin\phi = -\frac{g}{R\cos\phi}\frac{\partial \zeta}{\partial \lambda}$$

$$-\frac{1}{2}\frac{1}{R\cos\phi}\frac{\partial q}{\partial\lambda}-\frac{1}{2}\frac{q}{DR\cos\phi}\frac{\partial(\zeta-h+\eta)}{\partial\lambda}-n^2\frac{g}{D^{1/3}}\frac{U\sqrt{U^2+V^2}}{D} \tag{2}$$

$$\frac{\partial V}{\partial t}+\frac{U}{R\cos\phi}\frac{\partial V}{\partial\lambda}+\frac{V}{R}\frac{\partial V}{\partial\phi}+\left(2\Omega+\frac{U}{R\cos\phi}\right)U\sin\phi=-\frac{g}{R}\frac{\partial\zeta}{\partial\phi}$$

$$-\frac{1}{2}\frac{1}{R}\frac{\partial q}{\partial\phi}-\frac{1}{2}\frac{q}{DR}\frac{\partial(\zeta-h+\eta)}{\partial\phi}-n^2\frac{g}{D^{1/3}}\frac{V\sqrt{U^2+V^2}}{D} \tag{3}$$

$$\frac{\partial W}{\partial t}=\frac{q}{D} \tag{4}$$

$$\frac{\partial(\zeta-\eta)}{\partial t}+\frac{1}{R\cos\phi}\frac{\partial(UD)}{\partial\lambda}+\frac{1}{R\cos\phi}\frac{\partial(V\cos\phi D)}{\partial\phi}=0 \tag{5}$$

where U, V, and W are depth-averaged velocity components in the λ, ϕ, and z directions; q is the non-hydrostatic pressure at the seafloor; g is acceleration due to gravity; and n is Manning's coefficient accounting for surface roughness. Because of the assumption of a linear distribution, W is the average value of the vertical velocity at the free surface and seafloor given by the simplified kinematic boundary conditions:

$$w=\frac{\partial\zeta}{\partial t}+\frac{U}{R\cos\phi}\frac{\partial\zeta}{\partial\lambda}+\frac{V}{R}\frac{\partial\zeta}{\partial\phi} \qquad \text{at } z=\zeta \tag{6}$$

$$w=\frac{\partial\eta}{\partial t}-\frac{U}{R\cos\phi}\frac{\partial(h-\eta)}{\partial\lambda}-\frac{V}{R}\frac{\partial(h-\eta)}{\partial\phi} \quad \text{at } z=-h+\eta \tag{7}$$

Equations (6) and (7) describe the average vertical velocity W as a function of U, V, ζ, and η to close the depth-integrated governing equations for non-hydrostatic flows.

The depth-integrated non-hydrostatic equations describe wave dispersion through the non-hydrostatic pressure and vertical velocity. Although the basic assumptions are consistent with those in the classical Boussinesq equations of Peregrine (1967), the dispersion characteristics differ due to the variables employed and truncation of terms in the derivation of the governing equations. The linearized, depth-integrated, non-hydrostatic governing equations in the x direction read:

$$\frac{\partial U}{\partial t}+g\frac{\partial\zeta}{\partial x}+\frac{1}{2}\frac{\partial q}{\partial x}-\frac{1}{2}\frac{q}{h}\frac{\partial h}{\partial x}=0 \tag{8}$$

$$\frac{\partial}{\partial t}\left(\frac{w_\zeta+w_{-h}}{2}\right)-\frac{q}{h}=0 \tag{9}$$

$$\frac{\partial\zeta}{\partial t}+h\frac{\partial U}{\partial x}=0 \tag{10}$$

where w_ζ and w_{-h} denote the vertical velocity at the free surface and the seafloor. The one-dimensional kinematic conditions on the free surface and the seafloor are given by

$$w_\zeta=\frac{\partial\zeta}{\partial t}+U\frac{\partial\zeta}{\partial x} \tag{11}$$

$$w_{-h} = -U\frac{\partial h}{\partial x} \tag{12}$$

The non-hydrostatic pressure q in terms of ζ and U can be obtained from the vertical momentum equation (8) by substitution of the kinematic boundary conditions (11) and (12). The resulting governing equations for constant water depth become

$$\frac{\partial U}{\partial t} + g\frac{\partial \zeta}{\partial x} + \frac{1}{4}h\frac{\partial^3 \zeta}{\partial t^2 \partial x} = 0 \tag{13}$$

$$\frac{\partial \zeta}{\partial t} + h\frac{\partial U}{\partial x} = 0 \tag{14}$$

Following Madsen et al. (1991) and Nwogu (1993), the linear dispersive relation is derived by considering a system of small amplitude periodic waves in the form:

$$\zeta = \zeta_0 e^{ik(x-ct)} \tag{15}$$

$$U = U_0 e^{ik(x-ct)} \tag{16}$$

where k and c denote the wave number and celerity. Substitution of (15) and (16) into the linearized depth-integrated, non-hydrostatic equations (13) and (14) yields the dispersion relation:

$$c^2 = \frac{gh}{1 + \frac{1}{4}(kh)^2} \tag{17}$$

where k is wave number and kh is the water depth parameter. Figure 7-2 compares the linear dispersion relations of the depth-integrated, non-hydrostatic equation (17) and the classical Boussinesq equations of Peregrine (1967) with the exact relation from Airy wave theory. The applicable range of a model is up to an error of 5% in the linear dispersion relation according to Madsen et al. (1991). Within the intermediate water depth of $\pi/10 < kh < \pi$, the dispersion relation of the depth-integrated non-hydrostatic equations has an error less than 5%. The classical Boussinesq equation of Peregrine (1967) has an error of 5% at kh = 1.35 and a maximum of 20% within the intermediate depth range. This provides a theoretical proof of the observations by Stelling and Zijlema (2003), Walters (2005), and Yamazaki et al., (2009) that their non-hydrostatic models produce better dispersion characteristics than the classical Boussinesq equations.

7.1.2 Numerical formulation

The numerical formulation includes the solution schemes for the hydrostatic and non-hydrostatic components of the governing equations. Figure 7-3 shows the space-staggered grid for the computation. The model calculates the horizontal velocity components U and V at the cell interface, and the free surface elevation ζ, the non-hydrostatic pressure q, and the vertical velocity W at the cell center, where the water depth h is defined.

Integration of the continuity equation (5) provides an update of the surface elevation at the center of cell (j, k) in terms of the fluxes, FLX and FLY along the longitude and latitude, at the cell interfaces as

$$\zeta_{j,k}^{m+1} = \zeta_{j,k}^{m} + \left(\eta_{j,k}^{m+1} - \eta_{j,k}^{m}\right) - \Delta t \frac{FLX_{j+1,k} - FLX_{j,k}}{R\Delta\lambda\cos\phi_k} - \Delta t \frac{FLY_{j,k}\cos\left(\phi_k + \Delta\phi/2\right) - FLY_{j,k-1}\cos\left(\phi_{k-1} + \Delta\phi/2\right)}{R\Delta\phi\cos\phi_k} \tag{18}$$

where m denotes the time step, Δt is the time step size, and $\Delta\lambda$ and $\Delta\phi$ are the respective grid sizes. The flux terms at (j, k) are estimated using the upwind flux approximation of Mader (1988) as

$$FLX_{j,k} = U_p^{m+1}\zeta_{j-1,k}^{m} + U_n^{m+1}\zeta_{j,k}^{m} + U_{j,k}^{m+1}\frac{\left(h_{j-1,k} - \eta_{j-1,k}^{m}\right) + \left(h_{j,k} - \eta_{j,k}^{m}\right)}{2} \tag{19a}$$

$$FLY_{j,k} = V_p^{m+1}\zeta_{j,k}^{m} + V_n^{m+1}\zeta_{j,k+1}^{m} + V_{j,k}^{m+1}\frac{\left(h_{j,k} - \eta_{j,k}^{m}\right) + \left(h_{j,k+1} - \eta_{j,k+1}^{m}\right)}{2} \tag{19b}$$

in which

$$U_p^m = \frac{U_{j,k}^m + \left|U_{j,k}^m\right|}{2},\ U_n^m = \frac{U_{j,k}^m - \left|U_{j,k}^m\right|}{2};\ V_p^m = \frac{V_{j,k}^m + \left|V_{j,k}^m\right|}{2},\ V_n^m = \frac{V_{j,k}^m - \left|V_{j,k}^m\right|}{2} \tag{20}$$

The horizontal momentum equations provide the velocity components U and V at (m+1) in (19) for the update of the surface elevation in (18). Integration of the momentum equations (2) and (3) is performed in two steps. With the non-hydrostatic terms omitted, an explicit hydrostatic solution is given by

$$\begin{aligned}\widetilde{U}_{j,k}^{m+1} = {} & U_{j,k}^m - \frac{g\Delta t}{R\Delta\lambda\cos\phi_k}\left(\zeta_{j,k}^m - \zeta_{j-1,k}^m\right) + \Delta t\left(2\Omega + \frac{U_{j,k}^m}{R\cos\phi_k}\right)\overline{V}_{x\,j,k}^{\,m}\sin\phi_k \\ & - \frac{\Delta t}{R\Delta\lambda\cos\phi_k}U_p^m\left(U_{j,k}^m - U_{j-1,k}^m\right) - \frac{\Delta t}{R\Delta\lambda\cos\phi_k}U_n^m\left(U_{j+1,k}^m - U_{j,k}^m\right) \\ & - \frac{\Delta t}{R\Delta\phi}\overline{V}_{x\,p}^{\,m}\left(U_{j,k}^m - U_{j,k-1}^m\right) - \frac{\Delta t}{R\Delta\phi}\overline{V}_{x\,n}^{\,m}\left(U_{j,k+1}^m - U_{j,k}^m\right) - n^2 g\frac{\Delta t U_{j,k}^m\sqrt{\left(U_{j,k}^m\right)^2 + \left(\overline{V}_{x\,j,k}^{\,m}\right)^2}}{\left(D_{j-1,k}^m + D_{j,k}^m\right)^{\frac{4}{3}}}\end{aligned} \tag{21}$$

$$\begin{aligned}\widetilde{V}_{j,k}^{m+1} = {} & V_{j,k}^m - \frac{g\Delta t}{R\Delta\phi}\left(\zeta_{j,k+1}^m - \zeta_{j,k}^m\right) - \Delta t\left(2\Omega + \frac{\overline{U}_{y\,j,k}^{\,m}}{R\cos\left(\phi_k + \Delta\phi/2\right)}\right)\overline{U}_{y\,j,k}^{\,m}\sin\left(\phi_k + \Delta\phi/2\right) \\ & - \frac{\Delta t}{R\Delta\lambda\cos\left(\phi_k + \Delta\phi/2\right)}\overline{U}_{y\,p}^{\,m}\left(V_{j,k}^m - V_{j-1,k}^m\right) - \frac{\Delta t}{R\Delta\lambda\cos\left(\phi_k + \Delta\phi/2\right)}\overline{U}_{y\,n}^{\,m}\left(V_{j+1,k}^m - V_{j,k}^m\right) \\ & - \frac{\Delta t}{R\Delta\phi}V_p^m\left(V_{j,k}^m - V_{j,k-1}^m\right) - \frac{\Delta t}{R\Delta\phi}V_n^m\left(V_{j,k+1}^m - V_{j,k}^m\right) - n^2 g\frac{\Delta t V_{j,k}^m\sqrt{\left(\overline{U}_{y\,j,k}^{\,m}\right)^2 + \left(V_{j,k}^m\right)^2}}{\left(D_{j,k}^m + D_{j,k+1}^m\right)^{\frac{4}{3}}}\end{aligned} \tag{22}$$

where the subscripts p and n indicates upwind and downwind approximations of the advective speeds and the over bar denotes average quantities.

Stelling and Duinmeijer (2003) proposed an alternate shock-capturing scheme for finite-difference and finite volume solutions of the nonlinear shallow-water equations. The discretization scheme of the advective speeds in the horizontal momentum equations approximate breaking waves as bores or hydraulic jumps and conserves flow volume across discontinuities. NEOWAVE utilizes the momentum conserved advection (MCA) scheme of Yamazaki et al. (2009 and 2011), which embeds the upwind flux approximation of Mader (1988) in the shock-capturing scheme of Stelling and Duinmeijer (2003) to handle flow discontinuity associated with tsunami wave breaking and bore as part of the hydrostatic solution.

The numerical scheme for the non-hydrostatic solution is implicit. Integration of the non-hydrostatic terms in the horizontal momentum equations completes the update of the horizontal velocity from (21) and (22)

$$U_{j,k}^{m+1} = \tilde{U}_{j,k}^{m+1} - \frac{\Delta t}{R\Delta\lambda\cos\phi_k} A_{j,k} \frac{\left(q_{j,k}^{m+1} + q_{j-1,k}^{m+1}\right)}{2} - \frac{\Delta t}{R\Delta\lambda\cos\phi_k} \frac{\left(q_{j,k}^{m+1} - q_{j-1,k}^{m+1}\right)}{2} \tag{23}$$

$$V_{j,k}^{m+1} = \tilde{V}_{j,k}^{m+1} - \frac{\Delta t}{R\Delta\phi} B_{j,k} \frac{\left(q_{j,k+1}^{m+1} + q_{j,k}^{m+1}\right)}{2} - \frac{\Delta t}{R\Delta\phi} \frac{\left(q_{j,k+1}^{m+1} - q_{j,k}^{m+1}\right)}{2} \tag{24}$$

where

$$A_{j,k} = \frac{\left(\zeta_{j,k}^{m} - h_{j,k} + \eta_{j,k}^{m}\right) - \left(\zeta_{j-1,k}^{m} - h_{j-1,k} + \eta_{j-1,k}^{m}\right)}{\left(D_{j,k}^{m} + D_{j-1,k}^{m}\right)} \tag{25a}$$

$$B_{j,k} = \frac{\left(\zeta_{j,k+1}^{m} - h_{j,k+1} + \eta_{j,k+1}^{m}\right) - \left(\zeta_{j,k}^{m} - h_{j,k} + \eta_{j,k}^{m}\right)}{\left(D_{j,k}^{m} + D_{j,k+1}^{m}\right)} \tag{25b}$$

Discretization of the vertical momentum equation (4) gives the vertical velocity at the free surface as

$$w_{s\,j,k}^{m+1} = w_{s\,j,k}^{m} - \left(w_{b\,j,k}^{m+1} - w_{b\,j,k}^{m}\right) + \frac{2\Delta t}{D_{j,k}^{m}} q_{j,k}^{m+1} \tag{26}$$

The vertical velocity on the seafloor is evaluated from the boundary condition (7) as

$$\begin{aligned} w_{b\,j,k}^{m+1} = {} & \frac{\eta_{j,k}^{m+1} - \eta_{j,k}^{m}}{\Delta t} - \overline{U}_{z\,p}^{\,m} \frac{\left(h_{j,k} - \eta_{j,k}^{m}\right) - \left(h_{j-1,k} - \eta_{j-1,k}^{m}\right)}{R\Delta\lambda\cos\phi_k} - \overline{U}_{z\,n}^{\,m} \frac{\left(h_{j+1,k} - \eta_{j+1,k}^{m}\right) - \left(h_{j,k} - \eta_{j,k}^{m}\right)}{R\Delta\lambda\cos\phi_k} \\ & - \overline{V}_{z\,p}^{\,m} \frac{\left(h_{j,k} - \eta_{j,k}^{m}\right) - \left(h_{j,k-1} - \eta_{j,k-1}^{m}\right)}{R\Delta\phi} - \overline{V}_{z\,n}^{\,m} \frac{\left(h_{j,k+1} - \eta_{j,k+1}^{m}\right) - \left(h_{j,k} - \eta_{j,k}^{m}\right)}{R\Delta\phi} \end{aligned} \tag{27}$$

in which

$$\overline{U}_{z\,p}^{\,m} = \frac{\overline{U}_{z\,j,k}^{\,m} + \left|\overline{U}_{z\,j,k}^{\,m}\right|}{2} \quad \overline{U}_{z\,n}^{\,m} = \frac{\overline{U}_{z\,j,k}^{\,m} - \left|\overline{U}_{z\,j,k}^{\,m}\right|}{2} \quad \overline{V}_{z\,p}^{\,m} = \frac{\overline{V}_{z\,j,k}^{\,m} + \left|\overline{V}_{z\,j,k}^{\,m}\right|}{2} \quad \overline{V}_{z\,n}^{\,m} = \frac{\overline{V}_{z\,j,k}^{\,m} - \left|\overline{V}_{z\,j,k}^{\,m}\right|}{2} \tag{28}$$

where

$$\overline{U}_{z\,j,k}^{\,m} = \frac{U_{j,k}^{m} + U_{j+1,k}^{m}}{2} \quad \overline{V}_{z\,j,k}^{\,m} = \frac{V_{j,k}^{m} + V_{j,k-1}^{m}}{2} \tag{29}$$

The horizontal velocity components and the vertical velocity at the free surface are now expressed in terms of the non-hydrostatic pressure.

The non-hydrostatic pressure $q_{j,k}^{m+1}$ is calculated implicitly using the three-dimensional continuity equation discretized in the form

$$\frac{U_{j+1,k}^{\,m+1} - U_{j,k}^{\,m+1}}{R\Delta\lambda\cos\phi_k} + \frac{V_{j,k}^{\,m+1}\cos(\phi_k + \Delta\phi/2) - V_{j,k-1}^{\,m+1}\cos(\phi_{k-1} + \Delta\phi/2)}{R\Delta\phi\cos\phi_k} + \frac{w_{s\,j,k}^{\,m+1} - w_{b\,j,k}^{\,m+1}}{D_{j,k}^{m}} = 0 \tag{30}$$

Substitution of (23), (24), and (26) into the continuity equation (30) gives a linear system of Poisson-type equations

$$[P]\{q\} = \{Q\} \tag{31}$$

which provides the non-hydrostatic pressure at each time step. The matrix equation (31), in which [*P*] is non-symmetric, can be solved by the strongly implicit procedure (SIP) of Stone (1968). At each time step, the computation starts with the calculation of the hydrostatic solution of the horizontal velocity using (21) and (22). The non-hydrostatic pressure is then calculated using (31) and the horizontal velocity is updated with (23) and (24) to account for non-hydrostatic effects. The computation for the non-hydrostatic solution is complete with the calculation of the free surface elevation as well as the free surface and the bottom vertical velocities from (18), (26), and (27), respectively.

The governing equations in the spherical coordinate system (λ, ϕ) can be transformed into the Cartesian system (*x*, *y*) for modeling laboratory and analytical numerical experiments. The grid spacing in the *x* and *y* directions becomes

$$\Delta x = R\Delta\lambda\cos\phi_k \quad \Delta y = R\Delta\phi \tag{32}$$

With ϕ = 0, the earth curvature effects and Coriolis terms in the horizontal momentum vanish. These modifications will recover the numerical formulation in the Cartesian coordinate system as derived by Yamazaki et al. (2009).

7.1.3 Wet-dry moving boundary condition

For inundation or runup calculations, special numerical treatments are necessary to describe the moving waterline in the swash zone. The present model tracks the interface between wet and dry cells using the approach of Kowalik and Murty (1993). The basic idea is to extrapolate the numerical solution from the wet region onto the beach. The non-hydrostatic pressure is set to be zero at the wet cells along the wet-dry interface to conform to the physical problem and to improve stability of the scheme.

The moving waterline scheme provides an update of the wet-dry interface as well as the associated flow depth and velocity at the beginning of every time step. A marker $CELL_{j,k}^{m}$ first updates the wet-dry status of each cell based on the flow depth and surface elevation. If the flow depth $D_{j,k}^{m}$ is positive, the cell is under water and $CELL_{j,k}^{m} = 1$, and if $D_{j,k}^{m}$ is zero or negative, the cell is dry and $CELL_{j,k}^{m} = 0$. This captures the retreat of the waterline in an ebb flow. The surface

elevation along the interface then determines any advancement of the waterline. For flows in the positive λ or *x* direction, if $CELL_{j,k}^{m}$ is dry and $CELL_{j-1,k}^{m}$ is wet, $CELL_{j,k}^{m}$ is reevaluated as

$CELL_{j,k}^{m} = 1$ (wet) if $\zeta_{j-1,k}^{m} > -h_{j,k}$

$CELL_{j,k}^{m} = 0$ (dry) if $\zeta_{j-1,k}^{m} \le -h_{j,k}$

If $CELL_{j,k}^{m}$ becomes wet, the scheme assigns the flow depth and velocity at the cell as

$$D_{j,k}^{m} = \zeta_{j-1,k}^{m} + h_{j,k}, \quad U_{j,k}^{m} = U_{j-1,k}^{m}$$

The marker $CELL_{j,k}^{m}$ is then updated for flows in the negative direction. The same procedures are implemented in the ϕ or *y* direction to complete the wet-dry status of the cell. If water flows into a new wet cell from multiple directions, the flow depth is averaged.

Once the wet-dry cell interface is open by setting $CELL_{j,k}^{m} = 1$, the flow depth $D_{j,k}^{m}$ and velocity ($U_{j,k}^{m}$, $V_{j,k}^{m}$) are assigned to the new wet cell to complete the update of the wet-dry interface at time step *m*. The surface elevation $\zeta_{j,k}^{m+1}$ and the flow velocity ($U_{j,k}^{m+1}$, $V_{j,k}^{m+1}$) over the computational domain are obtained from integration of the momentum and continuity equations along with the implicit solution of the non-hydrostatic pressure as outlined in Section 7.1.2. The moving waterline scheme is then repeated to update the wet-dry interface at the beginning of the (*m*+1) time step. This approach remains stable and robust for the non-hydrostatic flows without artificial dissipation mechanisms.

7.1.4 Grid refinement scheme (two-way, coupled grid nesting scheme)

Most grid-nesting schemes for tsunami models use a system of rectangular computational domains with the fluxes as input to a fine inner grid and the surface elevation as output to the outer grid (Liu et al., 1995b, Goto et al., 1997, and Wei et al., 2003). A non-hydrostatic model needs to input the horizontal velocity, surface elevation as well as the non-hydrostatic pressure to ensure propagation of breaking and dispersive waves across inter-grid boundaries. Figure 7-4 illustrates the grid setup and data transfer protocol. The outer and inner grids align at the cell centers, where they share the same water depth. The surface elevation and non-hydrostatic pressure are input at the cell centers as indicated by the red dots. While the tangential component of the velocity is applied along the inter-grid boundary, the normal component is applied on the inboard side of the boundary cells as indicated by the red dash. Existing grid-nesting schemes, which only input the normal velocity, cannot handle propagation of discontinuities through MCA scheme and Coriolis effects across inter-grid boundaries.

Figure 7-5 shows a schematic of the solution procedure with the two-way grid-nesting scheme. The time step Δt_1 of the outer grid must be divisible by the inner-grid time step Δt_2. The calculation begins at time *t* with the complete solutions at both the outer and inner grids. The time-integration procedure provides the solution over the outer grid at (t + Δt_1). Linear interpolation of the horizontal velocity, surface elevation, and non-hydrostatic pressure in time and space provides the input boundary conditions to the inner grid. The time-integration procedure then computes the inner grid solution at Δt_2 increments until (t + Δt_1). The hydrostatic solution is computed explicitly from the input surface elevation and horizontal velocity. The non-

hydrostatic solution is implicit and requires reorganization of the matrix equation (31) for the input non-hydrostatic pressure from the outer grid. After the computation in the inner grid reaches ($t + \Delta t_1$), the surface elevation at the outer grid is then updated with the average value from the overlapping inner grid cells to complete the procedure. This feedback mechanism is similar to the grid-nesting scheme of Goto et al. (1997).

7.1.5 Non-hydrostatic/hydrostatic hybrid (NH-Hybrid) scheme

Dispersive wave models often introduce numerical artifacts when waves break on a beach (Zelt, 1991). A narrow peak appears at the leading edge, and the peak grows narrower and higher during shoaling and runup processes leading to instability. This problem is observed only for high amplitude waves on a gentle slope. NEOWAVE utilizes the non-hydrostatic/hydrostatic hybrid (NH-Hybrid) scheme to solve this overshoot instability problem associated with energetic wave breaking. When steep waves approach the shore with energetic breaking, nonlinearity is predominant and dispersion becomes secondary (Tonelli and Petti, 2010). The dispersion terms, which cause the overshoot instability, can be disabled prior to wave breaking. This will allow the momentum conserved advection scheme to model the breaking waves as bores or hydraulic jump without artificial dissipation.

A marker $CELL\_B_{j,k}^m$ is used to track the breaking area. The cells with the non-hydrostatic solution are set to $CELL\_B_{j,k}^m = 0$. We use the breaking initiation criterion

$$\sqrt{U^2 + V^2} > 0.5\sqrt{gD} \tag{33}$$

to disable the dispersive terms locally and the breaking termination criterion

$$\sqrt{U^2 + V^2} < 0.15\sqrt{gD} \tag{34}$$

to reactivate the dispersion terms. These criteria are checked every time step for every individual grid cell, and there is no need to track the wave direction and breaking duration. Once a cell hit the breaking initiation criterion (33), $CELL\_B_{j,k}^m = 1$ is assigned to the cell. With the dispersion terms disabled locally, the non-hydrostatic pressure $q = 0$ is specified at all cells with $CELL\_B_{j,k}^m = 1$, and Dirichlet B.C. is applied at cell interface between $CELL\_B_{j,k}^m = 1$ and $CELL\_B_{j,k}^m = 0$. The status remains until the cell reaches the breaking termination criteria (34). The marker becomes $CELL\_B_{j,k}^m = 0$ and the cell includes computation of the non-hydrostatic pressure.

We implemented the NH-Hybrid scheme with the wave breaking criteria, (33) and (34), to model energetic breaking events. Tonelli and Petti (2010) and Xiao et al. (2010) implemented the similar schemes with different breaking criteria. Tonelli and Petti (2010) used the ratio of wave amplitude and water depth, while Xiao et al. (2010) used the surface elevation gradient as wave breaking criteria. The proposed breaking criteria are verified with laboratory experiments.

7.2 Model verification and validation

This section provides verification and validation of NEOWAVE with analytical solutions, laboratory data, and field measurements in five test cases. The first test case on solitary wave transformation over a compound slope provides an assessment of the basic hydrodynamic processes of wave propagation, shoaling, breaking, and reflection. The test cases on solitary

wave transformation on a plane beach, a conical island, and a reef system allow examination of the numerical schemes for wave breaking and swashing. The fifth test case involving laboratory and field data of the 1993 Hokkaido Nansei-Oki earthquake tsunami validates the model for practical application.

7.2.1 BP4: Solitary wave on compound slope

Briggs et al. (1996) conducted a laboratory experiment to examine solitary wave propagation and transformation over a compound slope and the subsequent runup on a vertical wall. Figure 7-6 shows the experiment setup in a 23.2-m long, 0.45-m wide flume at the U.S. Amy Engineer Waterways Experiment Station, Vicksburg, MS. The water is 0.218 m deep over the 15.05 m long flat bed in front of the compound slope of 1:53, 1:150, and 1:13. Capacitance wave gauges record surface elevation at ten locations along the flume. Runup on the vertical wall is measured visually at every run. A computer-controlled hydraulic wavemaker generates solitary waves toward the slope and wall complex. Gauge 4 with a variable location at half wavelength from the toe of the compound slope recorded incident wave heights of A/h = 0.039, 0.264 and 0.696 for the three cases A, B, and C. The approximate wavelength of a solitary wave is given by

$$L = \frac{2}{k}\arccos\mathrm{h}\left(\sqrt{\frac{1}{0.05}}\right) \tag{35}$$

in which the wave number $k = \sqrt{3A/4h^3}$ (Synolakis, 1987).

We first verify the linear shallow-water component of NEOWAVE with the analytical solution of Kânoğlu and Synolakis (1998). The analytical solution describes linear wave transformation and reflection from the compound slope beginning with the recorded surface elevation at gauge 4. The computational domain covers the flume between gauge 4 and the vertical wall. The time series of the recorded solitary wave is input at the left boundary, which turns into an open boundary afterward. The computation uses $\Delta x = \Delta y = 1$ cm for the one-dimensional problem and $\Delta t = 0.002$ s to achieve a Courant number of $Cr = 0.41$. A Manning's roughness coefficient $n = 0.0$ is used according to the linear solution of Kânoğlu and Synolakis (1998). Figure 7-7, Figure 7-8, and Figure 7-9 compare the computed and analytical solutions at gauges 4 to 10 in the experiment of Briggs et al. (1996) as well as an artificial gauge 11 at the vertical wall. The excellent agreement for all for three cases verifies the linear shallow-water solver of NEOWAVE to appropriately model wave propagation, shoaling, and reflection. The small hump toward the end of the computation in cases B and C are reflection from the open boundary because of the steep nonlinear input profile.

The laboratory data include a wide range of wave amplitudes including non-breaking and breaking events for validation of the wave breaking criteria, (33) and (34) and the NH-hybrid scheme for modeling the wave breaking processes. The computational domain covers the entire length of the flume with $\Delta x = \Delta y = 1$ cm and a Manning's roughness coefficient of $n = 0.01$ for the smooth glass beach. The solitary wave is initiated at 4 m from the left boundary with the initial wave heights of $A/h = 0.039$, 0.264 and 0.8716, which provide best fits with the recorded wave heights at gauge 4. An extremely high amplitude of $A/h = 0.8716$ is used in case C to reproduce the recorded wave amplitude at gauge 4 because the present model cannot accurately describe the dispersion and nonlinearity of such high amplitude solitary waves. The recorded data at gauge 4 are also used as a reference for adjustment of the timing of the computed waveforms with and without the NH-hybrid scheme.

Figure 7-10 and Figure 7-11 compare the two solutions with the measurements at gauges 4 to 10 for case A and case B, respectively. Case A is a non-breaking event, while case B produced a wave breaker at or near the wall. Both solutions show very good agreement of the amplitude and waveform with the measurements, despite slight phase lags in the reflected wave. The solutions with and without the NH-Hybrid scheme are identical in case A confirming that the hybrid scheme does not modify the solution in non-breaking cases. The hybrid scheme avoids overshoot from dispersion when wave breaking occurs and produces a smaller reflected wave amplitude in case B. Figure 7-12 shows the comparison for case C, in which the wave breaks between gauges 7 and 8 and then re-forms and shoals to the vertical wall without further breaking. The NH-Hybrid scheme shows very good agreement of the amplitude and waveform with measurements. Without it, the solution shows a strong artificial peak and the wave propagates faster due to the artificially high amplitude.

Table 7-1. Runup comparisons on vertical wall.

Case No.	Measured runup (cm)	Computed runup with hybrid scheme (cm)	Computed runup without hybrid scheme (cm)
A	2.74	2.22	2.22
B	46.72	19.53	22.98
C	27.43	24.11	58.99

Table 7-1 provides a comparison of the measured runup at the wall and the solutions with and without the NH-Hybrid scheme. The NH-Hybrid scheme provides good predictions of the runup for case A and case C, but significantly underestimates the runup in case B. Because the wave broke near the wall, the depth integrated model cannot reproduce the splash from the jet. The computed results with and without the NH-Hybrid scheme are the same in case A, showing that the hybrid scheme does not alter the solution in non-breaking waves. On the other hand, the computed runup without the NH-Hybrid scheme in case B and case C is much higher due to artificial overshoot. The results verify the proposed wave breaking criteria (33) and (34) and the NH-Hybrid scheme for computation of wave transformation and runup over a wide range of wave amplitudes.

7.2.2 BP1/5: Solitary wave on a plane beach

Synolakis (1987) derived an analytical solution from the non-linear shallow water equations for solitary wave transformation and runup on a plane beach. Figure 7-13 provides a schematic of the physical problem with A indicating the incident wave height, β the beach slope, and R the runup. The solitary wave is initiated at a half wavelength from the toe of the beach. The analytical solution allows verification of the non-linear shallow water solution and the moving boundary condition of NEOWAVE. We consider a beach slope of 1:19.85 and a wave height of A/h = 0.019 and ignore surface roughness as in the analytical solution. The grid and time step size of $\Delta x/h$ = 0.025 and $\Delta t(g/h)^{1/2}$ = 0.025 gives a Courant number of Cr = 0.19. Figure 7-14 and Figure 7-15 show excellent agreement between the computed and analytical surface profiles along the model domain and at x/h = –9.95 and –0.25. We recomputed the surface profiles at $t(g/h)^{1/2}$ = 50 and 70 with additional grid resolutions of $\Delta x/h$ = 0.0625, 0.125, and 0.25. As observed in Figure 7-16, the higher the grid resolution, the better the convergence is to the analytical solution. These agreements of computed and analytical solutions verify the NEOWAVE model's moving boundary condition and the convergence of the model's solution.

Synolakis (1987) also conducted a series of laboratory experiments that have become the standard for validation of runup models. In the numerical model, we use $\Delta x/h = 0.125$ and a Courant number of $Cr = 0.2$. Surface roughness becomes important for runup over gentle slopes and a Manning's coefficient $n = 0.01$ describes the surface condition of the smooth glass beach in the laboratory experiments (Chaudhry, 1993). Synolakis (1997) provided a series of surface profiles with a beach slope of 1:19.85 and solitary wave heights of $A/h = 0.0185$ and $A/h = 0.3$. Figure 7-17 shows a comparison of the measured profiles with the computed results for the non-breaking conditions with $A/h = 0.0185$. The computed results, with and without the MCA shock capturing scheme, provide identical solutions in the non-breaking case. The model reproduces the runup and drawdown processes and gives very good agreement with the laboratory data.

The MCA scheme is instrumental in modeling the breaking conditions for $A/h = 0.3$. Figure 7-18 and Figure 7-19 compare the laboratory data, the non-hydrostatic solution with the MCA scheme, and the hydrostatic solutions with and without the MCA scheme. The laboratory data show wave breaking between $t(g/h)^{1/2} = 20$ and 25 as the solitary wave reaches the beach and development of a hydraulic jump at $t(g/h)^{1/2} = 50$ when the water recedes from the beach. The non-hydrostatic solution with MCA scheme reproduces wave breaking without the use of predefined criteria and matches the surface elevation and runup on the beach. Both hydrostatic solutions fail to reproduce the surface profile at $t(g/h)^{1/2} = 25$ immediately after wave breaking. The solution without the MCA scheme shows significant volume loss and underestimates the surface elevation on the beach and eventually the runup. The MCA scheme conserves the water volume and provides good agreement with laboratory data in the subsequent runup and drawdown process. A minor discrepancy on the location of the hydraulic jump occurs around the peak of the return flow at $t(g/h)^{1/2} = 55$. The finite volume model with Reimann solver of Wei et al. (2006) also produces a similar discrepancy with the laboratory data. This may be attributed to the three-dimensional flow structure that is not amenable to depth-integrated solutions. The comparisons show that the MCA scheme can effectively capture discontinuous flows associated with energetic wave breaking and can describe the subsequent runup on the beach without an empirical dissipation term in both the hydrostatic and non-hydrostatic solutions.

7.2.3 BP6: Solitary wave transformation on conical island

Briggs et al. (1995) conducted a large-scale laboratory experiment to investigate solitary wave runup on a conical island at the U.S. Army Engineer Waterways Experiment Station, Vicksburg, MS. The collected data have become a standard for validation of runup models (Liu et al., 1995a; Titov and Synolakis, 1998; Chen et al., 2000; Lynett et al., 2002; and Wei et al., 2006; and Yamazaki et al. 2009). Figure 7-20 shows a schematic of the experiment. The basin is 25 m by 30 m. The circular island has the shape of a truncated cone with diameters of 7.2 m at the base and 2.2 m at the crest. The island is 0.625 m high and has a side slope of 1:4. The surface of the island and basin has a smooth concrete finish. A 27.4-m long directional spectral wavemaker, which consists of 61 paddles, generates solitary waves for the experiment. Wave absorbers at the three sidewalls reduce reflection in the basin.

The experiment covers the water depths $h = 0.32$ and 0.42 m and the solitary wave heights $A/h = 0.05$, 0.1 and 0.2. The present study considers the smaller water depth $h = 0.32$ m, which provides a more critical test case for the non-hydrostatic model. In the computation, the solitary wave is generated from the left boundary with the measured initial wave heights of $A/h = 0.045$, 0.096, and 0.181 at gauge 2. These measured wave heights, instead of the target wave heights $A/h = 0.05$, 0.1, and 0.2 in the laboratory experiment, better represent the recorded data and thus

the incident wave conditions to the conical island. The open boundary condition is imposed at the lateral boundaries to model the effects of the wave absorbers. We use $\Delta x = \Delta y = 5$ cm, $\Delta t = 0.01$ sec, and a Manning's roughness coefficient $n = 0.012$ for the smooth concrete finish according to Chaudhry (1993).

A number of gauges recorded the transformation of the solitary wave around the conical island. Figure 7-21 shows the time series of the measured and computed free surface elevations at selected gauges. With reference to Figure 7-20, gauges 2 and 6 are located in front of the island and 9, 16, and 22 are placed just outside the still waterline around the island. These gauges provide sufficient coverage of the representative wave conditions in the experiment. The measured data at gauge 2 provide a reference for adjustment of the timing of the computed waveforms. The computed result shows excellent agreement with the measured time series, including the depression following the leading wave that was not adequately reproduced in previous studies. The present model well describes the phase of the peak, but slightly overestimates the leading wave amplitude at gauges 9 and 22 as the wave height increases. Figure 7-22 shows good agreement of the measured and computed inundation and runup around the conical island.

Most of the previous studies neglected friction in this numerical experiment (Liu et al., 1995a; Titov and Synolakis, 1998; Chen et al., 2000; and Lynett et al., 2002). A test of the model with n = 0.0 gave very similar results as n = 0.012. As pointed out in Liu et al. (1995a), the computed results are not sensitive to the surface roughness coefficient due to the steep 1:4 slope of the conical island. The computed results are comparable or slightly better than the extended Boussinesq solutions of Chen et al. (2000) and Lynett et al. (2002) that use empirical relations with adjustable coefficients to describe wave breaking. The overall agreement between the computed results and laboratory data indicates the capability of the present model to estimate wave transformation, breaking, and inundation in the two horizontal dimensions.

7.2.4 ISEC BM1/2: Solitary wave transformation over complex reef system

NEOWAVE entered the 2009 Benchmark Challenge at the Inundation Science and Engineering Cooperative (ISEC) Community Workshop, Corvallis, Oregon (http://isec.nacse.org/workshop/2009_isec/). The two benchmarks are based on the laboratory experiment of Swigler and Lynett (2011) at the large wave basin in the O.H. Hinsdale Wave Research Laboratory, Oregon State University. The basin is 48.8 m long, 26.5 m wide, and 2.1 m deep. The 26.5-m long piston-type wavemaker consists of 29 paddles. Swigler and Lynett (2011) constructed the 43.5 m long, 26.5 m wide experiment setup of a complex reef system shown in Figure 7-23. That figure shows the setup of ISEC BM1 with a triangular reef on a compound slope of 1:15.5, 1:31.25, and 1:550. The reef is flat with a gentle slope of 1:620. The top flat portion of the compound slope is 0.69 m high where it begins underwater and reaches 0.95 m high on shore. The reef has a maximum slope of 1:3.5 at the apex that gradually transitions to 1:31.25 on the compound slope. ISEC BM2 includes a cone near the apex of the reef as shown in Figure 7-24. The cone has a 0.45 m height and 3 m radius at water level.

Figure 7-25 and Figure 7-26 show laser scans of the finished reef-slope configurations and the instrument layouts. Resistance-type wire and ultrasonic wave gauges were used to measure surface elevation and the Norteck Vectrino 3D acoustic-Doppler velocimeters (ADV) were used to record velocity. In the numerical model, we use $\Delta x = \Delta y = 5$ cm and $\Delta t = 0.002$ s for a Courant number of $Cr = 0.16$. The computational grid captures the surface pattern and a

Manning coefficient of n = 0.012 accounts for the subgrid roughness of the finished concrete surface. Both benchmarks have the same water depth of 0.78 m and the incident solitary wave height of A/h = 0.5. We examine the model results with and without the NH-Hybrid scheme, because energetic wave breaking occurred during the laboratory experiment.

Figure 7-27(a) and (b) show the time series of the two solutions and the measured free surface elevations at the gauges along the centerline and at 5 m offset. The measured data at (x,y) = (7.5 m, 0 m) provides a reference for adjustment of the timing of the computed waveforms. Wave breaking occurs near (15 m, 0 m) at the center and (17 m, 5 m) when the wave approaches the edge of the shallow reef flat. Figure 7-27(c) indicates the subsequent bore propagates across the reef flat to the row of gauges near the waterline. The solution without the NH-Hybrid scheme produces an anomalous peak at the gauges in the surf zone. On the other hand, the solution with the NH-Hybrid scheme reproduces the amplitude and phase of the wave breaker. The subsequent reflected waves show clear phase lags from the measurement because the horizontal movement of the wavemaker, which is about 1 m, is not considered in computation. Figure 7-27(d) shows the velocity comparison at the three ADVs. The computed results agree with the first wave very well.

The addition of the cone in ISEC BM2 modifies the wave processes on the reef flat. Figure 7-28 shows comparisons of the two solutions with the measurements of the free surface elevation and velocity at the gauges. The model with the NH-Hybrid scheme successfully reproduces the wave transformation and energetic breaking over the complex reef system. There are some discrepancies in both the surface elevation and velocity comparisons, while the overall agreement is very good considering the strong nonlinearity and energetic wave breaking. These numerical experiments have validated the capability of NEOWAVE in handling wave processes beyond what are required of tsunami modeling.

7.2.5 BP7/9: The 1993 Hokkaido Nansei-Oki Earthquake Tsunami

An Ms 7.8 earthquake occurred west of Hokkaido, Japan on July 12, 1993 at 13:17 GMT. The subsequent tsunami hit the west coast of Hokkaido and devastated an entire coastal community on Okushiri Island along its way. The runup reached 31.7 m in a small valley near Monai on the west side of the island. Shuto and Matsutomi (1995) and Takahashi et al. (1995) conducted a field survey and a numerical model study after the event. The Hokkaido Tsunami Survey Group studied the impacts and characteristics of the earthquake and tsunami, including runup, ground deformation, arrival time, and structural damage (Shuto and Matsutomi, 1995). The Disaster Control Research Center (DCRC) in Tohoku University investigated the focal mechanism and derived a set of fault parameters (DCRC-17a) summarized in Table 7-2 that produces overall good agreement with recorded runup and bottom deformation (Takahashi et al., 1995). DCRC provided the measured runup, recorded tide gauge data, initial deformation, and digitized bathymetry from nautical charts as a field benchmark for tsunami models (Takahashi, 1996).

Table 7-2: Fault parameters of DCRC-17a (Takahashi et al., 1995).

No	Length (km)	Width (km)	Strike angle (º)	Dip angle (º)	Rake angle (º)	Dislocation (Slip) (m)	Depth (km)	Latitude (ºN)	Longitude (ºE)
1	90	25	188	35	105*	5.71	10	43.130*	139.400
2	30	25	175	60	80*	2.50	5	42.340	139.250
3	24.5	25	163	60	80*	12.00	5	42.100	139.300

* Modifications based on the initial deformation profile of Takahashi et al. (1995).

The present study uses three levels of nested grids to model the tsunami runup on Okushiri Island due to the 1993 Hokkaido Nansei-Oki earthquake. Figure 7-29(a) shows the level-1 grid at 450 m resolution off western Hokkaido and the coverage of the level-2 and level-3 grids. An open boundary condition allows radiation of tsunami waves away from the domain. The level-2 grid resolves the shelf and slope off Hokkaido at 150 m resolution and provides a transition to the level-3 grid at 50 m resolution around Okushiri Island as shown in Figure 7-29(b). The digital elevation model is derived from the 450-m, 150-m, and 50-m gridded datasets from DCRC as well as the JMA 20-sec bathymetry data. The Generic Mapping Tools (GMT) interpolates the data to produce the nested computational grids. The computation with the 3 levels of nested-grids covers 1 hour of elapsed time, and uses $\Delta t = 0.5$ s ($Cr = 0.3$) for the level-1 grid, $\Delta t = 0.125$ s ($Cr = 0.2$) for the level-2 grid, and $\Delta t = 0.125$ s ($Cr = 0.2$) for the level-3 grid, with a Manning's coefficient of $n = 0.025$ for the ocean bottom.

The planar fault model of Okada (1985) describes the earth surface deformation in terms of the depth, orientation, and slip of a rectangular fault as shown in Figure 7-30. The deformation is a linear function of the slip and dimensions of the fault. Superposition of the planar fault solutions from the subfaults gives vertical displacement of the seafloor as a function of the longitude and latitude (λ, ϕ):

$$\eta(\lambda,\phi) = \sum_{i=1}^{n} \eta_i(\lambda,\phi) \tag{36}$$

where $n = 3$ is the number of subfaults for DCRC-17a model, η_i is the vertical earth surface deformation associated with rupture of subfault i from Okada (1985). Figure 7-31 shows initial sea surface deformation, which is obtained from (36) with the fault parameters in Table 7-2.

Figure 7-32 shows the computed and recorded surface elevations at the Esashi and Iwanai tide gauges on the west coast of Hokkaido. The computed results with the 150-m grid at Esashi show good agreement of the arrival time and amplitude, but do not reproduce the waveform. The computed waves at Iwanai in the 450-m grid arrive about 5 min earlier than the recorded data. Esashi and Iwanai Bays are surrounded by multiple breakwaters and the available tide gauge coordinates are accurate to the arcmin. The bathymetry data at both tide gauges come from the 450-m grid, which does not show breakwaters and indicates the tide gauges are on land. The computed surface elevations are obtained at the nearest locations with different water depths. The discrepancies between the computed and recorded surface elevations come from multiple factors.

Figure 7-33 shows the computed and measured runup around Okushiri. The present model produces good agreement with measurements around most of the island, but underestimates the runup on the southwest coast from Monai to Aonae, consistent with previous studies (e.g., Takahashi et al., 1995, and Tanioka and Satake, 1996). Takahashi et al. (1995) derived the fault parameters to reproduce the overall tsunami runup around the entire island as well as the vertical ground deformation over the Island. The parameters do not reflect either the 20-m runup at Hamatsuma (due to lack of detailed topography data) or the largest recorded runup of 31.7 m in Moani Valley (due to the low-resolution computation). Shuto and Matsutomi (1995) suggested the fault parameters and the 45-m grid should produce 10-25 m of runup near the Moani valley. We computed the results with and without dispersion and shock capturing in this benchmark and obtained identical solutions meaning that this tsunami is fully hydrostatic and does not involve energetic wave breaking. Even though the computed results show discrepancies with the recorded tide gauge and runup data, the present model reproduces the overall patterns and very similar results as the previous studies. This validates that NEOWAVE is capable modeling field tsunamis with at least the same level of accuracy as the existing tsunami models in fully hydrostatic and non-breaking events.

Matsuyama and Tanaka (2001) conducted a laboratory study at the Central Research Institute for Electric Power Industry (CRIEPI) to investigate the runup in Monai Valley during the 1993 Hokkaido Nansei-Oki earthquake tsunami. Eyewitnesses reported an initial withdrawal of the water followed by a large tsunami wave at the coast, causing the 31.7-m runup. Such observations fit the description of the leading-depression N-wave, which is often used in laboratory studies of tsunami impact close to the source. The CRIEPI wave flume is 205 m long, 3.4 m wide, and 6 m high with a hydraulic, piston-type wavemaker capable of generating N-waves. The 1:400-scale coastal relief model around Monai Valley was constructed of painted plywood and installed approximately 140 m from the wavemaker. The initial N-wave was relatively long with a very gentle profile and dispersed into a series of short-period waves over the coastal relief model in the experiment. Figure 7-34(a) shows the setup of the numerical experiment over the 5.475-m-long and 3.4-m-wide relief model. We use $\Delta x = \Delta y = 1.25$ cm (5 m full scale) and $\Delta t = 0.0025$ sec to achieve a Courant number of $Cr = 0.23$. A Manning's coefficient $n = 0.012$ describes the surface roughness of the painted plywood relief model (Chaudhry, 1993). Figure 7-34(b) shows the input N-wave profile at the left boundary with 0.135 m (54 m full scale) water depth. The incident waves shoal over a plane slope before refracting and diffracting around a small island on a shallow bank. Figure 7-35 shows very good agreement of the computed surface elevations with the laboratory measurements at three gauges behind the island. The model reproduces the small-amplitude dispersive waves generated by reflection from the coast. The minor phase lag in the dispersive waves is likely due to errors in the small-scale laboratory experiment.

Table 7-3: Recorded runup for the six trials from Matsuyama and Tanaka (2001).

Trial No.	Maximum, Rmax (cm) (Full scale in m)	y = 2.2062 m R (cm) (Full scale in m)	y = 2.32 m R (cm) (Full scale in m)
209_105	8.75 (35.0)	5.25 (21.0)	5.25 (21.0)
209_106	9.00 (36.0)	5.75 (23.0)	5.50 (22.0)
209_107	8.00 (32.0)	5.50 (22.0)	5.50 (22.0)
210_101	9.00 (36.0)	6.50 (26.0)	5.75 (23.0)
210_102	10.00 (40.0)	6.75 (27.0)	5.75 (23.0)
210_103	9.00 (36.0)	6.50 (26.0)	5.75 (23.0)
Mean	8.97 (35.8)	6.04 (24.2)	5.58 (22.3)

Table 7-3 lists the runup measurements along transects at y = 2.2062 and 2.32 m as well as the maximum value inside Monai Valley from a series of tests in the laboratory experiment of Matsuyama and Tanaka (2001). Figure 7-36 shows the computed runup and inundation with the range and mean value of the recorded runup. The computed results show good agreement with the measured data despite the uncertainty in the laboratory experiment. Comparisons of the surface elevation, runup, and inundation from the Monai Valley experiment validate the model's ability to handle dispersive wave and runup processes over complex nearshore bathymetry and topography.

7.3 Proposed field benchmark problems

7.3.1 29 September 2009 South Pacific tsunami: water level records and runup

7.3.1.1 Introduction

The Samoa-Tonga earthquake occurred near the Tonga trench on 29 September 2009 at 17:48:10 UTC. The US Geological Survey (USGS) determined the epicenter at 15.509°S 172.034°W and estimated the moment magnitude Mw of 8.1. Figure 7-37 shows the epicenter and the locations of the water-level stations in the region. The main energy of the resulting tsunami propagated toward Tonga and American Samoa. The tide gauge in Pago Pago Harbor, Tutuila (American Samoa) and the DART buoys 51425, 51426, and 54401 surrounding the rupture area recorded clear signals of the tsunami. The destructive waves arrived at mid tide and produced maximum runup of 17.6 m with detrimental impact on Tutuila. Several field survey teams recorded and documented the tsunami runup and inundation around Tutuila and provided useful data for model validation (Jaffe et al., 2010, Koshimura et al., 2009, and Okal et al., 2010).

The source mechanism is still an on-going research topic, but the data are available to reproduce the tsunami with reasonable accuracy. The high resolution bathymetry and topography data around American Samoa and the well-recorded water level and runup will be one of the best datasets for tsunami model validation. This report provides a description of the field benchmark and demonstrates its use in the validation of NEOWAVE (Yamazaki et al., 2009; 2011).

7.3.1.2 Bathymetry and topography data

The digital elevation model is derived from a blended dataset of multiple sources. The 0.5-arcmin (≈ 900-m) General Bathymetric Chart of the Oceans (GEBCO) from the British

Oceanographic Data Centre (BODC) provides the bathymetry for the Pacific Ocean. The Coastal Relief Model from the National Geophysical Data Center (NGDC) covers the American Samoa region and Tutuila at 3 and 0.3333 arcsec (~90 and 10 m) resolution respectively. Embedded in the NGDC dataset are multibeam and satellite measurements around Tutuila and high-resolution LiDAR (Light Detection and Ranging) survey data at Pago Pago Harbor. We have converted the datasets to reference the WGS 84 datum and the mean-sea level (MSL). The Generic Mapping Tools (GMT) interpolates the data to produce computational grids.

Four levels of nested grids are used to reconstruct the 2009 South Pacific Tsunami from its generation at the earthquake source to runup at Pago Pago Harbor. Figure 7-37(a) shows the coverage of the level-1 grid, which extends across the south-central Pacific at 1-arc min (≈ 1800-m) resolution. An open boundary condition in the level-1 grid allows radiation of tsunami waves away from the domain. Figure 7-38(a) shows a close-up view around the source and the outlines of the grids at the next three levels. The level-2 grid in Figure 7-38(b) covers American Samoa and the surrounding seabed at 7.5-arcsec (≈ 225-m) resolution to capture wave transformation around the island group. The level-3 grid in Figure 7-38(c) resolves the insular shelf and slope of Tutuila at 1.5 arcsec (~ 45 m). The rugged, volcanic island sits on a shallow shelf of less than 100 m depth covered by mesophotic corals (Bare et al., 2010). The insular slope is steep with gradients up to 1:2 on the west side and drops off abruptly to over 3000 m depth in the surrounding ocean. The level-4 grid in Figure 7-38(d) covers Pago Pago Harbor at 0.3 arcsec (~9 m) resolution for computation of inundation as well as tide gauge signals. This nested-grid system describes wave dynamics at resolutions compatible with the physical process and spatial scale for optimization of computational resources.

Dispersive wave models including non-hydrostatic and Boussinesq-type models are prone to instability over localized, steep bottom gradients at high-resolution computations (Horrillo et al., 2006; Løvholt and Pederson, 2008). The depth-dependent Gaussian function of Yamazaki et al. (2011) smooths localized bottom features in relation to the water depth while retaining the bathymetry important for modeling of tsunami transformation and runup. Figure 7-39 shows the smoothed bathymetry and topography using the depth-dependent Gaussian function. Modelers can use either the original or smoothed dataset depending on the model being validated.

7.3.1.3 Fault parameters and initial condition

Great earthquakes typically involve rupture of a single fault or a fault network with an overall distribution of coseismic motion that can be characterized by a dominant geometry (e.g., thrust faulting, normal faulting, or strike-slip faulting). However, when stress from one rupture immediately activates faulting on a very distinct fault orientation, a non-double-couple point-source mechanism may be obtained by seismic wave analysis, and the precise orientation of any of the activated fault geometries may not be directly inferred from the point-source representation. This was the case for the 29 September 2009 Mw = 8.1 Samoa-Tonga earthquake (17:48:11 UTC, 15.51°S, 172.03°W) located near the northern Tonga subduction zone (Figure 7-37). The global centroid-moment tensor analysis (Ekström G, GCMT Project. http://www.globalcmt.org/, 2009) obtained an unusual non-double couple moment tensor for this great event.

Subsequent detailed analysis of seismic waves ranging from 1-s period body waves to ~3000-s normal modes demonstrated that this event actually involved two great earthquake ruptures with distinct faulting geometries. The main earthquake resulted from extensional

intraplate faulting with Mw = 8.1 in the shallow Pacific plate near the outer Tonga trench slope and followed within 40 s by compressional thrust faulting with Mw ~ 8.0, 50-100 km to the southwest along the subduction zone megathrust fault between the underthrusting Pacific plate and the overriding Tonga Block (Lay et al., 2010). Campaign GPS measurements on the Samoa islands and Niuatoputapu, and the computed tsunami signals at DART buoys 51425, 51426, and 54401 also suggested that composite extensional and compressional faulting had occurred (Beavan et al., 2010). The latter study noted that the polarities and waveforms for the tsunami recordings could not be matched by the extensional faulting alone, and even use of the full non-double couple point-source mechanism could not match the signals. Similarly, the NOAA PMEL assumed thrust faulting for a Tonga subduction zone event of this size could not match all polarities of the three nearest DART buoys (e.g., NOAA Center for Tsunami Research. Tsunami event—September 29, 2009 Samoa. http://nctr.pmel.noaa.gov/samoa20090929/, 2009).

This great Samoa-Tonga earthquake doublet is certainly unusual, but presents an opportunity to assess the superposition of tsunami signals from the two great earthquakes with different geometries. The relatively slow phase speed of the tsunami waves allow refinements of aspects of the doublet source model that are not well-resolved by seismic wave analysis due to the strong interference of signals from the two events. Table 7-4 lists the fault parameters deducted from Lay et al. (2010) and Beavan et al. (2010) through a sensitivity analysis of tsunami signals at the Pago Pago tide gauge and DART 51425, 51426, and 54401 using NEOWAVE. The event includes a normal fault and two thrust faults. The sensitivity analysis over strike angles from 320° to 350°, dip angles from 15° to 35°, fault lengths from 91 to 120 km, and fault widths from 15 km to 35 km covers the NE dipping normal fault of Lay et al. (2010) and the USGS finite fault solution used in Yamazaki et al. (2011). The computed surface elevations obtained from the NE dipping (shallow dipping) normal fault plane provide better agreement with recorded data than the SW dipping (steeply dipping) normal fault in Lay et al. (2010). This is consistent with tsunami modeling results and GPS measurements in Beavan et al. (2010) as well as tsunami modeling results in Yamazaki et al. (2011).

Table 7-4: Fault parameters for the 29 September 2009 Mw = 8.1 2009 Samoa-Tonga Earthquake

No	Length	Width	Strike angle	Dip angle	Rake angle	Slip	Depth	Latitude	Longitude	Rise time	Rupture initiation
	(km)	(km)	(º)	(º)	(º)	(m)	(km)	(ºN)	(ºW)	(s)	time (sec)
1	110	35	340	35	265	6.60	5.2	16.0151	171.9693	41	0
2	50	75	175	20	90	4.62	5	15.5260	172.3703	40	49
3	50	75	180	20	90	4.71	5	16.0402	172.3250	40	90

The planar fault model of Okada (1985) describes the earth surface deformation in terms of the depth, orientation, and slip of a rectangular fault. The deformation is a linear function of the slip and dimensions of the fault. Let t denote time and (λ, ϕ) the longitude and latitude. Superposition of the planar fault solutions from the subfaults gives the time sequence of the vertical displacement of the seafloor:

$$\eta(\lambda,\phi,t) = \sum_{i=1}^{n} \eta_i(\lambda,\phi) f_i(t) \tag{37}$$

in which

$$f_i(t) = \begin{cases} 0 & \text{if } t < t_i \\ \dfrac{t - t_i}{\tau_i} & \text{if } t_i \le t \le (t_i + \tau_i) \\ 1 & \text{if } t > (t_i + \tau_i) \end{cases} \tag{38}$$

where $n = 3$ is the number of subfaults for the 2009 Samoa-Tonga Earthquake, η_i is the vertical earth surface deformation associated with rupture of subfault i from Okada (1985), and t_i and τ_i are the corresponding rupture initiation time and rise time. The source time function (38) defines a linear motion of the slip at each subfault to approximate the rupture process in the absence of detailed source time information (Irikura, 1983).

7.3.1.4 Results and discussion

The 2009 South Pacific Tsunami is reconstructed from its generation at the earthquake source to runup at Pago Pago Harbor with the four levels of nested grids and the smoothed bathymetry data in Figure 7-39. A Manning's coefficient $n = 0.035$ represents the surface roughness of the coral reefs in the near-shore seabed according to Bretschneider et al. (1986). The momentum-conserved advection scheme is used at the level-4 grid to describe flow discontinuities associated with wave breaking and bore formation.

Tsunami energy propagation is directional with the majority perpendicular to the fault-line. The main energy propagates toward Tonga and American Samoa, where the tide gauge in Pago Pago Harbor recorded a strong signal of the tsunami. The three DART buoys, which are located roughly along the strike direction off the main energy beams, also recorded clear signals. Figure 7-40 shows a comparison of the recorded and computed waveforms and spectra at the Pago Pago tide gauge and at the three DART buoys. The computed results show good agreement of the arrival time, amplitude, and frequency content with the measurements. The model reproduces the initial negative wave at the tide gauge and captures the distinct 11- and 18-min oscillations at Pago Pago Harbor. The computed surface elevations at the three DART buoys show very good agreement with the recorded data. NEOWAVE, with the fault parameters in Table 7-4, successfully reproduces the arrival time, amplitude, and polarity of the recorded signals at the three DART buoys, which could not be achieved with a single normal fault (Yamazaki et al., 2011). DART 51426 and 54401 recorded the high-amplitude reflected waves from Tutuila arriving at 1.6 and 3.2 hours after the earthquake. The computed results at DART 51426 cannot reproduce the amplitudes, but reasonably predicts the reflected wave's arrival time. The computed results at DART 54401 show excellent agreement with recorded data, including the reflected waves.

Figure 7-41 compares the computed runup and inundation around Pago Pago Harbor with the measurements from Koshimura et al. (2009) and Okal et al. (2010). The model reproduces the overall pattern and height of the runup along the coast. The minor discrepancies between the computed results and the measurements are primarily due to the difficulties in modeling inundation in the built environment around Pago Pago Harbor. The large runup at the tip and low values in the outer harbor are results of resonance. Such oscillations, which extend over the

entire insular shelf and slope, provide an explanation for the local amplification and the disparate property damage along the coastlines of Tutuila (Roeber et al., 2010; Yamazaki et al., 2011). NEOWAVE reproduces the surface elevations at the Pago Pago tide gauge and the DART buoys as well as the runup around the harbor. The proposed field benchmark problem demonstrates the model capability in describing generation, propagation, and runup of tsunamis.

The 2009 South Pacific Tsunami is an excellent benchmark with high quality bathymetric and topographic data, water level records, and runup and inundation measurements. This is the first complete dataset of a significant event that has both water level as well as runup and inundation records at the same location. On the other hand, the initial condition is still an ongoing research topic. Modelers may use any suitable fault parameters in the validation.

7.3.2 2006 Kuril and 2010 Chile tsunamis: nearshore surface elevation and current

7.3.2.1 Introduction

Concurrent surface elevation and flow measurements of tsunamis in nearshore waters have been rare. The Kilo Nalu Observatory, which is a cabled coastal monitoring station at the south shore of Oahu, shown in Figure 7-42, represents an important asset in tsunami research. The facility is managed by the Department of Ocean and Resources Engineering, School of Ocean and Earth Science and Technology (SOEST), University of Hawaii (UH) to provide real-time hydrodynamic and geochemical data since 2004 (Pawlak et al., 2009). The observatory extends from 12 to 20 m water depth on an open coast. An acoustic Doppler current profiler (ADCP) was deployed at the observatory in 2006 to measure real-time velocity and pressure at 12 m depth and 400 m from the shore (21.2885°N, 157.8648°W). The ADCP has detected several tsunami events since its deployment and recorded clear signals of the 2006 Kuril and 2010 Chile tsunamis.

The Honolulu tide gauge (21.3033°N, 157.8645°W) adjacent to the Kilo Nalu Observatory also recorded clear signals of the 2006 Kuril and 2010 Chile tsunamis. The recorded data reflect the flows in a basin through narrow harbor channels. In contrast, the surface elevation and velocity data at the Kilo Nalu ADCP represents nearshore wave processes on an open coast. The recorded tsunami data and high-resolution bathymetry in the region provide a valuable field benchmark to examine model capabilities in describing detailed nearshore flow conditions and their transformation into harbor basins. The use of the USGS finite fault solutions of the 2006 Kuril and 2010 Chile earthquakes as initial conditions for tsunami modeling have been validated with DART and tide gauge data by Munger and Cheung (2006) and Yamazaki and Cheung (2011). We demonstrate the implementation of this benchmark with the non-hydrostatic free surface flow model NEOWAVE (Yamazaki et al., 2009; 2011).

7.3.2.2 Bathymetry and topography data

The digital elevation model is derived from a blended dataset from multiple bathymetry and topography data sources. The 1-arcmin (≈ 1800-m) ETOPO1 from National Geophysical Data Center (NGDC) provides the bathymetry for the Pacific Ocean. The 1.5-arcsec (≈ 50-m) SOEST mutibeam data covers the Hawaiian Islands bathymetry and the gaps are filled with the 5-arcsec (≈ 150-m) Japan Marine Science and Technology Center (JAMSTEC) and US Geological Survey (USGS) data. The 4-m Scanning Hydrographic Operational Airborne LiDAR Survey (SHOALS) data from U.S. Army Corps of Engineers (USACE) covers the nearshore bathymetry

from 40 m water depth to the coast, while the 1-m LiDAR topography from the Federal Emergency Management Agency (FEMA) and the U.S. Army Corps of Engineers (USACE) covers the coastal area up to 15 m elevation. The areas above the 15-m contour are filled with the 30-m National Elevation Dataset (NED) from USGS. The multiple datasets were merged with ArcGIS, converted to reference the WGS 84 datum and the mean-sea level (MSL). The Generic Mapping Tools (GMT) interpolates the data to produce nested computational grids.

Four levels of nested grids are used to reconstruct the 2006 Kuril and 2010 Chile tsunamis from the respective source to the south shore of Oahu. Figure 7-43(a) shows the coverage of the level-1 grids for the 2006 Kuril and 2010 Chile tsunamis over the north and southeast Pacific at 2-arc min (≈ 4000-m) resolution. An open boundary condition allows radiation of tsunami waves away from the computational domain. The level-2 grid in Figure 7-43(b) covers the Hawaiian Islands at 15-arcsec (≈ 500-m) resolution to capture wave transformation around the island group. The level-3 grid in Figure 7-43(c) resolves the insular shelf and slope of Oahu at 3 arcsec (~ 100 m) and provides a transition to the level-4 grid, which covers the south shore of Oahu at 0.3 arcsec (~10 m) resolution for computation of tsunami signals at the Kilo Nalu ADCP and at the Honolulu tide gauge, as shown in Figure 7-42. This nested-grid system describes wave dynamics at resolutions compatible with the physical process and at spatial scales that optimize computational resources.

Dispersive wave models, including the present depth-integrated, non-hydrostatic models and Boussinesq-type models, are prone to instability over localized, steep bottom gradients at high-resolution computations (Horrillo et al., 2006; Løvholt and Pederson, 2008). In this study, the depth-dependent Gaussian function of Yamazaki et al. (2011) is used to smooth bathymetric features smaller than the water depth to resolve the stability issues without significantly modifying the nearshore wave transformation shown in Figure 7-44. Modelers can use either the original or smoothed datasets depending on the type of models being examined.

7.3.2.3 Finite fault models and initial conditions

The Mw 8.3 Kuril earthquake occurred along Kuril Trench 495 km SSW of Severo-Kuril'sk, on 15 November 2006 at 11:14:17 UTC or 1:14:17 a.m. Hawaii Standard Time (HST). The resulting tsunami traveled across the Pacific reaching Hawaii at 7:20 a.m. (HST), 6 hours after the earthquake. The Mw 8.8 Chile earthquake occurred along the Peru-Chile Trench offshore of Maule, Chile (105 km NNE of Concepcion) on 27 February 2010 at 6:34:14 UTC (8:34:14 p.m. HST), and generated a destructive tsunami in the near field that resulted in warnings across the Pacific. The tsunami reached Hawaii at 11:19 a.m., 14.5 hours after the earthquake. Neither tsunami caused major damage in Hawaii, but prolonged oscillations and strong currents associated with tsunamis were observed at harbors and embayments around the Hawaiian Islands (Bricker et al., 2007, and Munger and Cheung, 2008).

USGS analyzed the 2006 Kuril and the 2010 Chile earthquake using the finite fault algorithm of Ji et al. (2002). For the 2006 Kuril earthquake, the finite fault solution utilizes a 400 km long and 137.5 km wide fault, which is sub-divided into 220 subfaults of 20 km long and 12.5 km wide, each with strike angle = 220° and dip angle = 14.89°, and hypocenter, 46.616°N, 153.224°E, at 26.7-km depth. The resulting finite fault solution, shown in Figure 7-45(a), estimates seismic moment of 3.9×10^{21} N·m (Mw 8.3). (Ji C, 2010, http://earthquake.usgs.gov/earthquakes/eqinthenews/2006/usvcam/finite_fault.php). For the 2010 Chile earthquake, the

solution utilized a fault of 540 km long and 200 km wide subdivided into 180 subfaults of 30 km by 20 km, with strike angle = 16.13 ° and dip angle = 14.84°, and hypocenter, 35.83°S, 72.67°W, at 35-km depth (Hayes G, 2010, http://earthquake.usgs.gov/earthquakes/eqinthenews/2010/us2010tfan/finite_fault1.php). The resulting finite fault solution in Figure 7-45(c) estimates seismic moment of 2.0×10^{22} N·m (Mw 8.8). The USGS finite fault solutions of the 2006 Kuril and 2010 Chile earthquakes in Figure 7-45(a) and (c) provide the sea surface deformations in Figure 7-45(b) and (d) through (36) as the initial conditions of the two benchmarks.

7.3.2.4 Results and discussion

The 2006 Kuril and 2010 Chile tsunamis are reconstructed from the generation at the earthquake sources to the nearshore transformation at the south shore of Oahu, using the smoothed bathymetry. A Manning's coefficient $n = 0.035$ represents the surface roughness of the coral reefs in the near-shore seabed according to Bretschneider et al. (1986). The momentum-conserved advection scheme is used at the level-4 grid to describe flow discontinuities associated with wave breaking and bore formation.

Figure 7-46 shows a comparison of the recorded and computed data at the Honolulu tide gauge and at Kilo Nalu for the 2006 Kuril tsunami. The computed surface elevations show very good agreement of the arrival time, amplitude, and frequency content with the measurements. However, the computed velocity component, u, along the longitude cannot capture the first distinct signal and underestimates the overall amplitude. The computed velocity component, v, along the latitude shows very good agreement of the arrival time and amplitude, of the first two waves especially, but it still underestimates the overall amplitudes.

Figure 7-47 compares the recorded and computed data at the Honolulu tide gauge and at Kilo Nalu for the 2010 Chile tsunami. The model reproduces the measured surface elevations at both the Honolulu tide gauge and at the Kilo Nalu ADCP well, but slightly overestimates the subsequent waves at the tide gauge. On the other hand, the computed subsequent waves at the Kilo Nalu ADCP show very good agreement of the arrival time, amplitude, and frequency content. The measured velocity show a strong noise level compared to the surface elevation. Both computed velocity components show overall good agreement of the arrival time and amplitude with the measurements.

The computed results at the Honolulu tide gauge for both the 2006 Kuril and 2010 Chile tsunamis shows slight overestimations of the amplitude at subsequent waves. The 10-m grid may not be able to describe detailed features of the wharves in the harbor to appropriately model harbor oscillation. Inaccurate harbor oscillation prediction could lead the growing amplitude in the computed surface elevation at the Honolulu tide gauge. Considering the long distance propagation across the Pacific, scattering around the many islets and seamounts, and the effects of background currents, NEOWAVE successfully reproduces the Honolulu tide gauge records and the surface elevation and velocity at the Kilo Nalu ADCP. This validates its capability to predict surface elevations and currents for distant tsunamis.

7.4 Conclusions

This report has demonstrated the versatility and robustness of the shock-capturing, dispersive wave model, NEOWAVE, for tsunami propagation, transformation, and runup. The formulation in the spherical coordinate system accounts for the earth's curvature in basin-wide

tsunami propagation and yet is flexible enough to model inundation at a regional scale through a system of two-way nested grids. Implementation of an upwind flux approximation in the momentum-conserved advection scheme and a mixed non-hydrostatic and hydrostatic hybrid scheme allows modeling of flow discontinuities associated with bores and hydraulic jumps during the runup and drawdown process. A series of numerical experiments with analytical solutions, laboratory data, and field data have verified and validated NEOWAVE as a tool for tsunami inundation mapping.

7.5 References

Bare AY, Grimshaw KL, Rooney JJ, Sabater MG, Fenner D, Carroll B. 2010. Mesophotic communities of the insular shelf at Tutuila, American Samoa, *Coral Reefs*, 29(2), 369-377.

Beavan J, Wang X, Holden,C, Wilson K, Power W, Prasetya G, Bevis M, Kautoke R. 2010. Near-simultaneous great earthquakes at Tongan megathrust and outer rise in September 2009, *Nature*, 466(7309), 959-963.

Bretschneider CL, Krock HJ, Nakazaki E, Casciano FM. 1986. Roughness of Typical Hawaiian Terrain for Tsunami Run-up Calculations: A User's Manual. J.K.K. Look Laboratory Report, University of Hawaii, Honolulu, Hawaii.

Bricker JD, Munger S, Pequignet C, Wells JR, Pawlak G, Cheung KF. 2007. ADCP observations of edge waves off Oahu in the wake of the November 2006 Kuril Island Tsunami. *Geophysical Research Letters*, 34(23), L23617, doi: 10.1029/2007GL032015.

Briggs MJ, Synolakis CE, Harkins GS, Green DR. 1995. Laboratory experiments of tsunami runup on a circular island. *Pure and Applied Geophysics*, 144(3/4), 569-593.

Briggs MJ, Synolakis CE, Kanoglu U, Green DR. 1996. Benchmark Problem 3: runup of solitary waves on a vertical wall. In *Long-Wave Runup Models*, Yeh H, Liu PL-F, Synolakis C. (eds). World Scientific, Singapore, pp. 375-383.

Chaudhry MH. 1993. Open-Channel Flow. Prentice-Hall Inc., Englewood Cliffs, New Jersey, 483 p.

Chen Q, Kirby JT, Dalrymple RA, Kennedy AB, Chawla A. 2000. Boussinesq modeling of wave transformation, breaking, and runup. II: 2D. *Journal of Waterway, Port, Coastal, and Ocean Engineering*, 126(1), 48-56.

Goto C, Ogawa Y, Shuto N, Imamura F. 1997. IUGG/IOC Time Project: Numerical Method of Tsunami Simulation with the Leap-Frog Scheme, Manuals and Guides No. 35, Intergovernmental Oceanographic Commission of UNESCO, Paris.

Horrillo JJ, Kowalik Z, Shigihara Y. 2006. Wave dispersion study in the Indian Ocean tsunami of December 26, 2004. *Marine Geodesy*, 29(1), 149-166.

Irikura K. 1983. Semi-empirical estimation of strong ground motions during large earthquakes, *Bulletin of the Disaster Prevention Research Institute*, 33-2(298), 63-104.

Jaffe BE, Gelfenbaum G, Buckley ML, Watt S, Apotsos A, Stevens AW, Richmond BM. 2010. The limit of inundation of the September 29, 2009, tsunami on Tutuila, American Samoa. *US Geological Survey Open-File Report* 2010-1018, U.S. Geological Survey.

Ji C, Wald DJ, Helmberger DV. 2002. Source description of the 1999 Hector Mine, California, Earthquake, Part I: Wavelet domain inversion theory and resolution analysis. *Bulletin of the Seismological Society of America*, 92(4), 1192-1207.

Kânoğlu U, Synolakis CE. 1998. Long wave runup on piecewise linear topographies. *Journal of Fluid Mechanics*, 374, 1-28.

Koshimura S, Nishimura Y, Nakamura Y, Namegaya Y, Fryer GJ, Akapo A, Kong LS, Vargo D. 2009. Field survey of the 2009 tsunami in American Samoa. *EOS Transactions of the American Geophysical Union*, 90(52), Fall Meeting Supplemental Abstract U23F-07.

Kowalik Z, Murty TS. 1993. Numerical Modeling of Ocean Dynamics. World Scientific, Singapore, 481 p.

Lay T, Ammon CJ, Kanamori H, Rivera L, Koper K, Hutko A. 2010. The 2009 Samoa-Tonga great earthquake triggered doublet. *Nature*, 466(7309), 964-968.

Liu PL-F, Cho YS, Briggs MJ, Kânoğlu U, Synolakis CE. 1995a. Runup of solitary wave on a circular island. *Journal of Fluid Mechanics*, 302, 259-285.

Liu PL-F, Cho YS, Yoon SB, Seo SN. 1995b. Numerical simulations of the 1960 Chilean Tsunami propagation and inundation at Hilo, Hawaii. In Tsunami: Progress in Prediction, Disaster Prevention and Warning. Tsuchiya Y, Shuto, N. (eds). Kluwer Academic Publishers, Netherlands, pp. 99-116.

Løvholt F, Pederson G. 2008. Instabilities of Boussinesq models in non-uniform depth. *International Journal for Numerical Methods in Fluids*, 61(6), 606-637.

Lynett PJ, Wu TR, Liu PL-F. 2002. Modeling wave runup with depth-integrated equations. *Coastal Engineering*, 46(2), 89-107.

Mader CL. 1988. Numerical Modeling of Water Waves. University of California Press, California, 206 p.

Madsen PA, Murray R, Sørensen OR. 1991. A new form of the boussinesq equations with improved linear dispersion characteristics. *Coastal Engineering*, 15(4), 371-388.

Matsuyama M, Tanaka H. 2001. An experimental study of the highest run-up height in the 1993 Hokkaido Nansei-oki earthquake tsunami. In Proceedings of the International Tsunami Symposium 2001, Seattle, Washington, pp. 879-889.

Munger S, Cheung KF. 2008. Resonance in Hawaii waters from the 2006 Kuril Islands Tsunami. *Geophysical Research Letters*, 35(7), L07605, doi: 10.1029/2007 GL032843.

Nwogu O. 1993. Alternative form of Boussinesq equations for nearshore wave propagation. *Journal of Waterway, Port, Coastal, and Ocean Engineering*, 119(6), 618-638.

Okada Y. 1985. Surface deformation due to shear and tensile faults in a half space. *Bulletin of the Seismological Society of America*, 75(4), 1135-1154.

Okal EA, Fritz HM, Synolakis CE, Borrero JC, Weiss R, Lynett PJ, Titov VV, Foteinis S, Jaffe BE, Liu PL-F, Chan IC. 2010. Field Survey of the Samoa Tsunami on 29 September 2009. *Seismological Society of America*, 81(4), 577-591.

Pawlak G, De Carlo EH, Fram JP, Hebert AB, Jones CS, McLaughlin BE, McManus MA, Millikan KS, Sansone FJ, Stanton TP, Wells JR. 2009. Development, deployment, and

operation of Kilo Nalu nearshore cabled observatory. In *Proceedings of the IEEE OCEANS 2009*, Bremen, Germany, May 2009, pp 1-10.

Peregrine DH. 1967. Long waves on a beach. *Journal of Fluid Mechanics*, 27(4), 815-827.

Roeber V, Yamazaki Y, Cheung KF. 2010. Resonance and impact of the 2009 Samoa tsunami around Tutuila, American Samoa, *Geophysical Research Letters*, 37(21), L21604, doi: 10.1029/2010GL044419.

Shuto N, Matsutomi H. 1995. Field survey of the 1993 Hokkaido Nansei-oki earhtuquake tsunami. *Pure and Applied Geophysics*, 144(3/4), 649-663.

Stelling GS, Duinmeijer SP.A. 2003. A staggered conservative scheme for every Froude number in rapidly varied shallow water flows. *International Journal for Numerical Methods in Fluids*, 43(12), 1329-1354.

Stelling GS, Zijlema M. 2003. An accurate and efficient finite-difference algorithm for non-hydrostatic free-surface flow with application to wave propagation. *International Journal for Numerical Methods in Fluids*, 43(1), 1-23.

Stone HL. 1968. Iterative solution of implicit approximations of multidimensional partial differential equations. SIAM (Society for Industrial and Applied mathematics) *Journal on Numerical Analysis*, 5(3), 530-558.

Swigler DT, Lynett P. 2011. Laboratory study of the three-dimensional turbulence and kinematic properties associated with a solitary wave traveling over an alongshore-variable, shallow shelf. in review.

Synolakis CE. 1987. The runup of solitary waves. *Journal of Fluid Mechanics*, 185, 523-545.

Takahashi T. 1996. Benchmark problem 4; the 1993 Okushiri tsunami—Data, conditions and phenomena. In *Long-Wave Runup Models*, World Scientific, 384–403.

Takahashi T, Takahashi T, Shuto N, Imamura F, Ortiz M. 1995. Source models for the 1993 Hokkaido Nansei-oki earthuquake tsunami. *Pure and Applied Geophysics*, 144(3/4), 747-767.

Tanioka Y, Satake K. 1996. Tsunami runup on Okushiri Island. In *Long-Wave Runup Models*, Yeh H, Liu PL-F, Synolakis C. (eds). World Scientific, Singapore, pp. 249-257.

Titov VV, Synolakis CE. 1998. Numerical modeling of tidal wave runup. *Journal of Waterway, Port, Coastal, and Ocean Engineering*, 124(4), 157-171.

Tonelli M, Petti M. 2010. Finite volume scheme for the solution of 2D extended Boussinesq equations in the surf zone. *Ocean Engineering*, 37(7), 567-582.

Walters RA. 2005. A semi-implicit finite element model for non-hydrostatic (dispersive) surface waves. *International Journal for Numerical Methods in Fluids*, 49(7), 721-737.

Wei Y, Cheung KF, Curtis GD, McCreery CS. 2003. Inverse algorithm for tsunami forecasts. *Journal of Waterway, Port, Coastal, and Ocean Engineering*, 129(2), 60-69.

Xiao H, Young YL, Prévost JH. 2010. Hydro- and morpho-dynamic modeling of breaking solitary waves over a fine sand beach. Part II: Numerical simulation. *Marine Geology*, 269(3-4), 119-131.

Yamazaki Y, Cheung KF. 2011. Shelf resonance and impact of near-field tsunami generated by the 2010 Chile earthquake. *Geophysical Research Letters*, 38(12), L12605, doi: 10.1029/2011GL047508.

Yamazaki Y, Cheung KF, Kowalik Z. 2011. Depth-integrated, non-hydrostatic model with grid nesting for tsunami generation, propagation, and run-up. *International Journal for Numerical Methods in Fluids*, 67(12), 2081-2107.

Yamazaki Y, Kowalik Z, Cheung KF. 2009. Depth-integrated, non-hydrostatic model for wave breaking and runup. *International Journal for Numerical Methods in Fluids*, 61(5), 473-497.

Zelt JA. 1991. The run-up of nonbreaking and breaking solitary waves. *Coastal Engineering*, 15(3), 205-246.

7.6 Figures

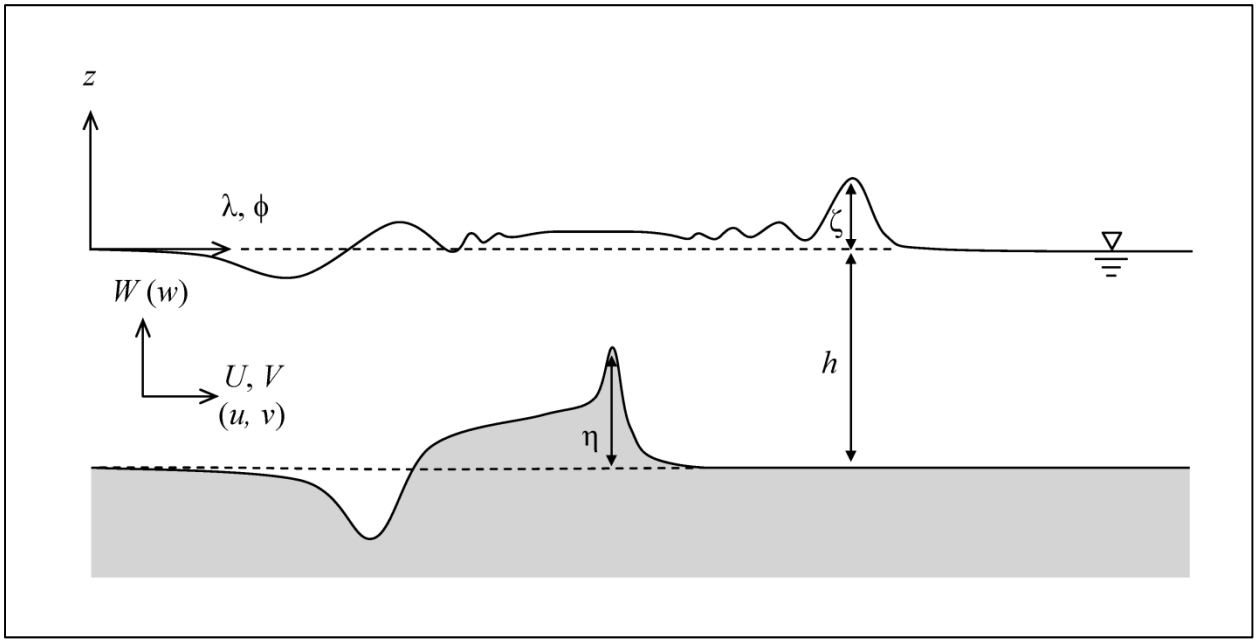

Figure 7-1: Schematic of free-surface flow generated by seafloor deformation.

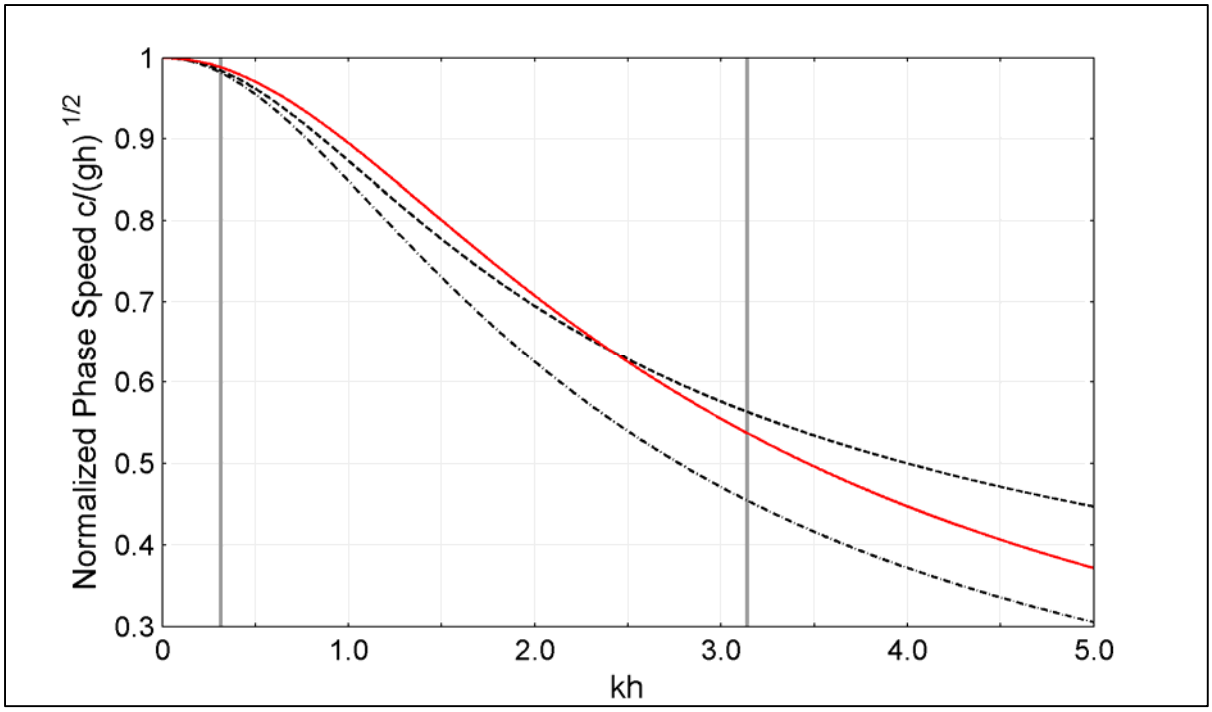

Figure 7-2: Linear dispersion relation. - - - -, Airy wave theory; -·-·-·-, classical Boussinesq equations of Peregrine (1967); ——(red), depth-integrated, non-hydrostatic equations.

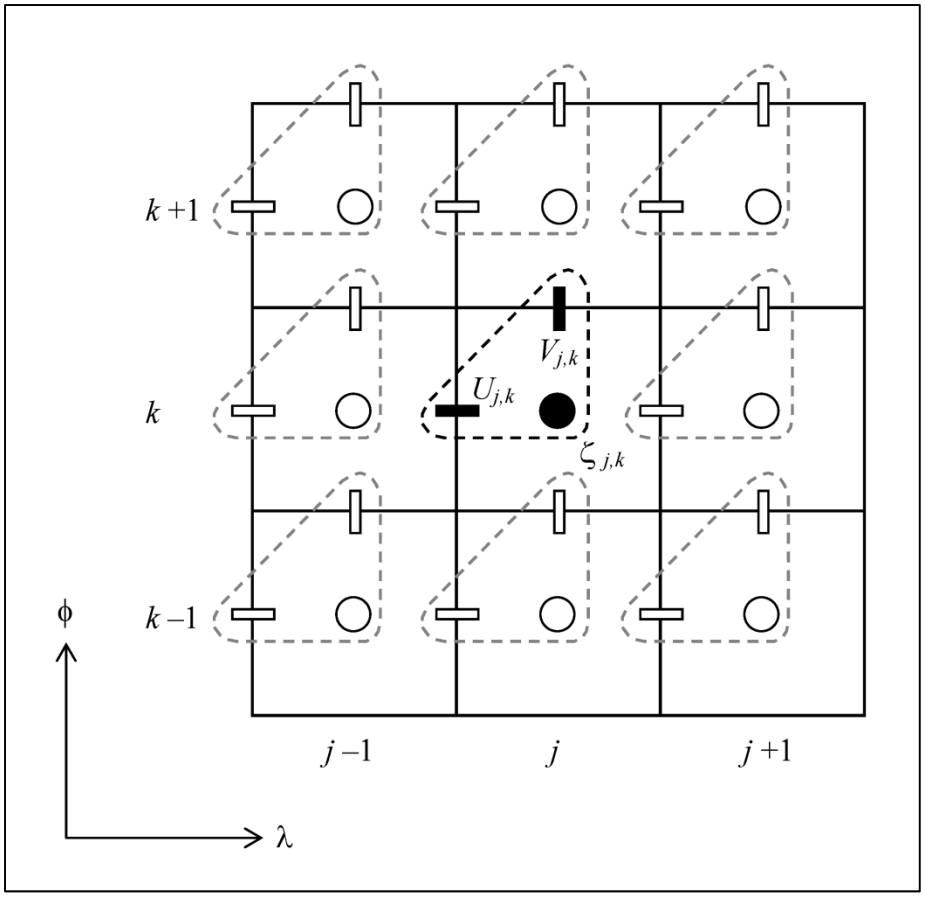

Figure 7-3: Definition sketch of the discretization scheme.

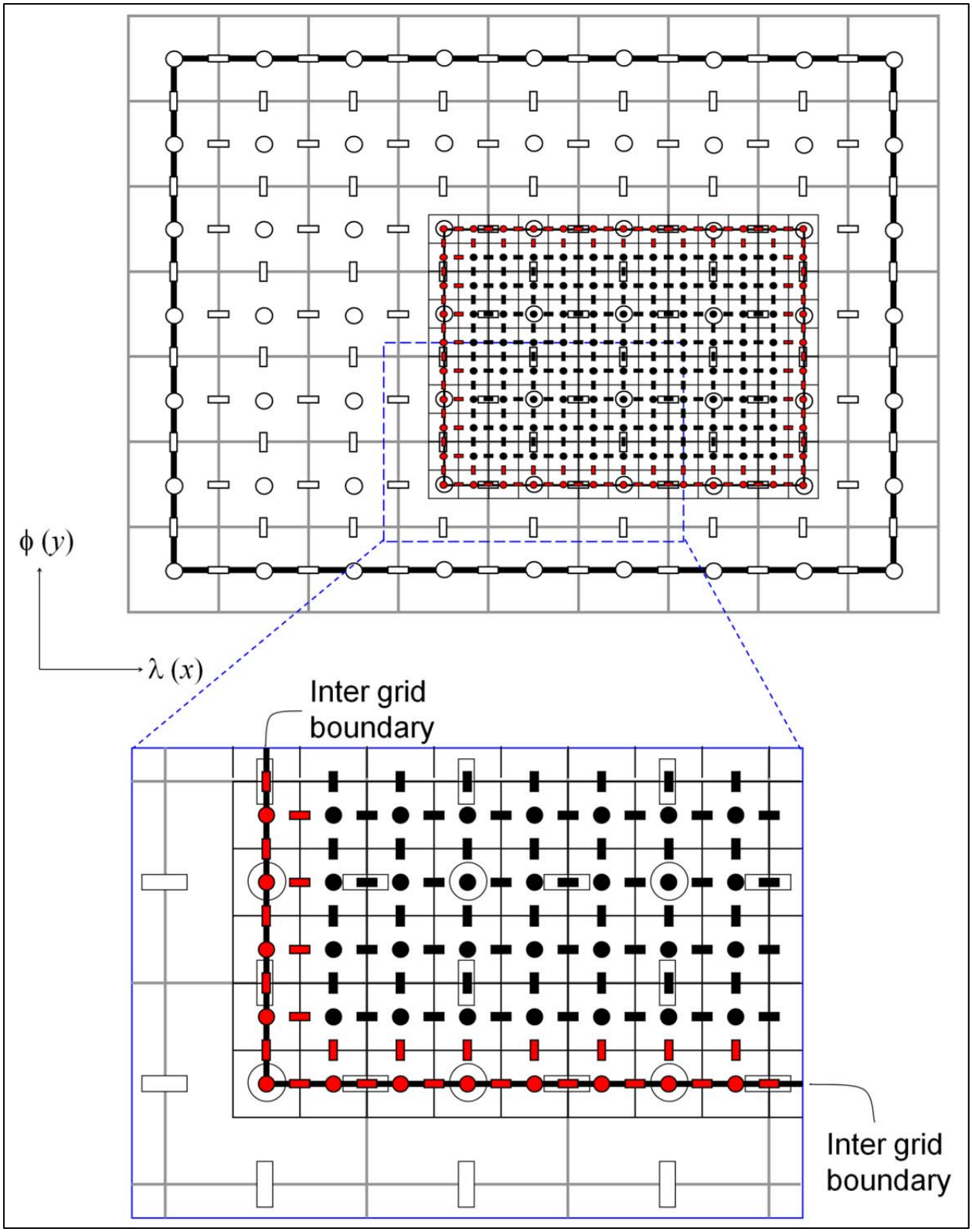

Figure 7-4: Schematic of a two-level nested grid system.

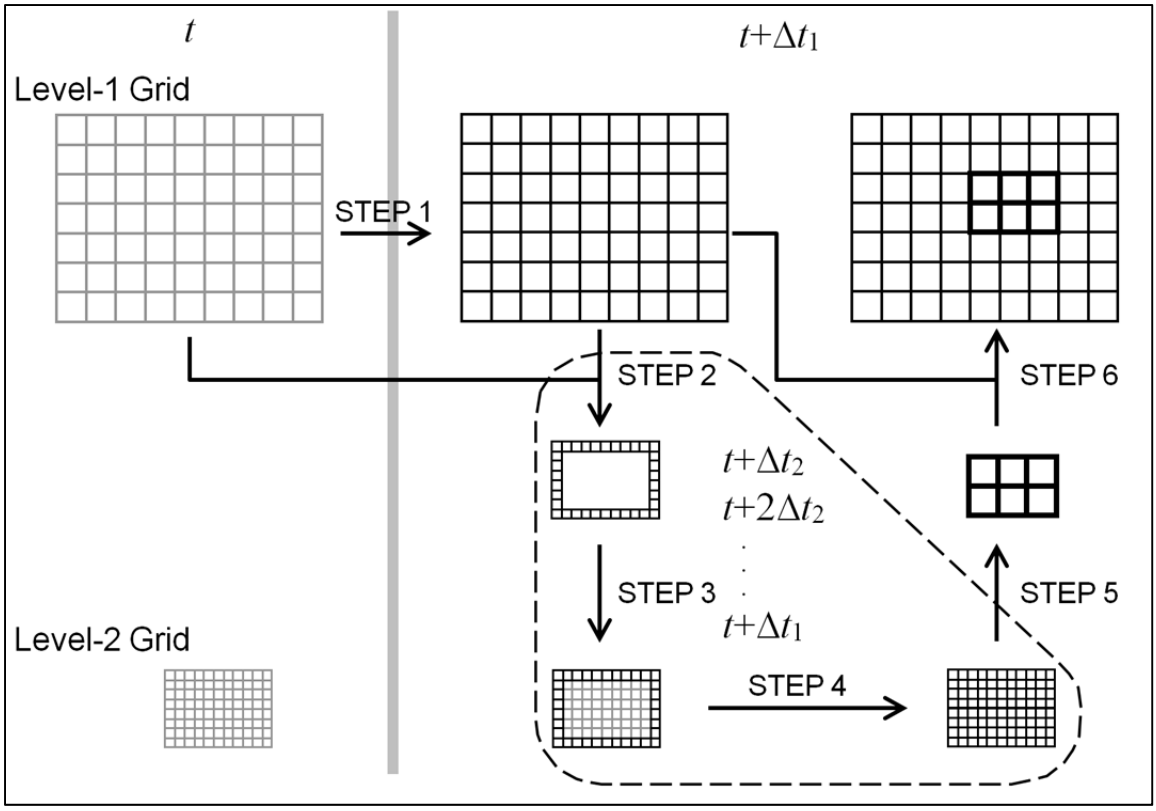

Figure 7-5: Schematic of two-way grid-nesting and time-integration schemes.

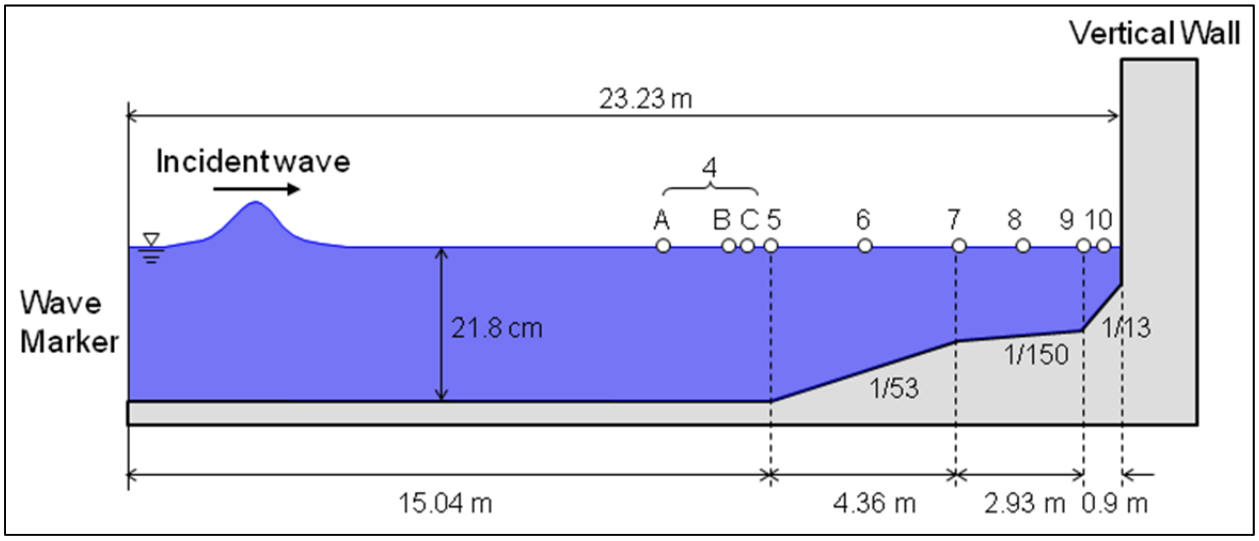

Figure 7-6: Definition sketch of solitary wave on compound slope. ○, gauge locations.

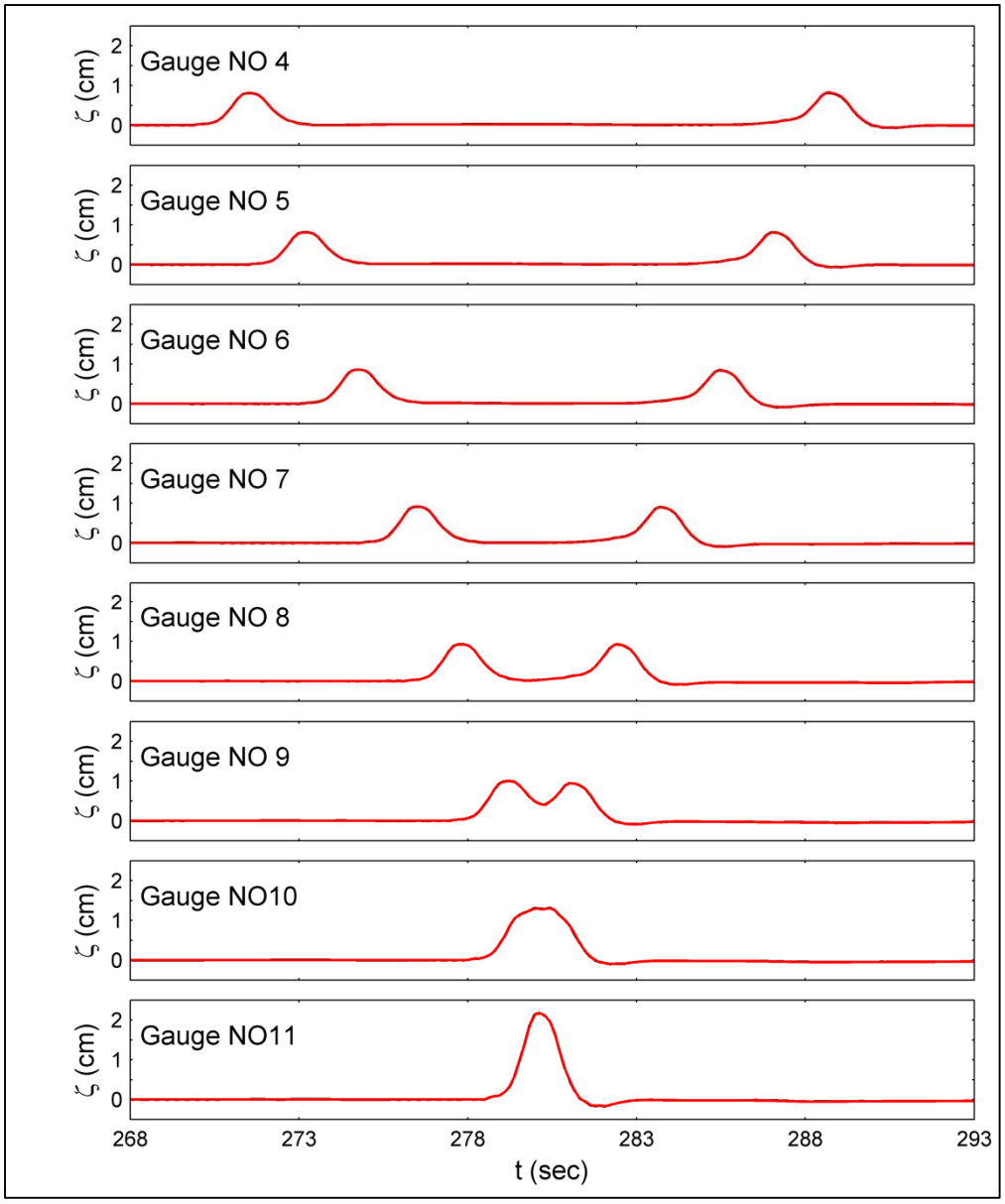

Figure 7-7: Time series of surface elevation at gauges on compound slope with A/h = 0.039. ——— (black), analytical solution of Kânoğlu and Synolakis (1998); ——— (red), computed data.

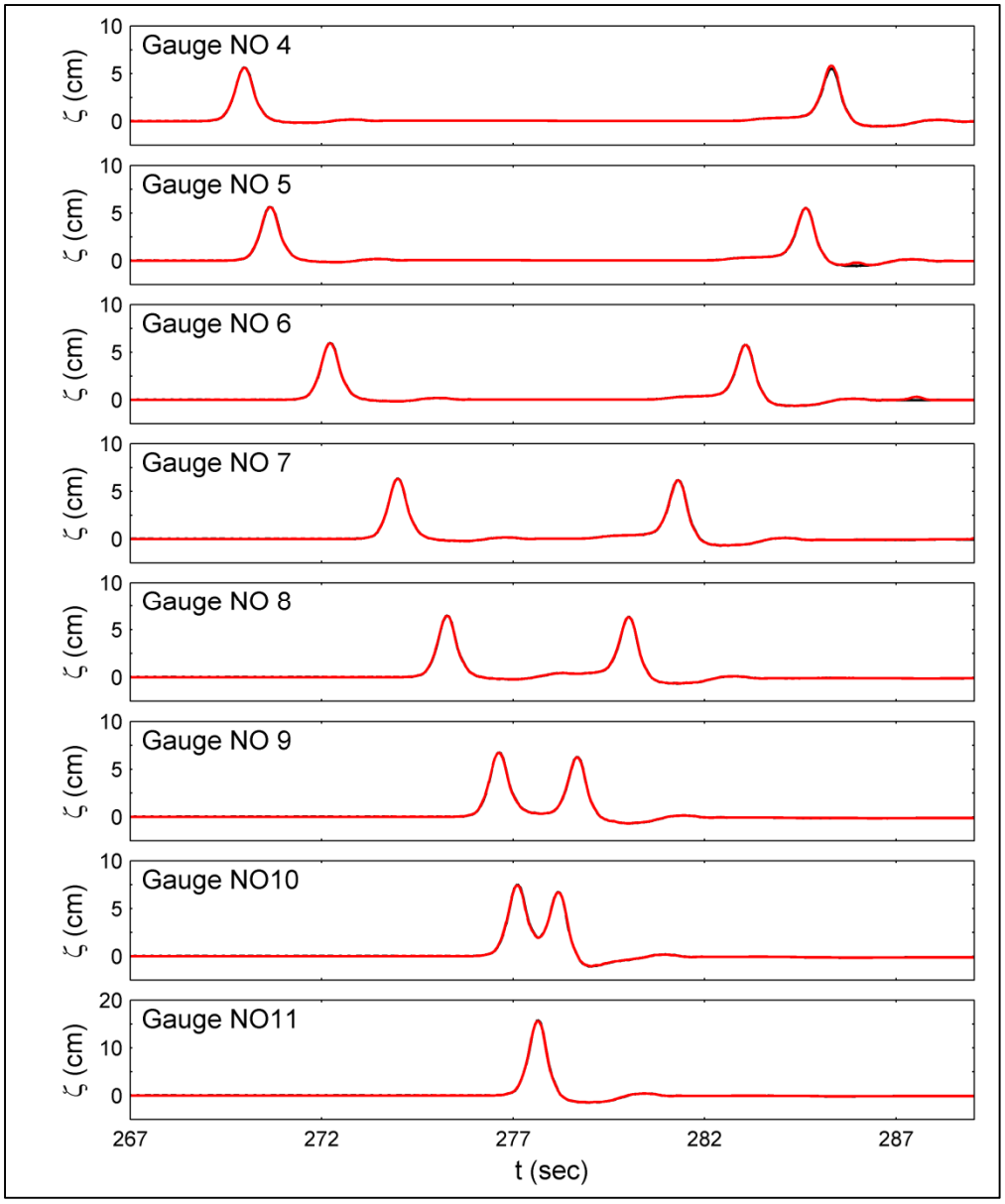

Figure 7-8: Time series of surface elevation at gauges on compound slope with A/h = 0.264. ——— (black), analytical solution of Kânoğlu and Synolakis (1998); ——— (red), computed data.

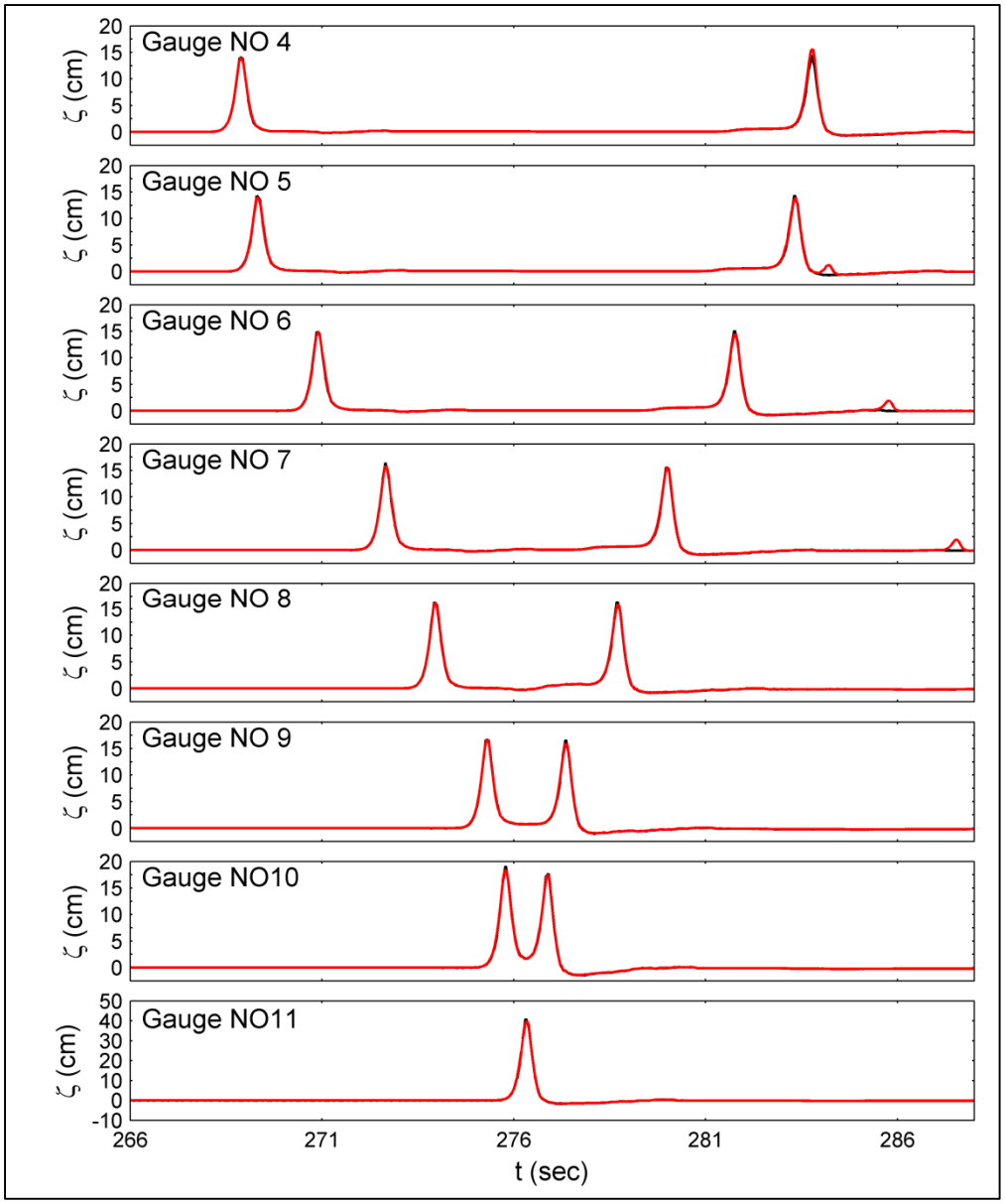

Figure 7-9: Time series of surface elevation at gauges on compound slope with A/h = 0.696. ——— (black), analytical solution of Kânoğlu and Synolakis (1998); ——— (red), computed data.

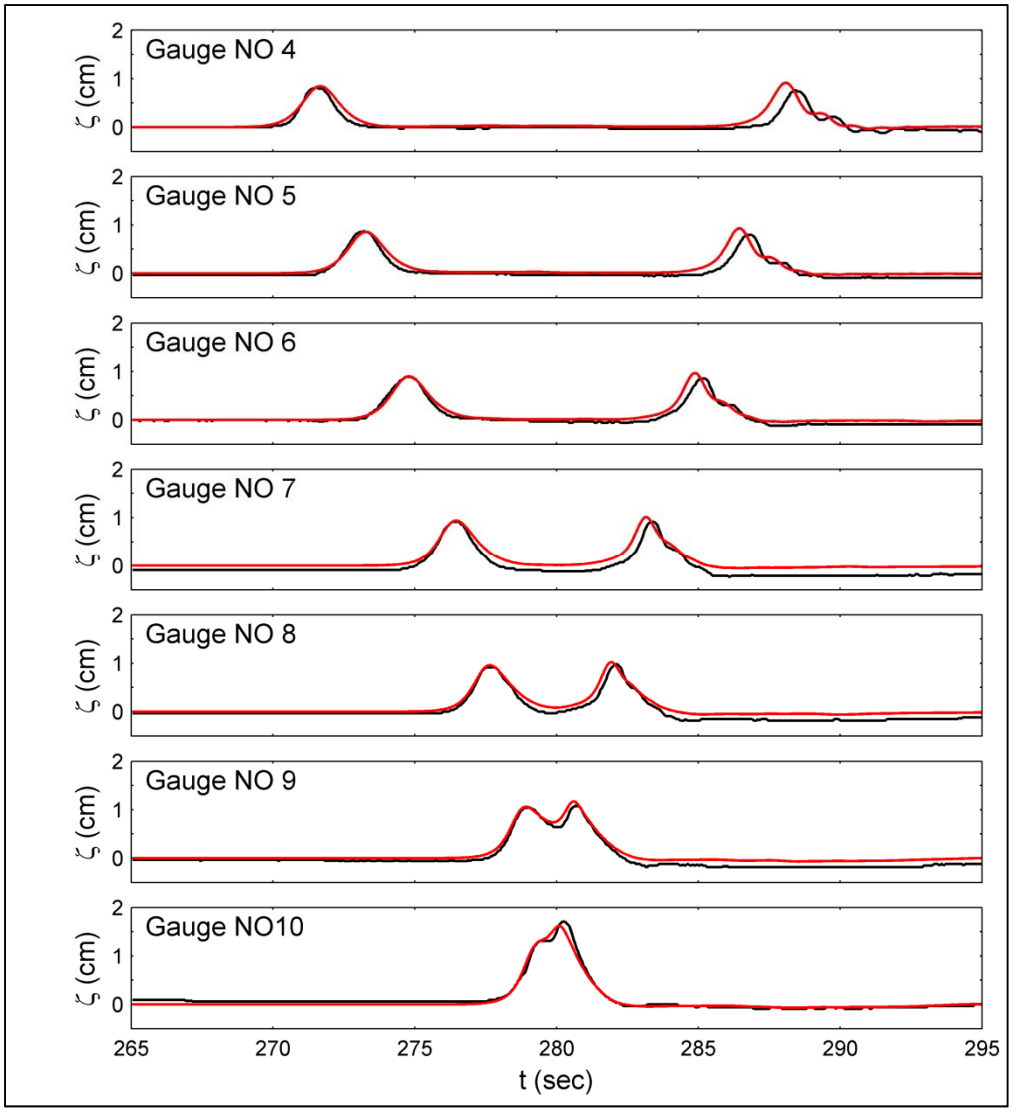

Figure 7-10: Time series of surface elevation at gauges on compound slope with A/h = 0.039. ——— (black), laboratory data of Briggs et al. (1996); ——— (red), solution with NH-Hybrid scheme; ——— (blue), solution without NH-Hybrid scheme.

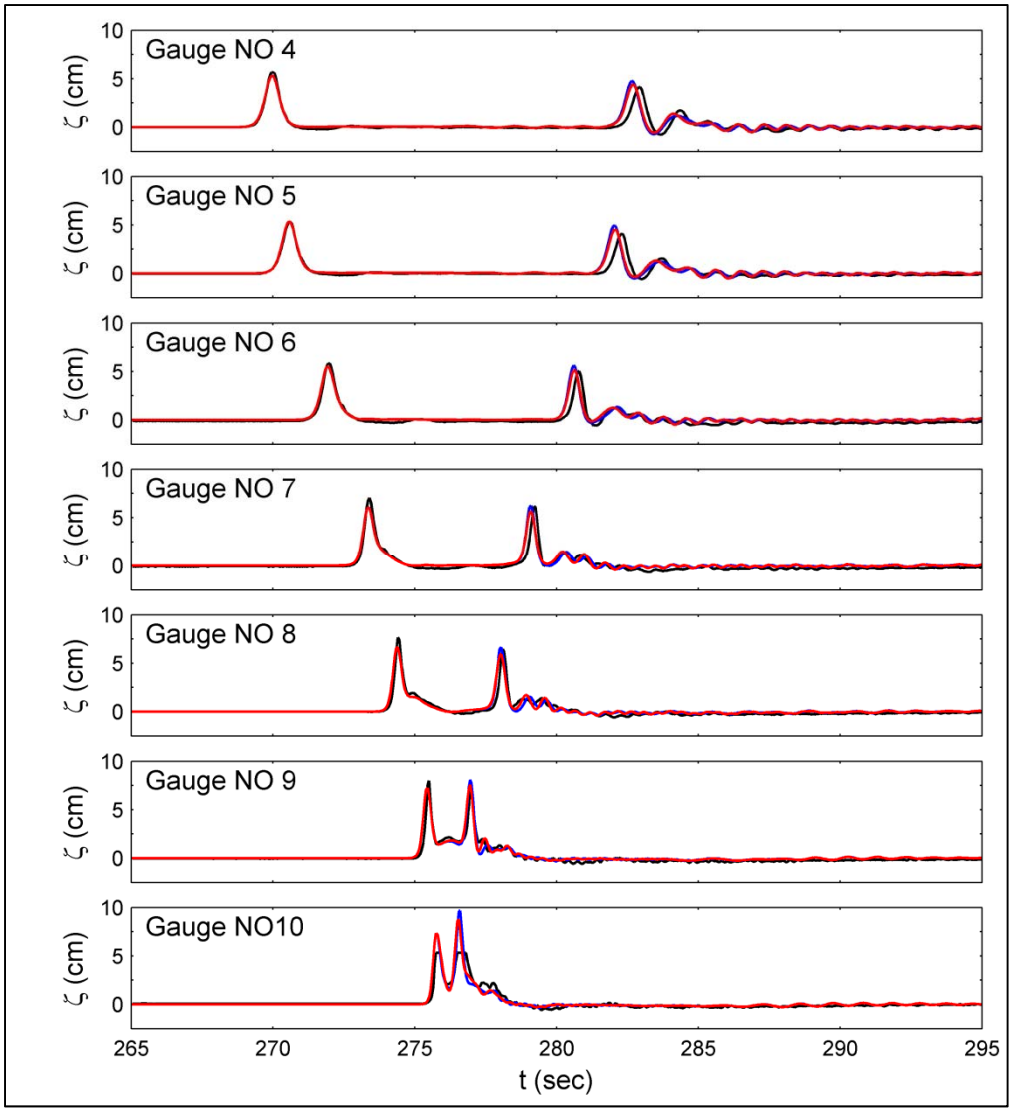

Figure 7-11: Time series of surface elevation at gauges on compound slope with A/h = 0.264. ——— (black), laboratory data of Briggs et al. (1996); ——— (red), solution with NH-Hybrid scheme; ——— (blue), solution without NH-Hybrid scheme.

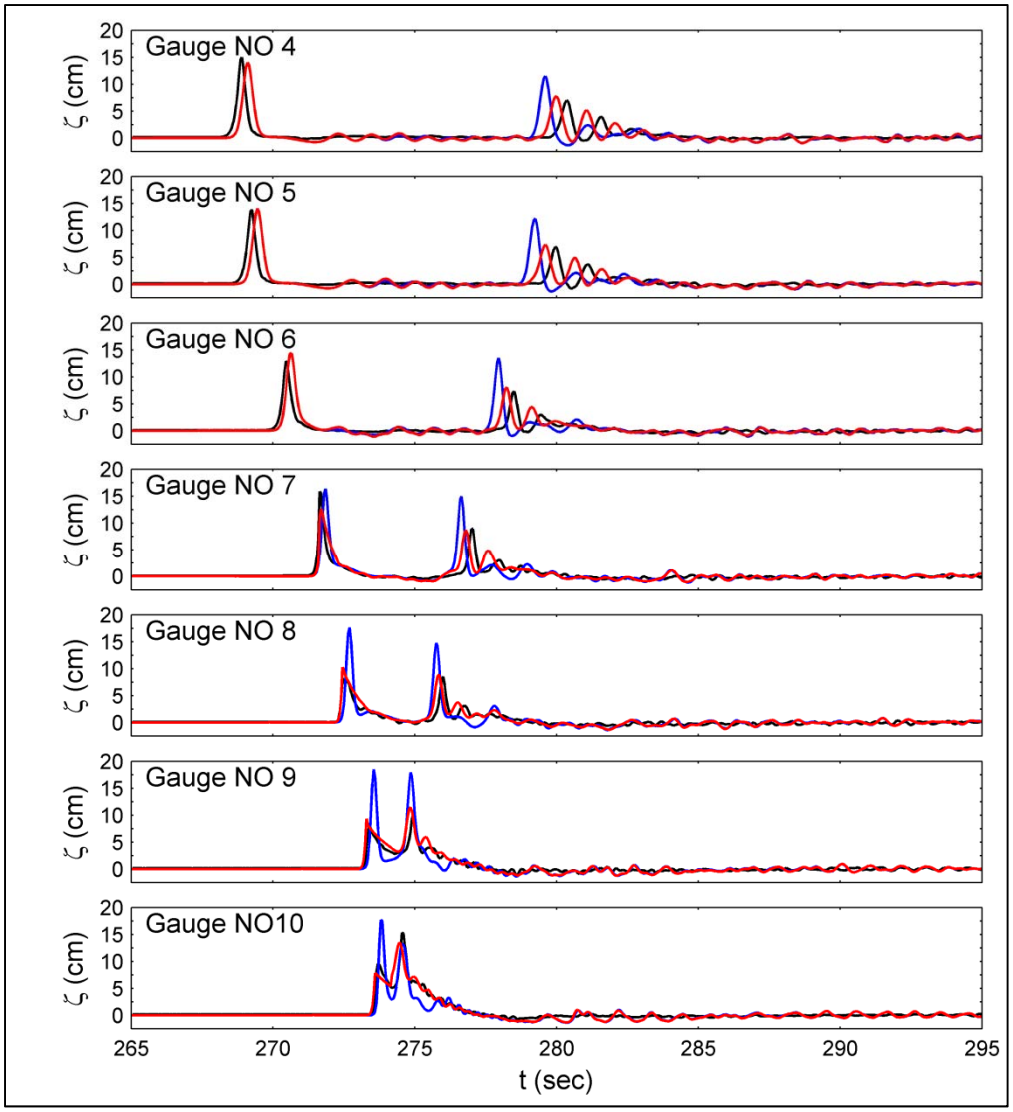

Figure 7-12: Time series of surface elevation at gauges on compound slope with A/h = 0.696. ——— (black), laboratory data of Briggs et al. (1996); ——— (red), solution with NH-Hybrid scheme; ——— (blue), solution without NH-Hybrid scheme.

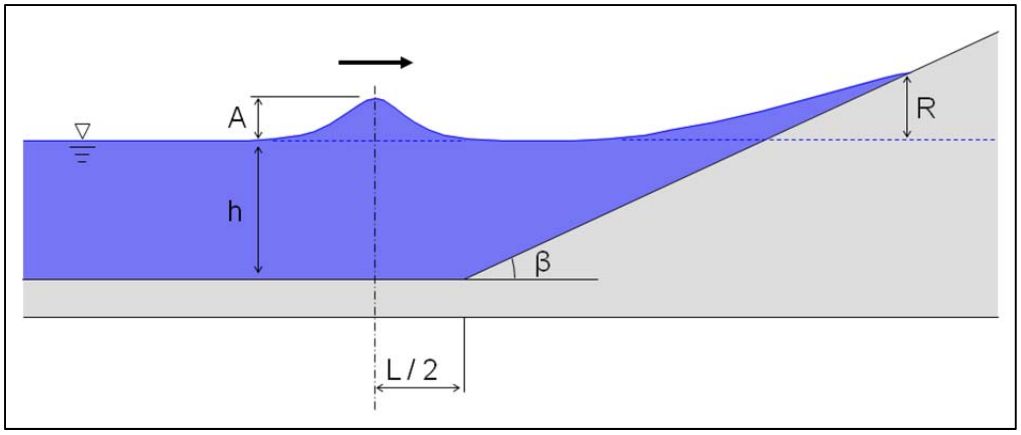

Figure 7-13: Definition sketch of solitary wave runup on plane beach.

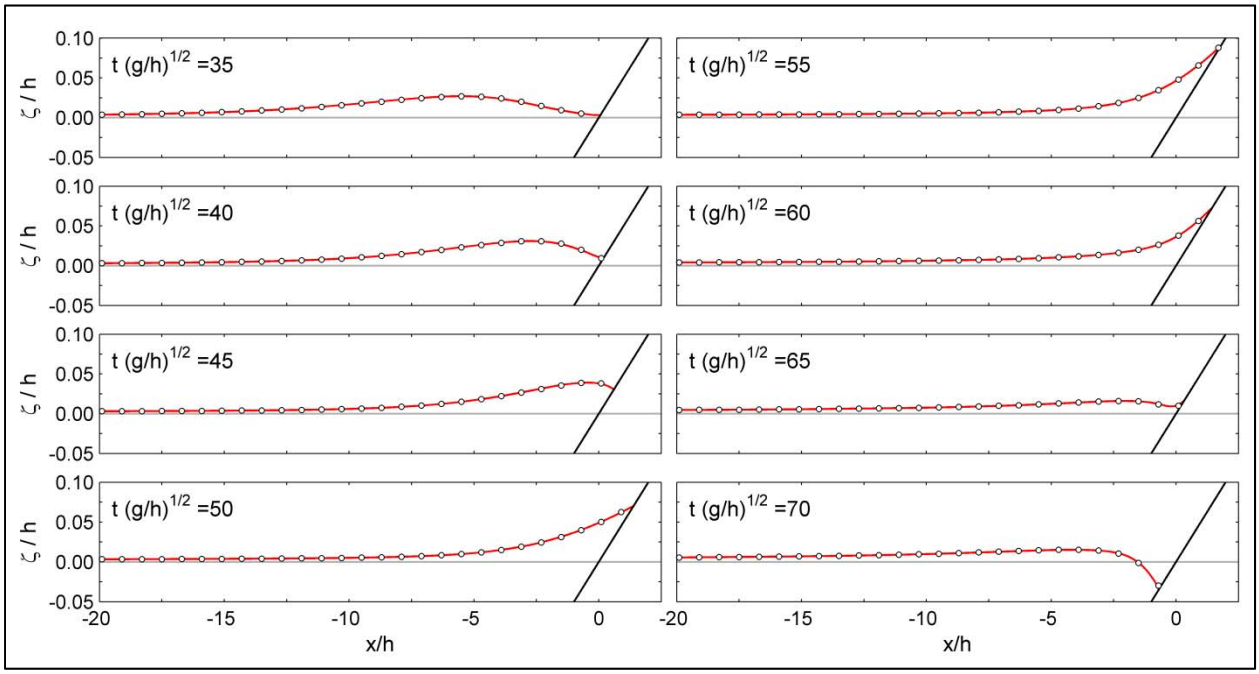

Figure 7-14: Transformation and runup of a solitary wave on a 1:19.85 plane beach with A/h = 0.019. ○, analytical solution of Synolakis (1987); —— (red), computed data.

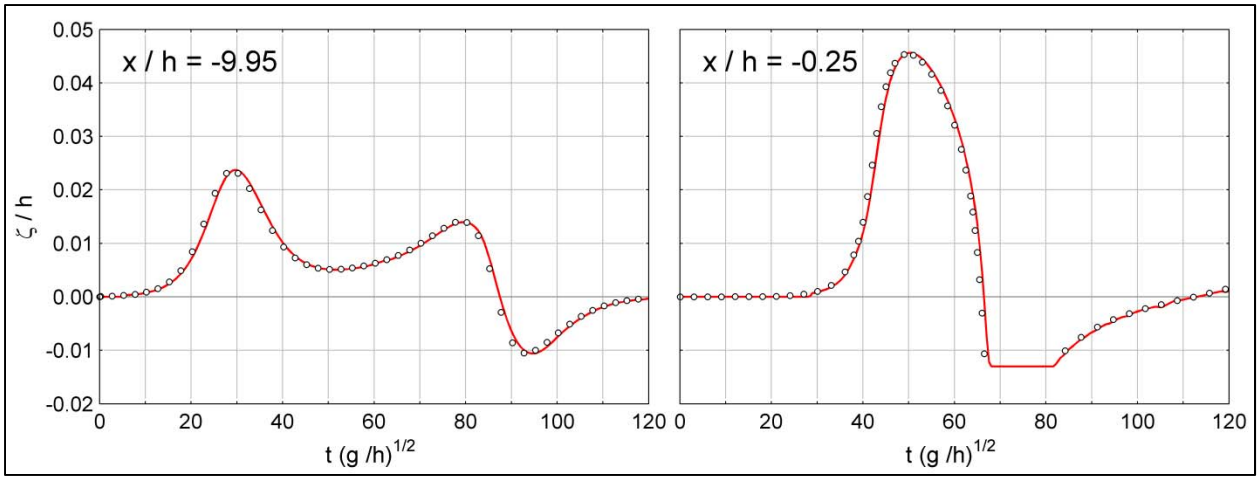

Figure 7-15: Time series of surface elevation at x/h = –9.95 and x/h = –0.25 on a 1:19.85 plane beach with A/h = 0.019. ○, analytical solution of Synolakis (1987); —— (red), computed data.

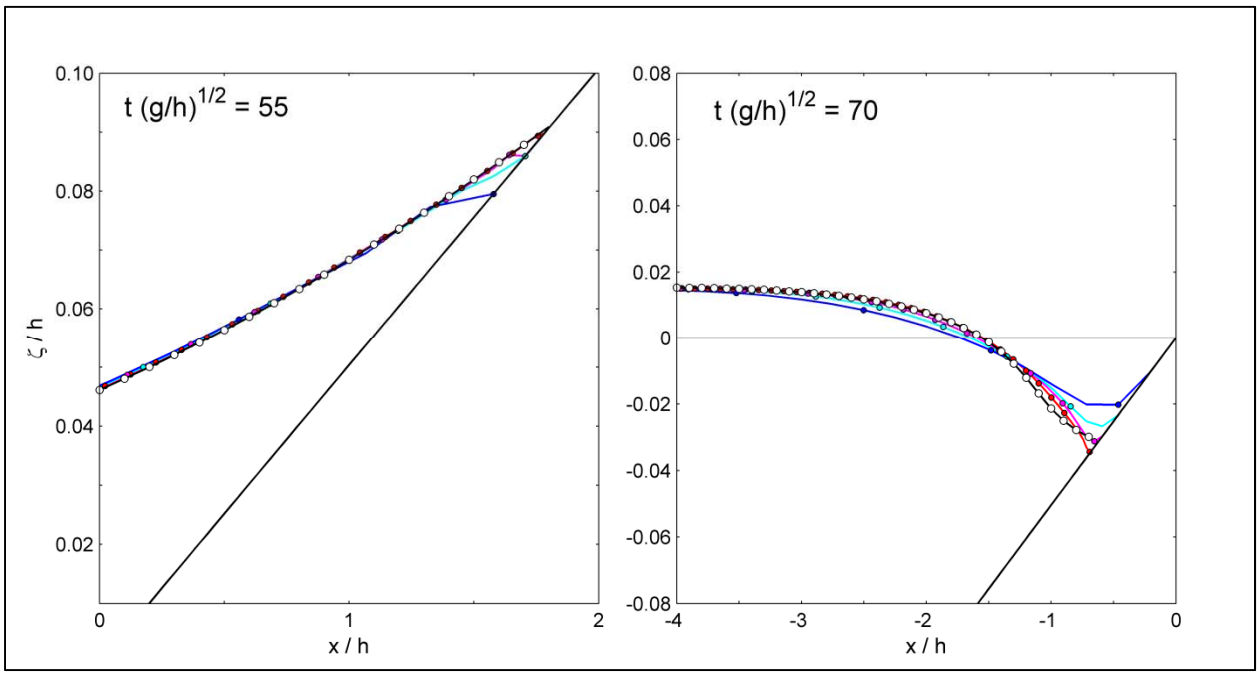

Figure 7-16: Convergence of numerical solution on a 1:19.85 plane beach with A/h = 0.019. ——, analytical solution of Synolakis (1987); —— (red), computed data with Δx/h = 0.025; —— (magenta), computed data with Δx/h = 0.0625; —— (cyan), computed data with Δx/h = 0.125; —— (red), computed data with Δx/h = 0.25.

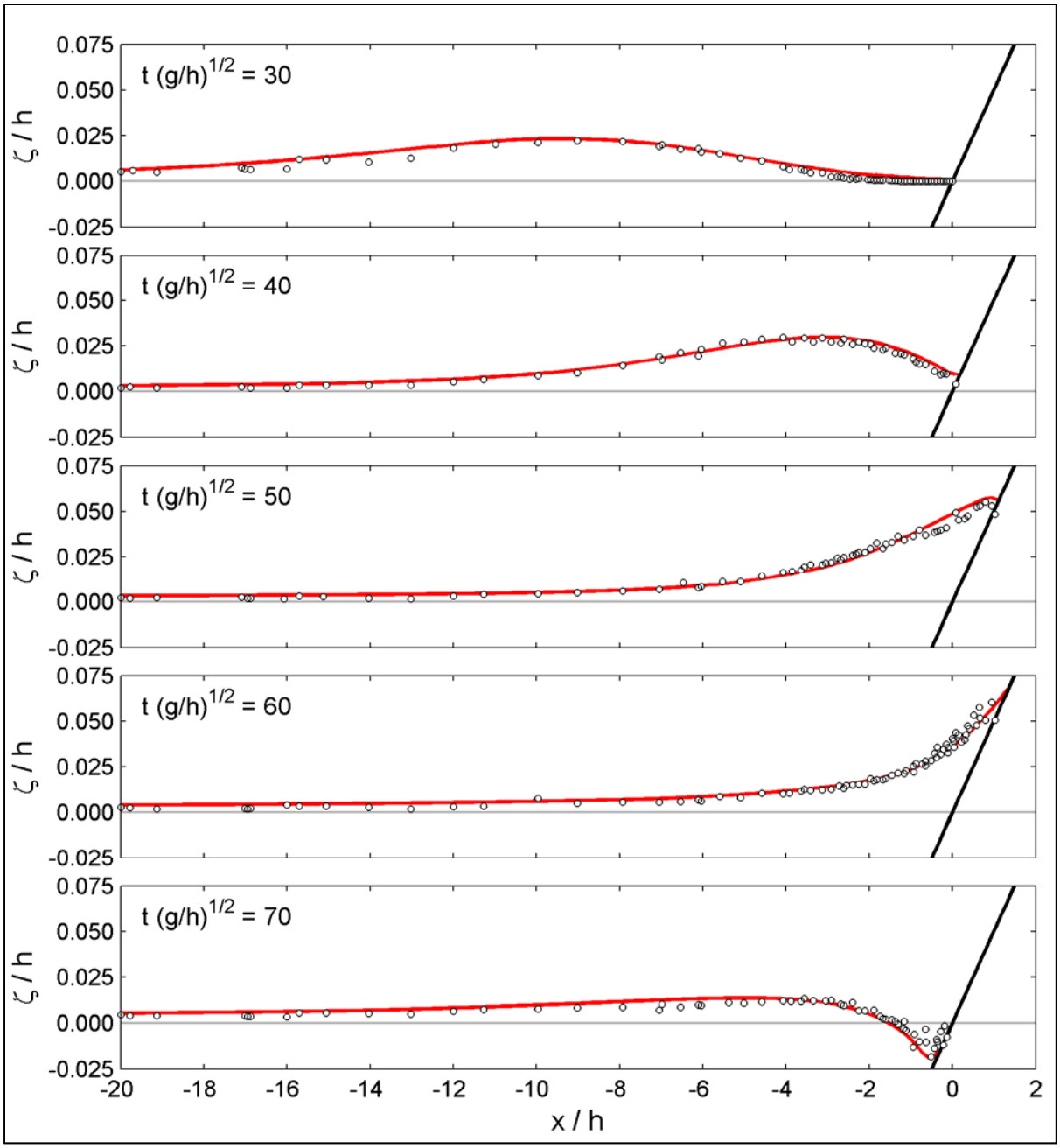

Figure 7-17: Transformation and runup of a solitary wave on a 1:19.85 plane beach with A/h = 0.0185. ○, laboratory data of Synolakis (1987); —— (red), computed data.

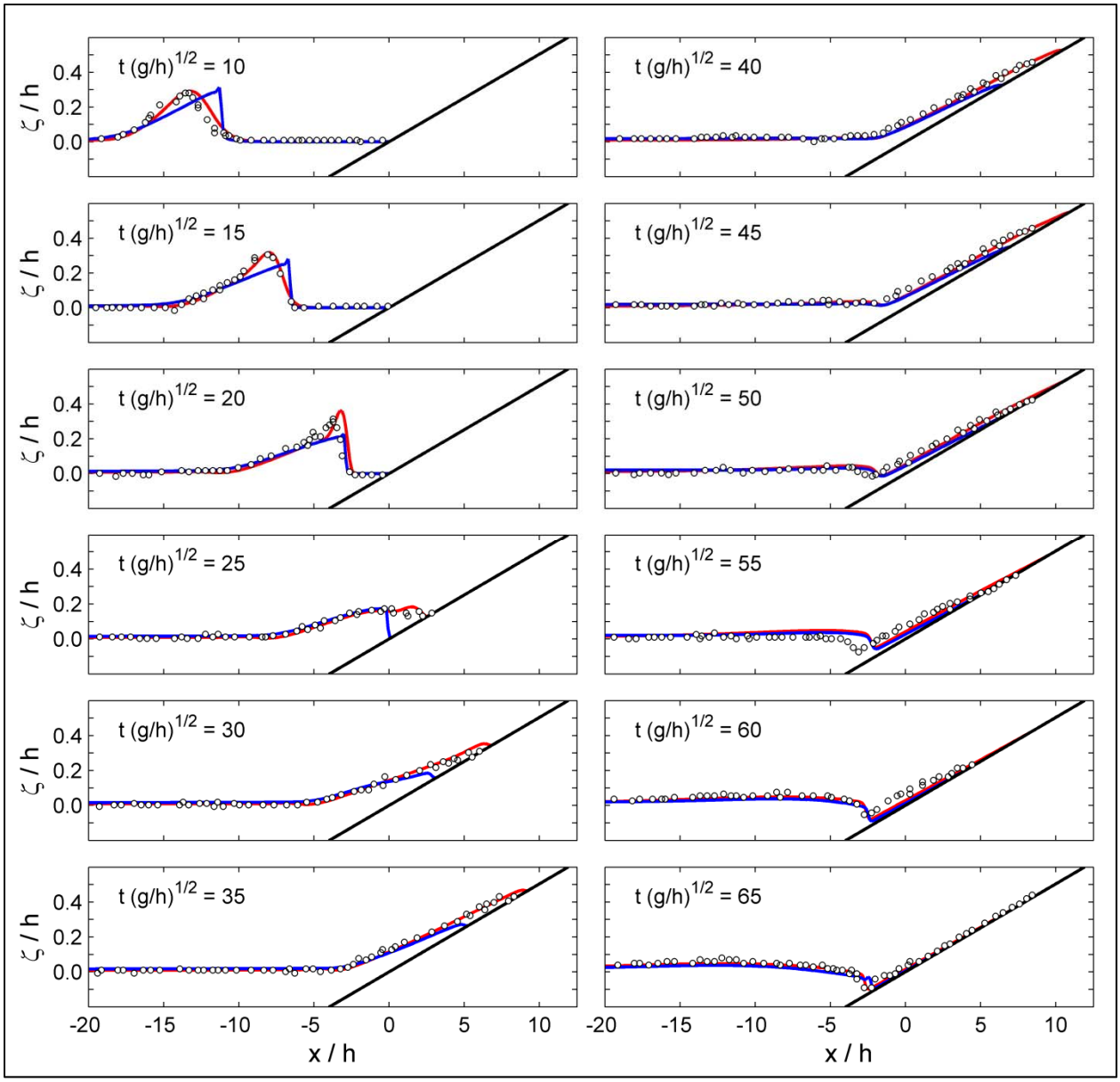

Figure 7-18: Transformation and runup of a solitary wave on a 1:19.85 plane beach with A/h = 0.03. ○, laboratory data of Synolakis (1987); —— (red), non-hydrostatic solution with MCA; —— (blue), hydrostatic solution without MCA.

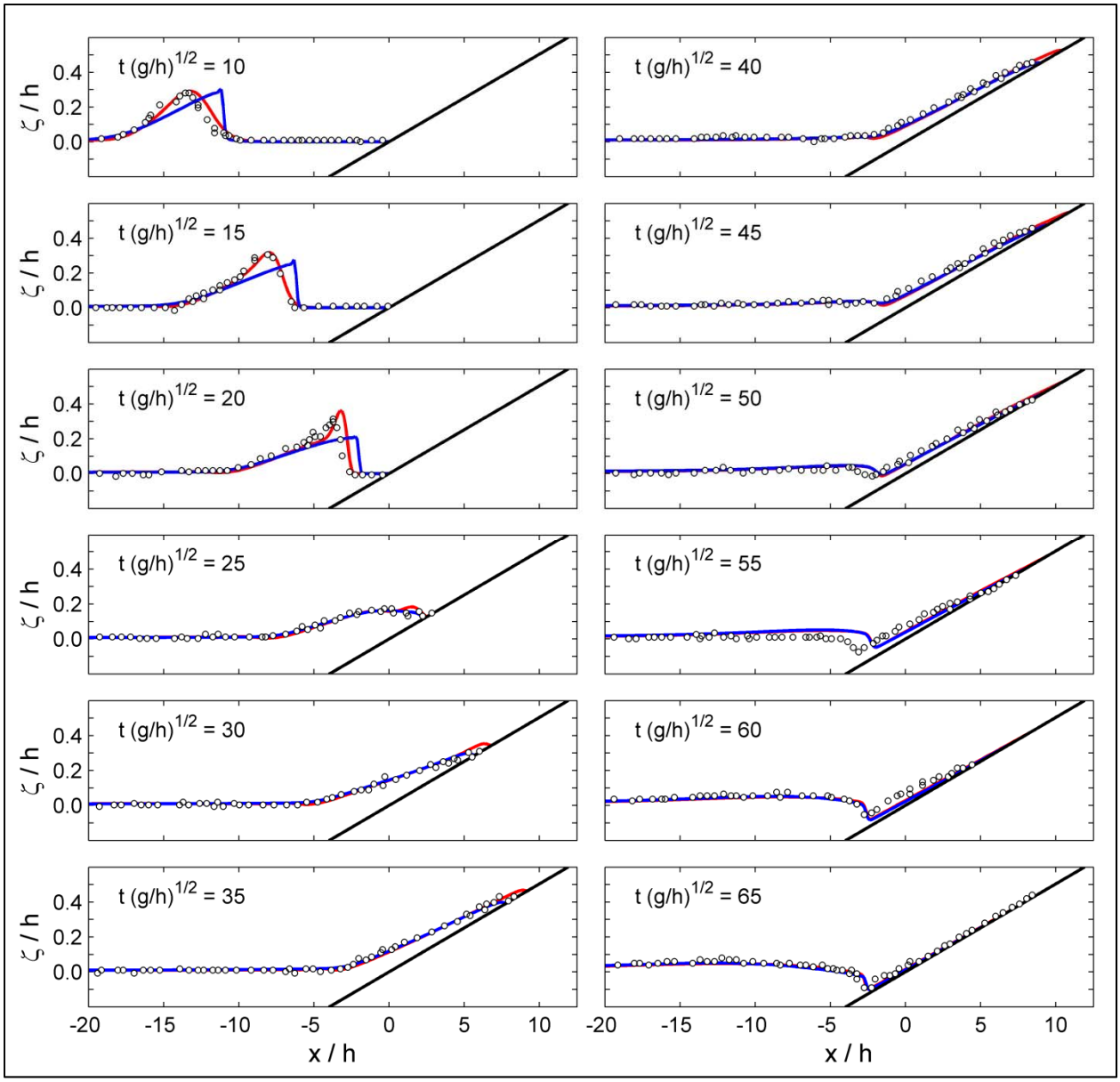

Figure 7-19: Transformation and runup of a solitary wave on a 1:19.85 plane beach with A/h = 0.03. ○, laboratory data of Synolakis (1987); —— (red), non-hydrostatic solution with MCA; —— (blue), hydrostatic solution with MCA.

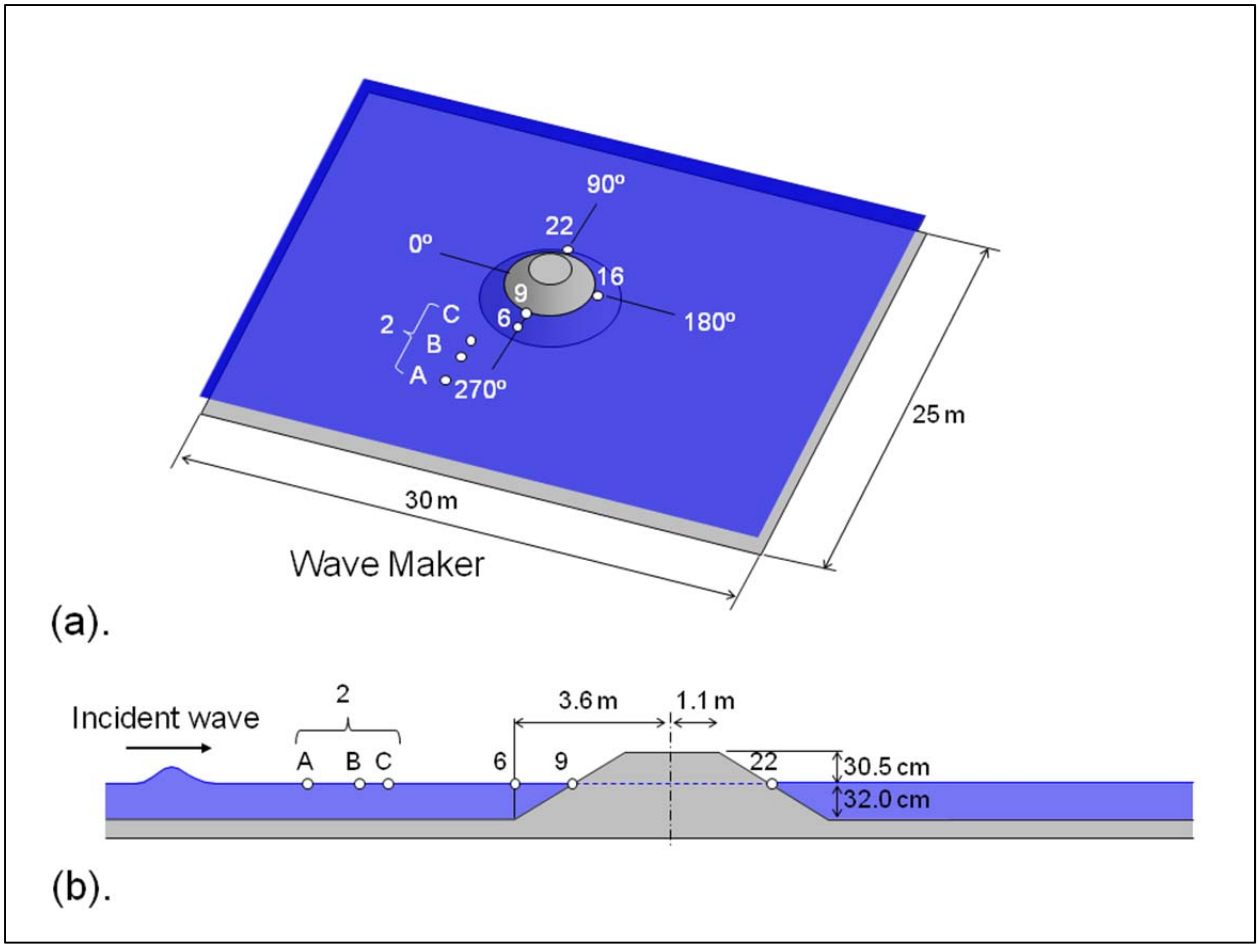

Figure 7-20: Schematic sketch of the conical island experiment. (a) Perspective view. (b) Side view (center cross section). ○, gauge locations.

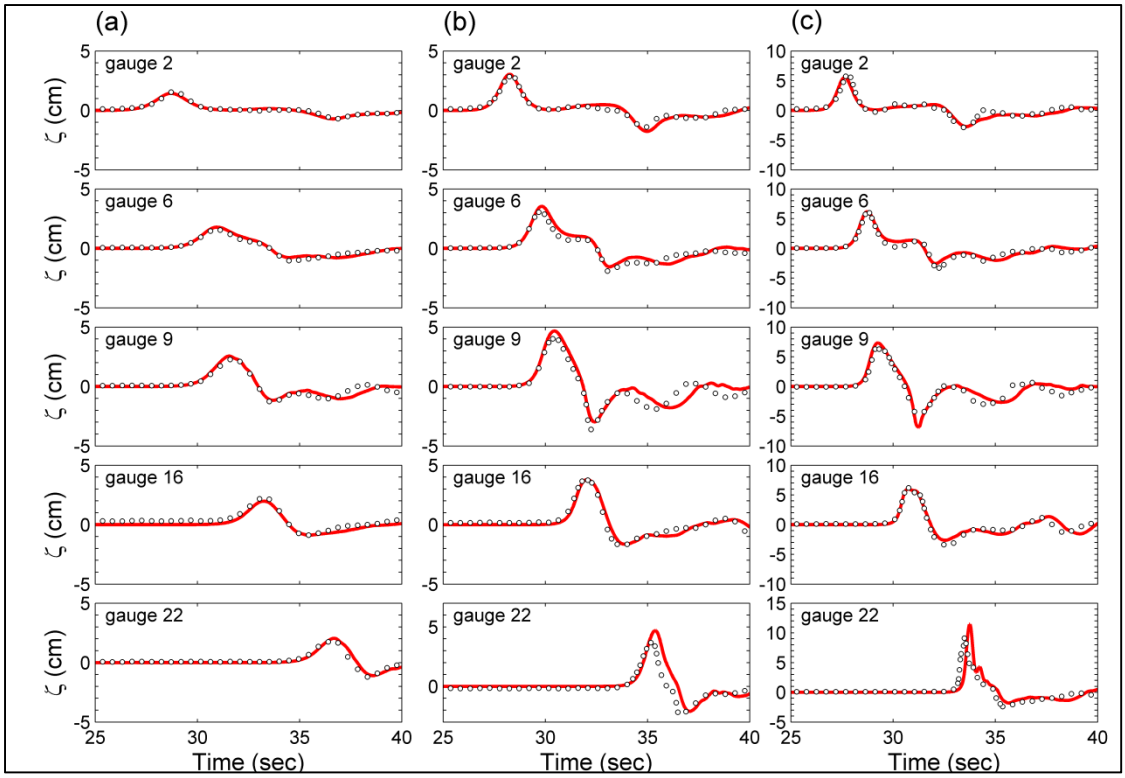

Figure 7-21: Time series of surface elevation at gauges around a conical island. (a) A/h = 0.045. (b) A/h = 0.096. (c) A/h = 0.181. ○, laboratory data from Briggs et al. (1995); ——(red), computed data.

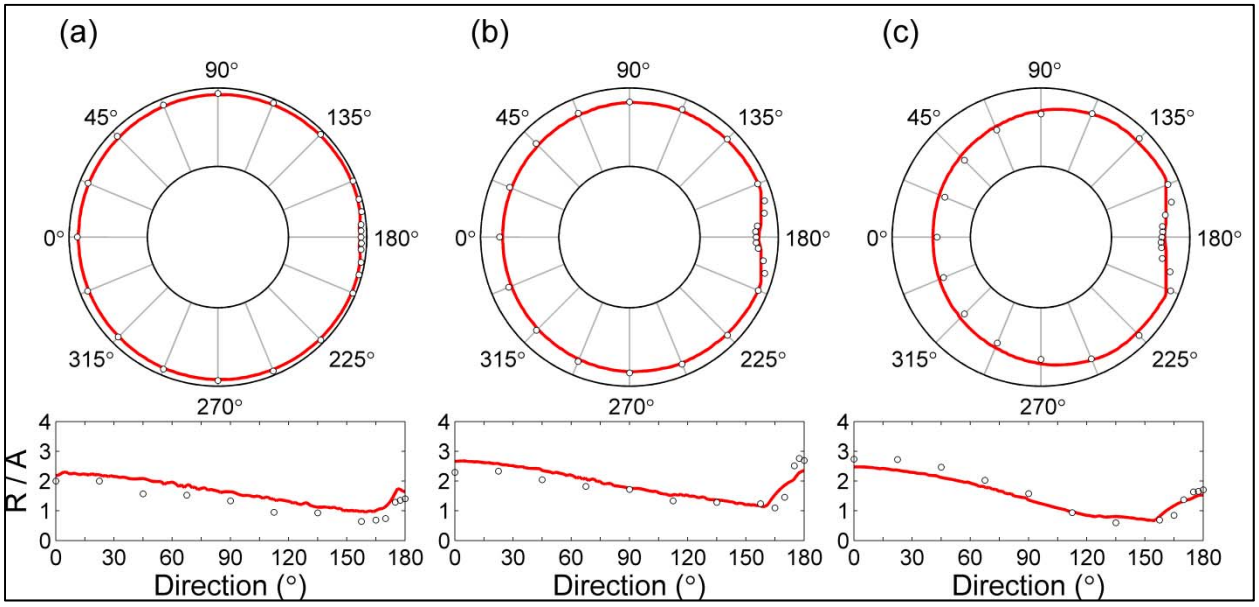

Figure 7-22: Inundation and runup around a conical island. (a) A/h = 0.045. (b) A/h = 0.096. (c) A/h = 0.181. ○, laboratory data from Briggs et al. (1995); ——(red), computed data.

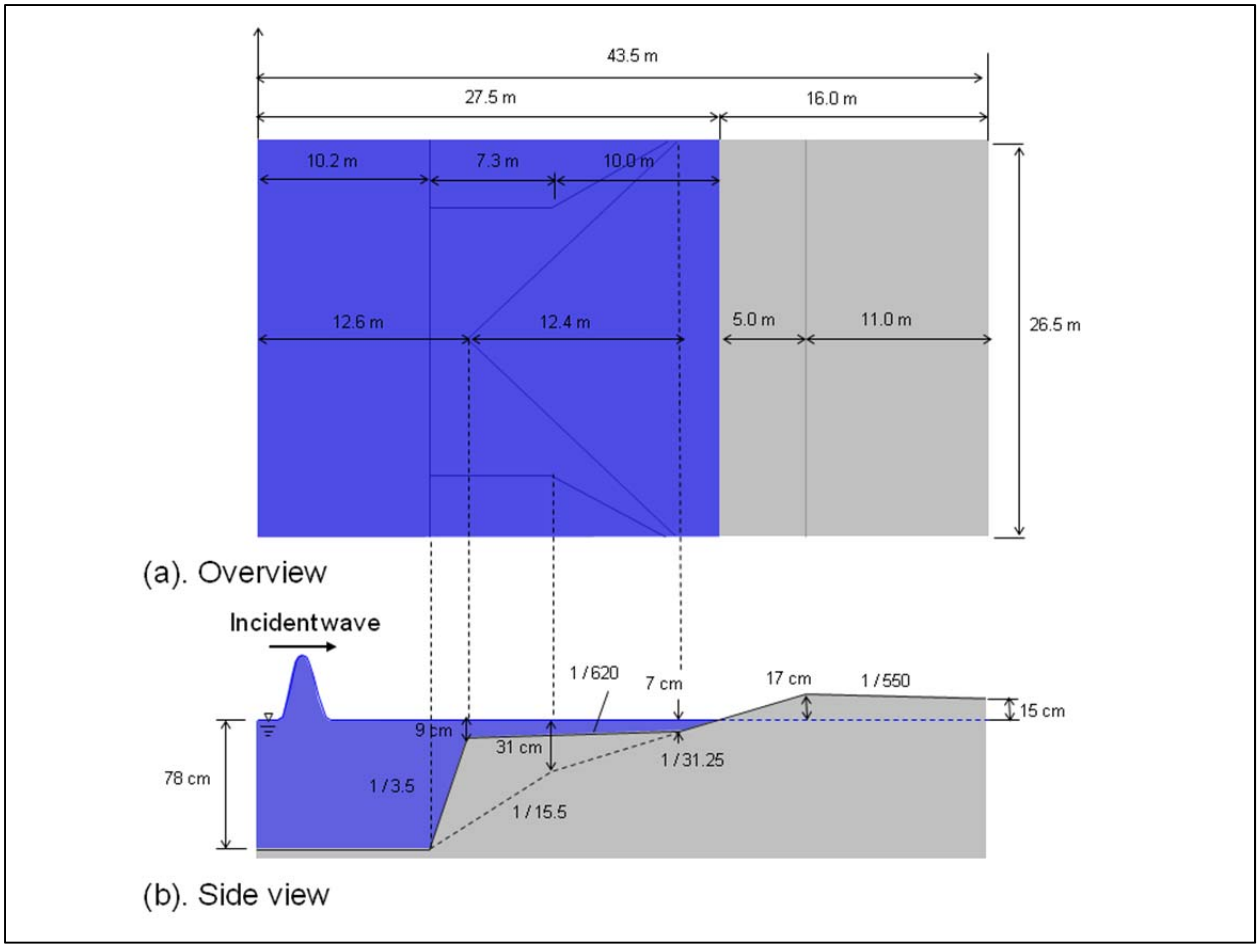

Figure 7-23: Schematic sketch of the complex reef system experiment in ISEC BP1. (a) Plain view. (b) Side view (center cross section).

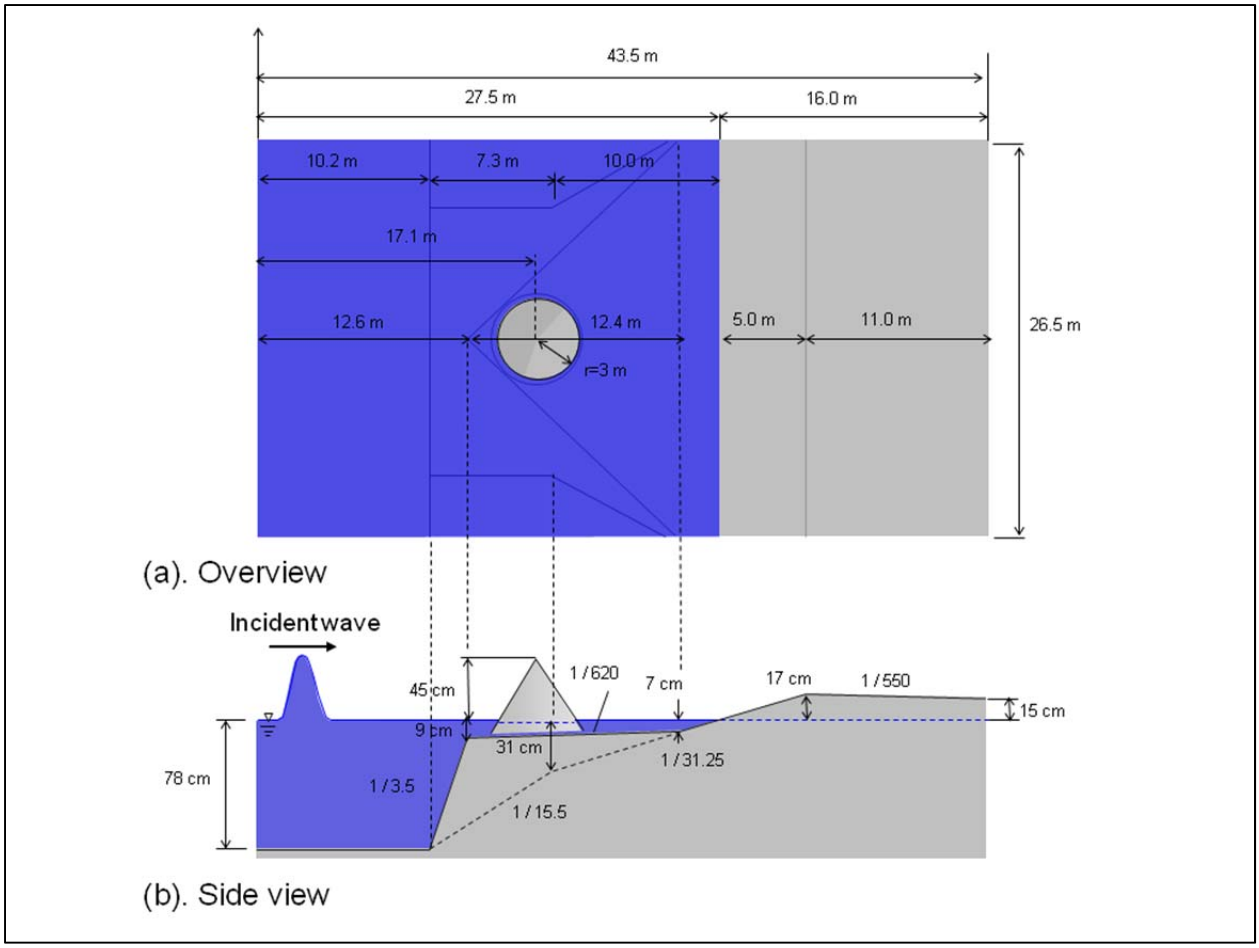

Figure 7-24: Schematic sketch of the complex reef system experiment in ISEC BP2. (a) Plain view. (b) Side view (center cross section).

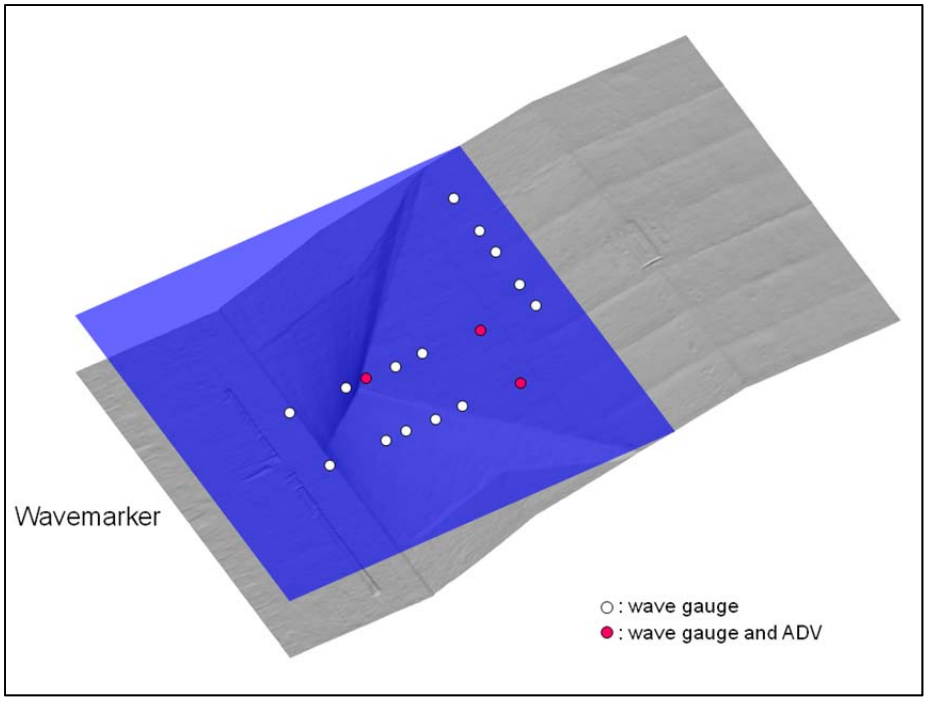

Figure 7-25: Geometry of reef system and wave gauge and ADV locations for ISEC BP1. ○ (white), wave gauge; ○ (red), wave gauge and ADV.

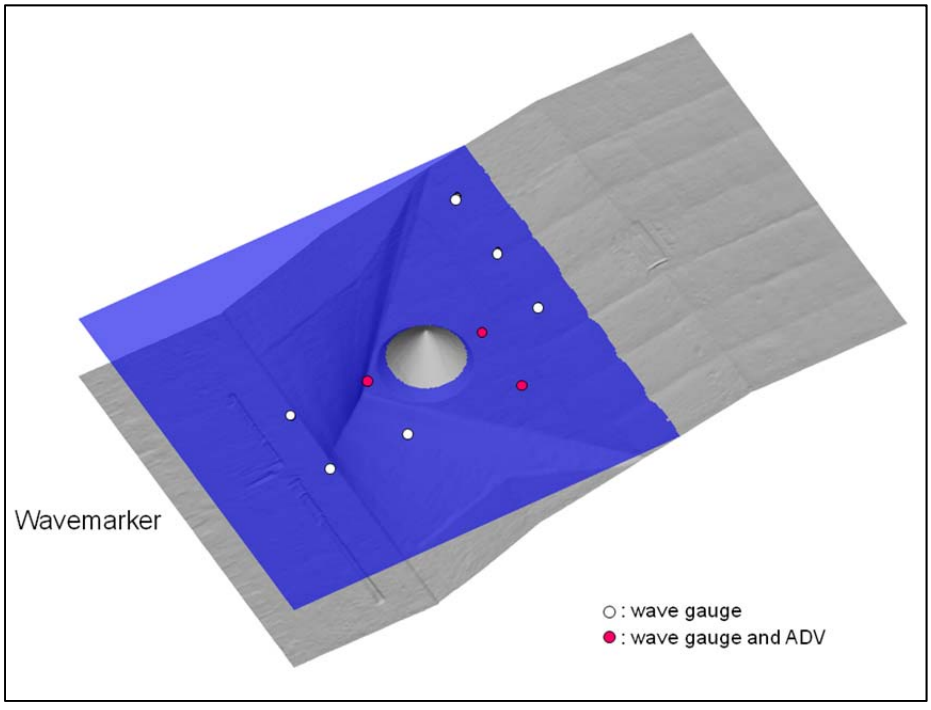

Figure 7-26: Geometry of reef system and wave gauge and ADV locations for ISEC BP2. ○ (white), wave gauge; ○ (red), wave gauge and ADV.

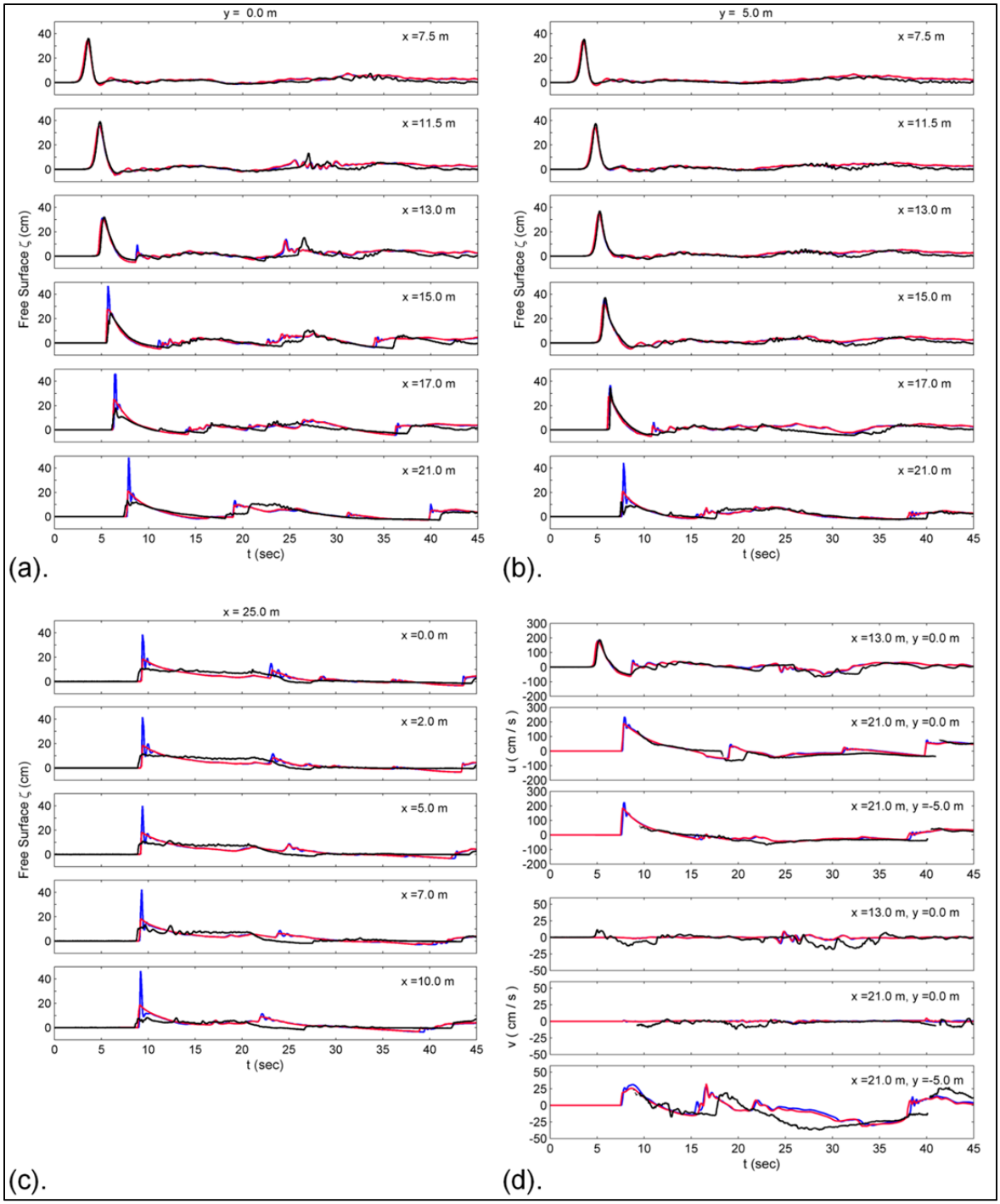

Figure 7-27: Time series of surface elevation and velocity at gauges for ISEC BP1. (a) Surface elevations at y = 0 m. (b) Surface elevations at y = 5 m. (c) Surface elevations at x = 25 m. (d) Horizontal velocity comparison at ADV. —— (black), laboratory data of Swigler and Lynett (2011); —— (red), solution with NH-Hybrid scheme; —— (blue), solution without NH-Hybrid scheme.

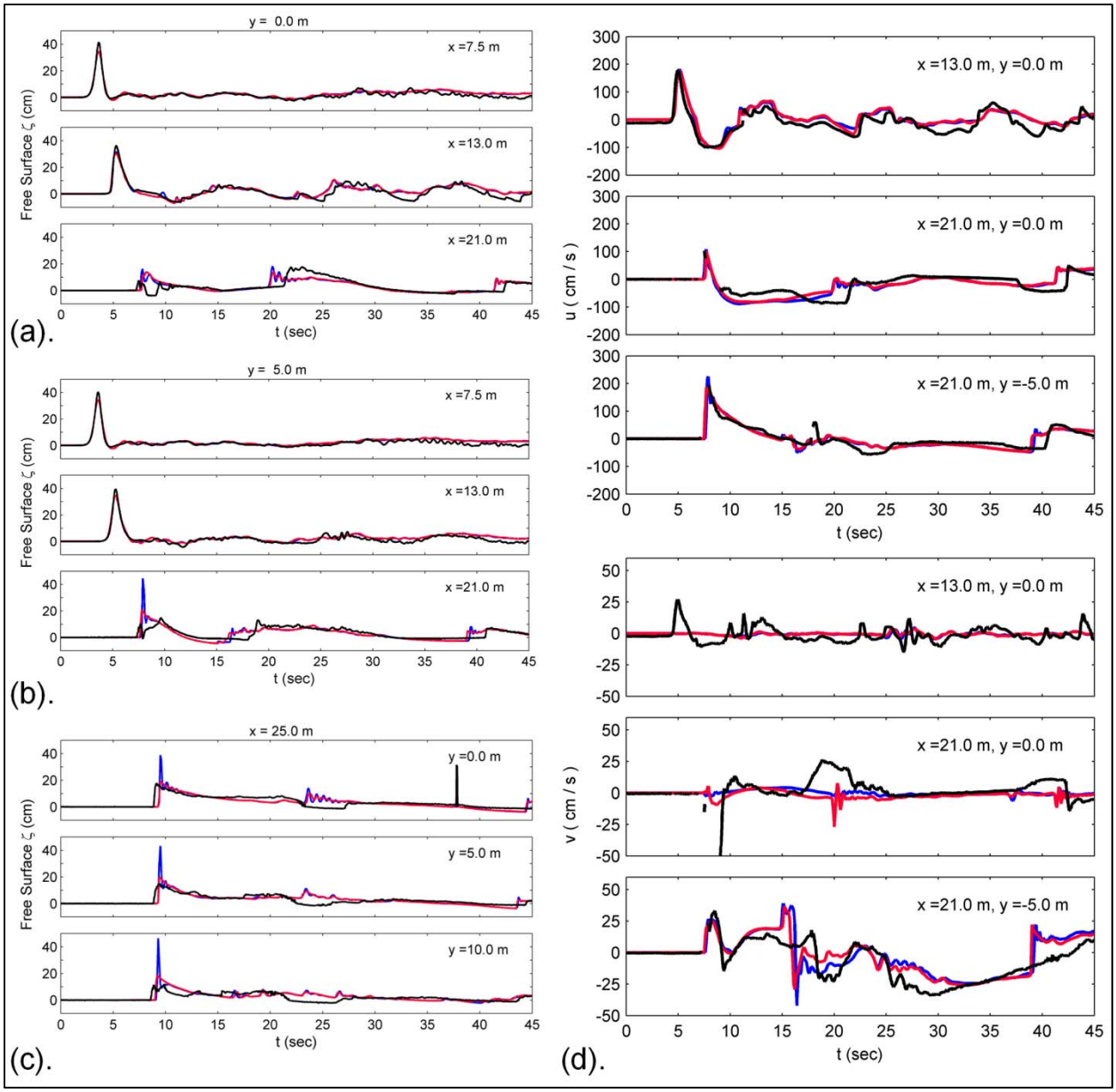

Figure 7-28: Time series of surface elevation and velocity at gauges for ISEC BP2. (a) Surface elevations at y = 0 m. (b) Surface elevations at y = 5 m. (c) Surface elevations at x = 25 m. (d) Horizontal velocity comparison at ADV. ——— (black), laboratory data of Swigler and Lynett (2011); ——— (red), solution with NH-Hybrid scheme; ——— (blue), solution without NH-Hybrid scheme.

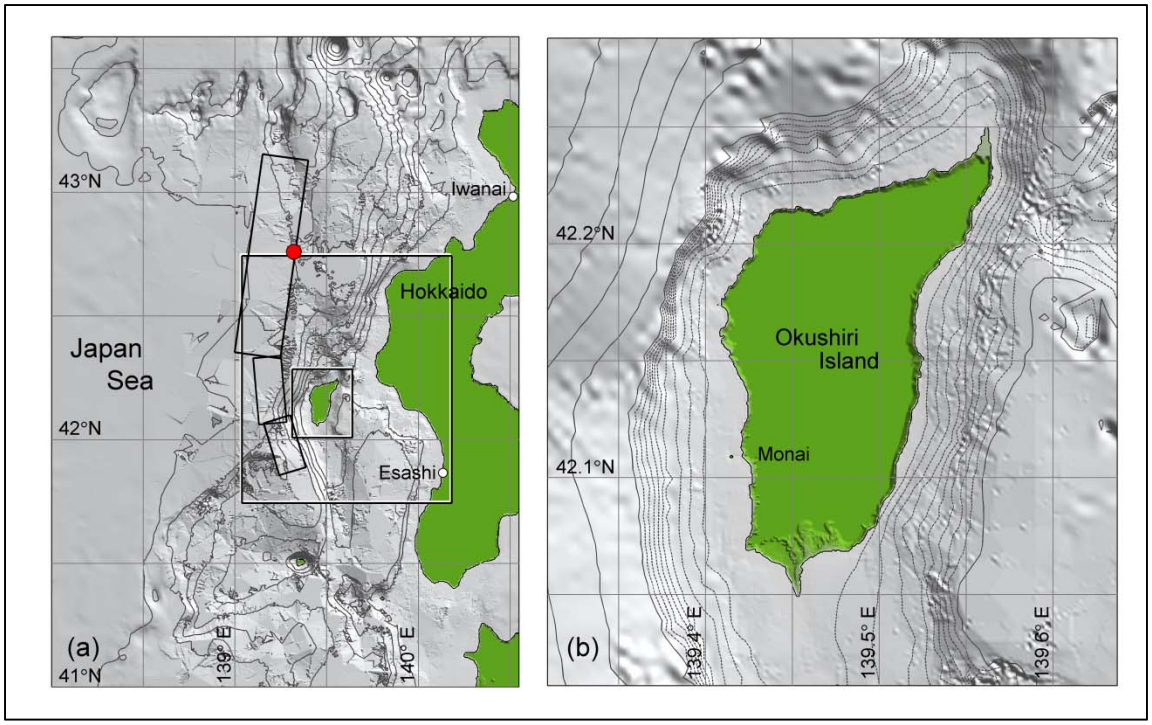

Figure 7-29: Bathymetry and topography in the model region for the 1993 Hokkaido Nansei-Oki tsunami. (a) level-1 computational domain, (b) level-3 domain. ○ (red), epicenter; ○ (white), tide gauge stations.

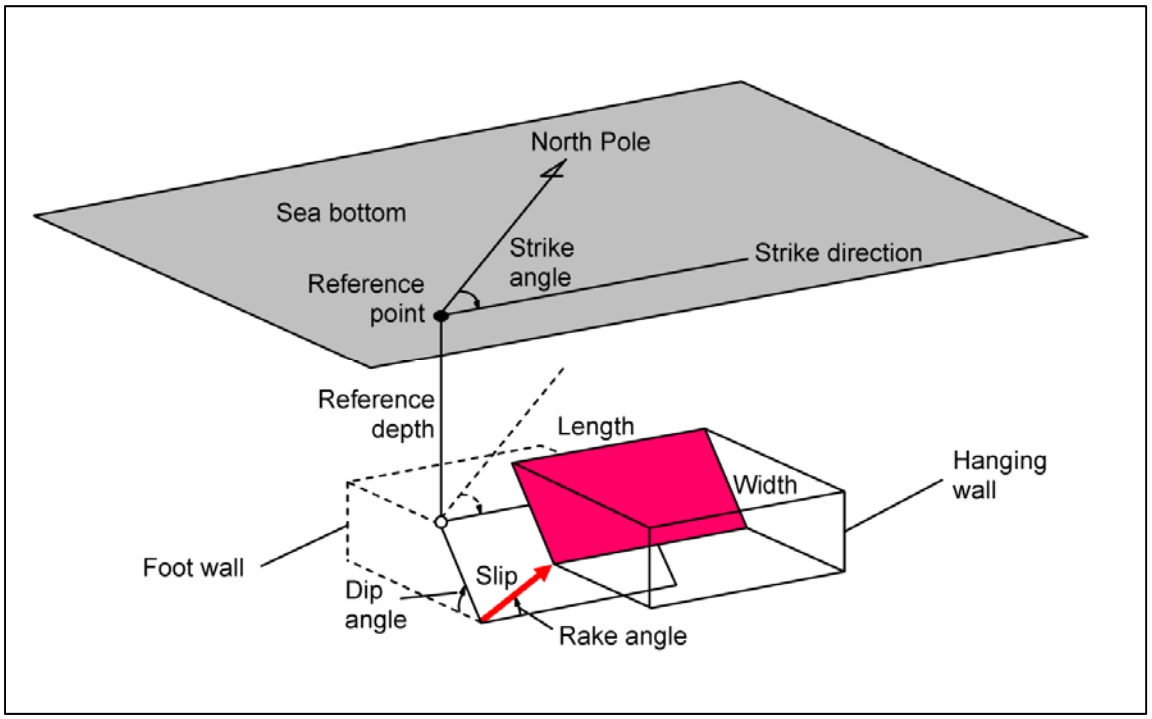

Figure 7-30: Schematic of planar fault model.

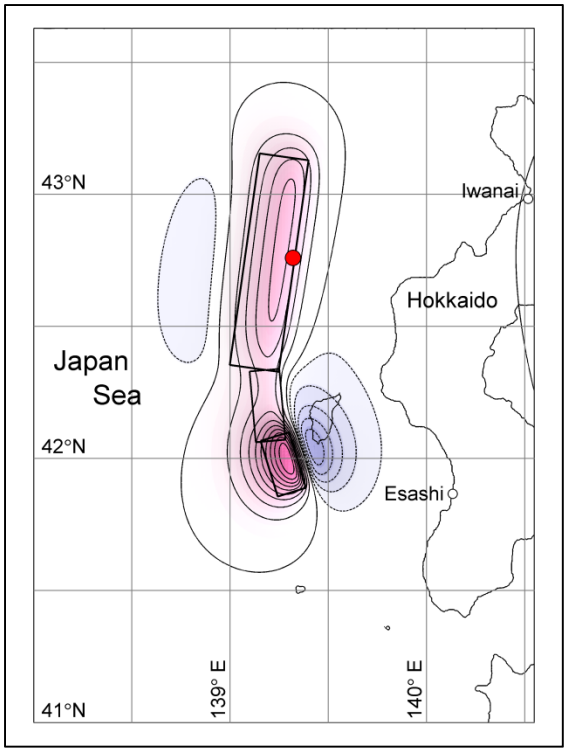

Figure 7-31: Initial sea surface elevation for the 1993 Hokkaido Nansei-Oki tsunami. Solid rectangles indicate subfaults; ——, uplift contours at 0.5-m intervals; - - - -, subsidence contours at 0.2-m intervals; ○ (red), epicenter; ○ (white), tide gauge stations.

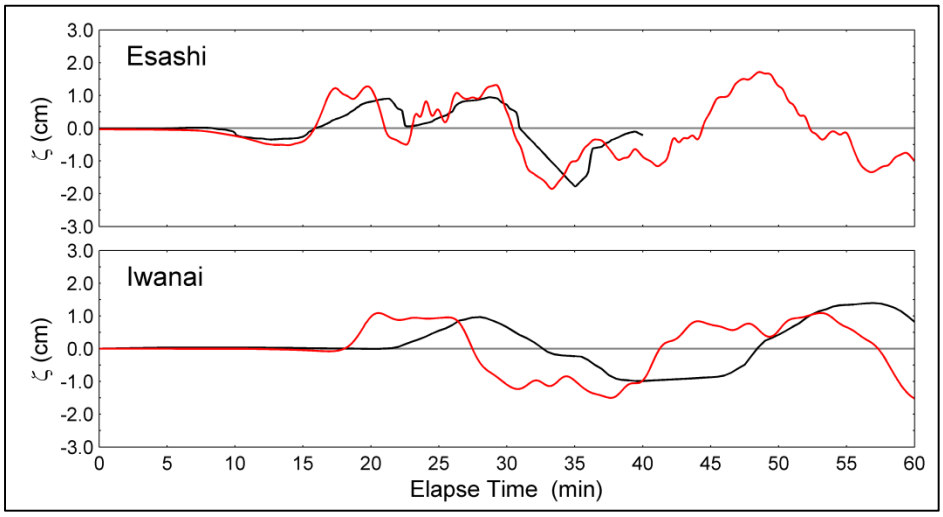

Figure 7-32: Time series of surface elevation at tide gauges. —— (black), recorded data; —— (red), computed data.

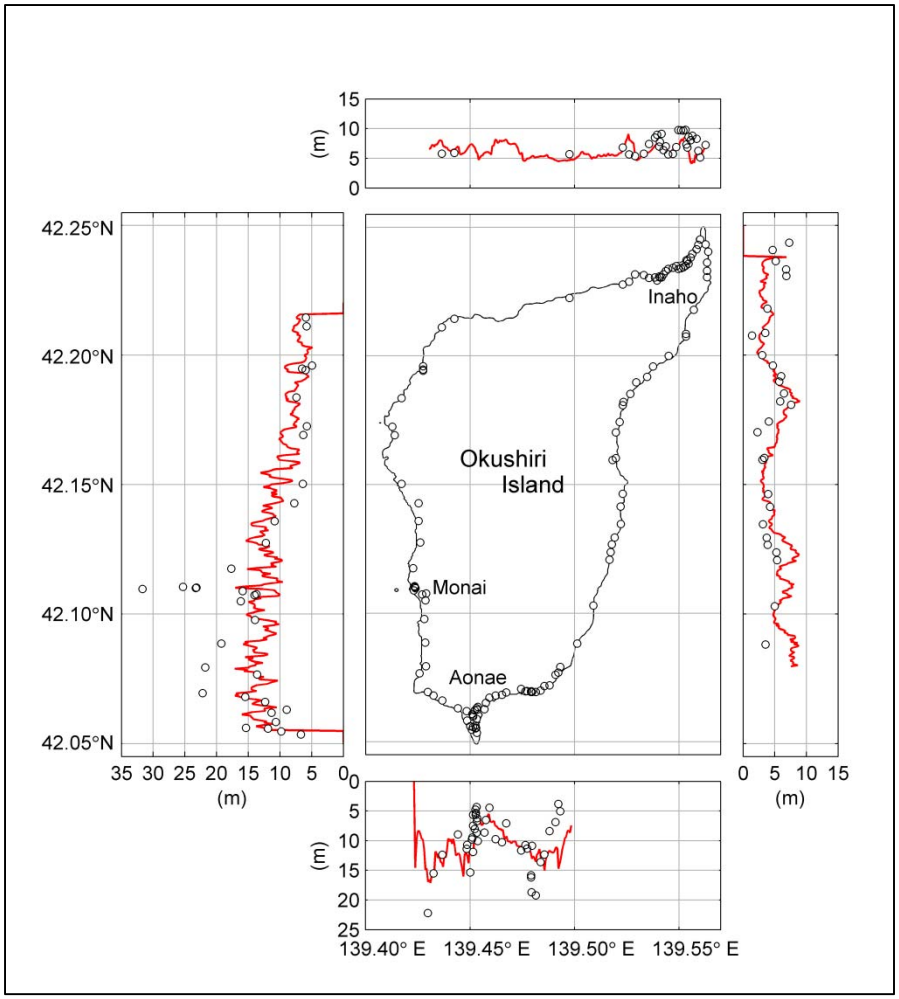

Figure 7-33: Runup around Okushiri Island. ○ (white): recorded runup; ——(red), computed runup.

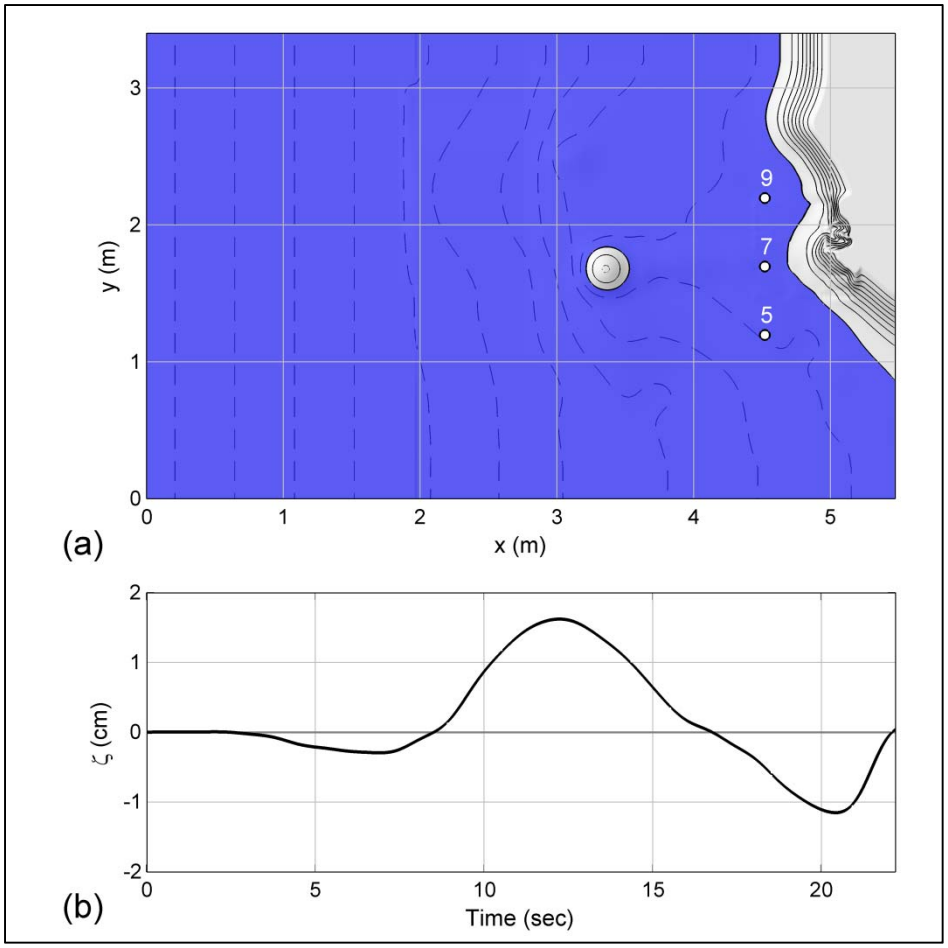

Figure 7-34: Input data for Monai Valley experiment. (a) Computational domain. (b) Initial wave profile. ○, gauge locations; ——— (black), topography contours at 0.0125-m intervals; - - - - (grey), bathymetry contours at 0.0125-m intervals; ———, initial profile.

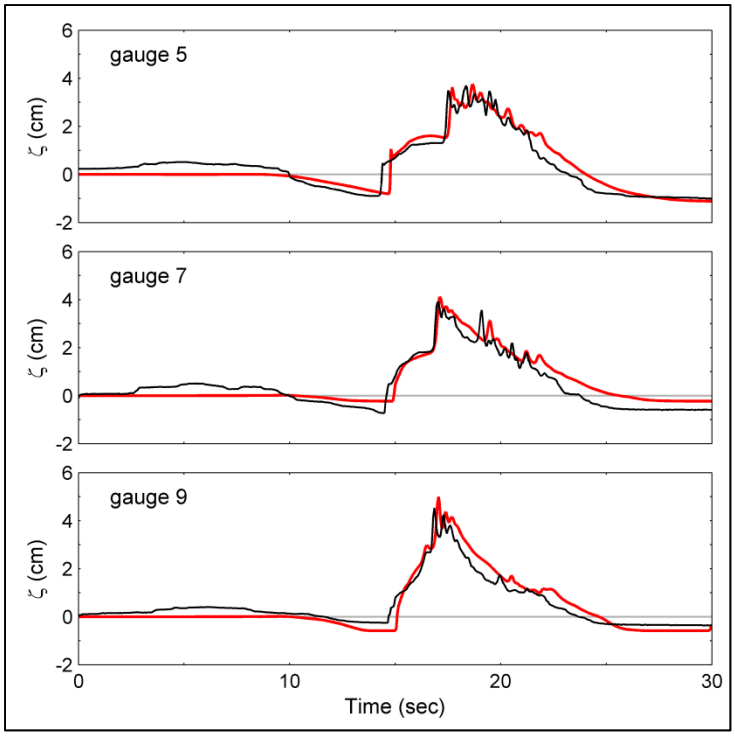

Figure 7-35: Time series of surface elevation at gauges in Monai Valley experiment. ——— (black), laboratory data of Matsuyama and Tanaka (2001); ——— (red), computed data.

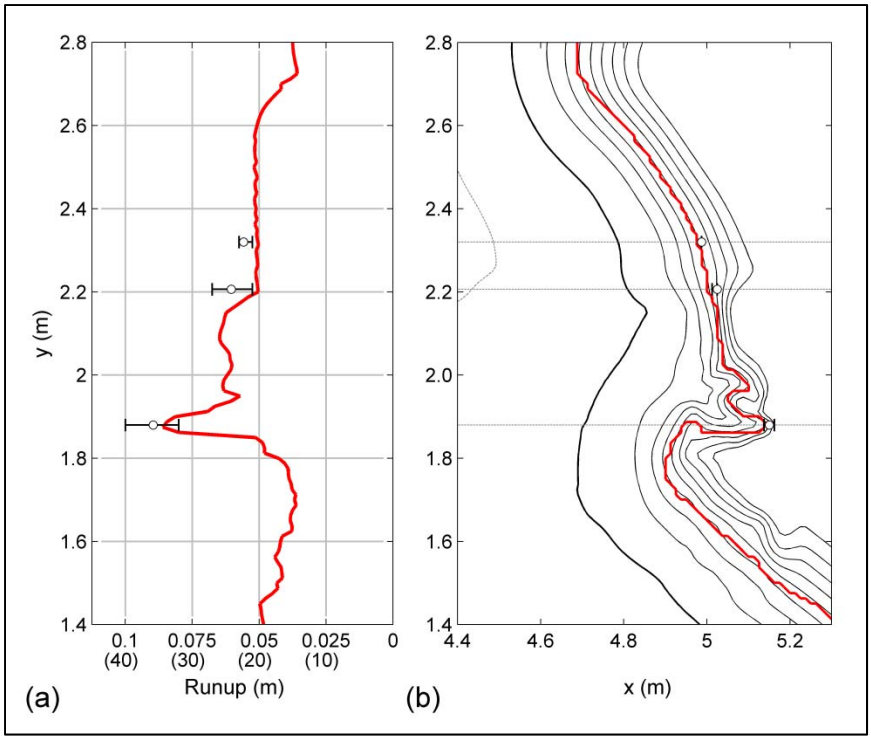

Figure 7-36: Runup and inundation comparisons. (a) Runup, (b) Inundation. ○, laboratory data of Matsuyama and Tanaka (2001); ——— (red), computed data; ——— (black), topography contours at 0.0125-m intervals; - - - - (grey), bathymetry contours at 0.0125-m intervals.

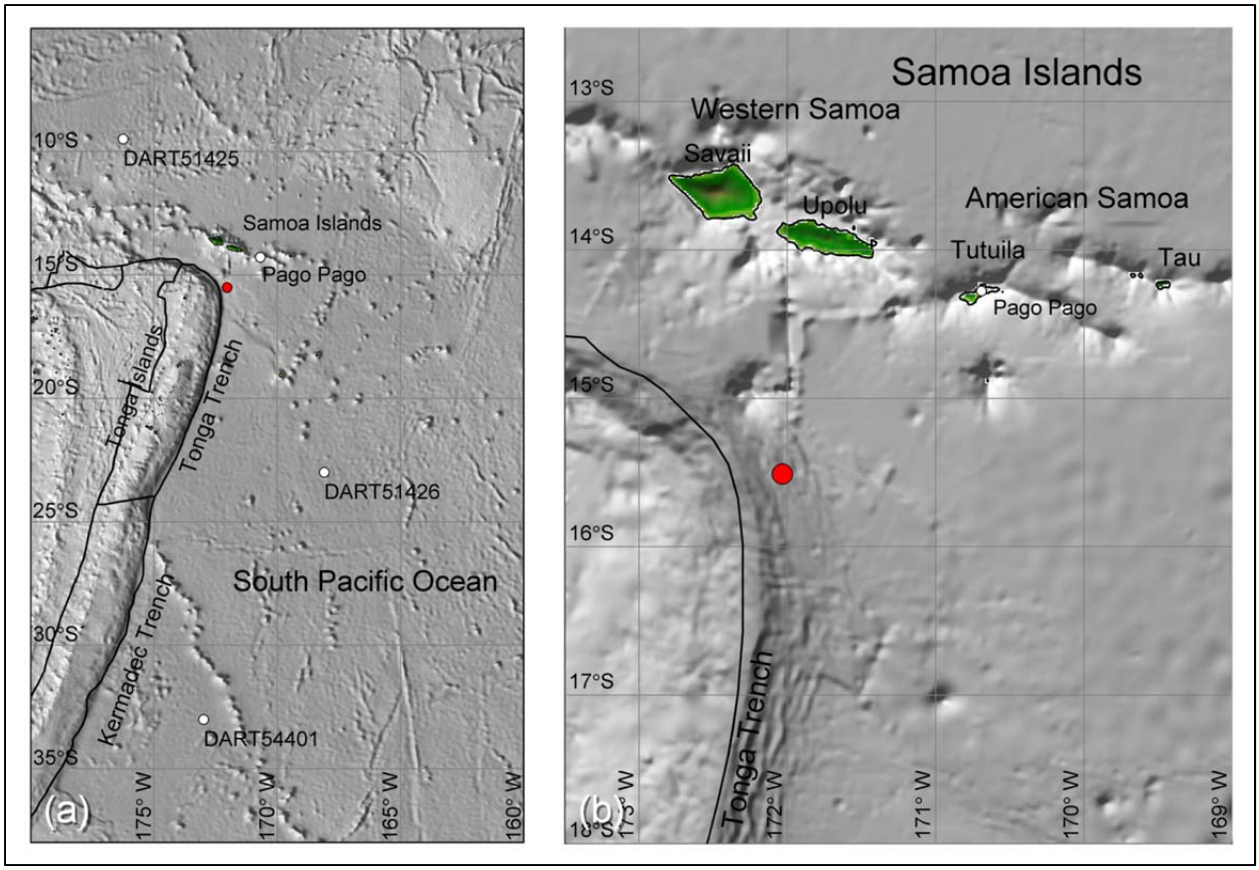

Figure 7-37: Bathymetry and topography in the model region for the 2009 Samoa Tsunami. (a) level-1 computational domain, (b) close-up view of epicenter and Samoa Islands. ○ (red), epicenter; ○ (white), water-level stations.

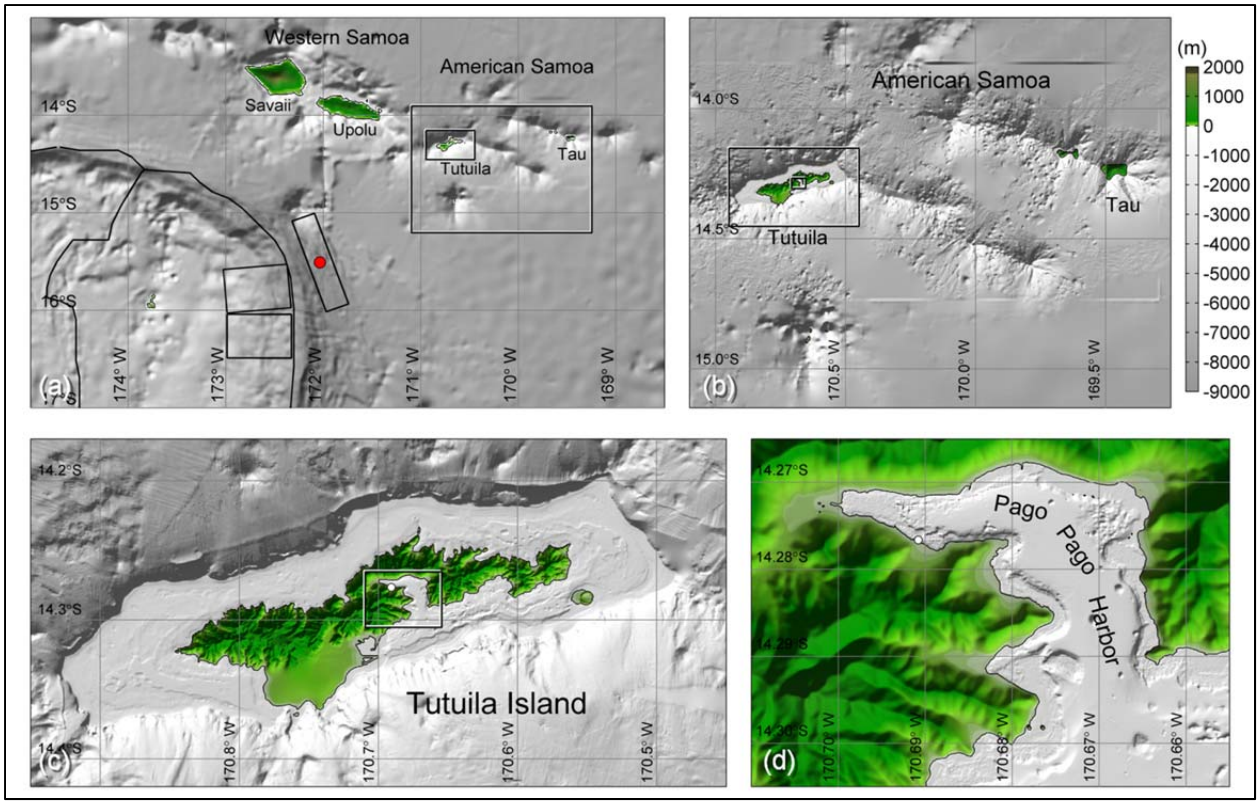

Figure 7-38: Original bathymetry and topography in the model region for the 2009 Samoa tsunami. (a) close-up view of faults and Samoa Islands in the level-1 computational domain, (b) level-2 domain, (c) level-3 domain , (d) level-4 domain. ○ (red), epicenter; ○ (white), water-level stations.

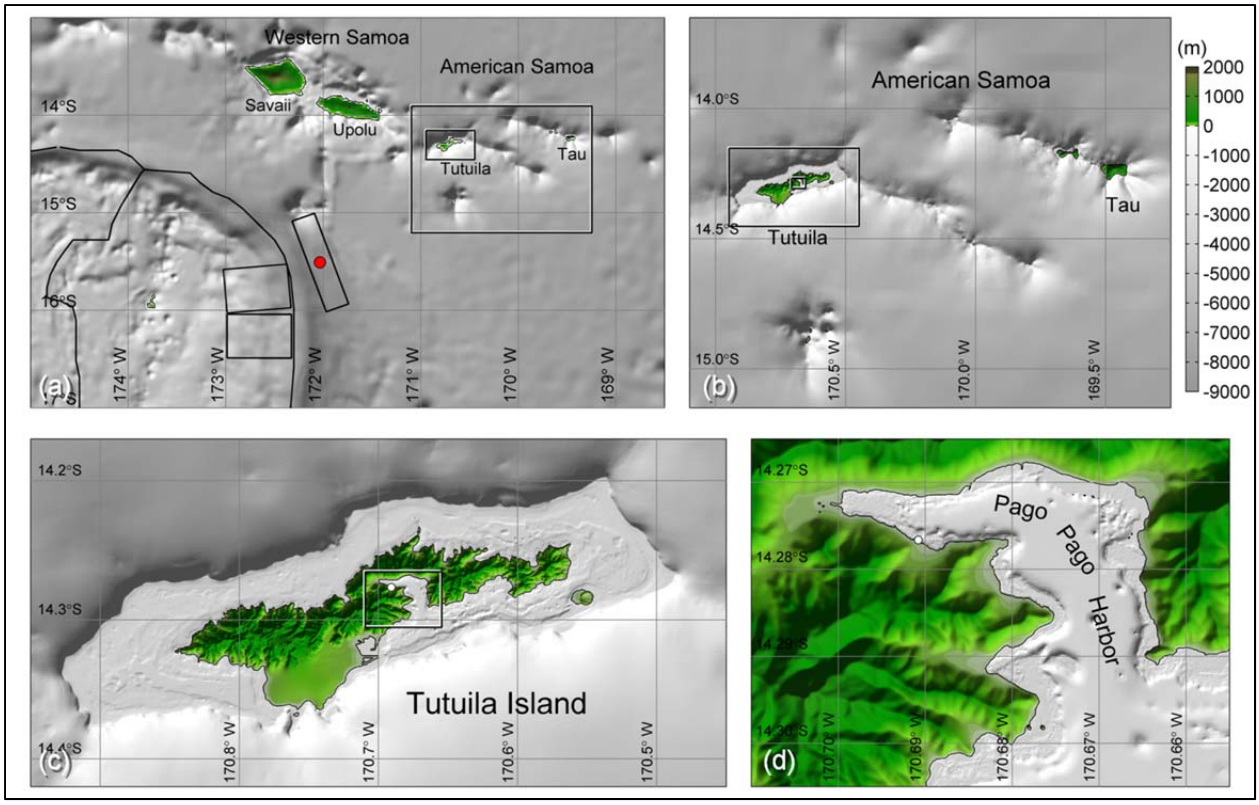

Figure 7-39: Smoothed bathymetry and topography with the depth-dependent Gaussian function in the model region for the 2009 Samoa tsunami. (a) close-up view of faults and Samoa Islands in the level-1 computational domain, (b) the level-2 domain, (c) the level-3 domain , (d) the level-4 domain. ○ (red), epicenter; ○ (white), water-level stations.

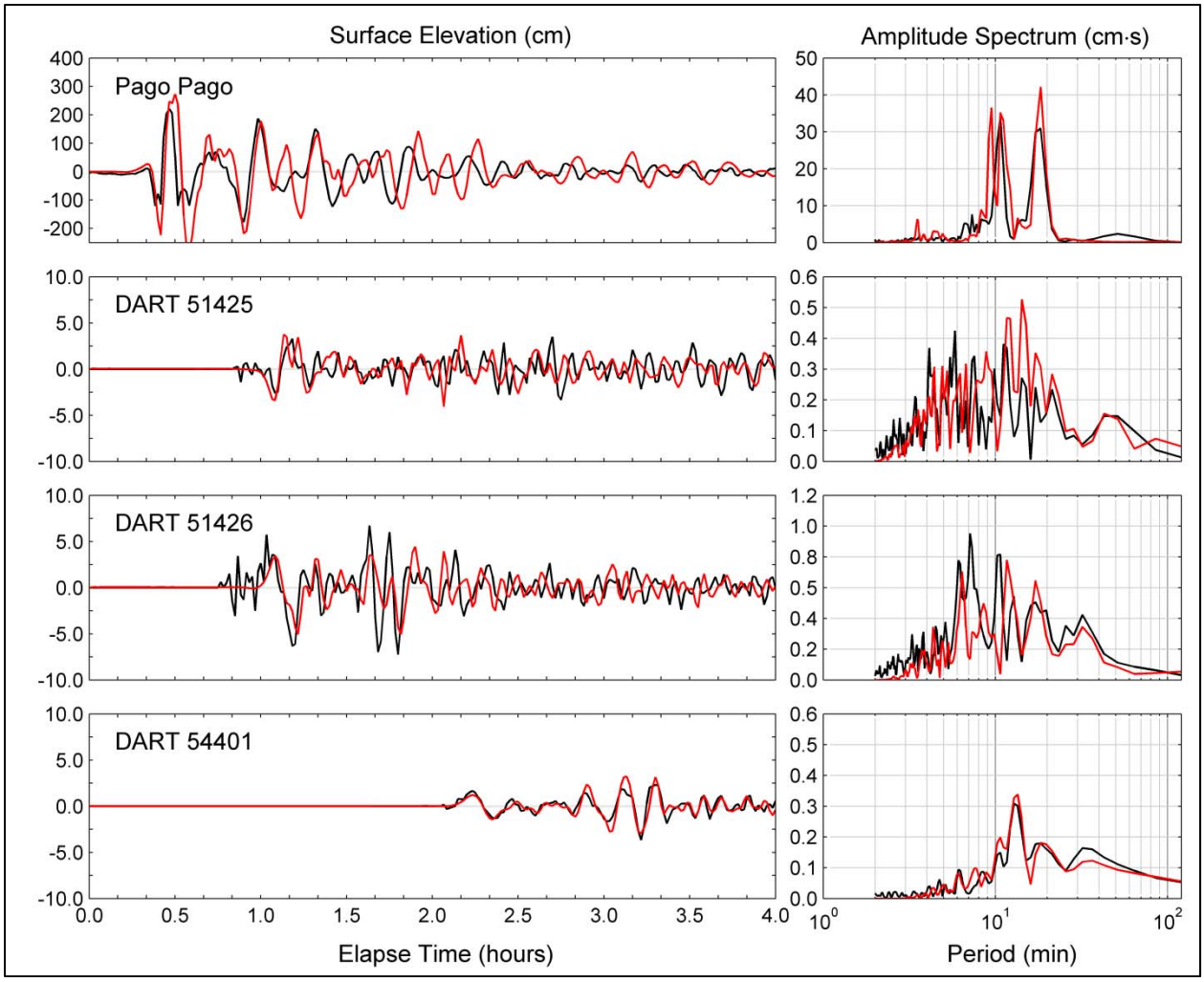

Figure 7-40: Time series and spectra of surface elevations at water level stations. (black), recorded data; (red), computed data.

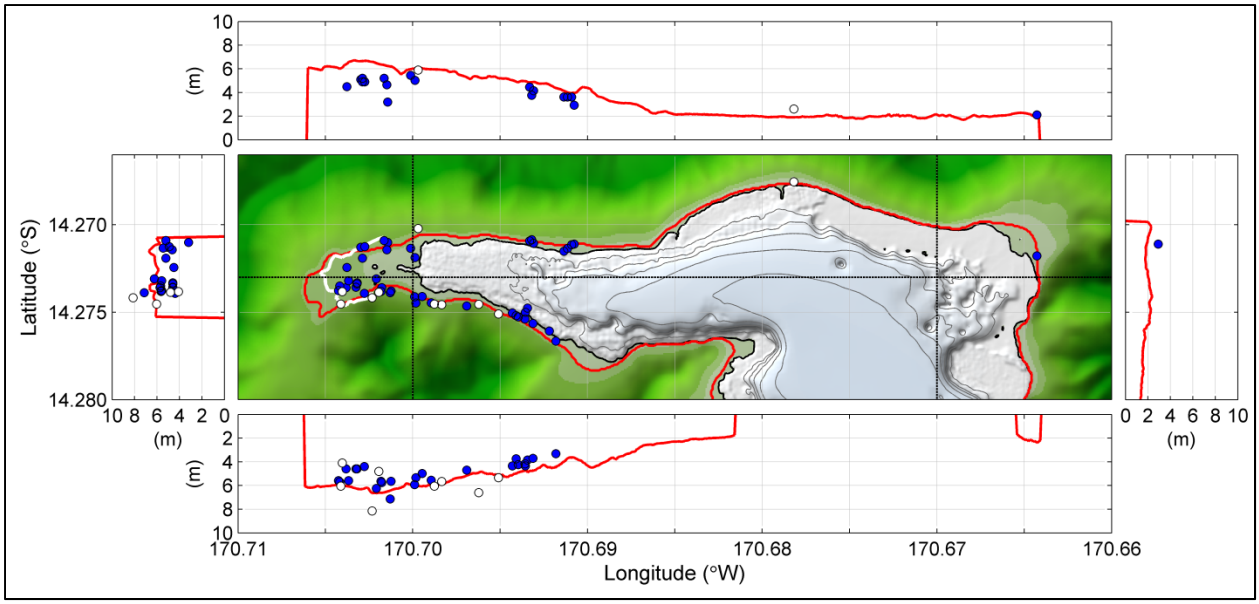

Figure 7-41: Runup and inundation at inner Pago Pago Harbor. ——— (white), recorded inundation; ○(white): recorded runup; ○(blue): recorded flow depth plus land elevation; (red), computed data; (black), coastline; (grey), depth contours at 10-m intervals.

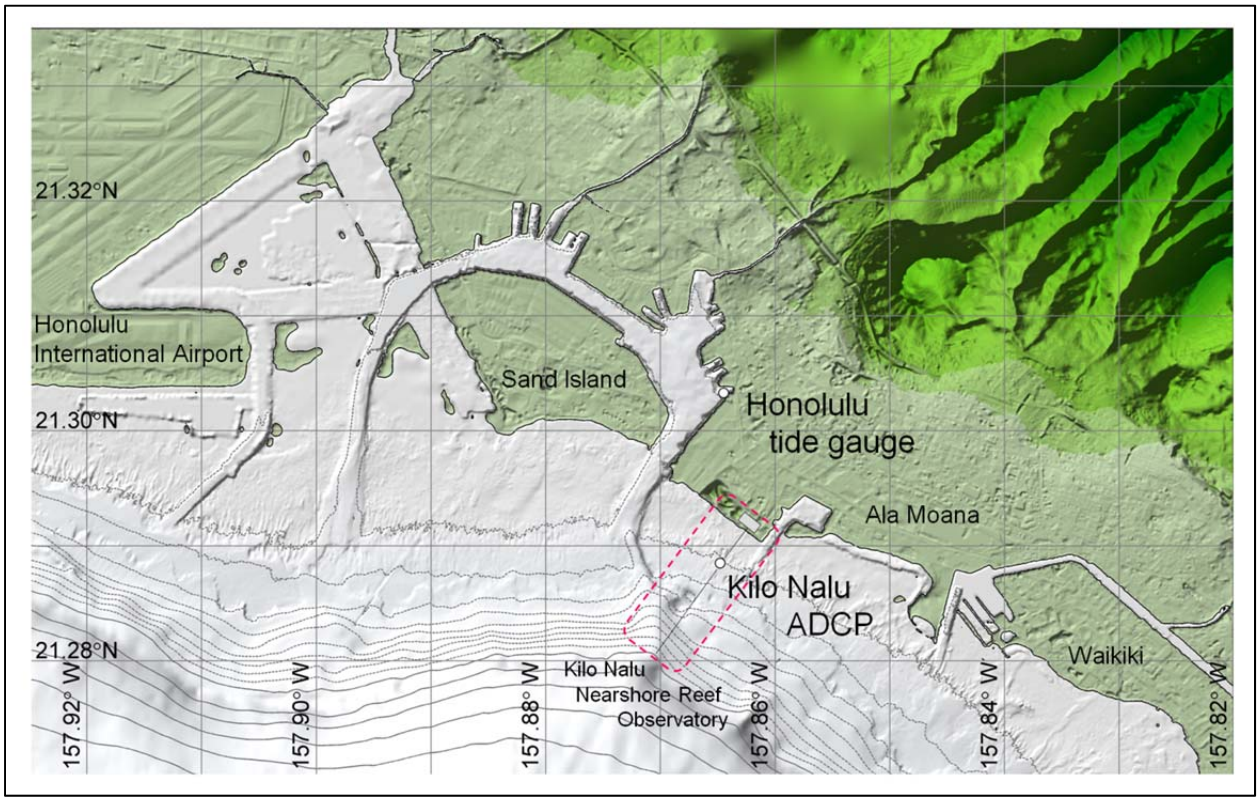

Figure 7-42: Original bathymetry and topography at south shore of Oahu, Hawaii and Kilo Nalu Nearshore Reef Observatory. ○ (white), water level and velocity measurement points.

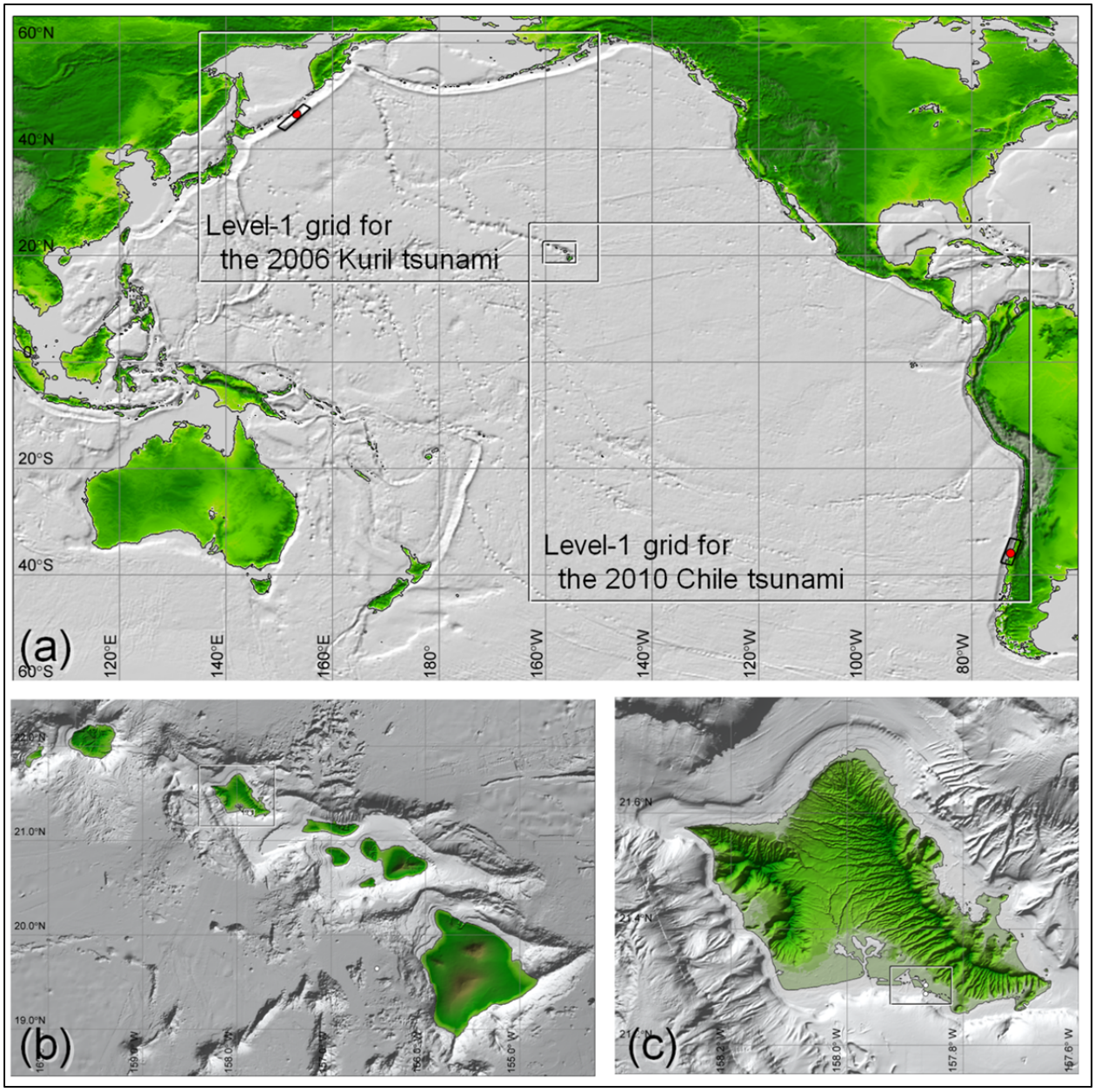

Figure 7-43: Original bathymetry and topography in the model region. (a) level-1 computational domains in the Pacific. (b) level-2 domain over Hawaiian Islands, (c) level-3 domain of Oahu. ○ (red), epicenter.

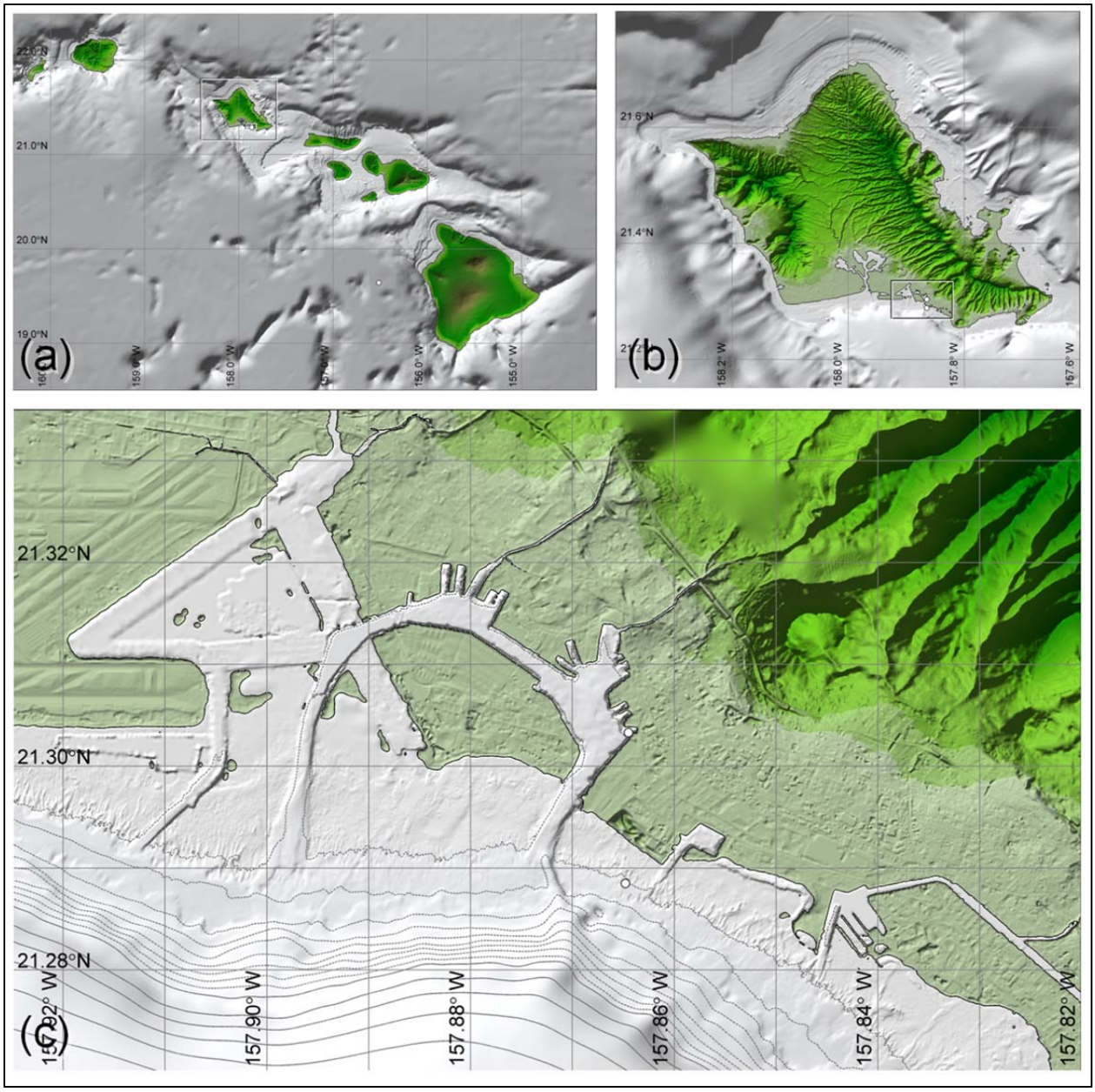

Figure 7-44: Smoothed bathymetry and topography with the depth-dependent Gaussian function. (a) level-2 domain over Hawaiian Islands, (b) level-3 domain of Oahu, (c) level-4 domain of the south shore of Oahu.

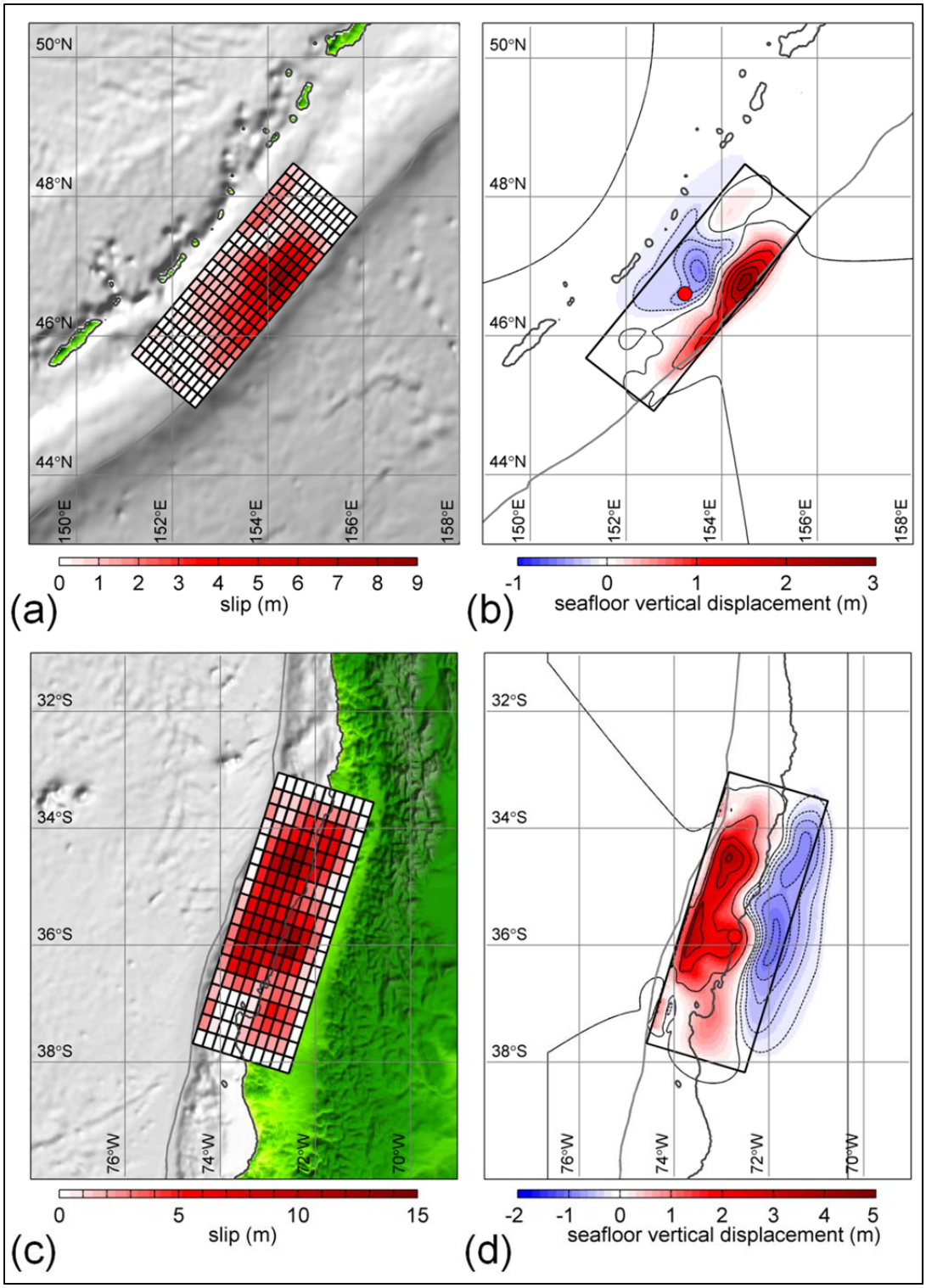

Figure 7-45: Slip distribution and initial sea surface deformation. (a) USGS finite fault solution for the 2006 Kuril earthquake, (b) Sea surface deformation for the 2006 Kuril tsunami, (c) USGS finite fault solution for the 2010 Chile earthquake, (d) Sea surface deformation for the 2010 Chile tsunami. ○ (red), epicenter.

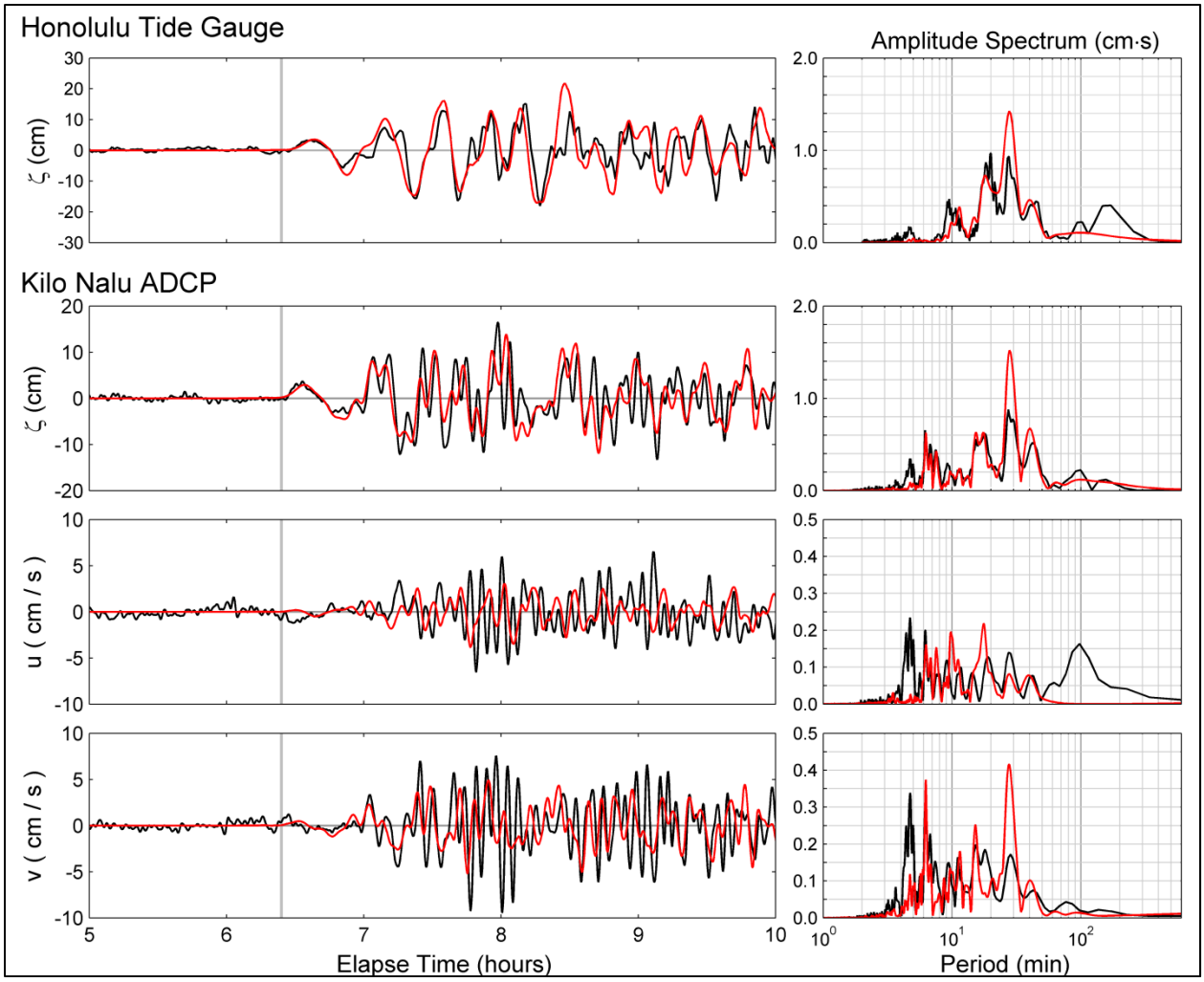

Figure 7-46: Time series and spectra of surface elevation and velocity at Honolulu tide gauge and Kilo Nalu ADCP for the 2006 Kuril tsunami. ——(black), recorded data; ——(red), computed data.

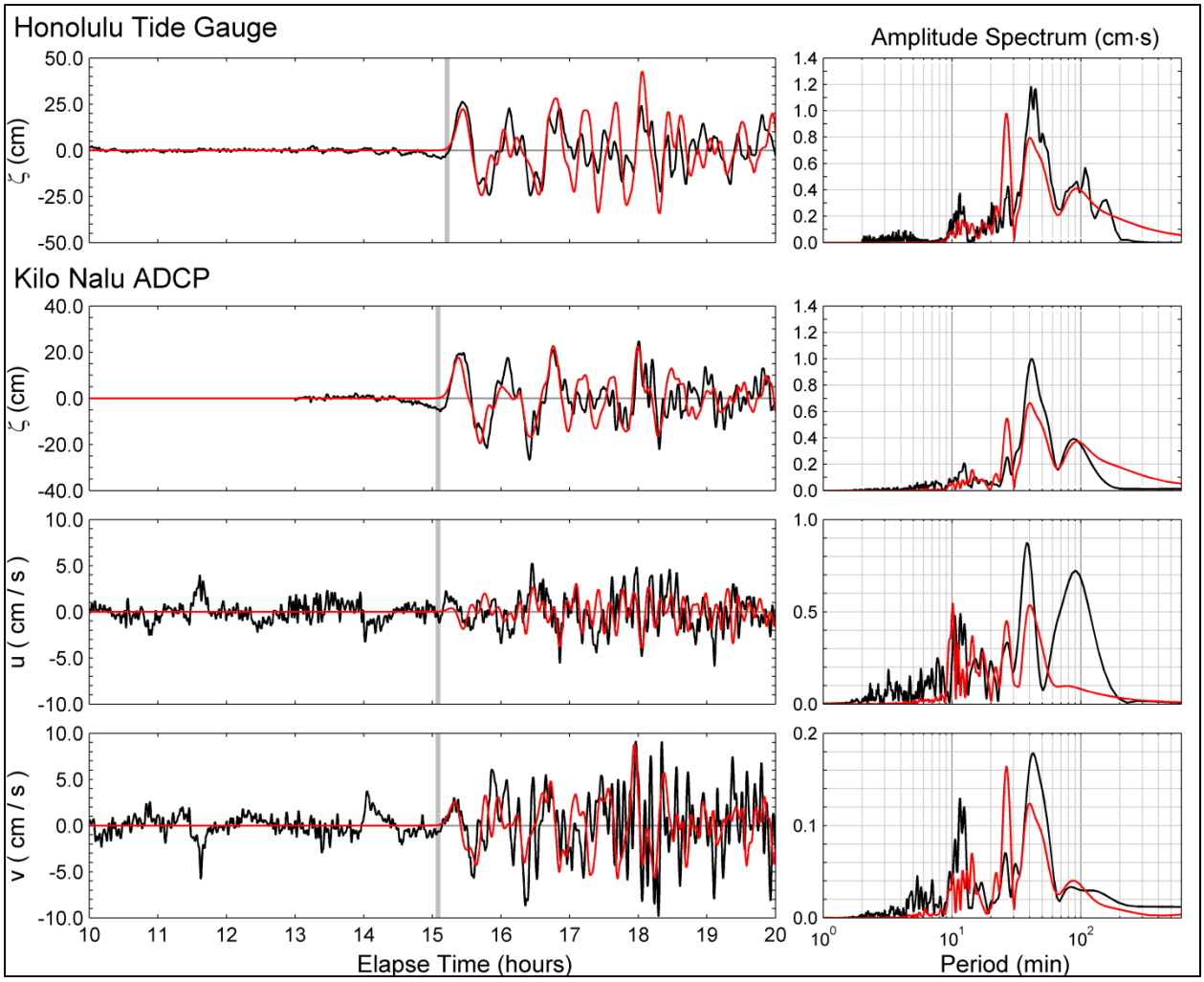

Figure 7-47: Time series and spectra of surface elevation and velocity at Honolulu tide gauge and Kilo Nalu ADCP for the 2010 Chile tsunami. ——— (black), recorded data; ——— (red), computed data.

8 SELFE

Y. Joseph Zhang (OHSU)

Oregon Health & Science University (OHSU) and Oregon Department of Geology & Mineral Industries (DOGAMI)

8.1 Introduction

The state of Oregon is part of the US Pacific Northwest (PNW) region with extensive coastline and vibrant coastal communities. The primary tsunami hazards posed to these communities come from the seismic sources including both local (Cascadia Subduction Zone – CSZ) and remote sources, with landslides being of relatively minor concern. We (OHSU) have been working in partnership with DOGAMI in the preparation and dissemination of inundation maps since the 1990s, first under Oregon Senate Bill 379. Current funding from NTHMP has enabled us to apply state-of-the-art technology, i.e., new geological and computational models, the latter based on unstructured grids, to remap the entire OR coastal counties for both local and remote sources. Because we are primarily focusing on seismic tsunamis, the tsunami propagation and inundation model we used has been carefully benchmarked for this purpose. We have however, also preliminarily benchmarked the non-hydrostatic version of the model for landslide problems and we may consider formally doing so in the future.

8.2 Model description

The fault dislocation model we use for the CSZ earthquakes is based on Okada's point source model but with extensive geophysical constraints (Priest et al., 2009; Witter et al., in review). We have developed 15 full-margin rupture models for Cascadia subduction zone earthquakes that define vertical seafloor deformation used to simulate tsunami inundation at Bandon, Oregon. Rupture models include slip partitioned to a splay fault in the accretionary wedge and models that vary the updip limit of slip on a buried megathrust fault. Coseismic slip is estimated from turbidite paleoseismic records (Goldfinger et al., in press) and constraints from tsunami simulations at Bradley Lake (Witter et al., in review). Alternative earthquake source scenarios are evaluated using a logic tree that ranks model performance based on geophysical and geological data. Scenario weights at the branch ends of the logic tree are the products of the weights of the two parameters, earthquake size and fault geometry, and represent the relative confidence that a particular model represents a reasonable rupture scenario based on geological and geophysical data, theoretical models and the judgment of the scientific team. The basal (and most important) branch of the logic tree, estimated fault slip from recurrence interval, is based on the frequency of turbidite interevent times over the last 10,000 years. The second branch of the logic tree evaluates three rupture geometries that vary the distribution of slip on the updip end of the locked zone: (1) activation of a shallow splay fault in the accretionary wedge; (2) shallow buried rupture that tapers slip to zero at the deformation front; and (3) a deeper buried rupture

that tapers slip to zero beneath a sharp break in the slope of the accretionary wedge offshore Washington and northern Oregon.

For remote sources we have limited ourselves to the Alaska-Aleutian subduction zone as historically it poses the most severe threat to the Oregon coast. We have considered two scenarios: the 1964 Great Alaska earthquake and a hypothetical worst case scenario. The source model for the 1964 event came from Johnson et al. (1996) while that for the worst case scenario was originally used for a pilot study at Seaside, OR (TPSWG, 2006). Both scenarios involve M_w ~9.2 earthquakes near the Gulf of Alaska. Results of simulations for the 1964 tsunami are checked against historical observations of water levels and wave runup along the Oregon coast, allowing verification of the hydrodynamic model.

The worst case Gulf of Alaska earthquake scenario, identified as "Source 3" in Table 1 of Gonzalez et al. (2009), has uniform slip on 12 subfaults with each subfault assigned an individual slip value of 15, 20, 25 or 30 m. These extreme parameters result in maximum seafloor uplift nearly twice as large as the uplift produced by the 1964 earthquake (as estimated by Johnson et al. (1996)). Analyses of the maximum tsunami amplitude simulated for this source show beams of higher energy directed toward the Oregon coast compared with other Alaska-Aleutian subduction zone sources (TPSWG, 2006). Because of its precedent use for the Seaside tsunami study by TPSWG (2006), we consider the hypothetical Gulf of Alaska scenario as a maximum distant tsunami source; however, testing the geological plausibility of the scenario was beyond the scope of this study.

The tsunami propagation and inundation model we use is SELFE (Zhang and Baptista 2008a), which was envisioned at its inception to be an open-source community-supported 3-D hydrodynamic/hydraulic model. This philosophy remains the corner stone of the model to this day. Originally developed to address the challenging 3-D baroclinic circulation in the Columba River estuary, it has since been adopted by 65+ groups around the world and evolved into a comprehensive modeling system encompassing such physical/biology processes as general circulation (Burla et al. 2010), tsunami and hurricane storm surge inundation (as in the on-going IOOS sponsored SURA project), ecology and water quality (Rodrigues et al. 2009ab), sediment transport (Pinto et al. 2011), wave–current interaction (Roland et al. 2011) and oil spill (Azvedo et al. 2009). Currently we maintain a central web site dedicated to this model (http://www.stccmop.org/CORIE/modeling/selfe/), maintain a user mailing list and mail archive system, organize annual user group meetings (since 2004), and occasionally conduct online training courses for users.

The rapid growth of the SELFE user community owes a great deal to the numerical scheme used in SELFE, which combines numerical accuracy with efficiency and robustness; the last two model traits are indispensable for large-scale practical applications as commonly found in tsunami hazard mitigation studies. The time stepping in SELFE is done semi-implicitly for the momentum and continuity equations, and together with the Eulerian-Lagrangian method (ELM) for the treatment of the advection, the stringent CFL stability condition is bypassed. The remaining stability conditions are related to the horizontal viscosity and baroclinic gradient terms, which are very mild (in the case of tsunami applications, these conditions are absent). The use of unstructured (triangular) grids in the horizontal dimension further enhances the model efficiency and flexibility due to their superior capability in fitting complex coastal boundary and resolving bathymetric features, topographic features, and coastal structures. The vertical grid used in SELFE (for 3-D model) uses hybrid terrain-following coordinates (generalized σ, or so-

called "*S*"; Song and Haidvogel 1994) and *Z* coordinates. The model can be configured in multiple ways: 2-D or 3-D; Cartesian (i.e., map projection) or spherical (latitude/longitude); hydrostatic or non-hydrostatic options, etc. In tsunami applications, we typically apply the 2-D hydrostatic configuration for maximum efficiency. An exception is for the land-slide generated tsunamis, to which we have applied the 3-D non-hydrostatic SELFE. For seismic tsunamis, we also explicitly model the earthquake stage (i.e., with moving bed) in order to obtain accurate initial acceleration (Zhang and Baptista 2008b).

The inundation algorithm in SELFE uses a simple iterative procedure to capture the moving shoreline as shown in Figure 8-1. Because a semi-implicit scheme is used, which enables exceptionally large time step, the iterative procedure allows wetting and drying over multiple layers of elements over a single time step (i.e., with local CFL number >1). This simple procedure has led to accurate and stable results even near the wet/dry front where supercritical flow is not uncommon.

The version used in this study (v3.1g) does not explicitly model wave breaking effects, and therefore breaking waves are often represented as shock fronts in the model results. This approach is consistent with the conservatism we attempt to build in for inundation maps. However, conceptually it is not difficult to include the breaking effects in the model in the future.

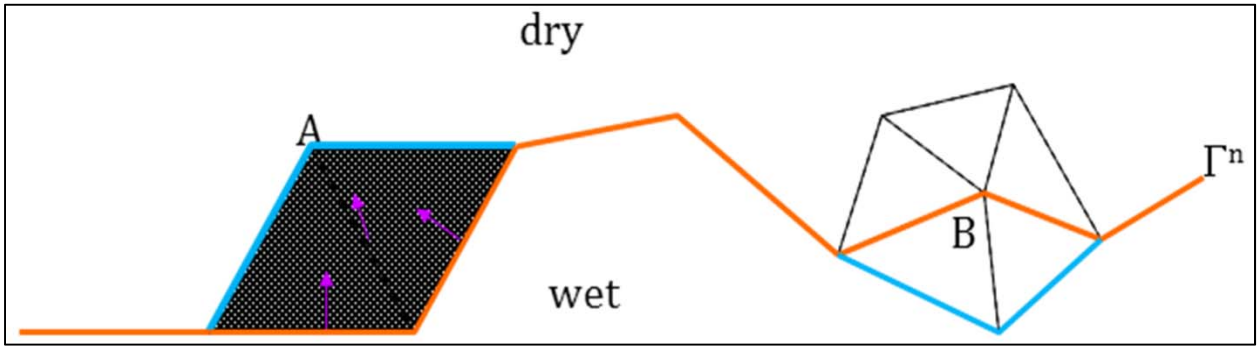

Figure 8-1: Inundation algorithm in SELFE. The orange line is the shoreline from the previous time step, and the cyan lines are corrections made to obtain the shoreline at the new time step because points A is wetted and B is dried.

Since 2007, all components of the SELFE modeling system have been fully parallelized using domain decomposition and Message Passing Protocol (MPI). This has further enhanced efficiency. For example, in the recent simulation of the impact of the 1964 Alaska event on the US west coast, we used a large grid (with 2.9 million nodes and 6 million elements) to resolve 12 major estuaries and rivers in the PNW (Zhang et al. 2011). With 256 CPUs on NASA's Pleiades cluster, the 6-hour simulation took only 2.25 hours wall-clock time. The largest grid we have implemented on Pleiades for SELFE so far has over 10 million nodes in the horizontal and 26 levels in the vertical.

8.3 Benchmark results

As mentioned before, here we will only report results for those benchmark problems relevant to seismic sources.

8.3.1 BP1: Solitary wave on simple beach – analytical

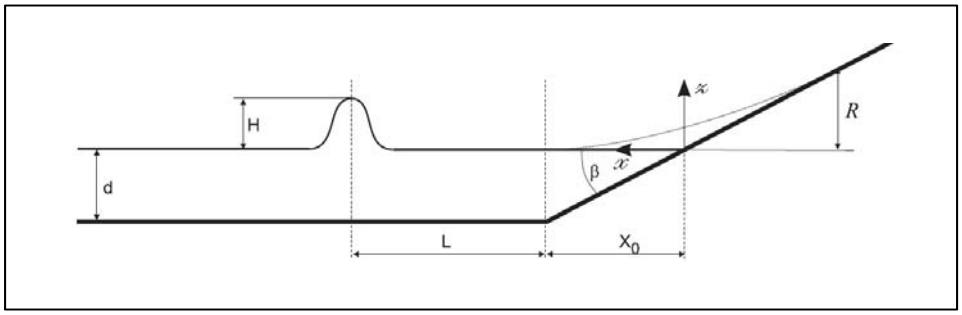

Figure 8-2: Domain sketch.

This canonical problem deals with a single solitary wave propagating along a constant depth and then over a sloping beach (Figure 8-2). The problem is completely defined by 3 parameters: *d* (offshore depth), β (beach slope) and *H* (height of the solitary wave over constant depth), and all variables are non-dimensionalized with respect to *d*. The goal is to validate the model for both propagation and inundation on the beach.

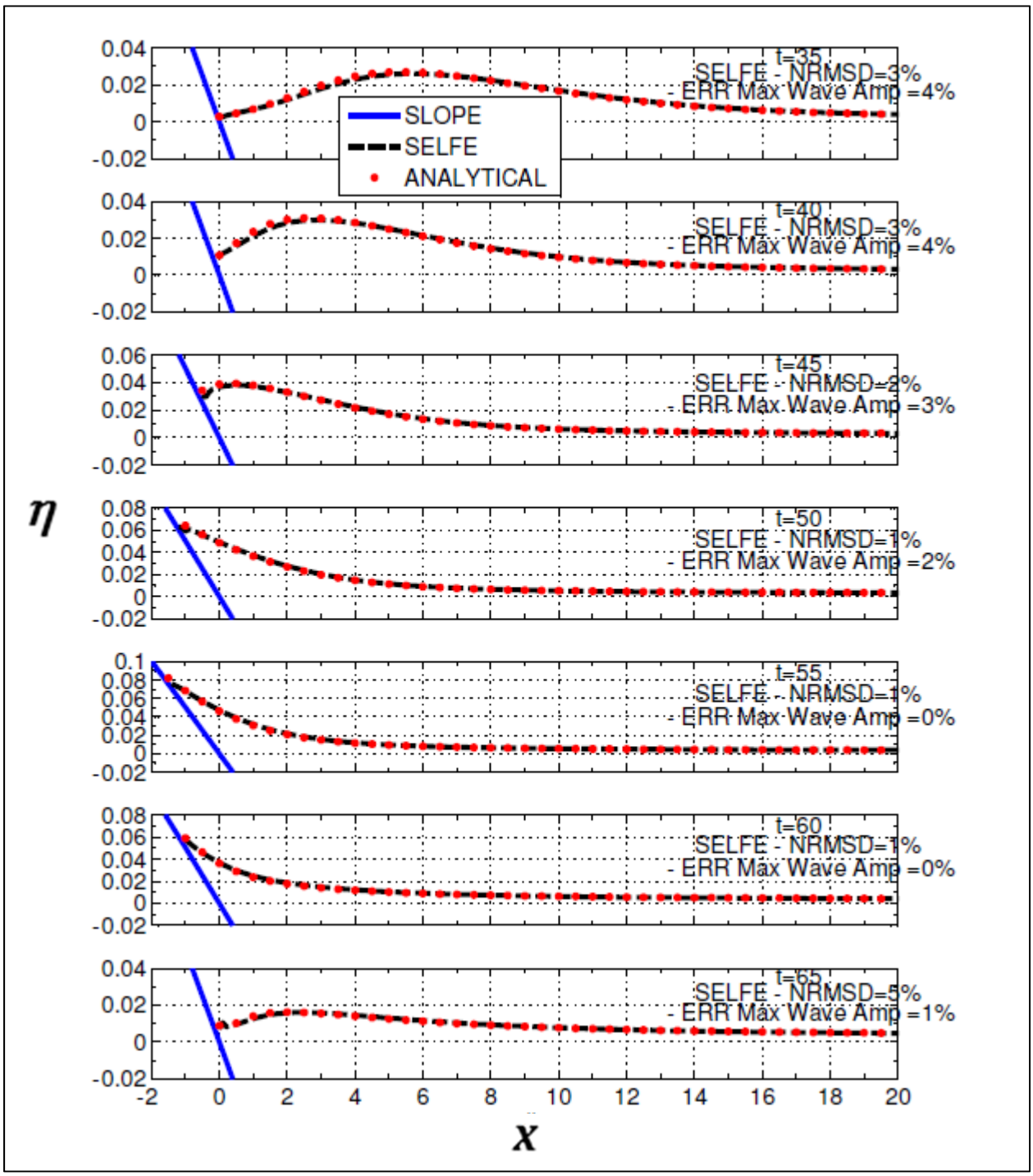

Figure 8-3: Comparison of surface profiles at various times for the non-breaking wave case A (H/d = 0.0185). All variables have been non-dimensionalized. The RMSE at t = 60 (near the maximum runup) is 0.001 and the Willmott skill is 0.998 (we have restricted the calculation of errors to x<2 to remove the uninteresting part of the solution offshore).

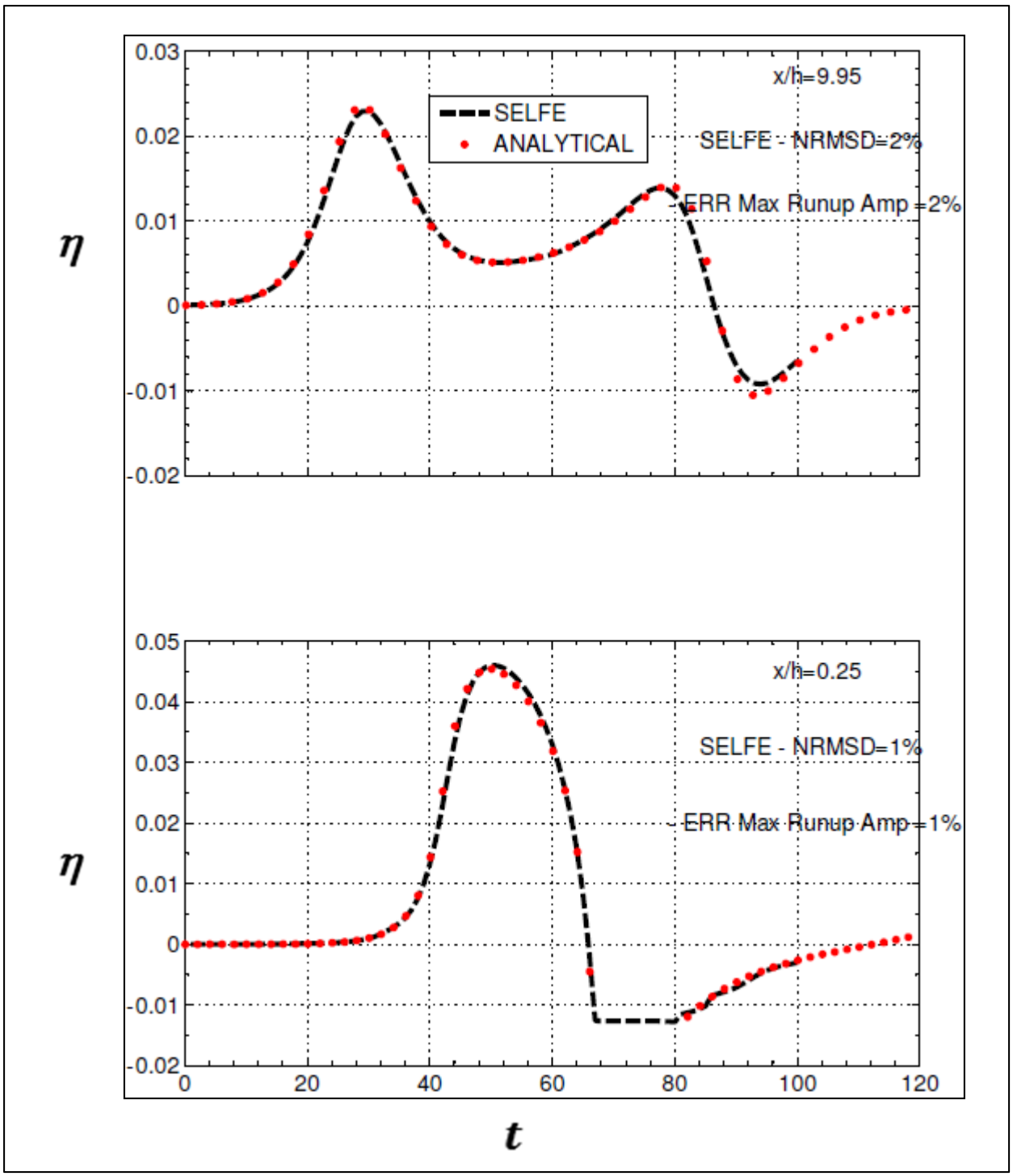

Figure 8-4: Comparison of elevation time series at two locations. The RMSE at the two stations are 0.0012 and 0.0008, and the Willmott skill are 0.994 and 0.999 respectively.

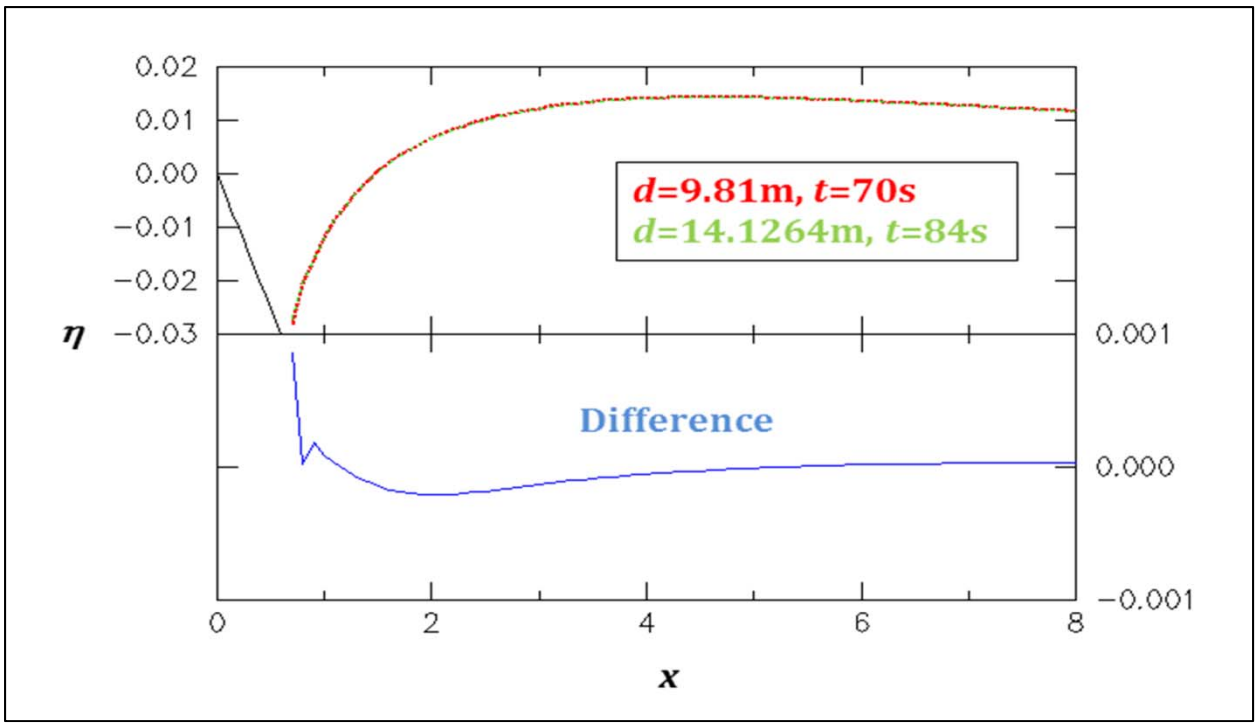

Figure 8-5: Scaling effects through comparison of surface profiles between model results using two different values of d. Note that the corresponding dimensional times are different due to the different scaling.

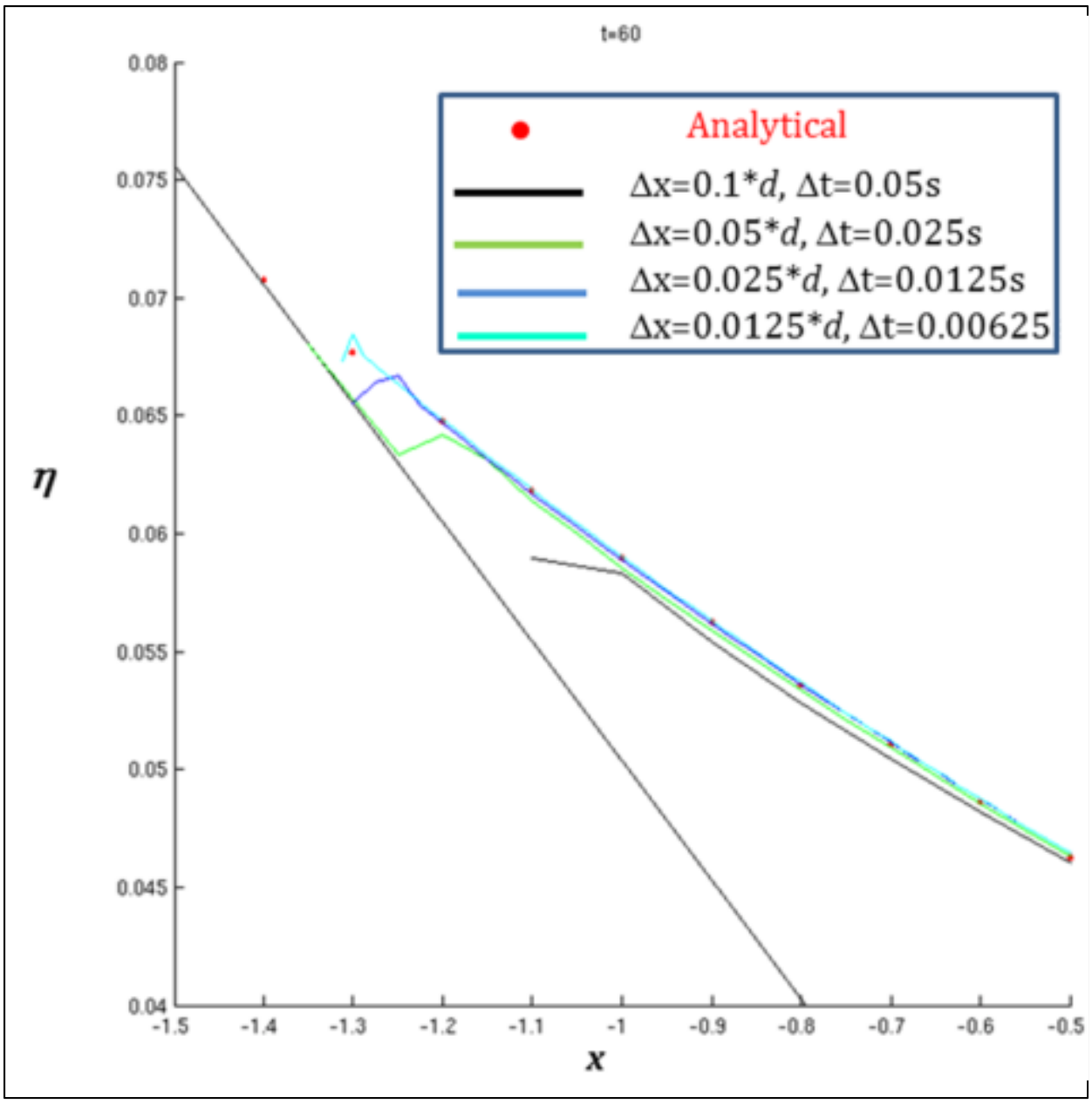

Figure 8-6: Convergence test for case A at a time near the maximum runup (t = 60).

For convenience, we chose $d = 9.81$ m in the model simulations, although scalability of the model is also tested below (Figure 8-5). The model grid covers $-98\,\text{m} \le x \le 686.7\,\text{m}$ and is 2 elements wide in the y direction. A "uniform" grid with $\Delta x = \Delta y = 0.1{*}d$ was used with each square divided into 2 triangular elements, and therefore there are altogether 2403 nodes in the grid. The time step was set at $\Delta t = 0.05$ s, and the implicitness factor at 0.6 (the maximum runup is somewhat sensitive to this factor; as explained in Zhang and Baptista (2008b), the best accuracy is achieved near 0.5). On the left boundary, a Flather type open boundary condition was imposed to minimize reflection there. We used frictionless bottom and nonlinear shallow-water equation (SWE) in order to be consistent with the assumptions made in the analytical solution.

The comparisons were made in several ways. First the surface profiles at multiple times are compared in Figure 8-3. The model is able to accurately simulate the entire runup and run-down process. In addition to the conventional root-mean-square error (RMSE) we also used the Willmott skill number which is defined as:

$$W = 1 - \frac{\sum (m - o)^2}{\sum \left[| m - \bar{o} | + | o - \bar{o} | \right]^2} \tag{1}$$

where m and o are model and data respectively, and $\bar{o}$ is the data mean. This number combines the contributions from both RMSE and the correlation (Willmott et al. 1985); a Willmott number of 1 indicates a perfect skill and the model is more skilled with a higher W.

Secondly, the time series at two stations were compared (Figure 8-4). Note that at one station (x = 0.25) wetting and drying occurred as indicated in both the model results and the analytical solution. Again the model skill is high in this aspect.

Thirdly, the scaling effects in the model were also examined. As mentioned before, there is only 1 parameter used in scaling all variables: the offshore depth d. Figure 8-5 shows model results from using different values of d and it can be seen that the difference in the elevations is very small, even near the instantaneous shoreline.

The convergence of the model is illustrated by using successively finer grid size and time step; the grid size and time step were varied in such a way that the CFL number remains constant as required by the model (Zhang and Baptista 2008a). The most challenging aspect of this test is to obtain the convergence for the maximum runup. As shown in Figure 8-6, the modeled runup indeed converges to the analytical value; at the finest resolution the error for the runup value is 3%.

Due to the small grid size used in this benchmark problem, the CPU time is modest. For example, the 100-time-unit run shown in Figure 8-4 took 1 min wall-clock time to complete with 1 CPU (all tests shown in this report, unless otherwise noted, were conducted on an Intel cluster running on Rocks version 5.0 with CPU clock speed of 2.66 GHz and gigabit copper Ethernet network connection).

8.3.2 BP2: Solitary wave on composite beach – analytical

This problem was modeled against the Revere Beach located approximately 6 miles northeast of Boston in the City of Revere, Massachusetts. A physical model was constructed at the Coastal Engineering Laboratory of the U.S. Army Corps of Engineers, Vicksburg, Mississippi facility. The model beach consists of three piecewise-linear slopes of 1:53, 1:150, and 1:13 from seaward to shoreward with a vertical wall at the shoreline (Figure 8-7). In the experiments, the wavemaker was moved to different locations for each of the 3 cases: A, B and C. Here we simply used the measured time series at gauge 4 as the boundary condition for the model. For comparison with the analytical solution, which was derived from the linearized SWE, we will only consider case A for the reason stated below.

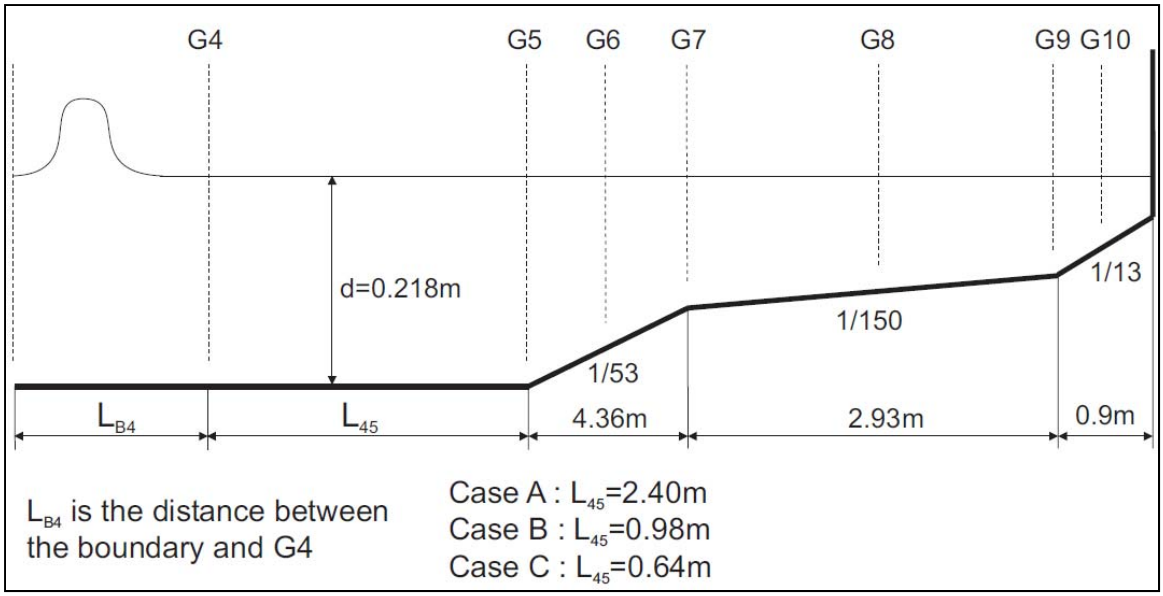

Figure 8-7: Schematics of the composite beach and locations of gauges.

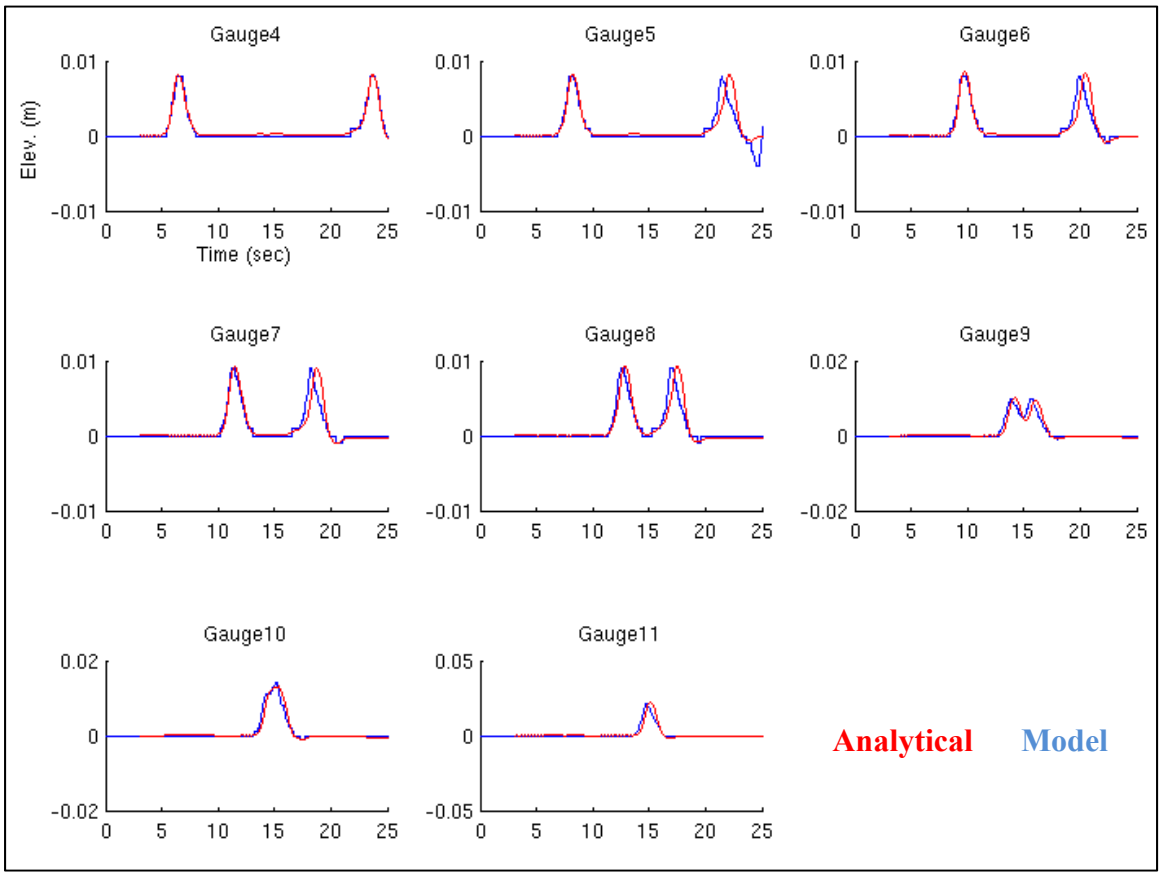

Figure 8-8: Comparison of elevation time history at 8 stations for case A. Gauge 4 is located at the domain boundary and serves as a check for the imposed boundary condition; gauge 11 is at the vertical wall, where the RMSE is 1.5 mm and the Willmott skill is 0.96.

In the model, a rectangular domain with variable grid size (Δy = 2.5 mm and Δx varies from 1 cm at the left boundary to 1 mm at the vertical wall, in order to capture the large runup there) was used to cover $12.64m \le x \le 23.23m$ (case A), $14.06m \le x \le 23.23m$ (case B), and $14.4m \le x \le 23.23m$ (case C). Note that no non-dimensionalization was done for this test. The time step was set at 0.08 s and the total run time was 30 s. The grid for case A was the largest with 11679 nodes, and it took 2 min wall-clock time to complete with 2 CPUs.

Figure 8-8 shows the comparison at various gauges along the flume. Good agreement is observed in general. The "errors" in the numerical solution can be partly attributed to the different assumptions used in the analytical and numerical solutions; in SELFE a strict "linear" solution of the SWE is not possible as the flux term in the integrated continuity equation can only be treated nonlinearly.

For the other two cases (B and C), the amplitude of the incident wave is not small as compared to the water depth, and therefore the analytical solution, which linearizes the SWE around $\eta = 0$, is definitely not valid even as a 1st-order approximation of the SWE. Consequently, we excluded these in the comparison. Comparison with the lab data will be presented in Section 8.3.4.

8.3.3 BP4: Solitary wave on simple beach – laboratory

The description of the problem can be found in Section 8.3.1. Here we compare the results for cases A and C, as well as for the runups as a function of the incident wave height. The model parameters are the same as in Section 8.3.1,, except that non-zero bottom frictions based on the Manning formulation were used.

Figure 8-9 shows surface profiles at various times for the non-breaking case A. The model is able to capture the runup and rundown process well, and near the maximum runup/rundown (t = 60 and 70) the model results are more accurate than the analytical solution (cf. Figure 8-3).

For wave breaking case C, the SWE is no longer appropriate, and therefore the hydrostatic version of SELFE initially gave larger errors (Figure 8-10). The steepening of the crest as seen in the model results, is typical of any hydrostatic model due to lack of energy dissipation. After wave breaking occurs, however, the SWE is able to reasonably simulate the runup process (last panel of Figure 8-10). The modeled maximum runup is also slightly sensitive to the choice of the bottom friction, and a smaller friction leads to a larger runup.

The repeated experiments using different wave heights provided the runups as a function of the wave height, and the comparison is made in Figure 8-11. The experiments indicated that wave breaking initiates when H/d >0.045. The modeled runups are accurate up to this limit and are less accurate beyond (Figure 8-11). We expect better results to be obtained when we incorporate the wave breaking effects.

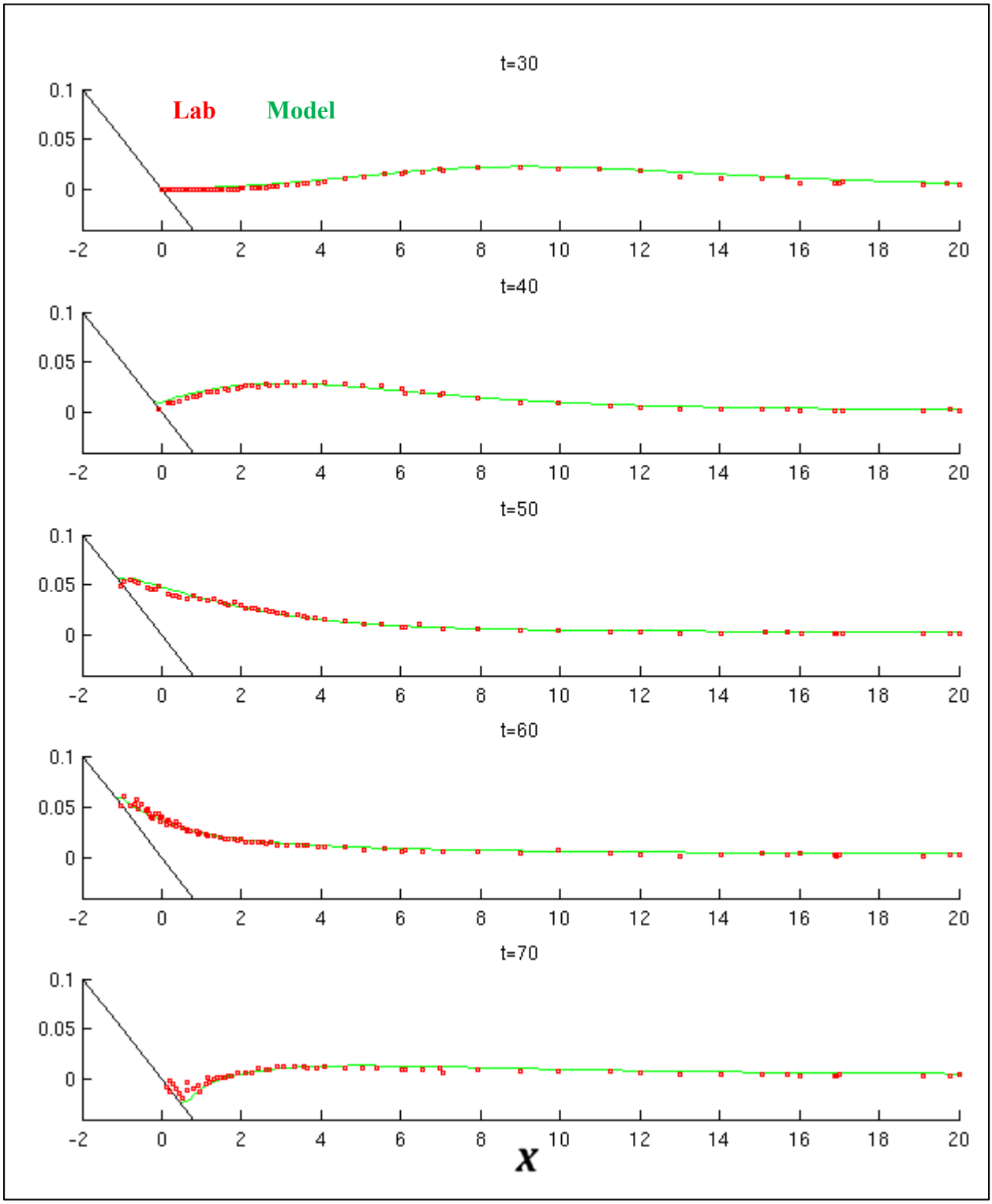

Figure 8-9: Comparison of surface profiles for case A. The Manning friction coefficient is n_0 = 0.016. The error for the maximum elevation at t = 60 (near the maximum runup) is 2%.

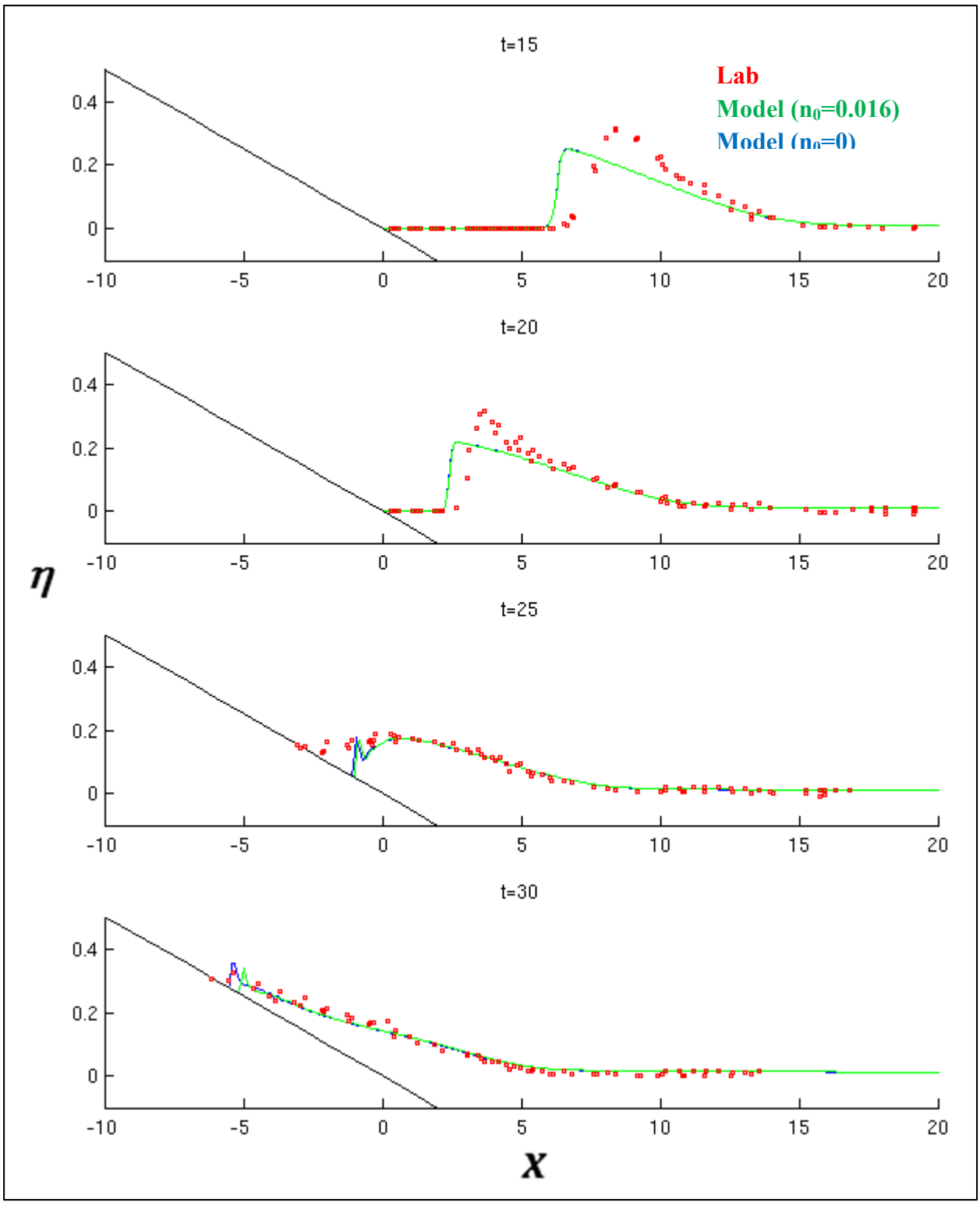

Figure 8-10: Comparison of surface profiles for breaking-wave case C (H/d = 0.3). Model results with two choices of bottom friction are shown.

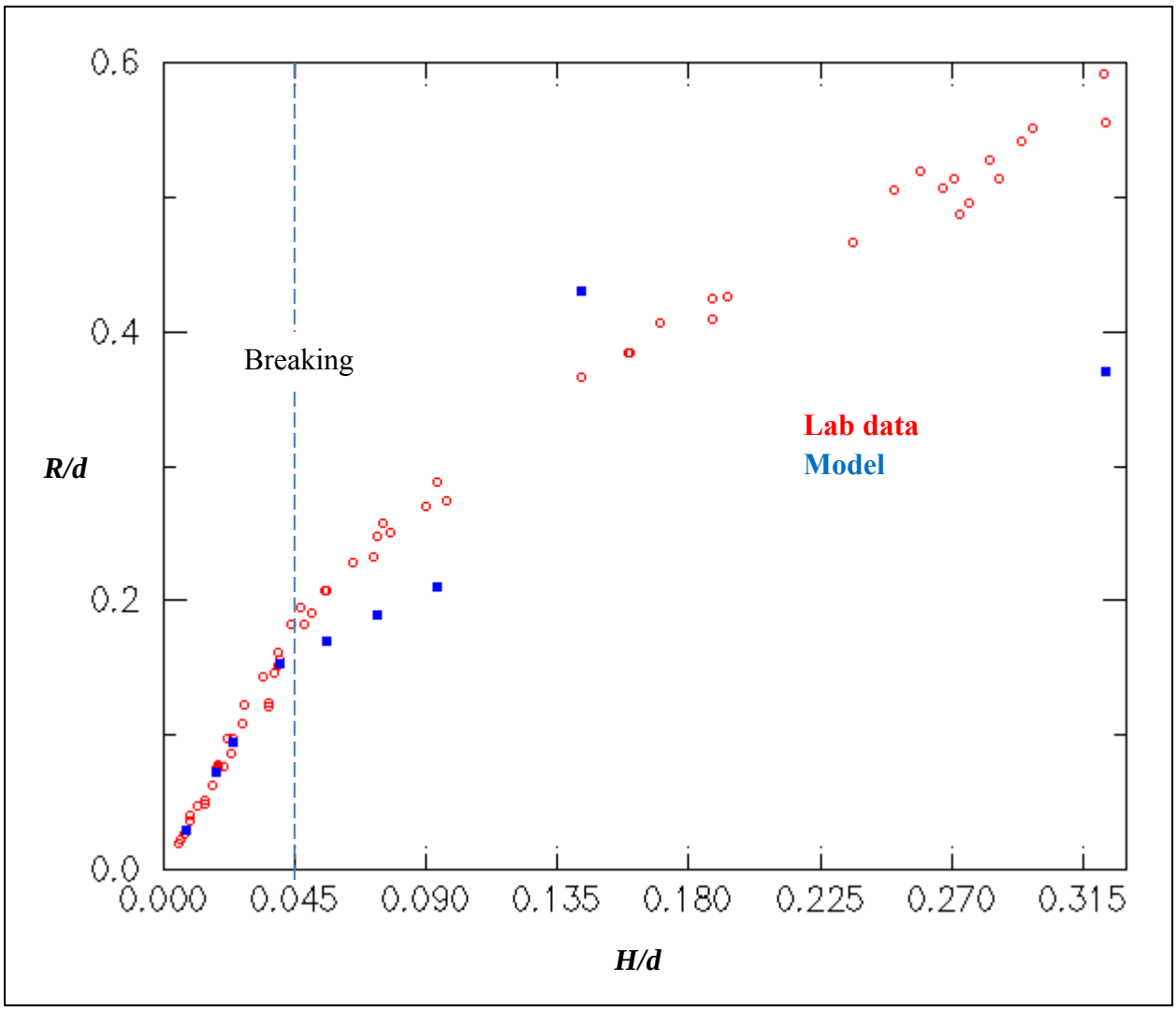

Figure 8-11: Runups as a function of the incident wave height. The maximum runup error for non-breaking waves is 1.9%.

8.3.4 BP5: Solitary wave on composite beach – laboratory

The set-up of the experiments has been described in Section 8.3.2. The model uses the nonlinear SWE instead of the linear SWE as in Section 8.3.2. We have also explored variation of the Manning coefficient (n_0) but found little sensitivity in the results to this parameter. The results presented below were obtained using $n_0 = 0$.

The elevation time series for all 3 cases (A, B, and C) are presented in Figure 8-12 through Figure 8-14. The mismatches in mean water level at gauge 7 in Figure 8-12, etc., suggest problems in the lab data. In general, the model results compare reasonably well with the lab data, except for the largest wave case C (Figure 8-14).

Furthermore, the modeled runups at the vertical wall are also in reasonable agreement with the data for cases A and C. For case A, the modeled and lab measured runups are 2.3 cm and 2.7 cm respectively. For case C, they are 24.9 cm and 27.4 cm. For case B, the large waves colliding with the wall generated very high splash which explains the largest runup measured

among the 3 cases (45.7 cm). Because the model does not explicitly simulate this process, the modeled runup was substantially lower (19.1 cm). In all three cases, the model runs were stable with no sign of instability.

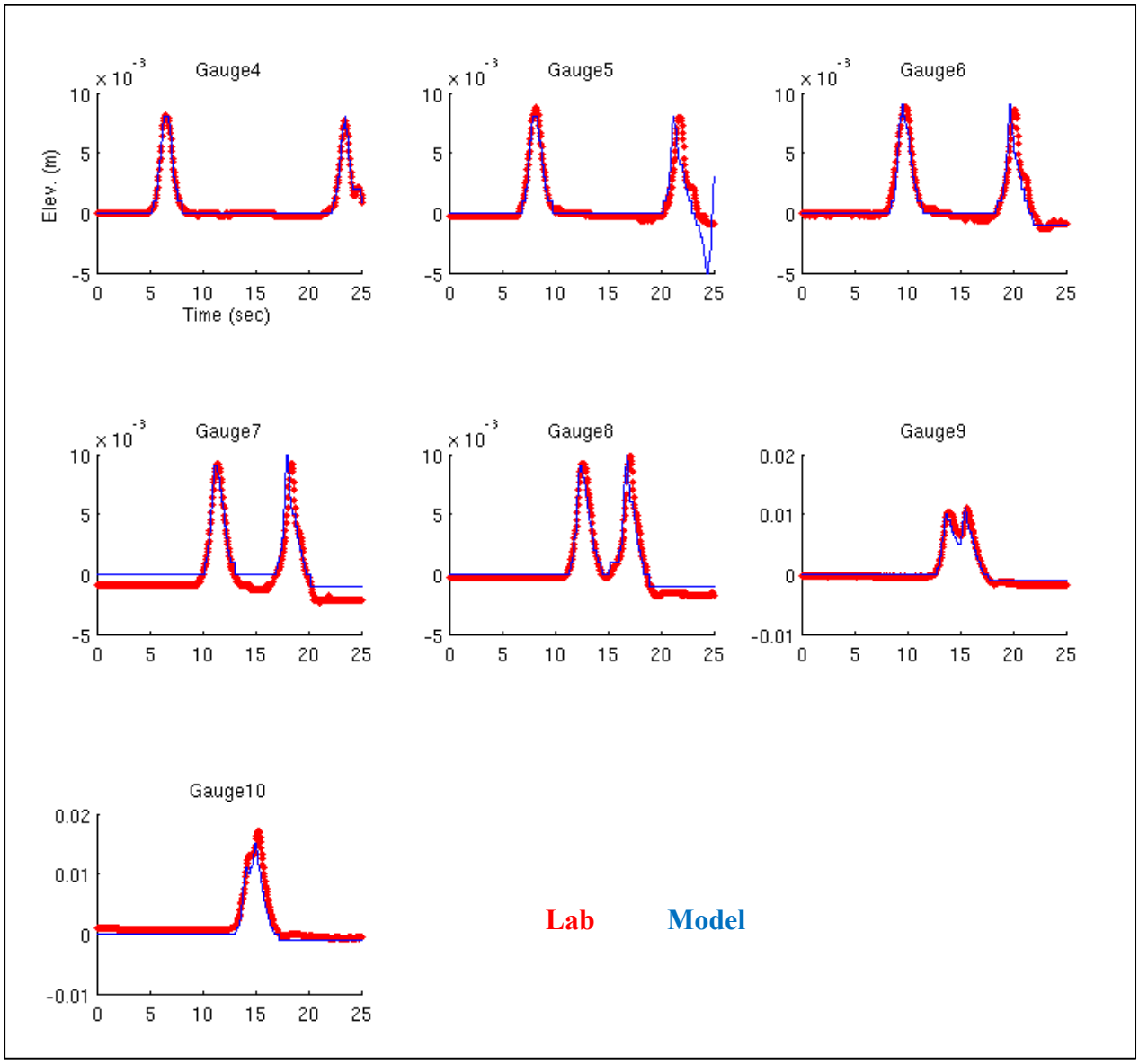

Figure 8-12: Comparison of elevation time series for case A.

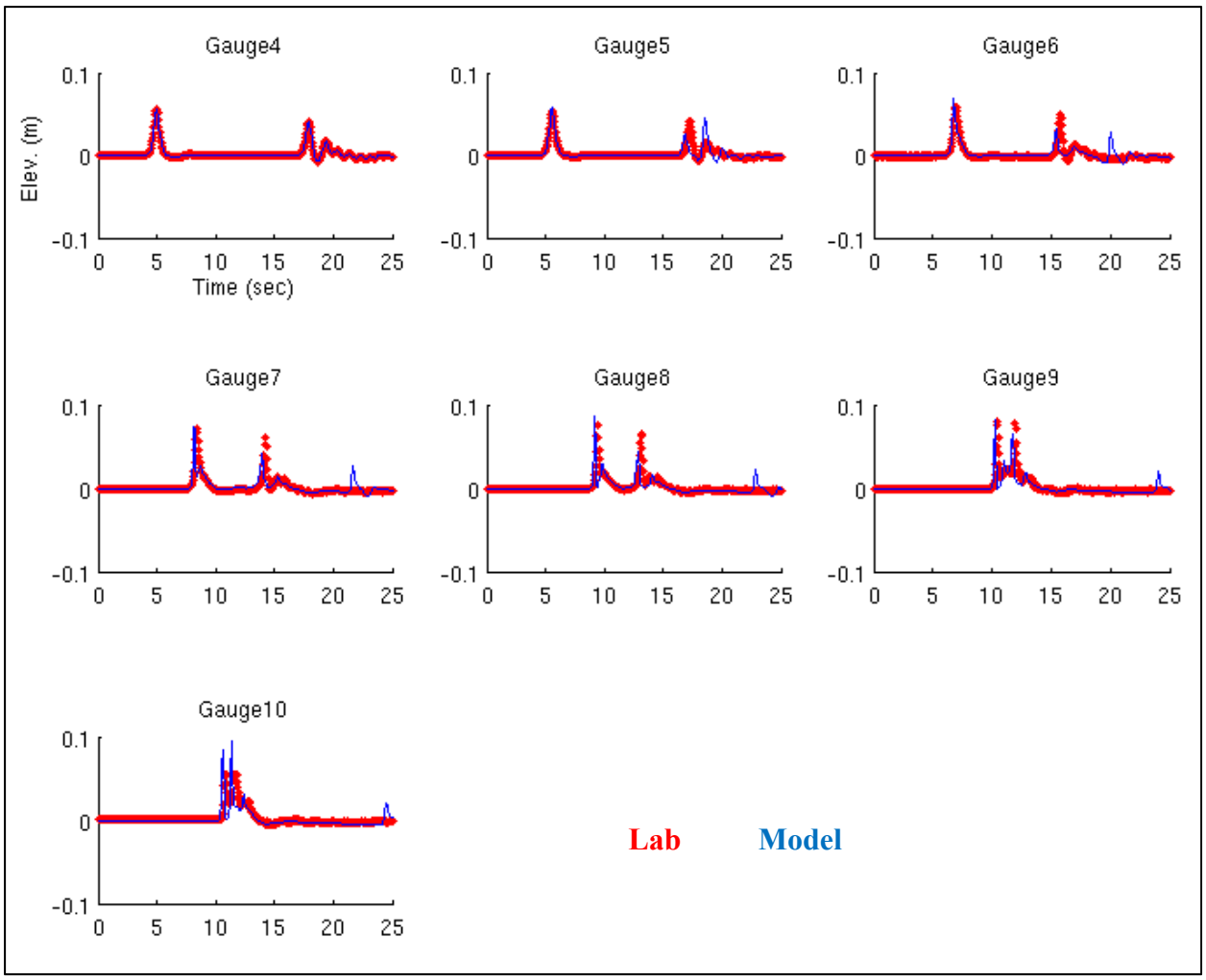

Figure 8-13: Comparison of elevation time series for case B.

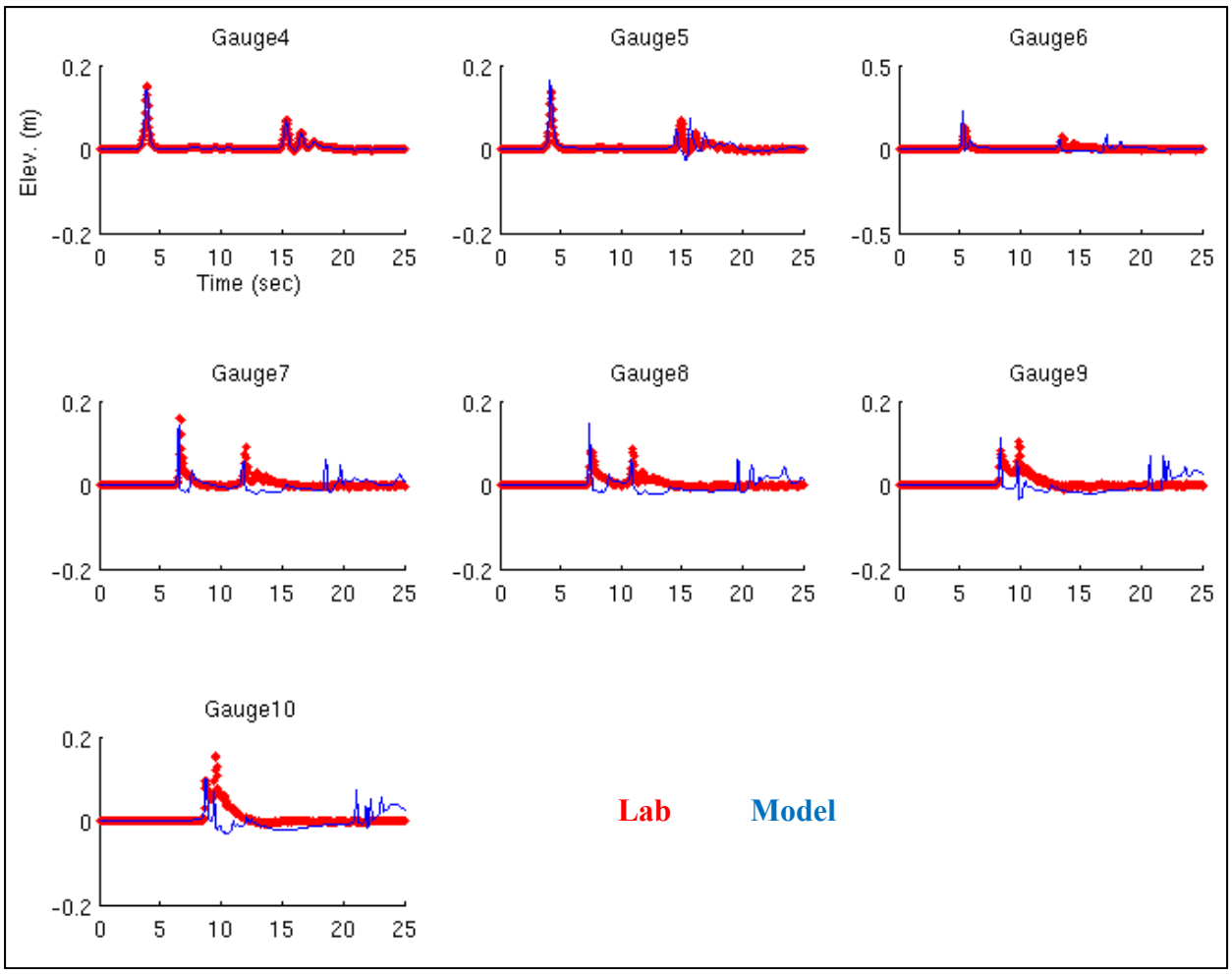

Figure 8-14: Comparison of elevation time series for case C.

8.3.5 BP6: Solitary wave on a conical island

To examine the model performance in more than one dimension, the experiment of solitary wave around a conical island (Figure 8-15a) is simulated numerically here. The lab data include time series at various gauges in the tank as well as runup measurements around the perimeter of the conical island.

We did not model the wavemaker in the experiment but instead used the time series at a gauge close to the wavemaker as the boundary condition. An unstructured grid was generated for this problem to better resolve the downwave side of the island where large runups due to collision of two waves were expected. A 10 cm grid size was used at the outer tank boundaries, 1 cm at the boundary of the flat top of the cone (which has a diameter of 2.2 m), and 5 cm in the upwave half of the circle that defines the toe of the conical island, and 2 cm for the downwave half (Figure 8-16). The total number of the nodes was 259231. The time step was set at 0.02 s, and the Manning's $n_0 = 0.01$. The total simulation time was 60 s, which took 38 min wall-clock time on 24 CPUs.

Figure 8-15 shows the comparison of elevation time series at 4 gauges for 3 cases, with a progressively larger incident wave amplitude. The modeled elevations are in good agreement with the lab data and the model was stable for all cases.

The modeled runup distribution around the island is compared to the measured values in Figure 8-17. Figure 8-18 is a spatial representation of the same information as in Figure 8-17. The agreement is excellent for cases A and B; the maximum errors were below 5%. For case C, the model results exhibit a slight asymmetry (Figure 8-18) and an under-estimation of the maximum runup at the back of the island. The wave breaking that occurred in this case cannot be accurately modeled by SELFE.

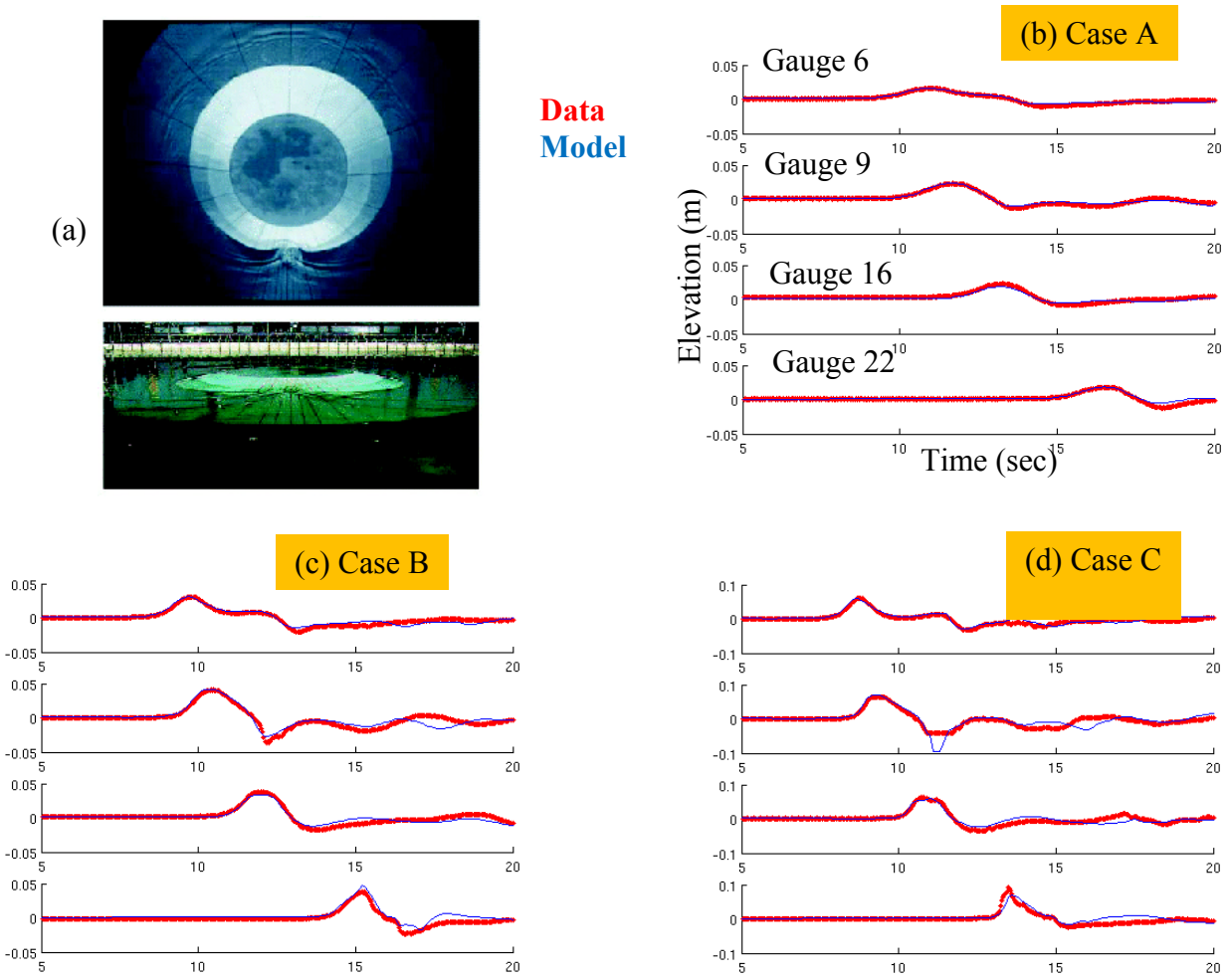

Figure 8-15: Comparison of elevation time series at 4 gauges for 3 cases. (a) shows the experimental setup.

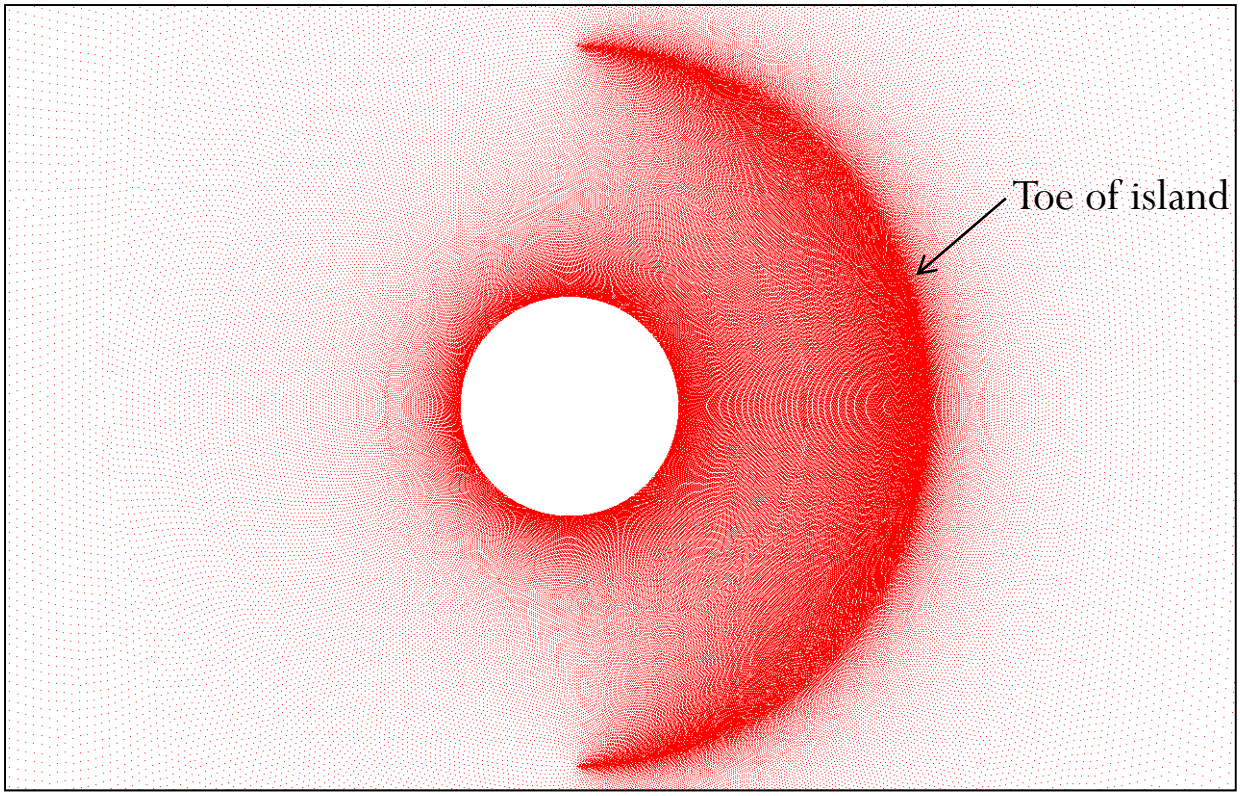

Figure 8-16: Nodes in the unstructured grid.

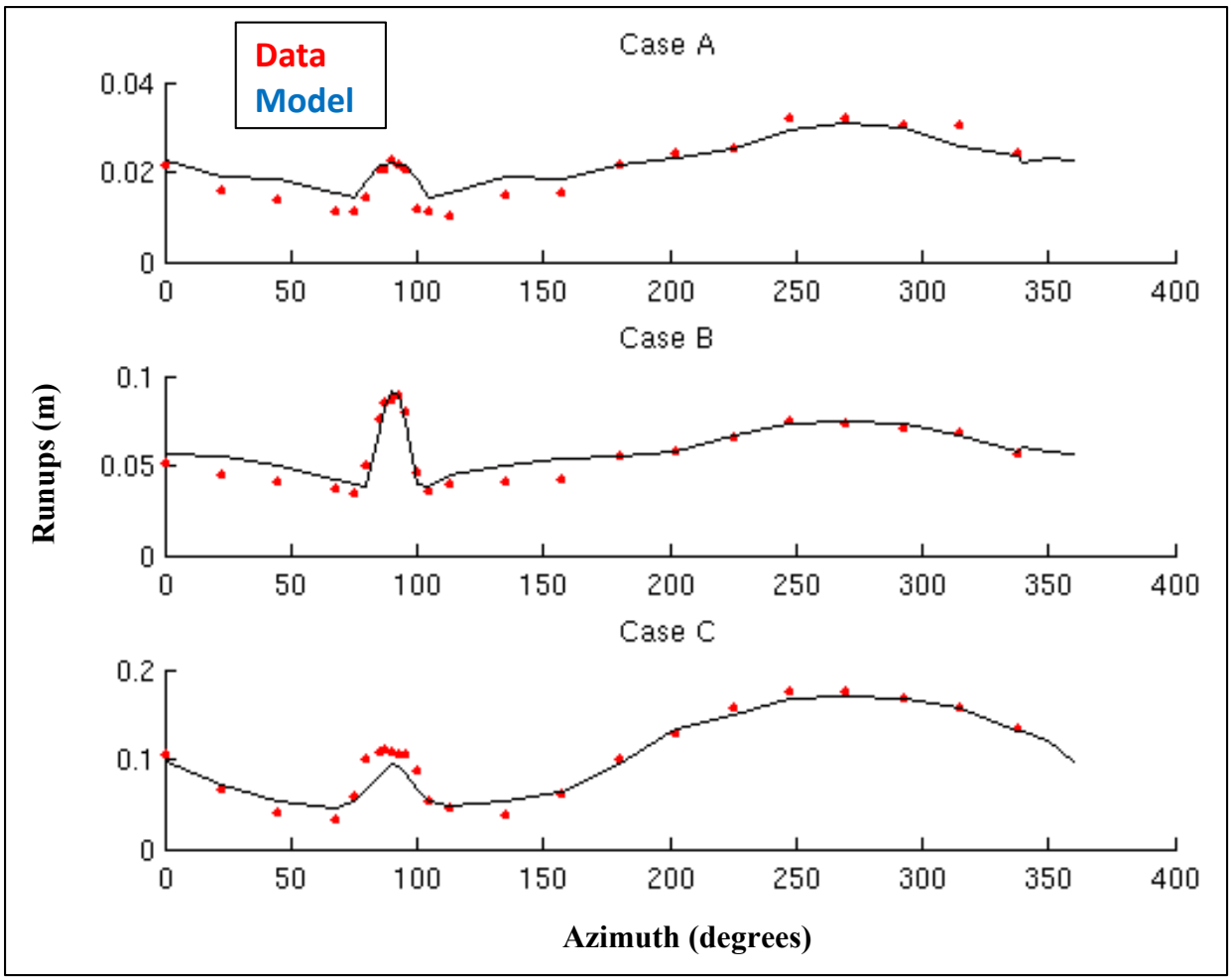

Figure 8-17: Comparison of runups around the conical island for the 3 cases. The errors at the back of the island are: 2.6%, 4.3% and 14% for the 3 cases.

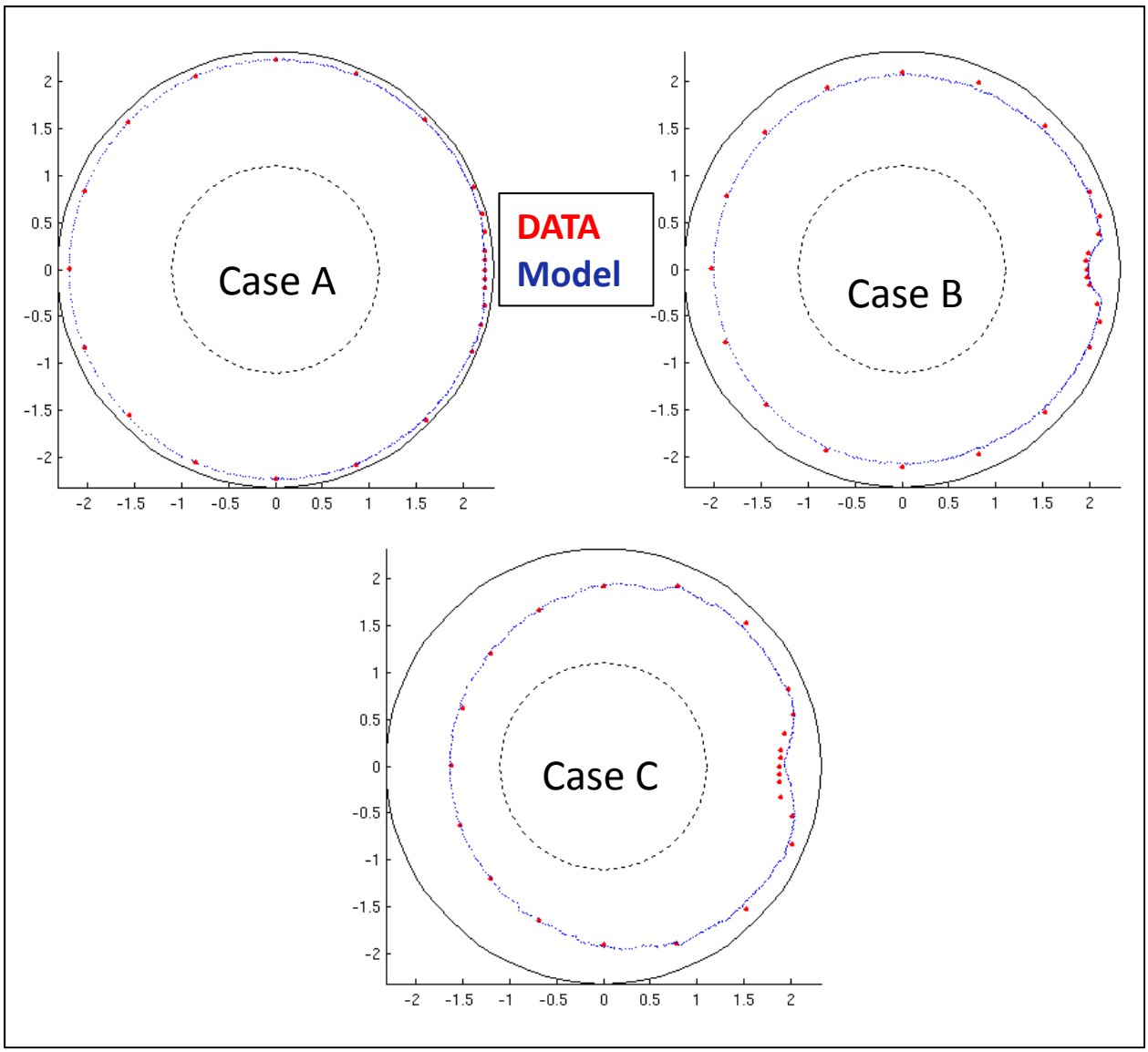

Figure 8-18: Comparison of runups around the conical island for the 3 cases, in spatial form.

8.3.6 BP7: Wave runup on Monai Valley

This test considers the wave tank experiment that models the 1993 Okushiri Island tsunami. The lab data include time series at 3 gauges (Figure 8-19a) as well as video images that illustrate the runup sequence in a narrow valley near Monai.

The model used a uniform grid resolution of 1.4 cm and a time step of 0.01 s . Therefore there were altogether 95892 nodes in the grid. We have tested the sensitivity to the Manning's n_0 and found little influence from this parameter. The results below were obtained using $n_0 = 0$. The total simulation time was 22.5 s, which took 9 min wall-clock time with 20 CPUs.

The comparison of time series at the 3 gauges in front of the valley is shown in Figure 8-19. The model was able to capture the arrival time and the amplitude of the first waves well. The inundation sequence in the narrow valley is shown in Figure 8-20, which agrees qualitatively

with the lab observation: the modeled maximum runup of 9 cm is close to the observed mean value of 10 cm.

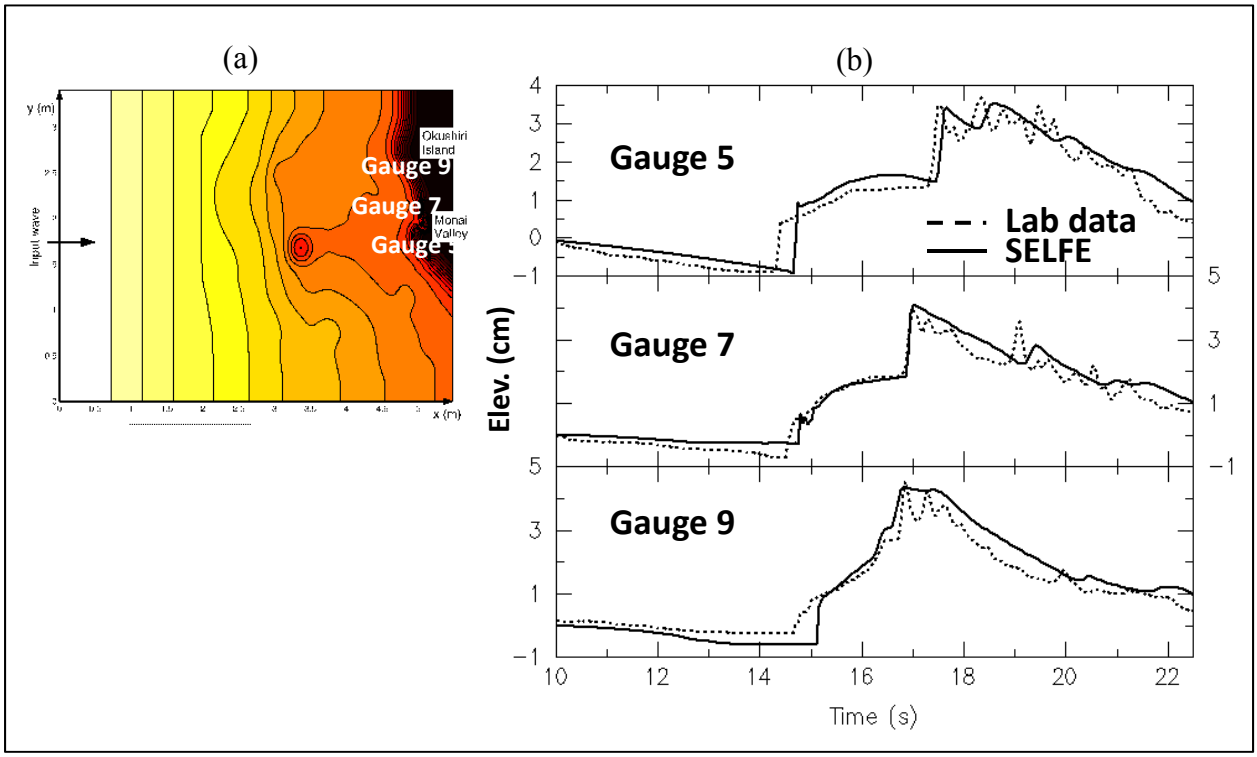

Figure 8-19: Comparison of elevations at 3 gauges in front of the valley as shown in (a).

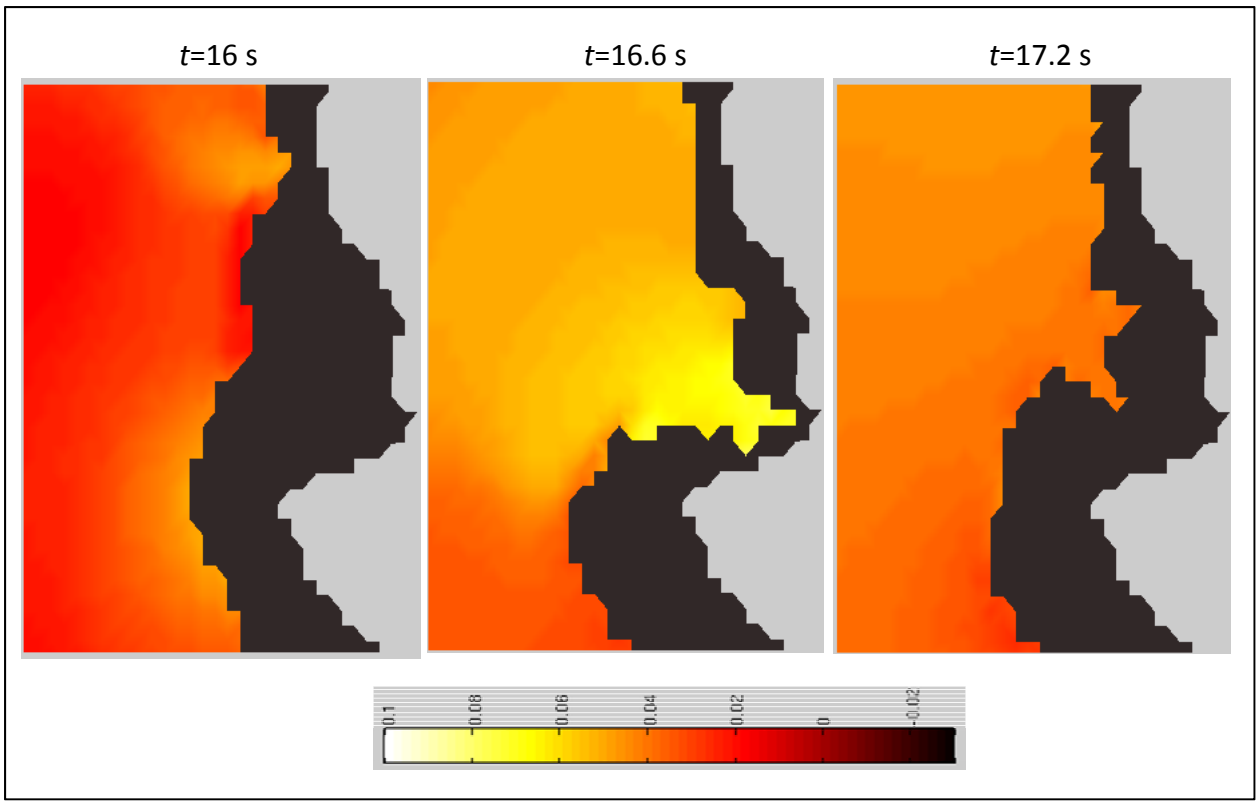

Figure 8-20: Inundation sequence near the narrow valley;. t = 16.6 is close to the maximum runup, which is ~9 cm .

8.3.7 BP9: Field – Okushiri Island

The first field test conducted was the 1993 Hokkaido-Nansei-Oki tsunami that impacted the Japanese island of Okushiri. The historical data were originally collected by the post-tsunami survey group and passed onto the author by Dr. Tomo Takahashi; they include the pre- and post-event bathymetry survey data, the estimated source information, tide gauge records at 2 gauges, and estimated runup distribution around the island. However, the horizontal datum used in the files was later found to contain errors when overlaid with modern maps. The files used in this study were corrected by Dr. Dmitry Nicolsky (U. Alaska Fairbanks). As shown in Figure 8-21a, there still appear to be mismatches among the various files that define the DEMs.

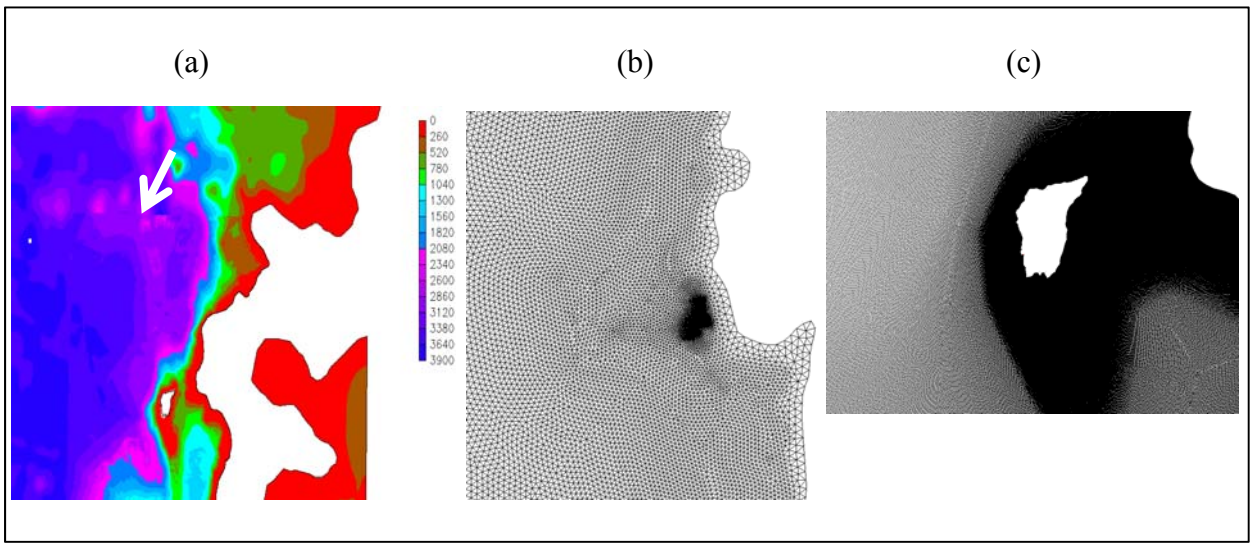

Figure 8-21: (a) Bathymetry as embedded in DEMs; (b) unstructured grid and (c) zoom-in around the Okushiri Island. The white arrow in (a) indicates a mismatch of bathymetry from multiple DEM sources.

To better capture the runup distribution around the island we used variable resolution around the island, with 30 m resolution at the shoreline, and ~5 m around the narrow Tsuji Valley where the maximum runup (~31 m) was observed (Figure 8-21). At the outer ocean boundary we used a coarse resolution of 7 km. The total number of nodes in the grid was 1,617,562 with over 95% spent around the island. A time step of 0.5 s was used to carry out the 1 hour simulation, which took 4.75 hours on 40 CPUs.

The comparison at the 2 tide gauges is shown in Figure 8-22. While the modeled arrival time approximately matched the gauge record at Esashi, it was too early at Iwanai, suggesting errors in the source information; note that a similar mismatch was also observed by Kato and Tsuji (1994).

On the other hand, the agreement between the model and data for the distribution of the runups around the island was much more reasonable (Figure 8-23). Note that the data were digitized from a figure in Kato and Tsuji (1994) and therefore the precise locations of observation were unknown. Nevertheless, the model seems to have captured well the variation along the west, north, and south coast, with large errors along the east coast, where the errors in the source information may be more pronounced. The model adequately simulated the large runups around the Tsuji Valley (with 20% error) on the west coast, and around Aonae-Hamatsumae on the south coast. The two waves reported in various post-tsunami surveys as arriving ~10 min apart devastated the town of Aonae; these were correctly simulated by the model (Figure 8-24).

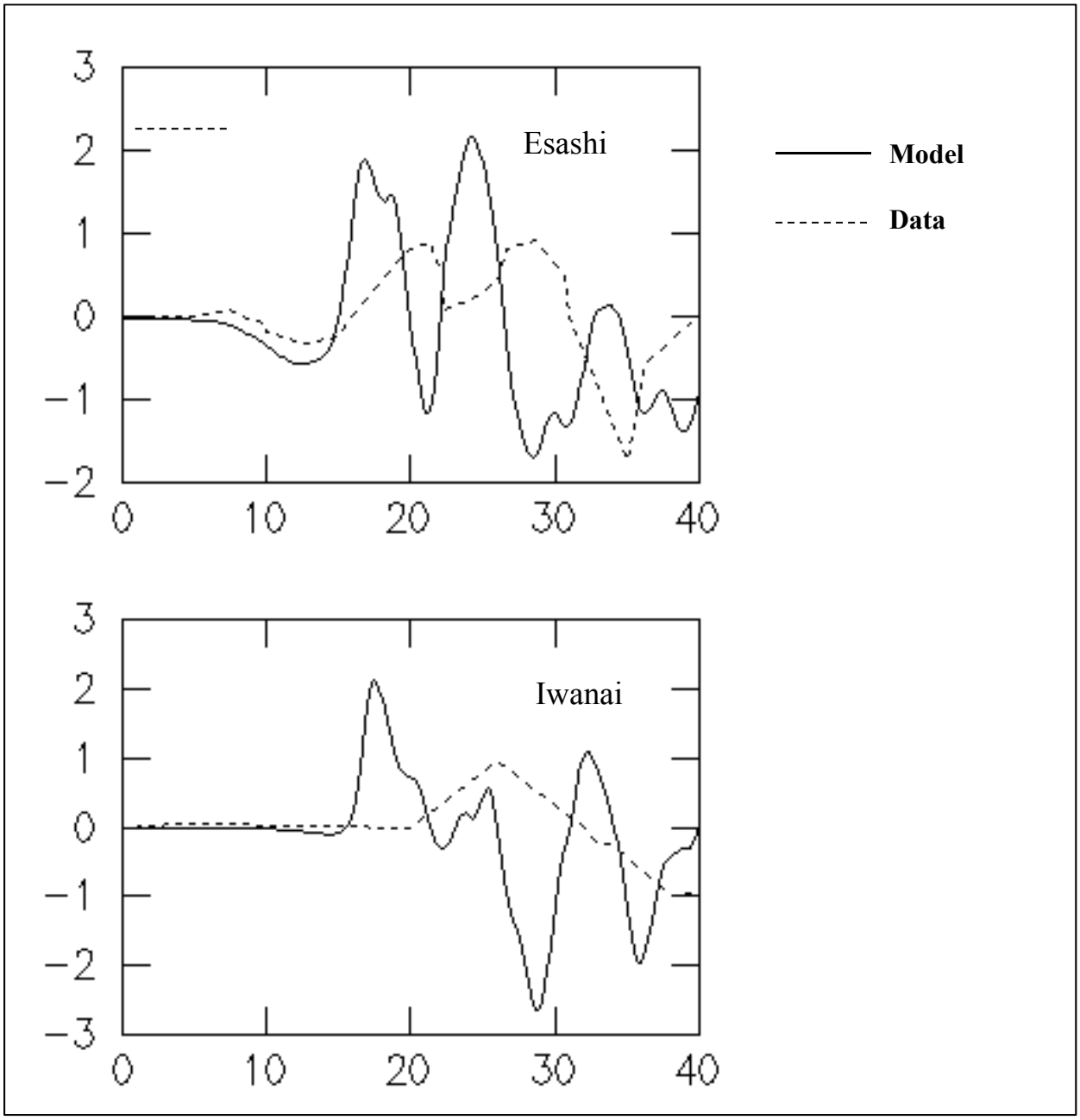

Figure 8-22: Comparison of elevations at 2 tide gauges.

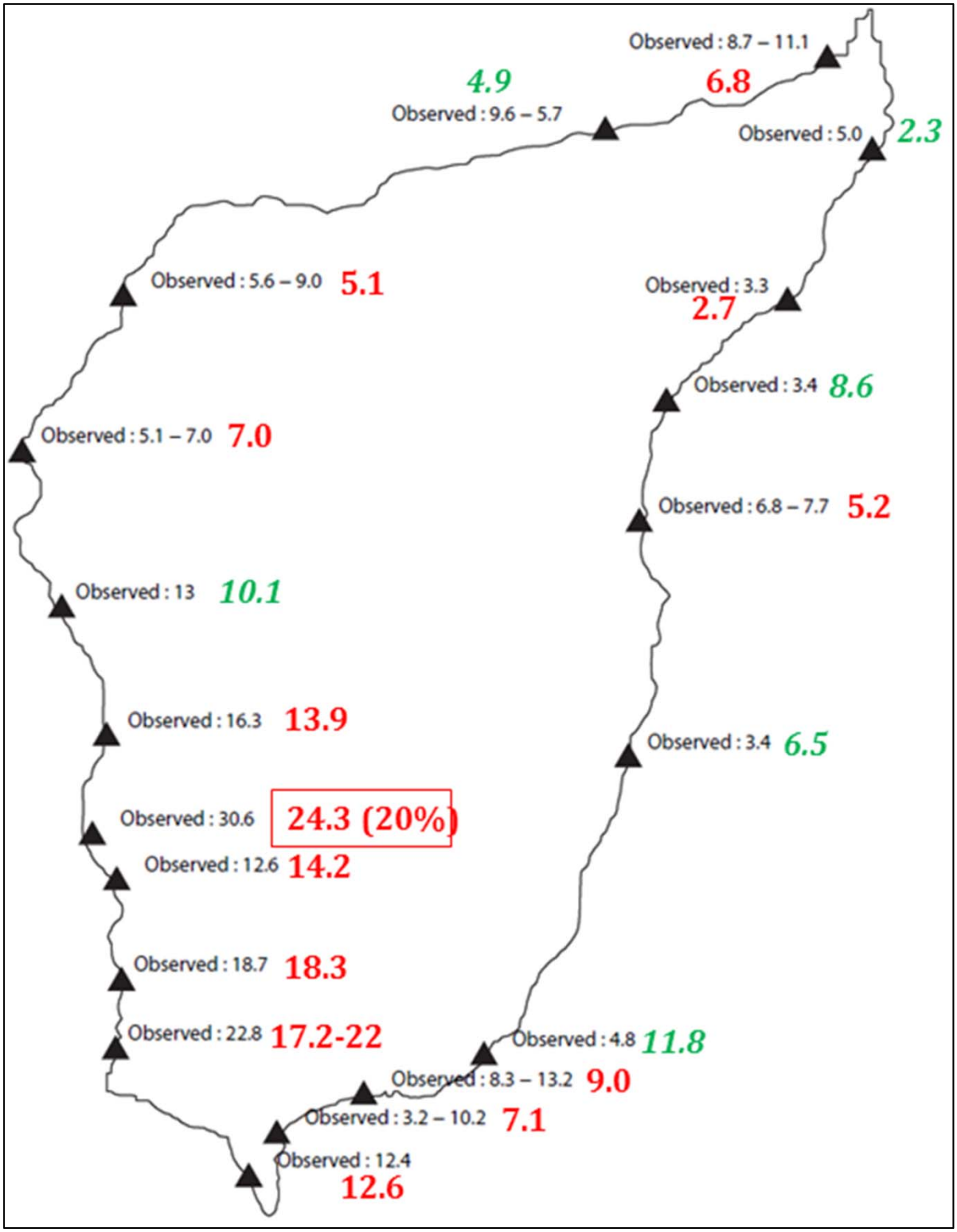

Figure 8-23: Comparison of runups around the island. Red and green numbers are from the model, with the green numbers indicating larger errors.

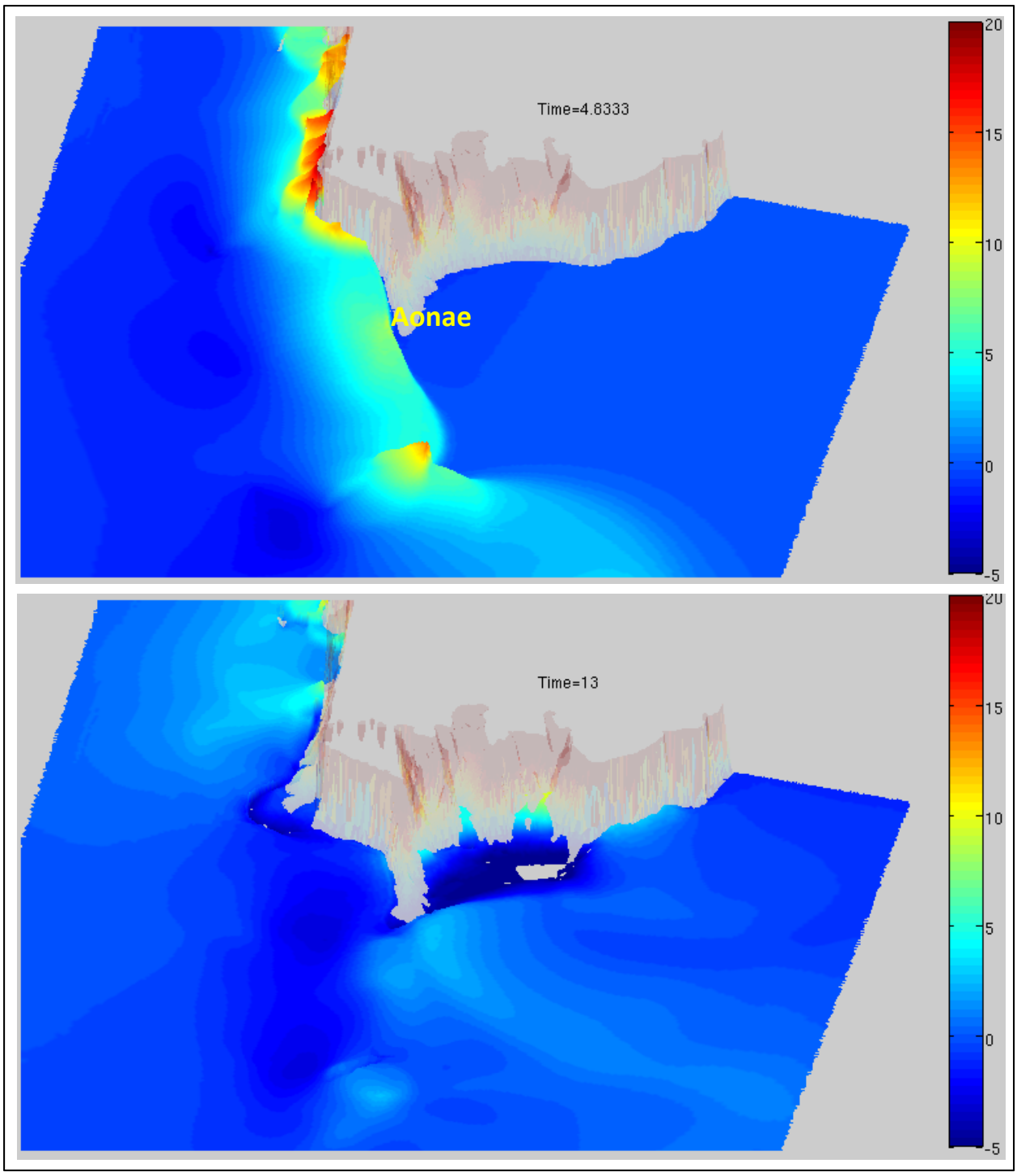

Figure 8-24: Arrival of 2 waves at Aonae. The 1st wave came from the west while the 2nd wave attacked from the east.

8.3.8 N-Wave runup on a beach

This test was originally proposed at the 3rd Workshop on Longwave Runup. The 1-D problem considers an initial N wave on a sloping beach (Figure 8-25) and has a nonlinear

analytical solution. Note that this test is more nonlinear than that for the solitary wave case (Section 8.3.1) and is therefore a good test for the nonlinear SWE solvers.

The model grid used a uniform resolution of 5 m in both x and y directions, a time step of 0.1 s and a frictionless bottom. The total number of nodes in the grid was 176011. With 25 CPUs, the 240 s-run took 24 min to complete.

Comparison of the along-slope elevation and velocity profiles at 3 times is shown in Figure 8-26; the errors for elevation were smaller than for the velocity, and the error for the runup was 5%. The model accurately simulated the entire runup and rundown phases.

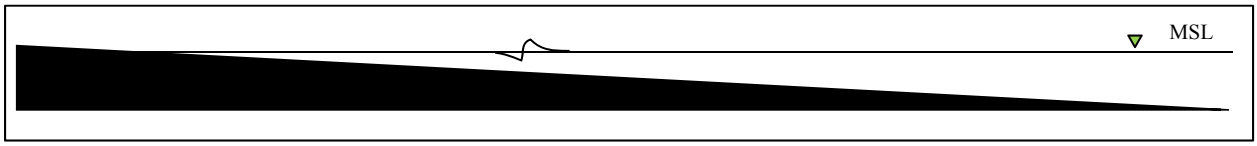

Figure 8-25: Domain sketch for N-wave runup.

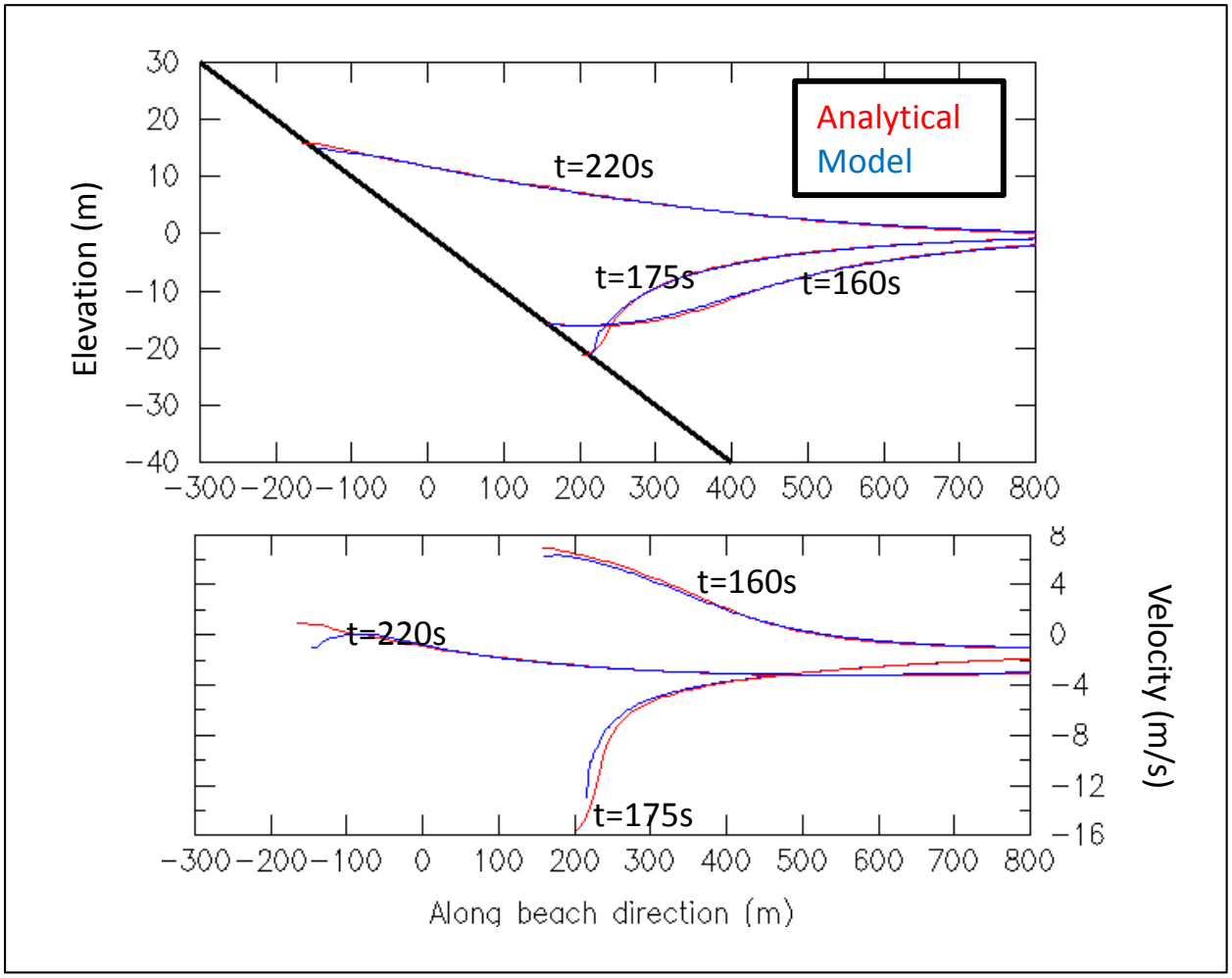

Figure 8-26: Comparison of elevation (top) and velocity (bottom) at 3 times. The error in the runup is 5%.

Comparison of the time history of shoreline position and velocity is shown in Figure 8-27. In general, larger errors were observed during the runup phase than in the rundown phase; in addition there appeared to be some minor instability during the runup phase as can be seen from the modeled shoreline velocity. Overall the model was able to adequately capture the shoreline evolution.

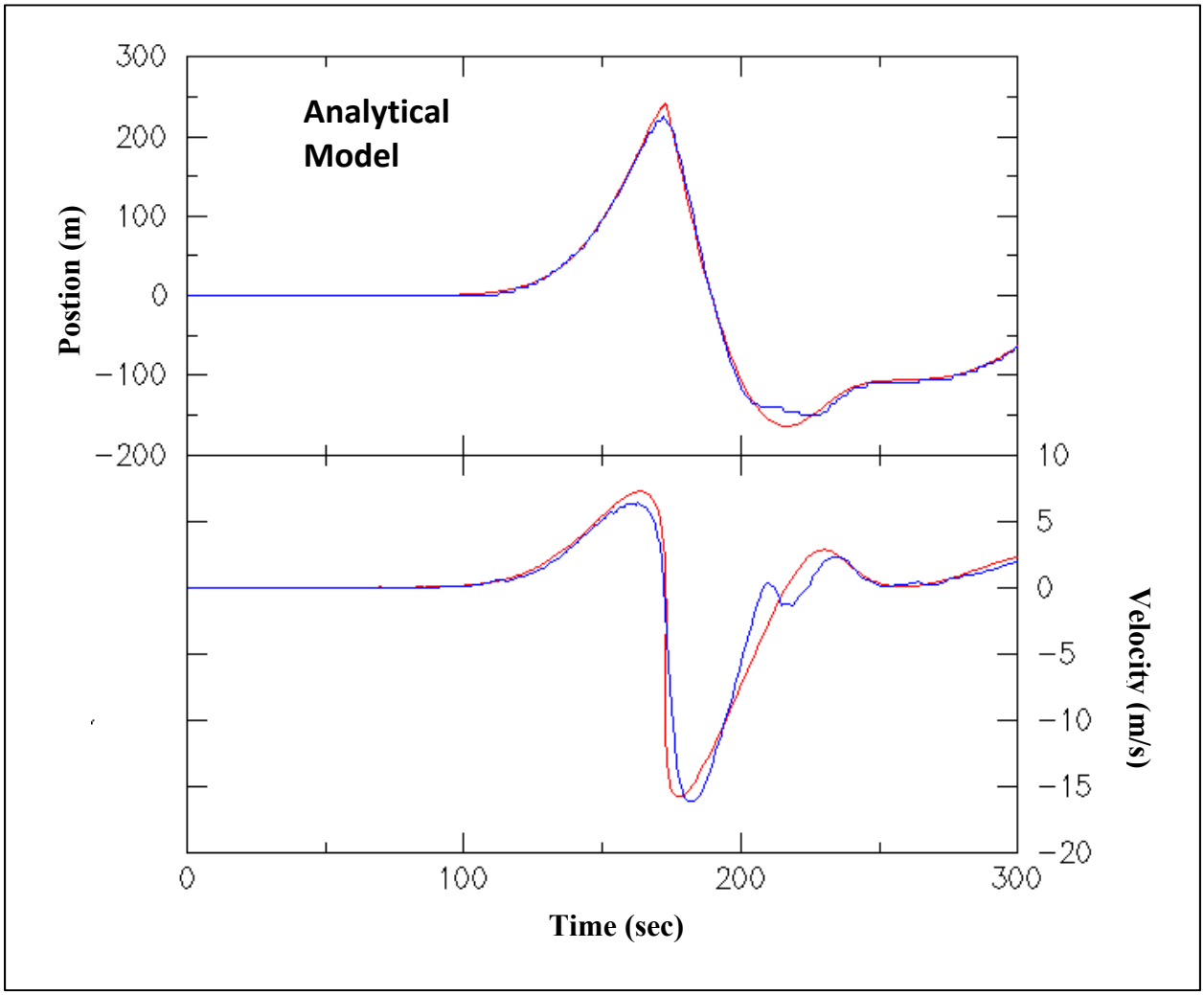

Figure 8-27: Comparison of time history of the shoreline position (top) and velocity (bottom).

8.3.9 1964 Alaska – field

The March 28, 1964 Prince William Sound (Alaska) earthquake produced a mega trans-oceanic tsunami that represented the largest tsunami that impacted US and Canadian west coast on record. There is a wealth of field records for this event from tide gauges and eyewitness reports. Therefore, we have been using this event as a representative of remote sources in our mitigation studies in Oregon.

We have recently conducted a detailed propagation and inundation study for this event for the Pacific Northwest coast (WA, OR and CA), and detailed model results are being reviewed as a journal publication (Zhang et al. 2011). Therefore we only present some highlights from this study below.

Using a large unstructured grid (with over 2.9 million nodes) to cover the Pacific from Prince William Sound to the west coast, we were able to resolve 12 major estuaries and rivers in Washington and Oregon (Figure 8-28). The resolution at the shoreline was 80 m in general, and 5-30 m in the 12 estuaries and rivers. The Manning $n_0 = 0.025$. The time step was set at 1 s .

A key question we strived to answer from this study was the role of tides in inundation. To this end, we have conducted two sets of simulation, one with static tides (with the vertical datum fixed at local MHW) and the other with dynamic tides. For the latter, we conducted a tidal simulation for 7.15 days before the event in order to reach a dynamic equilibrium.

Figure 8-29 shows the comparison of elevation time series at two tide gauges, one of which is located deep inside the Columbia River estuary, from the 2 simulations mentioned above. The main finding was that the linear superposition of tides on top of the static tide results led to an under-estimation of the wave amplitude as compared to the data due to significant nonlinear interaction between tides and tsunamis. The results with dynamic tides rectified this under-estimation (Figure 8-29).

The nonlinear interaction was even more pronounced in the maximum inundation extent as in the city of Cannon Beach, Oregon (Figure 8-30). With the static tides, the inundation extent was severely under-estimated, even though the starting water level was higher (MHW as opposed to MSL used in the dynamic tide simulations). The inundation line predicted by including dynamic tides significantly improved the model results (Figure 8-30b). Spectral analysis was conducted to verify that the nonlinear interaction occurred along the narrow Ecola Creek (not shown).

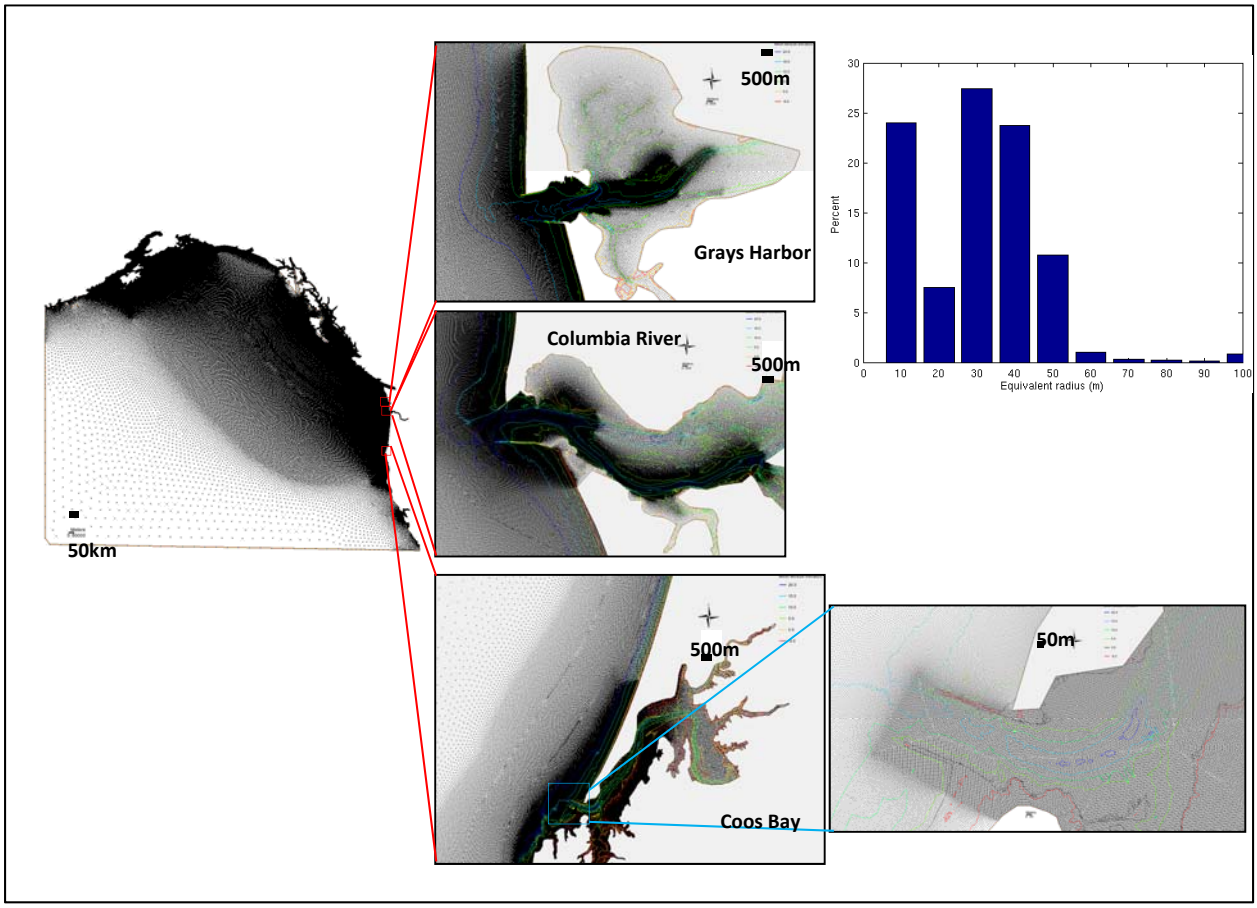

Figure 8-28: Grid used in the 1964 event, with multiple zooms. The insert histogram shows the distribution of equivalent radii of all elements; over 90% of the elements have a radius of 40 m or less.

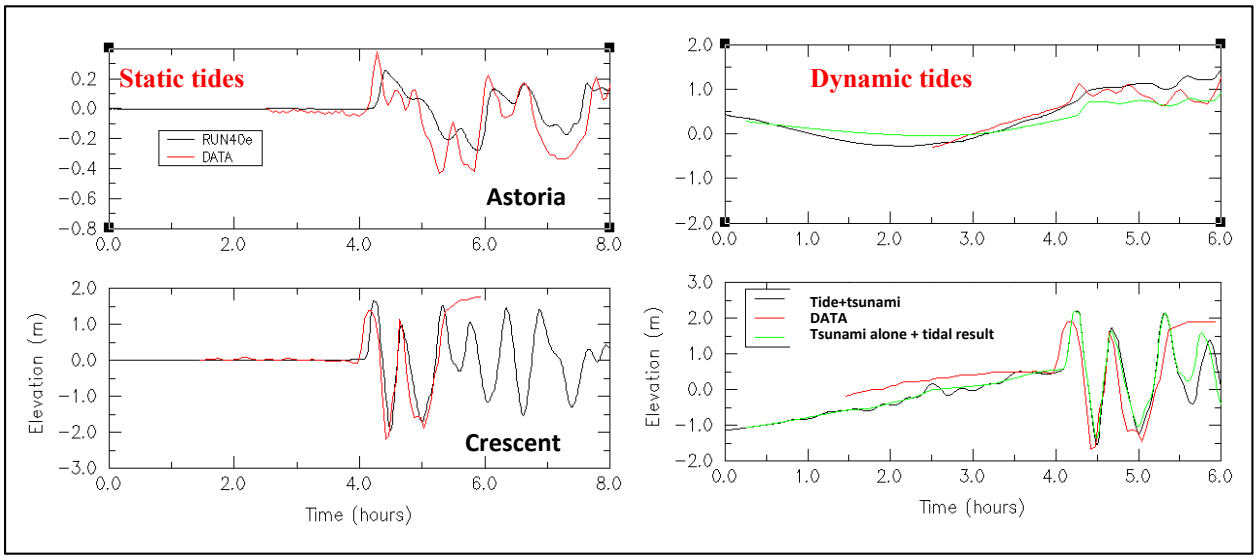

Figure 8-29: Comparison at two tide gauges; the model results are from (a) static tides; and (b) dynamic tide (black) or superposition of tides on top of static tide results (green).

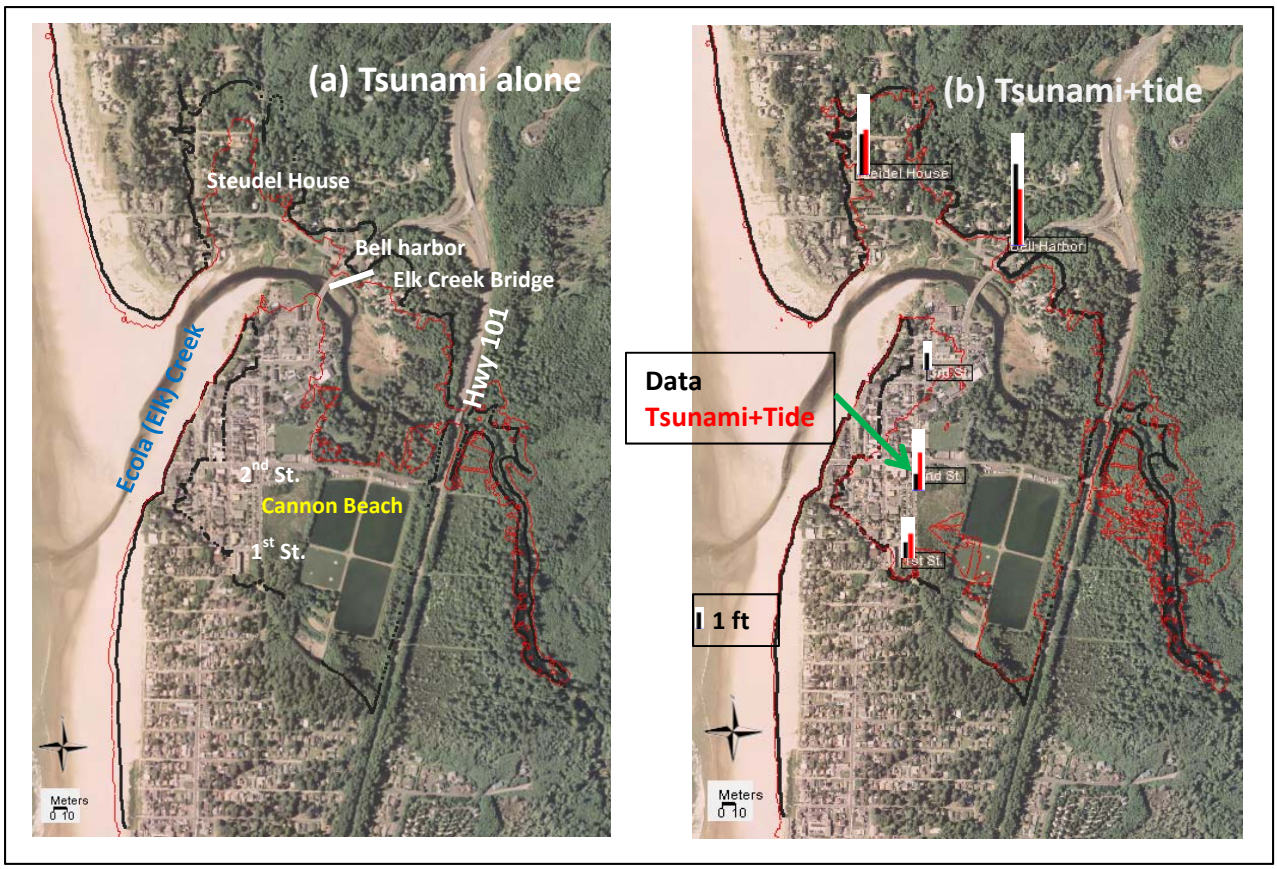

Figure 8-30: Comparison of inundation at Cannon Beach. The black dots are field estimates from Witter (2008) and the red dots are from the model, (a) with static tides, and (b) with dynamic tides.

The simulations were conducted at NASA's Pleiades cluster, and the 6-hour static tide simulation took 2.25 hours wall-clock time with 256 CPUs. The model efficiency has enabled us to effectively conduct simulations with even larger grids (~10 million nodes).

8.4 Lessons learned

During the benchmarking exercise, one of the most perplexing problems we have encountered was related to the incomplete information regarding those tests. We had to spend a considerable amount of time gleaning files from various sources. For the field tests (Okushiri, etc.) some critical pieces of information (such as the horizontal datums of the DEMs) are still missing. Perhaps the most serious problem with field tests is uncertainty about the geometry of the earthquake source. This issue causes serious errors in simulations for areas proximal to the source (e.g., poor match of simulated runup on the east coast of Okushiri Island).

The set of benchmark problems proposed in OAR-PMEL-135 was found to be mostly appropriate except for a few extreme cases (e.g., the larger wave breaking case C in the composite beach case). The combination of analytical, lab, and field tests adequately tests the performance of models.

Going forward we suggest inclusion of more recent field cases. These events have the advantage of better documentation and of the availability of new types of observation (satellite

imagery, amateur and professional videos, and DART buoy records, etc.), and therefore serve as better validation tools for models.

8.5 References

Azvedo A, Oliveira A, Fortunato AB, Bertin X. 2009. Applicaiton of an Eulerian-Lagrangian oil spill modeling system to the Prestige accident: trajectory analysis. *J. Coastal. Res*., 56, 777-781.

Burla M, Baptista AM, Zhang Y, Frolov S. 2010. Seasonal and inter-annual variability of the Columbia River plume: a perspective enabled by multi-year simulation databases. *Journal of Geophysical Research*, 115, C00B16.

Goldfinger C, Nelson CH, Johnson JE, Morey AE, Gutiérrez-Pastor J, Karabanov E, Eriksson AT, Gràcia E, Dunhill G, Patton J, Enkin R, Dallimore A, Vallier T, and the Shipboard Scientific Parties. 2010. Turbidite Event History: Methods and Implications for Holocene Paleoseismicity of the Cascadia Subduction Zone: U.S. Geological Survey Professional Paper 1661-F (in press).

Gonzalez FI., et al. 2009. Probabilistic tsunami hazard assessment at Seaside, Oregon, for near- and far-field seismic sources. *J. Geophys. Res.*, 114, C11023.

Johnson J, Satake K, Holdahl S, Sauber J. 1996. The 1964 Prince William Sound earthquake: joint inversion of tsunami and geodetic data. *J. Geophys. Res.*, 101(B1), 523–532.

Kato K, Tsuji Y. 1994. Estimation of fault parameters of the 1993 Hokkaido-Nansei-Oki earthquake and tsunami characteristics. *Bull. Earthq. Res. Inst.*, Univ. of Tokyo, vol. 69, 39-66.

Pinto L, Fortunato AB, Zhang Y, Oliveira A, Sancho FE.P. Development and validation of a three-dimensional morphodynamic modelling system, *Ocean Modelling* (submitted).

Priest GR, Goldfinger C, Wang K, Witter RC, Zhang YJ, Baptista AM. 2009. Confidence levels for tsunami-inundation limits in northern Oregon inferred from a 10,000-year history of great earthquakes at the Cascadia subduction zone: Natural Hazards, DOI 10.1007/s11069-009-9453-5.

Rodrigues M, Oliveira A, Queiroga H, Fortunato AB, Zhang Y. 2009a. Three-Dimensional Modeling of the Lower Trophic Levels in the Ria de Aveiro (Portugal), *Ecological Modelling*, 220(9-10), 1274-1290.

Rodrigues M, Oliveira A, Costa M, Fortunato AB, Zhang Y. 2009b. Sensitivity analysis of an ecological model applied to the Ria de Aveiro. *Journal of Coastal Research*, SI56, 448-452.

Roland A, Zhang Y, Wang HV, Maderich V, Brovchenko I. 2011. A fully coupled wave-current model on unstructured grids, *Compt. & Geosciences* (submitted).

Song Y, Haidvogel DB. 1994. A semi-implicit ocean circulation model using a generalized topography-following coordinate system. *J. Comp. Phys.*, 115(1), 228-244.

TPSWG (Tsunami Pilot Study Working Group). 2006. Seaside, Oregon tsunami pilot study—modernization of FEMA flood hazard maps. National Oceanic and Atmospheric Administration OAR Special Report, NOAA/OAR/PMEL, Seattle, WA.

Willmott CJ; Ackleson SG; Davis RE; Feddema JJ; Klink KM; Legates DR; O'Donnell J; Rowe CM. 1985. Statistics for the Evaluation and Comparison of Models, *J. Geophys. Res.*,Vol. 90, No. C5, pp. 8995–9005

Witter RC. 2008. Prehistoric Cascadia tsunami inundation and runup at Cannon Beach, Clatsop County, Oregon, Oregon Department of Geology and Mineral Industries, Open-File Report O-08-12, 36 p., appendices.

Witter RC, Zhang JY, Wang K, Priest GR, Goldfinger C, Stimely L, Ferro P, (in review) Simulating tsunami inundation at bandon, oregon using hypothetical Cascadia and Alaska earthquake scenarios: Oregon Department of Geology and Mineral Industries Special Paper.

Zhang Y, Baptista AM. 2008a. SELFE: A semi-implicit Eulerian-Lagrangian finite-element model for cross-scale ocean circulation. *Ocean Modelling*, 21(3-4), 71-96.

Zhang Y, Baptista AM. 2008b. An Efficient and Robust Tsunami Model on Unstructured Grids. Part I: Inundation Benchmarks. *Pure and Applied Geophysics*, 165, 2229–2248.

Zhang Y, Witter RW, Priest GP. 2011. Nonlinear Tsunami-Tide Interaction in 1964 Prince William Sound Tsunami, *Ocean Modelling* (submitted).

9 THETIS

Stéphane Abadie

Laboratoire SIAME, Université de Pau et des Pays de l'Adour, Anglet, France, and Fulbright Scholar at Department of Ocean Engineering, University of Rhode Island, Narragansett, USA

9.1 Introduction

THETIS is a multi-fluid Navier-Stokes (NS) solver developed by the TREFLE CNRS laboratory at the University of Bordeaux I. It is a multi purpose CFD code, freely available to researchers (http://thetis.enscbp.fr) and fully parallelized. THETIS solves the incompressible NS equations for water, air, and the slide. Basically, at any time, the computational domain is considered as being filled by one "equivalent" fluid, whose physical properties (namely density and viscosity) vary with space. Subgrid turbulent dissipation is modeled based on a Large Eddy Simulation approach, using a mixed scale subgrid model (Lubin et al., 2006). The governing equations (i.e., conservation of mass and momentum) are discretized on a fixed mesh, which may be Cartesian, cylindrical or curvilinear, using the finite volume method. These governing equations are exact, except for interfacial meshes, where momentum fluxes are only approximated, due to the presence of several fluids. NS equations are solved using a two-step projection method. Fluid-fluid interfaces are tracked using the VOF method. For most flows, the PLIC algorithm (e.g., Abadie et al., 1998) enables accurate tracking while keeping the interface discontinuous. However, for very violent flows with fast droplet ejection, the PLIC method may cause divergence of the projection algorithm. In such cases, the interface is smoothed either by allowing a slight diffusion process, after each PLIC iteration, or using a TVD scheme solving Eulerian advection equations for the interfaces.

THETIS has been extensively validated for many theoretical and experimental flow cases. Hence, each new version of THETIS has to successfully solve more than 50 validation cases within a certain expected accuracy, before being released.

Abadie et al. (2006, 2008, 2010) simulated classical landslide tsunami benchmarks involving rigid bodies using THETIS. In these papers, rigid slides are simulated as a Newtonian fluid, for which deformation is prevented by specifying an infinite viscosity. With the use of this so-called penalty method, the slide displacement is computed implicitly and thus no longer prescribed as in most other similar studies. Abadie et al. (2010) performed convergence studies and showed that result accuracy on the free surface is satisfactory as long as enough grid cells are used to ensure that the slide motion is correctly reproduced. Figure 9-1 shows an example of THETIS' results for the 2-D experiment of Heinrich (1992). In the latter experiment, waves were generated by a triangular rigid wedge sliding down a 45° slope. Figure 9-1a and Figure 9-1b show two snapshots of model results with interface contours and flow streamlines. The flow is solved within the wedge as well, where the very large viscosity, as expected, yields rectilinear streamlines (confirming that the rigid slide moves as a whole). Figure 9-1c shows the slide law

of motion simulated, as compared to experimental data, and Figure 9-1d shows the subsequent free surface deformation.

This penalty method is an improvement that may help NS models to become more suitable for more realistic applications or case studies, in which, of course, slide motion is always unknown. However, real slides are far more complex than solid bodies. Our next step is thus to validate the model for waves generated by deformable slides. For that purpose, we have implemented the generalized non Newtonian fluid model (i.e., a Herschel–Bulkley fluid) in THETIS and are currently performing tests using this constitutive law.

9.2 BP8: Three-dimensional landslide

Navier-Stokes multi-fluid models such as THETIS are adapted to wave generation by violent subaerial landslides, as they can deal with multiple interface reconnections (i.e., overturning/breaking waves). They may also be used for shallow water submarine landslide cases, provided that the ratio of slide thickness to depth is large enough, as the whole domain has to be meshed. For larger depth however, models relating pressure to free surface elevation will be less time consuming, for a comparable accuracy and thus more adapted.

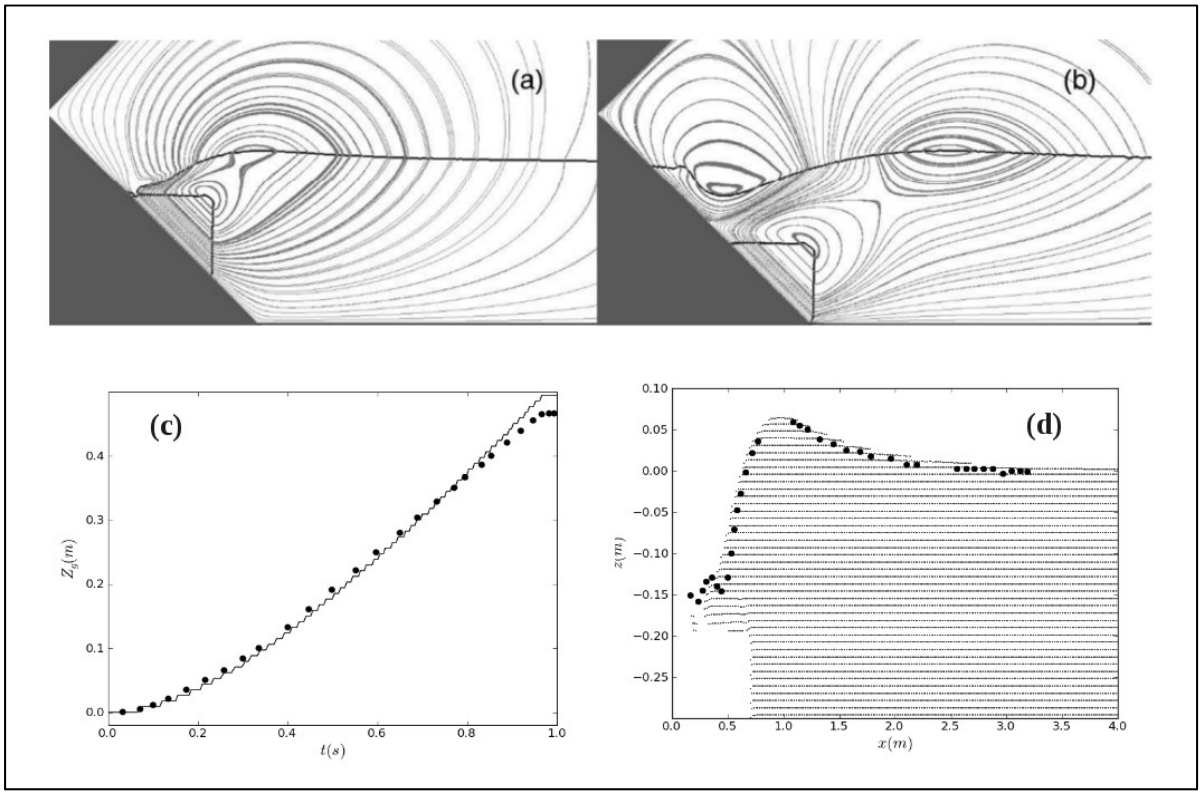

Figure 9-1: Simulation of Heinrich's experiment (Heinrich, 1992) using THETIS. Top panel: density contours and flow streamlines at time t =: (a) 0.5 s (b) 1 s, (c): Time evolution of vertical slide displacement. (•): Heinrich's (1992) experiments, (—): THETIS, (d): Free surface deformation at t = 0.5 s, (•): Heinrich's (1992) experiments, dot filled contour: THETIS.

In the NTHMP work along the East Coast, THETIS is used only to simulate the tsunami wave source in the potential case of Cumbre Vieja Volcano flank collapse (La Palma, Canary Islands), featuring a large subaerial landslide. For that reason, THETIS has only been tested

against BP8, which features a rigid body close to the free surface. Note also, that for the case of La Palma, runup is not studied with THETIS but instead, through a model coupling approach employing THETIS to compute the tsunami generation and later the long-wave propagation and coastal impact model FUNWAVE to study propagation and runup. For this reason, the THETIS model's results on runup in BP8 are only indicative.

In BP8, instead of prescribing slide motion (as in Liu et al., 2005, for instance), we solved for the full coupling between slide and water and hence calculated slide motion as part of the solution, where the rigid wedge is modeled as a Newtonian fluid of large viscosity ($10^5\ Pa.s$). Here, we present in detail the first benchmark case in which the slide initial submergence is $\Delta = -0.1\ m$ and slide density ratio is 2.14; x' is in the slope direction, z' is perpendicular to the slope plane (gravity being in this case inclined by 26.56° with respect to z'), $y = y'$ is in the longshore direction. Due to symmetry with respect to the middle vertical plane, the computational domain only represents half the experimental flume (including runup gauge 1 and wave gauge 1). Two numerical grids were tested to assess discretization effects on slide motion and, subsequently, on free surface deformation. Both grids were irregularly distributed over x' and z' to account for the need for finer resolution close to the generation zone. The first grid (mesh 1, with 62 x 76 x 24 cells) is comparable to the mesh used in Liu et al. (2005). The finest grid cell size is $\Delta x' = 0.039\ m$, $\Delta z' = 0.0196\ m$, $\Delta y'$ being constant and equal to 0.077 m. For the second mesh used (mesh 2, with 170 x 100 x 120 cells), the finest grid cell size is $\Delta x' = \Delta z' = 0.015\ m$, $\Delta y'$ was constant and also equal to $0.015\ m$. The nondimensional finest grid sizes are respectively $\Delta x'/L = \Delta z'/L = 3.8\%$ for mesh 1 and 1.4% for mesh 2 (with $L = 1.017\ m$). High resolution 3-D computations are very computationally intensive and therefore simulations were run using the parallel version of our model.

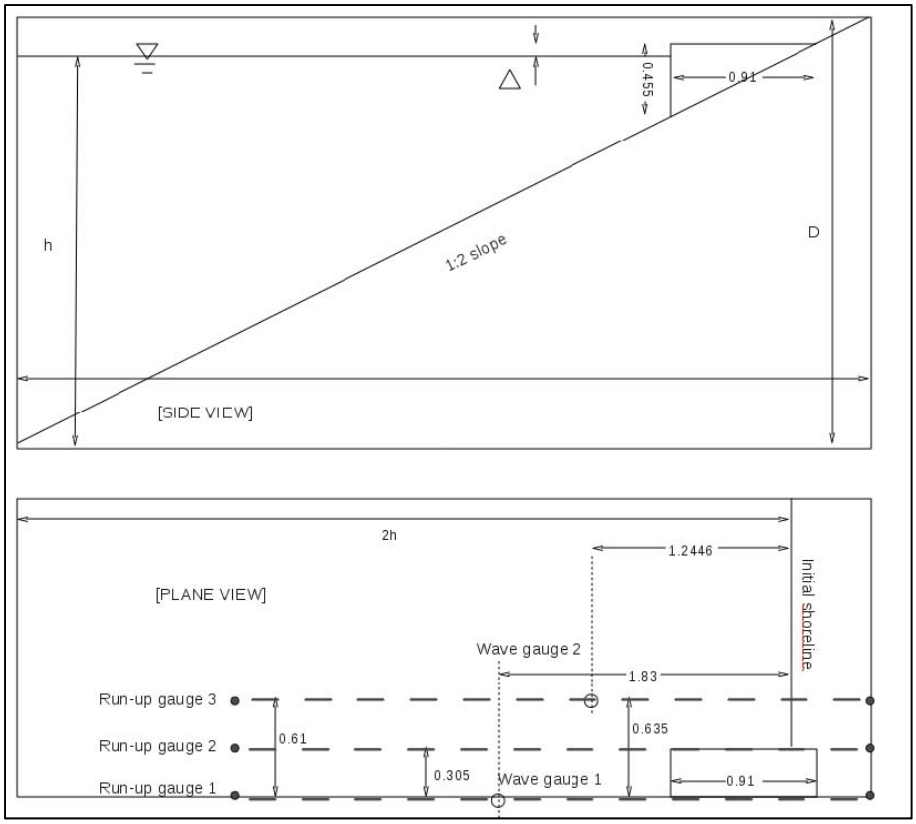

Figure 9-2: Sketch of BP8 (after Liu et al., 2005)

Figure 9-3 shows snapshots of water/air and slide/water interfaces computed at four different time steps for the finest mesh, using the NS-PLIC model. In the last image at t = 3.5 s, the slide has stopped on the horizontal bottom of the experimental flume, which is represented in simulations but not visible on Figure 9-3. In this snapshot sequence, we observe the generation of a wave train, and its subsequent propagation and reflection from the vertical sidewalls of the flume. Maximum runup, which occurs at the plane of symmetry on the flume axis, is seen to also propagate toward and reflect off the sidewalls.

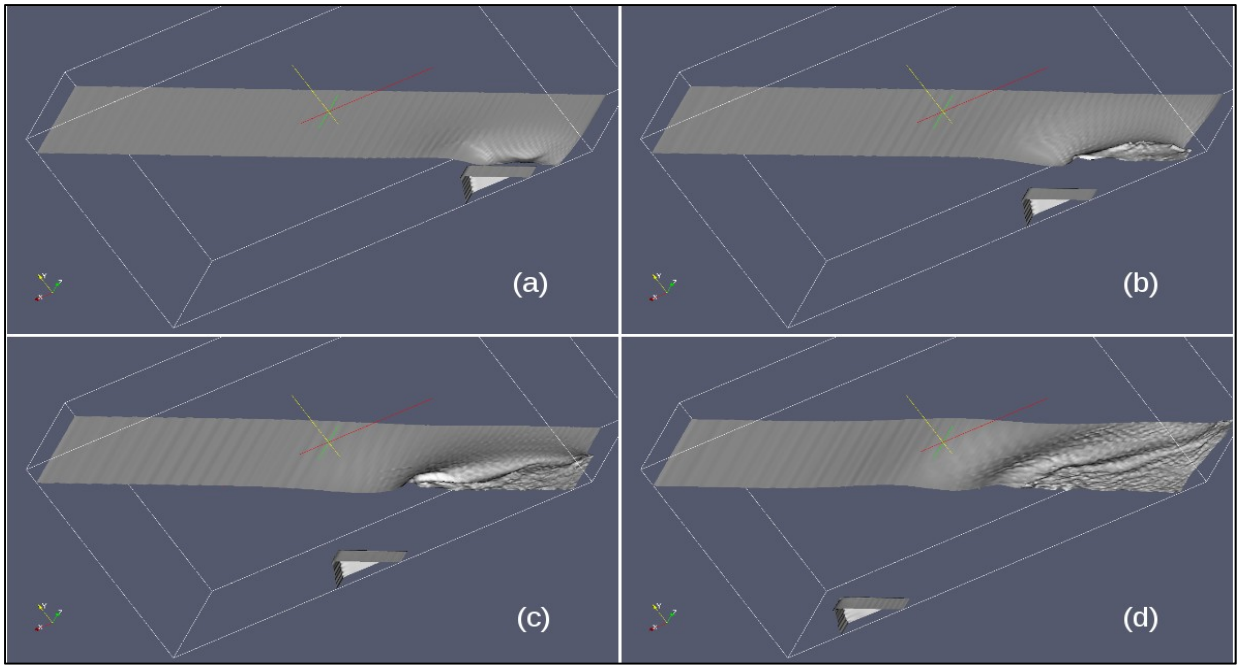

Figure 9-3: Snapshots of slide/water and water/air interfaces at different times for grid 2 with 170x100x120 cells, using the setup sketched in Figure 9-2. Slide initial submergence is D = -0.1 m, slide density is 2.14. (a) t = 0.7 s, (b) t = 1.4 s, (c) t = 2.1 s, (d) t = 3.5 s.

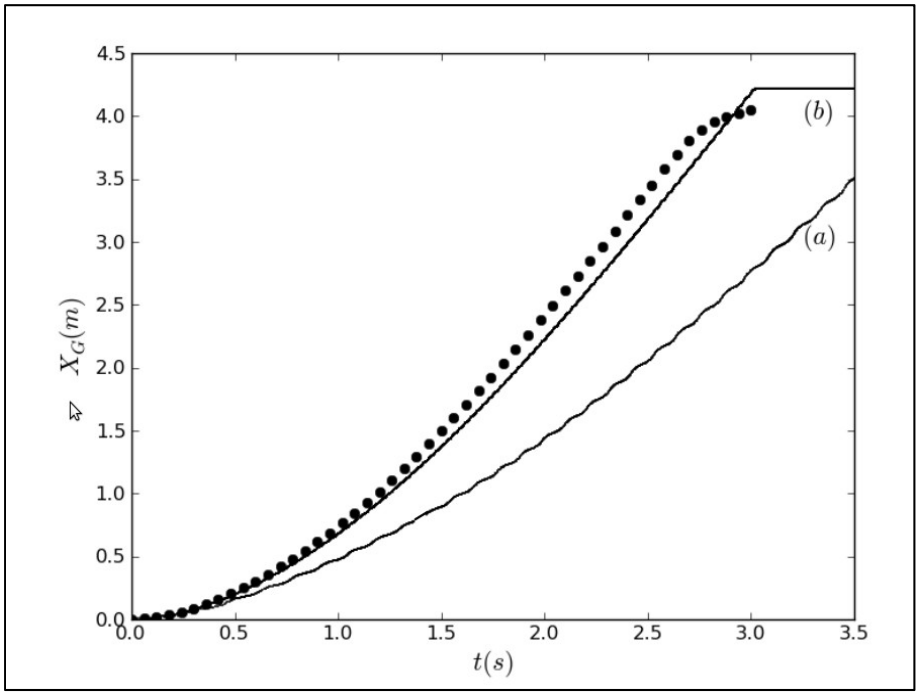

Figure 9-4: Time evolution of slide center of mass, using the setup sketched in Figure 9-2. Solid lines: numerical results with (a) 62x76x24 cells and (b) 170x100x120 cells ; (•): experimental data. Initial slide submergence is Δ = -0.1 m, slide density is 2.14.

Figure 9-4 shows the simulated slide center of mass motion as a function of time, as compared to experimental data. The measured slide motion is well reproduced in the finer mesh grid, with a *RMS* deviation of 0.16 m. In the coarser grid, the slide is much slower than in experiments (larger *RMS* deviation of 0.80 m). A computation performed using an intermediate grid size (not presented here) yielded a slide motion curve in between the two presented curves, indicating a consistent behavior of the model. Other computations for different initial submergence values also matched experimental data well, provided that a fine enough grid (i.e., with $\Delta x/L \sim 1\%$) is used. A closer inspection of our results indicates that resolving the coupling between slide motion and water flow in the numerical model is achievable with good accuracy, but requires an overall grid about 20 times larger than when slide motion is a priori specified, as in Liu et al. (2005).

Figure 9-5 compares the experimental data to the surface elevations simulated at wave gauges 1 and 2, both in the generation area (see Figure 9-2). At gauge 1, the first elevation wave and trough are both well modeled in the finer grid 2 (respectively 17% and 5% of relative errors), whereas the second wave is much higher (162%) than measured. This was also observed by Wu (2004) for this gauge location and a slide initial submergence $D = -0.05$. Our last attempt using a finer grid step (mesh: 260 x 200 x 120) helps, reducing the error from 162% to 114% for this second wave.

Wave phase and, hence, celerity, are correctly predicted in the finer grid 2, whereas the second wave is too slow in the coarser grid 1. Note that wave heights are also under-predicted in the latter grid, which is consistent with a slower slide. At gauge 2, the lateral spreading of the wave is also well simulated using grid 2; the simulated wave elevations are close to the experimental results (17%, 10%, 30% respectively for wave crest 1, trough 1, wave crest 2), even though waves seem to be a bit slower. In grid 1 again, the slower slide generates both smaller and slower waves as compared to experimental data.

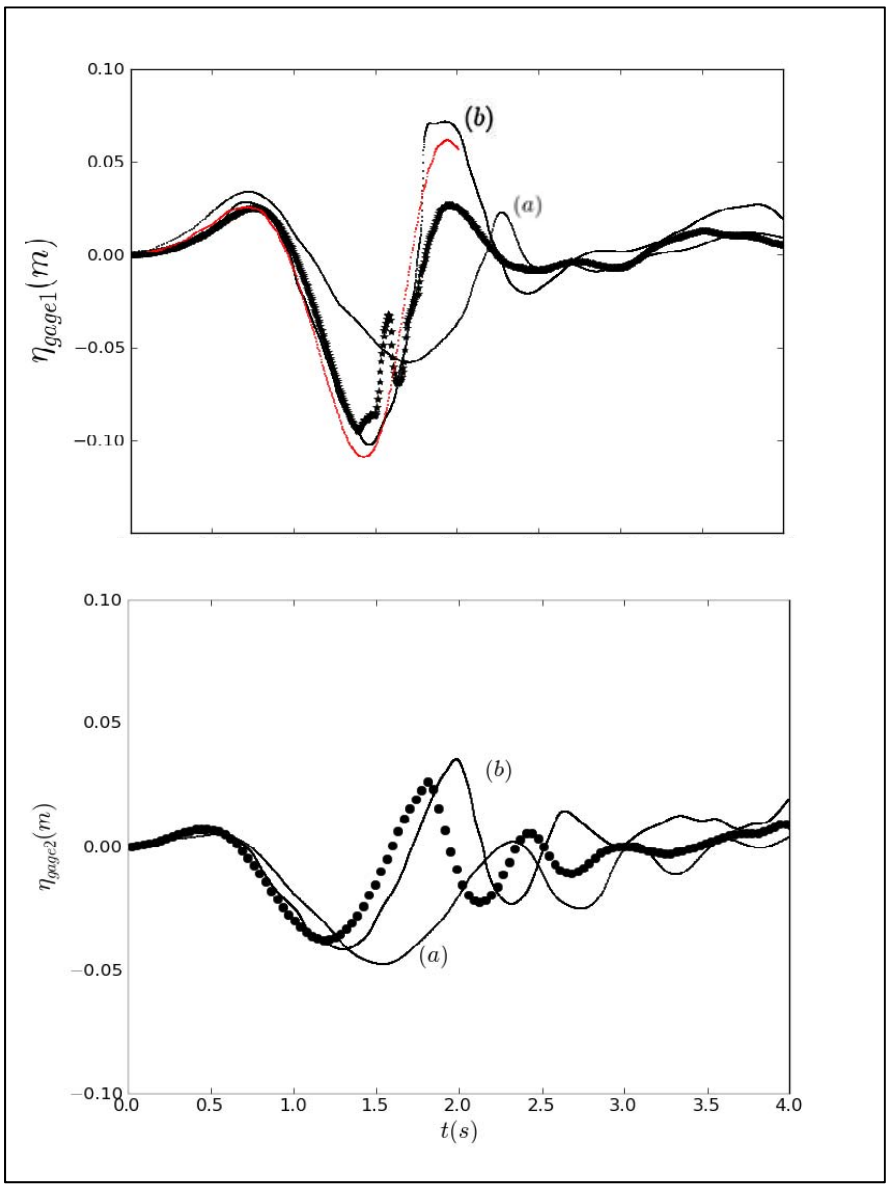

Figure 9-5: Comparison between numerical results (solid lines) and experimental data (•) for the time histories of free surface elevations at wave gauge 1 (top figure) and wave gauge 2 (bottom figure), using the setup sketched in Figure 9-2. Initial slide submergence is Δ = -0.1 m, slide density is 2.14, (a) 62x76x24 cells, (b) 170x100x120 cells, and (red curve) 260x200x120 cells.

Figure 9-6, similarly, compares runup simulated at runup gauges 2 and 3 (see Figure 9-2) to experimental data. At gauge 2, in the finer grid, numerical results closely match experiments, except during the first runup phase where the model overestimates the recorded runup value and generates a quicker runup motion. In the coarser grid, run-down and runup values are both overestimated. A similar behavior is observed at gauge 3. Wu (2004) also reported such discrepancies between runup data and numerical result with an initial submergence $\Delta = -0.05$. Note that we used here a free slip boundary condition on the bottom, which may explain the overestimation of the runup results. The model accuracy may be improved by using a no-slip condition.

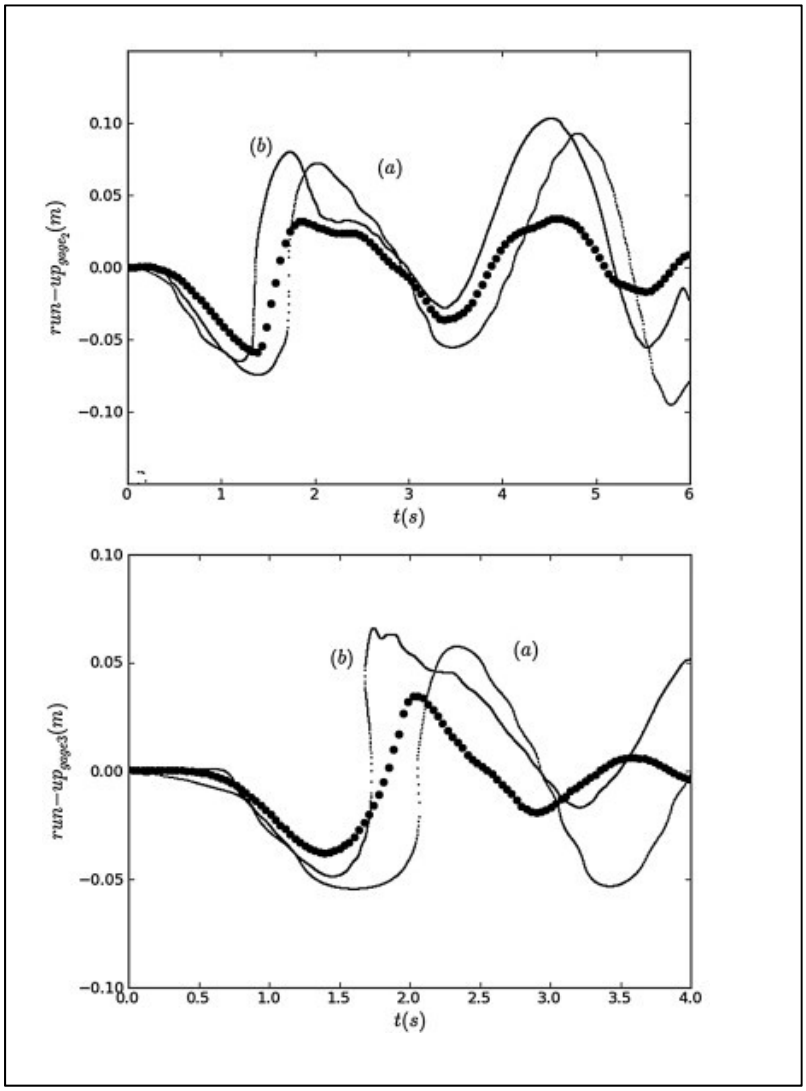

Figure 9-6: Comparison between numerical results (solid lines) and experimental data (•) for the time histories of runup at gauge 2 (top) and gauge 3 (bottom)), using the setup sketched in Figure 9-2. Initial submergence is Δ = -0.1 m, slide density is 2.14. (a) 62x76x24 cells, (b) 170x100x120 cells.

Finally, we also simulated the second benchmark case featuring the same rigid body, but with a lower submergence $\Delta = -0.025\, m$ and a higher slide density ratio of 2.79. In the finer mesh, the only results shown here, slide motion is accurately predicted (Figure 9-7). Also a comparison of free surface elevation at wave gauge 2, presented in Figure 9-8, shows the accuracy that may be expected by using THETIS in this kind of problem.

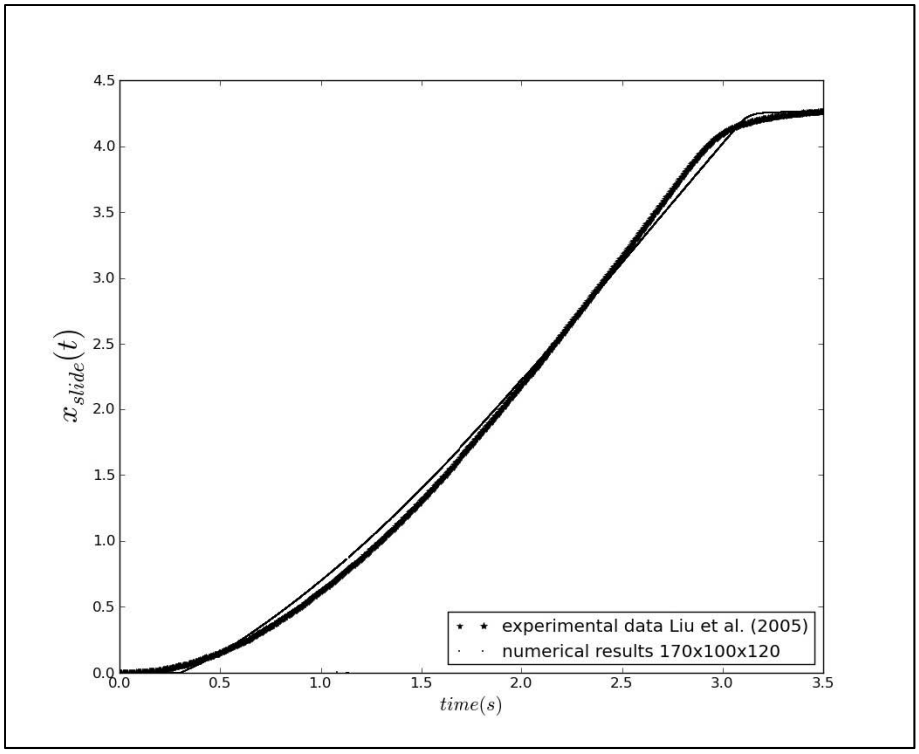

Figure 9-7: Time evolution of slide center of mass. Initial slide submergence is Δ = -0.025 m, slide density is 2.79. Solid line: numerical results with 170 x 100 x 120 cells; (•): experimental data.

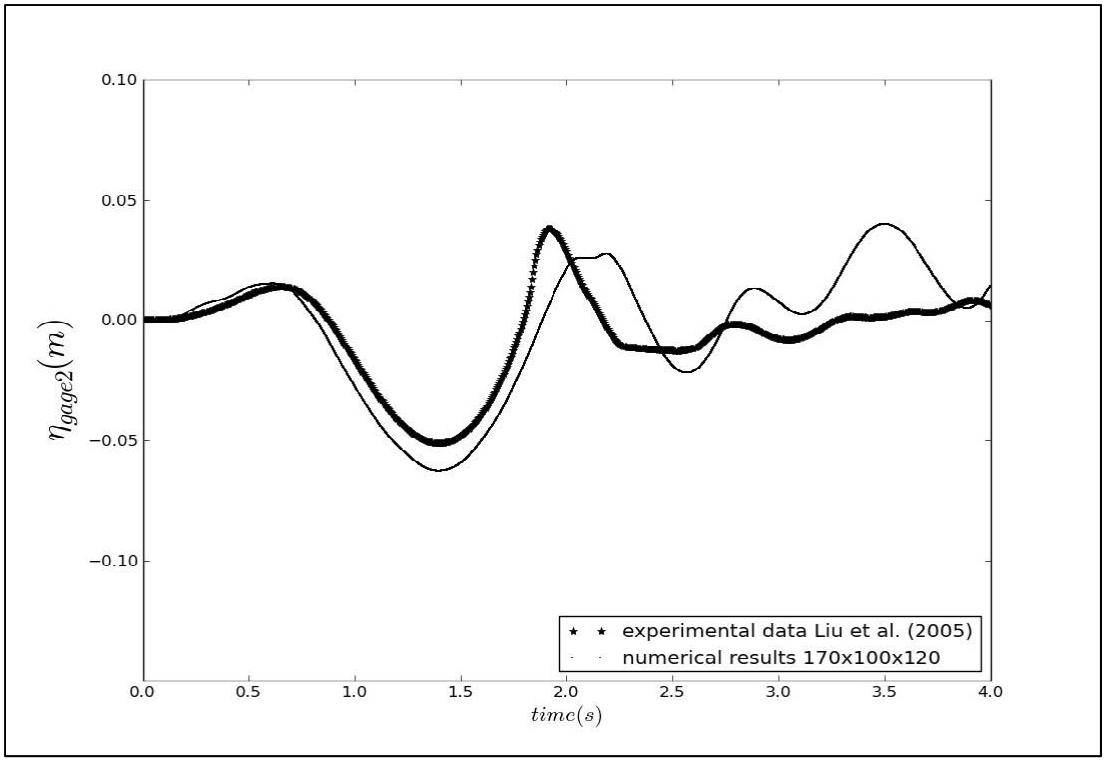

Figure 9-8: Comparison between numerical results (solid lines) and experimental data (•) for the time histories of free surface elevations at wave gauge 2 (Figure 9-2). Initial slide submergence is Δ = -0.025 m, slide density is 2.79. 170 x 100 x 120 cells.

9.3 References

Abadie S, Caltagirone JP, Watremez P. 1998. Splash-up generation in a plunging breaker . *Comptes Rendus de l'Académie des Sciences -Series IIB -Mechanics-Physics-Astronomy*, Volume 326, Issue 9, Pages 553-559

Abadie S, Grilli S, Glockner S. 2006. A coupled numerical model for tsunami generated by subaerial and submarine mass failures, in *Proc. 30th Intl. Conf. Coastal Engng.*, San Diego, California, USA. 1420-1431.

Abadie, S, Morichon, D, Grilli, S, Glockner, S. 2008. VOF/Navier-Stokes numerical modeling of surface waves generated by subaerial landslides, *La Houille Blanche*, 1, 21-26.

Abadie S, Morichon D, Grilli S, Glockner S. 2010 A three fluid model to simulate waves generated by subaerial landslides. *Coastal Engineering*, 57, 9, 779-794.

Heinrich P. 1992. Nonlinear water waves generated by submarine and aerial landslides. *J. Wtrwy, Port, Coast, and Oc. Engrg.*, ASCE, 118(3), 249-266.

Liu PL-F, Wu TR, Raichlen F, Synolakis CE, Borrero JC. 2005. Runup and rundown generated by three-dimensional sliding masses. *J. Fluid Mech.*, 536, 107-144.

Lubin P, Vincent S, Abadie S, Caltagirone JP. 2006. Three-dimensional Large Eddy Simulation of air entrainment under plunging breaking waves, *Coastal Engineering*, Volume 53, issue 8, .631-655.

Wu TR. 2004. A Numerical Study of Three-Dimensional Breaking Waves and Turbulence Effects. PhD Study. Cornell University.

10 TSUNAMI3D

Juan J. Horrillo, Amanda L. Wood, Gyeong-Bo Kim, Ashwin Parambath, Zygmunt Kowalik

Maritime Systems Engineering, Texas A&M University at Galveston, Texas; US
Ocean Engineering, Texas A&M University at College Station, Texas, US
Institute of Marine Science, University of Alaska Fairbanks, Alaska, US

10.1 Introduction

In accordance with National Tsunami Hazard Mitigation Program (NTHMP) guidance, tsunami numerical models need to be tested against the NOAA PMEL 135 validation benchmarks before receiving approval to be used as calculation tools for inundation mapping and mitigation. In this section, two experimental benchmarking problems have been selected to validate a proposed 3-D numerical model for tsunami generation by sub-aerial and submarine landslides. The 3-D model, dubbed TSUNAMI3D (for Tsunami Solution Using Navier-Stokes Algorithm with Multiple Interfaces), uses the Navier-Stokes approach and the Volume of Fluid Method (VOF) to track the fluid free surface. The model has been developed by the University of Alaska Fairbanks (UAF) and by Texas A&M University at Galveston (TAMUG).

TSUNAMI3D solves transient fluid flow with free surface boundaries, based on the concept of the fractional VOF. The code uses an Eulerian mesh of rectangular cells having variable sizes. The fluid equations solved are the finite difference approximation of the Navier-Stokes and the continuity equations. The basic mode of operation is for single fluid calculation having multiple free surfaces. However, TSUNAMI3D can also be used for calculations involving two fluids separated by either a sharp or indefinite (diffusive) interface, for instance, water and mud. In either case, the fluids may be treated as incompressible. Internal obstacles or topography are defined by blocking out fully or partly any desired combination of cells in the mesh.

The TSUNAMI3D code was exclusively developed for tsunami calculations. The first version of the code was developed under the direction of Professor Zygmunt Kowalik, UAF. Other important contributions to the code are due to William Knight, West Coast & Alaska Tsunami Warning Center (WC/ATWC) and Ed Kornkven, Arctic Region Supercomputing Center (ARSC). The code is based on development done at the Los Alamos National Laboratory (LANL) during the 70's, following the work done by C. W. Hirt and a group of researchers, including, among others, A. A. Amsden, T. D. Butler, L. D. Cloutman, B. J. Daly, R. S. Hotchkiss, C. Mader, R. C. Mjolsness, B. D. Nichols, H. M. Ruppel, M. D. Torrey and D. B. Kothe.

The current TSUNAMI3D code has undergone dramatic changes from its original conception in Horrillo's thesis (2006). In particular, the VOF algorithm for tracking the movement of a free surface interface between two fluids or between a fluid and a void has been simplified especially for the 3-D mode of operation. The simplification accounts for the horizontal distortion of the computational cells with respect to the vertical scale that is proper in

the construction of efficient 3-D grids for tsunami calculations. In addition, the pressure term has been split into two components, hydrostatic and non-hydrostatic. The splitting of the pressure term allows users of the model to obtain a hydrostatic solution by merely switching off the non-hydrostatic pressure term. Therefore, TSUNAMI3D can be used to separate out non-hydrostatic effects from the full solution while keeping the three dimensional structure. TSUNAMI3D is suitable for complex tsunami generation because it is capable of modeling: (1) moving or deformable objects, (2) subaerial/subsea landslide sources, (3) soil rheology, and (4) complex vertical or lateral bottom deformation.

TSUNAMI3D is in constant development and it requires FORTRAN and MATLAB (post-processing) programming skills to put it to work. Usually, a 3-D simulation requires a large amount of computer memory and CPU-wall-time to obtain the solution. A few subroutines, the most computational demanding, are parallelized using OPENMP directives. In the 2-D mode of operation, the code uses the PETSC-MPI library to solve the pressure field.

10.2 TSUNAMI3D Governing Equations

The governing equations to describe the flow of two incompressible Newtonian fluids (e.g., water and mud) in a domain $\Omega(t)$, are given by the equation of conservation of mass

$$\frac{\partial u}{\partial x}+\frac{\partial v}{\partial y}+\frac{\partial w}{\partial z}=0 \tag{1}$$

and the conservative equation of momentum given by:

A-water:

$$\frac{\partial u}{\partial t}+\frac{\partial uu}{\partial x}+\frac{\partial uv}{\partial y}+\frac{\partial uw}{\partial z}=$$
$$-g\frac{\partial \eta_1}{\partial x}-\frac{1}{\rho_1}\frac{\partial q}{\partial x}+\frac{\partial}{\partial x}\left[\frac{\mu_1}{\rho_1}\left(2\frac{\partial u}{\partial x}\right)\right]$$
$$+\frac{\partial}{\partial y}\left[\frac{\mu_1}{\rho_1}\left(\frac{\partial u}{\partial y}+\frac{\partial v}{\partial x}\right)\right]+\frac{\partial}{\partial z}\left[\frac{\mu_1}{\rho_1}\left(\frac{\partial u}{\partial z}+\frac{\partial w}{\partial x}\right)\right] \tag{2}$$

$$\frac{\partial v}{\partial t}+\frac{\partial uv}{\partial x}+\frac{\partial vv}{\partial y}+\frac{\partial vw}{\partial z}=$$
$$-g\frac{\partial \eta_1}{\partial y}-\frac{1}{\rho_1}\frac{\partial q}{\partial y}+\frac{\partial}{\partial x}\left[\frac{\mu_1}{\rho_1}\left(\frac{\partial v}{\partial x}+\frac{\partial u}{\partial y}\right)\right]$$
$$+\frac{\partial}{\partial y}\left[\frac{\mu_1}{\rho_1}\left(2\frac{\partial v}{\partial y}\right)\right]+\frac{\partial}{\partial z}\left[\frac{\mu_1}{\rho_1}\left(\frac{\partial v}{\partial z}+\frac{\partial w}{\partial y}\right)\right] \tag{3}$$

$$\frac{\partial w}{\partial t}+\frac{\partial uw}{\partial x}+\frac{\partial vw}{\partial y}+\frac{\partial ww}{\partial z}=$$
$$-\frac{1}{\rho_1}\frac{\partial q}{\partial z}+\frac{\partial}{\partial x}\left[\frac{\mu_1}{\rho_1}\left(\frac{\partial w}{\partial x}+\frac{\partial u}{\partial z}\right)\right]$$

$$+\frac{\partial}{\partial y}\left[\frac{\mu_1}{\rho_1}\left(\frac{\partial w}{\partial y}+\frac{\partial v}{\partial z}\right)\right]+\frac{\partial}{\partial z}\left[\frac{\mu_1}{\rho_1}\left(2\frac{\partial w}{\partial z}\right)\right] \tag{4}$$

where, $u(x,y,z.t)$, $v(x,y,z,t)$ and $w(x,y,z,t)$ are the velocity components along the coordinate axes of the fluid at any point $x=x\hat{i}+y\hat{j}+z\hat{k}$ at time t, $\eta_1(x,y,t)$ is the water-surface elevation measured from a vertical datum, ρ_1 is the density of the fluid, and q is the non-hydrostatic pressure. The kinematic viscosity μ_1/ρ_1 can be related to the water eddy viscosity and g is the acceleration due to gravity. The total pressure, $p = p_{hyd} + q$, has been divided into the hydrostatic pressure $p_{hyd} = \rho_1 g(\eta_1 - z)$ such that $\partial p_{hyd}/\partial z = -\rho_1 g$ and the dynamic pressure q. Here z is the elevation measured from a vertical datum to the cell center. The velocities u, v and w associated with a computational cell are located at the right, back and the top face of the cell respectively. The non-hydrostatic pressure $q(x,y,z,t)$ is located at the cell center as the hydrostatic pressure is.

For the simulation of landslide induced-tsunami waves, an additional set of equations are included for the second fluid (mud) with density ρ_2. Here, for this particular set of equations, the mud is considered as a Newtonian fluid (mud rheology is not considered). Then, the set of governing equations for the momentum in the second layer (mud) are given by:

B-mud:

$$\frac{\partial u}{\partial t}+\frac{\partial uu}{\partial x}+\frac{\partial uv}{\partial y}+\frac{\partial uw}{\partial z}=$$
$$-g\left(\alpha\frac{\partial \eta_1}{\partial x}+(1-\alpha)\frac{\partial \eta_2}{\partial x}\right)-\frac{1}{\rho_2}\frac{\partial q}{\partial x}+\frac{\partial}{\partial x}\left[\frac{\mu_2}{\rho_2}\left(2\frac{\partial u}{\partial x}\right)\right]$$
$$+\frac{\partial}{\partial y}\left[\frac{\mu_2}{\rho_2}\left(\frac{\partial u}{\partial y}+\frac{\partial v}{\partial x}\right)\right]+\frac{\partial}{\partial z}\left[\frac{\mu_2}{\rho_2}\left(\frac{\partial u}{\partial z}+\frac{\partial w}{\partial x}\right)\right] \tag{5}$$

$$\frac{\partial v}{\partial t}+\frac{\partial uv}{\partial x}+\frac{\partial vv}{\partial y}+\frac{\partial vw}{\partial z}=$$
$$-g\left(\alpha\frac{\partial \eta_1}{\partial y}+(1-\alpha)\frac{\partial \eta_2}{\partial y}\right)-\frac{1}{\rho_2}\frac{\partial q}{\partial y}+\frac{\partial}{\partial x}\left[\frac{\mu_2}{\rho_2}\left(\frac{\partial v}{\partial x}+\frac{\partial u}{\partial y}\right)\right]$$
$$+\frac{\partial}{\partial y}\left[\frac{\mu_2}{\rho_2}\left(2\frac{\partial v}{\partial y}\right)\right]+\frac{\partial}{\partial z}\left[\frac{\mu_2}{\rho_2}\left(\frac{\partial v}{\partial z}+\frac{\partial w}{\partial y}\right)\right] \tag{6}$$

$$\frac{\partial w}{\partial t}+\frac{\partial uw}{\partial x}+\frac{\partial vw}{\partial y}+\frac{\partial ww}{\partial z}=$$
$$-\frac{1}{\rho_2}\frac{\partial q}{\partial z}+\frac{\partial}{\partial x}\left[\frac{\mu_2}{\rho_2}\left(\frac{\partial w}{\partial x}+\frac{\partial u}{\partial z}\right)\right]$$

$$+\frac{\partial}{\partial y}\left[\frac{\mu_2}{\rho_2}\left(\frac{\partial w}{\partial y}+\frac{\partial v}{\partial z}\right)\right]+\frac{\partial}{\partial z}\left[\frac{\mu_2}{\rho_2}\left(2\frac{\partial w}{\partial z}\right)\right] \tag{7}$$

Again, here $u(x,y,z.t)$, $v(x,y,z,t)$ and $w(x,y,z,t)$ are the velocity components of the fluid along the coordinate axes at time t. $\eta_2(x,y,t)$ is the mud-surface elevation measured from a vertical datum; ρ_2 is the mud density and α is the fluid-mud density ratio given by ρ_1/ρ_2. The kinematic viscosity μ_2/ρ_2 can be related to a constitutive model for mud rheology for a non-Newtonian fluid (not discussed here). The total pressure, $p = p_{hyd} + q$, has been divided into the hydrostatic pressure $p_{hyd} = g[\rho_1(\eta_1-\eta_2)+\rho_2(\eta_2-z)]$ and the dynamic pressure q.

Both interfaces, water surface elevation (water-void) and mud surface elevation (fluid/void-mud), are traced using a simplified VOF method based on the donor-acceptor algorithm of Hirt and Nichols (1981). The simplified VOF method features a scalar function $F_{1,2}(x,y,z,t)$ to define the water/mud region in space and time. Here, sub-indices 1 and 2 represent water and mud respectively. The F function accounts for the fractional volume of fluid/mud contained in the cell (fluid concentration in the computational cell). A unit value for F corresponds to a fluid cell totally filled with water/mud, while a value of zero indicates an empty cell. Therefore, a cell with an F value between zero and one is a surface cell or a water-mud interface cell. The equation describing the F function is given by

$$\frac{dF_{1,2}}{dt}=\frac{\partial F_{1,2}}{\partial t}+\frac{\partial uF_{1,2}}{\partial x}+\frac{\partial vF_{1,2}}{\partial y}+\frac{\partial wF_{1,2}}{\partial z}=0 \tag{8}$$

which states that $F_{1,2}$ propagates with the fluid velocities u, v and w. Physical properties in each cell element, i.e., the density and eddy viscosity, can be weighted in terms of the $F_{1,2}(x,y,z,t)$ function. For example, a general expression for density is determined by the following equation and condition,

$$\begin{aligned}\rho(x,y,z,t) &= \rho_1(F_1-F_2)+\rho_2F_2\\ F_1 &>= F_2\end{aligned} \tag{9}$$

Eq. 9 indicates that advection or transportation of the second fluid (mud) requires the existence of the first fluid (water) in the cell such that $F_1 >= F_2$ (saturated condition). For instance, in a mud parcel that is isolated from the atmosphere / void (the subaerial landslide case), the initial value of F_1 always equals F_2 in the control volume cell ($F_2 = F_1$).This technique greatly simplifies calculations of both free surfaces, because the advection algorithm for the second fluid (mud) is an external procedure that is completed once the advection of the first fluid (water) is done.

The scalar function F is located at the cell center as the hydrostatic (p_{hyd}) and non-hydrostatic (q) pressures. Eq. 8 is only solved in the water and mud domains. The water and mud surface elevations $\eta_{1,2}(x,y,t)$ are a mere byproduct of $F_{1,2}$ and they are calculated by locating the water/void or mud/water interfaces along the water/mud column at each (x,y) location in time. This implies that breaking waves are not allowed, because just one value of η_1 and η_2 are kept for each (x,y) location. This assertion is valid for cells with a large distortion

ratio (horizontal/vertical scale ratio) much greater than two $(>> 2)$, which is a common case in mesh generation for practical tsunami calculations.

The code uses an Eulerian mesh of rectangular cells having variable sizes. The governing equations are solved by using the standard volume difference scheme starting with field variables such as u, v, w, q and F, which are known at time $t = 0$. Notice that η is a function of F and is known once F is determined. All variable are treated explicitly with the exception of the non-hydrostatic pressure field q which is treated implicitly. The governing equations are solved by discretizing field variables spatially and temporally in the domain to obtain new field variables at any required time. Nonlinear terms are approximated using an up-wind down-wind approach up to the third order. The hydrodynamic pressure field q is calculated through the Poisson's equation by using the incomplete Choleski conjugate gradient method to solve the resulting system of linear equations.

Turbulence closure approximations are not considered in the model solution. Instead, the scale of turbulence is mainly accomplished using a simplified general eddy viscous formulation described by two phase fluids, water and mud (Direct Numerical Simulations (DNS)). The DNS approximation is presumably correct when the computational domain is relatively well resolved. In addition, for rapid landslide tsunami generation (very steep slope), the energy transfer mechanism is mainly the pressure. Therefore, energy loss due to turbulence is expected to be small and comparable to other numerical assumptions and physical processes. Even though the turbulence mechanisms are solved in a very simple manner, the final solution is expected to be adequate. The simplified general eddy viscous formulation indicated previously in the momentum equations is discussed in more detail in the following lines.

The friction term can be tuned for internal friction within the water body by means of the water eddy viscosity. For instances, in practical tsunami calculations, a value for μ_1/ρ_1 typically ranges from $10^{-6}\ m^2/sec$ to $10^{-5}\ m^2/sec$. For mud, on the other hand, a typical value for μ_2/ρ_2 ranges from $10^{1}\ m^2/sec$ to $10^{3}\ m^2/sec$. At the water-mud interfaces, the eddy viscosity is calculated by a weighting function similar to the expression and condition indicated for density expression in Eq. 9. The eddy viscosity expression for water-mud interface cells is

$$\frac{\mu}{\rho}(x,y,z,t) = \frac{\mu_1}{\rho_1}(F_1 - F_2) + \frac{\mu_2}{\rho_2}F_2 \tag{10}$$

For a well resolved domain (very high resolution), additional friction mechanisms can be implemented, for instance, the no-slip condition. The no-slip condition is enforced at all computational cells that are in contact with the sea-bottom or walls, i.e., $\partial \vec{u} / \partial \vec{z} \neq 0$. In addition, to mimic further the bottom friction, an exponential function is provided to increase the fluid eddy viscosity to one or several orders of magnitude at computational fluid cells located at some short distance from the sea-bottom or walls.

10.3 Lab experiments

It is important for any tsunami numerical model to be evaluated against standard benchmarking cases suggested by National Tsunami Hazard Mitigation Program (NTHMP), National Oceanic and Atmospheric Administration (NOAA). In this section, two experimental

landslide cases have been chosen to validate the TSUNAMI3D code for tsunami generation caused by sub-aerial and sub-sea landslides. The two test cases are:

- Tsunami generation and runup due to 3-D landslide
- Tsunami generation and runup due to 2-D landslide

10.3.1 BP8: Tsunami generation and runup due to 3-D landslide

This test compares TSUNAMI3D numerical results with laboratory data obtained in a series of 3-D experiments carried out at Oregon State University (OSU) by Raichlen et al., (2003) and Synolakis et al., (2003).

In the 3-D lab experiments, a solid wedge was used in a large wave tank to represent a landslide inducing tsunami waves, see Figure 10-1.

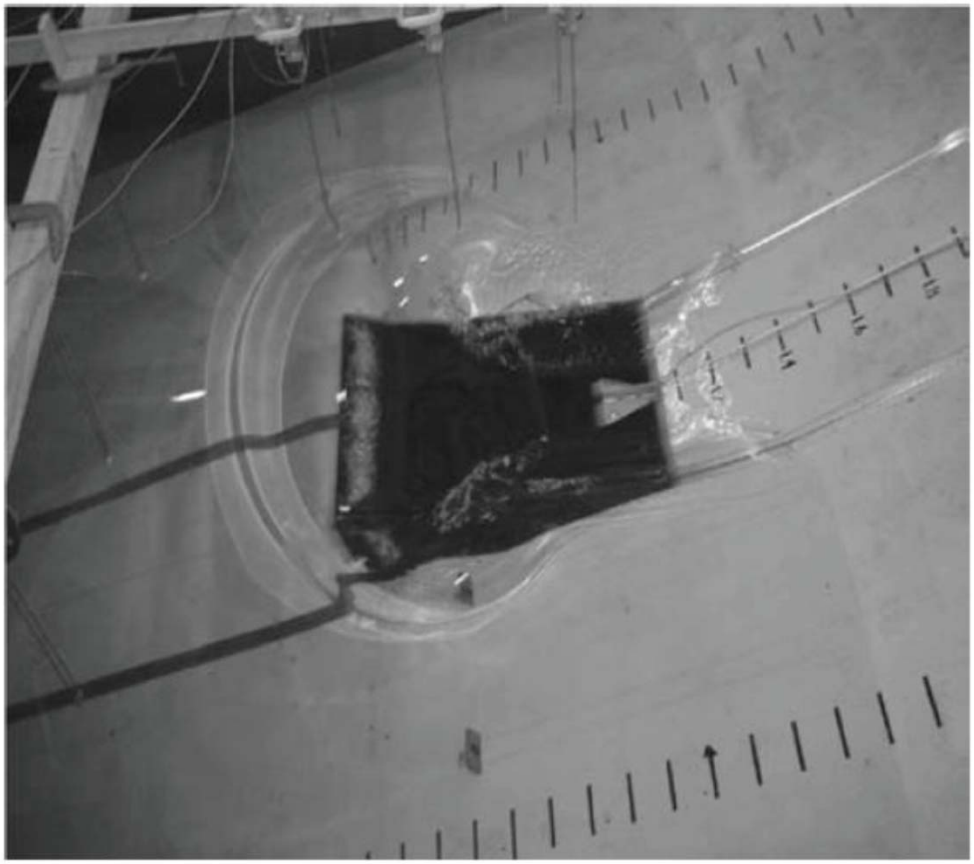

Figure 10-1: Experiment of a solid wedge induced waves. Tsunami generation and runup due to three-dimensional landslide (Synolakis et al., 2007).

The solid wedge has a triangular section with a horizontal length of 91cm, a height of 45.5 cm, and a width of 61 cm. The wedge rests in a sloping bottom of the wave tank and is released from repose. The horizontal surface of the wedge was positioned in two different small distances below the still water level (case $\Delta = 0.025$ m and case $\Delta = 0.10$ m) to generate waves with different energies and characteristics. Detailed information and access to the data are found in

the report, Tsunami Generation and Runup Due to Three dimensional Landslide, Synolakis et al., (2007), OAR PMEL 135.

TSUNAMI3D was tested against the experimental results for cases $\Delta = 0.025$ m and $\Delta = 0.10$ m. Figure 10-2 shows a set of snapshots for the case $\Delta = 0.025$, taken from the 3-D numerical model result. Domain dimensions, free surface elevation, and velocity vectors projected at plane $y = 0$ for time 1.0, 1.5, 2.0 and 2.5 sec are displayed in the figure. For numerical efficiency, the domain is reduced in half by cutting it through its plane of symmetry at $y = 0$, see Figure 10-2. The dimension of the computational box in the x, y and z direction is 6.10 m × 1.85 m × 3.05 m, respectively; total number of computational cells is 4.6 million (246 × 76 × 246); space step 0.025 m × 0.025 m× 0.0125 m; and maximum time step of 0.001 sec. The motion of the solid block was prescribed in the 3-D model according to a given wedge location time series. The computation time for 4 sec of simulation took 4 hours using a PC with 8 CPUs.

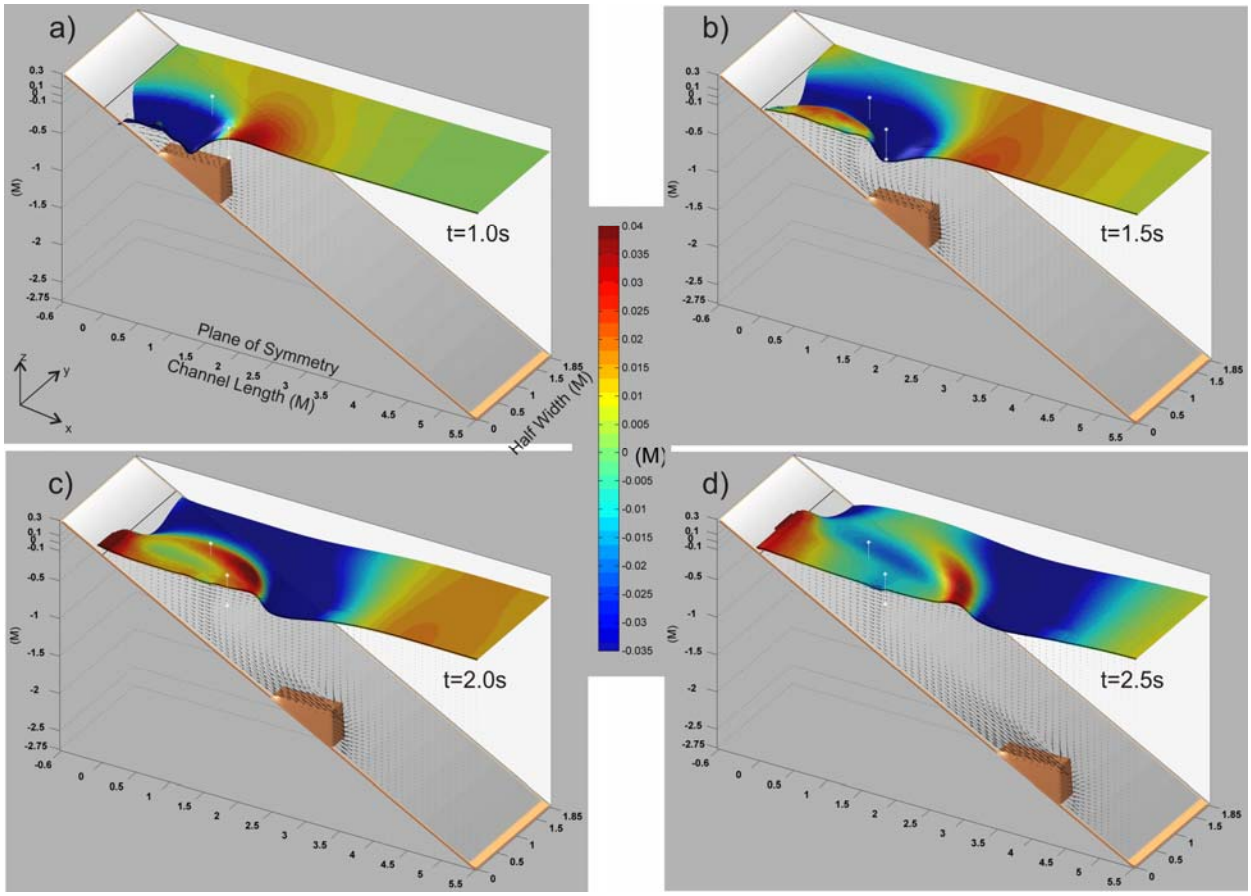

Figure 10-2: TSUNAMI3D snapshots of the solid wedge sliding down the slope and induced waves at time = [1.0, 1.5, 2.0 and 2.5] sec after slide initiation.

The TSUNAMI3D model's results are portrayed against the experimental results in Figure 10-3 and Figure 10-4. Overall numerical results agree fairly well with the experimental results. Some discrepancies in timing are evident, especially in the runup results. The rebound wave (second wave recorded in case $\Delta = 0.025$ m by gauge #1 resulting from the drag of the wedge) is slightly overestimated by the model. Similar overestimation in the rebound wave has been

reported by other authors, e.g., Abadie et al., (2010). The model has been tuned for internal friction by means of the eddy viscosity value of $10^{-6}\ m^2/sec$. The no slip condition is used for sea-bottom friction. In addition, an exponential function increases the internal friction by one or several orders of magnitude at all computational fluid cells in contact with walls or sea-bottom. The small discrepancy observed in the model's results is mainly attributable to energy dissipation due to turbulence processes. As previously indicated, a turbulence mechanism is not incorporated in the model solution, so the scale of turbulence is calculated by using the DNS approximation. Therefore, energy loss due to turbulence is expected to be small and comparable to other numerical assumptions and physical processes.

The normalized error (*ERR*) shown in Figure 10-3 and Figure 10-4 is used to measure model accuracy in time. The *ERR* is defined as

$$ERR(t) = \frac{1}{\zeta_{e_{max}} - \zeta_{e_{min}}} \frac{\sum_{i=1}^{n(t)} | \zeta_{e.i} - \zeta_{m,i} |}{n(t)} \tag{11}$$

$ERR(t)$ is the accumulative error between the values predicted by the model (ζ_m) and the values observed in the physical experiment (ζ_e). The error is normalized with respect to the distance between the maximum and minimum values obtained in the lab experiment ($\zeta_{e_{max}} - \zeta_{e_{min}}$), which usually corresponds to the first or second wave height. $n(t)$ is the number of observed points at a given time, so errors can be calculated as a function of time. This method permits measuring model accuracy for the first, second and subsequent waves. For instance, At *Gage* 1 for the lab experiment with $\Delta = 0.025$ m, the accumulative model error for predicting the wave height at t = [0.95, 2.25, 3.85] sec. are *ERR*(t) = [1.5%, 7.6%, 6%] respectively. Notice that the selected times are associated with the first, second and third waves respectively.

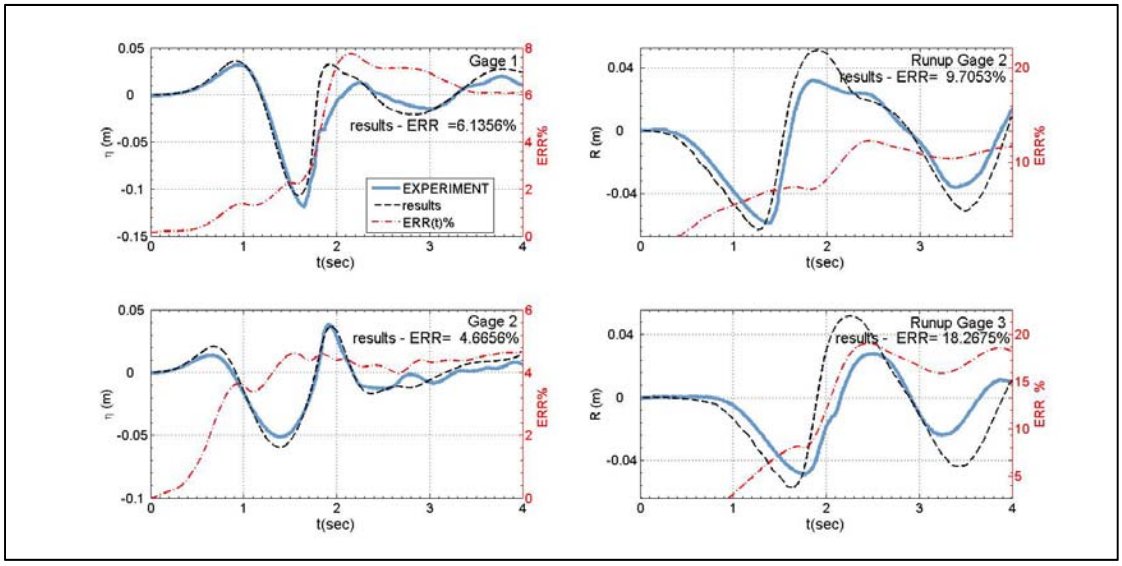

Figure 10-3: Comparison of TSUNAMI3D numerical result (black broken line) against experiment (blue solid line), case Δ = 0.025 m. Red line is the normalized error plotted in time.

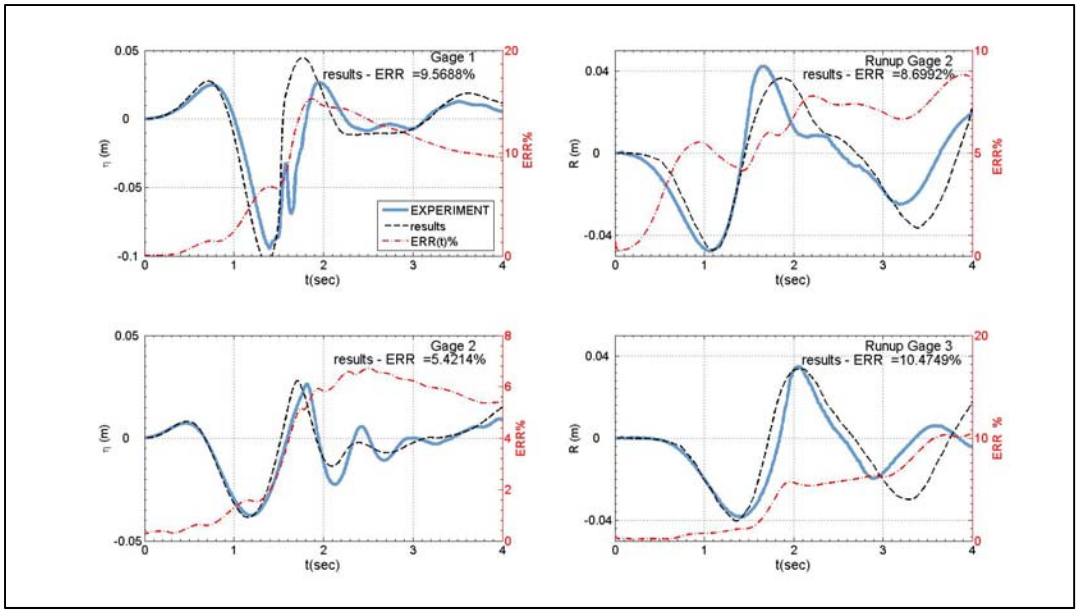

Figure 10-4: Comparison of TSUNAMI3D numerical result (black broken line) against experiment (blue solid line), case Δ = 0.010 m. Red line is the normalized error plotted in time.

10.3.2 BP3: Tsunami generation and runup due to 2-D landslide

The second experiment aims to predict the free surface elevation and runup associated with a 1-D translating Gaussian shaped mass which is initially at the shoreline (Synolakis et al. 2007). In dimensional form, the seafloor deformation can be described by

$$\eta(x,t) = H(x) + \eta_{\circ}(x,t) \tag{12}$$

$$H(x) = x\tan(\beta) \tag{13}$$

$$\eta_{\circ}(x,t) = \delta\, exp\left(-\left(2\sqrt{\frac{x\mu^2}{\delta\tan(\beta)}} - \sqrt{\frac{g}{\delta}}\mu t\right)^2\right) \tag{14}$$

where $\eta_{\circ}$ is the slide thickness, δ is the maximum slide thickness, $\mu = \delta/L$ is the thickness slide length ratio, β is the slope angle, and L is the slide length. After it begins to move, the landslide mass moves at constant acceleration. The experimental case and its analytical solution are described in great detail in Liu et al., (2003).

For this experiment, only the benchmark Case B has been chosen to test TSUNAMI3D because Case B offers higher nonlinearity than its counterpart, Case A. The experimental setup information for Case B follows.

Case B: $\tan\beta/\mu = 1$, $\beta = 5.7^{\circ}$, $\delta = 1$ m, $\mu = 0.1$; and snapshots of the free surface are determined at non-dimensional time: $\sqrt{\frac{g}{\delta}}\mu t = 0.5,\ 1.0,\ 2.5\ 4.5$

To solve Case B numerically, an additional 1-D hydrostatic numerical model has been considered to compare with the analytical linear-solution and visualize model differences and

behaviors with respect to TSUNAMI3D (non-hydrostatic). The 1-D hydrostatic model is based on the linear and non-linear shallow water approximation, LSW / NLSW respectively. It is expected that the LSW numerical solution will match the analytical linear-solution because both use the linear approach. On the other hand, if nonlinear effects are important, the NLSW results should depart from the linear solution and the free surface profile might be comparable to the TSUNAMI3D results, which are non-linear too. It is important to mention that TSUNAMI3D includes the vertical component of velocity and acceleration (non-hydrostatic), so dispersive effects might cause the solution to differ from shallow water (SW) solutions, which are, in principle, depth integrated methods. If non-hydrostatic effects are weak, the NLSW result will be comparable to the full solution of TSUNAMI3D.

The finite difference solution of momentum equation for the LSW or NLSW approximation is solved on a staggered grid using the original depth integrated code (an early version of NEOWAVE, Yamazaki et al., 2008), Kowalik and Murty, 1993. The nonlinear term for the NLSW method has second order approximation in space and first order in time.

The TSUNAMI3D model has been extended to deal with deformable moving objects in the computational domain, so the Gaussian slide deformation and motion is prescribed according to Eq. 12. As can be gleaned from Figure 10-5 and Figure 10-6, the TSUNAMI3D results agreed very well with the NLSW results. However, some differences are evident, such as the wave skewness and the location of the shoreline. It is important to mention that TSUNAMI3D solves the full Navier-Stokes equations with the vertical and horizontal velocities being variables along the water column, while the shallow water (SW) approximation assumes constant horizontal velocity and no vertical velocity. All SW numerical results, including the analytical solution, missed the effects caused by the vertical acceleration or the non-hydrostatic behavior of the generated impulsive wave.

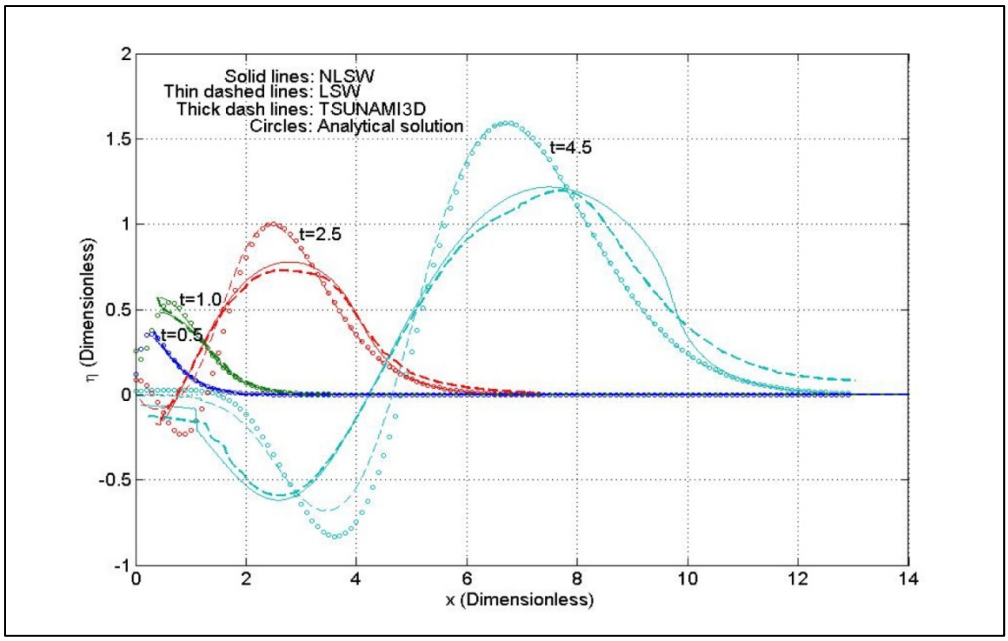

Figure 10-5: Comparison of the TSUNAMI3D model's numerical result against the analytical solution, nonlinear and linear shallow water approximation. Benchmark Tsunami generation and runup due to two-dimensional landslide, Synolakis et al., (2007), OAR PMEL-135.

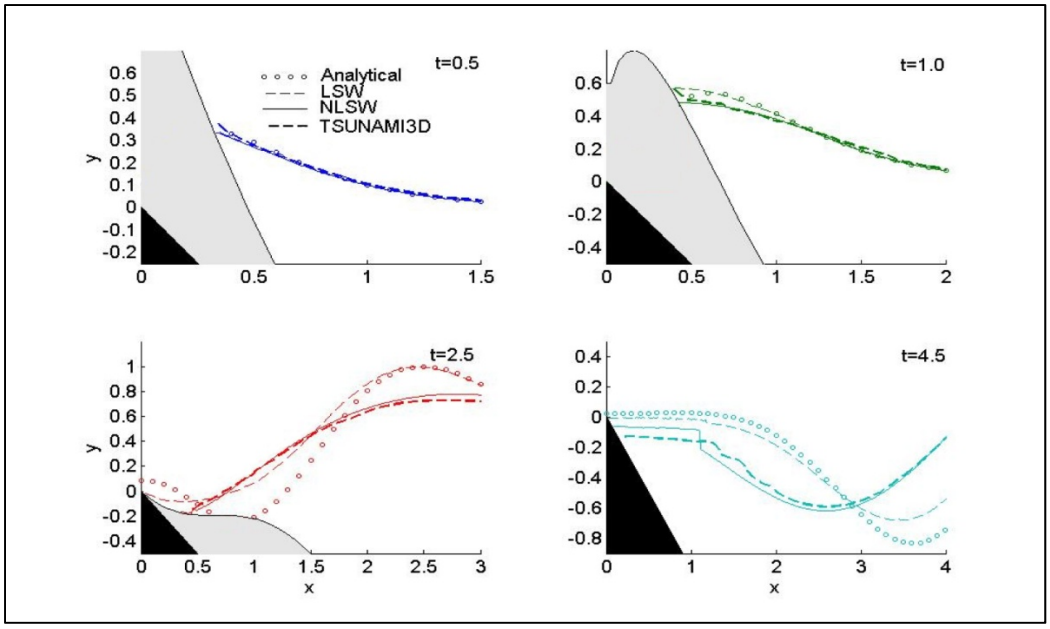

Figure 10-6: Comparison of the TSUNAMI3D model's numerical result (thick broken line) against the analytical solution. the nonlinear and linear shallow water approximation. Tsunami generation and runup due to two-dimensional landslide, Synolakis et al., (2007), OAR PMEL-135.

It is believed, that the full solution is ideally suited for cases where relatively high vertical velocity/acceleration occurs. In this particular case, as dispersion effects develop, TSUNAMI3D predicts a more elongated, skewed and less tall wave than the NLSW approach does for later times in the model run, i.e., $\sqrt{\frac{g}{\delta}}\mu t = 2.5$ and $\sqrt{\frac{g}{\delta}}\mu t = 4.5$. When nonlinearity is not strong, all numerical approximation agreed very well with the analytical solution, especially at earlier times in the model run, i.e., $\sqrt{\frac{g}{\delta}}\mu t = 0.5$ and $\sqrt{\frac{g}{\delta}}\mu t = 1.0$.

10.4 Conclusions

In accordance with National Tsunami Hazard Mitigation Program (NTHMP) guidance, tsunami numerical models must be tested against NOAA PMEL 135 benchmark standards for their approval. Therefore, TSUNAMI3D, a model solving Navier-Stokes equations for two fluids (water, mud and void), with a Volume of Fluid (VOF) algorithm to track fluid interfaces has been applied to the benchmark landslide problems. For the 3-D tsunami calculation, the algorithm has been simplified to account for the horizontal distortion of the computational cells with respect to the vertical scale. The pressure term has been split into two components, hydrostatic and non-hydrostatic. The splitting of the pressure term permits the determination of the hydrostatic solution by merely switching off the non-hydrostatic pressure terms. The turbulence process is solved in a very simple manner using Direct Numerical Simulations (DNS). TSUNAMI3D is validated against a set of established benchmarking problems for underwater and subaerial landslides. They are: a) Tsunami generation and runup due to 3-D landslide; b) Tsunami generation and runup due to 2-D landslide.

Both cases are simulated with a prescribed slide motion. Overall numerical results agree fairly well with the experimental data.

For the solid wedge experiment (3-D case), some small discrepancies in timing are evident, especially in the runup results. The rebound wave resulting from the drag of the landslide wedge is slightly overestimated by the model. The small difference is mainly attributed to the simplification of the model to account for energy loss due to the turbulence process. Even though the turbulence mechanism is solved in a very simple manner using DNS, the overall solution was adequate. The DNS assumption for this particular test correctly predicted the impulsive waves generated by the submarine solid slides, from generation to the propagation stages.

TSUNAMI3D code performed efficiently for the landslide simulation domain, with sizes on the order of 5 million cells. The computer time required to simulate 4 sec of landslide simulation was approximately 4 hours using a PC with 8 CPUs.

With respect to the 2-D analytical (linear-solution) experiment, all the models matched the analytical results at the early stages of the wave generation when nonlinearity effects are not strong. However, at later stages of wave generation, when nonlinearity and dispersive effects are important, the NLSW and TSUNAMI3D results are comparable, although some differences are visible due to the dispersive nature of the resulting wave. All SW numerical results, including the analytical solution, missed the complicated wave configuration caused by the vertical acceleration or the non-hydrostatic effects during the later stages of wave evolution.

10.5 References

Abadie SD, Morichon SD, Grilli S, Glockner S. 2010. Numerical simulation of waves generated by landslides using a multiple-fluid Navier-Stokes model. *Coastal Engineering*, 57:779-794.

Hirt CW, Nichols BD. 1981. Volume of Fluid Method for the Dynamics of Free Boundaries. *J. Comp. Phys.*, 39:201-225, 1981.

Horrillo J. 2006. Numerical Method for Tsunami Calculation Using Full Navier-Stokes Equations and Volume of Fluid Method. Thesis dissertation presented to the University of Alaska Fairbanks.

Kowalik Z, Murty TS. 1993. Numerical Simulation of Two-Dimensional Tsunami Runup. *Marine Geodesy*, 16:87-100.

Liu PL-F, Lynett P, Synolakis CE. 2003. Analytical solution for forced long waves on a sloping beach. *J. Fluid Mech.*, 478:101-109.

Raichlen F, Synolakis CE. 2003. Runup from three dimensional sliding mass. In Briggs, M. Coutitas, Ch., editors, in Proceedings of the long wave Symposium 2003, pages 247-256, XXX IAHR Congress Proceedings, ISBN-960-243-593-3.

Synolakis CE, Bernard EN, Titov VV, Kanoglu U, González FI. 2007. OAR PMEL-135 Standards, criteria, and procedures for NOAA evaluation of tsunami numerical models. Technical report, NOAA Tech. Memo. OAR PMEL-135, NOAA/Pacific Marine Environmental Laboratory, Seattle, WA.

Synolakis CE, Raichlen F. 2003. In Submarine Mass Movements and Their Consequences. Waves and Runup generated by a three-dimensional sliding mass, Advances in Natural Hazards. Locat, J. and Mienert, J.(Kluwer Academic publishers, Dordrect).

Yamazaki Y, Kowalik Z, Kwok Fai Cheung. 2008. Depth-integrated, non-hydrostaticmodel forwave breaking and run-up, *Int. J. Numer.Meth. Fluids*, DOI: 10.1002/fld.1952.

11 BOSZ

Volker Roeber, Kwok Fai Cheung

Department of Ocean and Resources Engineering, University of Hawaii at Manoa

11.1 Introduction

B O S Z (Boussinesq model for Ocean & Surf Zones) is a numerical model for propagation, transformation, breaking, and runup of water waves. BOSZ was specifically designed for nearshore wave processes in the presence of fringing reefs in tropical and sub-tropical regions around the world. The extended lagoons and steep flanks of most reef systems produce unique coastal wave processes that are challenging to numerical models used in coastal engineering design and flood hazard assessment. Typical nearshore processes that numerical models have to deal with are abrupt transitions from dispersion-dominated to flux-dominated flow through a wide range of wave breaking conditions. The formation, propagation, and runup of breaking waves or bores involve shock-related hydraulic processes in which additional treatments are necessary to enforce conservation laws across flow discontinuities. A numerical model designed for such extreme conditions provides a robust platform for a wide range of nearshore wave conditions elsewhere around the world. BOSZ was developed with the goal of obtaining reliable and robust results in addressing the complementary but somewhat opposing physical processes of flux and dispersion throughout a single numerical model. BOSZ was intentionally kept as simple as possible and yet containing the main features to accurately describe nearshore wave process. Often more sophisticated governing equations or numerical schemes encounter problems such as instabilities before they can utilize their theoretical advantages over a simpler solution.

BOSZ is primarily used for modeling nearshore and surf-zone processes of swell and wind waves. The model can be applied to near-field tsunami scenarios. However, to this date BOSZ is not based on spherical coordinates nor does it support nested grids.

11.2 Model description

11.2.1 Governing equations and numerical scheme

BOSZ combines the dispersive properties of a Boussinesq-type model with the shock-capturing capabilities of the conservative form of the nonlinear shallow-water equations. BOSZ allows the simulation of dispersive waves up to medium order as well as supercritical flows with discontinuities. The depth-integrated governing equations are derived from Nwogu's (1993) extended Boussinesq approach with conserved variables that satisfy conservation of mass and momentum for $Fr > 1$. The continuity and momentum equations contain the conservative form of the nonlinear shallow-water equations to capture shock-related hydraulic processes. In contrast, most depth-integrated formulations utilize physical variables and require additional treatments

for momentum conservation under supercritical flow conditions associated with breaking waves, bores or hydraulic jumps. The employed Boussinesq-type equations are given as

$$H_t + (Hu)_x + (Hv)_y + \left(\frac{z_\alpha^2}{2} - \frac{h^2}{6}\right) h\left(u_{xx} + v_{xy}\right) + \left(z_\alpha + \frac{h}{2}\right) h\left[(hu)_{xx} + (hv)_{xy}\right] + \left[\left(\frac{z_\alpha^2}{2} - \frac{h^2}{6}\right) h\left(u_{xy} + v_{yy}\right) + \left(z_\alpha + \frac{h}{2}\right) h\left[(hu)_{xy} + (hv)_{yy}\right]\right]_y = 0 \quad (1)$$

$$(Hu)_t + \left(Hu^2\right)_x + (Huv)_y + gH\eta_x + H\frac{z_\alpha^2}{2}\left[u_{xxt} + v_{xyt}\right] + Hz_\alpha\left[(hu_t)_{xx} + (hv_t)_{xy}\right] + u\left[\left(\frac{z_\alpha^2}{2} - \frac{h^2}{6}\right) h\left(u_{xx} + v_{xy}\right) + \left(z_\alpha + \frac{h}{2}\right) h\left[(hu)_{xx} + (hv)_{xy}\right]\right]_x + u\left[\left(\frac{z_\alpha^2}{2} - \frac{h^2}{6}\right) h\left(u_{xy} + v_{yy}\right) + \left(z_\alpha + \frac{h}{2}\right) h\left[(hu)_{xy} + (hv)_{yy}\right]\right]_y = 0 \quad (2)$$

$$(Hv)_t + \left(Hv^2\right)_y + (Huv)_x + gH\eta_y + H\frac{z_\alpha^2}{2}\left[v_{yyt} + u_{xyt}\right] + Hz_\alpha\left[(hv_t)_{yy} + (hu_t)_{xy}\right] + v\left[\left(\frac{z_\alpha^2}{2} - \frac{h^2}{6}\right) h\left(u_{xx} + v_{xy}\right) + \left(z_\alpha + \frac{h}{2}\right) h\left[(hu)_{xx} + (hv)_{xy}\right]\right]_x + v\left[\left(\frac{z_\alpha^2}{2} - \frac{h^2}{6}\right) h\left(u_{xy} + v_{yy}\right) + \left(z_\alpha + \frac{h}{2}\right) h\left[(hu)_{xy} + (hv)_{yy}\right]\right]_y = 0 \quad (3)$$

where H is total water depth, h is still water level, η is the free surface elevation, u and v are the horizontal flow velocities, g is gravitational acceleration and z_α is the reference depth at which the velocity is evaluated.

The governing equations are solved with a conservative finite volume Godunov-type scheme. The finite volume method benefits from a two-dimensional third-order TVD (Total Variation Diminishing) reconstruction procedure (Kim and Kim, 2005) that evaluates the inter-cell variables. The user can chose between the exact Riemann solver of Wu and Cheung (2008) and the approximate HLL Riemann solver for the solution of the inter-cell flux and bathymetry source terms. The flux and bathymetry source terms are well-balanced and the numerical scheme preserves continuity at moving boundaries over irregular topography. The moving waterline is part of the Riemann solution and does not require additional treatments. A second-order explicit Runge-Kutta scheme integrates the governing equations in time and evaluates the conserved variables, which in turn provide the two horizontal velocity components through the solution of

separate tri-diagonal matrices. The mixed spatial and temporal derivatives are split up throughout the solution procedure so that the two-dimensional equations can be treated as a series of one-dimensional problems in the x and y directions that can easily be processed on a parallel computer architecture. The solution procedure reduces numerical diffusion and provides accurate descriptions of the flow and runup over relatively coarse grids and with large time steps for efficient computation over large geographic areas.

11.2.2 Dispersion properties

In addition to the nonlinear shallow water equations, the governing Boussinesq-type equations contain parabolic terms to describe frequency dispersion. These terms involve the reference depth z_α, which can be used to optimize the dispersion properties. Comparing the linearized form of the governing equations with Airy wave theory leads to an optimum value of z_α over a range of water depth parameter kh. Moving the value of z_α toward the free surface gear the equations toward shorter period components, and vice versa. The optimum value is determined from an error analysis over the range of $0 < kh < 2\pi$ but with stronger emphasis on $kh < \pi$. Figure 11-1 illustrates the dispersion relation from the linearized version of the governing equations and Airy wave theory. The present value of $z_\alpha = -0.5208132$ results in less than 1% error in celerity for $kh < \pi$ and less than 4% at $kh = 5$. This means, that the model accounts reasonably well for wavelengths almost as short as the local water depth.

11.2.3 Wave breaking

Depth-integrated models do not describe overturning of the free surface and thus cannot fully reproduce the wave breaking processes. However, the use of conserved variables in the present governing equations allows approximation of breaking waves as discontinuous flows. The flow is flux dominated along the breaking wave front and non-hydrostatic effects are negligible. The Boussinesq-type equations locally reduce to the nonlinear shallow-water equations for the shock-related hydraulic processes, while the waves in the rest of the domain remain dispersive. Even though the flow is flux-dominated, the governing equations balance amplitude dispersion of the shock with frequency dispersion. This might lead to a local anomaly at the breaking location that results in numerical instability depending on the order of the dispersion terms, the numerical scheme, and most important, the grid size. This problem can be observed in a wide range of dispersive depth-integrated equations. Hence, the present solution to this issue can be applied to other numerical models in the same way.

BOSZ uses an approach to locally and momentarily deactivate the dispersion terms for the Riemann solver to describe the breaking wave as a bore or hydraulic jump. We utilize the local momentum gradients, $(HU)_x$ and $(HV)_y$, as the indicators consistent with the flux-based formulation in the governing equations. Dispersion terms are deactivated in cells where

$$0.5[|(HU)_x| + (HU)_x] \geq B\sqrt{gH} \tag{4}$$

and

$$0.5[|(HV)_y| + (HV)_y] \geq B\sqrt{gH} \tag{5}$$

with $B = 0.5$ denoting the onset criterion of wave breaking. Even though $(HU)_x$ and $(HU)_y$, in a strict sense, are not velocity terms, calibration with laboratory data would define their relations to the velocity for the wave-breaking criterion. BOSZ has been calibrated with laboratory data from

Ting and Kirby (1994) as well as a wide range of wave breaking scenarios in the benchmark test cases considered here.

The form of Eqs. (4) and (5) accounts for the direction of the flow and rules out wave breaking behind the crest, where large momentum gradients might occur in short period waves. This criterion focuses at the potential source of instability typically at the steep wave front instead of the wave crest and allows dispersion to take effects over most of the surf zone. Since the Riemann solver used in BOSZ is exact, the solution over the breaking cells satisfies exact conservation laws of mass and momentum. This provides a robust solution over an area that is often the source of instabilities. The approach determines the breaking threshold using only one coefficient without the need for a wave front tracking mechanism. This method eliminates a primary source of numerical instability while enabling the numerical solution to account for energy dissipation associated with wave breaking. For many practical applications, only a very limited number of cells represent the breaking wave front. The dispersion terms will hardly approach critical value and as a consequence, the threshold in Eqs. (4) and (5) will mostly not be exceeded even though the flow is locally supercritical. This means that if there is simply no potential instability arising along the wave front, the model run remains stable. Excessive suppression of dispersion based on the water depth to wave height criterion of Tonelli and Petti (2010) is not necessary. Independently of Eqs. (4) and (5), the governing equations in BOSZ automatically account for momentum conservation if $Fr > 1$ and therefore, no additional terms are needed nor does the numerical scheme require modifications under wave breaking conditions.

11.2.4 Model extensions

BOSZ has been greatly extended over the past months. The model package now gives the user the option to choose from two higher-order formulations:

- The conservative formulation of the extended Boussinesq equations of Wei. et al. (1995), similar to the governing equation of FUNWAVE-TVD
- The conservative formulation of the set fourth-order Boussinesq-type equations by Madsen and Schäffer (1998)

The higher-order formulations are based on the same numerical scheme as the standard governing equations with an identical treatment of wave breaking and moving boundary (runup). The different formulations are compatible and the model is arranged in modular form, thus giving the option to compute parts of the numerical grid with governing equations of different orders depending on the practical problem. The dispersion properties of the higher-order formulation based on the equations by Madsen and Schäffer (1998) show almost perfect agreement with Airy wave theory up to $kh = 2\pi$. However, satisfactory results can be achieved for most of the following benchmark problems with low order dispersion properties. Thus, all tests were conducted using the governing equations described in Section 11.2.1.

11.2.5 System requirements

The model has about 100 variables in matrix format and several other scalar variables that require roughly 750 MB of computer memory for a grid of 1000 by 1000 cells. The code is written in MATLAB with most of its processing in embedded pre-compiled C MEX subroutines. This combines fast computation with a user-friendly code development interface for debugging, modifying, and demonstration. BOSZ can be run on multiple processors through OMP parallel

processing of the C MEX routines. Parallel processing also includes the solutions of the linear systems of equations that are formed by the two momentum equations. The post-processing and plotting can also be done in MATLAB and useful scripts are provided with the model package. Software requirements include a MATLAB license as well as a compatible C compiler. The code has been successfully run on Mac OS, Windows, and Linux cluster platforms with MATLAB 2007 and 2010 in combination with GNU C and Microsoft Visual 2010 Express compilers.

11.3 Benchmark comparisons

11.3.1 BP4: Single wave on a simple beach

Solitary wave runup on a plane slope is one of the most intensively studied problems in long-wave modeling. In particular, the laboratory experiments of Hall and Watts (1953) and Synolakis (1987) have provided frequently used data for validation of wave breaking and runup models. Figure 11-2 shows a schematic of the experiment with A indicating the initial solitary wave height, R the runup, and β the beach slope. We first focus on case C from Synolakis (1987) with A/h = 0.3 that involves wave breaking in front of the slope. This simple two-dimensional geometry allows for testing of grid dependency and computation time. The computational domain is set up with a length of 25 m. The governing equations contain derivatives of up to the third order that need at least 6 cells in each horizontal direction in the computation. The model was tested with four different grids with identical model parameters. A Courant number of C_r = 0.45 ensures the stability of the time integration and a Manning coefficient of n = 0.01 s/m$^{1/3}$ defines the surface roughness of the smooth glass beach in the laboratory experiment. The initial solitary wave is located at x/h = -20 from the beach toe, allowing the initial wave profile to adjust to the governing equations before reaching the slope.

The runup on a beach with β = 19.85 and a wave height of A/h = 0.3 is first examined. Figure 11-3 compares the measured surface profiles and the model results. Different from nonlinear shallow-water models, which lack dispersion terms, the present model reproduces the shoaling process up to $t\sqrt{g/h} = 20$ at the onset of a plunging breaker as observed in the laboratory experiment. With the conserved variables, the model mimics the three-dimensional breaking process as a collapsing bore and conserves the flow volume and momentum during the process. The resulting surge reaches the maximum elevation of R/h = 0.55 around $t\sqrt{g/h} = 40$. The model shows a minor discrepancy with the laboratory data starting around $t\sqrt{g/h} = 50$, when a hydraulic jump begins to develop from the drawdown. Because the computed results agree with the measured data toward the end, the local disagreement might be due to a combination of instrumentation and model errors. The drawdown process introduces air entrainment in the water column and splashes at the surface that are difficult to measure by any instrument. The depth-integrated model also cannot fully capture the complex two-dimensional flow structure in the vertical plane.

Table 11-1: Convergence test and computation time for BP4.

Grid Size Δx/h	Number of Grid cells	Runup [cm]	Computation time 1 Intel Nehalem i7 CPU 2.66 GHz
0.25	1500	18.2	32 sec
0.125	3000	18.9	01 min 20 sec
0.0625	6000	19.0	04 min 18 sec
0.025	15000	18.9	21 min 35 sec

Table 11-1 shows the CPU time and computed runup for a range of grid resolutions for 20 sec of simulation time. The CPU time increases approximately as a quadratic function of grid resolution. A grid size of $\Delta x/h = 0.125$ is sufficient to reproduce the runup. The computed runup remains very similar at finer resolution, indicating convergence of the solution. This can be attributed to the low numerical diffusion of the finite volume scheme.

Figure 11-4 plots the measured and computed runup as a function of the initial solitary wave height A/h for beach slopes of 1:19.85, 1:15, and 1:5.67. The data show good agreement over a wide range of breaking and non-breaking events characterized by a bilinear distribution with a distinct transition. For the 1:19.85 and 1:15 slopes, the data to the right of the transition represent plunging breakers, whereas the relatively steep slope of 1:5.67 produces surging waves without flow discontinuities or breaking. The model is able to simulate the runup for incident wave heights of up to $A/h = 0.7$, which is beyond the model's range of nonlinearity. The tests prove the validity of the use of the Riemann solver in combination with local deactivation of dispersion terms for wave breaking in depth-integrated dispersive models. The model runs stably and the results are not grid sensitive as indicated in the table above.

11.3.2 BP2: Solitary wave on a composite slope

Briggs et al. (1996) conducted a laboratory experiment at the U.S. Army Corps of Engineers Waterways Experiment Station, Vicksburg, MS, to examine propagation and transformation of a solitary wave over a compound slope as well as the subsequent runup on a vertical wall. Figure 11-5 illustrates the test setup, which comprises a flat section of 15.05 m length and 0.218 m depth and a compound slope of 1:53, 1:150, and 1:13. Three cases, A, B, and C, were investigated with solitary wave heights of $A/h = 0.039$, 0.264 and 0.696 measured at gauge 4. The solitons then transform over the three slopes before being reflected from the right wall. Case A is a small-amplitude non-breaking solitary wave. Case B is a medium size soliton that undergoes significant shoaling over the slopes. The wave breaks over the 1:150 slope with the wave face slamming onto the wall causing a very high splash-up. Case C uses a large initial solitary wave with very high nonlinearity and dispersion that are beyond the range of applicability of the governing equation in Section 11.2.1. With intense breaking over the first slope, bore formation and subsequent transition of the bore into dispersive waves, this test is an interesting validation that pushes depth-integrated formulations to their limit. In all three cases the waves are initiated at the left boundary. Timing is adjusted by aligning the numerical solution with the measured peak at wave gauge 4. We conducted a convergence test similar to the one described in Section 11.3.1 and found that the numerical solutions agree well for grid sizes below $\Delta x = 1.5$ cm. All cases are run with $Cr = 0.45$ and a Manning coefficient $n = 0.01$ s/m$^{1/3}$.

Figure 11-6, Figure 11-7, and Figure 11-8 show comparisons between the computed and laboratory data. In Figure 11-6, the discrepancy between the numerical solution and the laboratory data can probably be attributed to the poorly defined initial solitary wave in the experimental study. The recorded profile is slightly narrower than the computed profile at gauge 4. The wavemaker is probably not calibrated to generate such a small amplitude wave. The initial wave profile is better defined for case B in Figure 11-7. The model well captures the shoaling and breaking processes over the slope as well as the subsequent reflection of the dispersive waves. A small discrepancy can be observed around gauge 10, where the model cannot fully account for the breaking wave with overturning of the free surface, resulting in larger amplitudes. The results of case C are shown in Figure 11-8. BOSZ is able to propagate a highly nonlinear and dispersive solitary over the flat bed. Although discrepancies arise in the shoaling and breaking processes, the amplitude and phase of the reflected dispersive waves match the measured data fairly well. This demonstrates that the wave breaking technique accurately reproduces transitions between flux and dispersion dominated flows even for conditions beyond the applicable range of the model. It should be noted that for case C the threshold for deactivation of the dispersion terms had to be elevated to $B = 0.6$ (see Eqs. (4) and (5)) to avoid anticipated negligence of dispersion due to very high flux gradients at the steep flanks of the initial solitary wave. This is of minor concern because the model was not primarily designed for propagation of highly nonlinear waves such as the one in this test case.

Table 11-2 compares the recorded and computed runup on the wall. The computed runup in cases A and C is about 80% of the measured values, which can be considered satisfactory for a depth-integrated model without an explicit description of the vertical motion of water particles. The large discrepancy in case B can probably be attributed to strong splash-up and to vertical sheet flow from the impinging wave that are beyond the scope of this model.

Table 11-2: Runup on vertical wall in BP2.

Case No.	Experimental runup [cm]	Computed runup from BOSZ [cm]
A	2.74	2.20
B	46.72	16.40
C	27.43	22.10

11.3.3 BP6: Solitary wave on conical island

Transformation of long waves around an island has attracted a lot of attention in the research community. Refraction and diffraction of long waves may result in significant inundation on the lee side and trapping of energy around an island. A common observation is that waves refract around an island on the two sides, collide in the back with additional energy from the diffracted waves, and continue to wrap around the island. Briggs et al. (1995) conducted a large-scale laboratory experiment to investigate solitary wave transformation around a conical island. Figure 11-9 shows schematics of the laboratory experiment. The basin is 25 m by 30 m. The circular island has the shape of a truncated cone constructed of concrete with diameters of 7.2 m at the bottom and 2.2 m at the top. The island is 0.625 m high and has a side slope of 1:4. A 27.4-m long directional wavemaker consisting of 61 paddles generates the input solitary waves for the laboratory test. Wave absorbers at the three remaining sidewalls reduce reflection in the basin.

The experiment covers the water depths h = 0.32 and 0.42 m and the solitary wave heights A/h = 0.05, 0.1 and 0.2. The present study considers the smaller water depth h = 0.32 m, which provides a more challenging test case for dispersive wave models. In the computation, the solitary wave is generated from the left boundary with the measured incident wave heights of A/h = 0.045, 0.096, and 0.181. These measured wave heights, instead of the target wave heights A/h = 0.05, 0.1, and 0.2 in the laboratory experiment, better represent the recorded data at gauge 2 and thus the incident wave conditions to the conical island. A solid boundary condition is imposed at the lateral boundaries. The wave absorbers, which are not effective for long waves, are not considered. The model is set up with a grid of $\Delta x = \Delta y$ = 5 cm. A Manning's roughness coefficient n = 0.014 s/m$^{1/3}$ accounts for the smooth concrete finish according to Chaudhry (1993). The Courant number is set to C_r = 0.45. Figure 11-10 shows a series of snapshots as the solitary wave with A/h = 0.181 propagates around the island. The result shows the maximum runup at the front and refraction and trapping of the solitary wave over the island slope. The trapped waves from the two sides superpose with the diffracted wave on the leeside of the island. Wave breaking occurs around the island according to Titov and Synolakis (1998) and reduces the runup particularly on the leeside of the cone. After the solitary wave passes the island, the trapped waves continue to wrap around to the front.

A number of gauges recorded the transformation of the solitary wave around the conical island. Figure 11-11 shows the time series of the solutions and the measured free surface elevations at selected gauges. With reference to Figure 11-9, gauges 2 and 6 are located in front of the island and 9, 16, and 22 are placed close to the still waterline at 0°, 270°, and 180° around the island. These gauges provide sufficient coverage of the wave conditions important to the experiment. The measured data at gauge 2 provides a reference for adjustment of the timing of the computed waveforms. The results show the incident wave profile and reflection from the island. With higher nonlinearity, the crest of the solitary wave is narrower and the reflection is more distinct. Wave breaking was observed at gauge 9 for A/h = 0.181 and 0.096. The model accurately describes the subsequent drawdown in all three cases, but just like most published models, does not reproduce the small amplitude short period waves afterwards. A careful inspection of the laboratory setup shows the wavemaker is 2.6 m shorter than the basin width and diffraction of the incident wave at the two ends of the wavemaker likely generated these short period waves. For A/h = 0.181, the wave breaks as it wraps around the island and the model approximates the wave breaking process as bores resulting in steep front faces. The waves wrapped around from the two sides superpose and break symmetrically as if it is a standing wave. This is a classic example of the two-shock interaction in the Riemann solver used in the present model. Most empirical wave breaking mechanisms cater to typical spilling and plunging wave breakers such as those examined by Ting and Kirby (1994) and might not correctly account for these conditions. Figure 11-12 compares the measured data and the computed inundation in its original resolution around the conical island. The computed results show good agreement with the laboratory data and are symmetric about the wave propagation direction despite the use of a Cartesian grid to describe curved surfaces. Especially the inundation at the lee side of the island is captured very well. Doubling the grid spacing to $\Delta x = \Delta y$ = 10 cm hardly affects the quality of the results. However, the maximum runup outline appears less detailed due to the coarser grid.

11.3.4 BP7: Runup at Monai valley

The 1993 Hokkaido Nansei-Oki tsunami is a well-studied event. In particular, Matsuyama and Tanaka (2001) conducted laboratory experiments at the Central Research Institute for

Electric Power Industry (CRIEPI) to examine the extreme runup of over 30 m at Monai Valley located between two headlands and sheltered by the small Muen Island. The CRIEPI wave flume is 205 m long, 3.4 m wide, and 6 m high with a hydraulic wavemaker capable of generating leading depression N-waves, which are typical for near-field tsunamis. The area around Monai Valley was reconstructed in the tank at a 1:400 scale based on bathymetric data as shown in Figure 11-13. A wave gauge near the wavemaker recorded the initial low amplitude N-wave as shown in Figure 11-14 and is used in BOSZ as boundary input with the free surface elevation interpolated from the data according to the model time step. The computational domain is discretized with $\Delta x = \Delta y = 2$ cm. As in the other benchmark cases, the Courant number is kept consistent at $Cr = 0.45$. A Manning coefficient of $n = 0.014$ s/m$^{1/3}$describes the surface roughness of the plywood model (Chaudhry, 1993). Figure 11-15 shows the comparison between the computed and recorded data at the wave gauges located between Muen Island and Monai Valley in the experiment. The model cannot fully resolve all the details associated with the interactions between refracted and diffracted waves around Muen Island and the drawdown from Monai Valley. The scattered waves are not highly dispersive. The short period waves in the record probably result from scattering over the physical model terrain at small water depth. However, the model agrees well with the overall wave field. It should be noted that very similar results were obtained from non-dispersive shallow-water models, because dispersion has only marginal influence on this experiment.

The maximum inundation limit can be seen in Figure 11-16 and Figure 11-17. The well-balanced finite volume scheme reproduces the inundation at three monitored locations including one in the narrow Monai Valley without requiring an excessively fine grid resolution.

11.4 Proposed benchmark problems

11.4.1 Solitary wave over 2-D reef

We conducted two series of laboratory experiments at Oregon State University in 2007 and 2009 that included 198 tests with 10 two-dimensional reef configurations at a range of water depths. Each test included a series of incident solitary wave heights. These test cases are a logical extension of the current benchmark for validation of inundation models. Though the laboratory experiments focuses on shock-related hydraulic processes such as wave breaking and bore formation, the collected data allow examination of shoaling, reflection, wave breaking, and swashing dynamics. We propose the results from one of the test configurations with $A/h = 0.3$ as a future NTHMP benchmark problem and provide a detailed description of hydraulic processes with additional data from BOSZ. Additional experimental data for $0.05 < A/h < 0.5$ can be requested and we can also provide data for different bathymetries.

As we will demonstrate, this test is suitable for dispersive and non-dispersive models. Though the test is essentially two-dimensional, it is recommended to compute the numerical solution over the x and y directions by simply rotating the input grid. The solutions should be identical to ensure that the model works flawlessly and the computer code is free of errors. The proposed test case examines many aspects of numerical models that are important in tsunami inundation modeling:

- Wave breaking and bore formation
- Transitions between dispersion and flux–dominated flows
- Transitions between sub and supercritical flows

- Mass and momentum conservation for $Fr > 1$
- Mass and momentum conservation at moving waterlines
- Wave shoaling and reflection

11.4.1.1 Experiment setup

The test was conducted in the Large Wave Flume (LWF) at the Hinsdale Wave Research Laboratory at Oregon State University, Corvallis, OR. The LWF has a length of 104 m, a width of 3.66 m, and a height of 4.57 m. The wavemaker was installed in early 2009 prior to the series of experiments. A hydraulic actuator moves a single piston, which in turn drives a 4.57-m high waveboard at a maximum speed of 4.0 m/s. This facility can accommodate tests with a scale up to 2.5 times that in the Tsunami Wave Basin at the same laboratory. **Error! Reference source not found.** shows a schematic of the experiment setup. The effective length of the flume is 83.7 m with a 1:12 slope starting at 25.9 m from the wavemaker. The reef flat is at an elevation of 2.361 m from the tank floor. Because most fringing reefs have a sheltered lagoon, a reef crest composed of marine plywood is attached to the reef edge and smoothly transitions the reef slope to 2.565 m elevation. The reef crest is 1.25 m long and the offshore and onshore slopes are both 1:12. With a water level of 2.5 m, the lagoon has a shallow depth 0.136 m while the reef crest remains exposed by 0.065 m. Resistance-type and ultrasonic-type wave gauges recorded the free surface elevation along the tank. Two Acoustic Doppler velocimeters (ADV) recorded the three-dimensional flow velocity at 54.41 m and 58.07 m from the wavemaker. However, the particular location at 58.07 m was subject to very intensive wave breaking and air entrainment and the recorded ADV data show insufficient quality for this study and thus are omitted. More details about the experimental procedure can be found in Roeber et al. (2010) and Roeber (2010).

11.4.1.2 Hydraulic processes and model – data comparison

The hydraulic processes can be best explained by a combination of model and laboratory data. The computational domain uses a grid size of $\Delta x = \Delta y = 0.05$ m with a Courant number of $C_r = 0.45$. A Manning coefficient of $n = 0.014$ s/m$^{1/3}$ from Chaudhry (1993) describes the smooth, finished concrete and plywood surfaces of the flume. Figure 11-19 shows the computed and measured free surface profiles along the flume. The 0.75-m solitary wave gives a dimensionless wave height of $A/h = 0.3$. After being generated at the left boundary from an analytical solution, the solitary wave shoals over the relatively gentle slope. The profile becomes near vertical and the wave begins to break around $t\sqrt{g/h} = 65$. Observations during the laboratory experiment indicate subsequent overturning of the free surface and the development of a plunging breaker impinging on the reef crest with a large air cavity and subsequent splash-up around $t\sqrt{g/h} = 69$. BOSZ mimics the plunging breaker as a collapsing bore and correctly describes the free surface profile during the entire process. The flow transitions to advection- or flux-dominated over the reef flat such that the conservative form of the governing equations becomes instrumental in capturing the pertinent hydraulic processes. Around $t\sqrt{g/h} = 70$, the broken wave begins to travel down the back slope of the reef crest and generates a supercritical flow displacing the initially still water in the lagoon. The flow generates a hydraulic jump off the back reef and a propagating bore downstream. Laboratory observations indicate overturning of the free surface at the hydraulic jump as the supercritical flow transfers volume and momentum to the subcritical flow that fuels a propagating bore at the front. The hydraulic jump initially moves downstream with the strong supercritical flow. Around $t\sqrt{g/h} = 80$, the momentum flux

balances at the flow discontinuity and the hydraulic jump becomes stationary momentarily. The present model detects the breaking at the hydraulic jump during the process through the momentum gradient in the Riemann solver approach that would otherwise not be accounted for by conventional methods based on free surface motion. The hydraulic jump subsequently diminishes with the flow and moves back to the reef crest as a bore. In the meanwhile, the propagating bore shows a gradual reduction in amplitude and continues to propagate downstream.

The end wall of the flume reflects the bore back to the lagoon that in turn overtops the reef crest as sheet flow generating a hydraulic jump on the fore reef. The reflected bore, which has lower Froude number, produces a series of dispersive waves that warrant a closer examination. Figure 11-20 compares the computed and recorded surface elevation time series. The wave gauge right next to the wall at x = 80 m shows superposition of the approaching and reflected bores propagating in the opposite directions. The time series at x = 65.2 on the reef flat shows the approaching bore and the reflected bore from the end wall as well as its reflection from the reef crest. The process continues with the subsequent reflection from the end wall. The steep wave fronts demonstrate the shock-related hydraulic processes in the flux-dominated flow. The time series at x = 57.9 m shows overtopping at the reef crest. As the water rushes down the fore reef, the flow transitions to dispersion-dominated through a hydraulic jump. Observations during the experiments confirm an overturning free surface with air entrainment near x = 54.4 m. The hydraulic jump initially generates an offshore propagating bore, which transforms into a train of waves over the increasing water depth at the fore reef for $x \leq 50.4$ m. The resulting undulations intensify as higher harmonics are released from the wave packet. At the same time, a long period reflected wave propagates in onshore direction and superposes with the released higher harmonics from the offshore propagating bore. Wave gauges located near the toe of the slope record highly dispersive waves of $kh > 15$. Figure 11-21 shows a close up view of the free surface at the wave gauge at x = 35.9 m in about 1.7 m water depth. Though the wavelengths of these harmonics are below the applicable range of the model, the waveforms are well captured with good agreement of the phase and only slight over-predictions in the amplitude. Figure 11-22 shows the velocity in the x direction at a location in front of the reef crest, where the laboratory wave already overturns. Despite its depth-integrated structure, the model captures the velocity of the initial strong supercritical flow conditions ($Fr \sim 3.5$) and subsequent dispersive waves.

The model reproduces the long and intermediate-period oscillations even after a long simulation involving a series of wave breaking and reflection in the flume. The conservative structure of the model allows description of the transition between super and subcritical flows and the present wave-breaking model reproduces the surging and plunging waves over the reef. This test also demonstrates the applicability of the Riemann solver model for wave breaking. The local deactivation of dispersion terms efficiently eliminates potential instabilities, and at the same time, does not alter the dispersion properties of subsequent wave transformation processes such as the release of higher order dispersive waves from a decaying bore.

11.4.1.3 Grid dependency and dispersion

Figure 11-23 and Figure 11-24 illustrate the model grid dependency and resolution of shock and dispersive waves. Despite the fact that the tank geometry cannot be perfectly resolved with Δx = 0.1 and 0.2 m, the model shows good agreement with the measurements. The model is able to resolve most of the dispersive waves at x = 35.9 m with Δx = 0.10 m and only a small phase shift can be observed. This might be due to a small offset of the wall location in the coarse grid

that alters the timing of the reflection. Even with a grid of Δx = 0.20 m the model is able to resolve the main features of the recorded waveform including the leading dispersive waves. The results for the coarser grids are very satisfying considering the much shorter computation time and smaller output files.

11.4.1.4 Comparison between dispersive and hydrostatic solutions

BOSZ has an option to use the embedded nonlinear shallow-water equations by turning off the dispersion terms in the computation. We recomputed the bore propagation over the reef flat using the same discretization, Courant number, and Manning's coefficient without the dispersion term. The computation starts off with the full model up to $t\sqrt{g/h} = 64.8$, which allows the solitary wave to propagate up to its breaking point without any difference. The dispersion terms are turned off in the entire domain afterward and the computation continues based on the nonlinear shallow-water equations describing only hydrostatic effects. Figure 11-25 through Figure 11-28 show comparisons of the solutions. Despite the fundamental differences in the governing equations, as the flow becomes completely flux-dominated, both solutions become almost identical. The subsequent bore formation does not depend on dispersion, and as long as the governing equations conserve momentum, the shock front moves at the correct speed and height. The small difference in phase speed results from the small changes in the remaining wave field to the left of the reef crest that fuel the bore. Especially as the bore decays along the flume, its Froude number decreases and the bore approaches the stage toward an undular bore. As the hydrostatic solution continues to dissipate energy through the hydraulic jump, the Boussinesq solution conserves energy in the vicinity of the weakening shock and correctly reproduces its speed. After the wave gets reflected from the wall and propagates over the reef crest back into the deeper part of the tank, the shallow-water solution fails to resolve the dispersive wave train, which develops from the decaying bore along the offshore slope. Instead, the shallow-water solution describes the wave train as a decaying discontinuity. The lack of dispersive effects can also be seen in the velocity profile that essentially follows the trend of the free surface profile.

This example has demonstrated the key features for a tsunami inundation model. The results from the nonlinear shallow-water equations can give very satisfying predictions of the flux-dominated processes. We would like to encourage modelers using nonlinear shallow-water models to undertake this test case by simply initializing the calculation with the initial solitary wave placed at the first wave gauge instead of generating the input from the left boundary.

11.4.2 ISEC BM1, ISEC BM2: Solitary wave over 3-D reef system

The National Science Foundation funded a workshop and a benchmarking exercise for inundation models at Oregon State University in 2009. The organizer provided two benchmark test cases with data from laboratory experiments at the Tsunami Wave Basin. Swigler and Lynett (2011) provided a detailed description of the experiments, instrumentation, and data post-processing. These test cases, which involve wave transformation over three-dimensional reef configurations, are logical extensions of the two-dimensional reef experiments from Section 11.4.1. The laboratory data allows validation of models in handling dispersion and flux-dominated processes simultaneously. Information about the test cases can be found at

http://isec.nacse.org/workshop/2009_isec/benchmarks.html.

Figure 11-29 shows the reef configuration determined from a laser scan and the setup of the instrumentation for ISEC BM1. The neutral position of the wavemaker is at x = 0. The main

feature in the experiment is a triangular reef flat submerged between 7.5 and 9 cm below the still water level. The reef sits on top of a bilinear background profile extending from x = 10.2 to 17.7 m at a slope of 1:16 and from x = 17.7 to 32.4 m at 1:32. The slope of the reef is 1:3.5 at the apex and flares to 1:16 over a distance of 9 m on either side to converge the wave energy. The water depth in front of the bilinear profile varies slightly around 0.78 m. The top of the relief model has an elevation between 0.16 to 0.13 m above the still water level with a mild grade to the back of the basin. Time series of the water surface elevation were recorded along transects at the centerline from gauges 1 to 7, at 5 m offset from gauges 8 to 13, and at the edge of the reef flat from gauges 7 and 14 to 17. Velocity measurements are available at gauges 3, 6, and 13. Because of the limited supply of instruments, the data were recorded over several weeks from a number of repetitions of the same test conditions with the instrument array repositioned along the basin.

The model is set up with a grid of $\Delta x = \Delta y = 0.1$ m, a Courant number of $Cr = 0.45$, and a Manning roughness of $n = 0.014$ s/m$^{1/3}$ as in the two-dimensional reef experiments. On a single CPU, the model takes almost 2 hours of runtime for 90 sec of simulation. With parallel computation, the computation time reduces almost linearly; the simulation finishes in around 16 minutes on 8 CPUs. The incident solitary wave has a height of 0.39 m giving rise to strongly nonlinear conditions with $A/h = 0.5$. Figure 11-30 shows a series of snapshots as the solitary wave transforms over the reef and slope complex. In the laboratory experiment, spilling at the crest occurred locally at t = 5 sec, when the solitary wave reached the apex of the reef with little shoaling over the steep slope. With shoaling of the wave along the sides, plunging waves subsequently developed along the entire length of reef edge at t = 8 sec. The model reproduces the breaking process as a collapsing bore spreading across the triangular reef flat. The flow transitions into a surge moving up the initially dry slope and overtops the reef and slope complex. At t = 21 sec, drawdown of the water has already occurred on the slope, while the sheet flow on the top continues to move forward. As observed in the laboratory experiment, the upper slope is mostly dry with water trickling down the streaks of the concrete surface and the sheet flow at the top has been reflected from the back wall as a bore over the impounded water by t = 35 sec. The panel at t = 48 sec shows the second reflection from the wavemaker and sloshing of the impounded water at the top separated by the dry upper slope. Though the test uses a high solitary wave as input that itself poses challenging dispersive conditions, the flow stays mainly flux-dominated throughout the entire experiment after wave breaking occurs. For this part, nonlinear shallow-water models can give satisfying results if the initial solitary wave is placed at about 6 m from the left boundary. Dispersion, however, is responsible for many of the flow details in Figure 11-30.

The data from the laboratory experiment allow a quantitative comparison with the model prediction. Figure 11-31 and Figure 11-32 show good agreement of the computed and recorded surface elevations during the initial steepening and breaking of the solitary wave along the two cross-shore transects of the basin. Figure 11-33 shows good agreement of the bore propagation in the alongshore direction. The timing of the first and second reflection from the wavemaker mainly depends on the water depth over the reef. Figure 11-34 compares the recorded and computed flow velocity components at three of the gauges in the x and y directions. At the apex of the shelf, the model reproduces the entire recorded time series of the x component of the velocity. The recorded data are not continuous at the two other locations at the reef flat but generally agree with the model output in the x and y directions, albeit with minor phase shift of

the reflection. We noticed a slight decrease of the phase lag of the reflection through shortening the domain by 0.5 m at the offshore boundary and increasing the water depth by ~1.5 cm, that correspond to the final wavemaker position and the equivalent volume displaced. However, this adjustment does not account for the dynamics that is induced by the forward motion of the wavemaker as it generates the initial wave.

ISEC BM2 utilizes the same relief model but with a concrete cone of 6 m diameter and 0.45 m height fitted to the apex of the reef between x = 14 and 20 m. Figure 11-35 shows the test configuration and instrumentation layout. The presence of the cone modifies the hydraulic processes over the reef flat and provides even more complex wave dynamics for model validation. The model setup is similar to that for ISEC BM1 with a grid of $\Delta x = \Delta y = 0.10$ m, a Courant number of $Cr = 0.45$, and a Manning roughness of $n = 0.014$ s/m$^{1/3}$. Figure 11-36 shows snapshots of the computed free surface elevation in the basin. The solitary wave breaks at the apex of the reef flat at t = 5.1 sec and the resulting surge completely overtops the cone at t = 6.6 sec. The refracted waves from the two sides of the cone and the diffracted waves converge in the back at t = 8.6 sec. While the refracted waves continue to wrap around as trapped waves, the diffracted waves radiate from the back of the cone. During this process, the flux gradients in the x and y directions trigger the threshold to deactivate dispersion along the breaking wave front and the model is stable during this critical episode of the simulation. The diffracted wave on the leeside of the cone propagates up the slope reinforcing the refracted waves from the reef edge. The drawdown of the diffracted wave generates a bore, which collides with the reflection from the wavemaker over the reef flat around t = 17 sec and part of which is trapped around the cone as shown in the panel at t = 21.2 sec. After about 45 sec, and not shown in the snapshots, small vortices are generated in the vicinity of the reef edge and are moved around the conical island. Figure 11-37 compares the computed and recorded surface elevations. The model reproduces the recorded surface elevations in front of the cone and the collapse of the bore behind the cone. The model matches the x component of the velocity at gauge 3 reasonably well as shown in Figure 11-38. The recorded data immediately behind the cone at gauge 6 missed the initial wave probably due to the turbulence and air entrainment, which could be the reason for the small discrepancies in the alongshore velocity component. Gauge 10 recorded most of the initial wave and gives good agreement with the computed data. The y component of the velocity is only a fraction of the x component with distinct secondary flow features of which the overall trend is accounted for in the model. Simulations with a coarser grid of $\Delta x = 0.20$ m, which takes only 10 min of computation time, still account for the main flow structure and provide very reasonable agreement with the laboratory data - especially along the bore.

The overall agreement between the computed and recorded data demonstrates the validity of BOSZ in handling multiple hydraulic processes, transitions from flux to dispersion–dominated flows as well as a variety of wave breakers in the two-dimensional horizontal plane with a moving boundary.

11.5 References

Briggs MJ, Synolakis CE, Harkins GS, Green DR. 1995. Laboratory experiments of tsunami runup on a circular island. *Pure and Applied Geophysics*, 144(3/4), 569-593.

Briggs MJ, Synolakis CE, Kanoglu U, Green DR. 1996. Benchmark Problem 3: runup of solitary waves on a vertical wall. In Long-Wave Runup Models, Yeh, H, Liu PL-F., and Synolakis, C. (eds). World Scientific, Singapore, pp. 375-383.

Chaudhry MH. 1993. Open-Channel Flow. Prentice-Hall Inc., Englewood Cliffs, New Jersey, 483 p.

Hall JV, Watts JW. 1953. Laboratory investigation of the vertical rise of solitary waves on impermeable slopes. Technical Memo No. 33, Beach Erosion Board, US Army Corps of Engineers.

Kim KH, Kim C. 2005. Accurate, efficient and monotonic numerical methods for multidimensional compressible flows. Part II: Multi-dimensional limiting process. *Journal of Computational Physics* 208, 570-615.

Maden PA, Schäffer, HA. 1998. Higher-order Boussinesq-type equations for surface gravity waves: Derivation and Analysis. *Phil. Trans.: Math., Phys. and Eng. Sciences*, Vol. 356 (1749), 3123-3184.

Matsuyama M, Tanaka H. 2001. An experimental study of the highest run-up height in the 1993 Hokkaido Nansei-oki earthquake tsunami. In Proceedings of the International Tsunami Symposium 2001, Seattle, Washington, pp. 879-889.

Nwogu O. 1993. An alternative form of the Boussinesq equations for nearshore wave propagation. *Journal of Waterway, Port, Coastal, and Ocean Engineering*, 119 (6), 618-638.

Roeber V. 2010. Boussinesq-type model for nearshore wave processes in fringing reef environment. PhD Dissertation, University of Hawaii, Honolulu.

Roeber V, Cheung KF, Kobayashi MH. 2010. Shock-capturing Boussinesq-type model for nearshore wave processes, *Coastal Engineering*, 57 (4), 407–423.

Swigler DT, Lynett P. 2011. Laboratory study of the three-dimensional turbulence and kinematic properties associated with a solitary wave traveling over an alongshore-variable, shallow shelf. In review.

Synolakis CE. 1987. The runup of solitary waves. *Journal of Fluid Mechanics*, 185, 523-545.

Ting FC.K, Kirby JT. 1994. Observation of undertow and turbulence in a laboratory surf zone. *Coastal Engineering* 24 (3-4), 51-80.

Titov VV, Synolakis CE, 1998. Numerical modeling of tidal wave runup. *J. Waterw. Port Coast. Ocean Eng.*, 124(4), 157-171.

Tonelli M, Petti M. 2010. Finite volume scheme for the solution of 2D extended Boussinesq equations in the surf zone. *Ocean Engineering*, 37(7), 567-582.

Wei G, Kirby JT, Grilli ST, Subramanya R. 1995. A fully nonlinear Boussinesq model for surface waves: Part I. Highly nonlinear unsteady waves, *J. Fluid Mech.*, 294, 71-92.

Wu Y, Cheung KF. 2008. Explicit solution to the exact Riemann problem and application in nonlinear shallow-water equations. *International Journal for Numerical Methods in Fluids* 57 (11), 1649-1668.

11.6 Figures

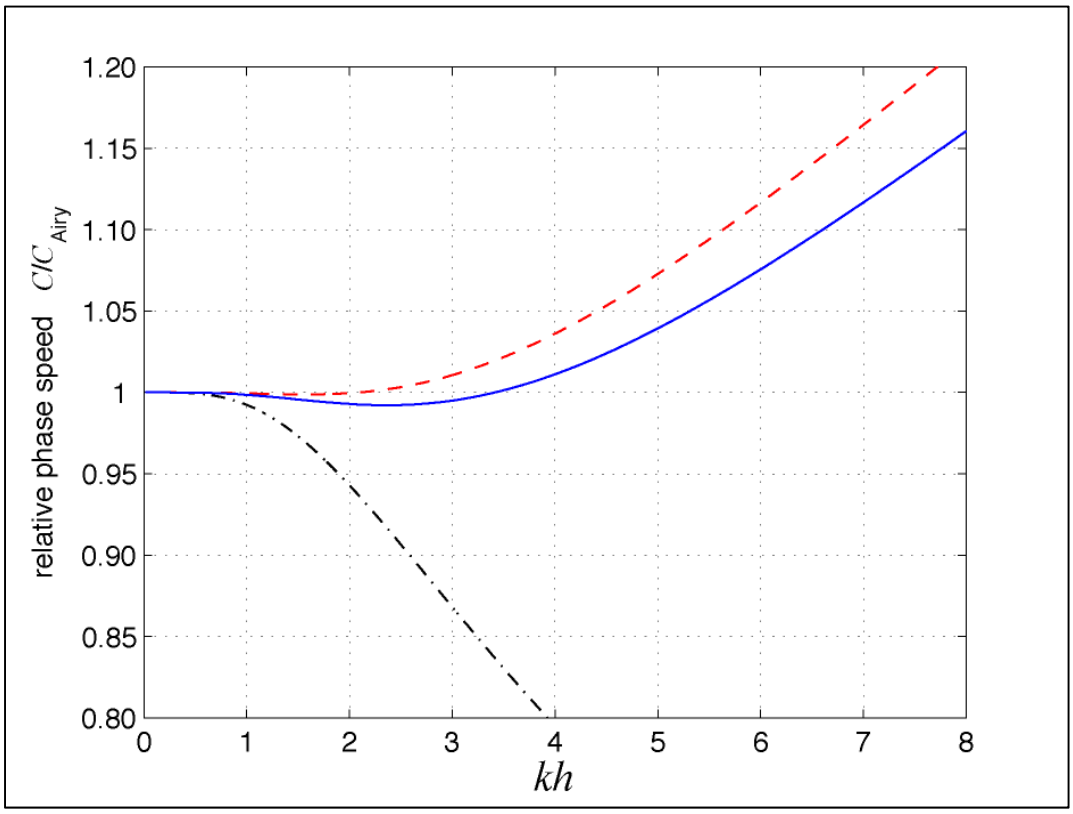

Figure 11-1: Linear dispersion properties. (blue), zα = -0.5208132 from BOSZ; (red), zα = -0.5375 from Nwogu (1993); (black), zα = -0.42265 equivalent to Peregrine (1967).

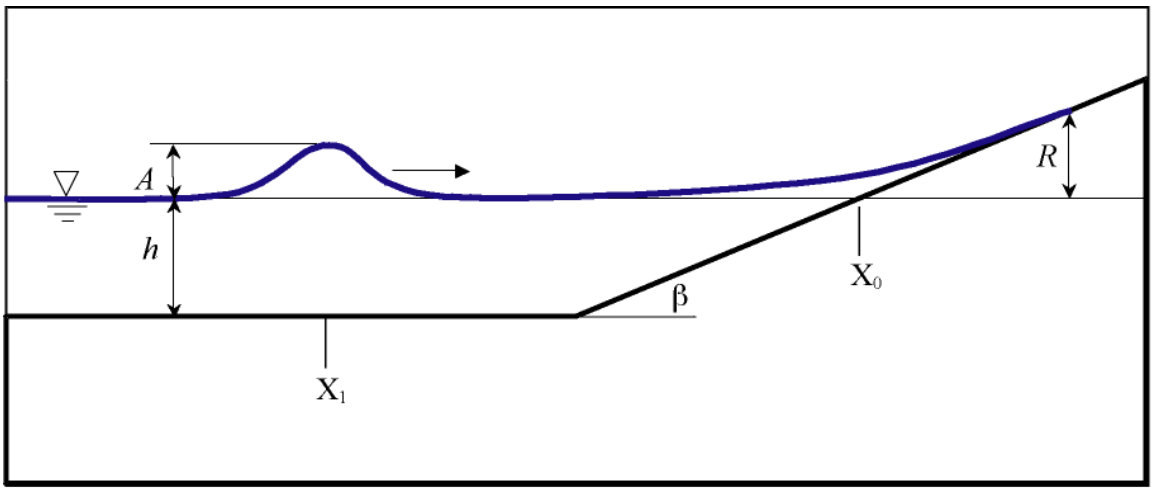

Figure 11-2: Definition sketch of BP4: Solitary wave runup on a simple beach.

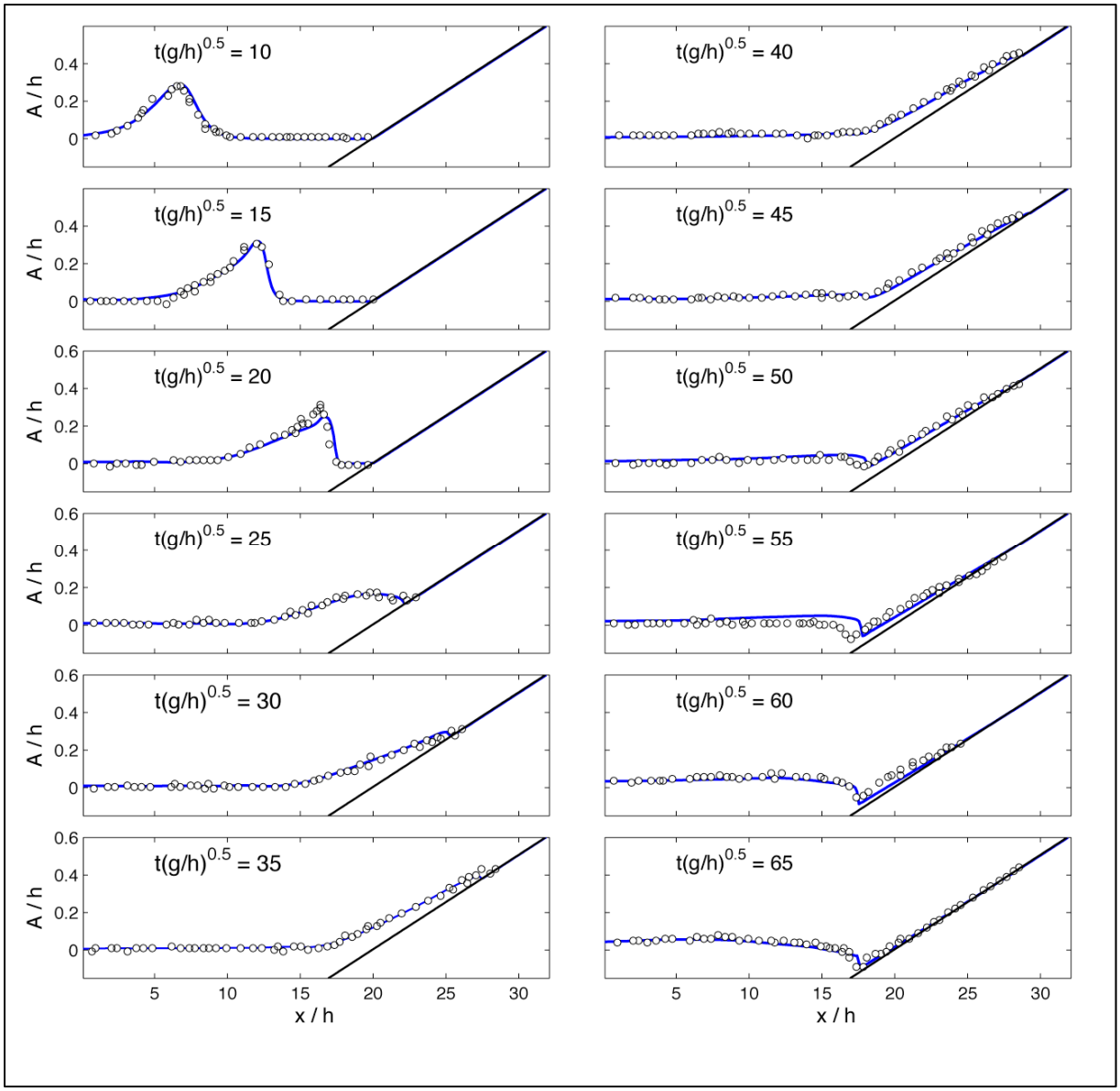

Figure 11-3: Free surface profiles of solitary wave transformation on a 1:19.85 simple beach with A/h = 0.3 and Δx/h = 0.125. Solid lines and circles denote BOSZ and measured data.

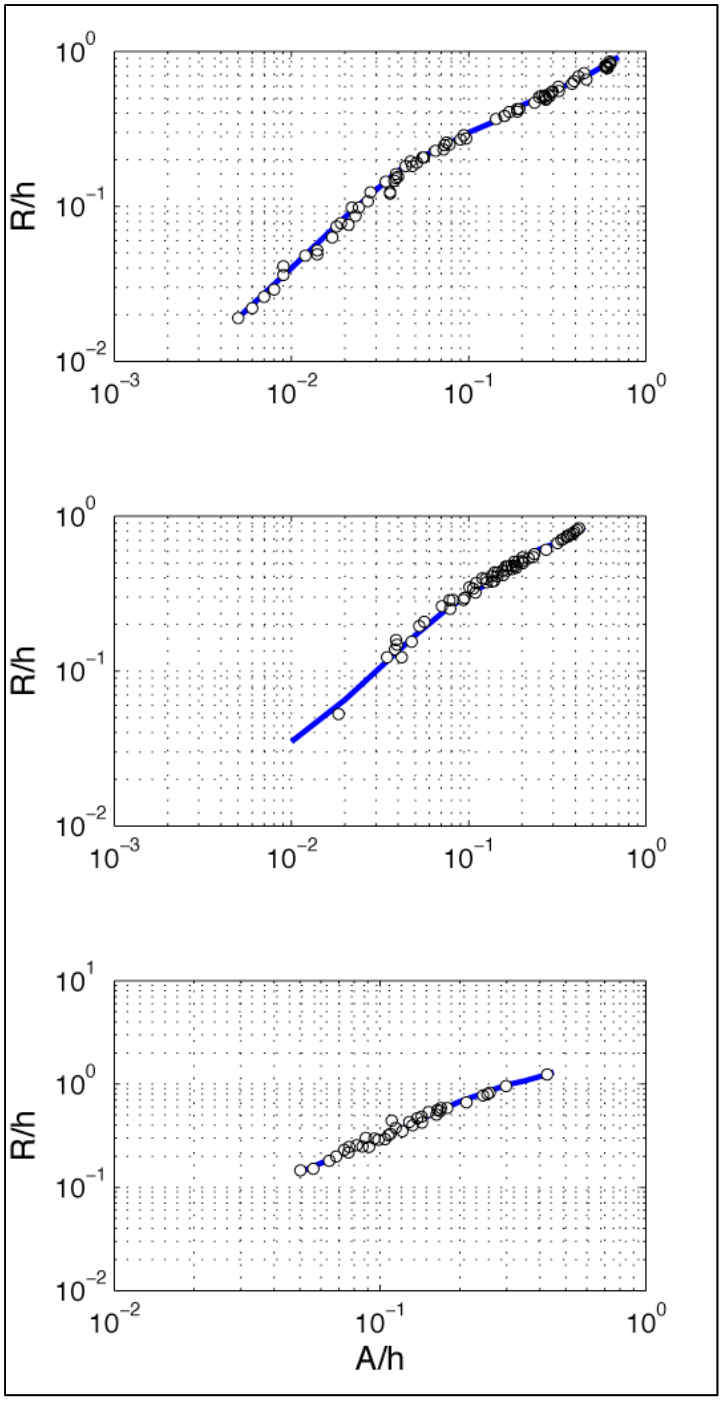

Figure 11-4: Solitary wave runup on a simple beach. (a) 1:19.85 (Synolakis, 1987). (b) 1:15 (Li and Raichlen, 2002). (c) 1:5.67 (Hall and Watts, 1953). Solid lines (blue), and circles denote computed and measured data.

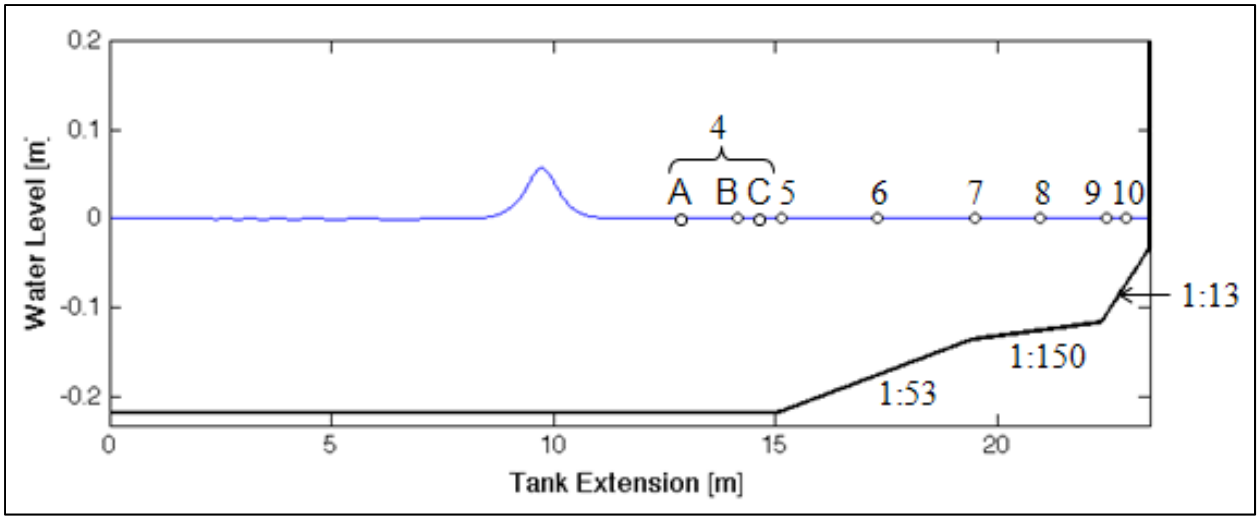

Figure 11-5: Definition sketch of BP2: Solitary wave on a composite beach. Circles denote wave gauge locations.

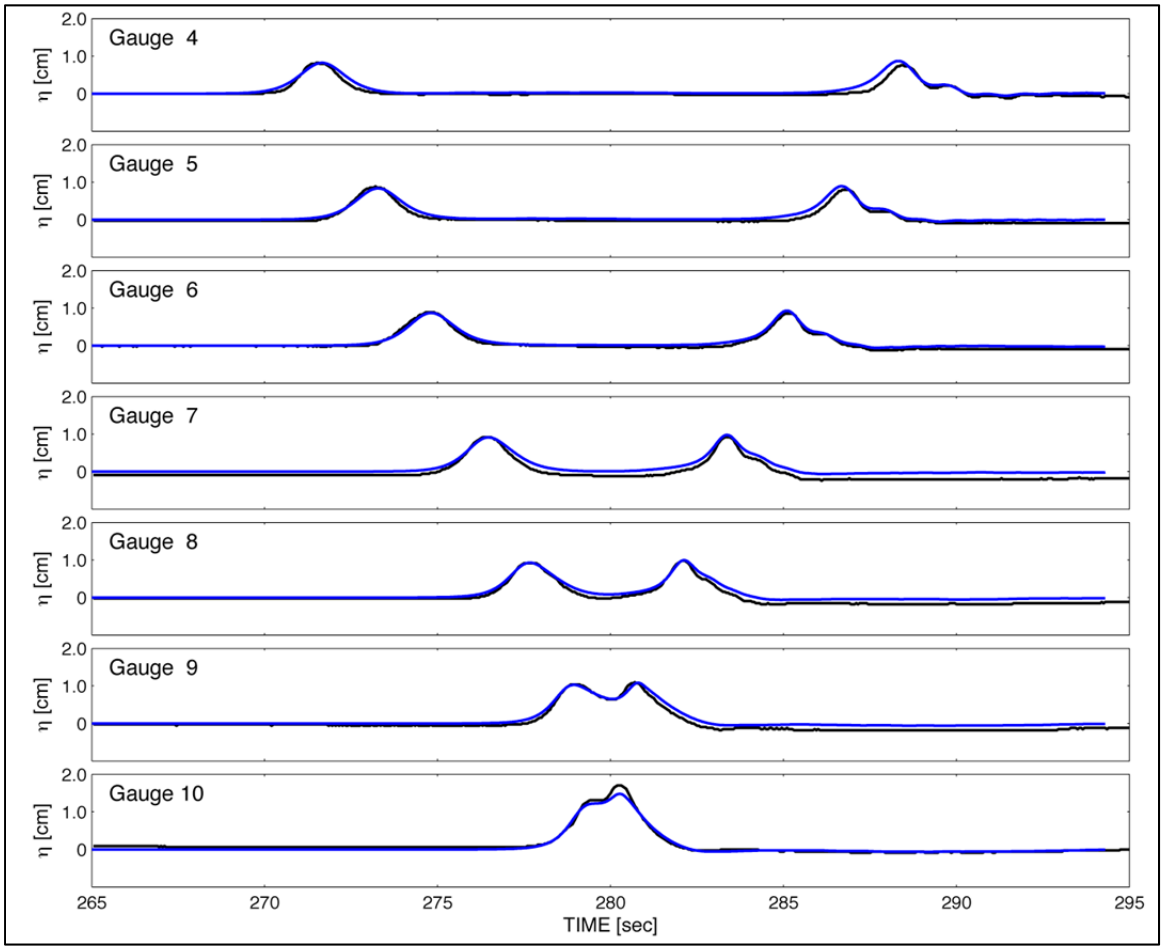

Figure 11-6: Solitary wave on a composite beach, BP2, case A. (blue) denotes solution from BOSZ. (black) indicates laboratory data from Briggs et al. (1996).

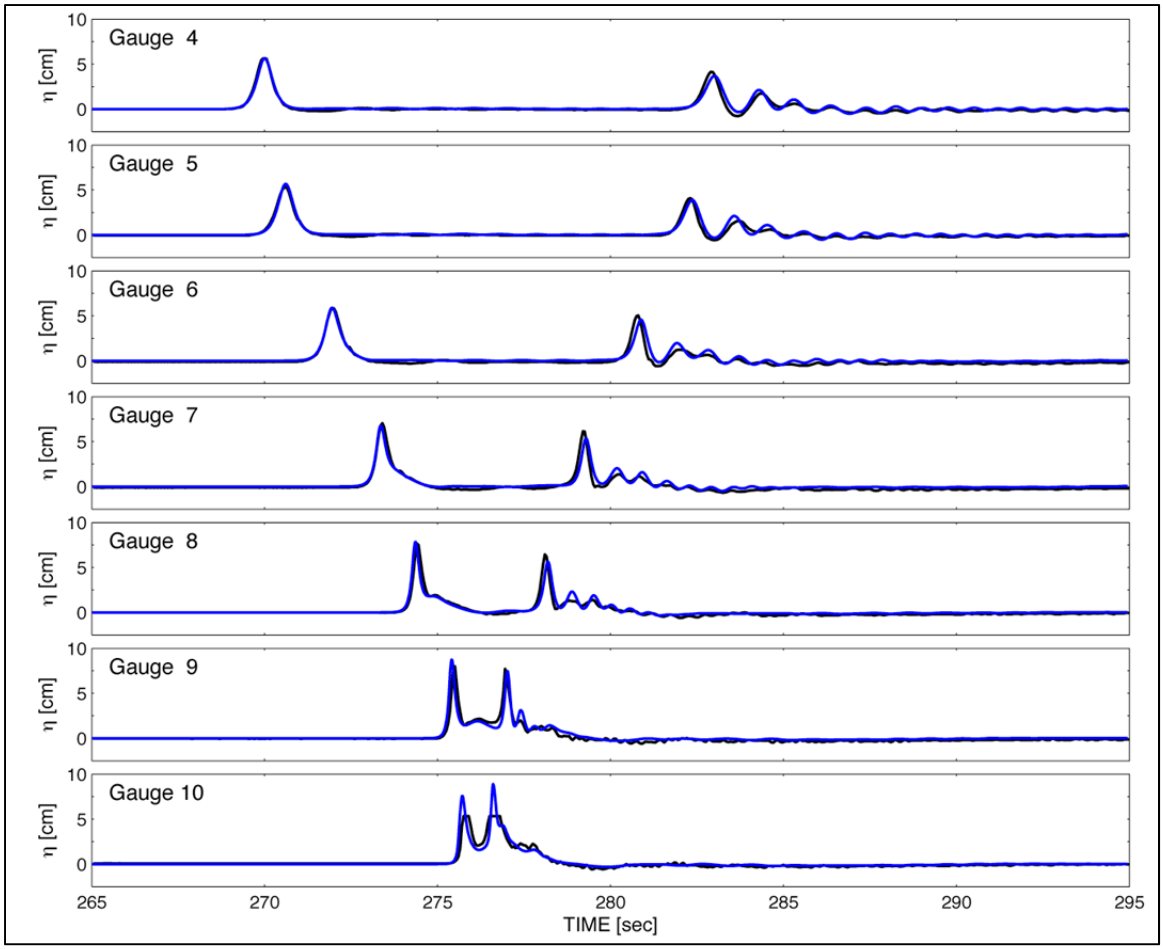

Figure 11-7: Solitary wave on a composite beach, BP2, case B. (blue) denotes solution from BOSZ. (black) indicates laboratory data from Briggs et al. (1996).

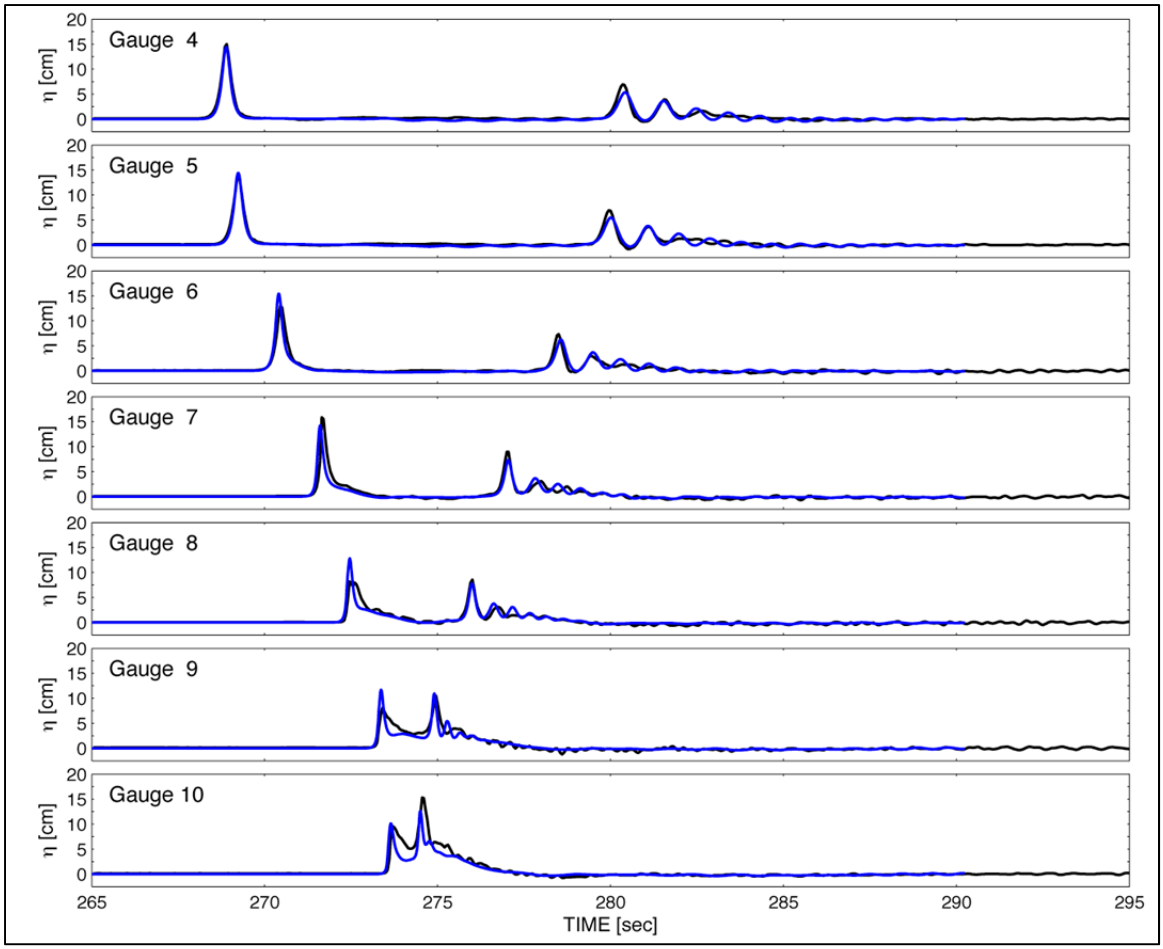

Figure 11-8: Solitary wave on a composite beach, BP2, case C. (blue) denotes the solution from BOSZ. (black) indicates laboratory data from Briggs et al. (1996).

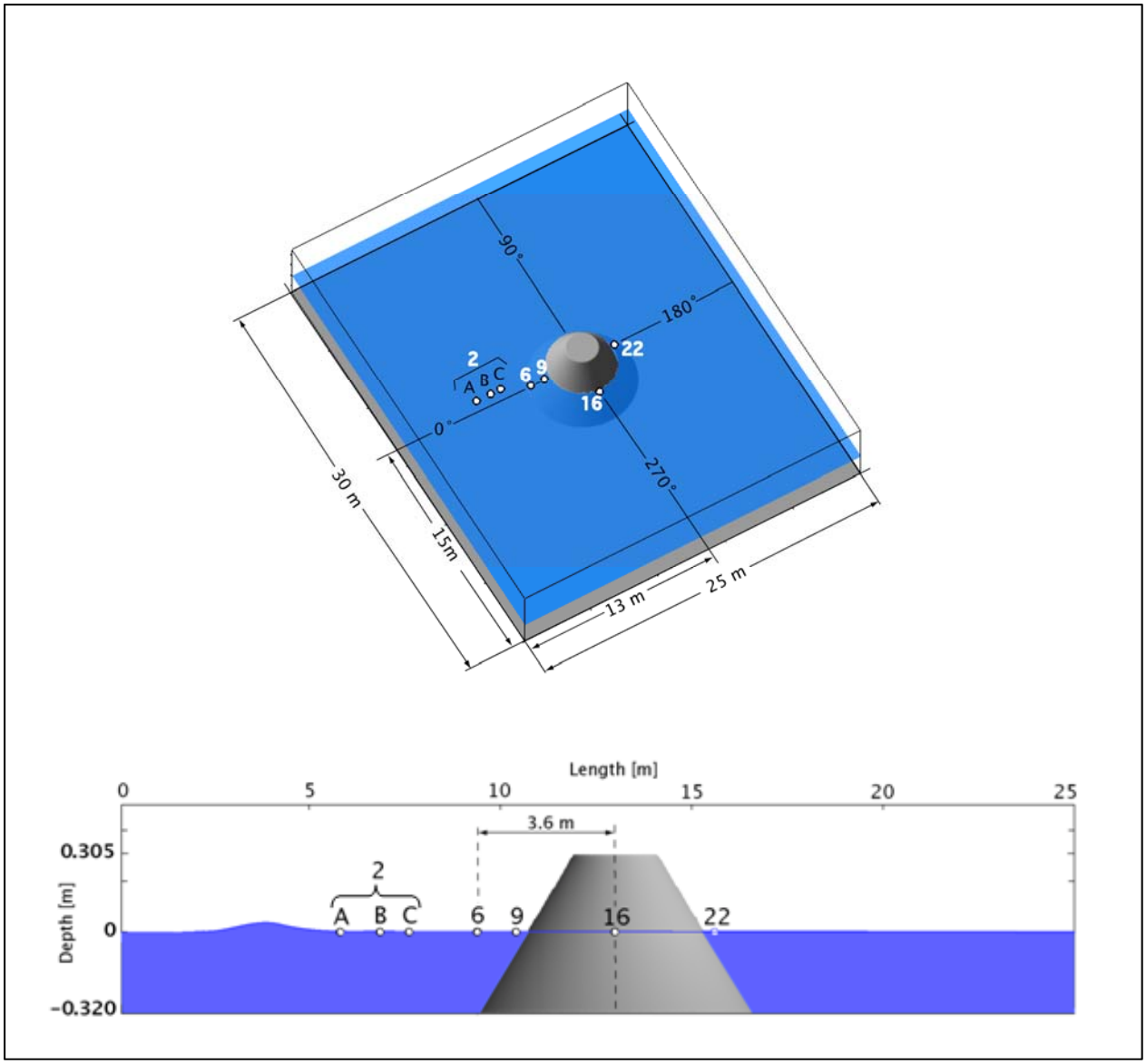

Figure 11-9: Schematics of the conical island laboratory experiment, BP6. (Top) Perspective view. (Bottom) Cross-sectional view along centerline. Circles denote gauge locations.

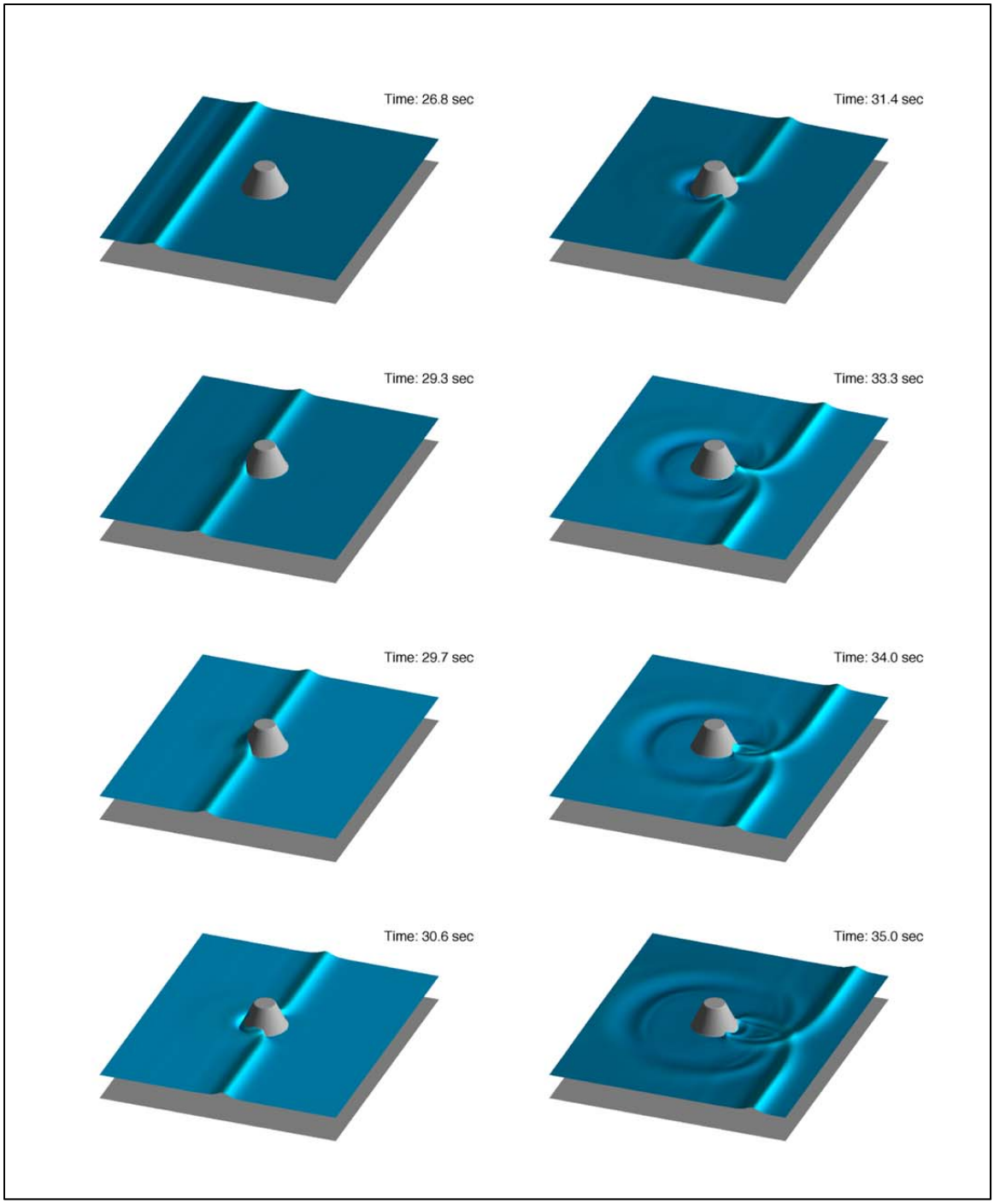

Figure 11-10: Wave transformation around the conical island, BP6 for A/h = 0.181.

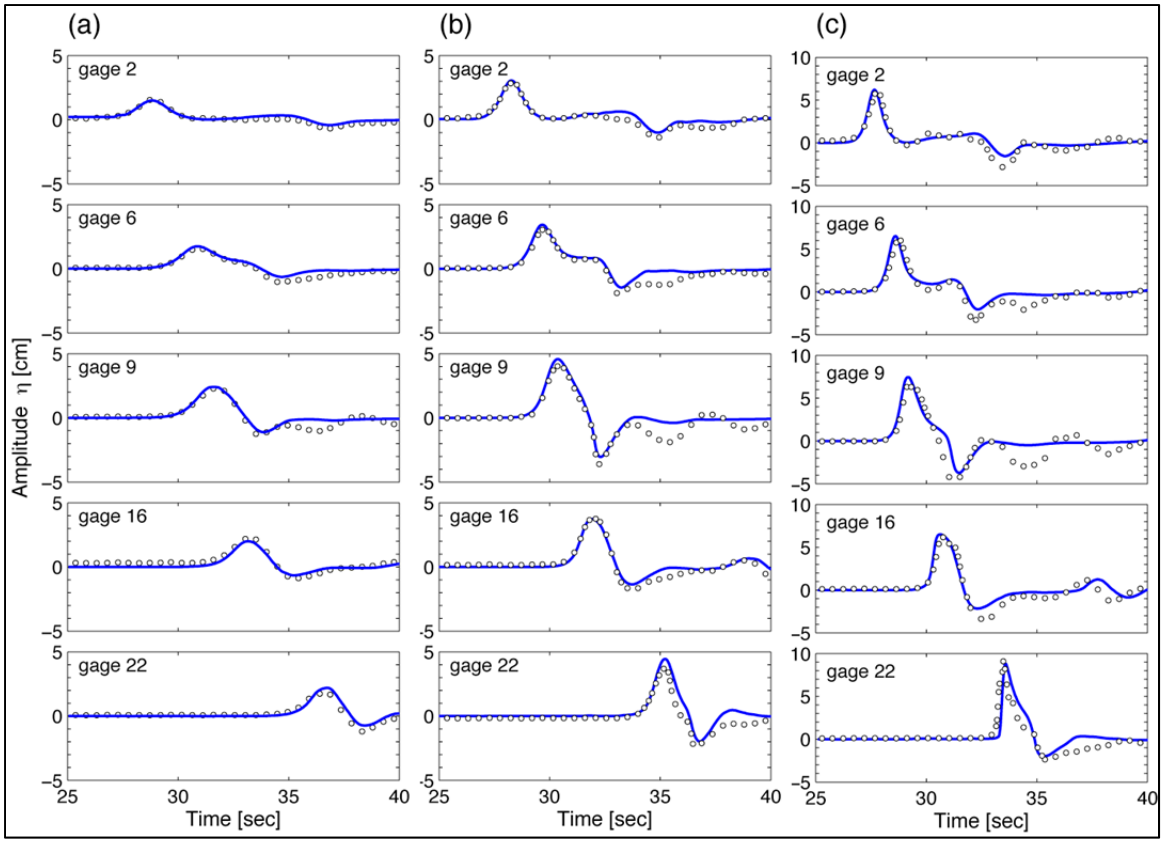

Figure 11-11: Free surface profiles of wave transformation around the conical island, BP6. (a) A/h = 0.045; (b) A/h = 0.096; (c) A/h = 0.181. Solid lines and circles denote computed and measured data.

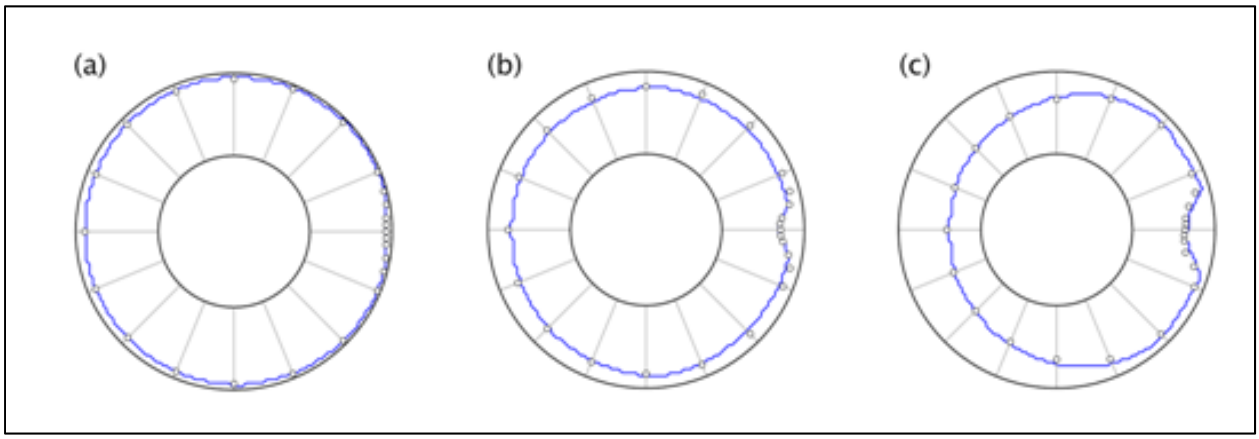

Figure 11-12: Maximum inundation around the conical island, BP6. (a) A/h = 0.045; (b) A/h = 0.096; (c) A/h = 0.181. Solid lines and circles denote computed and measured data.

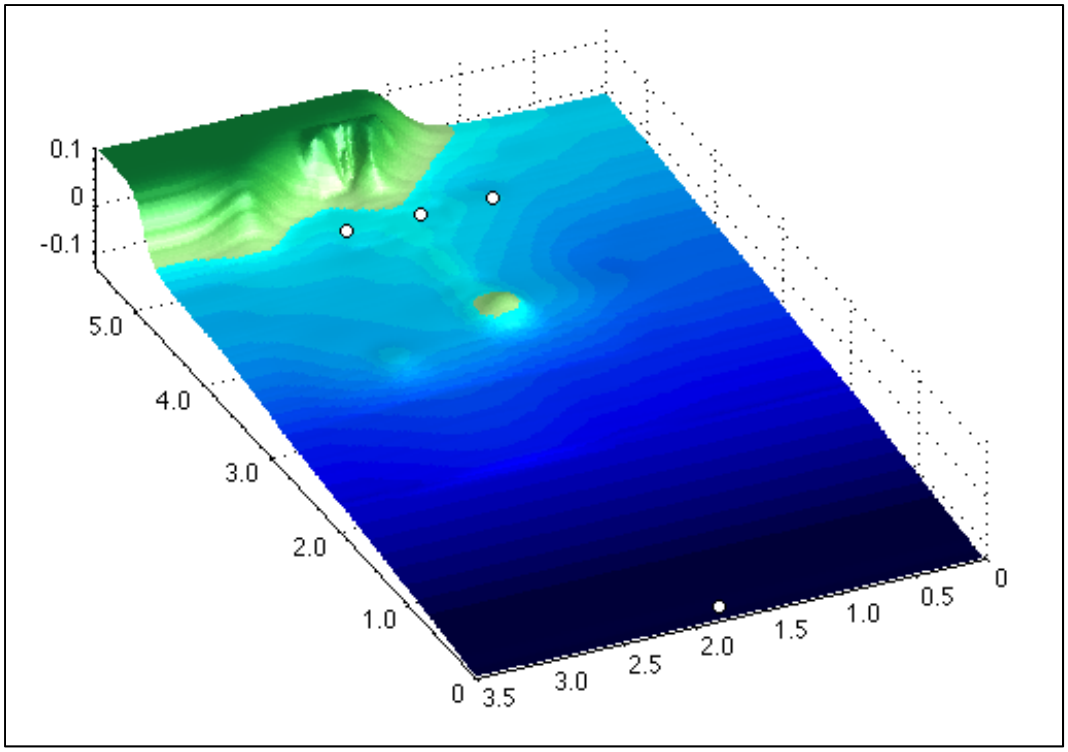

Figure 11-13: Bathymetry of the Monai valley experiment, BP7. White circles denote wave gauge locations. The gauge at the lower boundary is used as a control for the wave input (see Figure 11-14 below).

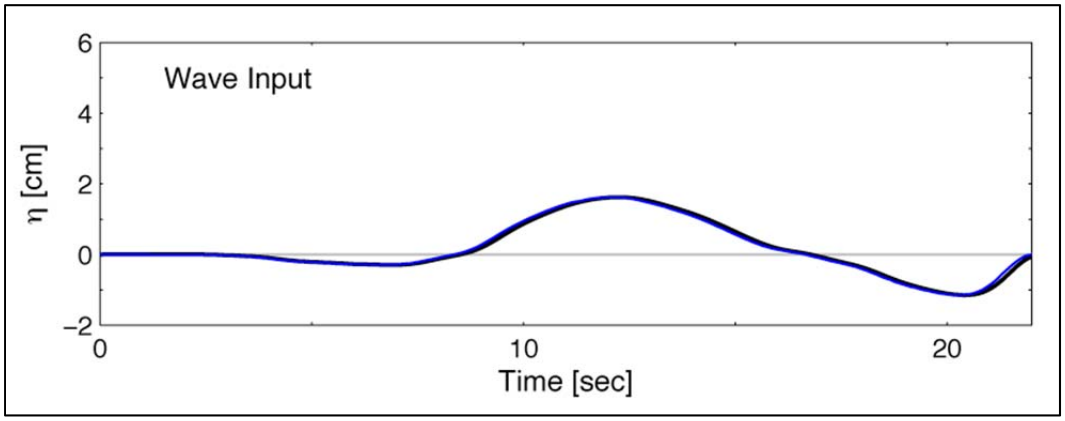

Figure 11-14: Initial N-wave profile near the left boundary, BP7. (blue) denotes solution from BOSZ. (black) indicates initial wave profile from Matsuyama and Tanaka (2001).

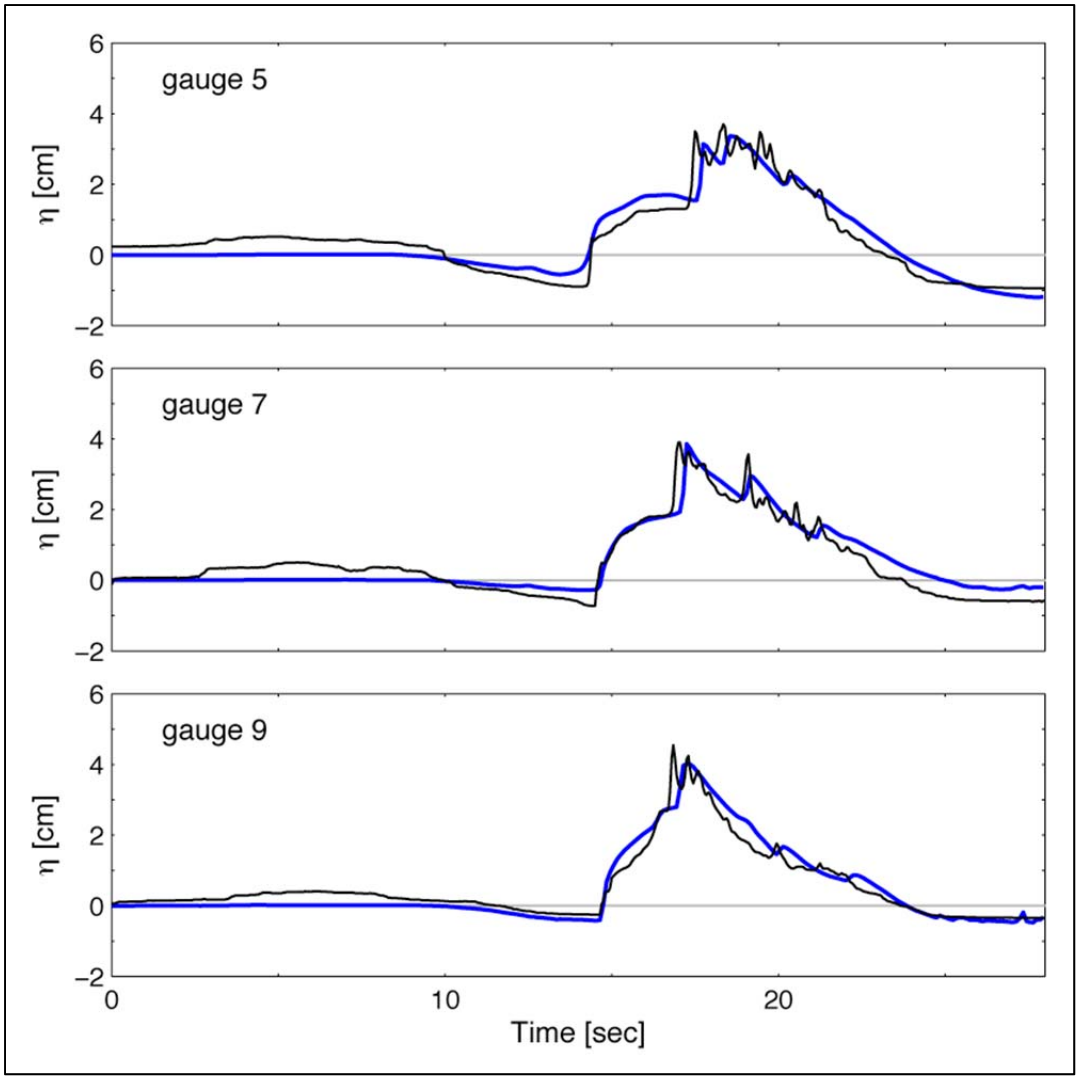

Figure 11-15: Time series of free surface elevation in Monai valley experiment, BP7. (blue) denotes solution from BOSZ. (black) indicates experimental data from Matsuyama and Tanaka (2001).

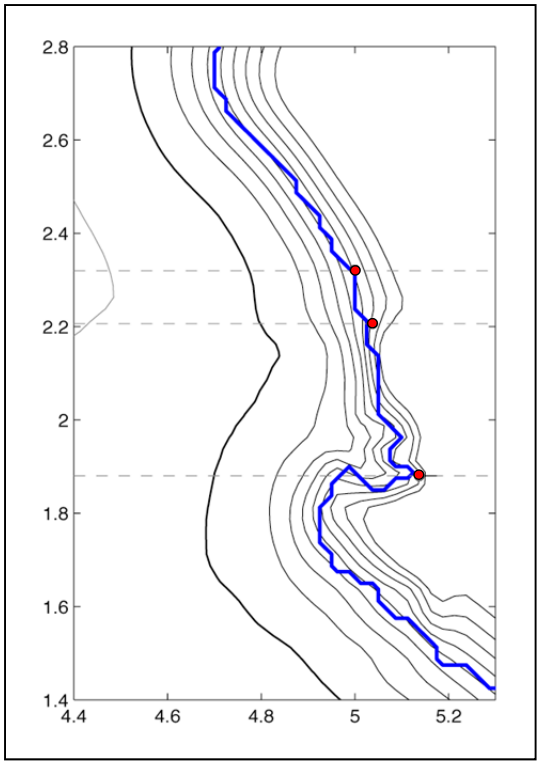

Figure 11-16: Maximum inundation in Monai valley experiment, BP7. (Blue) denotes solution from BOSZ. (Red) circles indicate observed inundation from Matsuyama and Tanaka (2001). Black lines are topographic contours at 1.25 cm intervals.

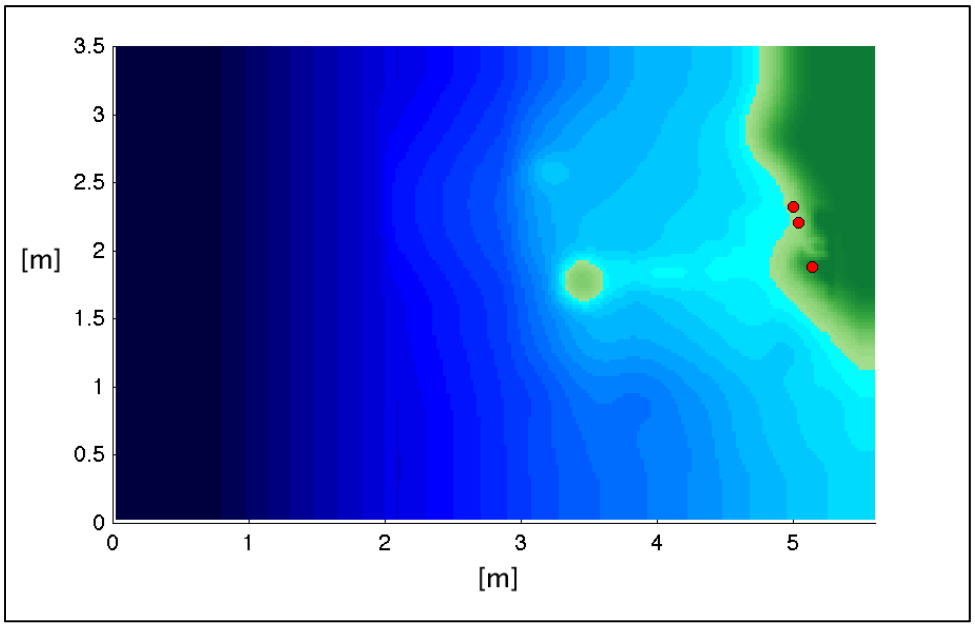

Figure 11-17: Maximum inundation in Monai valley experiment, top view, BP7. (Red) circles denote locations of observed inundation from Figure 11-16.

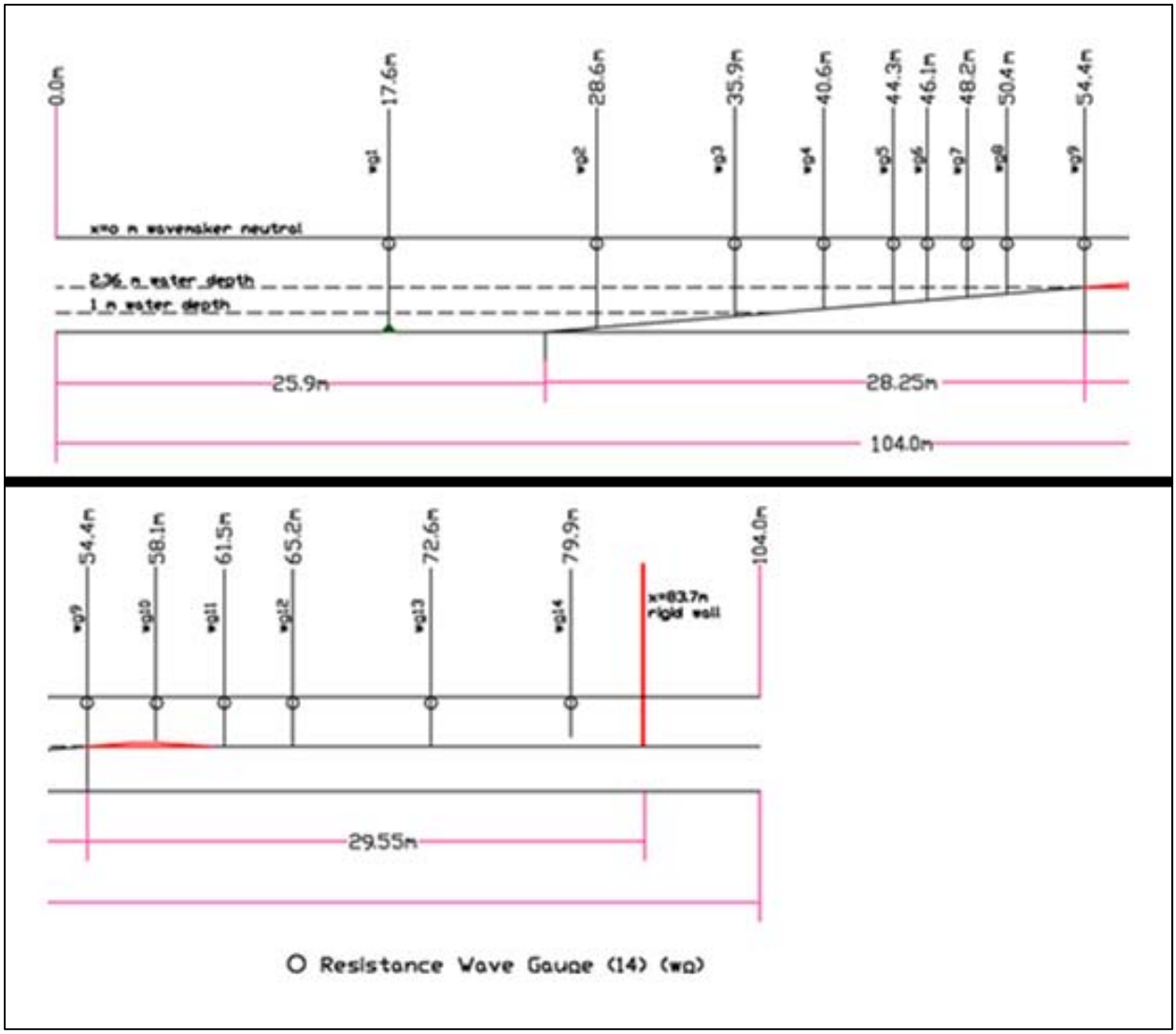

Figure 11-18: ISEC BM1 test. Two-dimensional reef model of 1:12 slope in the Large Wave Flume at Oregon State University (folded into two rows at the 28.25 m measurement point for better visibility). Circles and vertical lines indicate wave gauge locations. The water level in the Benchmark test case is 2.5 m resulting in a water depth of 0.136 m over the reef flat. The reef crest (red trapezoid) is 1.25 m long and rises 0.201 m above the reef flat (exposed by 0.065 m), with a 1:12 offshore and a 1:15 onshore slope. The plywood reef crest and the finished concrete tank are described by the same Manning coefficient of n = 0.014 m/s1/3. The tank is 3.66 m wide. A two-dimensional bathymetry file is provided in the benchmark package.

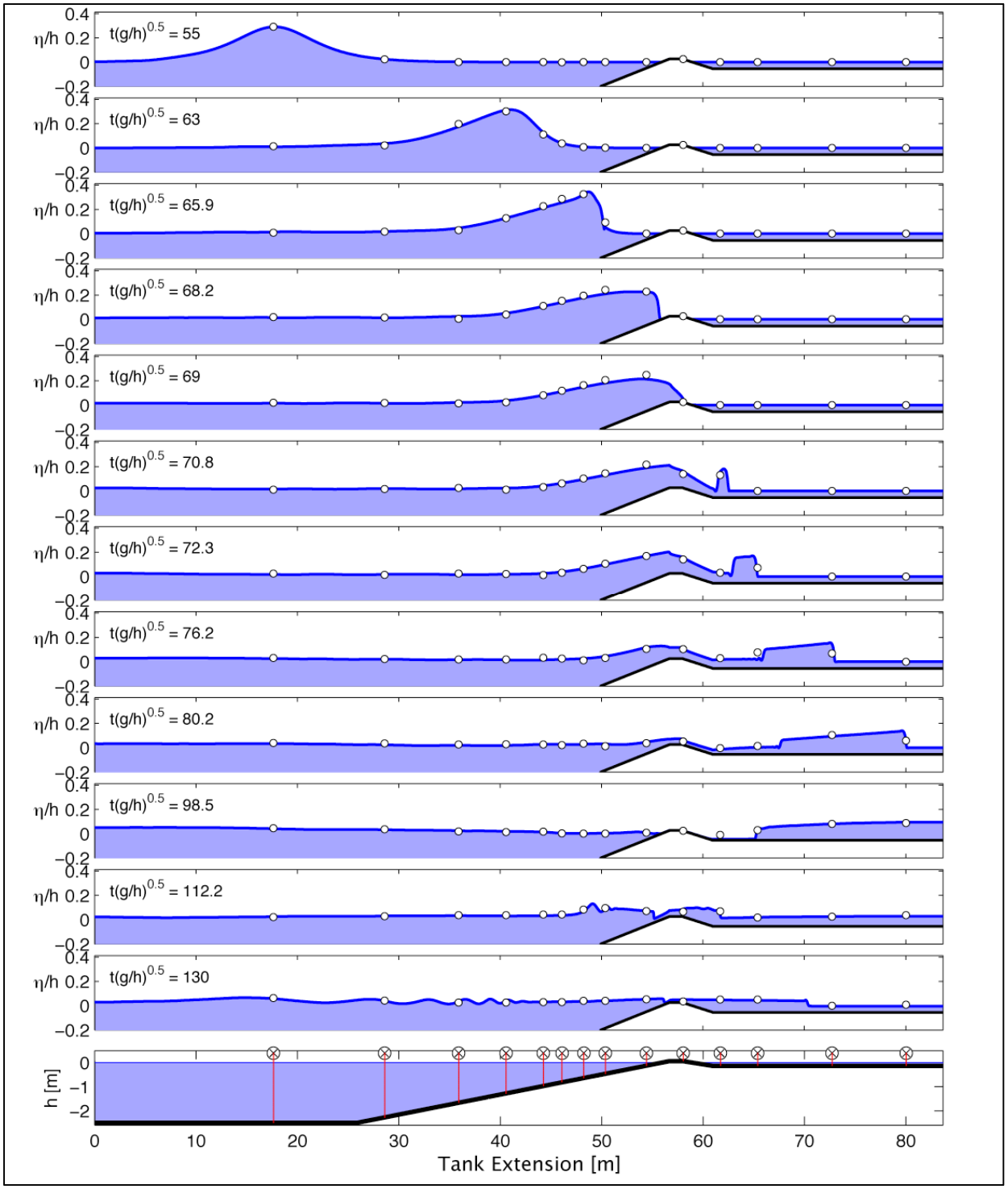

Figure 11-19: Snapshots of free surface profiles for propagation of solitary wave with A/h = 0.3 over 1:12 slope and exposed reef crest. Solid lines and circles denote computed and measured data. The experimental wave overturns describing a large air cavity. The depth-integrated numerical formulation approximates the 3-D process as a 2-D discontinuity with high accuracy.

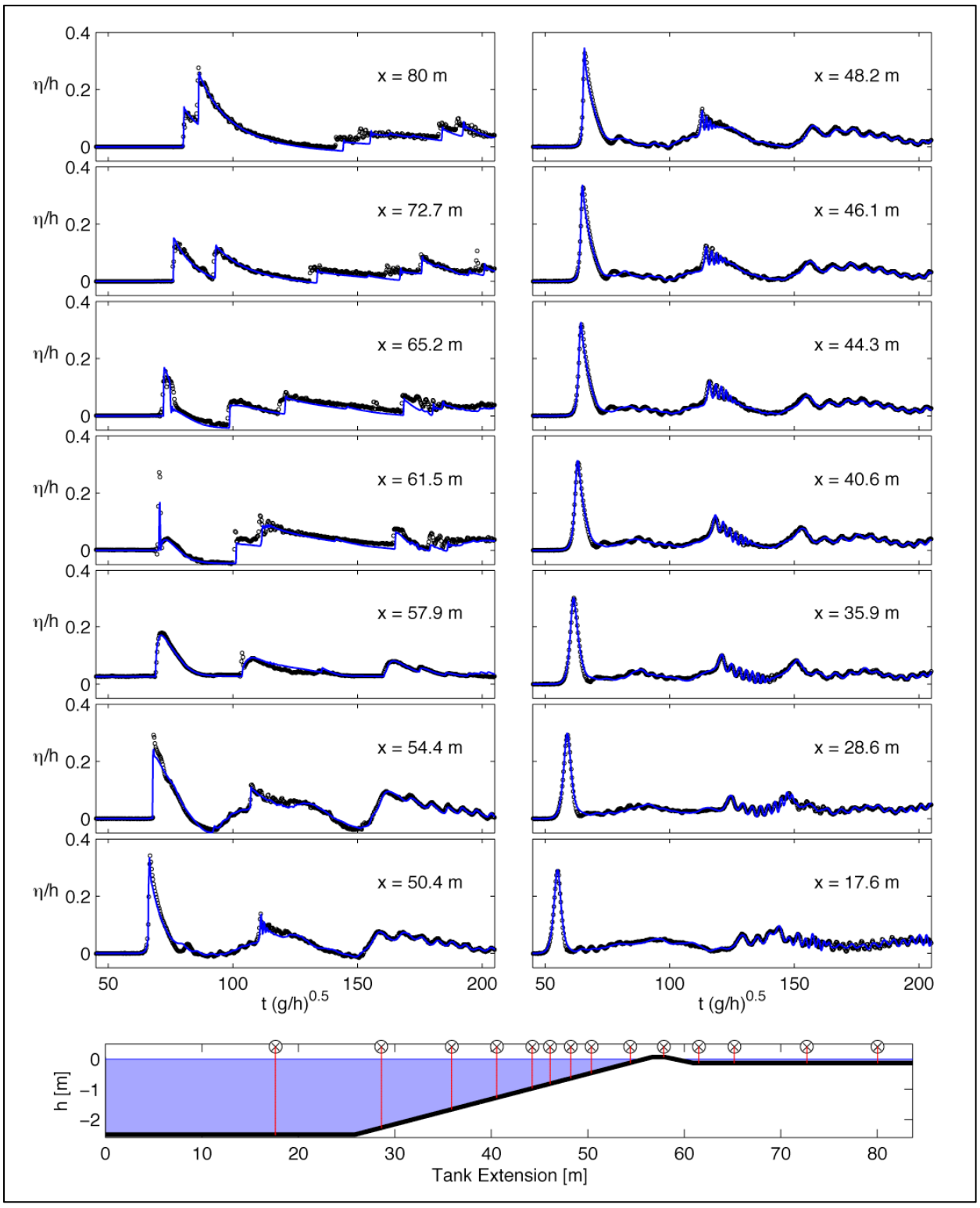

Figure 11-20: Time series of free surface at all wave gauges for propagation of solitary wave with A/h = 0.3 over 1:12 slope and exposed reef crest. Solid lines and circles denote computed and measured data. Notice the dispersive waves over the slope (30 – 50 m) generated from the reflected bore.

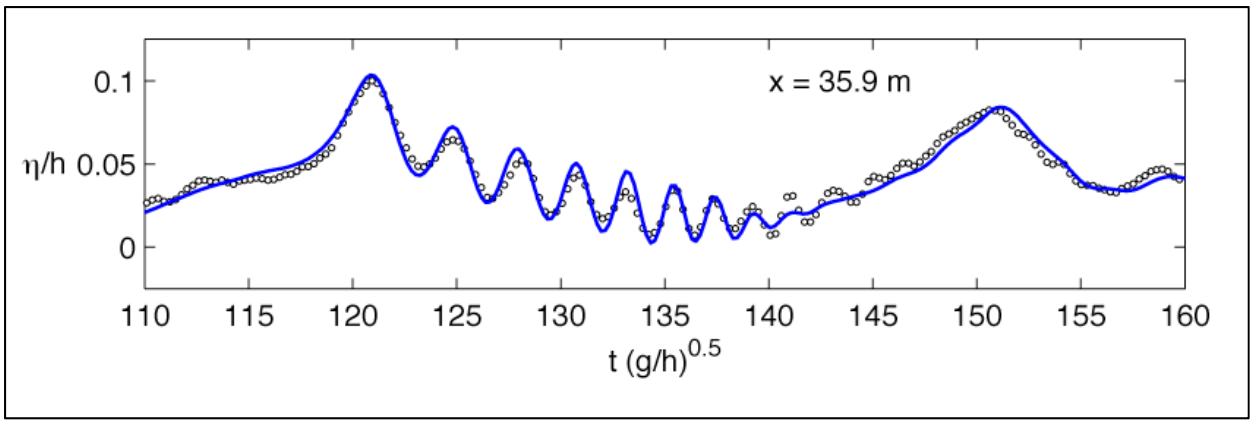

Figure 11-21: Close-up of time series of free surface at x = 35.9 m at beginning of 1:12 slope. Solid lines and circles denote computed and measured data. Signal showing dispersive waves generated from the reflected bore that propagated over the slope into the direction of the wavemaker.

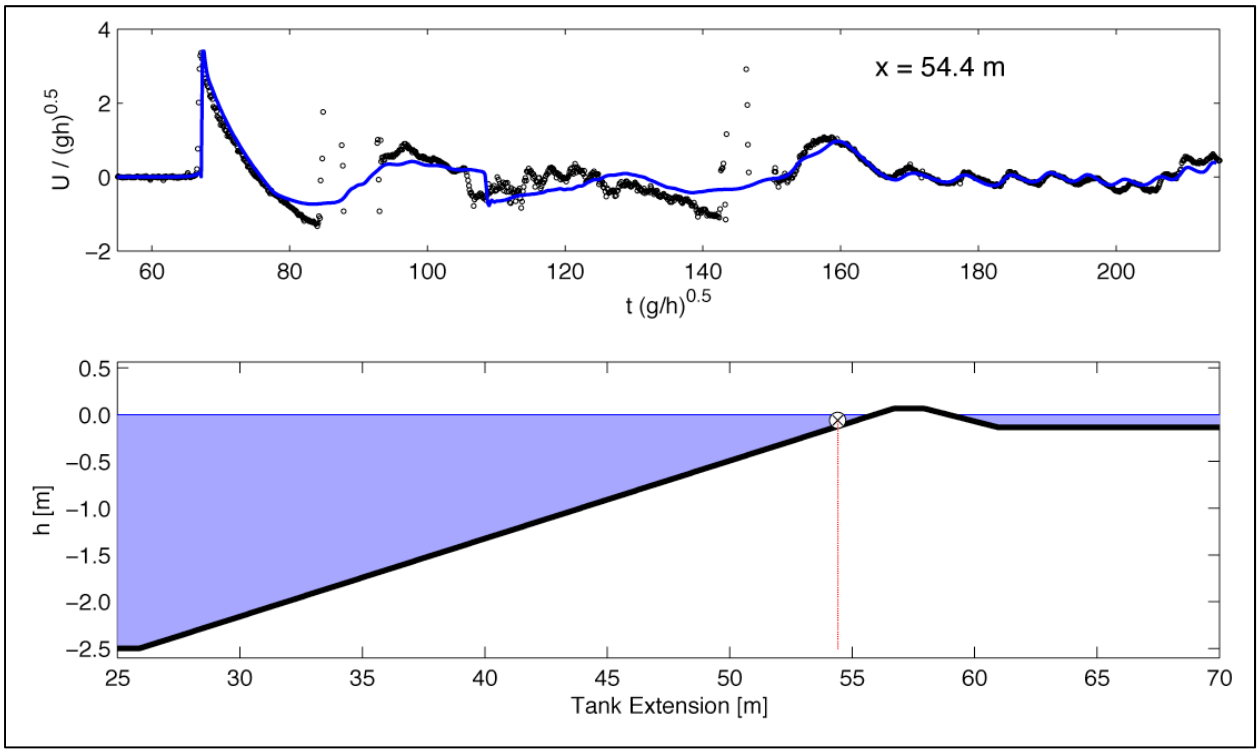

Figure 11-22: Time series of x-directed velocity at x = 54.4 m close to the reef crest. Solid lines and circles denote computed and measured data. The laboratory wave already overturned at this location causing strong supercritical flow.

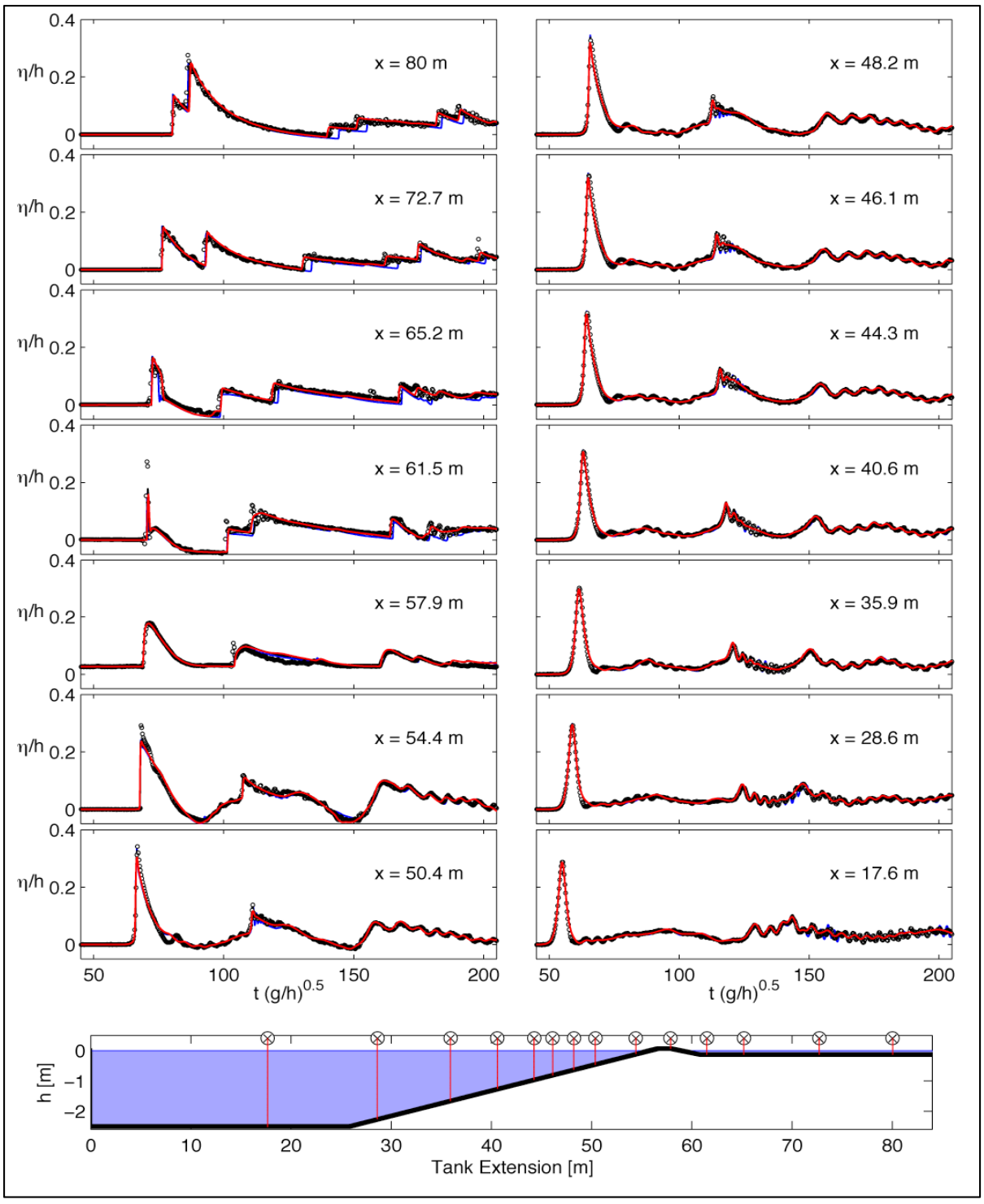

Figure 11-23: Time series of free surface at all wave gauges with different grid resolution and identical model setup.
(blue), BOSZ with Δx = 0.05 m
(black), BOSZ with Δx = 0.10 m
(red),BOSZ with Δx = 0.20 m

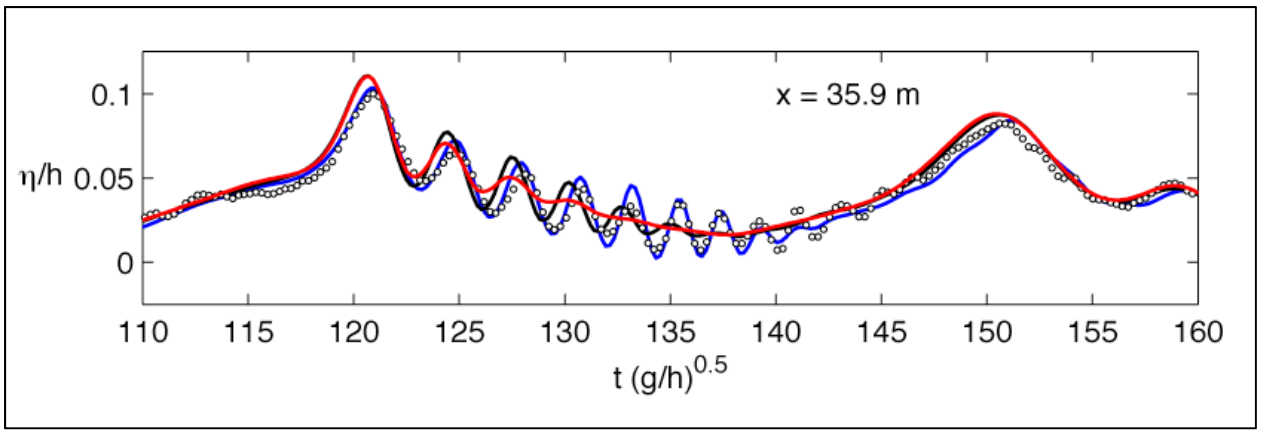

Figure 11-24: Close-up of time series of free surface at x = 35.9 m close to the reef crest with different grid resolution and identical model setup.
(blue), BOSZ with Δx = 0.05 m
(black), BOSZ with Δx = 0.10 m
(red),BOSZ with Δx = 0.20 m

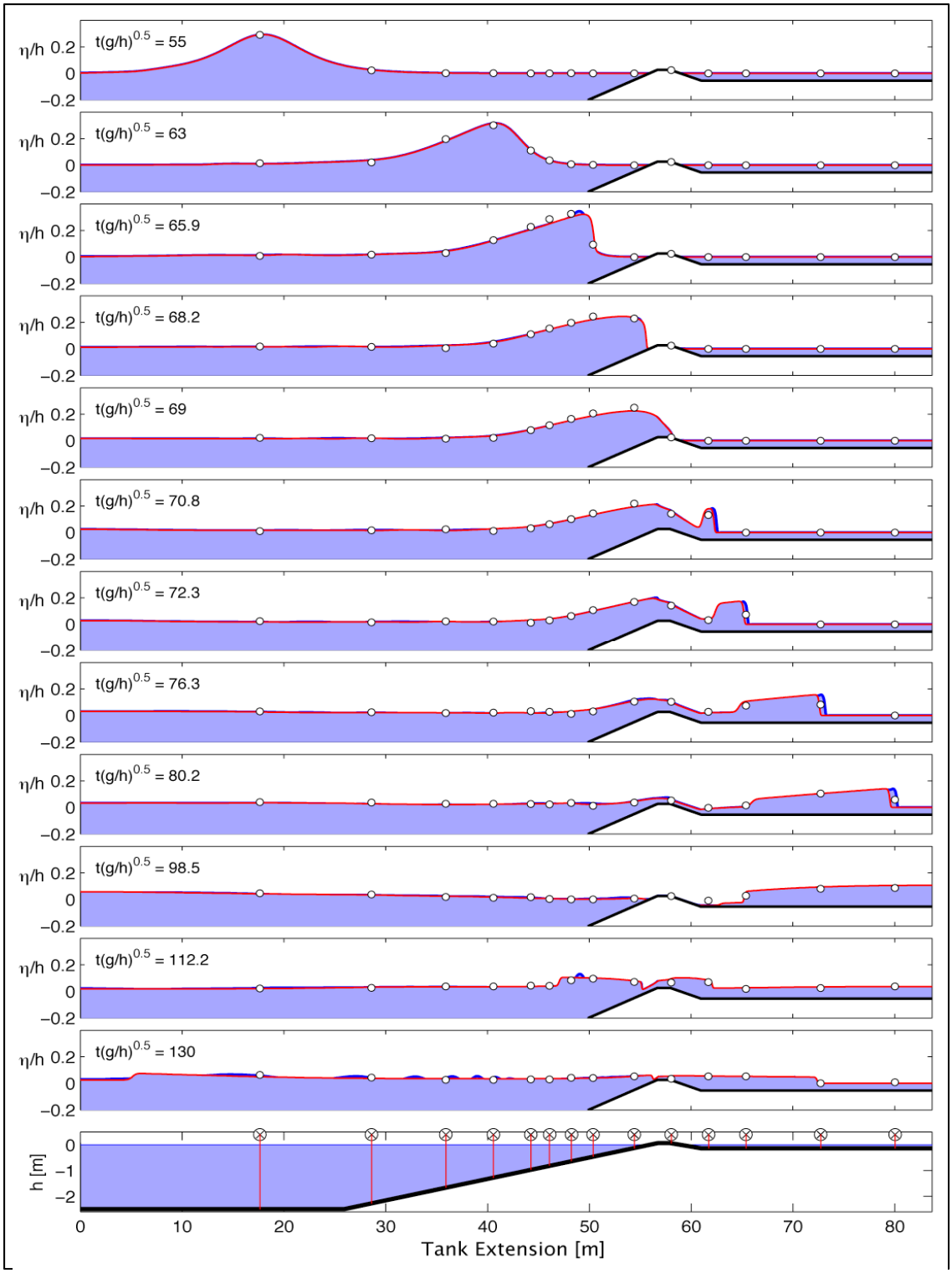

Figure 11-25: Snapshots of free surface profiles for propagation of solitary wave with A/h = 0.3 over 1:12 slope and exposed reef crest.
(blue), BOSZ dispersive,
(red), BOSZ hydrostatic (nonlinear shallow water equations)
after $t\sqrt{g/h} = 64.8$.

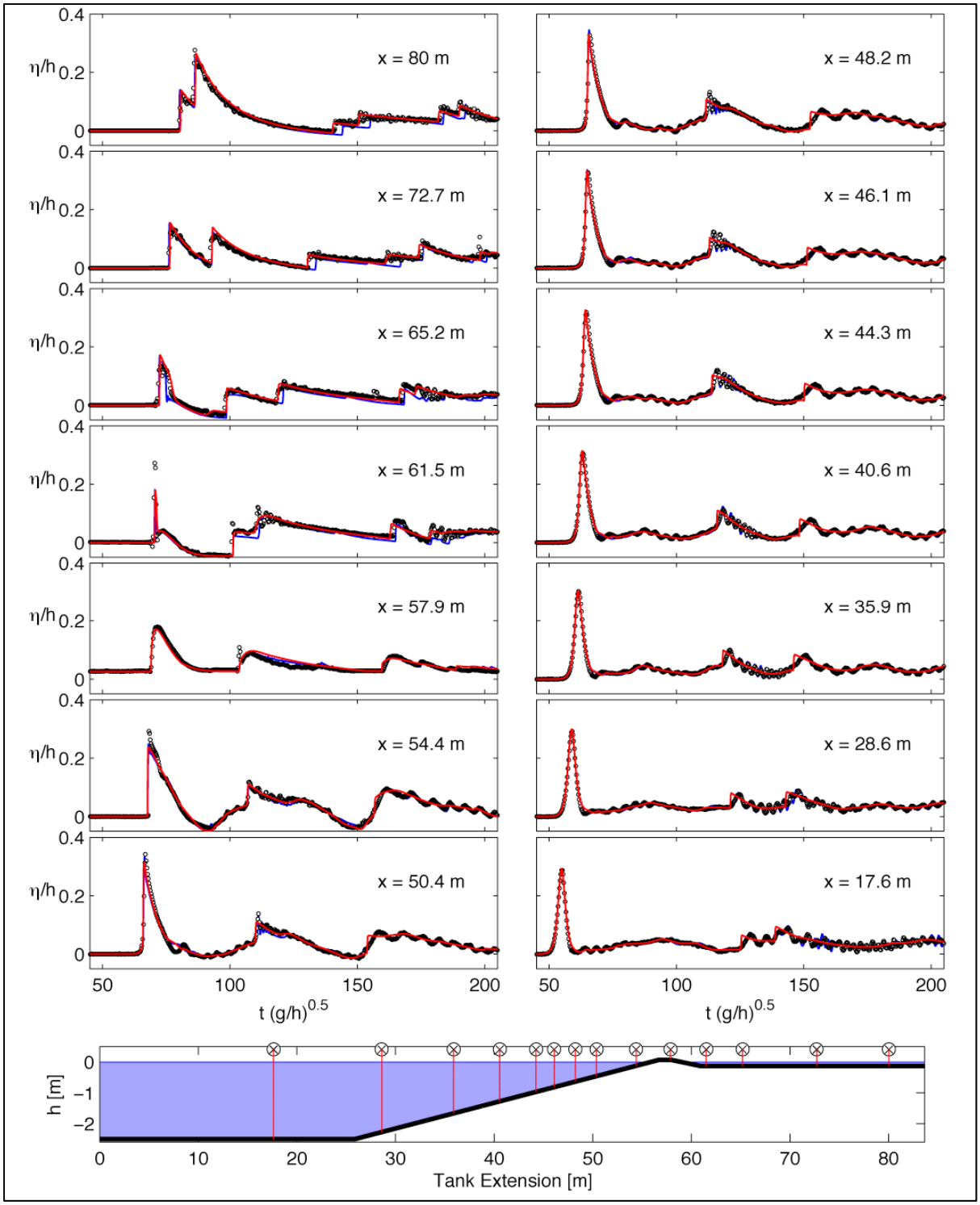

Figure 11-26: Time series of free surface at all wave gauges. Solutions from BOSZ with identical numerical scheme and input parameters for (blue), BOSZ dispersive, (red), BOSZ hydrostatic (nonlinear shallow water equations) after $t\sqrt{g/h} = 64.8$

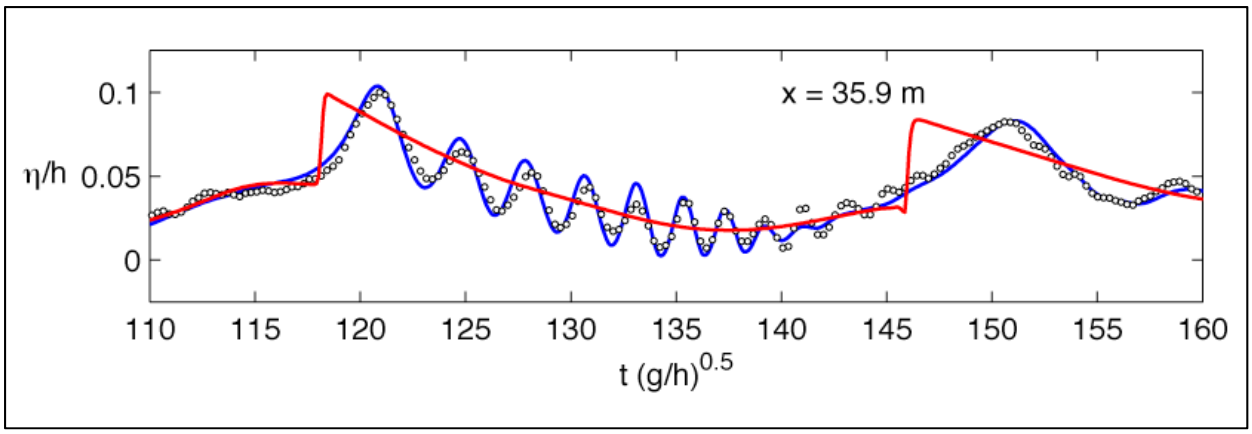

Figure 11-27: Close-up of time series of free surface at x = 35.9 m. Solutions from BOSZ with identical numerical scheme and input parameters for
(blue), BOSZ dispersive,
(red), BOSZ hydrostatic (nonlinear shallow water equations)
after $t\sqrt{g/h} = 64.8$.

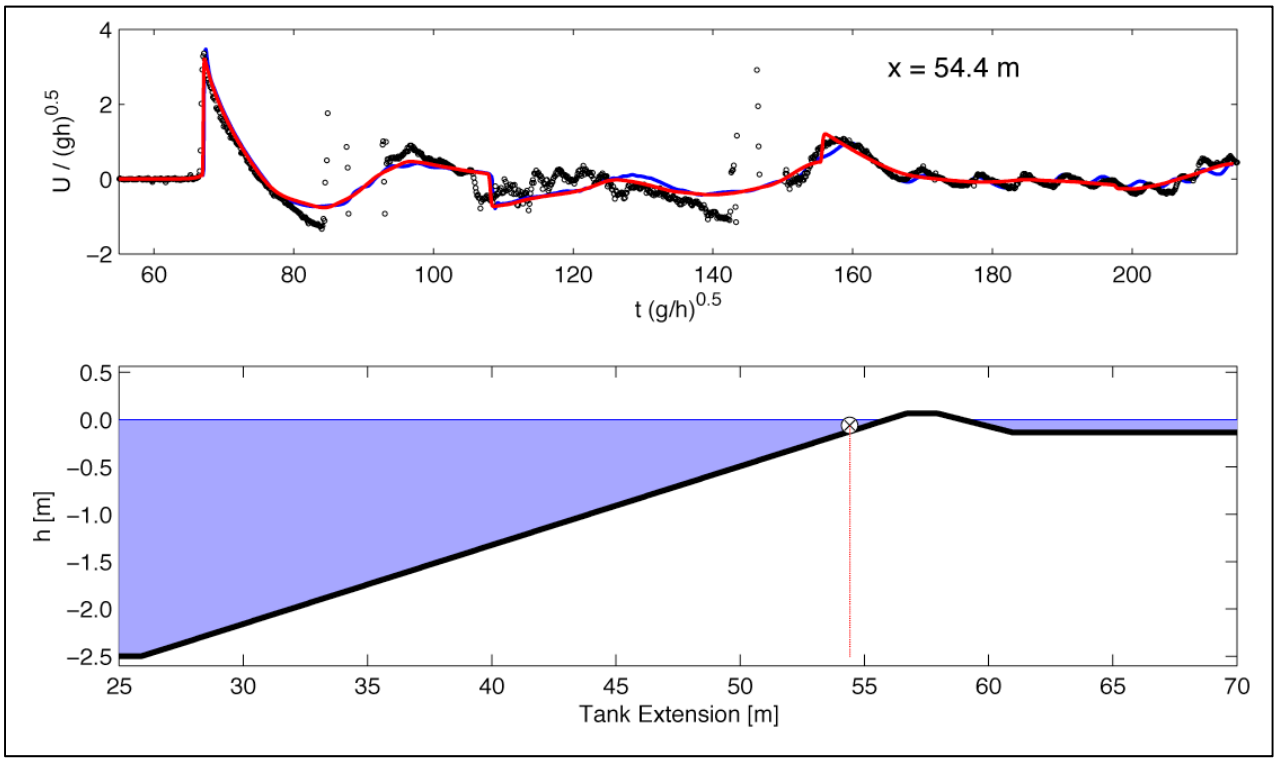

Figure 11-28: Time series of x-directed velocity at x = 54.4 m. Solutions from BOSZ with identical numerical scheme and input parameters for
(blue), BOSZ dispersive,
(red), BOSZ hydrostatic (nonlinear shallow water equations)
after $t\sqrt{g/h} = 64.8$.

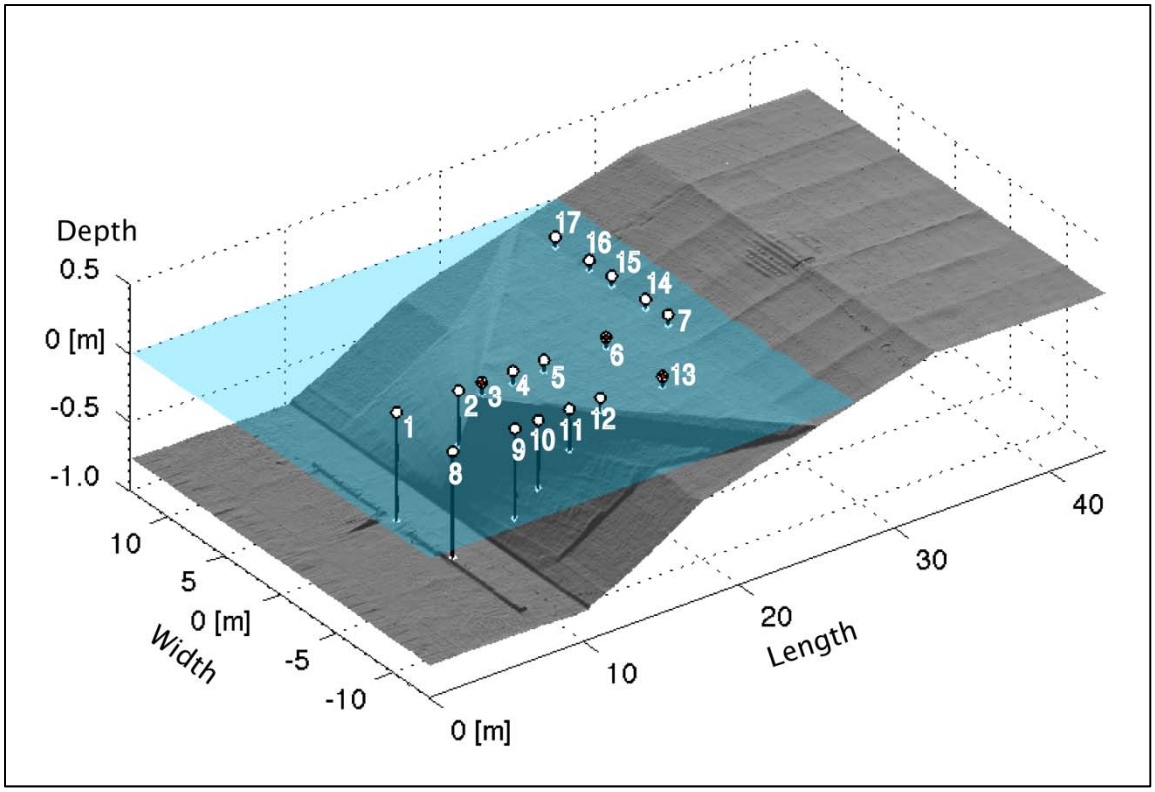

Figure 11-29: Perspective view of ISEC BM1 bathymetry from laser scan at original resolution of x = 5 cm. Circles denote wave gauge locations at free surface and corresponding location on tank bottom. Red crosses at gauges 3, 6, and 13 indicate positions of acoustic Doppler velocimeters for velocity measurements.

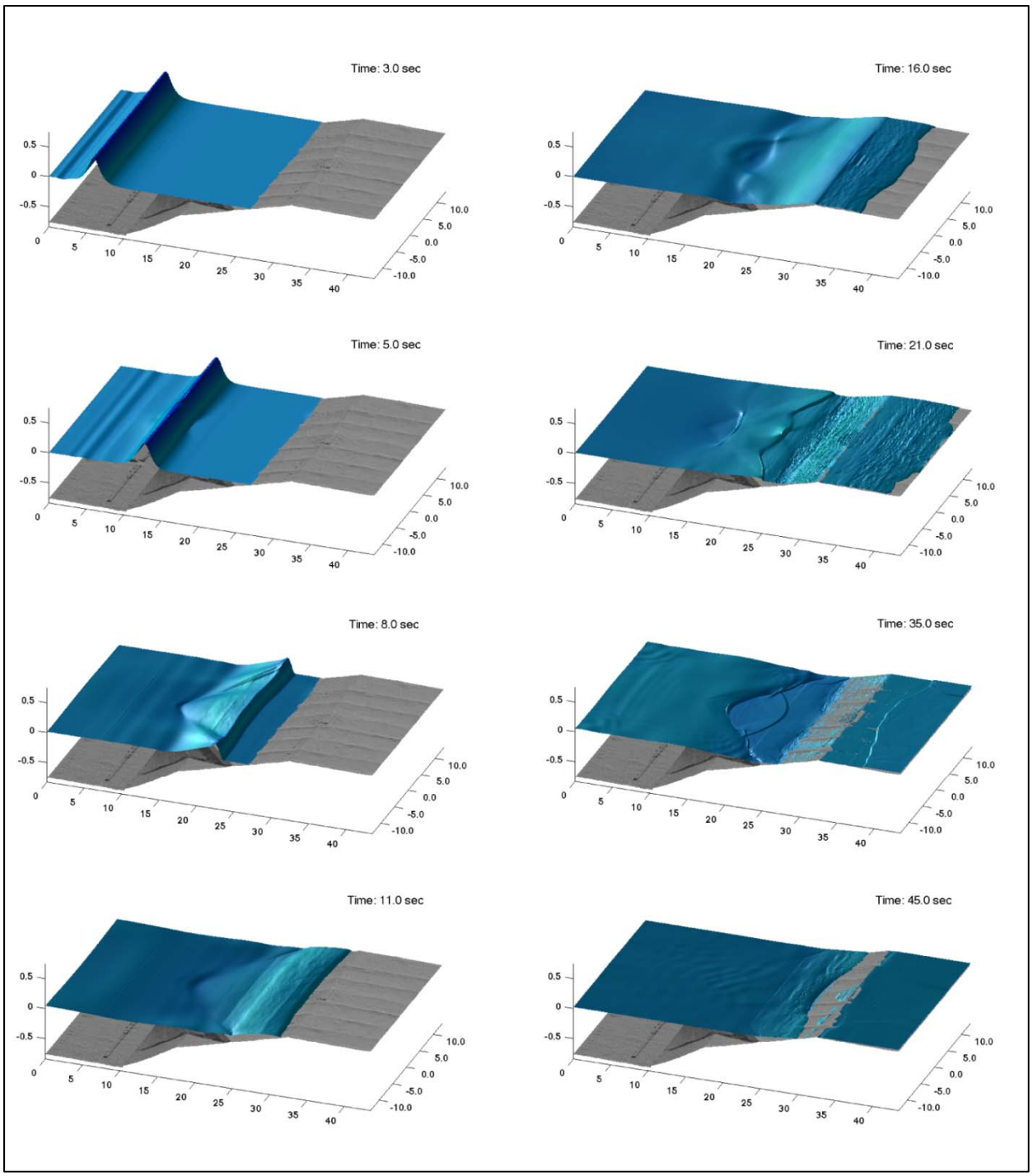

Figure 11-30: Snapshots of solitary wave transformation in ISEC BM1.

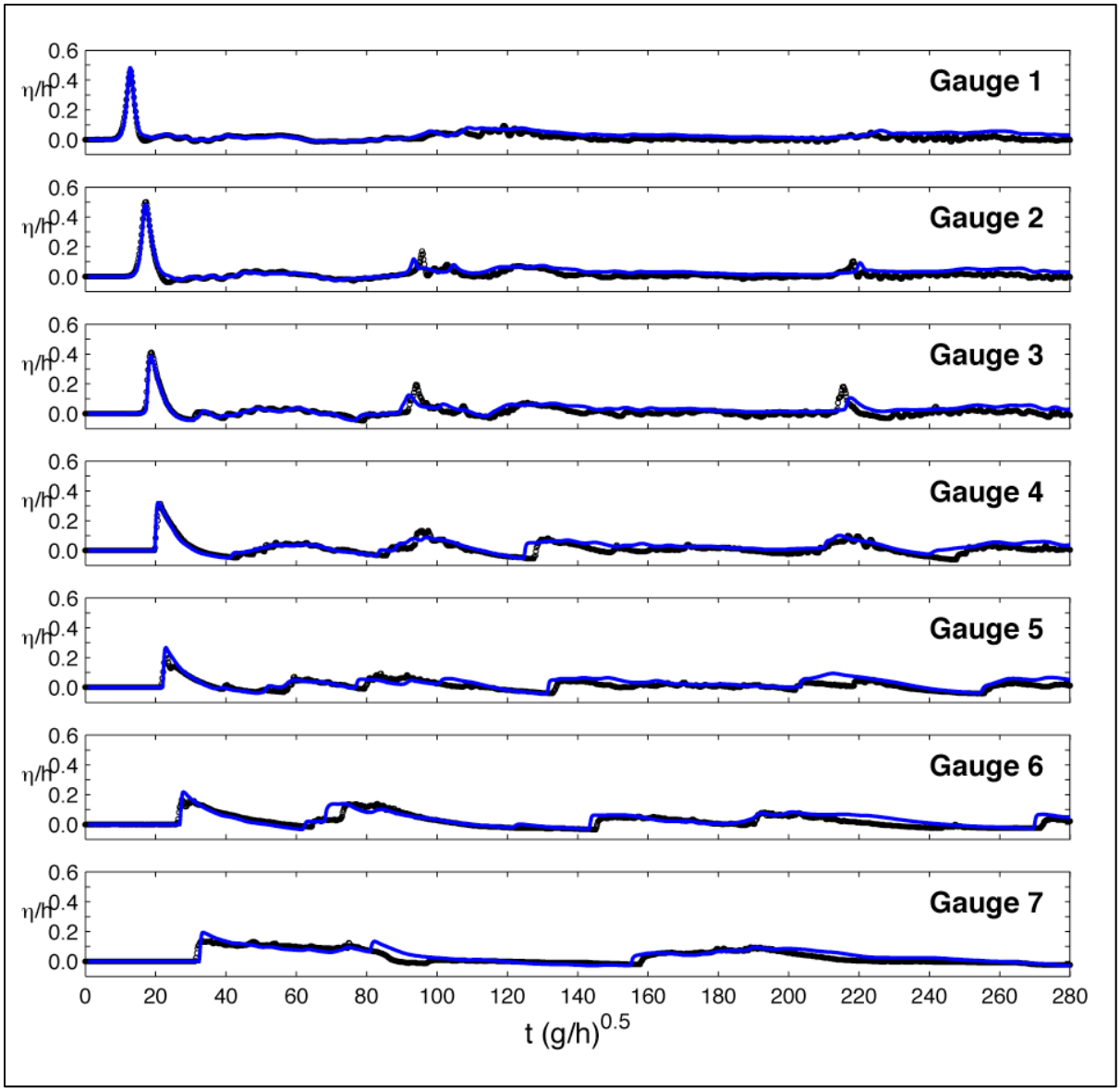

Figure 11-31: Time series of free surface profiles along basin centerline in ISEC BM1. Solid lines and circles denote computed and measured data.

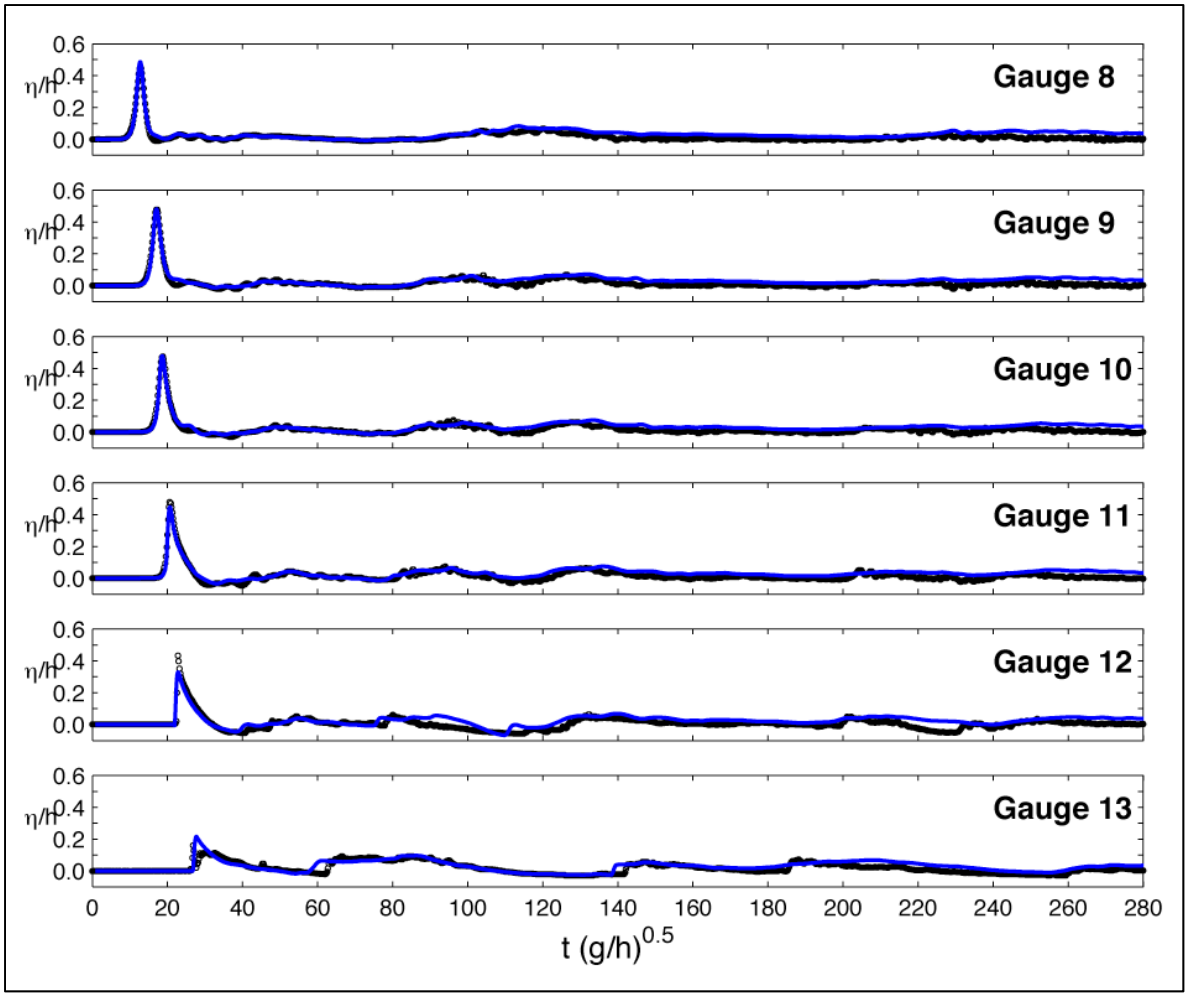

Figure 11-32: Time series of free surface profiles along transect at x = -5 m in ISEC BM1. Solid lines and circles denote computed and measured data.

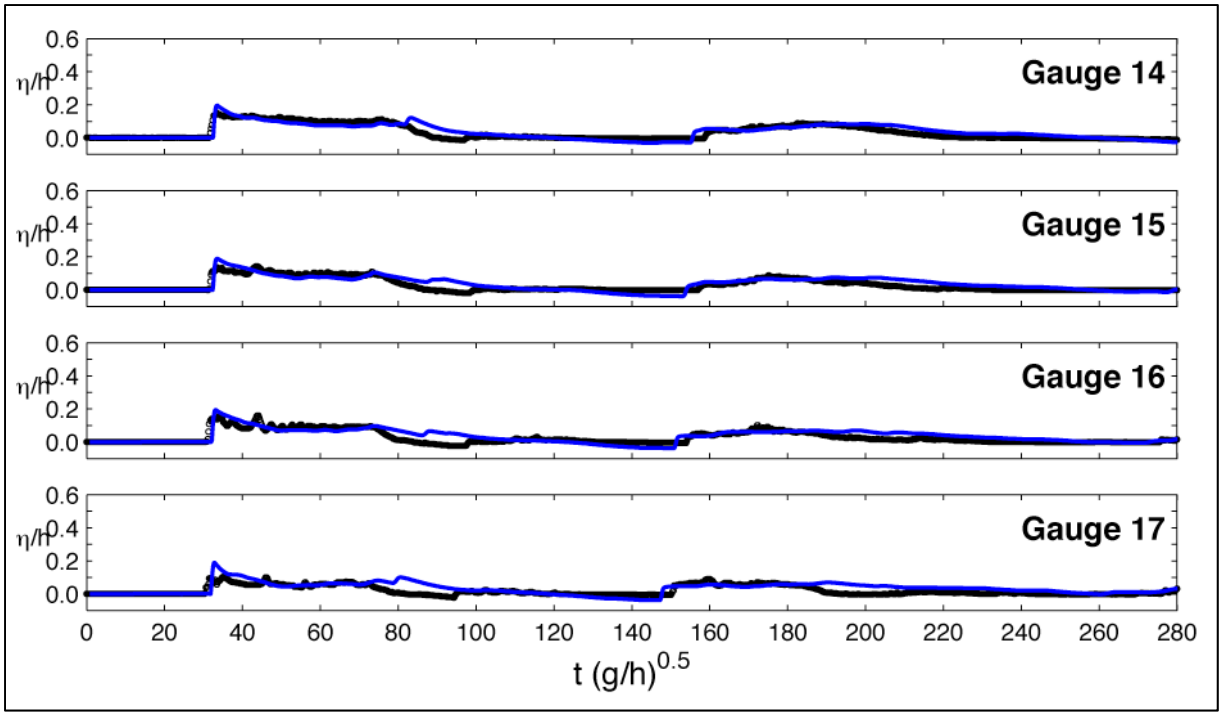

Figure 11-33: Time series of free surface profiles along alongshore transect in ISEC BM1. Solid lines and circles denote computed and measured data.

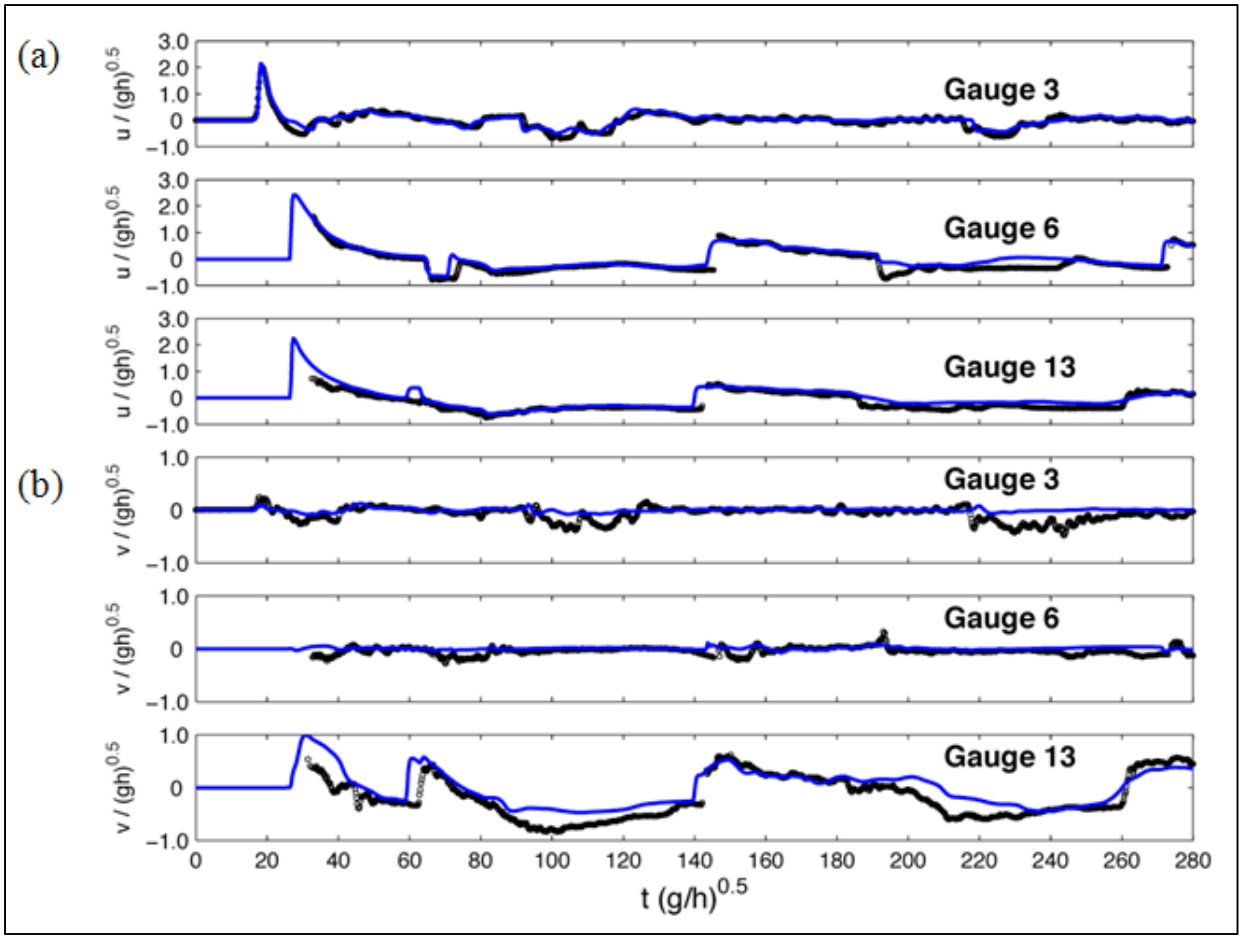

Figure 11-34: Time series of velocity in ISEC BM1. (a) Cross-shore component. (b) Alongshore component. Solid lines and circles denote computed and measured data.

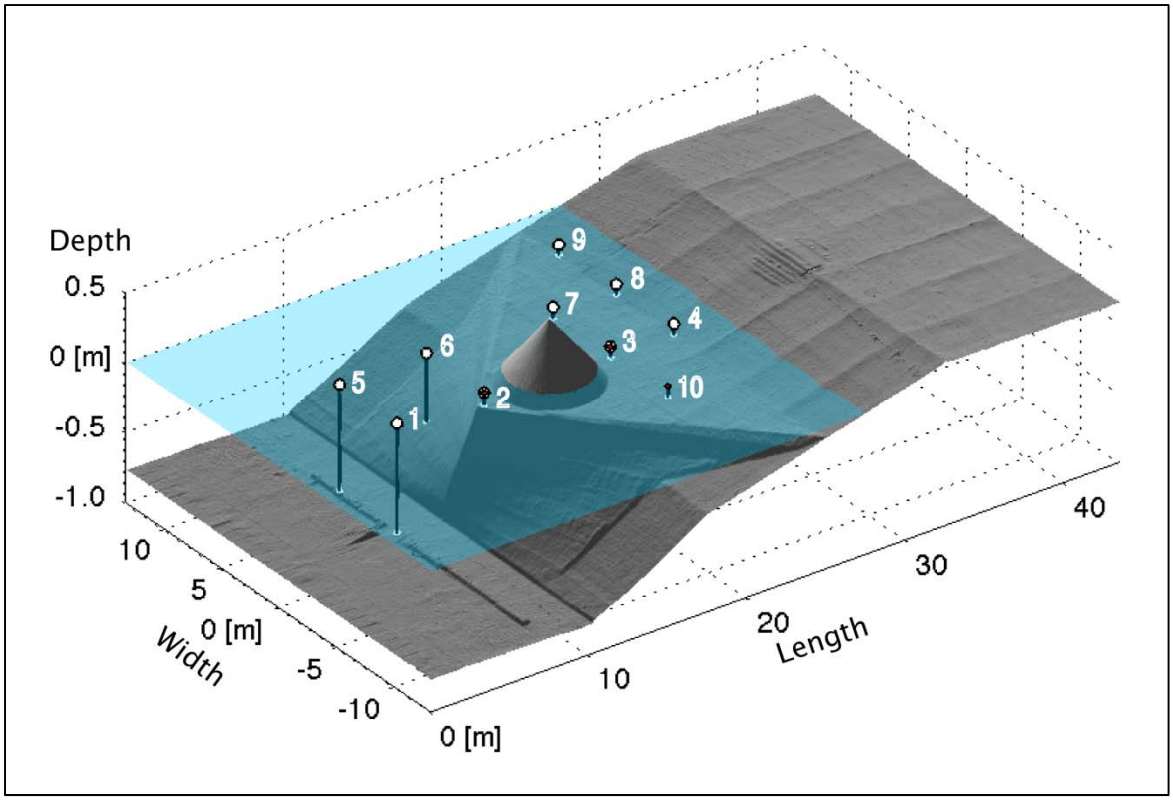

Figure 11-35: Perspective view of ISEC BM2 bathymetry from laser scan at original resolution of. Δx = 5 cm. Conical island was added after laser scan. Circles denote wave gauge locations at free surface and corresponding location on tank bottom. Red crosses at gauges 2, 3, and 10 indicate positions of acoustic Doppler velocimeters for velocity measurements.

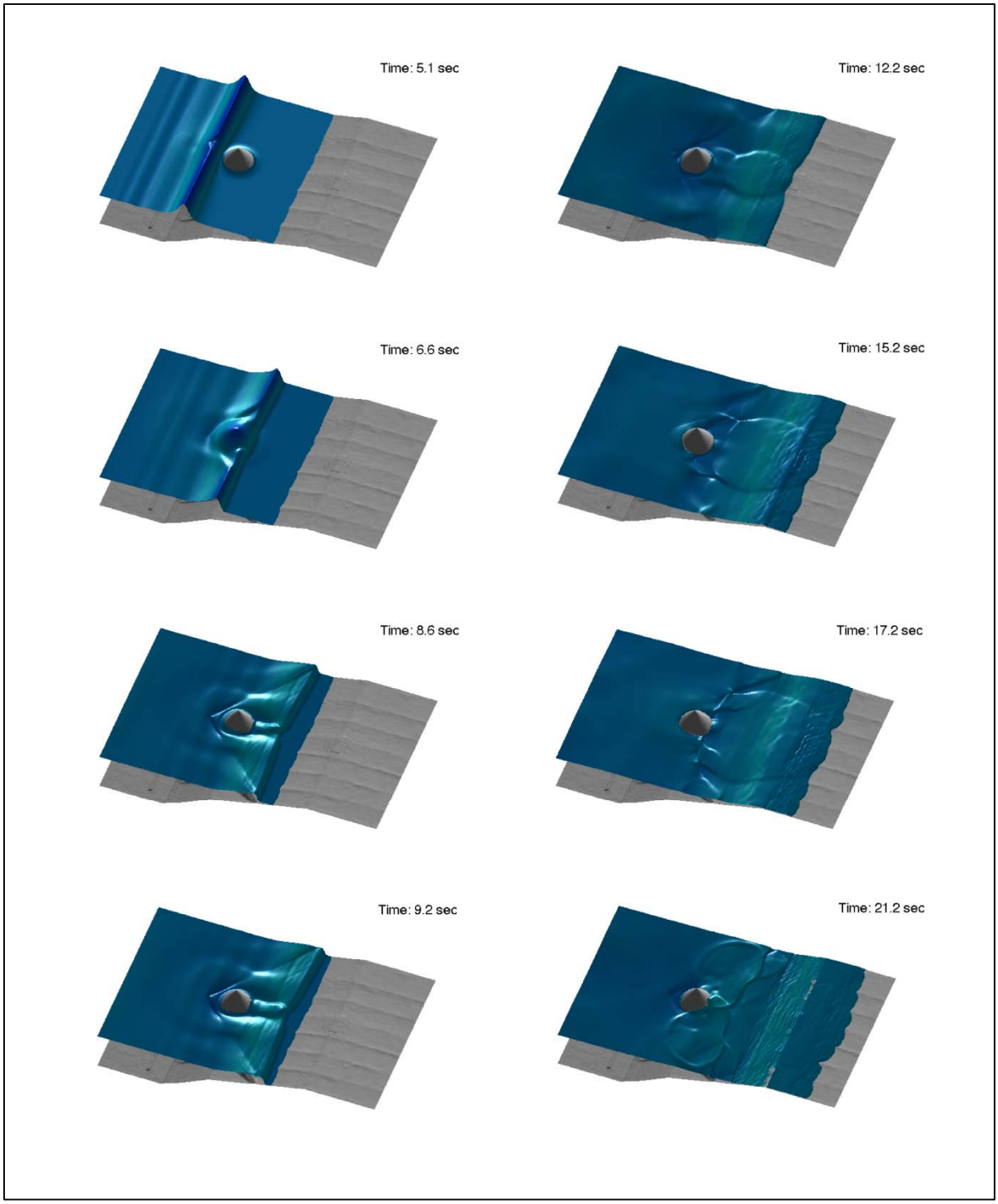

Figure 11-36: Snapshots of solitary wave transformation in ISEC BM2.

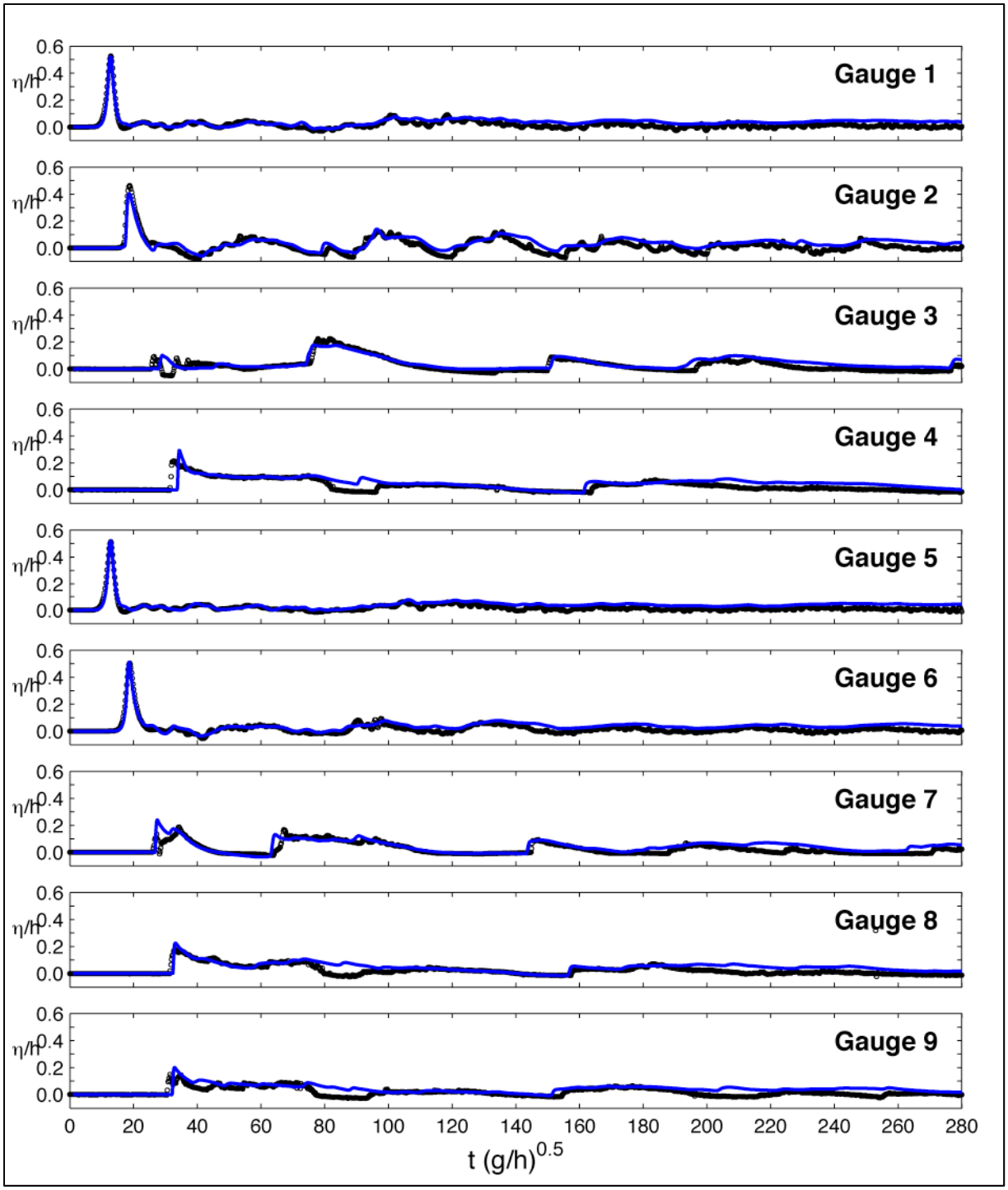

Figure 11-37: Time series of free surface profiles at wave gauges in ISEC BM2. Solid lines and circles denote computed and measured data.

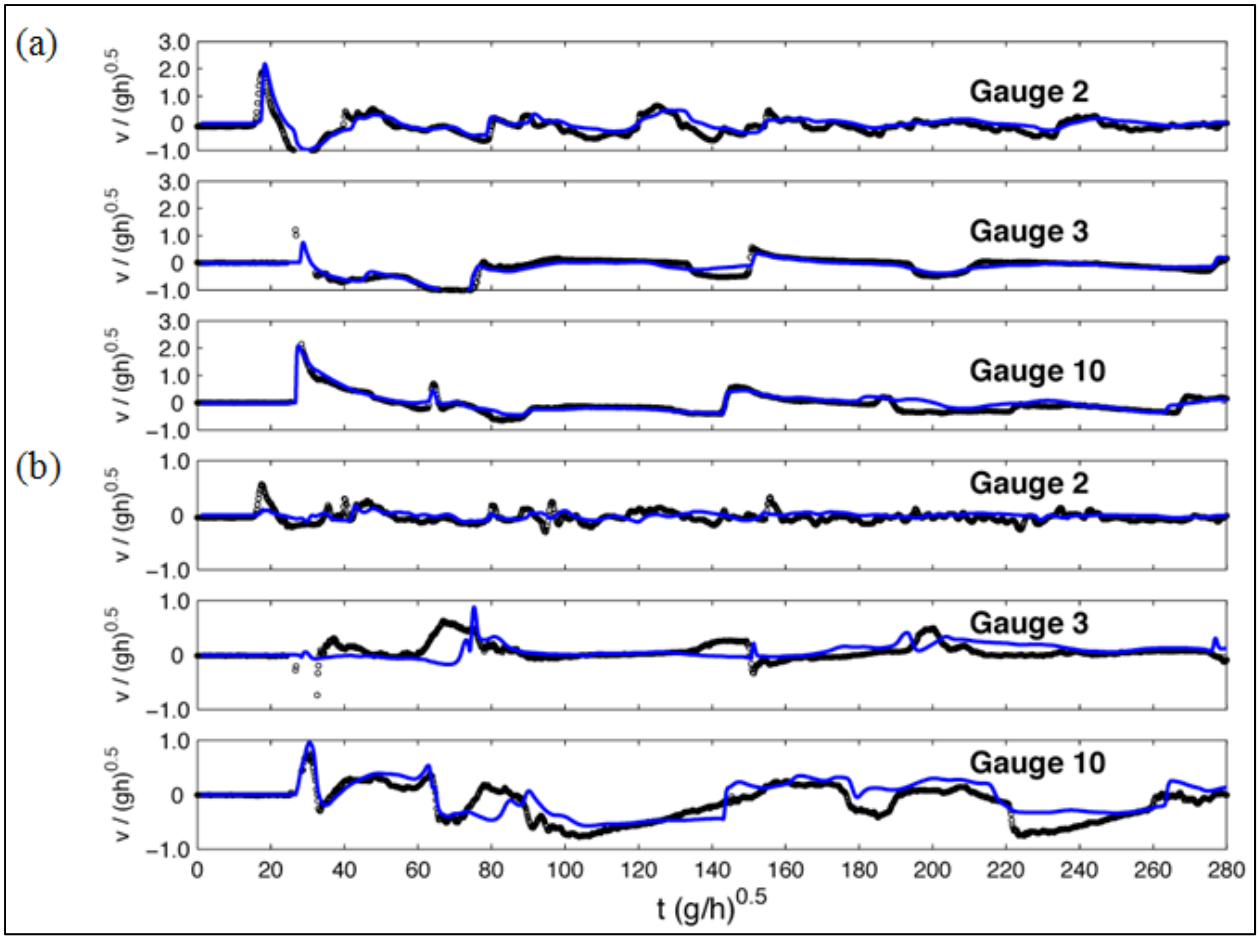

Figure 11-38: Time series of velocity in ISEC BM2. (a) Cross-shore component. (b) Alongshore component. Solid lines and circles denote computed and measured data.